AES 2014

3rd Advanced Electromagnetics Symposium

7 - 10 DECEMBER 2014, HANGZHOU

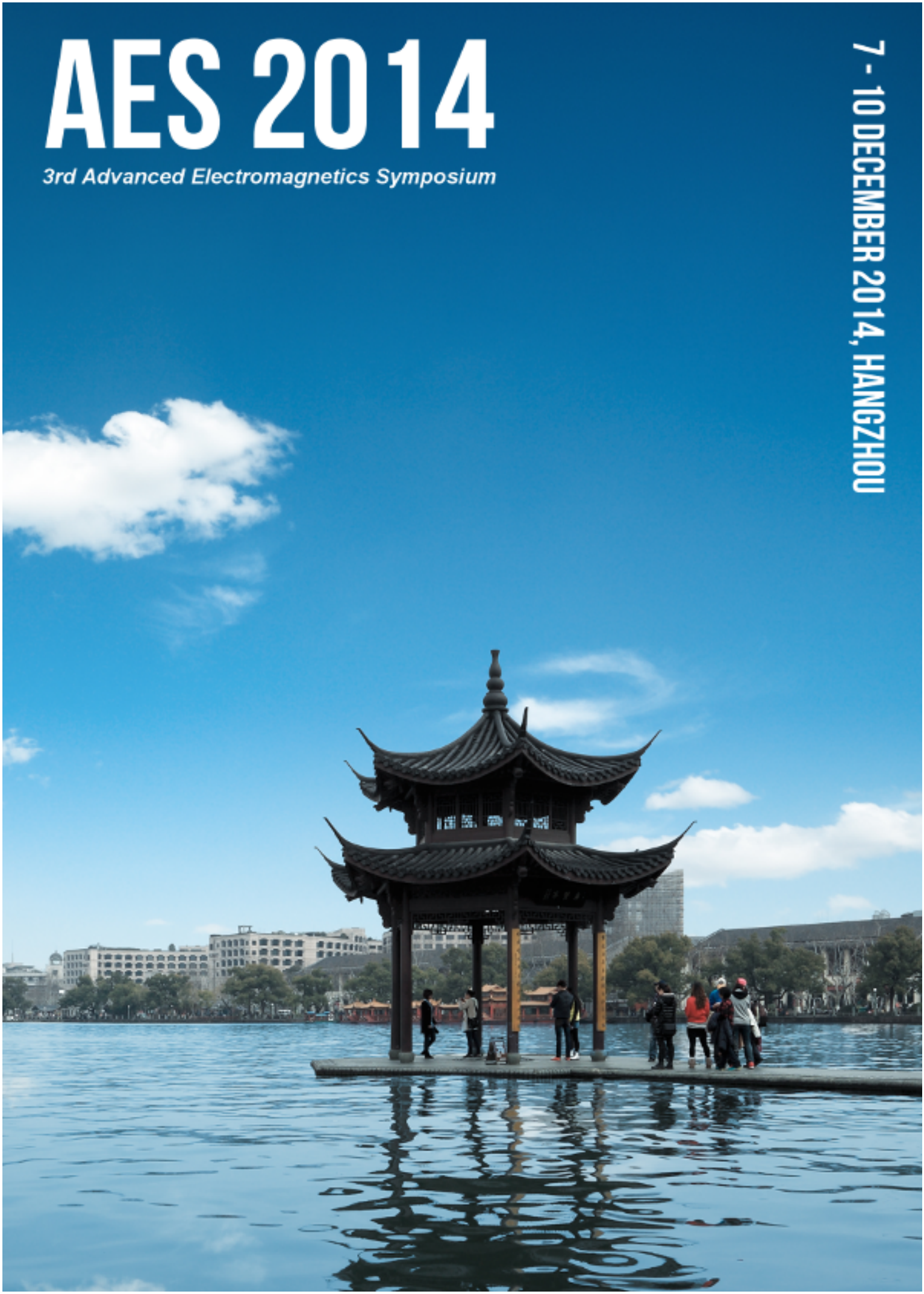

AES 2014 Hangzhou - China

The 3rd Advanced Electromagnetics Symposium

Proceedings

ISBN 978-2-9545460-5-6

www.mysymposia.org

AES 2014 Hangzhou - China

The 3rd Advanced Electromagnetics Symposium

Edited by

Said Zouhdi | Paris-Sud University, France
Lingling Sun | Hangzhou Dianzi University, China
Ke Wu | Ecole Polytechnique de Montreal, Canada

Contents

AES 2014 ORGANIZATION

AES General Chair

Said Zouhdi, Paris-Sud University, France

AES 2014 General Co-Chairs

Lingling Sun, Hangzhou Dianzi University, China
Ke Wu, Ecole Polytechnique de Montreal, Canada

Organizing Committee

Zhiqun Cheng (Chair), China
Wen-Yan Yin (Co-Chair), China
Youlin Geng (General Secretary), China
Tao Zhou, China
Laurent Santandrea, France
Romain Corcolle, France
Laurent Daniel, France

International Advisory Committee

Yahia Antar, Canada
Partha P. Banerjee, India
Madhukar Chandra, Germany
Jean Chazelas, France
Wen-Shan Chen, Taiwan
Christos Christopoulos, UK
Peter de Maagt, Netherlands
Apostolos Georgiadis, Spain
Dave V. Giri, United States
Xun Gong, United States
Lixin Guo, China
Yang Hao, United Kingdom
Nathan Ida, USA
Koichi Ito, Japan
Andrzej Karwowski, Poland
Le-Wei Li, China
Kwai Man Luk, Hong Kong
Claude Marchand, France
Adel Razek, France
Alain Sibille, France
Ari Sihvola, Finland
Paul Smith, Australia
C-K Clive Tzuang, China
J(Yiannis) C. Vardaxoglou, UK
Junhong Wang, China
Jian Wu, China
Yong-Jun Xie, China
Yu Zhang, China

Technical Program Committee

Boran Guan (Chair), China
A. Alu, USA
J.-C. Badot, France
S. E. Barbin, Brazil
M. S. Bawa'aneh, Jordan
X. Begaud, France
C. Craeye, Belgium
T. J. Cui, China
L. Daniel, France
S. Gonzalez Garcia, China
T.-S. Jason Horng, Taiwan
J. Hu, China
Z. Hu, UK
R.-B. Hwang, Taiwan
T. Isernia, UNIRC, Italy
A. Khenchaf, France
A. Kishk, Canada
K. Kitayama, Japan
M. Krawczyk, Poland
H. Kurt, Turkey
M Kuzuoglu, Turkey
J.-C. Levy, France
J.-M. Lopez, France
A. Massa, Italy
O. Ozgun, Turkey
L. Panina, UK
L. Pichon, France
C.-W. Qiu, Singapore
A. Raizer, Brazil
B. Ravelo, France
A. Shamim, Saudi Arabia
J.T. Sri Sumantyo, Japan
G. Stojanovic, Serbia
M. Tentzeris, USA
C-K Clive Tzuang, China
N. Vallestero, USA
V. Y. Vu, Viet Nam
A. I. Zaghloul, USA
Q.-J. Zhang, Canada
A. Zhukov, Spain

Special Session Organizers

Jin Chen, China
Laurent Daniel, France
Li Dongying, China
Youlin Geng, China
Ran Hao, China
Zhao Huapeng, Singapore
Yang Lixia, China
Xing Chang Wei, China
Sanshui Xiao, Denmark
Wen-Yan Yin, China
Jingjing Zhang, Denmark

TABLE OF CONTENTS

Keynote Lectures

Scattering and Electromagnetic Theory

Antennas and Microwave technologies

Optics and Photonics

Metamaterials, Plasmonics, Photonic Crystals and Complex Media

Remote Sensing, Inverse Problems, Imaging, Radar and Sensing

Bioeffects of EM fields, Biological media, Medical electromagnetics

Educational Electromagnetics

Nanoplasmonics

Material Modelling

Graphene electronics and photonics

Antenna Arrays: CEM Modeling and Array Signal Processing

Teaching and Training Electromagnetics around the world : what 's new?

Computational Electromagnetic Methods and Their Applications

Electromagnetic and Light Scattering

General Papers

Keynote Lectures

Smart Antennas for Space-borne Synthetic Aperture Radars

F. Qin[1], S. Gao[1], C. Mao[1], Z. Wang[1] ,
A. Patyuchenko[2], M. Younis[2], G. Krieger[2]

[1]School of Engineering and Digital Arts, University of Kent, Canterbury, UK
[2]Microwaves and Radar Institute, German Aerospace Centre (DLR), Wessling, Germany
f.qin@kent.ac.uk; S.gao@kent.ac.uk

Abstract

This paper discusses smart antennas for space-borne synthetic aperture radar (SAR). First, some recent development in smart antennas for space-borne SAR is reviewed. Then, the paper presents a low-cost space-borne SAR system using digital beamforming on receive. The smart antenna system is also discussed and some results are shown. The antenna system, consisting of a parabolic reflector and multi-feed array, is designed and optimized for dual-band dual-polarized digital beam-forming performance. The operating frequencies are at X and Ka bands with the center frequency of 9.6 GHz and 35.75 GHz, respectively. The stacked dipoles and square patches with parasitic elements are employed as the feed elements at X- and Ka-bands. Dual-band antenna arrays are combined in the same aperture, which not only reduce the aperture of the feed array, but also coincide the center of dual-band feed arrays.

Key words- digital beam-forming, smart antenna, SAR, dual-band, dual-polarization

1. Introduction

The importance of radar observations for civilian remote sensing and Earth observation has increased considerably in the last decade, which motives great development of synthetic aperture radar (SAR). AS a key component in SAR system, the antenna system is required to operate multiband and multi-polarized performance. For example, the Seasat in 1978, the Space-borne Imaging Radar-A (SIR-A) in 1981 and SIR-B in 1984 were all L-band systems with horizontal polarization transmit and receive. The SIR-C/X-SAR system, developed by the United States and German, was the first multiband space-borne imaging system operating at L-, C- and X-band. The SIR-C antenna had a capability of four simultaneous transmit/receive polarizations (HH, HV, VV, VH) [1].

The success of current space-borne SAR is boosting the further study and higher performance of next generation system. The concept of digital beam forming (DBF) used in SAR system is being considered as a promising candidate for future earth observation missions. This is evident both from research activities and space qualified technology demonstrations[2, 3]. There are two basic antenna systems can be applied in DBF SAR system. One is planar system and the other is reflector system. Typically, the planar system is composed of several sub-apertures connected with digital channels. The reflector system consists of a parabolic reflector and a digital feed array. The echoes from the targets are received by each digital sub-aperture, amplified, down-converted and digitized. These two antenna systems were compared in [4], which revealed that the reflector system can be realized with a simpler hardware and shows a performance advantage of several dBs in terms of ambiguity and signal-to-noise ratio.

This paper addresses the issue of designing smart feed arrays for a multi-feed reflector antenna system employed in a highly competitive and innovative SAR concept 'DIFFERENT' [5]. The DIFFERENT stands for 'Digital beam forming for low-cost multi-static space-borne synthetic aperture radars'. This proposed feed arrays are designed at X- and Ka-band with dual polarizations. One requirement of this system is that both of feed arrays should be at focus of the reflector system. Thus a shared-aperture antenna structure is considered to meet the requirement. Several works have been done to research dual-band antennas with common aperture in the past several decades [6-9]. Here, the microstrip dipoles are used as X-band radiating elements. Two parasitic dipoles are applied to enhance the bandwidth of this elements. Slot fed patches with a parasitic patch and cross dipole are designed as the Ka-band element. After the designs of feed elements, a Ka-band sub-array is modeled and simulated.

This paper is organized as follows: In section II, review of recent development in smart antenna for SAR will be given. The space-borne SAR system will be presented in section III. Then the reflector antenna system for DIFFERENT will be described in section IV. The designs of feed elements at X- and Ka- band will be given in section V. The performance of sub-array at Ka band and conclusion will be given in section VI and VII, respectively.

2. Review of Recent Development in Smart Antennas for SAR

2.1 ASAR

The first European SAR based on an active phase array was launched in 2002 [10]. The Advanced Synthetic Aperture Radar (ASAR) operates at C-band with the frequency of 5.331 GHz. This antenna system consists of 320 active elements distributed over an area of 1.3m×10m, with the performance of dual polarization in VV/HV or VH/VV.

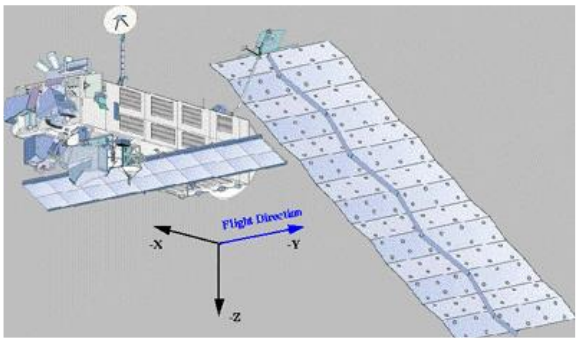

Fig.1. ASAR in flight configuration [10]

The active transmit/receive modules (T/R Modules) can provide low noise amplification and transmit power generation. In addition, the GaAs technology was employed in the design of active microwave components. The key components, SSPA, can deliver up to 10 Watts of peak power while the LNA has a noise figure of only 1.3 dB. In ASAR system, a 100 km swath width can be achieved in scanSAR mode compared to around 80 km in imaging mode.

2.2 COSMO-SkyMed

COSMO-SkyMed [11] (Constellation of small satellite for Mediterranean basin Observation) is the largest Italian investment in space systems for Earth Observation, funded by Italian Space Agency (ASI) ,Italian Ministry of Defense (MoD) and industry contribution (Alenia Spazio) with high-resolution capability. The system consists of a constellation of four Low Earth Orbit (LEO) mid-sized satellites, each is equipped with a multi-mode high resolution SAR operating at X-band and fitted with particularly flexible and innovative data acquisition and transmission equipment.

The SAR system carried by each LEO satellite has a total antenna area of 1.4 m×5.6 m. This large antenna is folded during launched and deployed in orbit. This antenna also can achieve dual polarization mode. In order to stabilize the beam in high-resolution modes at large scan angles, the antenna is equipped with true time delay elements.

2.3 TerraSAR-X

TerraSAR-X [12] is Germany's first national remote sensing satellite being implemented in a public–private partnership (PPP) between DLR and EADS Astrium GmbH. This system is based on advanced active phased array technology, which allows operation in Stripmap-, Spotlight- and ScanSAR-mode. Hence, it combines the ability to acquire high-resolution images for detailed analysis as well as wide swath images for overview applications. It also allows full polarimetric imaging. Imaging bandwidth is up to 300 MHz for high-resolution operation whereas 150 MHz are used for normal operation.

The TerraSAR-X system has an Antenna with 384 linear arrays organized in 12 columns of 32 radiators, as described in [13]. Each column of TR modules corresponds to a tile, inside which two power supplies, two digital controllers, harness, and RF distribution are mounted. The dual-polarized linear arrays in waveguide technology realize

Fig.2. COSMO-SkyMed in flight configuration [11]

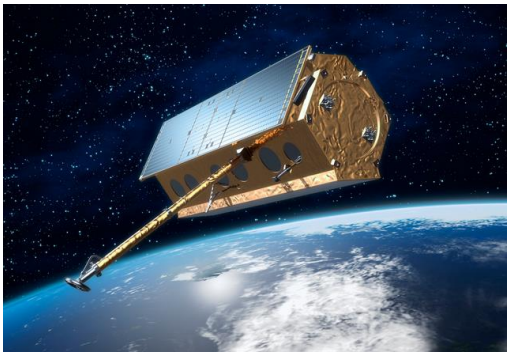

Fig.3. TerraSAR-X in flight configuration [12,13]

the mechanical supporting frame for the tile electronics. The tiles are directly mounted to a side wall of the satellite.

2.4 NovaSAR-S

NovaSAR-S [14-16] is a small Synthetic Aperture Radar (SAR) mission operating at S band and designed for low-cost programmes and optimised for shared launch opportunites. The system baselines SSTL-300 avionics flying on NigeriaSat-2, with an imaging payload developed by the space borne SAR team at Astrium UK, and S-band solid state power amplifer technology.

The antenna array in NovaSAR-S system is a microstrip-patch active phased array consisting of 18 sub arrays. The total size of the antenna array is 3 m×1 m. Multi-polarizations including VV, HH, VH and HV can achieve using this antenna system. To obtain electronic beam steering, the antenna is integrated with microwave phase shifters which are controlled by DC voltages. GaN technology is employed in NovaSAR-S is to reduce the size, mass and cost of SAR antenna system due to the high power density capability of GaN devices in comparison to conventional GaAs technologies.

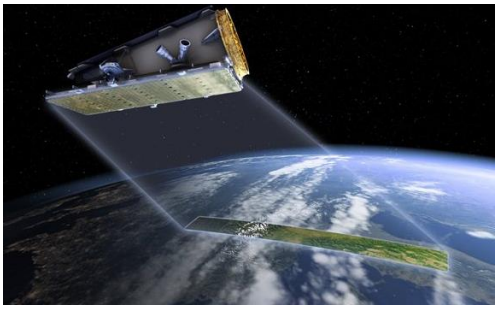

Fig.4. Nova SAR-S in flight configuration [14-16]

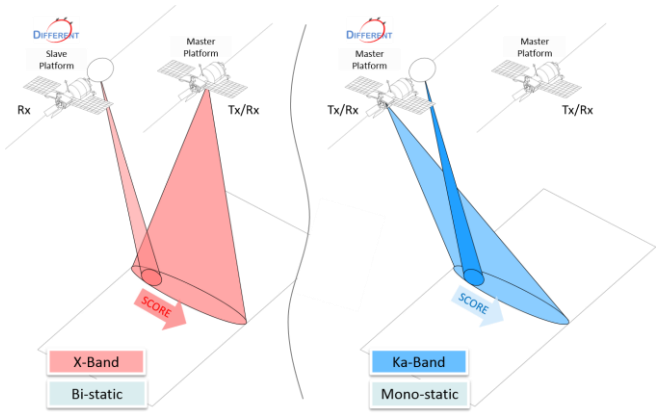

Fig.5. Mission concept of DIFFERENT: bi-static X-band sub-system (left) and mono-static Ka-band sub-system (right).

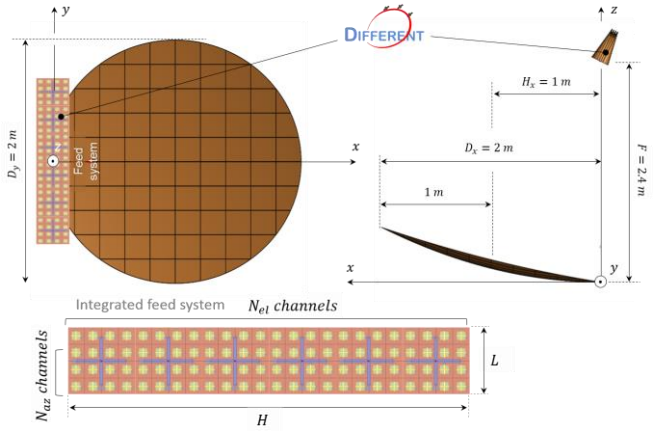

Fig.6. Geometry of the reflector based dual-band DIFFERENT

3. Space-Borne SAR System using Digital Beamforming on Receive

DIFFERENT is a highly integrated modular system enabling the realization of various configurations of spaceborne SAR missions. One of the potential mission concepts is schematically illustrated in Fig. 5. In the proposed dual-band mission, DIFFERENT is operated as a receiver in a formation flying bi-static configuration with an X-band master satellite and in a mono-static configuration with a dedicated on-board Ka-band transmitter.

The proposed mission is based on a dual-polarimetric mode and utilizes SCORE in elevation [17] and multiple phase centers technique in azimuth [18]. The dual-polarimetric mode is realized by transmitting either vertically or horizontally polarized pulses and coherently receiving echoes by using independent channels dedicated to both polarizations.

The bi-static X-band mission concept shown in Fig. 5 (left) uses similar configuration employed in SAR systems based on a constellation of two or more satellites such as TanDEM-X [19]. DIFFERENT receiver system paired with an existing or future X-Band SAR system (e.g. TanDEM-X [19], HRWS [17], or a custom satellite) provides a wide range of applications including glaciology, oceanography, imaging of urban areas, and moving target indication.

The mono-static Ka-band sub-system of DIFFERENT mission shown in Fig. 5 (right) utilizes a small low weight and cost effective on-board transmitter ensuring a high level of compactness of the imaging platform. Potential applications of the Ka-band sub-system include ocean surface topography, oil spills monitoring as well as ocean temperature and current monitoring.

4. Reflector Antenna System for DIFFERENT

This section presents the designs of a multi-feed reflector antenna system for the DIFFERENT. This system consists of a parabolic reflector and a feed array, which is a key module of realizing the concept of DIFFERENT, as shown in Fig.6. The parabolic reflector is designed by our partner, German Aerospace Centre (DLR). This parabolic reflector is defined in a Cartesian coordinate system where x-axis coincides with an along track (azimuth) and y-axis with a cross-track (elevation) direction of the imaging platform. The reflector antenna is given by its focal length, F=2.4 m, azimuth diameter D_x=2 m, elevation diameter D_y=2 m and offset clearance H_x=1 m. The offset configuration is used to avoid the blockage effect degrading the antenna performance which would be present if the feed system was placed in the zone of the main beam.

The feed system is constructed by its dimensions L (azimuth) and H (elevation) and by the number of digital channels N_{az} and N_{el} in azimuth and elevation correspondingly. More importantly, the feed system is working at two bands, X and Ka bands, with the operation of dual-polarization. Due to the requirement of same focus at both bands in the reflector system, combining the dual polarized antenna arrays in the same aperture is considered in our design.

5. Feed Elements Design

5.1. Feed elements at X band

This section presents the feed elements at X band. Microstrip dipoles are employed as the radiation elements. One of the advantages of choosing dipoles is that it takes up less space than patches and exhibits some advantages in combining dual-band arrays. The structure of X-band elements is shown in Fig.7. Two stacked dipoles with different polarizations are located orthogonally, forming a cross shape in the top view. The function of these parasitic dipoles are to broaden the antenna's bandwidth. The width of the dipoles in two polarizations is same as the feeding microstrip line. The simulated S parameters of this elements are shown in Fig.8 (a). The bandwidth of more than 400 MHz in both orthogonal polarizations is obtained, which is from 9.43 GHz to 9.89 GHz and 9.25 GHz to 9.9 GHz, respectively. The isolation between two feeding points is higher than 30 dB at 9.6 GHz. The radiation patterns in Phi=0° and Phi=90° plane at 9.6 GHz are shown in Fig.8 (b). It shows that the realized gain of this element achieves 7.87 dBi and the cross polarization discrimination (XPD) is better than 30 dB.

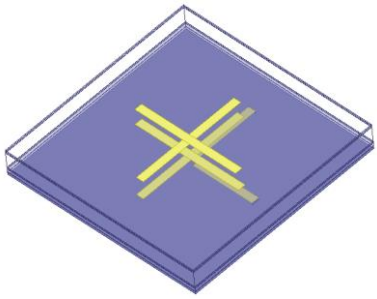

Fig.7. Structure of X-band element

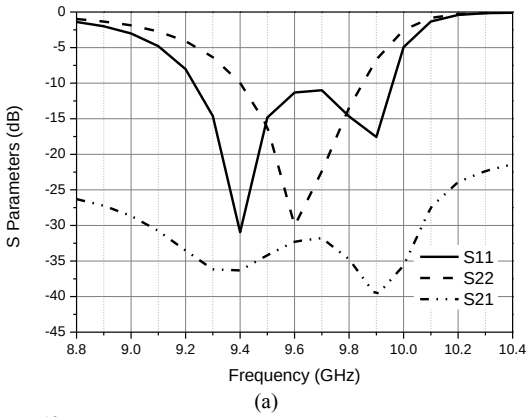

(a)

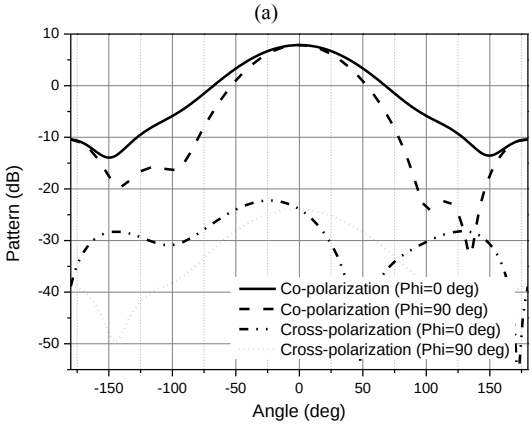

(b)

Fig.8. Simulation results: (a) S parameters; (b) Radiation patterns

5.2. Feed elements at Ka band

The Ka-band radiation element is composed of a slot-fed patch, a parasitic patch and perpendicular dipoles in different layers. The geometry of this element is shown in Fig.9. The simulated S parameters, shown in Fig.10 (a), reveals that the bandwidth of this antenna is wider than 1 GHz in both polarizations. An isolation of 32 dB between two feeding points is obtained at 35.75 GHz. Fig.10 (b) shows the radiation patterns in two polarizations. The realized gain is 8.1 dBi and the XPD is better than 30 dB at 35.75 GHz, respectively.

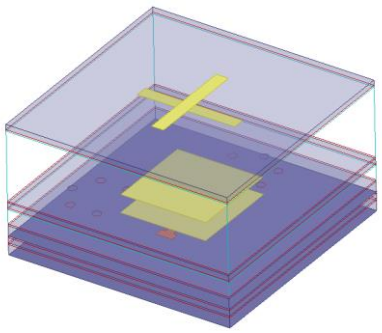

Fig.9. Structure of Ka-band element

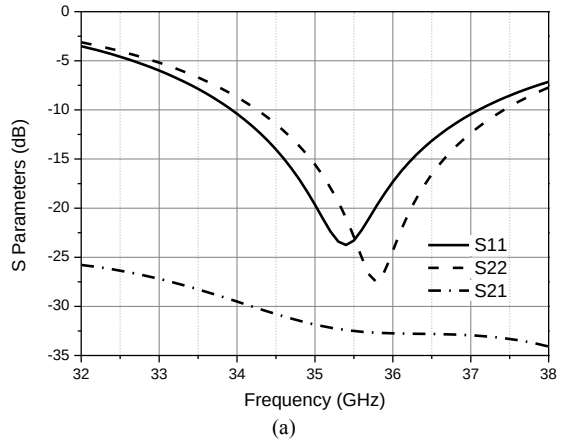

(a)

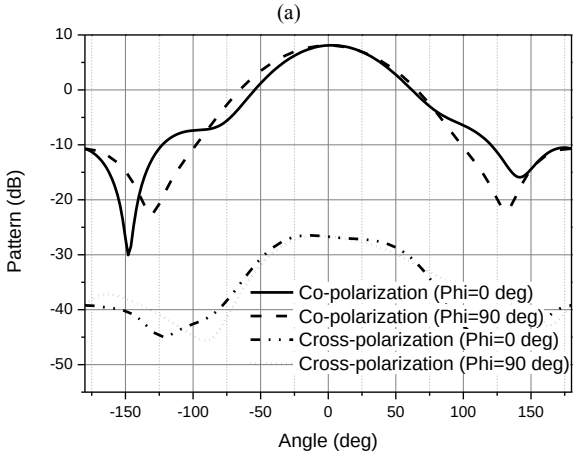

(b)

Fig.10. Simulation results: (a) S parameters; (b) Radiation patterns

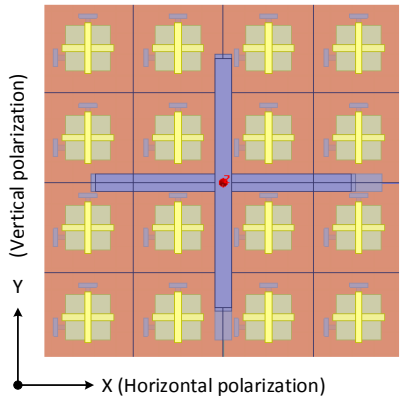

Fig.11. Geometry of Ka-band sub-array with X-band dipole

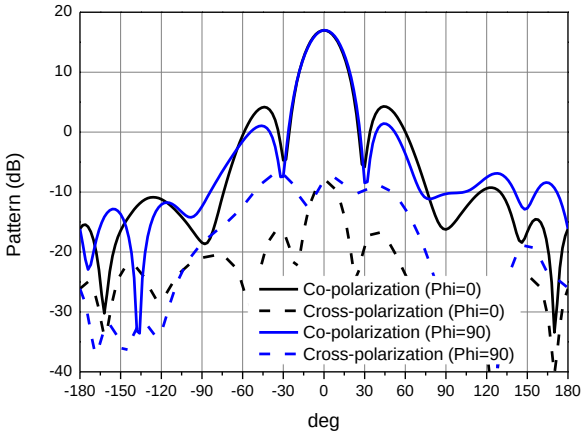

Fig.12. Radiation patterns for Ka-band sub-array

6. Sub-array at Ka Band

Due to the reflector system, the dual band antenna arrays must be combined in the same board, namely sharing the common aperture. Thus, a 4×4 Ka band array with an X-band parasitic dipole in the center is built and simulated to demonstrate the performance of feed array. Fig.11 presents the geometry of the Ka band antenna array. Fig.12 shows the radiation patterns of the sub-array in one polarization. The 3-dB beamwidth is around 24° with the realized gain of 17 dBi. The sidelobe level is around -12.9 dB in the plane of phi=0° and -15.5 dB in the plane of phi=90°, respectively. Since the symmetry structure of sub-array, the radiation patterns has the similar performance in the other polarization.

7. Conclusions

The paper provides a brief overview of recent development in smart antennas for space-borne SAR systems. Then digital beam-forming SAR system on receive is described. After that, the antenna system used in advanced concept of 'DIFFERENT' SAR system is introduced. The reflector antenna, consisting of a parabolic reflector and a multi-feed antenna array, is employed in this system. The antenna elements for DBF feed array is designed with the operation of dual-band and dual-polarizations. Some results of the DBF Ka/X band SAR system are presented and discussed. Hardware implementation of the DBF SAR system is ongoing at the moment and will be reported in future conferences.

Acknowledgements

This work is part of the project 'DIFFERENT' funded by EC FP7 (grant number: 6069923).

References

[1] W. A. Imbriale, S. Gao, and L. Boccia, *Space antenna handbook*: Wiley Online Library, 2012.

[2] S. Huber, M. Younis, A. Patyuchenko, and G. Krieger, "Digital beam forming techniques for spaceborne reflector SAR systems," in *Synthetic Aperture Radar (EUSAR), 2010 8th European Conference on*, 2010, pp. 1-4.

[3] D. Perkovic-Martin, J. P. Hoffman, and L. Veilleux, "Instrument concept for the proposed DESDynI SAR instrument," 2012.

[4] M. Younis, S. Huber, A. Patyuchenko, F. Bordoni, and G. Krieger, "Digital beam-forming for spaceborne reflector-and planar-antenna SAR—A system performance comparison," in *Geoscience and Remote Sensing Symposium, 2009 IEEE International, IGARSS 2009*, 2009, pp. III-733-III-736.

[5] M. Y. Anton Patyuchenko, Zhengpeng Wang, Steven Gao, Fan Qin, Srdjan Glisic, Wojciech Debski, Luigi Boccia, G. Amendola, E. Arnieri, Milos Krstic, Elisabeth Celton, Piotr Penkala, "Spaceborne X/Ka-Band Digital Beamforming Synthetic Aperture Radar for Earth Observation," presented at the Proceedings of the KEO Workshop (Ka-band Earth Observation Radar Missions), November 2014.

[6] L. L. Shafai, W. A. Chamma, M. Barakat, P. C. Strickland, and G. Seguin, "Dual-band dual-polarized perforated microstrip antennas for SAR applications," *Antennas and Propagation, IEEE Transactions on,* vol. 48, pp. 58-66, 2000.

[7] X. Qu, S. Zhong, Y. Zhang, and W. Wang, "Design of an S/X dual-band dual-polarised microstrip antenna array for SAR applications," *Microwaves, Antennas & Propagation, IET,* vol. 1, pp. 513-517, 2007.

[8] S.-C. Gao, L.-W. Li, M.-S. Leong, and T.-S. Yeo, "Dual-polarized slot-coupled planar antenna with wide bandwidth," *Antennas and Propagation, IEEE Transactions on,* vol. 51, pp. 441-448, 2003.

[9] S. Gao and A. Sambell, "Dual-polarized broad-band microstrip antennas fed by proximity coupling," *Antennas and Propagation, IEEE Transactions on,* vol. 53, pp. 526-530, 2005.

[10] M. Ludwig, C. Buck, F. Coromina, and M. Suess, "Status and trends for space-borne phased array radar," in *Microwave Symposium Digest, 2005 IEEE MTT-S International*, 2005, p. 4 pp.

[11] P. Capece, "Active SAR antennas: design, development, and current programs," *International Journal of Antennas and Propagation,* vol. 2009, 2009.

[12] B. Grafmuller, A. Herschlein, and C. Fischer, "The TerraSAR-X antenna system," in *Radar Conference, 2005 IEEE International*, 2005, pp. 222-225.

[13] S. Buckreuss, R. Werninghaus, and W. Pitz, "The German satellite mission terraSAR-X," *Aerospace and Electronic Systems Magazine, IEEE,* vol. 24, pp. 4-9, 2009.

[14] P. Iervolino, R. Guida, and P. Whittaker, "NovaSAR-S and Maritime Surveillance," in *IGARSS Proceedings*, 2013.

[15] S. Gao and J. T. S. Sumantyo, "SAR Antenna Development in the UK."

[16] R. Di Bari, T. Brown, S. Gao, M. Notter, D. Hall, and C. Underwood, "Dual-polarized printed S-band radar array antenna for spacecraft applications," *Antennas and Wireless Propagation Letters, IEEE,* vol. 10, pp. 987-990, 2011.

[17] M. Süß, B. Grafmüller, and R. Zahn, "A novel high resolution, wide swath SAR system," in *Geoscience and Remote Sensing Symposium, 2001. IGARSS'01. IEEE 2001 International*, 2001, pp. 1013-1015.

[18] M. Younis, C. Fischer, and W. Wiesbeck, "Digital beamforming in SAR systems," *Geoscience and Remote Sensing, IEEE Transactions on,* vol. 41, pp. 1735-1739, 2003.

[19] G. Krieger, I. Hajnsek, K. P. Papathanassiou, M. Younis, and A. Moreira, "Interferometric synthetic aperture radar (SAR) missions employing formation flying," *Proceedings of the IEEE,* vol. 98, pp. 816-843, 2010.

RADIATION CONTROL OF ELECTRICALLY SMALL ANTENNA USING SUPERDIRECTIVITY

A. Sharaiha[1], A. Clemente[2;3], A. Haskou[1], M. Smierzchalski[1]
Ch. Delaveaud[2;3], S. Collardey[1], L. Rudant[2;3], and K. Mahdjoubi[1]

[1]IETR UMR CNRS 6164- Université de Rennes 1, Rennes, France
[2]Univ. Grenoble-Alpes, Grenoble, France
[3]CEA, LETI, Minatec Campus, 17 rue des Martyrs, 38054 Grenoble, France

ABSTRACT:

By focusing the radiation in useful directions, directional antennas offer new opportunities for wireless applications in terms of spectral efficiency, reduced environmental impact and use modes. However the conventional techniques for enhancing the directivity often lead to a significant increase in the size of the antenna. Consequently, the integration of directional antennas in small wireless device is limited. This difficulty is particularly critical for the frequency bands below one gigahertz if objects dimensions are limited to a few centimeters. However, the Internet of Things requires radiation control to reduce the electromagnetic pollution, which limits the acceptability of wireless communications, as well as to allow coexistence of ubiquitous systems. The radiation control is an important issue for future smart radio, with a limited impact on environment of the users.
The recent state-of-the art in the field of miniature antennas shows new perspectives for the development of compact antennas presenting directivities higher than accepted normal limits (super-directivity properties). The increase of low directivity of electrically small-sized antennas is a modern motivation for super-directivity. Moreover, recent research activities in the field of active antennas offer new opportunities for practical super-directivity implementation. Already, the state-of-the art shows concrete experiments of these issues.

This presentation gives some results and examples on improving the directivity of electrically small antennas. This work is in the framework of a national project "SOCRATE" with the funding of the French National Research Agency and the support of the « Images et Réseaux », “Minalogic” and “SCS” clusters, France including research teams from CEA-Leti and IETR and industrial partners Movea and Tagsys whose applications require directional small antennas.

Common-mode Filter for EMC Design in 10+Gbps High-speed Circuits: A story from academic research to industrial application

Tzong-Lin Wu

National Taiwan University, Taiwan
*corresponding author, E-mail: tlwu@ntu.edu.tw

Abstract

Based on metamaterial concept, a novel common-mode filter (CMF) which can behave as bandstop filter the common-monde noise on high-speed differential circuits and give all-pass characteristics for the differential signals will be demonstrated. Through the miniaturization and bandwidth-enhanced techniques, the CMF is becoming available for industrial application to solve the EMC or RFI problems for high-speed differential interfaces such as USB, PCIe, and so on.

Multiscale Computational Electromagnetics for Applications in Subsurface Sensing, Microwaves, and Nanophotonics

Qing Huo Liu

Duke University, USA

Abstract

Electromagnetic sensing and system-level design problems are often multiscale and very challenging to solve. They remain a significant barrier to system-level sensing and design optimization for a foreseeable future. Such multiscale problems often contain three electrical scales, i.e., the fine scale (geometrical feature size much smaller than a wavelength), the coarse scale (geometrical feature size greater than a wavelength), and the intermediate scale between the two extremes. Most existing commercial solvers are based on single methodologies (such as finite element method or finite-difference time-domain method), and are unable to solve large multiscale problems. We will present our recent work in solving realistic multiscale simulation and imaging problems. Applications will be illustrated for subsurface sensing, microwaves, and nanophotonics.

Scattering and Electromagnetic Theory

Analysis of Electromagnetic Wave Propagation in Plasma Sheath when Reentry into Atmosphere

Chen Wei, Guo Lixin, Li Jiangting, Guo Linjing

School of Physics and Optoelectronic Engineering, Xi Dian University, Xi'an, China

Abstract

One-dimensional inhomogeneous plasma sheath properties are analyzed by using the finite-difference time-domain (FDTD) algorithm. By using the differential Gauss pulse as the excitation source, calculate the transmission coefficient of the non- uniform plasma sheath and also discuss the behavior of electromagnetic (EM) wave in the sheath. At last, Analyses the characteristics in time domain and frequency domain, when the EM wave through the plasma sheath the electromagnetic wave through a plasma sheath set is given of the time domain and frequency domain graph. The simulating results can provide a way to solve the blackout problem.

Key words**:** finite difference time domain method; plasma sheath; inhomogeneous plasma

1. Introduction

Near space high-speed process is called reentry to landing process. Reentry process, when aircraft flying high in the atmosphere with the surrounding air friction, the surrounding temperature increase rapidly, which leads to dense air ionization. As temperatures continue to rise, aircraft surface material ablation, the formation of gas and the gas at high temperatures and ionization, the two forms a layer of plasma ionization. This layer of plasma cladding craft forms around a contains a lot of free electrons, plasma cladding of inhomogeneous flow field, the plasma sheath [1,2] . Plasma sheath of the electromagnetic parameter is a function of the flow field parameters and their distribution characteristics closely related to the hypersonic flow field characteristics, at the same time is related to aircraft shape, flight Mach number and altitude. The existence of the plasma sheath sets can make the power attenuation and phase shift of propagation of electromagnetic waves, time delay and dispersion effect, the change of vehicle antenna impedance characteristics, influence the normal work of the antenna, which may lead to a ground station and the target vehicle communication interrupt, namely "blackout" phenomenon [3]. Communication blackout will track of vehicle registration effect etc, serious when even endanger the safety of the pilot's life. Therefore, solve the problem of black barrier is the development direction of aerospace measurement and control [4] is now an international problem. Mechanism of communication blackout for people a lot of research and put forward many methods to eliminate, mainly includes: change the aircraft aerodynamic structure, magnetic open window [5], introduce cross electromagnetic fields, using high frequency communication, Raman scattering communication, etc.

This article uses the finite difference time domain (FDTD) algorithm analyzes the one-dimensional case of the aircraft under the condition of different altitude electron density, and calculated the inhomogeneous plasma sheath of the resulting set of reflection and transmission coefficients, and aircraft dropped in the process of using the L, C, S, X, Ka band measured attenuation coefficient with the time graph and get some conclusions.

2. The FDTD iterative of inhomogeneous plasma

Maxwell equations and related constitutive equation is expressed in the anisotropic dispersive media collision in magnetized plasma

$$\nabla \times \mathbf{E} = -\mu_0 \frac{\partial \mathbf{H}}{\partial t} \tag{1}$$

$$\nabla \times \mathbf{H} = \varepsilon_0 \frac{\partial \mathbf{E}}{\partial t} + \mathbf{J} \tag{2}$$

$$\frac{d\mathbf{J}}{dt} + \nu \mathbf{J} = \varepsilon_0 \omega_p^2(z)\mathbf{E} + \boldsymbol{\omega}_b \times \mathbf{J} \tag{3}$$

During difference discrete the FDTD iterative of the electric field and the magnetic field can be written as

$$H_x^{n+1/2}\left(k+\frac{1}{2}\right) = H_x^{n-1/2}\left(k+\frac{1}{2}\right) + \frac{\Delta t}{\mu_0 \Delta z}\left[E_y^n(k+1) - E_y^n(k)\right] \tag{4}$$

$$H_y^{n+1/2}\left(k+\frac{1}{2}\right) = H_y^{n-1/2}\left(k+\frac{1}{2}\right) - \frac{\Delta t}{\mu_0 \Delta z}\left[E_x^n(k+1) - E_x^n(k)\right] \tag{5}$$

$$E_x^{n+1}(k) = E_x^n(k) - \frac{\Delta t}{\varepsilon_0 \Delta z}\left[H_y^{n+1/2}\left(k+\frac{1}{2}\right) - H_y^{n+1/2}\left(k-\frac{1}{2}\right)\right] - \frac{\Delta t}{\varepsilon_0} J_x^{n+1/2}(k) \tag{6}$$

$$E_y^{n+1}(k) = E_y^n(k) + \frac{\Delta t}{\varepsilon_0 \Delta z}\left[H_x^{n+1/2}\left(k+\frac{1}{2}\right) - H_x^{n+1/2}\left(k-\frac{1}{2}\right)\right] - \frac{\Delta t}{\varepsilon_0} J_y^{n+1/2}(k) \tag{7}$$

3. Numerical examples validate

Using the FDTD method compared with WKB method, calculate parameters are ν =10GHz, $\omega_p = 10GHz$, the angle of incidence is 30°,the thickness of plasma sheath is 10cm. The calculation results as shown in figure 1.

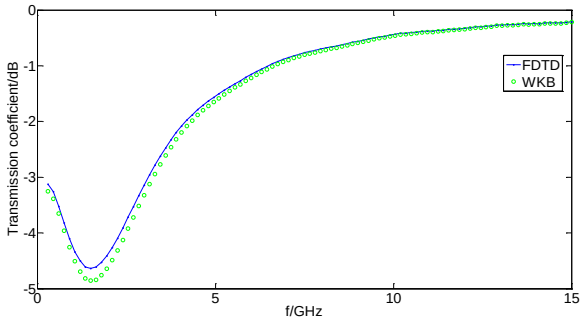

Figure 1: Numerical examples validate.

From Figure 1 the FDTD solutions and the WKB solutions results are mainly unison, verify the algorithm's accuracy.

4. EM wave propagation characteristics of inhomogeneous plasma sheath

The electron density in the process of reentry [6]is shown as figure 2(a). Here we get the density distribution of 76km for example. The plasma sheath is divided into 29 layers and is shown as figure 2(b).Calculated and analyzed the transmission coefficient of inhomogeneous plasma sheath.

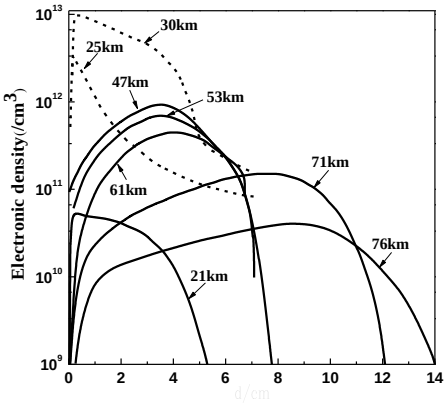

Figure 2 (a):In the process of reentry electron density distribution

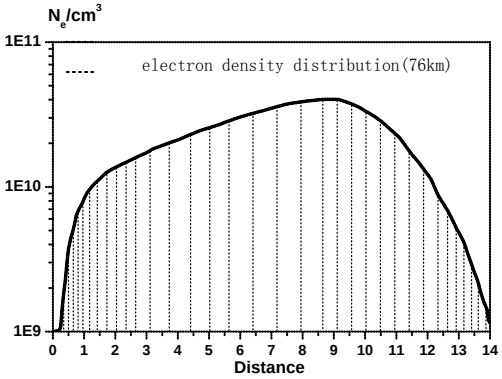

Figure 2 (b): In the process of reentry electron density distribution

4.1. The transmission coefficient of inhomogeneous plasma sheath

The calculate model is shown as figure 3, it is divided into 29 layers between the two edges are Mur absorbing boundary, the EM waves incident from air into the plasma. During the calculation, the space step is $dz = 60\times10^{-6}\,\mathrm{m}$, time step is $dt = \dfrac{dz}{2c} = 1.0\times10^{-14}\,\mathrm{s}$.

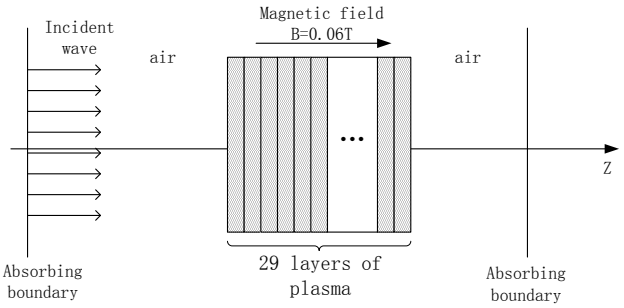

Figure 3: the calculate model of inhomogeneous plasma sheath.

4.2. Magnetized (Non magnetized) plasma sheath

For magnetized （$\omega_b = 10GHz$， B=0.06T） and non magnetized （$\omega_b = 0$） two cases of plasma sheath, we Calculate the transmission coefficient and the transmitted wave time-domain graphics, the flight heights, respectively are 76km,71km,61km,53km,47km,30km,25km,21km. The transmission coefficient are shown as figure 4 and figure 5 and the transmitted wave time-domain graphics are shown as figure 6 and figure 7.

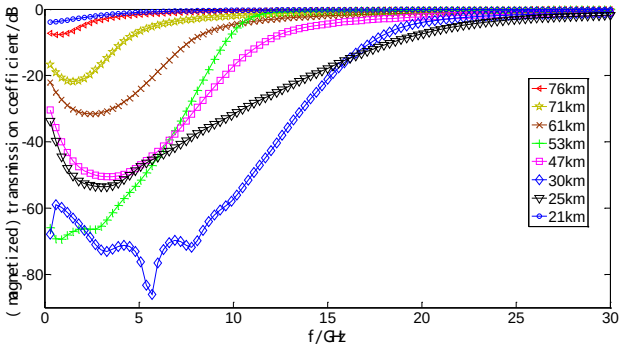

Figure 4: Magnetized transmission coefficient.

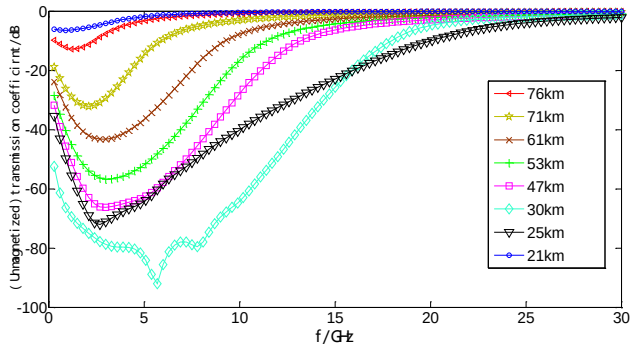

Figure 5: Non magnetized transmission coefficient

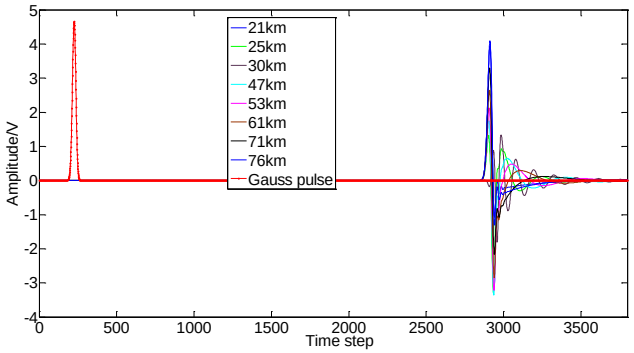

Figure 6: Different height of time domain response.

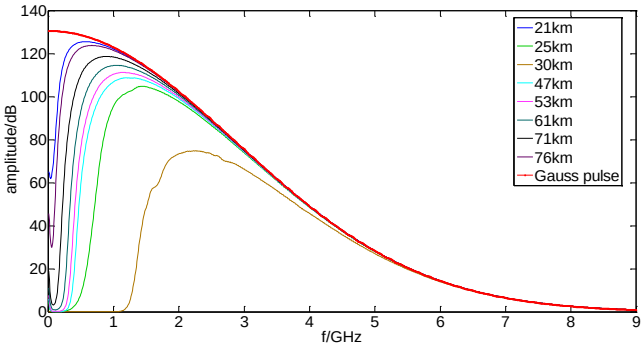

Figure 7: Different heights of frequency response.

In figure 4 and figure 5 we can see in both magnetized and non magnetized cases, the space vehicle decreased from 76km to 30km the transmission coefficient with the height of the lower and lower then rise. The reason for this is that: 1.due to the speed of decline increasing the air ionization more intense, thus increasing the electron density. 2. because of the speed of decline increasing the air temperature become higher and higher it increasing the electron density on the other hand. Otherwise, from the figure in about 3-5 GHz electromagnetic wave frequency has an obvious attenuation, as the height of the drop, the center frequency of transmission coefficient has a tendency to move to higher frequency. Figure 6 and figure 7 are the different height in the process of time domain response and frequency response of the electromagnetic wave transmission. It can be seen from the figure 7 of the transmitted wave frequency bandwidth are better than gauss pulse frequency domain narrow, and there is a decrease in the amplitude is obvious. It is know from figure that 8 high amplitude attenuation of 21km, 76km, 71km, 61km, 53km, 47km, 25km and 30km, and they are obtained with figure 4 and figure 5.

5. The transmission characteristics of different frequencies in plasma sheath

When the space vehicle in the process of into the ground we Intercepting the height is 76 km, 71km, 61km, 53km, 47km, 30km, 25km, 21km eight different high moment of electromagnetic wave attenuation coefficient figure change over time, as is shown in figure 8.

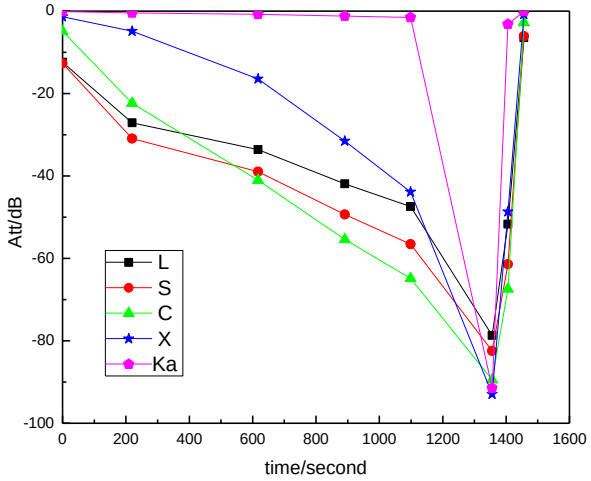

Figure 8: Attenuation coefficients of different frequencies changing with time.

Figure 8 shows the L, S, C, X, Ka, five different frequency attenuation coefficients. The attenuation from weak to strong, in turn, is ka band and X band, C band and S band and L band. That is to say, the higher the frequency the smaller the attenuation, which is in line with the prevailing in most of the literature of conclusions. Overall, the general trend of 5 articles is similar, about 1100 seconds began to have obvious attenuation and then back up again. It is because with increasing vehicle speed, its temperature increase and atmospheric friction more intense. Thus air ionization more frequently increasing the electron density. Otherwise, due to the increasing of temperature also makes free electrons in the plasma collision more intense. It will inevitably make the plasma to increase the absorption of electromagnetic wave, so that the attenuation is more obvious.

6. Conclusions

By using the FDTD algorithm to study the one-dimensional inhomogeneous plasma sheath properties and using the differential Gauss pulse for excitation source and calculating the transmission coefficient of the inhomogeneous plasma sheath. Discussing the inference to electromagnetic (EM) wave when a space vehicle reentry the atmosphere and the electronic density varying with the height of space. Then analyze the aircraft dropped in the process of using the L, C, S, X, Ka band measured attenuation coefficient with the time graph and get some conclusions. The simulating results give the theoretic testimony to solve the blackout problem.

Acknowledgements

This work was supported by the National Natural Science Foundation of China (Grant No.61431010 and Grant No.61301065), The authors thank the reviewers for their helpful and constructive suggestions.

References

[1] Masoudi S F, Salehkoutahi S M. The dynamics of ions entering the magnetized plasma sheathobliquely - collisional and collisionless situations, *EUROPEAN PHYSICAL JOURNAL D.* 57(1):71-76,2010.

[2] Liu J Y, Wang F, Sun J. Properties of plasma sheath with ion temperature in magnetic fusion devices. *Physics of Plasmas*, 18(1):013506, 2011.

[3] Cheng G X, Liu L. Direct Finite-Difference Analysis of the Electromagnetic-Wave Propagation in Inhomogeneous Plasma,*TRANSACTIONS ON PLASMA SCIENCE*, 38(11):3109-3115,2010.

[4] Minkwan Kim, Michael Ke idar, Iain D. Boyd. Electrostatic Manipulation of a Hypersonic Plasma Layer: Images of the Two-Dimensional Sheath. *TRANSAC TIONS ON PLASMA SCIENCE*,36(4):1198-1199,2008.

[5] Jiang-Fan Liu, Xiao-Li Xi, Guo-Bin Wan, Li-Li Wan. Simulation of Electromagnetic Wave Propagation Through Plasma Sheath Using the Moving-Window Finite-Difference Time-Domain Method. *TRANSACTIONS ON PLASMA SCIENCE*,39(3):852:855,2011.

[6] C. T. Swift, F. B. Beck, J. Thomson, et al. RAM C-III S-band diagnostic experiment[C].*NASA,* Washington, 137-155, 1971.

The Calculation of Irregularities scattering and Delay Power Spectrum in Mid-latitude Es Layer

Cheng Qi , Guo Lixin , Li Jiangting ,He long

School of Physics and Optoelectronic Engineering, Xi Dian University, Xi'an, China

Abstract

On the basis of the existing theoretical and experimental studies about the ionosphere , in this paper ,a new method is adopted to simulate the delay power spectrum of irregularities' multipath scattering in the ionosphere .We establish a mathematical model of irregularities' multipath scattering by a geometric model of irregularities scattering along the ionosphere's field ,then we analyzes the impact of electron density and electromagnetic wave propagation distance of irregularities in the ionosphere to multi-path delay. The result shows that RCS (Radar cross section) can obtain the maximum scattering cross-sectional area when the geomagnetic angle is fixed. At the same time, the delay power spectrum, which is obtained by the simulation based on the simulated data of the electron density in the ionosphere, has a good applicability, so the practicability of the result is approved.

1. Introduction

Since the 1970s, irregularities scattering in the ionosphere has received widespread attention. Various nonlinear effects which occurred in the ionosphere have great values in scientific research and practical applications[1-3]. For example, ionosphere will generate irregularities distributed along the magnetic field direction of different sizes and shapes, which can be used for ionosphere scattering communication and so on. Irregularities generated in the ionosphere can cause changes in the communication signal's amplitude, group path and phrase path and other parameters. Additionally, different natural conditions in the outside may also cause the distinction of irregularities' shape, drift velocity and other parameters. Thus the impact on the communication signal will be different too. In the paper, we focus on the relationship between irregularities' electron density along the geomagnetic field in the ionosphere and the received signal's multipath delay during the communication process. We also verify the theory that the RCS can get maximum scattering cross-sectional area when the geomagnetic angle is a constant.

2. The RCS model of irregularity along the geomagnetic field in the ionosphere

Irregularities scattering along the field in the ionosphere has a strong directivity. Based on characteristics of scattering along the field in Es layer [4], we have an analysis of the geometric relationship among the incident wave, the scattering wave and the geomagnetic direction of the scattering point. Within the scope of the ionosphere over the Earth, random perturbation of electron density will lead to a corresponding change in the refractive index of irregularities in the ionosphere, and irregularities are along the direction of the magnetic field. However, random variation in refractive index is anisotropic. As a result, the total power of the received signal is expressed as follows:

$$P_r = P_t G_t G_r e^{-0.23K_A} \frac{1}{4\pi R_r^{\,2}} \iiint_V \sigma dV \tag{1}$$

Where P_t is the power of incident wave. G_t, G_r are gain modes of the transmitting antenna and the receiving antenna. K_A is the power loss when the incident wave and the scattering wave get through the D layer of the ionosphere. In the paper we only care of irregularities in Es layer, so we suppose $K_A = 0$. σ is irregularities' radar cross section(RCS) per unit volume. Rr is the distance from the receiving point to the scattering point. The scattering coefficient is equal to 4π . The integration region is the common area irradiated by both the transmitting antenna and the receiving antennas. Assuming there is a single scattering when the incident waves pass irregularities. According to Booker theory[5], scattering sectional area of irregularities per unit volume is calculated as follows:

$$\sigma = \frac{\pi^2}{\lambda^4} \sin^2 \chi \overline{\left|\frac{\Delta\varepsilon}{\varepsilon}\right|^2} \tag{2}$$
$$P\left[k(l_2 - l_1), k\left(m_2 - m_1\right), k\left(n_2 - n_1\right)\right]$$

Where χ is the angle between the direction of the incident wave's electric field and the direction of the scattered wave. λ is the wavelength of the incident wave. $\overline{\left|\frac{\Delta\varepsilon}{\varepsilon}\right|^2}$ shows mean square variation of the dielectric constant. $P\left[k(l_2 - l_1), k\left(m_2 - m_1\right), k\left(n_2 - n_1\right)\right]$ is three-dimensional wave number spectrum of the dielectric constant's disturbance. k is the wave vector of the incident wave. l_1 , m_1 , n_1 and l_2 , m_2 , n_2 are direction cosines of the incident and the scattered wave. For the plasma in the ionosphere

$$\overline{\left|\frac{\Delta\varepsilon}{\varepsilon}\right|^2} = \left(\frac{\lambda}{\lambda_P}\right)^4 \overline{\left(\frac{\Delta N}{N}\right)^2} \tag{3}$$

Where $\overline{\left(\frac{\Delta N}{N}\right)^2}$ is electron density disturbance of the corresponding region in the ionosphere. λ_P is the wavelength of irregularities' plasma. Eq. (3) is put into eq. (2),we can obtain

$$\sigma = \frac{\pi^2}{\lambda_P{}^4}\sin^2\chi\overline{\left(\frac{\Delta N}{N}\right)^2} \quad (4)$$
$$P\left[k(l_2-l_1),k\left(m_2-m_1\right),k\left(n_2-n_1\right)\right]$$

Gaussian random perturbation is adopted for the electron density perturbation of irregularities, the form of which is as follows:

$$r(x,y,z)=\exp\left[-\frac{1}{2}\left(\frac{x^2}{a^2}+\frac{y^2}{b^2}+\frac{z^2}{c^2}\right)\right] \quad (5)$$

Where (x,y,z) is the coordinate of every integral scattering point in space. (a,b,c) is the perturbation intensity of the corresponding point. Three-dimensional wave number spectrum of random perturbation of irregularities' electron density can be written in the following form:

$$P\left\{k(l_2-l_1),k(m_2-m_1),k(n_2-n_1)\right\}= \quad (6)$$
$$\left(2\pi\right)^{3/2}abc\cdot\exp\{-\frac{1}{2}k^2$$
$$\left[a^2(l_2-l_1)^2+b^2(m_2-m_1)^2+c^2(n_2-n_1)^2\right]\}$$

Irregularities in the magnetic field direction are considered to be cylindrical symmetry. Suppose $a=b=T$ and $c=L$ are irregularities' horizontal and vertical size of the relevant scale, then eq. (6) can be further written in the form

$$P\left[k(l_2-l_1),k\left(m_2-m_1\right),k\left(n_2-n_1\right)\right] \quad (7)$$
$$=P_{\perp}\{k[(l_2-l_1)^2+(m_2-m_1)^2]^{1/2}\}+P_{//}\{k(n_2-n_1)\}$$

$$P_{\perp}\{k[(l_2-l_1)^2+(m_2-m_1)^2]^{1/2}\}= \quad (8)$$
$$2\pi T^2\exp\{-\frac{1}{2}k^2[T^2(l_2-l_1)^2+T^2(m_2-m_1)^2]\}$$

$$P_{//}\{k(n_2-n_1)\}=(2\pi)^{1/2}L\exp\{-\frac{1}{2}k^2L(n_2-n_1)^2]\} \quad (9)$$

According to the geometric relationship among the emission point, the receiving point and the scattering point, the scattering angle is denoted as ϕ_s, the complementary angle of the angle between the Geomagnetic field and bisector of the angle ,which is between incident wave vector and scattering wave vector, is represented as φ . Based on scattering characteristics of the heating ionosphere forming irregularities, we can achieve

$$\sigma=\overline{\left(\frac{\Delta N}{N}\right)^2}\frac{\pi^2\sin^2\chi}{\lambda_P^4}(2\pi)^{3/2}T^2L \quad (10)$$
$$\exp\{-2k^2[T^2\sin^2(\frac{\phi_s}{2})\cos^2\varphi$$
$$+L^2\sin^2(\frac{\phi_s}{2})/\sin^2\varphi]\}$$

Because of the effective scattering confined to the central location of irregularities within a small range, after finishing, eq. (10) is into the following form

$$\sigma=\overline{\left(\frac{\Delta N}{N}\right)^2}\frac{\pi^2\sin^2\chi}{\lambda_P^4}(2\pi)^{3/2}T^2L \quad (11)$$
$$\exp\{-2k^2[T^2\sin^2(\frac{\phi_s}{2})+L^2z^2/R'^2]\}$$

Where z represents the position coordinate along the longitudinal direction of irregularities, that is, the direction of Geomagnetic field. The equivalent distance is $R'=2R_tR_r/(\mathrm{R}_t+\mathrm{R}_r)$. R_t is the distance from the emission point to the scattering point.

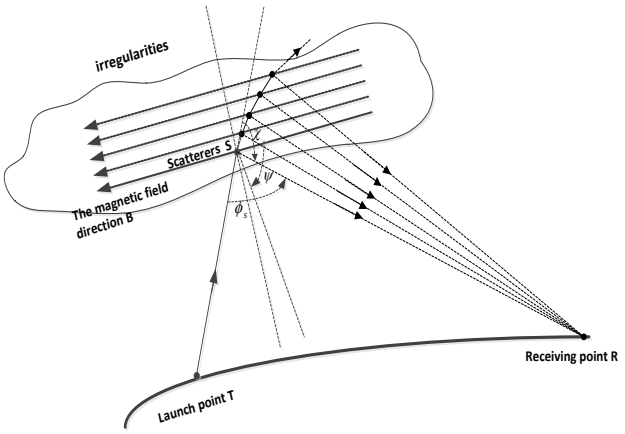

Figure1. The geometric relationship of scattering along the field

In the paper, we assume that a large irregularity along the geomagnetic field can be equivalent to a series of small scatterers along the direction of geomagnetic field, which have same geometric dimensions and are aligned as the vertical direction. Every small scatterer will scatter the incident wave [5]. Assuming that every small scatterer's transverse radius is W_1 , the half thickness is W_2 , and the value of every scatterer's center electron density perturbation is $\overline{\left(\frac{\Delta N}{N}\right)^2}_0$ .We also suppose that the center point is the origin of the large coordinate system, the direction of z-axis is perpendicular to the ground, and the horizontal surface is OXY . Presuming that electron density perturbation at the center is a Gaussian disturbance, the form is as follows

$$\overline{\left(\frac{\Delta N}{N}\right)^2}=\overline{\left(\frac{\Delta N}{N}\right)^2}_0\exp\left(-\frac{X^2}{W_1^2}-\frac{Y^2}{W_1^2}-\frac{Z^2}{W_2^2}\right) \quad (12)$$

When calculating the total scattering cross section of irregularities by integral, we consider valid scatter is mainly in the surface S ,which is perpendicular to the direction of geomagnetic field. The origin of the coordinate system xyz is also the center position of irregularity. The direction of z-axis is opposite to the direction of

geomagnetic field. After the coordinate conversion of XYZ and xyz , we can achieve the total RCS of the receiving point is expressed as

$$\begin{aligned}\sigma_z &= \iiint_V \sigma dV\infty \\ &= \frac{4\pi^5 \sin^2\chi}{\lambda_P^2}\overline{\left(\frac{\Delta N}{N}\right)^2}_0 W_1^2 \lambda T^2 R' \cdot \\ &\exp\{-2k^2[T^2\sin^2(\frac{\phi_s}{2})]\}\Big/\sqrt{\cos^2\theta_1+\frac{W_1^2}{W_2^2}\sin^2\theta_1}\end{aligned} \tag{13}$$

Where θ_1 is the angle between the horizontal plane and the geomagnetic inclination θ. Putting eq. (11) into eq. (1), we can calculate the power of the receiving point.

Before studying multipath scattering signal, we have to determine the time delay of the scattered signal. This article assumes that the propagation velocity of electromagnetic waves in plasma is a constant of c, so the delay expression is

$$\tau = \frac{R_t + R_r}{c} - \frac{R_{ro}+R_{to}}{c} \tag{14}$$

R_{ro} and R_{to} are distances of which receive the scattered signal fastest[6]. If the scattering coherence of each of the small scatterers is not taken into consideration, every received signal will have appropriate power and time delay. In this way, if the distribution of the internal electron density of irregularities in the ionosphere is known in advance, the corresponding relationship between power and time delay of the multipath scattering signal can be calculated.

3. The simulation and analysis of delay power spectrum of irregularities scattering along the field

In order to verify the feasibility of the model, in this paper a simulation calculation is made for analog electron density in the ionosphere. According to the simulation of relevant parameters in the ionosphere, it can be achieved that the transverse component of perturbation wave number spectrum of electron density is:

$$\begin{aligned}&P_\perp\{k[(l_2-l_1)^2+(m_2-m_1)^2]^{1/2}\} = \\ &2\pi\{\alpha T_1^2[e^{-(1/2)(kT_1)^2}]+(1-\alpha)T_2^2[e^{-(1/2)(kT_2)^2}]\}\end{aligned} \tag{15}$$

Where Values of α, T_1 and T_2 are 0.24,. 1, 0.5.

For the mid-low latitudes, simulation parameters are set as: The transverse radius of scatterer is 50km. The half thickness is 5km. In the case of dual station communication, the corresponding scattering height is 85-120km. The spacing between the transmitting and receiving station is 200km. Assuming the relative change in electron center density is 1.5%, horizontal polarization is used for transmitting signals.

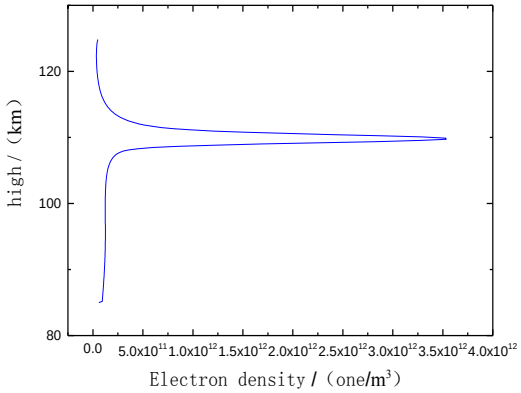

Figure3. The simulation of ionospheric electron density distribution

According to the simulation of ionospheric electron density distribution (Figure3), it can be calculated that the variation of RCS with the height when the geomagnetic direction and the radar beam have a fixed angle of 45^0, as the figure4 shows. The peak of RCS at about 110km verifies the theory that the RCS can get maximum scattering cross-sectional area when the geomagnetic angle is a constant..

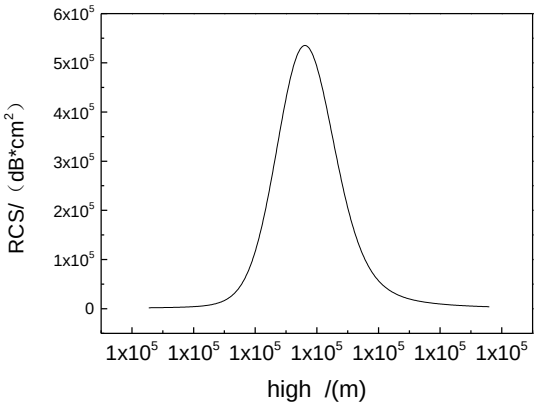

Figure4. The variation of RCS of the dual station path with the height when the geomagnetic direction and the radar beam have an angle of 45^0.

It is shown by the figure5 the resulting delay power spectrum at the transmitting frequency of 20 HZ,40 HZ and 60 HZ. In the figure of simulation result, ordinate represents the accepted power, and abscissa represents the accepted time delay. With the increase of communication frequency, the scattering accepted power is reduced overall. Even at the frequency of 60Hz, the power is also at the order of 20 $dB \cdot m$. Such a large accepted power has a sound advantage in scattering communication along the field. The accepted power has no significant fluctuation in the first half; however a significant fluctuation occurs at the peak of the ionospheric electron density. The electron density of the background has a close relationship with the accepted power in communication.

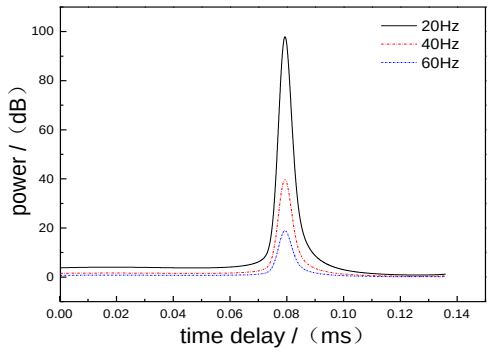

Figure5. The delay power spectrum at different frequencies when the geomagnetic direction and the radar beam have a fixed angle of 45^0

The figure6 shows the delay power spectrum when the emissive frequency is $60MHz$ and the geomagnetic direction and the radar beam has an angle of $30^\circ, 45^\circ$ and 60° .It can be seen that the geomagnetic field has a great influence on the accepted power. The larger the angle between the incident direction and the geomagnetic field is, the greater the accepted power of ionospheric scattering will be. The influence of the geomagnetic field plays a key role in the communication of scattering along the field in the ionosphere. RCS changes with variation of the angle between the direction of the geomagnetic field and the radar beam. Therefore, the textual scattering model can be used to calculate the received power at different angles between the radar beam and the geomagnetic field, and make an analysis of impact of the geomagnetic field on the scattering along the field in the ionosphere. These obtained results, which are in good agreement with conclusions of the literature [10], verify the feasibility of this idea.

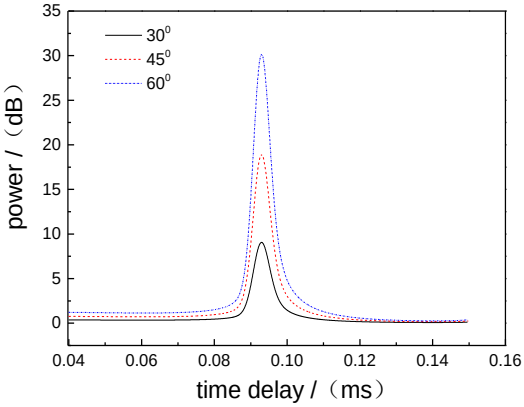

Figure6. The delay power spectrum when the geomagnetic direction and the radar beam have different angles

4. Conclusions

In the paper a new idea is adopted, which is also a bold attempt. Leaving the conventional delay estimation method aside, such as the cross-correlation method, spectral estimation, interpolation method and so on, on the theoretical basis of the existing irregularities scattering along the geomagnetic field in the ionosphere, the multipath scattering model of ionospheric scatter communication is established.According to the distribution of simulated electron density in the ionosphere, we derive the multipath delay power spectrum of ionospheric scatter communication, thus analyze the impact of electron density of irregularities in the ionosphere and the angle between the radar beam and the geomagnetic field on the multi-path delay. The electron density of irregularities is the most direct factor affecting the received power. At the same time, the theory that when the geomagnetic angle is fixe, the RCS can get maximum scattering cross-sectional area d is verified. In scattering communication along the field, such a large accepted power has a sound advantage. Finally, the feasibility of this idea is verified by comparison with the literature [7], which has a great help for further research on irregularities scattering in the ionosphere.

Acknowledgements

This work was supported by the Foundation of the China Research Institute of Radio Wave Propagation The authors thank the reviewers for their helpful and constructive suggestions.

References

[1] Song Jipeng, Skywave Propagation Prediction and Analysis of Assistant Decision Making [J], Journal of Xidian University, 2007, 30(2):50-53.

[2] Yan Yubo, Lv Libin, Li lingliang. Design of communication circuits based on AFAS [J]. Chin. J. Radio Sci，2008, 23(3):520-524. in Chinese

[3] Booker H G. A theory of scattering nonisotropic irregularities with application to radar reflections from the aurora[J]. J. Atmos. Tern. Phys., 1956, 8:204-221

[4] Long He, Li-xin Guo, Jiang-ting Li, The Simulation of Short Wave Propagation Ray Tracing in Sporadic E layer of Ionosphere, Third Asia-Pacific Conference on Antennas and Propagation(APCAP), 2014, in Press.

[5] Tan Hui, Simulation and Statistic Analysis on Mid-Latitude Sporadic E-Layers [D], Wuhan Institute of Physics and Mathematics, 2004.

[6] Y.Y Chen, J.T Chan, Time Delay and DOA Estimation Using TST-ESPRIT in wireless channel[C]. in Proceedings of the 32th Annual Asilomar Conference on Signals. 2001，3 02-3 O5.

[7] Lv Libin, Li Qingliang,Yan Yubo. Estimating of RCS of AFAS based on ionospheric heating. Chin. J. Space Sci., 2009, 29(6):558-562

Analysis of the EM Wave Propagation Characteristic in the Time Varying Plasma Sheath

Li Jiangting ,Guo Lixin ,Cheng Qi ,Chen Wei

(School of Physics and Optoelectronic Engineering, Xidian University, Xi'an 710071, China)

Abstract

By solving Navier-Stokes equations with AUSMPW+ format, the flow field of blunt cone model is simulated, the electron density distributions in plasma sheath at different flight speeds are obtained, and the impact of aircraft on the electron density distribution at different accelerations is also received. On the basis of these, time domain and frequency domain characteristics of electromagnetic wave are calculated through this time-varying plasma sheath using FDTD method based on time. The results show that: In the process of electromagnetic waves' transmission in a time-varying plasma sheath, if the speed and acceleration of the aircraft are higher, waves will decay more significantly. At the same flight speed, the greater the acceleration is, the more significantly the low frequency electromagnetic pulses decay. Research results in this paper will have a certain significance in measurement, control and communication of reentry vehicle.

1. Introduction

In the process of reentry, when the friction occurs between the aircraft with a high speed and the gas, the temperature in the ambient increases rapidly, which results in ionization of dense air, the aircraft will be coated with a layer of plasma, this layer generates plasma sheath[1-3]. Electromagnetic parameters of the plasma sheath are functions of the flow field parameters, their distributions are closely related to the characteristics of hypersonic flow field, while they are related to the aircraft shape, flight Mach number and altitude. Since the plasma sheath generated by the surface of high-speed aircraft has a significant impact on radio signals, the study on the electromagnetic properties of the plasma sheath shows great significance for reentry communication, measurement and control.

With the rapid development of computer technology and computational fluid dynamics calculating, numerical simulation has played an increasingly important role in engineering practice. This paper established a typical blunt cone aircraft model, since many aircraft have a blunt head or blunt leading edge. On the basis of this, for the calculation of reentry vehicle flow field, Navier-Stokes equations are used in this paper as control equations. AUSMPW+ format with simple structure, no matrix operation, strong ability to capture the shock waves and good stability is for solving control equations. Flow field distribution around the blunt body moving at high speed is simulated. The influence of high-speed and mobility state of aircraft on the electromagnetic characteristics of the plasma sheath is considered to analyze the influence of different accelerations on dielectric constant of plasma sheath, and propagation characteristics of electromagnetic wave in time-varying plasma sheath using the shift operator method.

2. Page layout and style

2.1. The flow field equations

Dimensionless equation of high-speed aircraft flow field is

$$\frac{\partial \mathbf{Q}}{\partial t}+\frac{\partial \mathbf{F}}{\partial x}+\frac{\partial \mathbf{G}}{\partial r}+\mathbf{H}=\frac{1}{R_e}\left(\frac{\partial \mathbf{F}_V}{\partial x}+\frac{\partial \mathbf{G}_V}{\partial r}+\mathbf{H}_V\right)+\mathbf{W} \tag{1}$$

Q is the vector of conservative variable. **F** and **G** are the vectors of convection flux along the direction of x and r. $\mathbf{F_V}$ and $\mathbf{G_V}$ are the viscosity vectors along the direction of x and r. **H** and $\mathbf{H_V}$ are viscous source vector and nonviscous source vector. **W** is source vector of vibrational energy term[4].

In view of the two-temperature models in high-speed aircraft circumferential flow, the nonequilibrium pressure is[5-6]

$$p=\rho T\sum_{i=1}^{N_i-1}\frac{c_i}{M_i}+\rho T_V\frac{c_e}{M_e} \tag{2}$$

Internal energy of two-temperature model is

$$E=e+E_v+\frac{1}{2}(u^2+v^2) \tag{3}$$

The vibration energy of each component is

$$E_V=\sum_M\frac{c_i}{M_i}e_{vi}+\frac{3}{2}\frac{c_e}{M_e}T_V \tag{4}$$

ρ_i is the density, c_i is the quality percentage, and e_{vi} is the molecular vibration energy.

2.2. Simulation of plasma sheath

Take the aircraft reentry process as an example, Figure 1 shows a typical curve of vehicles reentry track[7]. The aircraft's flight speed and altitude information at different heights can be drawn from the figure. Plasma sheath model as described above is adopted to calculate the electron density distribution at a position outside the aircraft.

The spherical cap radius of blunt cone model is 0.15m. The cone angle is 9°, and it's length is 1.3m. The space craft's background pressure and background temperature in the examples are obtained from IRI2000 models.

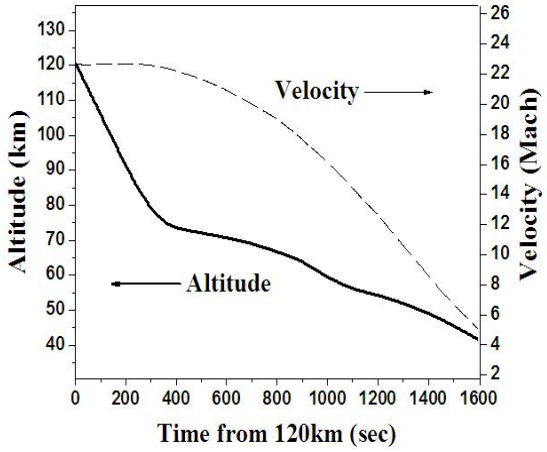

Figure 1 Reentry trajectory

The simulation results are shown in Figure 2. It shows that after friction and ionization, the high temperature gas formed on the surface of aircraft generates electron density sheath.

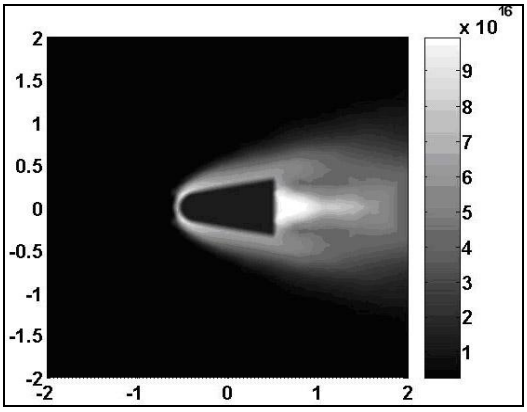

Figure 2 Electron number density profile

Figure 2 indicates that the electron density in the head area of the aircraft is about 1e16m^{-3}, and the density is gradually reduced along the axial direction.

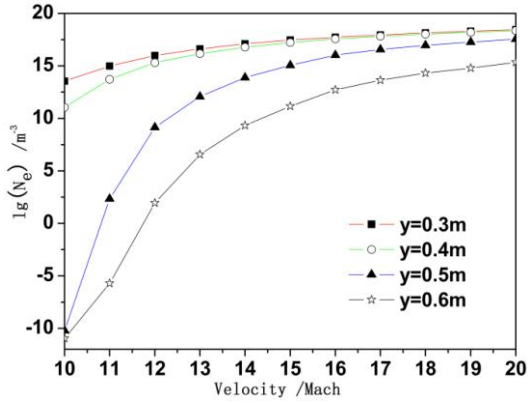

Figure 3 Electron number density profile at different speed

Figure 3 shows electron density at the direction perpendicular to the axis of the aircraft. Electron density decreases along the axial direction of the aircraft. As the flight speed increasing, the electron density at various locations gradually increases, eventually becoming saturated. When the vehicle speed changes, the electron density in plasma sheath changes over time. The plasma frequency and the electron collision frequency are also functions of time. The plasma frequency in sheath is

$$\omega_p(t) = (n_e(t)e^2 / m_e\varepsilon_0)^{1/2} \tag{5}$$

We can gain from the formula above

$$d\omega_p = \frac{1}{2\omega_p} \cdot \frac{e^2}{m_e\varepsilon_0} dn_e \tag{6}$$

Electron collision frequency is

$$\upsilon(t) = 5.2\times10^{13} n_e(t)\kappa T \tag{7}$$

We can gain from the formula above

$$d\upsilon = 5.2\times10^{13}\kappa T dn_e \tag{8}$$

According to formula (6) and (8), the plasma sheath model previously described is adopted to calculate the electron density distributions as the speed of the aircraft changes. Figure 4 shows the electron density changes at different accelerations.

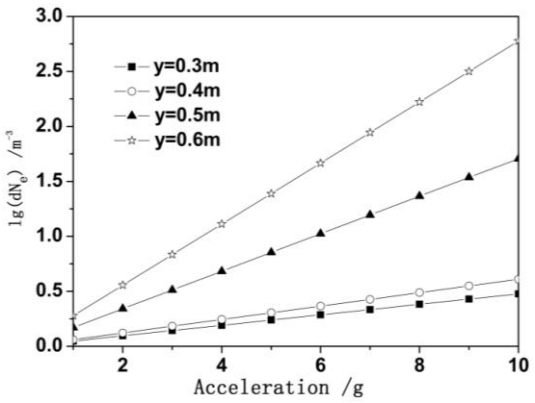

Figure 4 Electron number density profile at different acceleration

Figure 4 shows the variation of the electron density perpendicular to the axial direction of the vehicle. It is increasing along a direction perpendicular to the axis of the aircraft. As the acceleration increasing, the electron density at various locations gradually increases. The electron density at the edge of the sheath changes more obviously than the surface of the aircraft.

3. Wave propagation in the time varying plasma sheath

When the electromagnetic waves propagate in the plasma sheath, phase shift, delay, dispersion, reflection, refraction and absorption effects will be aroused. With high-speed maneuvering of vehicle, plasma sheath flow field characteristics change with flight speed. The propagation of

electromagnetic wave in the time-varying sheath is also affected by sheath characteristic changes[8].

This paper adopts FDTD method of time-varying plasma to analyze the electromagnetic wave transmission characteristics in plasma sheath. The changes of plasma frequency and the plasma collision frequency over time are determined by formula (6) and (8). Suppose that plasma electron density changes according to different accelerations, when the electromagnetic waves are in sheath[9-10].

As calculating, the Gaussian pulse propagating along the z-axis positive is taken, the expression of the pulse is

$$E_x = -A(t-5\tau)\exp\left(-\frac{(t-5\tau)^2}{2\tau^2}\right), \quad t \le 10\tau \qquad (9)$$

$$E_x = 0, \qquad t > 10\tau$$

Figure 5 present the time-domain waveforms of electromagnetic waves in plasma sheath at different accelerations. It is shown that as the vehicle acceleration increasing, the plasma sheath decays significantly. At the same flight speed, if vehicle acceleration is bigger, maneuvering change is fiercer and the electromagnetic wave decay more obviously by the plasma sheath.

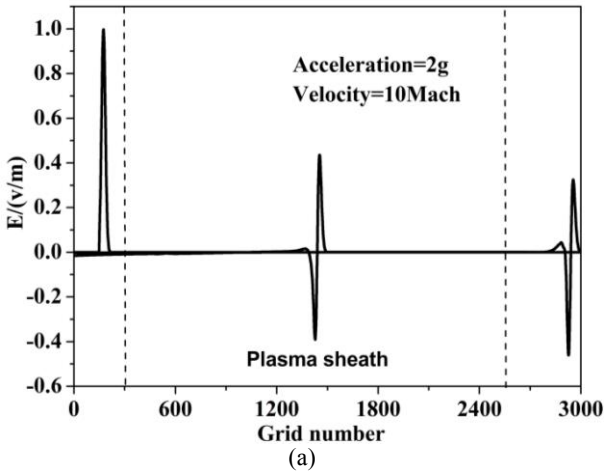

(a)

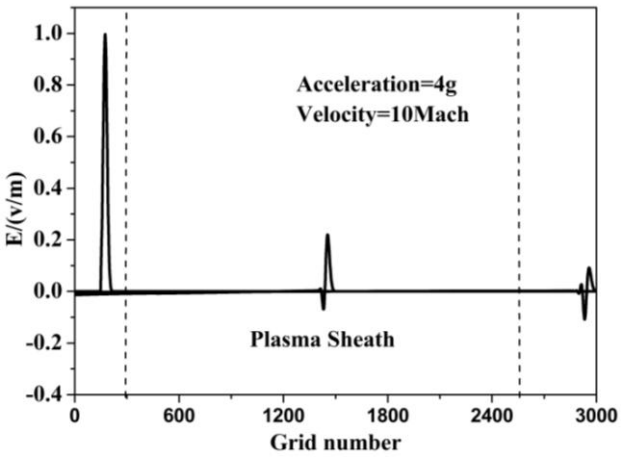

(b)

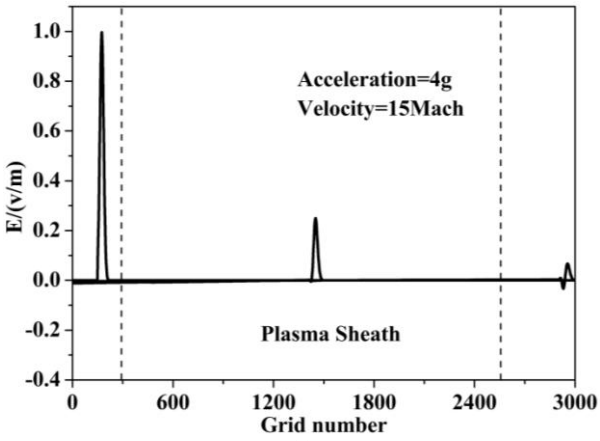

(c)

Figure 5 EM wave propagation in the time varying plasma sheath

Figure 6 is a spectrogram of electromagnetic waves through plasma sheath at different accelerations, when the reentry velocity is 15Mach.

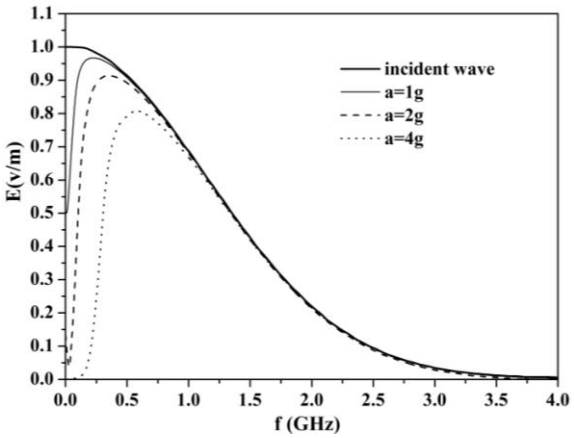

Figure 6 spectrum of electromagnetic wave

The figure shows that the width of frequency-domain of transmitted wave is shorter than incident Gaussian pulse, and the amplitude is decreased significantly, the greater the maneuvering acceleration, spectral peaks shift to the right, the more significantly the low frequency parts decay.

4. Conclusions

In this paper, the math format AUSMPW + was used to solve the NS equation of aircraft surface flow field. Electron density profile of plasma sheath was simulated. Time domain and frequency domain characteristics of electromagnetic wave are calculated in the time-varying plasma sheath at different flight speeds and accelerations, conclusions are as follows: (1) The higher the vehicle speed, the greater the electron density in the plasma sheath. And the electron density in outside of plasma sheath increases with vehicle acceleration. (2) In the process of electromagnetic waves' transmission in a time-varying plasma sheath, if the speed and acceleration of the aircraft are higher, waves will

decay more significantly. (3) At the same flight speed, the greater the acceleration is, the more significantly the low frequency electromagnetic pulses decay.

Acknowledgements

This work was supported by the National Natural Science Foundation of China (Grant No.61431010 and Grant No.61301065), The authors thank the reviewers for their helpful and constructive suggestions.

References

[1]Mather D E, Pasqual J M, Sillence J P. Radio frequency(RF) blackout during hypersonic reentry[R]. AIAA/CIRA 13th International Space Planes and Hypersonic Systems and Technologies, 2005.

[2]Usui H, Mat S H, Yamashita F,et al. Computer experiment s on radio blackout of a reentry vehicle[R] . 6th Spacecraft Charging Technology Conference , AFRL-VS-TR- 220001578, 2000: 107- 110.

[3]R.L.Stenzel and J.M.Urrutia, A new method for removing the blackout problem on reentry vehicles, journal of applied physics,Vol113,103303,2013.

[4]Kim K H, Kim C, Rho O H. Methods for the Accurate Computations of Hypersonic Flows I. AUSMPW+ Scheme[J]. Joumal of Computational Physics, 2001, 174(1):38-80.

[5]Boyd I D, Modeling of Associative Ionization Reactions in Hypersonic Rarefied Flows[J], Physics of Fluids, 2007,19:3-14.

[6]Gupta R N, Yos J M, Thompson R A. A review of reaction rates and thermodynamic and transport properties for an 11-species air model for chemical and thermal nonequilibrium calculations to 30000 K, NASA-TM- 101528, 1989.

[7]Hartunian RA, Stewart GE, Seibold RW. Causes and mitigation of radio frequency blackout during reentry of reusable launch vehicles. Rep. ATR-2007(5309)-1. EI Segundo (CA): Aerospace Corporation; 2007.

[8]Guoin Cheng and Lie Liu, Direct finite-difference analysis of the electromagnetic-wave propagation in inhomogeneous plasma, IEEE transactions on plasma science, Vol38,No11,2010.

[9]Ahmad A. Al-jabr,Tien Khee and Boon S.Ooi, A simple FDTD algorithm for simulating EM-wave propagation in general dispersive anisotropic material, IEEE transactions on antenna and propagation, Vol.61,No3,2013.

[10]Jiang-fan Liu, Xiao-Li Xi,Guo-Bin Wan and Li-Li Wang, Simulation of electromagnetic wave propagation through plasma sheath using the moving-window finite-difference time-domain method, IEEE transactions on plasma science, Vol39,No3,2011.

Antennas and Microwave technologies

Capacity Analysis of Antenna Arrays with Various Transmitting Angles

Shu-Han Liao[1*], Chien-Ching Chiu[2] and Su-Ei Wu[2]
[1]Smart Network System Institute, Institute for Information Industry, Taipei, Taiwan, R.O.C.
[2]Electrical Engineering Department, Tamkang University
Tamsui, Taipei, R.O.C.
[*]corresponding author: shliao@iii.org.tw

Abstract- This paper focuses on the research of channel capacity of Multiple-Input Multiple-Output (MIMO) system with different transmitting angles in straight tunnels. The channel capacities of MIMO Long Term Evolution (MIMO-LTE) system using spatial and polar antenna arrays by different transmitting angles are computed. Numerical results show that, The channel capacity for transmitting angle at 15 degrees is largest compared to the other angles in the tunnels. Moreover, the channel capacity of Polar Array (PA) is better than that of Spatial Array (SA) in the straight tunnels. Besides, the channel capacity for the tunnels with traffic is larger than that without traffic.

MIMO technology has attracted huge attention in wireless communications, due to its ability of offering significant increase in data throughput and link range without additional bandwidth or transmit power in the presence of multi-path scattering. In this paper, channel capacities of MIMO-LTE system [1], [2] by using spatial and polar antenna arrays at different transmitting angles are computed. The most suitable transmitting angle is investigated. The channel capacities for spatial array (SA) and polar array (PA) are compared in the straight tunnels with and without traffic.

After normalizing process, equation can be rewritten as follow:

$$\boldsymbol{C_{SE}^{LTE}} = \frac{1}{\boldsymbol{BW}} \sum_{\boldsymbol{f}=1}^{\boldsymbol{N_f}} \boldsymbol{B} \log(\det(\boldsymbol{I} + \boldsymbol{SNR_r} \times \hat{\boldsymbol{R}}_{\boldsymbol{H,f}})) \tag{1}$$

Where $SNR_r = \frac{SNR_t}{N_t} \times H_n^2$ denotes the ratio of average receiving signal power to noise power on each receiving antenna and $\hat{R}_{H,f}$ is the normalized eigenmatrix at the fth frequency component.

By using these images and received fields, the channel frequency response can be obtained as following:

$$H(f) = \sum_{p=1}^{N_p} a_p(f) e^{j\theta_p(f)} \tag{2}$$

where *p* is the path index, N_p is the number of paths, f is the frequency of sinusoidal wave, $\theta_p(f)$ is the *p*th phase shift and $a_p(f)$ is the *p*th receiving magnitude. Note that the channel frequency response of LTE systems can be calculated by equation (2) in the frequency range of LTE for desired signal.

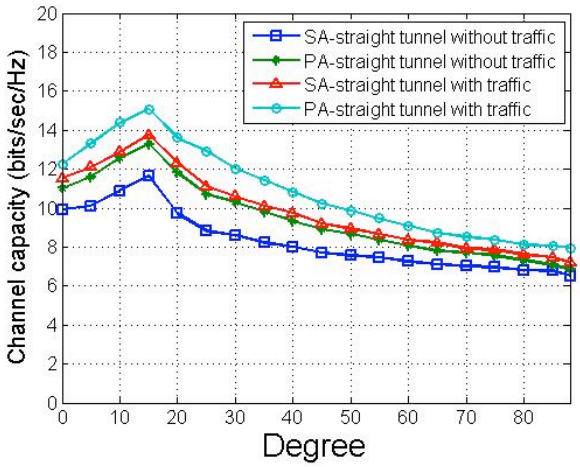

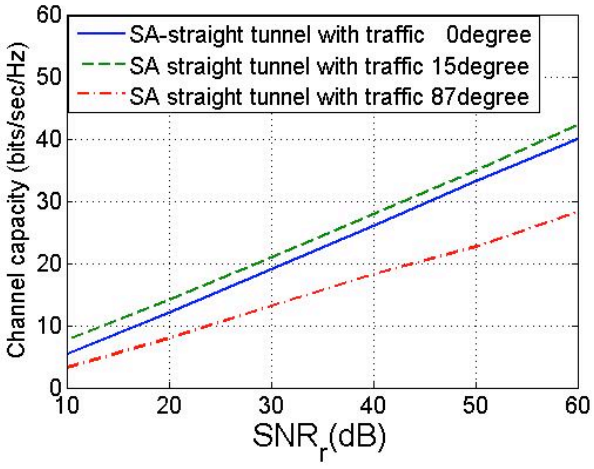

Fig 1. The average capacities of MIMO-SA and MIMO-PA system Fig 2. The average capacities of MIMO-SA system

The average capacities at SNRr=20dB for different transmit angles of Spatial Array Multiple-Input Multiple-Output (MIMO-SA) and Polar Array Multiple-Input Multiple-Output (MIMO-PA) in the straight tunnel are shown in Figure 1. It is clear the channel capacity for the transmit angle of 15 degrees is the largest. The average channel capacity at transmitting angle of 15 degrees without traffic for MIMO-PA and MIMO-SA is 13.26 (bits/sec/Hz) and 11.66 (bits/sec/Hz), respectively. The average channel capacity with traffic for MIMO-PA and MIMO-SA is 15.05 (bits/sec/Hz) and 13.76 (bits/sec/Hz), respectively. It is seen that the capacity for MIMO-SA is smaller than that for MIMO-PA. In other words, when the MIMO-SA system breaks a multipath channel into several individual spatial channels to enhance the capacity, the individual spatial channels are affected by each other. As a result, the correlation of MIMO-SA is stronger compared to MIMO-SA. Numerical results show that changing the polarization can improve the channel capacity effectively. It is also clear that the capacity for the tunnel with traffic is larger than that without traffic, no matter what MIMO-SA or MIMO-PA is employed.

The channel capacities of MIMO-SA at transmitting angles of 0, 15 and 87 degrees for different SNRr in the straight tunnel with traffic are plotted in Fig. 2. It is seen that the channel capacity is almost linearly proportional to single to noise ratio. The average channel capacity of MIMO-SA at SNRr=30dB for transmit angles of 0, 15 and 87 degrees is 19.01 (bits/sec/Hz), 20.91 (bits/sec/Hz) and 13.21 (bits/sec/Hz), respectively. The channel capacities for MIMO-PA is larger than those for MIMO-SA when the SNRr is the same.

Knox [3] presents a full-duplex design using a single circularly polarized antenna. Since we do not need to allocate different antennas for receiving and transmitting, and will be the subject of a future study.

Acknowledgements

A special thanks goes to Institute for Information Industry in Taiwan, for its great help to this study.

REFERENCES

1. Jae-Young Chung , Taesik Yang . Juhyung Lee ”Low correlation MIMO antenna for LTE 700MHz band” *IEEE International Conference on Acoustics, Speech, and Signal Processing*, pp. 2202-2204.
2. W.F. Young ”A Channel Propagation Model for the 700MHz Band” *IEEE Wireless Personal Communication* ,May. 2010 , pp.1-6.
3. M. Knox, “Single antenna full duplex communications using a common carrier,” *in 13th Annual Wireless and Microwave Technology Conference*, Apr. 2012.

Recent Development of Millimeter-Wave Bi-CMOS Multi-Band Amplifiers

Cuong Huynh, Jaeyoung Lee, and Cam Nguyen

Department of Electrical and Computer Engineering, Texas A&M University, College Station, Texas, 77840, U.S.A.
E-mail: cam@ece.tamu.edu

Abstract

Recent developments of millimeter-wave BiCMOS multiband amplifiers including 0.18-μm SiGe BiCMOS concurrent dual-band power amplifier (PA) and tri-band low-noise amplifier (LNA) are presented. The PA can work in concurrent dual-band mode at 25.5 and 37 GHz as well as single-band mode at 25.5 or 37 GHz. In the dual-band mode, the measured maximum output power is 13 and 9.5 dBm at 25.5 and 37 GHz, respectively, and the total maximum PAE is 7.1 %. The LNA operates concurrently around 13/24/35 GHz and achieves power gain of 22.4/23.7/20.2 dB at 13.5/24/35 GHz, respectively. It has the best noise figure of 3.4/3.2/3.7 dB and IIP_3 of -13.5/-17.1/-16.1 dBm in the 13.5/24/35 GHz pass-band, respectively. The LNA achieves less than 3.5-dB gain imbalance and 41/30-dB stopband rejection ratios in the low/high stopbands, respectively.

1. Introduction

Advanced communication and radar systems working "concurrently" over multiple bands provide numerous advantages and have more capabilities as compared to their single-band counterparts for communications and sensing. Achieving concurrent functions over multiple bands enables one single system to be used at multi-band simultaneously, leading to optimum size, cost and power consumption, and ease in realization for the system. True concurrent multiband systems require many components to work concurrently in multiple bands. Two of the most important components for concurrent multiband systems are power amplifier (PA) and low-noise amplifier (LNA). Several concurrent multiband PA's [1]-[2] and LNA's [3]-[4] have been reported.

This paper reports recent developments of millimeter-wave BiCMOS multiband PA and LNA. The PA operates concurrently over dual-band at 25.5 and 37 GHz and was designed based on concurrent dual-band matching. The LNA works concurrently over tri-band at 13, 24 and 35 GHz and implements a tri-band load composed of two feedback notch filters.

2. 25.5/37-GHZ Concurrent Dual-Band PA

The 25.5/37-GHz concurrent dual-band PA was designed and fabricated using Jazz 0.18-μm SiGe BiCMOS process [5]. Fig. 1 shows the schematic of the concurrent dual-band PA and Fig. 2 shows its photograph.

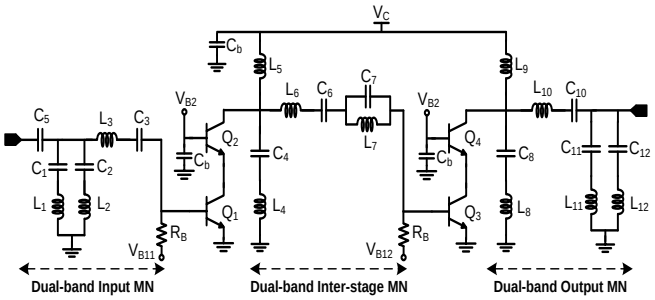

Fig. 1. Schematic of the 25.5/37-GHz concurrent dual-band PA.

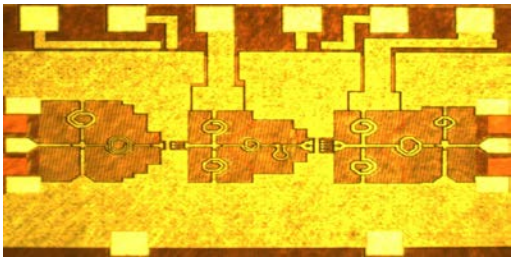

Fig. 2. Microphotograph of the 25.5/37-GHz dual-band PA.

Fig. 3 shows the simulated and measured S-parameters of the concurrent dual-band PA under small-signal conditions. The dual-band PA exhibits gains (S21) of 21.4 dB and 17 dB, 3-dB bandwidths of 3.7 GHz and 1.8 GHz, input return losses (S11) of 14.8 and 9 dB, and output return losses (S22) of 12.5 and 15 dB at 25.5 GHz and 37 GHz, respectively. The PA has a good dual-band gain response with out-of-band rejection below 0 dB from DC to 20, 30.5 to 34, and above 43 GHz. The rejection of signals at 32.5 GHz is 15 dB, while that at

frequencies below 10 GHz and above 50 GHz is larger than 30 dB, resulting in good suppression of the harmonics, IMPs and out-of-band signals. Fig. 4 shows the measured and simulated gain, output power, and PAE in the dual-band mode, in which two CW signals at 25.5 and 37 GHz are applied to the PA simultaneously. As shown in Fig. 4, the measured output power of the 25.5- and 37-GHz signals are the same until their input power P_{in} reach -12.5 dBm. The measured results in Fig. 4 show that, in the dual-band mode, the maximum output powers are 13 and 9.5 dBm, and the output 1-dB compression powers are 6.8 and 4.6 dBm at 25.5 and 37 GHz, respectively.

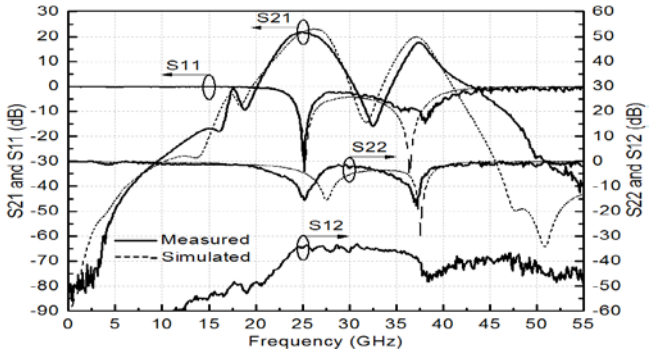

Fig. 3. Measured and simulated small-signal S-parameters.

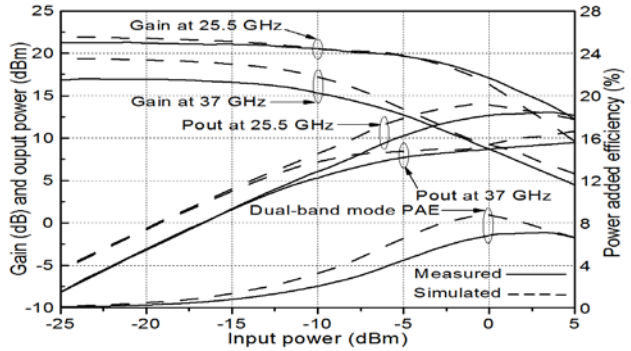

Fig. 4. Measured and simulated gain, output power and PAE at 25.5 and 37 GHz in dual-band mode.

3. 13/24/35-GHz Concurrent Tri-Band LNA

The 13/24/35-GHz concurrent tri-band LNA was designed and fabricated using Jazz 0.18-µm SiGe BiCMOS process [5]. Figs. 5 and 6 show the schematic and photograph of the concurrent tri-band LNA based on a two-stage cascode topology employing a tri-band load with two feedback notches, respectively.

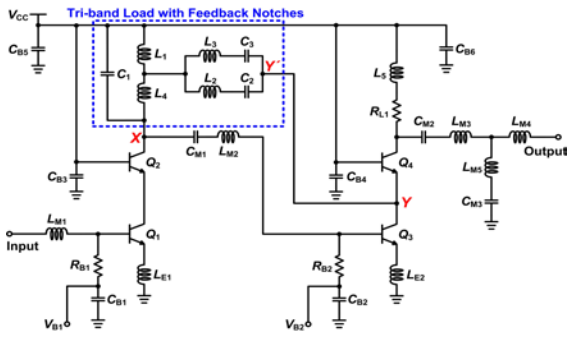

Fig. 5. Concurrent tri-band LNA schematic.

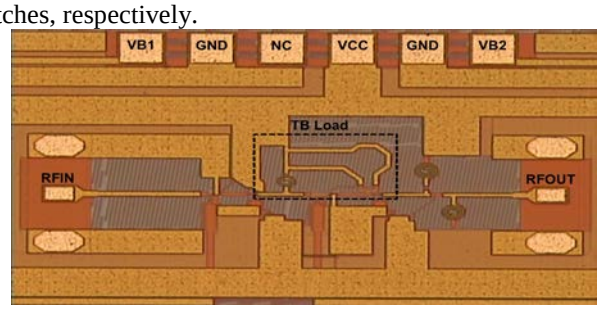

Fig. 6. Microphotograph of the 13/24/35-GHz tri-band LNA.

Fig. 7 shows the S-parameters and NF of the tri-band LNA. The power gain is 22.4/23.7/20.2 dB at 13.5/24/35 GHz, respectively. The minimum NF is 3.4/3.2/3.7 dB at each corresponding pass-band.

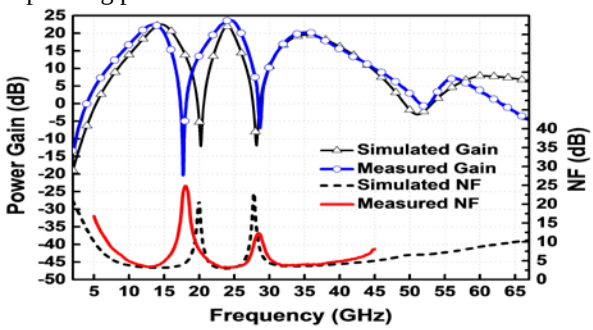

Fig. 7. Simulated and measured power gain and NF.

4. Conclusion

Recently developed concurrent dual-band PA and tri-band LNA working at 25.5/37 and 13/24/35 GHz, respectively, have been presented. The dual-band PA and tri-band LNA exhibit good performance, making them attractive for multi-band communication and radar systems. The proposed architectures and designs can be implemented at other frequencies and for other concurrent multiband design.

Acknowledgement

This paper was made possible by NPRP grant # 6-241-2-102 from the Qatar National Research Fund (a member of Qatar Foundation). The statements made herein are solely the responsibility of the authors.

References

[1] S.-F. R. Chang, W. L. Chen, S. C. Chang, C. K. Tu, C. L. Wei, C. H. Chien, C. H. Tsai, J. Chen, and A. Chen, "A dual-band RF transceiver for multistandard WLAN applications," *IEEE Trans. Microwave Theory and Techniques*, vol. 53, no. 3, pp. 1048–1055, Mar. 2005.

[2] C. Huynh and C. Nguyen, "New technique for Synthesizing Concurrent Dual-Band Impedance-Matching Filtering Networks and 0.18-µm SiGe BiCMOS 25.5/37-GHz Concurrent Dual-Band Power Amplifier," *IEEE Trans. on Microwave Theory and Techniques*, vol. 61, no. 11, pp. 3927–3939, Nov. 2013.

[3] C. W. Ang, Y. Zheng, and C. H. Heng, "A multi-band CMOS low noise amplifier for multi-standard wireless receivers," in *IEEE Int. Symp. on Circuits and Systems Dig.*, 2007, pp. 2802–2805.

[4] J. Lee and C. Nguyen, "A Concurrent Tri-Band Low-Noise Amplifier with a Novel Tri-Band Load Resonator Employing Feedback Notches," *IEEE Trans. on Microwave Theory and Techniques*, vol. 61, no. 12, pp. 4195–4208, Dec. 2013.

[5] TowerJazz Semiconductor, 4321 Jamboree Road, Newport Beach, CA 92660.

Dual-Band Circularly Polarized Rectangular Slot Antenna

Tao Zhou[1], Mian Pan[1], Hua-jie Ke[1], Zhi-hua Dong[1],Guo-hua Liu[1], Hai-jun Gao[1],Jin-cai Wen[1], Zhi-qun Cheng[1], Ling-ling Sun[1]

[1]Hangzhou Dianzi University, Electronics and and Information College, Hangzhou, China
*corresponding author, E-mail: zhou.tao@hdu.edu.cn

Abstract

A coplanar waveguide fed dual-band circularly polarized rectangular slot antenna is presented. The proposed antenna consists of a rectangular slot as a ground and an S-shaped monopole as a radiator. The composite vector current analysis is utilized to demonstrate that the circular polarization is generated by the S-shaped monopole which controls the path of the surface currents. A prototype is fabricated on a FR4 substrate with dielectric constant 4.4 and the overall dimension of the antenna is 37×37×1 mm3. The proposed antenna achieves a 10 dB return loss bandwidth of 2.27-2.81 GHz and 4.94-6.08 GHz respectively. It also exhibits a 3 dB axial ratio bandwidth of 2.39-2.98 GHz and 5.42-5.92 GHz, which can cover the bands of WLAN and WiMAX.

1. Introduction

The rapid development in wireless communications with different standards has resulted in a huge demand for multi-band antennas. Various types of multi-band antennas have been proposed [1-3]. Coplanar waveguide (CPW) fed slot antennas exhibit attractive features for dual-band applications because of its favorable characteristics, such as wide bandwidth, light weight, low profile, less sensitivity to manufacturing tolerances and easy integration with microwave integrated circuits. Circularly polarized (CP) antennas have attracted much attention in wireless systems due to the greater flexibility in orientation angle between signal and receiving antennas, and can avoid the effect of multipath reflection caused by walls and ground surfaces. Moreover, the circular polarization provides better mobility and weather penetration than linear polarization in WLAN and WiMAX applications. The essence of designing a CP antenna is the two required orthogonal resonant modes with 90° phase difference and equal amplitude [4, 5]. As known to all, CP antennas are usually divided into two types: single-feed and dual-feed configurations [6, 7]. Since the single-fed antennas can realize CP operation without using an external polarizer and can be arrayed like linearly polarized antennas [8, 9].

Several single-fed dual CP bands designs have been proposed recently [10-18]. There are many methods to realize the dual-band CP operations, such as introducing an inverted-L slit [15] or two spiral slots [16, 17] in the ground plane. In [18], a dual-frequency annular slot antenna with identical circular polarization is discussed. However, relatively few designs of coplanar waveguide single-fed dual-frequency slot antennas with circular polarization have been reported [14, 17, 18], and they all have complicated structure. In this paper, a novel design of a CPW-fed CP antenna with dual-band operation is introduced. The S-shaped monopole changed the path of the currents and the composite vector current analysis is utilized to demonstrate CP operation. Details of the antenna design and both theoretical and experimental results are presented and discussed.

This paper mainly consists of three parts. Firstly, the configuration of the proposed antenna is illustrated. And the mechanism for the dual-band and CP operation is analyzed with some discussions of the parameters of the S-shaped monopole and the rectangle slot. Secondly, the measured and simulated results for the S_{11}, AR, gain and radiation efficiency of the proposed antenna are described. Finally, the paper is summarized.

2. Antenna Design

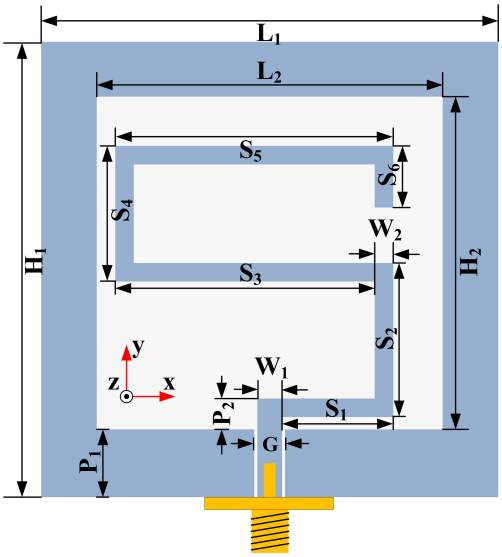

Figure 1: Geometry and photograph of the proposed antenna.

Figure 1 presents the configuration of the proposed rectangular slot antenna with dual-band circular polarization. The antenna is constructed by printing it on a 1 mm thick low cost suspended FR4 substrate with dielectric constant 4.4 and loss tangent 0.02. The area of the antenna is $L_1 \times H_1$. L_2 and H_2 are the width and height of the rectangle slot. The S-shaped monopole with the width of W_2 and the length of S_1, S_2, S_3, S_4, S_5 and S_6 for each stub is fed by the coplanar waveguide. The CPW is designed for a 50 Ohms characteristic impedance with slot and feed line widths equal to 0.25 mm and 2 mm respectively. The feed line is terminated with a standard SMA connector.

3. Discussion

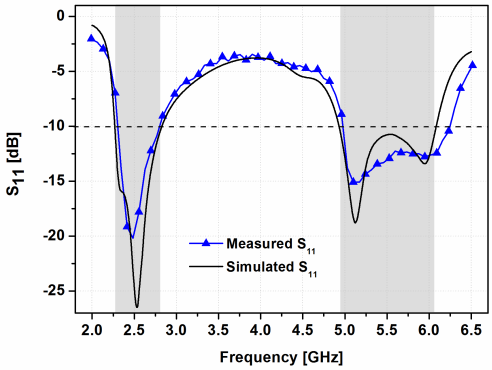

Figure 2: Measured and simulated S11 of the proposed antenna.

The measured and simulated S parameters results are depicted in figure 2. The antenna provides a $S_{11} \leq -10$ dB bandwidth of 21.3% (2.27-2.81 GHz) and 20.7% (4.94-6.08 GHz) in the first and second band in simulation, and 18.5% (2.31-2.78 GHz) and 22.6% (4.99-6.26 GHz) in measurement. The simulated and measured ARs in maximum radiation direction (z-axis direction as shown in figure 1) are shown in figure 3. The proposed CP antenna has a wide 3 dB axial-ratio bandwidth of 21.9% (2.39-2.98 GHz) and 8.8% (5.42-5.92 GHz) in simulation and of 19.6% (2.30-2.80 GHz) and 8.8% (5.40-5.90 GHz) in measurement. It is evident from the plot that the measured and simulated results are in good agreement.

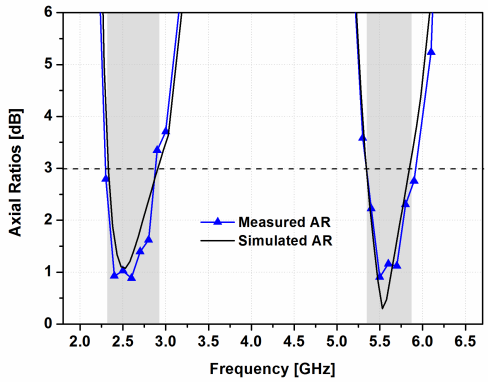

Figure 2: Measured and simulated axial ratio of the proposed antenna.

4. Conclusions

In this study, a novel dual-band circularly polarized CPW-fed rectangular slot antenna is presented and discussed. The S-shaped monopole controls the surface currents and generates the circular polarization, which is demonstrated by using composite vector current analysis. Experimental results show that the proposed antenna achieves a 10 dB return loss bandwidth of 2.31-2.78 GHz and 4.99-6.26 GHz respectively. It also exhibits a 3 dB axial ratio bandwidth of 2.30-2.80 GHz and 5.40-5.90 GHz. The proposed antenna is a good candidate for communications requiring circular polarizations at WLAN and WiMAX bands.

5. Acknowledgements

This work was supported by the National Natural Science Foundation of China (No.61331006, No.61001066 and No.61372021), Natural Foundation of Zhejiang Province (No.LY13F010018 and No.LQ14F010012).

References

[1] Liu, W. C., Optimal design of dual-band CPW-fed G-shaped monopole antenna for WLAN application, *Progress In Electromagnetics Research*, Vol. 74, 21-38, 2007.

[2] Liang, X. L., S. S. Zhong and, L. N. Zhang, Printed S-shaped monopole antenna for tri-band WLAN application, *Antennas, Propagation & EM Theory*, 2006. ISAPE '06. 7th International Symposium on, 26-29, 2006.

[3] Liu, W. C., W. R. Chen and, C. M. Wu, Printed double S-shaped monopole antenna for wideband and multiband operation of wireless communications, *Microwaves, Antennas & Propagation, IET*, Vol. 151, No. 6, 473-476, 2004.

[4] Chen, H. M., Y. K. Wang, Y. F. Lin, C. Y. Lin and, S. C. Pan, Microstrip-fed circularly polarized square-ring patch antenna for GPS applications, *Antennas and Propagation, IEEE Transactions on*, Vol. 57, No. 4, 1264-1267, 2009.

[5] Yen, T. Bee, R. Cahil,l and V. F. Fusco, Understanding and measuring circular polarization, *Education, IEEE Transactions on*, Vol. 46, No. 3, 313-318, 2003.

[6] Caso, R., A. Buffi, M. R. Pino, P. Nepa, and G. Manara, A novel dual-feed slot-coupling feeding technique for circularly polarized patch arrays, *Antennas and Wireless Propagation Letters*, IEEE, Vol. 9, 183-186, 2010.

[7] Pan, M. C., and K. L. Wong, Circularly polarized microstrip antenna with dual-CPW feed, *APSURSI* 2000, Vol. 2, 996-999, 2000.

[8] Chiu, C. N., and C. C. Yang, A new board-integrated single microstripfed circularly polarized monopole antenna for global positioning satellite receivers, *Journal of Electromagnetic Waves and Applications,* Vol. 24, No. 7, 903-909, 2010.

[9] Deng, J. Y., L. X. Guo, T. Q. Fan, Z. S. Wu, Y. J. Hu, and J. H. Yang, Wideband circularly polarized suspended patch antenna with indented edge and gap-coupled feed, *Progress In Electromagnetics Research*, Vol. 135, 151-159, 2013.

[10] Yang, J., C. H. Liang, and T. Wang, Novel dual-band circularly polarized wideband antenna for WLAN and WiMAX, *Journal of Electromagnetic Waves and Applications,* Vol. 26, No. 14-15, 1881-1888, 2012.

[11] Nayeri, P., K. F. Lee, A. Z. Elsherbeni, and F. Yang, Dual-band circularly polarized antennas using stacked patches with asymmetric U-slots, *Antennas and Wireless Propagation Letters, IEEE*, Vol. 10, 492-495, 2011.

[12] Heidari, A. A., M. Heyrani, and M. Nakhkash, A dual-band circularly polarized stub loaded microstrip patch antenna for GPS applications, *Progress In Electromagnetics Research*, Vol. 92, 195-208, 2009.

[13] Shao, Y., and Z. Chen, A design of dual-frequency dual-sense circularly-polarized slot antenna, *Antennas and Propagation, IEEE Transactions on*, Vol. 60, No. 11, 4992-4997, 2012.

[14] Chen, C. H., and E. K. N. Yung, Dual-band circularly-polarized CPW-fed slot antenna with a small frequency ratio and wide bandwidths, *Antennas and Propagation, IEEE Transactions on*, Vol. 59, No. 4, 1379-1384, 2011.

[15] Jou, C. F., J. W. Wu, and C. J. Wang, Novel broadband monopole antennas with dual-band circular polarization, *Antennas and Propagation, IEEE Transactions on*, Vol. 57, No. 4, 1027-1034, 2009.

[16] Bao, X. L., and M. J. Ammann, Monofilar spiral slot antenna for dual-frequency dual-sense circular polarization, *Antennas and Propagation, IEEE Transactions on*, Vol. 59, No. 8, 3061-3065, 2011.

[17] Chen, C. H., and E. K. N. Yung, Dual-band dual-sense circularly polarized CPW-fed slot antenna with two spiral slots loaded, *Antennas and Propagation, IEEE Transactions on*, Vol. 57, No. 6, 1829-1833, 2009.

[18] Chang, D. C., B. H. Zeng, and J. C. Liu, CPW-fed circular fractal slot antenna design for dual-band applications, *Antennas and Propagation, IEEE Transactions on*, Vol. 56, No. 12, 3630-3636, 2008.

[19] Chen, Z. N., K. Hirasawa, and K. Wu, A broad-band sleeve monopole integrated into parallel-plate waveguide, *Microwave Theory and Techniques, IEEE Transactions on*, Vol. 48, No. 7, 1160-1163, 2000.

[20] Pozar, D. M., and B. Kaufman, Comparison of three methods for the measurement of printed antenna efficiency, *Antennas and Propagation, IEEE Transactions on*, Vol. 36, No. 1, 136-139, 1988.

Miniaturized coupled-fed printed antenna for WWAN/WLAN/WiMAX communication

Yi Chen SONG[1*], Jiang Sheng ZHOU[2], Yun Long LU[3]

[1]Hangzhou Dianzi University, Information Engineering School, Hangzhou Zhejiang, PRC
[2]Jiang Nan Electronic and Communication Research Institute, Jiaxing Zhejiang, PRC
[3]Ningbo University, College of Information Science and Engineering, Ningbo Zhejiang, PRC
*corresponding author, E-mail: 506724608@qq.com

Abstract

A miniaturized coupled-fed printed antenna for multi-band WWAN/WLAN/WiMAX communication is presented. The proposed antenna consists of a long radiation strip, a short-circuited inductive shorting strip, and a coupling strip. By using the capacitive excitation of the coupling strip, the long radiating strip with the shorting strip can generate a wide lower band to cover the GSM850/900 operation, and the coupling strip can also form a wide upper band to cover GSM850 /900 /1800 /1900 /UMTS2100, WLAN2400, and WiMAX2300 /2500 operations. The antenna is suitable to be disposed on a small no-ground board space (15 x 45 mm^2) of the system circuit board and enclosed by an L-shaped system ground plane. Details of the proposed antenna are described, and the measurement and simulation results are presented and discussed.

1. Introduction

Owing to the demands of low-profile and multiband mobile applications, the design of compact multiband or wideband internal antennas has become a necessity and a challenge. To achieve small size, easy fabrication, and multiband operation, the on-board internal printed antennas such as the capacitively coupled-fed antennas [1-5], monopole antennas [6, 7] and slot antennas [8, 9] are attractive for the modern mobile applications. Various designs of wideband antennas [10-19] with printed structure or 3-D structure have been recently proposed to cover the WWAN, WLAN or WiMAX operation required by modern mobile devices.

Recently, a multiple printed branches monopole antenna operating for GSM/DCS/PCS/UMTS/BT/WLANs/WiMAX for mobile handset applications is reported in [10], which size of 17.5 x 36 mm^2, but this antenna does not cover all of the GSM bands. Another multiband antenna for WWAN/WLAN/WiMAX operation in the internal mobile phone is demonstrated in [11], which has a three-dimensional structure and a chip inductor needs to be loaded. The internal multiband loop antennas have also been reported in [18, 19], however they are also three-dimensional and not easy for fabrication.

In this article, we propose a miniaturized coupled-fed antenna for achieving multiband operation which covers not only all the five operating bands for WWAN operation, including the GSM850, GSM900, GSM1800, GSM1900, UMTS, but also the WLAN2400 and the WiMAX2300, WiMAX2500. That is, WWAN/WLAN/WiMAX multi-network operation can be achieved by the proposed antenna without any external matching circuit [20] or setting additional resonators [21], which introduce Ohm loss or occupy additional size.

The antenna has a small footprint of 15x45mm^2 and is suitable to be disposed on a no-ground board at either the top or bottom edge of the system circuit board. Further, the no-ground board space occupies only a fractional portion of the edge and is enclosed by an L-shaped system ground plane of the mobile device. A universal series bus (USB) connector [22] for the data port of the mobile devices or other associated electronic elements can be disposed on the protruded ground of the L-shaped system ground plane. The proposed antenna is suitable to be directly printed on the system circuit board of the mobile device, making it easy to fabricate at low cost and attractive for mobile applications. Detailed operating principle of the proposed antenna is described in the article. Results of the fabricated prototype of the proposed antenna are presented and discussed.

2. Proposed antenna configuration

The geometry of the proposed antenna is shown in Figure 1. In this study, the antenna is printed on one corner of the bottom edge of the main circuit board, which is a FR4 substrate (relative permittivity 4.4 and conductivity 0.02 S/m) of length 115mm and width 60 mm. The proposed antenna occupies a no-ground region of 15x45 mm^2 and enclosed by a L-shaped system ground plane printed on the back side of the system circuit board. Note that there is a 1mm spacing between the protruded ground and the printed metal pattern of the antenna. This spacing influences the impedance matching of the antenna's upper band. A USB connector is mounted on the protruded ground of the L-shaped system ground plane. Although a USB connector is near the antenna, there is no noticeable effects on the performances of the antenna. For measuring the antenna in the experiment, a 50ohms coaxial feed line is used to excite the proposed antenna at the feeding point A. In addition, to simulate practice case, a 1mm thick plastic housing (with height 9mm, relative permittivity 3.3, and loss tangent 0.02)

is used, where a gap (width 1mm) between the PCB and plastic housing exist.

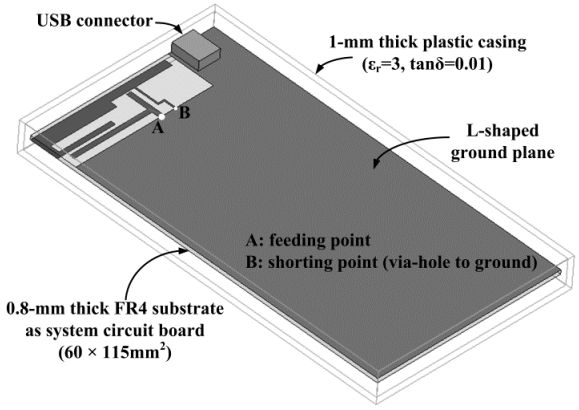

Figure 2: Measured and simulated return loss for the proposed printed antenna.

3. Results and Disussion

A prototype of the proposed antenna was fabricated and tested. The measured and simulated return losses of the antenna is shown in Figure 2. The experimental data was measured on an Agilent N5247A vector network analyzer, which agree well with the simulation results giving by HFSS. With the definition of 3:1 VSWR (-6dB return loss) generally used for internal mobile device antenna design, a wide lower band from 800 to 1010 can easily cover GSM 850/900 operation. Then a wide upper band with a measured 2:1 VSWR (or -10 dB return loss) bandwidth of 1060 MHz (1700-2760 MHz) is also obtained. For frequencies cover the GSM1800/1900/UMTS2100 bands, the impedance matching is better than not only 3:1 VSWR but also 2:1 VSWR. The upper band also covers the WLAN2400 and the WiMAX2300/2500 bands, with the impedance matching better than 2:1 VSWR. Some discrepancies were found due largely to system circuit board manufacture tolerance and the effects of the 50ohms coaxial cable as well as the hand soldering that was performed.

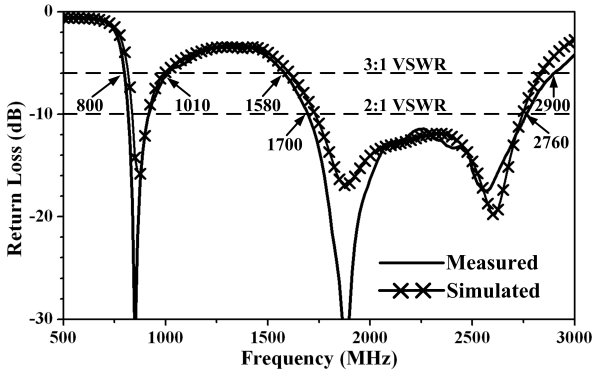

Figure 2: Geometry of the proposed printed antenna

Radiation characteristics of the constructed prototype are also studied. In the three azimuthal planes (xy-planes), smooth variations in the vertical polarization E_θ over all of the φ angles are seen, which can provide good coverage for the antenna. Large differences in the radiation patterns at lower and higher frequencies are related to the different excited surface currents on the system ground plane and the metal pattern of the mobile device. Comparable E_θ and E_φ components are observed in the radiation patterns, which is advantageous since the wave propagation environment is usually complex for practical applications.

4. Conclusions

A small-size coupled-fed printed antenna for internal mobile applications is proposed, fabricated and studied in the paper. The proposed antenna is formed by a radiating strip, an inductive shorting strip and a coupling strip, which can generate multiple resonant modes over the desired operating bands to cover GSM850/900/1800/1900/ UMTS2100, WLAN2400, and WiMAX2300 / 2500 operation. The proposed antenna element is easily printed on the no-ground portion of the system circuit board at low cost and occupies a very small area of 15×45 mm^2 only, and the antenna can also integrate with a USB connector as the data port at the bottom edge of the mobile device. Good radiation characteristics over the operating bands have also been observed. Owing to its all printing structure and good performance, the proposed antenna is very suitable for thin mobile device applications.

References

[1] C. C. Yu, J. H. Yang, C. C. Chen, and W. C. Hsieh, A compact printed multi-band antenna for laptop applications, *PIER Online*, Vol. 7, 605-608, 2011.

[2] J. H. Chen, Y. L. Ban, H. M. Yuan, and Y. J. Wu, Printed coupled-fed PIFA for seven-band GSM/UMTS/LTE WWAN mobile phone, *J. of Electromagn. Waves and Appl.*, Vol. 26, 390-401, 2012.

[3] K. L. Wong, M. F. Tu, C. Y. Wu, and W. Y. Li, Small-size coupled-fed printed PIFA for internal eight-band LTE/GSM/UMTS mobile phone antenna, *Microwave Opt. Technol. Lett.*, vol. 52, pp. 2123–2128, 2010.

[4] D. B. Lin, I. T. Tang, and M. Z. Hong, A compact quad-band PIFA by tuning the defected ground structure for mobile phones, *Progress In Electromagnetics Research B*, Vol. 24, 173-189, 2010.

[5] Y. L. Ban, C. Q. Lei, J. H. Chen, et. al., Compact coupled-fed PIFA employing T-shaped monopole with two stubs for eight-band LTE/WWAN internal mobile phone, *J. of Electromagn. Waves and Appl.*, Vol.26, 973-985, 2012.

[6] W. S. Chen and B. Y. Lee, A meander PDA antenna for GSM/DCS/PCS/UMTS/WLAN applications, *Progress In Electromagnetics Research Letters,* Vol. 14, 101-109, 2010.

[7] J. Y. Sze and Y. F. Wu, A compact planar hexa-band internal antenna for mobile phone, *Progress In Electromagnetics Research,* Vol. 107, 413-425, 2010.

[8] W. J. Lu, W.S.W. Cheung, Y. Cheng, and H.B. Zhu, Ultra-wideband antipodal slot antenna with improved radiation performance, *International Journal of Electronics*, Vol. 1, 1–17, 2012.

[9] Z. Chen, Y. L. Ban, J. H. Chen, L. W. Li, and Y. J. Wu, Bandwidth enhancement of LTE/WWAN printed mobile phone antenna using slotted ground structure (accepted), *Progress In Electromagnetics Research*, 2012.

[10] W. J. Liao, S. H. Chang, and L. K. Li, A compact planar multiband antenna for integrated mobile devices, *Progress In Electromagnetics Research*, Vol. 109, 1-16, 2010.

[11] K. L. Wong and C. T. Lee, Small-size wideband monopole antenna closely coupled with a chip-inductor-loaded shorted strip for 11-band WWAN/WLAN/WiMAX operation in the slim mobile phone, *Microw. Opt. Technol. Lett.*, Vol. 53, No. 2, 361-366, 2011.

[12] S. C. Chen and K. L. Wong, Small-size 11-band LTE/WWAN/WLAN internal mobile phone antenna, *Microw. Opt. Technol. Lett.*, Vol. 52, No. 11, 2603-2608,2010.

[13] W. S. Chen and B. Y. Lee, A meander PDA antenna for GSM/DCS/PCS/UMTS/WLAN applications, *Progress In Electromagnetics Research Letters*, Vol. 14, 101-109, 2010.

[14] J. R. Panda and R. S. Kshetrimayum, A printed 2.4 GHz/5.8 GHz dual-band monopole antenna with a protruding stub in the ground plane for WLAN and RFID applications, *Progress In Electromagnetics Research*, Vol. 117, 425-434, 2011.

[15] Y. L. Ban, H. M. Yuan, J. H. Chen, L. W. Li, and Y. J. Wu, A novel ultra-wideband antenna with distributed inductance for wireless USB dongle attached to laptop computer, *J. of Electromagn. Waves and Appl.*, Vol. 26, 179-191, 2012.

[16] Y. L. Ban, J. H. Chen, L. J. Ying, Joshua L. W. Li, and Y. J. Wu, Ultrawideband antenna for LTE/GSM/UMTS wireless USB dongle applications, *IEEE Antennas Wirel. Propag. Lett.*, Vol. 11, 403-406, 2012.

[17] A. H. Kusuma, A. F. Sheta, I. Elshafiey, Z. Siddiqui, M. A. Alkanhal, S. Aldosari, and S. A. Alshebeili, A new low SAR antenna structuer for wireless handset applications, *Progress In Electromagnetics Research*, Vol. 112, 23-40, 2011.

[18] M. R. Hsu and K. L. Wong, Seven-band folded-loop chip antenna for WWAN/WLAN/WIMAX operation in the mobile phone, *Opt. Technol. Lett.*, Vol. 51, No. 2, 543-549, 2009.

[19] W. Y. Li and K. L. Wong, Seven-band surface-mount loop antenna with a capacitively coupled feed for mobile phone application, *Opt. Technol. Lett.*, Vol. 51, No. 1, 81-88, 2009.

[20] M. Tzortzakakis and R. J. Langley, Quad-band internal mobile phone antenna, *IEEE Trans. Antennas Propag.*,Vol 55, 2097-2103, 2007.

[21] K. L. Wong, L.C. Chou and C. M. Su, Dual-band flat-plate antenna with a shorted parasitic element for laptop applications, *IEEE Trans. Antennas Propag.*,Vol. 53, 539-544, 2005.

[22] S. C. Chen and K. L. Wong, Planar strip monopole with a chip-capacitor-loaded loop radiating feed for LTE/WWAN slim mobile phone application, *Opt. Technol. Lett.*, Vol. 53, No. 4, 952-958, 2011.

A Novel Compact Microwave Dual-Band Bandpass Filter Using Stub-Loaded Resonators

Bin You[1], Long Chen[1]*, Xuan Wen[2]

[1]Circuits and Systems Key Laboratory of the Ministry of Education, Hangzhou Dianzi University, China
[2]Nokia Solutions and Networks System Technology (Beijing) Co., Ltd, China
*corresponding author, E-mail: alanchenlong2@gmail.com

Abstract

A novel compact microwave dual-band bandpass filter using stub-loaded resonators (SLR) is presented in this paper. The proposed dual-band filter comprises two dual-mode single band filters using common input/output lines. Each single band filter comprises a SLR. By tuning the length of main line or stub-loaded line of the resonator, either the passband center frequency or the fractional bandwidth can be easily controlled and designed independently. The filter has the advantage of two passband center frequencies and two FBWs can be controlled by only few parameters. Meanwhile, this filter is implemented with three transmission zeros. This paper presents the brief analysis of the SLRs and introduces the structure and design approach of the proposed filter. Finally a dual-band bandpass filter is designed and realized to prove the analysis.

1. Introduction

With an explosive growth in wireless communications, the research on dual-band wireless systems becomes the hotspot since the 21st century [1]. As an important and essential component of these systems, a high-performance dual-band bandpass filter (BPF) is in great demand. In this case, the design of dual-band BPF with easy-control center frequency and bandwidth becomes an important issue to reduce system size and complexity. To meet these requirements, various approaches have been applied to design dual-band BPFs. The step impedance resonators (SIR) are used in designing dual-band BPFs [2]. However, these designs can't control the bandwidth easily. The stub-loaded resonator (SLR) is widely and successfully uesd in designing bandwidth and center frequencies easy-control dual-band BPF [3]. Recently, SLR is also adapted in the tunable center frequencies and bandwidth filter designs [4]. Those researches present various dual-band BPFs. Nevertheless, from the perspective of simple applications with different center frequencies and FBWs, there still lacks of design tools. In this paper, a compact microstrip dual-band BPF using $\lambda/2$ SLR is presented. The proposed dual-band BPF has the characteristic of two passband center frequencies and two FBWs which can be easily controlled by only few parameters and can be designed independently.

Later parts in this paper, the $\lambda/2$ SLR is brief analysed and the main design process of the proposed filter is introduced. Finally, for the demonstration, a dual-band BPF with an extremely small area, shown in Fig. 1, has been designed and implemented to verify the analyses.

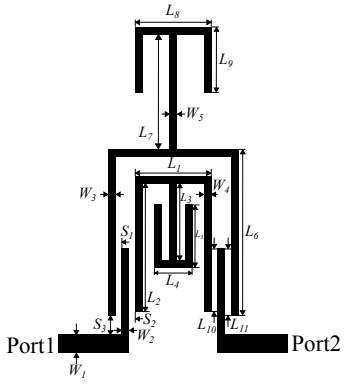

Figure 1: Structure of the proposed dual-band BPF.

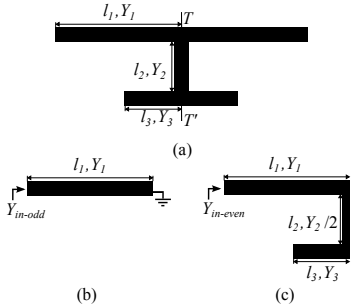

Figure 2: (a) The $\lambda/2$ stub-loaded resonator. (b) Odd-mode equivalent circuit. (c) Even-mode equivalent circuit.

2. Analysis and design

2.1. Analysis

As shown in Fig.1, the proposed filter comprises two parallel dual-mode single band filters using common input/output lines. Each single band filter comprises a $\lambda/2$ SLR. The first passband is designed based on the larger resonator with an outside stub-loaded line and the second passband is designed based on the small one with an inside stub-loaded line. This parallel structure makes these two passband responses not interact with each other. Ignoring the influence of the microstrip corner, the two $\lambda/2$ SLRs both

can be made into a more simple structure as shown in Fig.2 (a), which comprises a conventional $\lambda/2$ resonator and a bifid open stub-loaded line in the center. After study in [3], odd- and even-mode analysis is used for characterizing the resonator. In Fig.2, $Y_{1\sim3}$ and $l_{1\sim3}$ denote the characteristic admittances and the lengths of each microstrip lines.

For odd-mode excitation, Fig.2 (b) presents the equivalent circuit. The input admittance for odd-mode can be expressed as

$$Y_{\text{in-odd}} = \frac{Y_1}{j\tan(\beta l_1)} \tag{1}$$

From the resonance condition of $Y_{\text{in-odd}} = 0$, the odd-mode resonant frequencies can be deduced as

$$f_{\text{odd}} = \frac{(2n-1)\,c}{4l_1\sqrt{\varepsilon_{\text{eff}}}} \tag{2}$$

where n=1,2,3$\cdots$, c is the speed of light in free space, and ε_{eff} denotes the effective dielectric constant of the substrate. (2) proves that the stub-line has no effect on the odd-mode resonant frequencies. By tuning the length of $\lambda/2$ line, the odd-mode resonant frequencies can be easily controlled.

For even-mode excitation, Fig.2 (c) presents the equivalent circuit. The input admittance for even-mode can be deduced as

$$\begin{aligned} &Y_{\text{in-even}} = \\ &jY_1[Y_2Y_3\tan(\beta l_3) + \frac{1}{2}Y_2\tan(\beta l_2) + Y_1Y_2\tan(\beta l_1) \\ &- 2Y_1Y_3\tan(\beta l_1)\tan(\beta l_2)\tan(\beta l_3)]/[Y_1Y_2 \\ &- 2Y_1Y_3\tan(\beta l_2)\tan(\beta l_3) - Y_2Y_3\tan(\beta l_1)\tan(\beta l_3) \\ &- \frac{1}{2}Y_2^2\tan(\beta l_1)\tan(\beta l_2)] \end{aligned} \tag{3}$$

From the resonance condition of $Y_{\text{in-even}} = 0$, and considering the special case of $Y_1 = \frac{1}{2}Y_2 = Y_3$, (3) can be derived as $\tan(\beta l_1 + \beta l_2) + \tan(\beta l_3) = 0$. Then the resulting even-mode resonant frequencies can be derived as

$$f_{\text{even}} = \frac{nc}{2(l_1+l_2+l_3)\sqrt{\varepsilon_{\text{eff}}}} \tag{4}$$

where n=1,2,3$\cdots$. (4) proves that the stub-loaded line and the $\lambda/2$ line both have effect on the even-mode resonant frequencies. According to (2) and (4), by tuning the length of the stub-loaded line, the even-mode resonant frequencies can be easily controlled without changing the odd-mode resonant frequencies.

2.2. Design

To verify the above results, the 3D EM simulation is carried out by using Ansoft.HFSS.V13.0. Fig.3 shows the simulated results of the $\lambda/2$ SLR under weak coupling against L_5. When the length of L_5 is increased from 5mm to 6.5mm, f_{even} is lower than f_{odd}. When the length of L_5 is reduced from 3mm to 2.5mm, f_{even} is higher than f_{odd}. The location of the transmission zero is also well controlled by the length of L_5. Fig.4 shows the simulated results of the $\lambda/2$ SLR under weak coupling against $\lambda/2$ line. Both (2) and simulated results in Fig.4 prove f_{odd} is mainly controlled by the length of L_2, and both (4) and simulated results in Fig.3 prove f_{even} can be controlled by the length of L_5 without changing f_{odd}. The simulation results also show that the passband center frequency is characterized by the midpoint of f_{odd} and f_{even} and the FBW is characterized by the difference between f_{odd} and f_{even}.

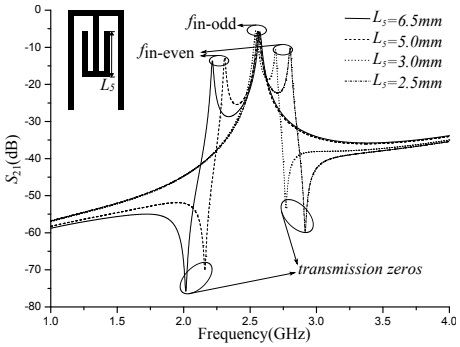

Figure 3: Simulated results of the $\lambda/2$ stub-loaded resonator under weak coupling against stub-loaded line.

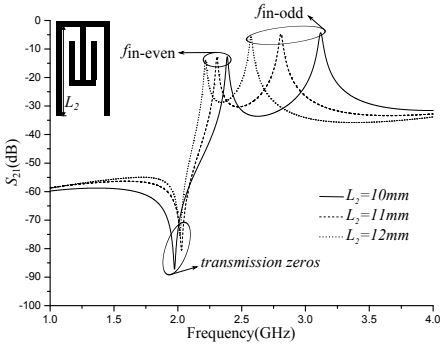

Figure 4: Simulated results of the $\lambda/2$ stub-loaded resonator under weak coupling against $\lambda/2$ line.

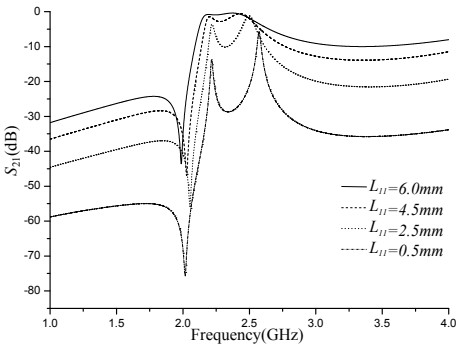

Figure 5: Simulated results of the $\lambda/2$ stub-loaded resonator against feeder line.

According to the above characteristics, dual-band BPFs can be easily designed to meet the requirements of different center frequencies and FBWs. The second passband is chosen as an example to explain the main design process. Firstly, deriving the cut-off frequency according to the ex-

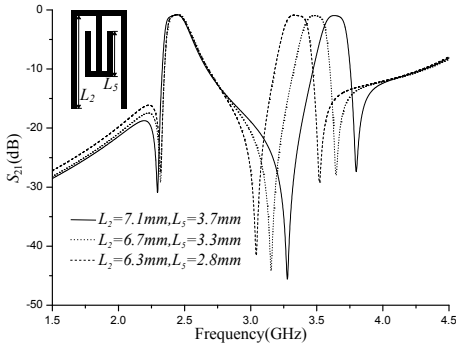

Figure 6: Design of the proposed filter with different center frequencies.

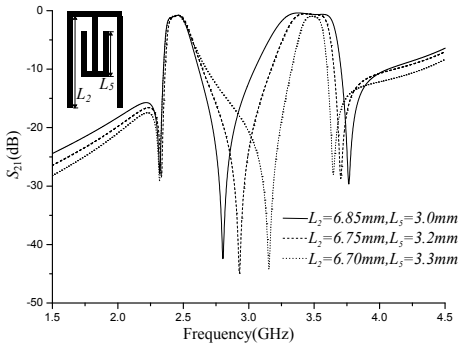

Figure 7: Design of the proposed filter with different FBWs.

pected passband center frequency and the expected FBW, then setting the length of L_2, which is a part of $\lambda/2$ line, to make the f_{odd} equal to the expected upper cut-off frequency or the lower cut-off frequency. Secondly, setting the length of L_5, which is a part of stub-loaded line, to make the f_{even} equal to another cut-off frequency. Meanwhile, the transmission zero is near to the f_{even}. Finally, regulate the feeder line L_{10} to make the passband response flat, as shown in Fig.5. Fig.6 and Fig.7 show different center frequencies and different FBWs simulation results to prove the design process is adapted. Besides, because of the parallel structure, this design process is also adapted to the first passband. The simulation results prove that the proposed filter has the advantage of two passband center frequencies and two FBWs which can be easily controlled by only few parameters and can be designed independently. To proving the simulation, a 2.35G/3.35G dual-band BPF with same FBW of 5% is designed and fabricated. The substrate we used in this design is Rogers RT/Duriod 6010, whose ε_{eff} is 10.8, $\tan\delta$ is 0.0023, substrate thickness is 1.27mm, and the copper thickness is 0.07mm. The dimensions are chosen as follows: W_1=1.0mm, W_2=W_3=W_4=W_5=0.4mm, S_1=S_2=0.3mm, S_3=1mm, L_1=4mm, L_2=7.1mm, L_3=4mm, L_4=2mm, L_5=2.9mm, L_6=8.7mm, L_7=6mm, L_8=4mm, L_9=3mm, L_{10}=3.3mm, L_{11}=3.5 mm. Its photograph and the S-parameter simulation and measurement results are shown

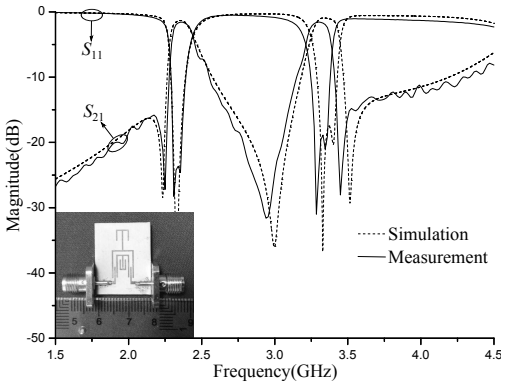

Figure 8: Simulated and measured results.

in Fig.8. The first passband with center frequency of 2.35-Ghz has less than 1.4-dB insertion loss and greater than 23-dB return loss. The second passband with center frequency of 3.35-Ghz has less than 1.5-dB insertion loss and greater than 20-dB return loss. In addition, three pairs of transmission zeros provide a better cutoff rate in the stopband.

3. Conclusions

This paper presented a compact microstrip dual-band BPF using $\lambda/2$ SLRs. The proposed dual-band filter comprises two dual-mode single band filters using common input/output lines. Each single band filter comprises a $\lambda/2$ SLR. The proposed dual-band BPF possesses the advantage that the passband center frequency and the FBW can be easily controlled by tuning only few parameters and designed independently. This paper presents the brief analysis of the SLRs and introduces the structure and design approach of the proposed filter. A dual-band BPF is designed and physical realized to prove that the analysis and the measured results agree with simulations very well.

References

[1] Y.P. Zhang and M. Sun, Dual-Band microstrip bandpass filter using stepped-impedance resonators with new coupling schemes, *IEEE Trans. Microw. Theory Tech.* 54: 3779-3785, 2006.

[2] C.-H. Lee, Hsu, C.-I.G. and H.-K. Jhuang, Design of a new tri-band microstrip BPF using combined quarter-wavelength SIRs, *IEEE Microw. Wireless Compon. Lett.* 16: 594-596, 2006.

[3] X.Y. Zhang and J.X. Chen, Dual-band filters using stub-loaded resonators, *IEEE Microw. Wireless Compon. Lett.* 17: 583-585, 2007.

[4] G. Chaudhary, Y. Jeong and J. Lim, Dual-band bandpass filter with independently tunable center frequencies and bandwidths, *IEEE Trans. Microw. Theory Tech.* 61: 107-116, 2013.

Triplexers based on coupled resonators: design and comparision of two different topologies

Lidiane da Silva Araújo
Antonio Jeronimo Belfort de Oliveira
Dep. de Eletrônica e Sistemas
Universidade Federal de Pernambuco
Recife, Brasil
lidiane-sac@hotmail.com
belfort@ufpe.br
*corresponding author, E-mail: lidiane-sac@hotmail.com

Abstract

This paper presents results of computer simulations of two triplexers with 9 resonators each one, conceived in two different topologies. One of them is designed with 6 resonators on its stem and the other one, with the topology of 3. Results show that the triplexer with 6 resonators presents lower performance than the one with 3 as for the reflection and insertion losses and isolation between their output ports. Results were obtained by optimizing the coupling coefficient matrix using the a Gradient based Method.

1. Introduction

Multiplexers are devices widely used in telecommunication systems to separate, in the same transmission medium, signals in different frequency bands. So, for example, a satellite antenna that receives signals from Earth, gets them into different channels totaling a very wider band. These signals before being returned back to Earth, need to be regenerated. Satellite microwave circuits that handle these signals cannot operate with such wide bandwidth. They need to be separated and thus its signals are treated by devices operating in their respective bands. They are afterwards multiplexed, i.e. gathered again in a single transmission medium, and taken to another antenna that retransmits them back to Earth. As the transmission of data, voice and images becomes increasingly larger, so the multiplexers involved must also be. In order to meet that requirement, designers have to compact them in a smaller volume to reduce the room they occupy in the telecommunications systems that must be installed. Conventional multiplexers using physical junctions that have the function of dividing the input signal in several frequency bands need matching circuits to make them operate satisfactorily [1, 2, 3]. As a result, they would turn out to be bulkier sistems. Coupled resonator-based multiplexers have revealed suitable to provide size reduction [4, 5.6]. One of the attractive features is that their design also takes into account the matching procedure, which means no extra circuit is needed to match them. The values of the coupling coefficients obtained by optimization are such that the task of matching is inherent.

This paper uses the coupling theory to design two triplexers with 9 resonators. The technique used to design these triplexers is an adaptation of the one developed by Hong and Lancaster [7], and extended by Skaik and Lancaster [8]. Each design involves the optimization of the coupling matrix by a Gradient based Method which searches for local minimum. A comparative study between them for two different topologies are presented. The tested topologies differ from each other by the number of resonators existing on the stem of each triplexer. The first of these includes 3 resonators on its stem, while the second includes 6 resonators, both totaling 9 resonators. The triplexers were designed with the same characteristics; that is, Tchebyshev frequency response with ripple 0.04321 dB and 3rd order Filtering Function. Curves showing reflection and insertion losses and isolation were obtained after optimized coupling matrix is achieved for each triplexer. The results show that the topology that has 6 resonators on its stem presents lower performance compared to the one with only 3 resonator.

2. Triplexers descriptions

2.1. Topology of the proposed triplexers

Two triplexers have been designed and their performances analyzed from computer simulations. Both triplexers were designed with 9 resonators, which yield better selectivity. Fig. 1 shows the topology of each triplexer. The first triplexer, illustrated in Fig. 1 (a), presents 3 resonators on the stem and 2 resonators in each output branch after the distributor resonator, which is the resonator of number 3. The second triplexer presents 6 resonators on the stem and only one resonator in each output branch after the distributing resonator, which is the one of number 6, as shown in Fig. 1 (b). The resonators are characterized by their resonance frequency and the relation between neighboring resonators e represented by the coupling coefficient m_{ij}. Given the geometry of the resonator, the coupling between them can be electric, magnetic or mixed. Coupling coefficients and the external quality factors q_{ei} are important elements in the design of a triplexer. For the desired center frequency, those parameters depend on the resonator chosen geometry.

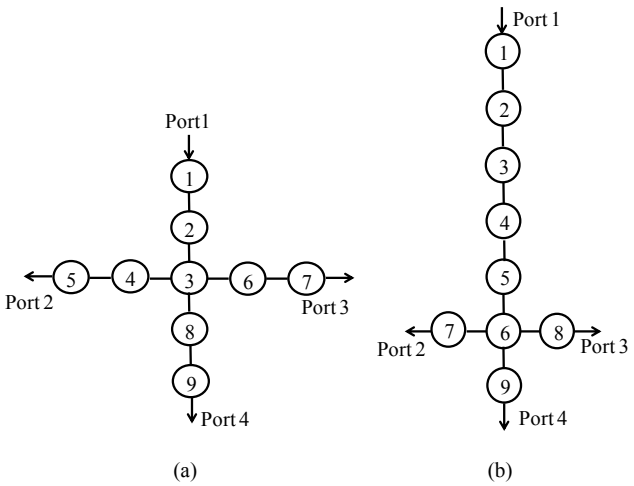

Figure 1: Topology of the proposed triplexers: (a) triplexer with 3 resonators on the stem; (b) triplexer with 6 resonators on the stem.

3. Computer simulation results for the two triplexers

3.1 Triplexer with 3 resonators on the stem

Considering 0.125 Hz as the normalized bandwidth, a Tchebyshev response with ripple of 0.04321 dB and a 3rd order Filtering Function for each one of the output bands of the triplexer, the optimized coupling coefficients obtained from computer simulation were: m_{12}= 0.6543; m_{23}= 0.6816; m_{34}= 0.0963; m_{45}= 0.0569; m_{44}= 0.9263; m_{55}= 0.9343; m_{38}= 0.1349; m_{89}= 0.0887. The external quality factors calculated are [7]: q_{e1}= 4.54; q_{e5}=q_{e7}= 13.62 and q_{e9}= 11.0. The return and insertion losses for the triplexer are shown in Fig. 2. The return loss was very close to the value for which it was designed (-20 dB). The bandwidth of the output signal from port 2 is greater than the ones from the side ports because the coupling coefficient m_{38} is different from the coefficients m_{34} and m_{36}. The curves for the isolation between ports 2 and 3, 2 and 4 are shown in Fig. 3. It can be observed that the responses for the reflection and insertion losses are very good. It can also be observed that the isolation between ports 2 and 4 reach excellent values, around -40 dB.

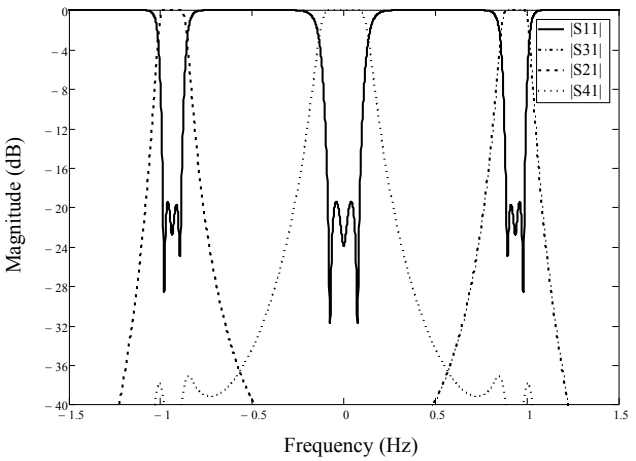

Figure 2: Reflection and transmission losses for the triplexer of Figure 2(a).

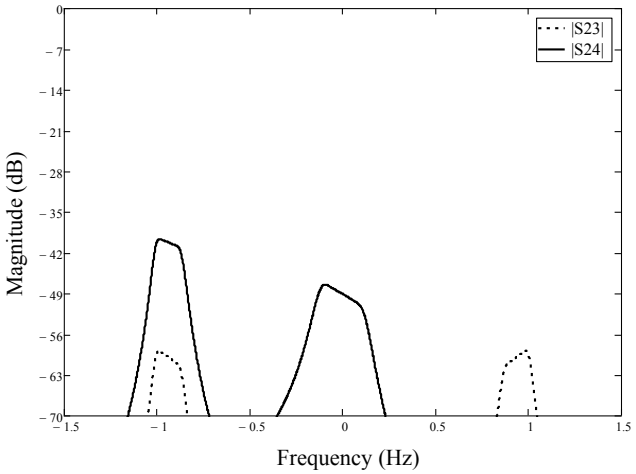

Figure 3: Isolation performance between ports 2 and 3, and between ports 2 and 4 for the triplexer with 3 resonators on the stem.

3.2 Triplexer with 6 resonators on the stem

Considering also a normalized bandwidth of 0.125 Hz, a Tchebyshev response with ripple of 0.04321 dB and a 3rd order Filtering Function for each one of the output bands, the optimized coupling coefficients obtained from computer simulation were: m_{12}= 0.7494; m_{23}= 0.5810; m_{34}= 0.2158; m_{45}= 0.8149; m_{56}= 0.4237; m_{67}= 0.1947; m_{69}= 0.0802; m_{77}= 0.8955. The external quality factors were calculated [7]: q_{e1}= 4.54; q_{e5}=q_{e7}= 13.62 and q_{e9}= 11.0. The return and insertion losses for the triplexer are shown in Fig. 4. The responses for the isolation between ports 2 and 3, 2 and 4, are shown in Fig. 5.

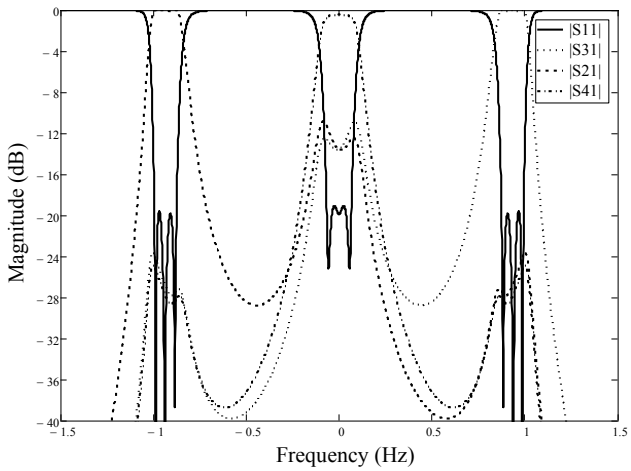

Figure 4: Reflection and transmission losses for the triplexer of Fig. 2(a).

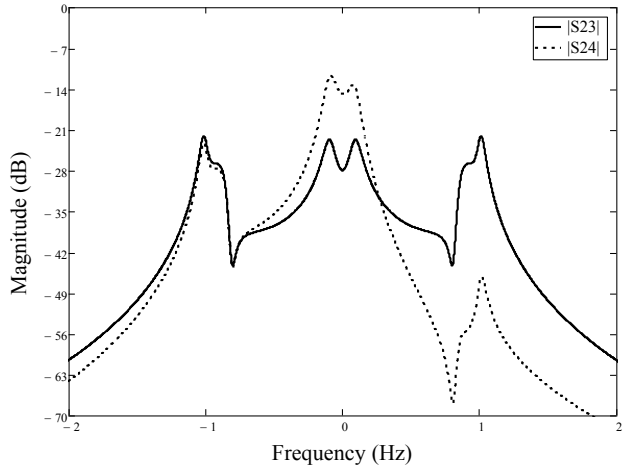

Figure 5: Isolation performance between ports 2 and 3, and between ports 2 and 4 for the triplexer with 6 resonators on the stem.

The reflection loss of the sidebands showed excellent performance as the zeros of reflection and the maximum value of the peaks were very close to the value for which it was designed; i.e. -20 dB. The central band no longer had equal performance. Their corresponding curve presented peaks of return loss a bit larger than the one for whicht it was designed. It can be seen that increasing the number of resonators in the design of a multiplexer, does not necessarily improve its performance. The topology used in the design plays very important role in obtaining the expected performance for the triplexer. It can be observed that the isolation is not very good for this topology, especially for the central band, where its peak is around -11 dB.

4. Conclusions

Two triplexers of 9 coupled resonators were designed with the same features for the same normalized frequency band. One of them was conceived with 3 resonators on the stem and the other with 6 resonators. For both triplexers, the coupling matrix has been optimized by a Gradient based Method searching for local minima. Results of computer simulations showed curves of reflection and transmission losses and also isolation between the output ports of each triplexer. They suggest that, in the design, the maximum number of resonators must be used after the distributing resonator in order to increase the isolation between the output ports, which also contributes to the overall performance of the triplexer. Isolation for the triplexer with 3 resonators on the stem reached excellent values less, than -40dB, whereas the triplexer with 6 achieved values as high as -11 dB.

References

[1] P. Deng, M.. Lai, S. Jeng and C. H. Chen, “Design of Matching Circuits for Microstrip Triplexers Based on Stepped-Impedance Resonators. IEEE Trans. on Mircowave Theory and Technique, vol. 54, n.. 12, dez. 2006.

[2] G. Macchiarella and S. Tamiazzo, “Design of triplexer combiners for base stations of mobile communications,” IEEE MTT-S International Microwave Symposium Digest, Milan, Itália, 2010, pp. 429-432.

[3] S. Bastioli, L. Marcaccioli and R. Sorrentino, “An original resonant Y-junction for compact waveguide diplexers,” IEEE MTT-S International Microwave Symposium Digest, Boston, USA, junho 2009, pp. 1233-1236.

[4] C. Chen, T. Huang, T. Shen and R. Wu, “A miniaturized microstrip common resonator triplexer without extra matching network,” Asia-Pacific Microwave Conference, Yokohama, Japan, 2006.

[5] X. Zhang, M. He and X. Zhao, “Compact design of high temperature superconducting duplexer and triplexer for satellite communications,” Supercond. Sci. Technol., vol. 25, pp. 1-5, julho, 2012.

[6] P. Castilllo-Aranibar, P. Rodriguez-Postigo, A. Garcia-Lamperez e D. Segovia-Vargas, “Compact Triplexer w Bandpass Filters for Asymetric Bandpass Filters for Asymetric Response,” IMOC2013 International Microwave and Optical Electronics Conference, Rio de Janeiro, Brasil, setembro, 2013.

[7] J. S. Hong and M. J. Lancaster, “Microstrip filters for RF/microwave applications. New York, Wiley, 2001.

[8] T. F. Skaik, M. J. Lancaster and F. Huang, “Synthesis of multiple output coupled resonator circuits using coupling matrix optimization, ” IET Microwave, Antennas and Propagation, vol. 5, ed.9, pp. 1081-1088, June,2011.

Wideband Circularly-Polarized Smart-Skin Microstrip Antenna

Ming-Tao Tan and Bing-Zhong Wang

Institute of Applied Physics,University of Electronic Science and Technology of China,Chengdu, China
*corresponding author, E-mail: mingtaotan@163.com

Abstract

This paper presents a novel wideband circularly-polarized smart-skin antenna. The smart skin is an organic honeycomb sandwich structure. When the antenna is embedded in honeycomb sandwich structure, smart-skin antenna is formed. Electromagnetic simulation shows that the proposed smart-skin antenna has a good impedance match and circular polarization performances around 20GHz.

1. Introduction

Traditional practice in antenna design has been to design the radome and antenna as separate entities, and resolve any interface problems afterwards. Recently there has been interest in designing a structurally-integrated antenna, the so-called smart-skin antenna. Smart-skin antenna emerged from the rise of conformal antenna. Smart-skin antenna technique is to satisfy both structural efficiency and antenna performance. Structures, electronics, materials, and manufacturing should be considered in the design of smart-skin antenna. In particular, it is important to satisfy mechanical and electrical requirements. Since the early 1990s, much research has been done on the embedding of antennas in load-bearing structural surfaces [1-5]. In [2], a smart-skin antenna using a multilayer honeycomb sandwich structure was presented, as well as a design procedure that includes structure design, material selection, and radiator design so as to achieve high electrical and structural performance. Ref. [3] points out that a high gain is obtained by placing an outer facesheet at a half wavelength distance from a radiating patch antenna. The honeycomb sandwich structures embedded with antenna was investigated experimentally and good structural performance was confirmed [4].

Wideband circularly-polarized smart-skin antennas have wide applications in satellite communication, navigation, radar, and so on. This paper presents a structurally-integrated smart-skin microstrip antenna. The antenna has not only a good impedance match and circular polarization performances around 20GHz, but also an excellent structural performance.

2. Antenna Design

Fig. 1 shows the geometrical configuration of the proposed wideban circularly-polarized smart-skin antenna. The antenna has eight layers, which includes facesheet, upper honeycomb, upper patch, lower honeycomb, lower patch, substrate, ground plane, and back facesheet. In order to make the structurally-integrated antenna sustain axial loads, honeycomb layers are positioned on two sides of the radiation patch. In electromagnetic simulation process, honeycomb material is approximately modeled using a material with a relative permittivity of 1.1. The thicknesses of the upper honeycomb layer and the lower one are 3.5mm and 2mm, respectively. The two facesheets can mechanically carry a significant portion of in-plane loads, contribute to overall panel buckling resistance, and provide low velocity impact and environmental resistance. The facesheet uses a glass/epoxy composite with a relative permittivity of 4, and a loss tangent of 0.03. The thicknesses of facesheet and back facesheet are 3mm. The upper patch and lower patch resonate at a little different frequencies because the sizes of the two patches differ slightly, which can enhance the impedance bandwidth of the smart-skin antenna. The dielectric substrate below lower patch uses RogersRT5880 material with a thickness of 0.254mm and a relative permittivity of 3.48. The truncated corners on the two patches are used to disturb current distributions on the patch so that circular polarization can be excited. Designed antenna elements with their dimensions are shown in Fig. 2. The units of the dimensions are millimeter (mm).

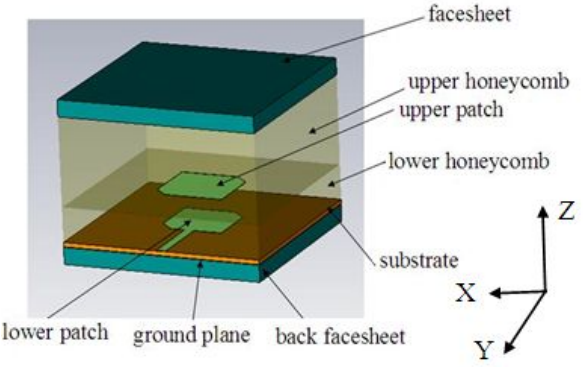

Figure 1: Configuration of the proposed antenna.

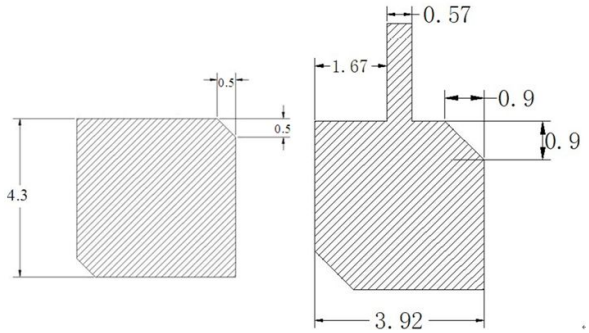

Figure 2: Designed antenna elements: upper patch (left); lower patch (right). (unit: mm)

3. Simulated Results

The antenna design and optimization are carried out using CST Microwave Studio. Fig. 3 shows the simulated reflection coefficient of the proposed antenna. The simulated -10dB impedance bandwidth is from 18.7 to 22.1GHz. The simulated variations of axial-ratio (AR) against frequency of proposed antenna in the $+z$ axis direction are shown in Fig. 4. It is seen from the figure that 3-dB AR bandwidth of the proposed antenna ranges from 19.2 to 21.1GHz. Fig. 5 presents the simulated far-field radiation patterns of proposed antenna in zoy plane (E-plane) and zox plane (H-plane) at 20.4GHz; good broadside radiation patterns are observed. Fig. 6 shows the simulated antenna gains in the $+z$ axis direction. The gains are steady and above 10dB from 19.0 to 22.5GHz.

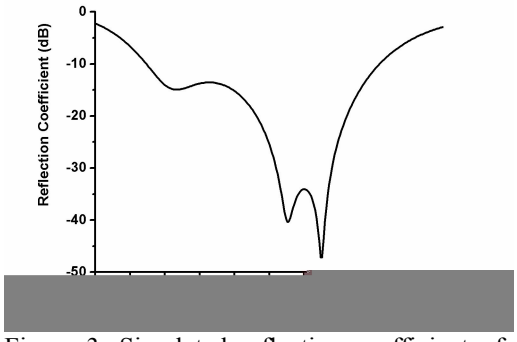

Figure 3: Simulated reflection coefficient of the proposed antenna.

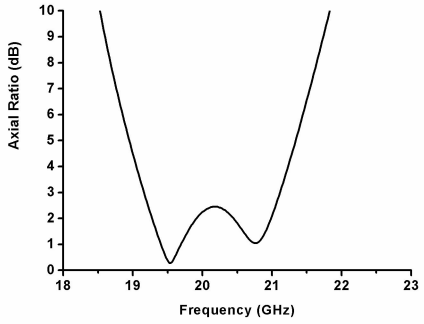

Figure 4: Simulated AR of the proposed antenna.

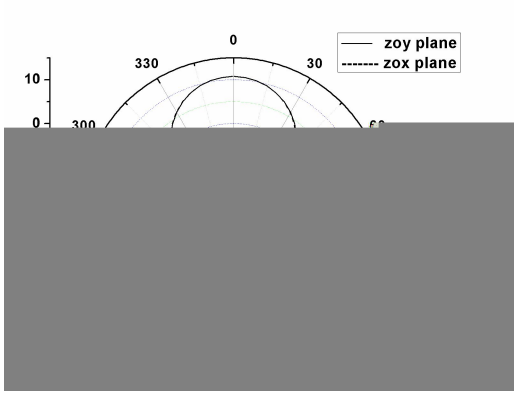

Figure 5: Simulated radiation patterns of the proposed antenna at 20.4 GHz.

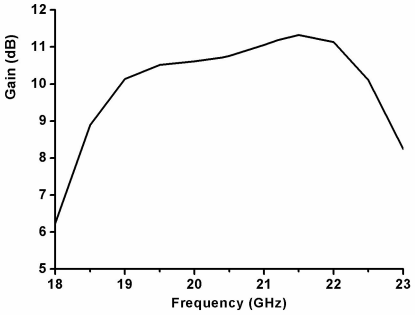

Figure 6: Simulated gains for the proposed antenna.

4. Conclusions

A novel structurally-integrated and wideband circularly-polarized smart-skin antenna is presented. The antenna has not only an excellent structural performance, which can sustain axial loads and in-plane loads, but also a good impedance match and circular polarization performances around 20GHz. These good performances make the antenna can be used in practical aircrafts, ships, and so on.

Acknowledgements

This work was supported by the National Natural Science Foundation of China (No. 61331007 and No. 61361166008), the Research Fund for the Doctoral Program of Higher Education of China (No. 20120185130001), and the Project ITR1113.

References

[1] C. S. You, M. M. Tentzeris, and W. B. Hwang, "Multilayer effects on microstrip antennas for their integration with mechanical structures," IEEE Transactions on Antennas and Propagation, vol. 55, pp. 1051-1058, Apr 2007.

[2] C. S. You and W. B. Hwang, "Design of load-bearing antenna structures by embedding technology of microstrip antenna in composite sandwich structure," Composite Structures, vol. 71, pp. 378-382, Dec 2005.

[3] C. S. You, W. Hwang, and S. Y. Eom, "Design and fabrication of composite smart structures for communication, using structural resonance of radiated field," Smart Materials & Structures, vol. 14, pp. 441-448, Apr 2005.

[4] J. H. Jeon, W. Hwang, H. C. Park, and W. S. Park, "Buckling characteristics of smart skin structures," Composite Structures, vol. 63, pp. 427-437, Feb-Mar 2004.

[5] S. H. Son, S. Y. Eom, and W. B. Hwang, "Development of a smart-skin phased array system with a honeycomb sandwich microstrip antenna," Smart Materials & Structures, vol. 17, Jun 2008

A Low-Profile and Tightly-Coupled Microstrip Array with Wide-Angle Scanning Performance Based on Time Reversal Synthesis Method

Ren Wang, Bing-Zhong Wang*, Xiao Ding, and Ya-Qing Wen

Institute of Applied Physics, University of Electronic Science and Technology of China, Chengdu, China
*corresponding author, E-mail: bzwang@uestc.edu.cn

Abstract

A low-profile and tightly-coupled microstrip array with wide-angle scanning performance based on time reversal synthesis method is proposed. The profile of the antenna is only 0.03λ and the distance between elements is 0.25λ, where λ is the wavelength in free space corresponding to the designed operation frequency 5.8 GHz. The excitation signals of the array are determined with time reversal synthesis method. The main lobe of the array can scan from -73° to +73° with a directivity fluctuation less than 3 dB and the scanning beamwidth of 3 dB can cover a large range from -86° to +85°. It shows that the time reversal synthesis method can be used to optimize tightly-coupled array efficiently.

1. Introduction

Generally, the main lobe of a planar array can only scan from -50° to +50° with a gain fluctuation of 4-5 dB because of the limited beamwidth of elements and mutual coupling between elements [1], [2]. In reference [3], a multi-panel approach for phased array to obtain wide-angle scanning performance is introduced, but its mechanical adjusting is not suitable for fast beam-scanning. In references [4] and [5], jointly covering a large scanning range with some narrow beam using pattern reconfigurable elements is proposed. The planar phased array can scan its main lobe to ±60° or even more with this method. However, side lobe level (SLL) can reach to -3.2 dB because the mutual coupling problem is not solved well. Besides, the profile of the arrays is 0.15-0.25λ [4], [5].

Time reversal electromagnetic wave can focus temporally and spatially in the location of the wave source at the same time [6]. Recently, time reversal technique has been used to steer beam of arrays and the main lobe can be scan to ±60° [7], [8]. Reference [9] introduced a synthesis method for beam-steering arrays based on the focusing characteristic of time-reversed electromagnetic wave. This method can optimize arbitrarily structured array adaptively. But the time reversal synthesis method has not been used for wide-angle scanning array with tight coupling.

In this paper, a low-profile and tightly-coupled microstrip array with wide-angle scanning performance based on time reversal synthesis method is proposed. The main lobe of the array can scan from -73° to +73° in the *yoz* plane with a directivity fluctuation less than 3 dB.

2. Low-profile and tightly-coupled microstrip array design

The structure and dimension of the low-profile microstrip antenna element is shown in Figure 1. Its radiator is a rectangular patch fed from the back of dielectric substrate with a full ground by a 50Ω coaxial cable. The feeding point is located in the middle of the long side of the rectangular patch. The substrate has a thickness of 1.6 mm and a relative dielectric constant of 4.4. The profile of the antenna is only 0.03λ, where λ is the wavelength in free space corresponding to the designed operation frequency 5.8 GHz.

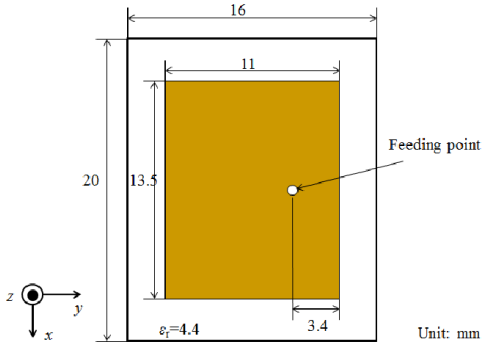

Figure 1: Structure of the low-profile microstrip antenna.

The proposed antenna is designed using CST Microwave Studio. Its simulated reflection coefficient and radiation patterns are shown in Figure 2. The S11 is less than -10 dB in the frequency band from 5.68 GHz to 5.95 GHz. In the E plane (*yoz* plane), its main lobe points at direction θ=+2° with a directivity of 5.8 dBi and a half power beam width (HPBW) of 101°. In the H plane, its main lobe points at direction θ=0° with a directivity of 5.8 dBi and a HPBW of 92.6°. Next, we will arrange the antenna array along the *y* axis because of the wide beamwidth in the E plane. The structure of the low-profile and tightly-coupled microstrip array with 16 elements is shown in Figure 3. The distance between each element is about 0.25λ.

Figure 4 is the comparison of the radiation patterns between the single antenna and some elements in the array. The active radiation patterns have some fluctuation at the main beam. The half power beams of elements 1, 5, 9, and 13 are from -10° to +78°, from -75° to +25°, from -73° to +40°, and from -45° to 74°, respectively. By using the coupling between elements, the beam coverage area of the elements in the array is larger than the single antenna, which is helpful to wide-angle scanning.

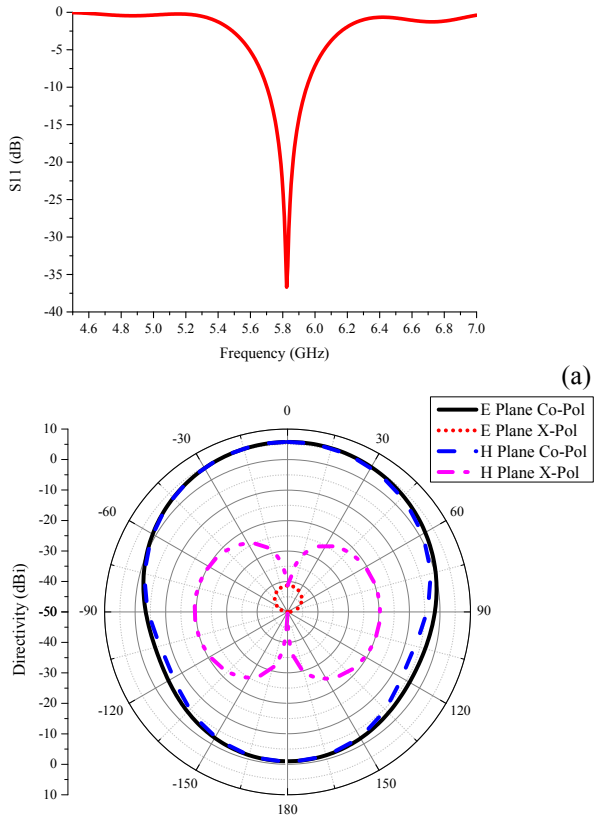

Figure 2: (a) S11 and (b) radiation patterns of the low-profile microstrip antenna.

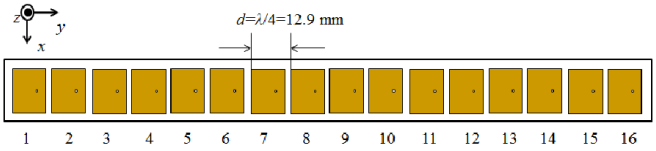

Figure 3: Structure of the low-profile and tightly-coupled microstrip array.

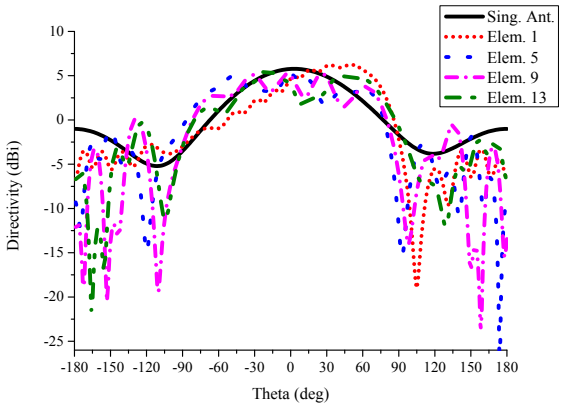

Figure 4: Comparison of radiation patterns of *yoz* plane between the single antenna and some antenna elements in the array.

3. Performance of the wide-angle scanning array based on time reversal synthesis method

Generally, it is difficult and time-consuming to optimize radiation patterns of tightly-coupled array based on pattern multiplication theorem. However, time reversal synthesis method which can consider coupling adaptively will deal with the problem well without repeated optimization.

The basic process of time reversal synthesis method is: (1) The array to be optimized is illuminated by a plane wave with a temporal waveform that covers the operating frequency bandwidth of the array from the desired steering angle; (2) Each element of the array receives the signal at the same time and time-reverses it; (3) Each element of the array transmits the time-reversed signal, which is noted as the time-reversal excitation signal method (TRESM); (4) The signal focuses to the direction that the plane wave comes from, so that the desired main beam direction will be obtained.

In the simulation, the plane wave signal is a Gaussian-modulated sinusoidal pulse with a frequency range of 0-2f_0, where f_0 is the operation frequency of the array, and f_0=5.8GHz. It is worth noting that the signals of TRESM fed to the elements are not the modulated Gaussian pulse anymore because of the strong coupling between elements.

Figure 5 is the simulation scanning performance in *yoz* plane at 5.8 GHz of the array excited with TRESM. Table 1 is the radiation pattern information of scanning performance corresponding to Figure 5. The main lobe of the array can scan from -73° to +73° in the *yoz* plane with a directivity fluctuation less than 3 dB and SLL less than -7.8 dB using the time reversal synthesis method. The scanning beam-width of 3 dB can cover a large range from -86° to +85°.

From Table 1, when the desired steering angle is within the range of -60° to +60°, the main beam of the array can direct to the direction that the plane wave comes from accurately. However, when the desired steering angle is beyond the range of -60° to +60°, deviation between the main beam direction and the plane wave incidence direction will occur. In that case that the plane wave comes from -90°, the main beam direction is only -73°. This phenomenon is likely due to multiple factors and the following are two main reasons. Firstly, the half power beam of each element cannot cover the end-fire direction. Secondly, the effective aperture of the array to receive signals decreases with the increase of incident angle of the plane wave, so, at large scanning angle, the array cannot receive enough information of the plane wave to re-establish its wavefront.

Next, we suggest a method to build a simplified time reversal excitation signal suitable for phased arrays. After the nth element of the array receiving the Gaussian-modulated sinusoidal pulse plane wave, we do Fourier transform to the received signal and extract its amplitude A_n and phase φ_n at f_0. And then, the nth element of the array is excited with a Gaussian- modulated sinusoidal pulse with a frequency range of 0-2f_0 and a corresponding amplitude A_n and a opposite phase $-\varphi_n$ at f_0, which is noted as the simplified time reversal excitation signal method (S-

TRESM). The excitation signals of S-TRESM with the same spectrum distribution are suitable for phased array.

Figure 6 is the comparison of radiation patterns between TRESM and S-TRESM. The radiation patterns of the two excitation methods agree well, which means that the amplitude and phase of the excitation signal suitable for phased array can be determined with the time reversal synthesis method.

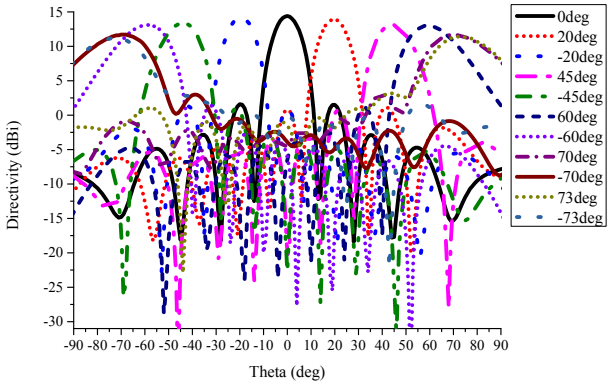

Figure 5: Simulation scanning performance in *yoz* plane at 5.8GHz of the array excited with TRESM.

Table 1: Radiation pattern information of scanning performance in *yoz* plane at 5.8GHz of the array. θ_1 is the incidence angle of the plane wave, θ_2 is the main lobe direction corresponding to θ_1.

θ_1 (degree)	θ_2 (degree)	Directivity (dBi)	SLL (dB)	HPBW (degree)
0	0	14	-12.8	11.9
20	20	13.8	-12.8	12.6
-20	-20	13.9	-12.8	12.6
45	45	13.1	-12.4	16.4
-45	-45	13.4	-12.3	16.2
60	60	13	-11.8	22.3
-60	-60	13.1	-11.9	22.4
72	70	11.7	-8.3	28.7
-72	-70	11.8	-8.4	28.6
90	73	11.4	-8	28.9
-90	-73	11.2	-7.8	29.3

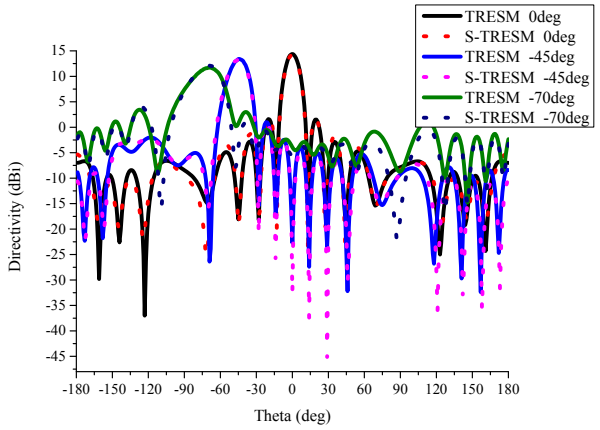

Figure 6: Comparison of radiation patterns in *yoz* plane at 5.8GHz of the array between TRESM and S-TRESM.

4. Conclusions

In this paper, a low-profile and tightly-coupled microstrip array with wide-angle scanning performance based on time reversal synthesis method is proposed. The distance between each element is about 0.25λ and the profile of the antenna is only 0.03λ. The main lobe of the array can scan from -73° to +73° with a directivity fluctuation less than 3 dB and the scanning beam-width of 3 dB can cover a large range from -86° to +85°. The time reversal adaptive synthesis method can be used to optimize tightly-coupled array efficiently.

Acknowledgements

This work was supported by the National Natural Science Foundation of China (No. 61371007, No. 61361166008 and No. 61401065), and the Research Fund for the Doctoral Program of Higher Education of China (No. 20120185130001).

References

[1] C. A. Balanis, *Antenna Theory, Analysis and Design*, 2nd ed., New York, NY, USA: Wiley, 1997.

[2] S. E. Valavan, D. Tran, A. G. Yarovoy, and A. G. Roederer, "Dual-band wide-angle scanning planar phased array in X/Ku-bands," *IEEE Trans. Antennas Propag.*, vol. 62, no. 5, pp. 2514-2521, May 2014.

[3] A. G. Toshev, "Multipanel concept for wide-angle scanning of phased array antennas," *IEEE Trans. Antennas Propag.*, vol. 56, no. 10, pp. 3330-3333, Oct. 2008.

[4] Y. Y. Bai, S. Q. Xiao, M. C. Tang, Z. F. Ding, and B.-Z. Wang, "Wide-angle scanning phased array with pattern reconfigurable elements," *IEEE Trans. Antennas Propag.*, vol. 59, no. 11, pp. 4071-4076, Nov. 2011.

[5] X. Ding, B.-Z. Wang, and G.-Q. He, "Research on a millimeter-wave phased array with wide-angle scanning performance," *IEEE Trans. Antennas Propag.*, vol. 61, no. 10, pp. 5319-5324, Nov. 2013.

[6] R. Carminati, R. Pierrat, J. Rosny, and M. Fink, "Theory of the time reversal cavity for electromagnetic fields," *Opt. Lett.*, vol.32, no. 21, pp. 3107-3109, Oct. 2007.

[7] D. Carsenat and C. Decroze, "UWB antennas beamforming using passive time-reversal device," *IEEE Antennas and Wireless Propagat. Lett.*, vol. 11, pp. 779-782, 2012.

[8] S. K. Hong, V. Mendez, W. S. Wall, and R. Liao, "Single-feed beam-steering of short pulses via time reversal," *IEEE Antennas and Wireless Propagat. Lett.*, vol. 13, pp. 794-797, 2014.

[9] D. Zhao, Y. Jin, B.-Z. Wang, R. Zang, "Time reversal based broadband synthesis method for arbitrarily structured beam-steering arrays," *IEEE Trans. Antennas Propag.*, vol. 60, no. 1, pp. 164-173, Jan. 2012.

Ultra-Compact Superdirective Two- and Three-Element Linear Arrays

Abdullah Haskou[1], Antonio Clemente[2,3], Ala Sharaiha[1], Christophe Delaveaud[2,3], Sylvain Collardey[1], and Lionel Rudant[2,3]

[1]IETR UMR CNRS 6164- Université de Rennes 1, Rennes, France
[2]Univ. Grenoble-Alpes, Grenoble, France
[3]CEA, LETI, Minatec Campus, 17 rue des Martyrs, 38054 Grenoble, France
*corresponding author, E-mail: abdullah.haskou@univ-rennes1.fr

Abstract

Superdirective parasitic arrays of two- and three-planar printed small loop antennas are presented. The unit-element dimensions are $\frac{\lambda}{14} * \frac{\lambda}{17}$. It is shown that these antenna arrays with an inter-element spacing of 0.064λ present maximum directivities of $6.3dBi$ and $9dBi$ respectively. Simulation results are provided and discussed.

1. Introduction

Antenna arrays are highly used in applications where directive beams are required. Superdirective antenna arrays are a class of arrays that can be designed to achieve higher directivities than those obtained from the uniformly excited equally spaced equivalent arrays. It was shown in [1, 2] that the end-fire directivity of collinear dipole radiators, one excited and the others parasitic, approaches a value of N^2 as the inter-element distance approaches zero. This is also desirable in some applications, where compact size arrays are required. Two electrically small superdirective antenna arrays were presented in [3, 4].
In this paper, loop parasitic arrays of two- and three- elements are proposed. The array parasitic elements are loaded with complex loads to enhance the array directivity.[1]

2. Single element description

The unit element used in these arrays is a shorted loop antenna loaded by a capacitance. The use of the capacitance and the short circuit allowed miniaturizing the antenna without significantly disturbing the performance of the antenna (narrower bandwidth). Thus, the single element is electrically small since its diameter is equal to $\lambda/11$. The capacitance of the single element shown in Fig. 1(a) is realized by two metallic strips (gap of $0.1mm$). The loop is realized on a 0.8mm-thick Rogers RO4003 substrate. The loop is fed by a capacitive coupling with a microstrip line placed on the opposite layer of the loop (Fig. 1(b)). The length and position of this microstrip feeding line allows shifting the resonance frequency and feeding coupling.

[1]This work was done with the funding of the French National Research Agency as part of the project "SOCRATE" and the support of the "Images et Reseaux" cluster of Brittany region, France.

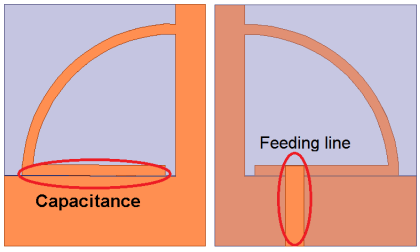

(a) (b)

Figure 1: The miniaturized unit-element. (a) Top view and (b) bottom view.

The single element presents a resonant frequency at $897MHz$, a radiation efficiency of 34%, and a directivity of $1.7dBi$ as shown in figures 2(a) and 2(b) respectively.

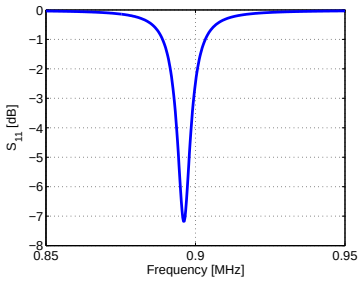

(a)

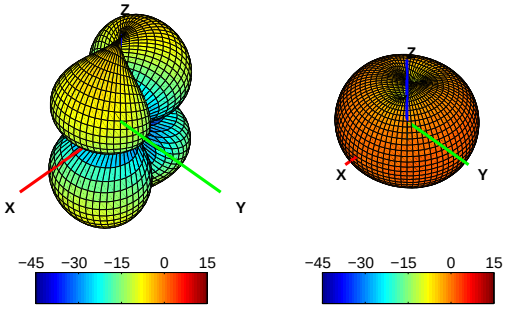

(b)

Figure 2: The miniaturized unit-element. (a) Antenna simulated input reflection coefficient and (b) antenna simulated 3D directivity (cross-polar (left) and co-polar (right)).

3. Parasitic array design

Two and three unit elements are placed in a row, as shown in Fig. 3(a) and Fig. 4(a) respectively. The inter-element distance is set to 0.064λ. Only the first element is fed while the other elements are parasitic. To improve the directivity of the arrays the most appropriate loadings are placed on the parasitic elements. These loads are calculated using the spherical wave expansion method [5]. As shown in Fig. 3(b) and Fig. 4(b), the maximum reached directivity for the two-element array is $6.3dBi$ and for the three-element array is $9dBi$.

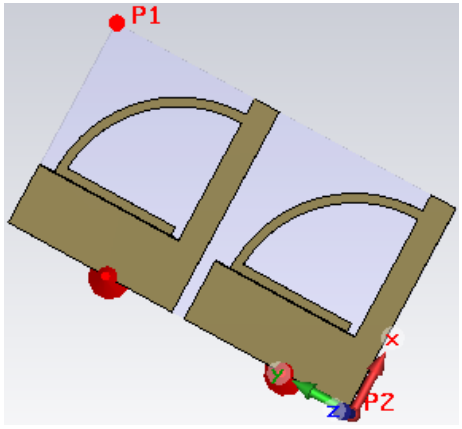

(a)

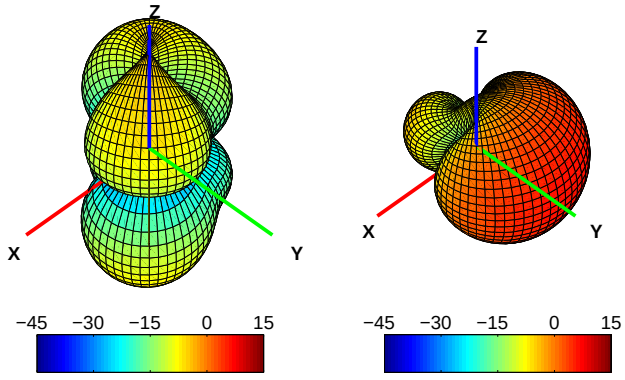

(b)

Figure 3: The two-element array. (a) The array geometry and (b) the array simulated 3D directivity (cross-polar (left) and co-polar (right)).

4. Conclusions

In this paper, parasitic two- and three-element superdirective electrically small antenna arrays were designed. Simulation results showed that these arrays have a maximum end-fire directivity of $6.3dBi$ and $9dBi$ respectively. Further details on the design procedure will be presented in the final version.

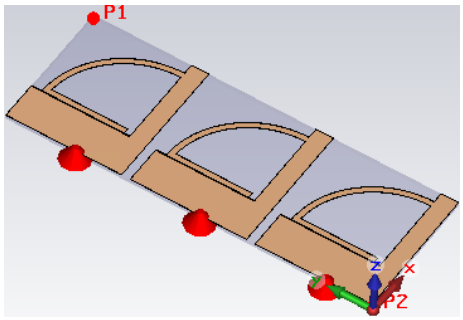

(a)

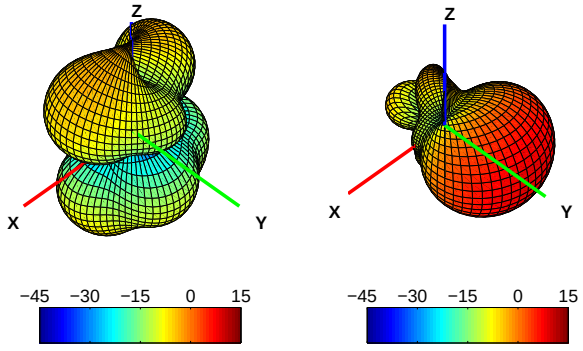

(b)

Figure 4: The two-element array. (a) The array geometry and (b) the array simulated 3D directivity (cross-polar (left) and co-polar (right)).

References

[1] T. H. O'Donnell, and A. D. Yaghjian, Electrically Small Superdirective Arrays Using Parasitic Elements, *IEEE Antennas and Propagation Society International Symposium 2006*, pp. 3111,3114, 9-14 July 2006.

[2] S. R. Best, E. E. Altshuler, A. D. Yaghjian, J. M. McGinthy, and T. H. O'Donnell, An Impedance-Matched 2-Element Superdirective Array, *IEEE Antennas and Wireless Propagation Letters*, vol. 7, pp. 302,305, 2008.

[3] M. Pigeon, A. Sharaiha, and S. Collardey, Miniature and Superdirective Two Elements Endfire Antenna Array, *8th European Conference on Antennas and Propagation (EuCAP 2014)*, 6-11 April 2014.

[4] A. Haskou, A. Sharaiha, S. Collardey, M. Pigeon, and K. Mahdjoubi, A Design Methodology for Electrically Small Superdirective Antenna Arrays, *2014 Loughborough Antennas and Propagation Conference (LAPC 2014)*, 10-11 November 2014.

[5] A. Clemente, M. Pigeon, L. Rudant, and C. Delaveaud, Super Directive Compact Antenna Design Using Spherical Wave Expansion, *2014 IEEE Antennas and Propagation Society International Symposium (APSURSI 2014)*, pp.571,572, 6-11 July 2014.

A Microstrip Triangular Spiral Resonator for a Tchebyshev Bandpass Filter Design

L. S. Araújo and A. J. Belfort de Oliveira

Department of Electronics and Systems
Federal University of Pernambuco
Recife-PE, Brasil
lidiane_sac@hotmail.com

Abstract

This paper presents the design and computer simulation results of a microstrip three pole Tchebyshev filter based on a triangular spiral resonator. Its performance is here reported and compared with the performance of a filter designed based on a simple microstrip triangular open loop resonator. The objective of the paper is to show that a triangular spiral resonator filter with 48% of the area of a filter based on the triangular open loop resonator can perform very similarly in the band of interest and with the same Tchebyshev characteristics.

1. Introduction

The use of coupled resonators in the design of microwave filters has drawn the interest of researchers specially because stringent requirements can only be met by using cross-coupled resonators. Besides, size reduction can also be achieved. Triangular resonators has drawn particular interest of filter designers because of the multiple schemes of coupling between them. Microstrip triangular coupled resonators used for bandpass filter design have been reported [1]. This paper describes how size reduction can be achieved for a Tchebyshev filter design by using triangular spiral resonators. Its performance is compared with the one of a single microstrip triangular open loop resonator filter here also designed and simulated for the same center frequency and Tchebyshev characteristics.

2. The three pole triangular resonator filters

Filter theory based on coupled resonators has been satisfactorily deployed in [1]. It has been shown therein that the external quality factor and the coupling coefficient (for a three pole filter, for instance) can be calculated by

$$Q_{e1} = \frac{g_0 g_1}{FBW} \tag{1}$$

$$Q_{e3} = \frac{g_3 g_4}{FBW} \tag{2}$$

$$M_{i,i+1} = \frac{FBW}{\sqrt{g_i g_{i+1}}} \quad \text{for } i=1, 2 \tag{3}$$

where g_i and FBW are the normalized low pass prototype element and fractional bandwidth, respectively. For a three pole Tchebyshev band pass filter with center frequency at 1.0 GHz, FBW=4% and a ripple of 0.1 dB (which means maximum reflection loss of -16 dB), the normalized low pass prototype elements can be found in [2]. They are g_0=1.0, g_1=1.0316, g_2=1.1474, g_3=1.0316 and g_4=1.0. Using (1), (2) and (3), the calculated values of the coupling coefficients and external quality factors are M_{12}=0.0552 and Q_{e1}=25.79. Also, $Q_{e1} = Q_{e3} = Q_e$.

2.1. Description of the coupled resonators

The two types of resonators employed to design the filters investigated here are shown in Fig. 1. The first one, depicted in Fig. 1(a), is the triangular open loop resonator (TOLR), and the second one, shown in Fig. 1(b), is called the triangular spiral resonator (TSR). Both resonators have resonance frequency around 1 GHz for the same value of gap g = 1 mm and width w = 1 mm on dielectric layers of thickness 1.27 mm and relative permittivity ε = 10.2. Their sides are 20.02 mm and 14.45 mm for the triangular open loop resonator (TOLR) and the triangular spiral resonator (TSR), respectively. The external quality factors, Q_e, for both resonators were extracted [2] for each feeding position t, using the expression

$$Q_e = 2\pi f_0 \cdot \tau_{S_{11}}(f_0)/4, \tag{4}$$

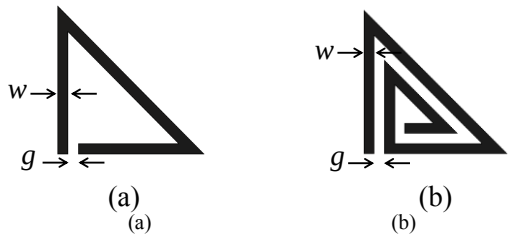

Figure 1: (a) Triangular Open Loop Resonator (TOLR) and (b) Triangular Spiral Resonator (TSR).

where $\tau_{S_{11}}(f_0)$ is the group delay of S_{11} for the frequency at which $\tau_{S_{11}}$ presents its maximum value (the resonance frequency, f_0).

The coupling coefficients (M) were extracted [2] as a function of s from expression

$$M = (f_{p2}^2 - f_{p1}^2)/(f_{p2}^2 + f_{p1}^2), \quad (5)$$

where f_{p1} and f_{p2} are the frequencies (obtained from computer simulations) for which the peaks of resonance are observed in the curve of $|S_{21}|$ for a pair of resonators being tested and for each separation s. The calculated values for the coupling coefficient M, from (3), are then taken into the curves of the extracted M, from which the physical spacing s is obtained. Similarly, the calculated values for the external quality factors, from (1) and (2), are taken into the extracted curves of Q_e, from which the feeding position t is obtained.

2.2. The three pole triangular open loop resonator filter (TOLR filter).

The layout of a three pole Tchebyshev filter using TOLRs is depicted in Fig. 2. The external quality factor calculated from (1) and (2), Q_e=25.79 was then extracted from computer simulation as a function of t and it was found to be t=8.44mm. As for the coupling coefficients, they were calculated from (3): M_{12}= M_{23}=0.036, which requires spacings of s_1=2.20 mm and s_2=2.32mm.

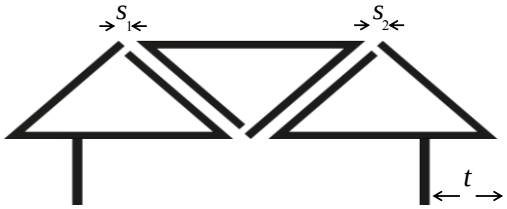

Figure 2: Scheme of a Tchebyshev three pole filter based on TOLRs.

2.3. The three pole triangular spiraled resonator filter (TSR filter).

The scheme of a three pole Tchebyshev band pass filter designed with microstrip triangular spiraled resonators is shown in Fig. 3. For the design, it is also required that Q_e=25.79 and M_{12}= M_{23}=0.036. As stated before, from computer simulations the coupling coefficients and external quality factors were extracted as functions of s and t, respectively. They were found to be t=11.6 mm, s_1=1.66mm and s_2=1.16mm.

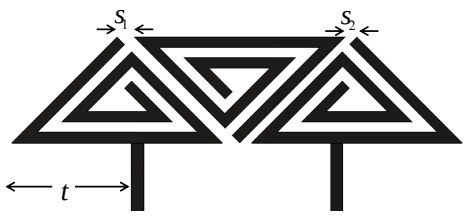

Figure 3: Scheme of a Tchebyshev three pole filter based on TSR.

2.4. Computer simulation results and comparison between the filters

Simulation results for both filters, based on TOLR and TSR, are shown in Figs. 4 and 5, respectively, using the same full wave software employed to extract the coupling coefficients and external quality factors. They show the reflection and transmission losses against frequency for f_0=1 GHz as the center frequency. It can be seen for the open loop resonator filter and also for the triangular spiraled resonator filter that the maximum peak value for the refection loss is around -14 dB. It can easily be seen that both filters cover very nearly the same frequency band.

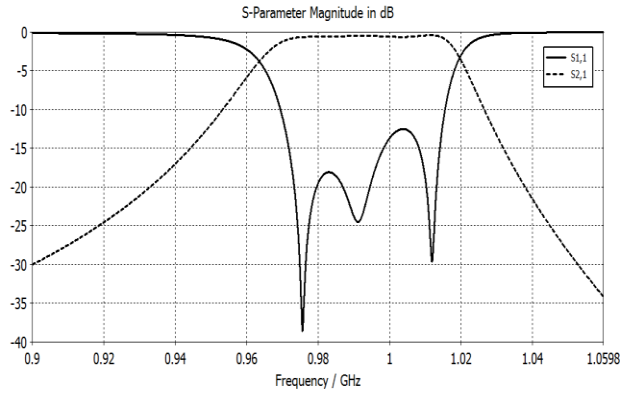

Figure 4: Simulation results obtained for the reflection and transmission losses for the TOLR filter.

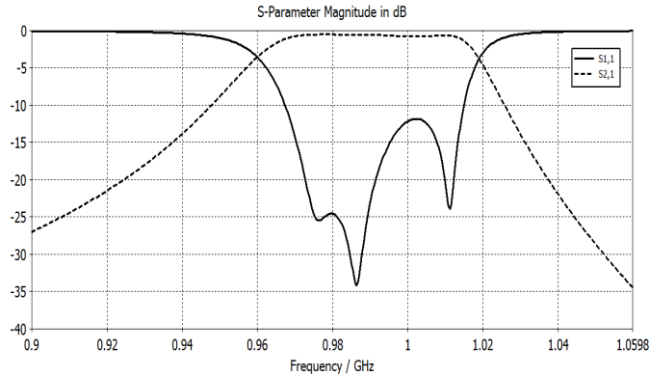

Figure 5: Simulation results obtained for the reflection and transmission losses for the TSR filter.

3. Conclusions

The proposed three pole bandpass filter, based on microstrip triangular spiral resonators(TSR), with the same specifications as the one with the triangular open loop resonators(TOLRS), was designed and computed simulated. For comparison, the filter based on TOLRS was also designed and simulated in this paper. The investigation concluded that having the same line width as the one of the open loop resonator, operating in the same frequency band and having the same Chebyshev characteristics, the area of the spiral resonator filter revealed to be the area of the open loop filter reduced of 48% . Clearly the performance of both

filters are very similar as far as the bandwidth, reflection and transmission losses are concerned. The center frequency turned out to be slightly shifted certainly because the extraction of the coupling coefficient and external quality factor presented intrinsic small errors.

References

[1] M. Hedayati, M. J. Kazemi, and R. Safian, "Design and implementation of a multi triangular microstrip resonator passband filter based on mixed coupling," Int. RF and Microwave Conference (RFM2011), Dec. 2011, Seremban, Malaysia, pp. 141–144.

[2] J. S. Hong and M. J. Lancaster, "Microstrip Filters for RF/Microwave Applications," Wiley, New York, 2001.

UWB Printed Monopole Antenna with Dual Band-Notched Characteristic at WLAN and X-Band Communication Frequency

Xiaomu Hu [1,2], Wenhu Yang[1], Shuhui Yu[1], Rong Sun[1]

1 Shenzhen Institutes of Advanced Technology, Chinese Academy of Sciences, Shenzhen 518055, China

2 Nano Science and Technology Institute, University of Science and Technology of China, Suzhou 215123, China

*corresponding author, E-mail: sh.yu@siat.ac.cn

Abstract

Abstract—A new kind of planar ultra-wideband (UWB) patch antenna with dual band-notched characteristics was proposed and analyzed. The structure of the antenna is composed of a radiation patch and a rectangular-shaped ground plane. A tapered microstrip transmission line was used to provide matching for the antenna. A folded slots and a dipole-like slot were etched out on the antenna patch to provide dual band-notched characteristic. The antenna has a relatively compact size of 22mm*34mm*0.8mm. The measured return loss of the antenna is lower than 10dB in 3.2-9.2GHz and has a dual band-notched characteristic at WLAN band and X-Band frequency respectively. The antenna shows a monopole-like radiation pattern and constant gain except in the notched bands. Good agreement between the simulation and measurement is observed.

Index terms—Dual band-notched, UWB, WLAN, X-Band satellite communication, Printed patch antenna

1. Introduction

The ultra-wideband (UWB) technology is an emerging technology on wireless communication. According to the standard of Federal Communication Commission (FCC), the spectrum from 3.1 GHz to 10.6 GHz has been allocated for the UWB measurement and communication applications after the year 2002 [1]. Since then, the technology has been extensively studied due to its numerous advantages, including simple structure, low profile, high data rate and easy integration with MMICs. However, the band overlap issue has always been a major challenge, due to the fact that some narrow bands are occupied by the existing wireless system, such as WLAN at 5.15-5.825GHz, and the X-Band satellite communication at 7.25-8.395GHz. To solve this problem, lots of research on UWB antenna with band-notched characteristic has been reported [1-9].

The present work is aimed at providing the dual/multiple band-notched characteristic at WLAN and X-Band communication frequency, where the rejection of X-Band communication frequency is less focused on in previews research. A new kind of compact dual band-notched UWB monopole antenna is proposed. The antenna is an inverted arch-shaped structure fed by a tapered microstrip line. A folded slot and a dipole-like slot are etched out on the patch, rejecting the bands at 5.15-5.825GHz and 7.25-8.395GHz respectively. The antenna has a relatively compact size of 22mm*34mm*0.8mm. The measured return loss shows a 2.99-9.2GHz 10dB bandwidth. The antenna shows a typical monopole-typed radiation pattern and constant gain, except at the two notched bands.

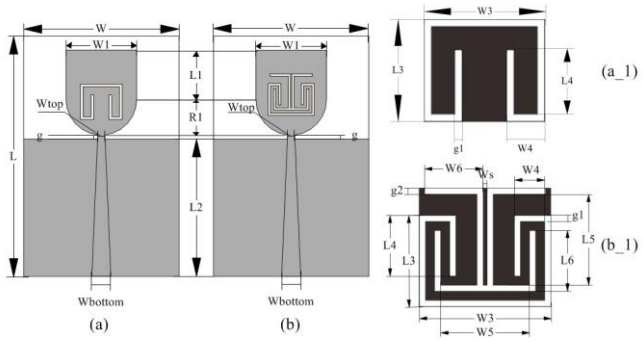

Figure 1. Proposed antenna's configuration: (a) single band-notched antenna (b) dual band-notched antenna (a_1) slot's parameters of the single band-notched antenna (b_1) slots' parameters of the dual band-notched antenna

2. ANTENNA DESIGN AND ANALYSIS

A. Tapered microstrip feedline

In this design the full-band antenna without any slots on is constructed on Rogers 5870 substrate, with a relative dielectric constant of 2.33 and a dielectric loss tangent of 0.0012. The substrate's thickness is fixed at 0.8mm.The antenna is fed by a tapered microstrip line for good impedance matching, which is mainly due to the fact that the port impedance of the microstrip is determined by its width. Empirical equations (1) & (2) are used to estimate the port characteristic impedance Z0:

$$Z_0 = \frac{376.8}{2\pi\sqrt{\varepsilon_{eff}}}\ln(8\frac{h}{w}+\frac{w}{4h}) \quad (1)$$

$$\varepsilon_{eff} = \frac{\varepsilon_r+1}{2}+\frac{\varepsilon_r-1}{2}[(1+12\frac{h}{w})^{-\frac{1}{2}}+0.04(1-\frac{w}{h})^2] \quad (2)$$

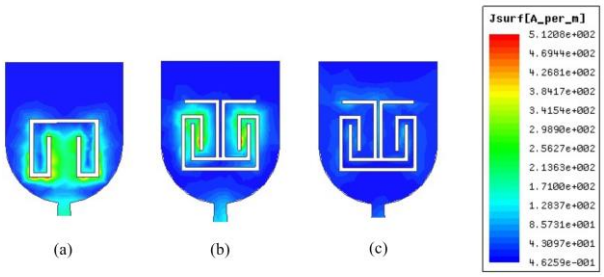

Figure 2. Simulated surface current on the antenna radiation patch: (a) 5.5GHz, single slot (b) 5.5GHz, dual slots (c) 7.8GHz, dual slots

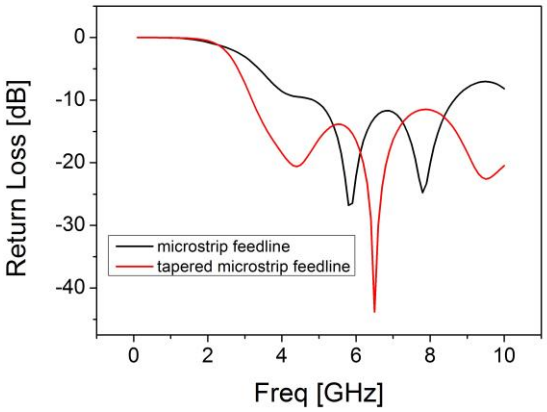

Figure 3. Simulated return loss of the full-band antenna

Here, ε_{eff} is the effective permittivity, ε_r is the relative permittivity, h is the thickness of the substrate and w is the width of the microstrip. It can be observed from Figure 3 that the antenna with tapered feed line shows better 10dB bandwidth. After optimization, the bottom width of the feed line (*Wbottom*) was fixed at 2.7 mm.

B. Single band-notched antenna

A single band-notched slot antenna (Figure 1(a) & (a_1)) was proposed to reject the WLAN band's interference in the UWB application. A folded slot was etched out on the radiation patch, which is approximately half of the wavelength of the desired rejected band. Figure 2(a) shows the surface current on the antenna patch at 5.5GHz. It can be observed that at the target notched band, the surface current mainly concentrated around the slot edges, indicating that the folded slot functioned as a band stop filter at the target notched band.

According to the following equations, Cs, the slot's inner perimeter can be written as:

$$C_s = \frac{\lambda_g}{2} = \frac{c}{2 f_n \sqrt{\varepsilon_{eff}}} \tag{3}$$

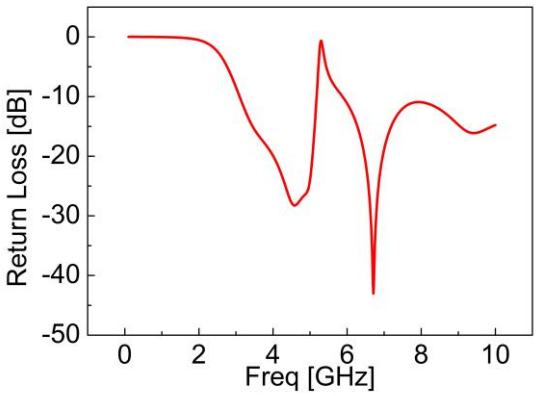

Figure 4. Simulated return loss of the single band-notched antenna

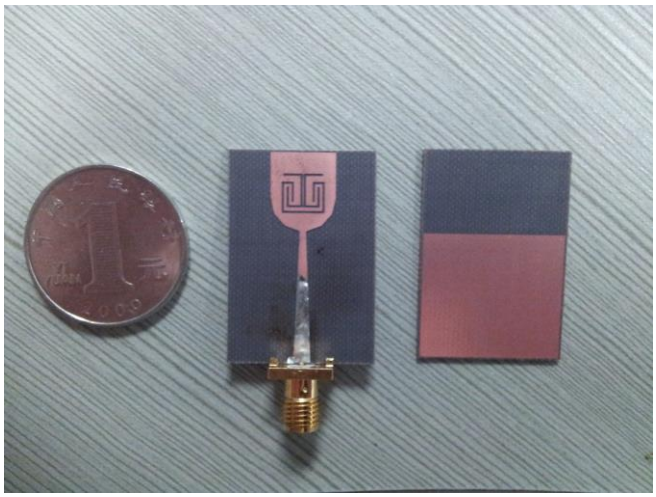

Figure 5. Fabricated antenna prototype

$$\varepsilon_{eff} = \frac{\varepsilon_r + 1}{2} + \frac{\varepsilon_r - 1}{2}\left(1 + \frac{12h}{w_f}\right)^{-0.5} \tag{4}$$

Here, λ_g is the wavelength on the microstrip, c is the speed of light, f_n is the notched band's center frequency, and ε_{eff} is the effective dielectric constant. In this design, Cs can be further described as:

$$Cs = \left(L_4 + W_4 + L_3 - 4*g\right) + W_3 - 2*g \tag{5}$$

Thus, by tuning the slot's parameters according to equation (3), the notched band's position and width can be adjusted. An obvious increase of the return loss at the notched band can be observed, as is shown in Figure 4.

C. Dual band-notched antenna

To minimize the interference of the X-Band system and the WLAN system at the same time, a double slotted patch antenna was proposed and shown in Figure 1(b) & (b_1). The folded slot from the single band-notched antenna was turned upside down for better spacing, while a

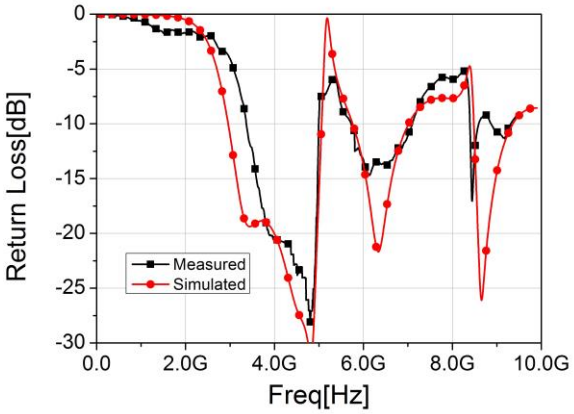

Figure 6. Measured and Simulated return loss of the proposed dual band-notched antenna

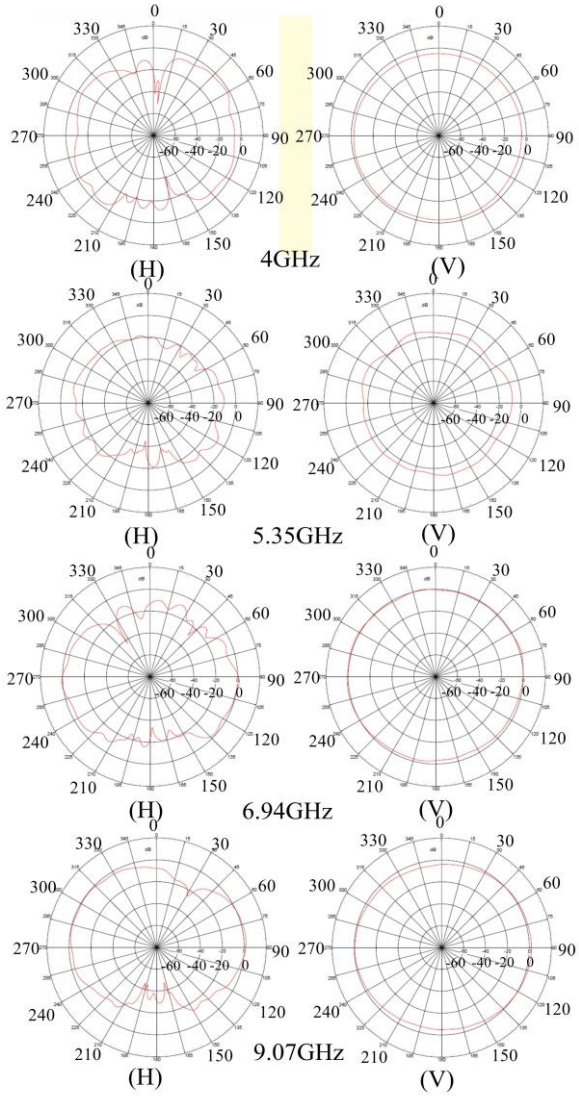

Figure 7. Measured far-field radiation pattern of the proposed antenna

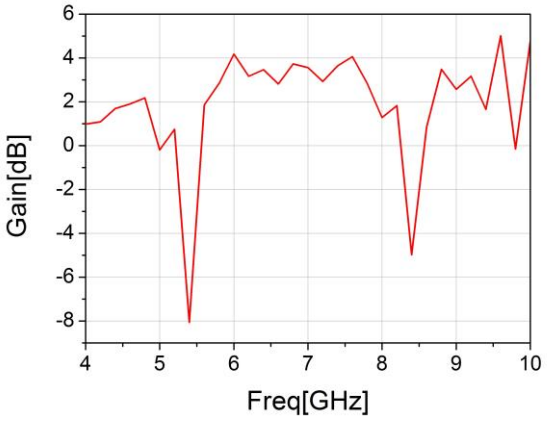

Figure 8. Measured return loss of the proposed antenna

dipole-like slot was carefully placed on the patch to avoid mutual coupling with the folded slot while providing rejection to the X-Band frequency. Figure 2(b) & (c) shows the simulated surface current on the patch. It can be observed from Figure 2(b) that the surface current at 5.5GHz is mostly concentrated around the folded slot. Meanwhile, Figure 2(c) shows that the surface current at 7.8GHz was mainly concentrated between the arms of the "dipole", indicating that the second notched band was mainly produced by the dipole-like slot. Careful placement and parameters choice can avoid mutual coupling of the two notched band. After optimization, the parameters of the proposed antenna were fixed as follows: L = 34 mm, W = 22 mm, $W1$ = 10mm, $L1$ = 7 mm, $L2$ = 19.8mm, $R1$ = 5mm, $Wtop$ = 1 mm, $Wbottom$ = 2.7 mm, g = 0.2 mm, $L3$ = 4.7 mm, $L4$ = 3 mm, $L5$ = 4.5 mm, $L6$ = 2.8mm, $W3$ = 6.5 mm, $W4$ = 1.5 mm, $W5$ = 4.4 mm, $W6$ = 2.6 mm, Ws = 0.2 mm, and $g1$ = $g2$ = 0.3 mm.

3. Measured results discussion

The fabricated antenna prototype is shown in Figure 5. The measurement of the proposed antenna was carried out with an Agilent N5227 vector network analyzer. In Figure 6, the measured and the simulated return loss of the antenna are presented. Good agreement on the notched bands between simulation and measurement is observed. The antenna shows a wide bandwidth within 3.2-9.2 GHz for |S11|< - 10 dB, and dual band-notched characteristic around 5.11-5.81GHz band and 7.05-8.4GHz band, which meets the frequency range of WLAN band and the X-Band frequency.

Figure 7 shows the horizontal (H) and Vertical (V) polarization in the far-field at the sampling frequencies of 4GHz, 5.35GHz, 6.94GHz, and 9.07 GHz. The designed antenna showed omnidirectional radiation patterns in the Vertical polarization plane and dipole like radiation patterns in the horizontal polarization plane. In Figure 8, the measured antenna shows a constant gain around 3dB throughout 4GHz-10GHz except in the notched bands, where obvious minimums occur around 5.5GHz and 8.4GHz.

4. Conclusions

In this letter, a UWB antenna with dual band-notched characteristic was presented. A folded slot and a dipole-like slot were etched out on the antenna patch to achieve dual band-notched characteristics at WLAN band and X-Band frequency. The antenna achieved a relatively compact size of 22mm*34mm*0.8mm, while showing good agreement between measured and simulated result on impedance matching. Constant gain and omnidirectional radiation pattern were also observed over the UWB application band.

Acknowledgements

This paper's research was supported by the Guangdong Innovative Research Team Program (No. 2011D052) and the Shenzhen Peacock Plan (KYPT20121228160843692). It was also supported by the SIAT Innovation Program for Excellent Young Researchers (201311).

References

[1] S. R. Emadian, C. Ghobadi, J. Nourinia, M. H. Mirmozafari, and J. Pourahmadazar, "Bandwidth Enhancement of CPW-Fed Circle-Like Slot Antenna With Dual Band-Notched Characteristic," Ieee Antennas And Wireless Propagation Letters, vol. 11, pp. 543-546, 2012.

[2] P. Gao, S. He, X. Wei, Z. Xu, N. Wang, and Y. Zheng, "Compact Printed UWB Diversity Slot Antenna With 5.5-GHz Band-Notched Characteristics," Ieee Antennas And Wireless Propagation Letters, vol. 13, pp. 4, 2014.

[3] F. G. Zhu, S. Gao, A. T. S. Ho, R. A. Abd-Alhameed, C. H. See, T. W. C. Brown, J. Z. Li, G. Wei, and J. D. Xu, "Multiple Band-Notched UWB Antenna With Band-Rejected Elements Integrated in the Feed Line," Ieee Transactions on Antennas And Propagation, vol. 61, no. 8, pp. 3952-3960, Aug, 2013.

[4] S. Koley, and S. Choudhury, "An Integrated Planar Bluetooth and UWB Monopole Antenna with Dual Notched Bands Based on Etched Slot on the Patch and Split Ring Resonators on the Ground Plane," 2013 Third International Conference on Advanced Computing & Communication Technologies (Acct 2013), pp. 4, 2013.

[5] M. Shokri, H. Shirzad, S. Movagharnia, B. Virdee, Z. Amiri, and S. Asiaban, "Planar Monopole Antenna With Dual Interference Suppression Functionality," Ieee Antennas And Wireless Propagation Letters, vol. 12, pp. 1554-1557, 2013.

[6] Y. E. Jalil, and B. Kasi, "A Compact Ultra Wideband Antenna with Dual Band-Notched Design," 2013 7th International Conference on Digital Object Identifier Signal Processing and Communication Systems (ICSPCS), pp. 5, 2013.

[7] T. Pechrkool, T. Hongnara, S. Chaimool, P. Akkaraekthalin, and K. Chung, "A Dual Band-notched UWB Monopole Antenna with C-shaped Slot and Hairpin Slot," TENCON Spring Conference, pp. 4, 2013.

[8] J. H. Wang, Y. Z. Yin, X. L. Liu, and T. Wang, "Trapezoid UWB antenna with dual band-notched characteristics for WiMAX/WLAN bands," Electronics Letters, vol. 49, no. 11, pp. 685-U76, May 23, 2013.

[9] Y.-Y. Yang, Q.-X. Chu, and J.-F. Li, "Dual Band-Notched Ultrawideband MIMO Antenna Array," 2013 IEEE International Wireless Symposium (IWS), pp. 4, 2013.

A Sierpinski Fractal Tag Antenna for RFID Applications

Yanzhong Yu, Xianhui Li, Xiaoying Wei

1. College of Physics & Information Engineering, Quanzhou Normal University, Fujian, 362000, China
2. Key Laboratory of Information Functional Materials for Fujian Higher Education, Fujian, 362000, China
*corresponding author, E-mail: yuyanzhong059368@gmail.com

Abstract

A design of Sierpinski fractal tag antenna at 2.45 GHz with match loop is presented in this paper. The Sierpinski fractal technology is employed to miniaturize the dimensions of tag antenna. And in order to realize impedance conjugate matching between tag antenna and chip, a match loop is introduced to tune flexibly the input impedance of tag antenna. Return loss of the proposed antenna at 2.45GHz is S11= –29.6 dB. Its impedance bandwidth (S11<= –10 dB) is about 90MHz, and the relative bandwidth reaches to 3.7%. Numerical results demonstrate that the designed tag antenna shows good performances and may satisfy the pragmatic RFID application requirements.

1. Introduction

With the rapid development of industrial automation and Internet of Things (IoT), RFID technology has attracted much attention and made great progress recently. So many RFID applications can be found in various trades, like distribution logistics, electronic toll collection, animal tracking, and intelligent transportation systems [1]. Usually, RFIDs can be classified by the operating frequency of system. They are operated in low-frequency (LF), high-frequency (HF), and ultra-high frequency (UHF) and microwave frequency bands or RF wavebands, respectively. Generally speaking, the read rang is longer and data transmission speed is higher when the operating frequency of system rises. Accordingly RFID systems present the growing trend to design higher frequency [2]. Operating frequency of the designed tag antenna in the present paper is 2.45 GHz.

A RFID system involves reader and tag which contains at least two parts: an integrated circuit (IC chip) and an antenna for receiving and transmitting the signal [3]. The tag antenna plays an important role in transferring data, and consequently the design of high performance tag antenna becomes a most challenging task in RFID system. The design requirements of tag antenna are becoming increasingly rigorous with the more popular applications of RFID. Nowadays the trend to miniaturize tag antenna is likely to continue for the purpose of concealing or embedding in other items conveniently [4].

Lots of methods have been suggested to miniaturize tag antennas. One of them is to employ a fractal theory and technology. The fractal possesses two important characteristics, i.e., self-similarity and space self-filling ability. If they are used to design tag antenna, the former can make an antenna has the multiband property and the latter can compact the volume of an antenna [5]. In order to miniaturize tag antenna, the Sierpinski fractal theory and technique are employed in the present paper. Additionally, the input impedance of tag antenna must be complex conjugate matching to that of IC chip for maximum power transferring [1]. However the IC chips fabricated from different companies own the different input impedances. Generally the input impedance of tag antenna can be varied readily and flexibly so as to conjugate match that of the IC chip, owing to a big and costly investment in design and manufacturing a new IC chip. To overcome this problem, a match loop is introduced and loaded to the tag antenna in our design. Numerical results indicate that input impedance of the designed antenna can be tuned easily through changing the parameters of match loop. Relevant performances of the designed antenna are calculated by HFSS. And the results demonstrate that the designed antenna can satisfy the requirements of practical RFID applications.

2. Antenna design and analysis

The fractal concept was firstly proposed by Mandelbrot in 1975. From then on many well-known and significant fractals have been constructed successively, such as Koch fractal, Hilbert fractal, and Sierpinski triangle fractal. It is known that fractals are typically self-similar patterns, and may be exactly the same at every scale, or, nearly the same at different scales. In the present paper, we are only concerned on Sierpinski fractal structures. It is named after the Polish mathematician Wacław Sierpiński for his outstanding contribution. The Sierpinski triangle may be constructed from an equilateral triangle by repeated removal of triangular subsets: (1) Start with an equilateral triangle; (2) Subdivide it into four smaller congruent equilateral triangles and remove the central one; (3) Repeat step 2 with each of the remaining smaller triangles, as depicted in Fig. 1. The fractal dimension of Sierpinski triangle may be calculated by: $D = \log 3/\log 2 = 1.58$.

Fractals have found lots of important and significant applications in many fields of science and engineering [5]. One such application is to analyze and design fractal

antennas, in which fractal geometry is combined with electromagnetic theory in order to develop a new class of antennas which are multi-band and/or compact in size [6]. In this paper a novel monopole antenna based on Sierpinski triangle fractal is proposed. Its schematic is illustrated in Fig. 2. The proposed antenna consists of three elements, a two-order Sierpinski triangle fractal used as radiation arm, a match loop (see Fig. 3), and a ground plate. The monopole antenna can produce the equivalent performances of dipole antenna by using the mirror image effect of the ground plate. Moreover, its dimensions are much smaller than the dipole one. In our design the epoxy_Kevlar, whose relative dielectric constant is $\varepsilon_r = 3.6$, is used as substrate material. The total sizes of the substrate are 24.9 mm×23.2 mm×1 mm. They meet entirely the requirements of miniature antenna. In order to construct antenna model conveniently, the height and width of the smallest triangle in radiation arm are taken as L and 2×W, respectively. H is the substrate height. R represents the ratio of the half width W to height L and is used to adjust the form of smallest triangle. Table 1 gives the sizes of the designed tag antenna.

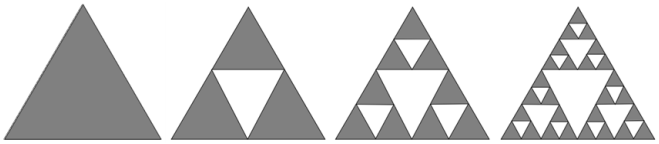

Fig. 1. 0～4 order Sierpinski triangle fractal

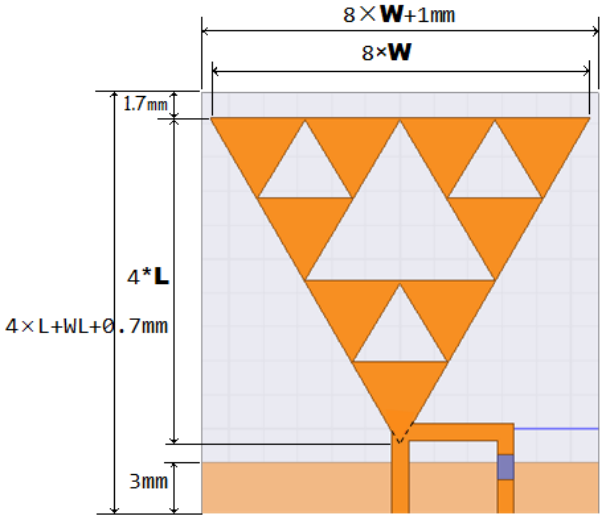

Fig. 2. Schematic of the proposed antenna.

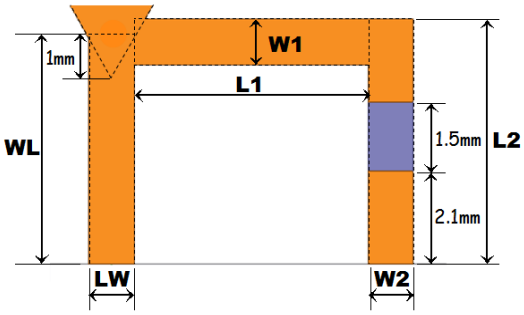

Fig. 3. Match loop

TABLE 1 PARAMETERS OF THE PROPOSED ANTENNA (MM)

Parameter	L	W	H	R	WL
Value	4.8	R×L	1	0.577	5
Parameter	LW	L1	W1	L2	W2
Value	1	5.2	1	5.3	1

Performances of the proposed antenna are calculated by using HFSS.13. Fig. 4 shows the return loss S11 as a function of frequency. It can be observed from Fig. 4 that the resonating frequency point is just located at the expect value of 2.45 GHz. The minimum of return loss is S11= –29.5999 dB and the operating bandwidth (S11<= –10 dB) is 2.41~2.50 GHz, which meets the bandwidth requirement of RFID tag applications. Input impedance of the designed antenna is depicted in Fig. 5. We can find that input impedance is inductive strongly due to the loaded match loop. The input impedance at 2.45 GHz is Z_{tag}=(28.3+j201) Ω that approaches to conjugate value of the supposed IC chip input impedance of Z_{chip}=(30–j200) Ω. This indicates a good match between the IC chip and the proposed antenna. The illustration of simulated 3D gain pattern is given in Fig. 6. The maximum total gain is G_{total}=2.0 dB and closely locates in Y-Z plane. Obviously it is an omnidirectional antenna. The 2D radiation patterns for the designed antenna are showed in Fig. 7. The maximum gain in Y-Z plane is $G_{y\text{-}z}$=2.0325 dB, which is a little smaller than the maximum total gain G_{total}.

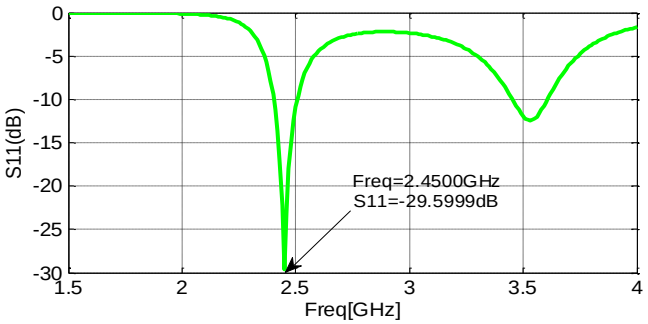

Fig. 4. Return loss S11 of the proposed antenna

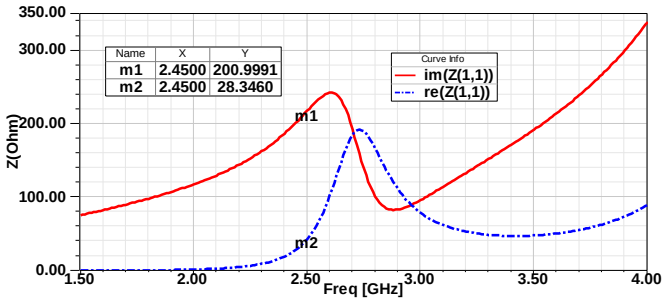

Fig. 5. Input impedance of the proposed antenna

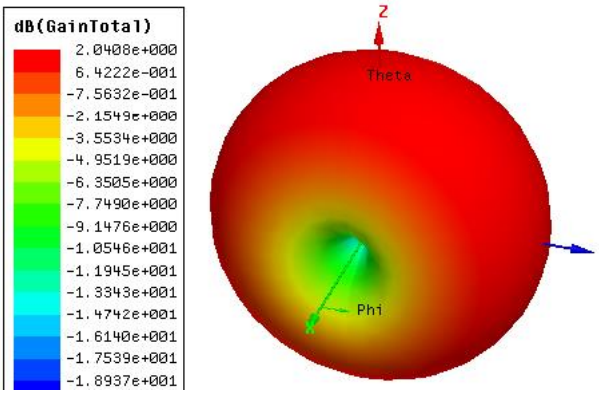

Fig. 6. 3D gain pattern of the proposed antenna

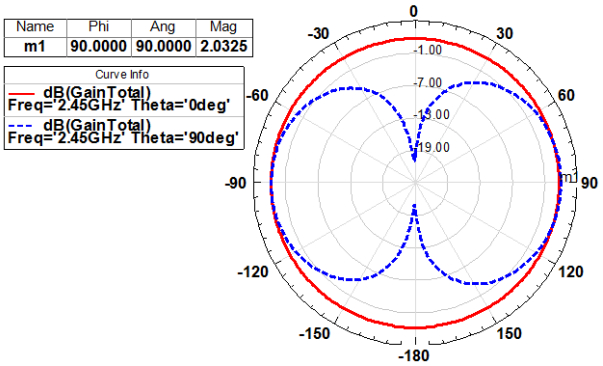

Fig. 7. 2D radiation patterns of the proposed antenna

The maximum read range is considered as the most important tag performance characteristic [1]. The tag read range for the far field passive RFID system can be calculated from two ways: one is a data link from reader to tag; and the other data link is from tag to reader. Usually, the reader is more sensitive when compared with the tag. Therefore the read range is mainly determined by the tag antenna. If the IC chip is more sensitive and its threshold voltage is lower, it means that the less power is necessary to active this IC chip. The Friis free-space formula can be employed to compute the read range and defined as [1]:

$$R_{\max} = \frac{\lambda}{4\times\pi}\sqrt{\frac{P_t G_t G_r \tau \rho}{P_{th}}} \qquad (1)$$

where λ is the wavelength, P_t denotes the power transmitted by the reader, P_{th} represents the minimum threshold power necessary to active the IC chip, G_t and G_r mark the gains of the read and the tag antennas, respectively. τ and ρ are the power transmission factor and mismatch factor, respectively. Now let us estimate the maximum read range. λ =0.1224 m at f =2.45 GHz. Referring to the practical reader antenna, we get P_t =1 W and G_t =8 dB=6.3096 W. Under the condition of polarization match and maximum radiated direction, τ and ρ can reach to 1. The typical value of threshold power is P_{th} = –8~ –20 dBm, and in our calculation we take the average value P_{th} = –14 dBm=0.0398 mW. From Fig. 7 one can get G_r =2.0408 dB=1.5999 W. Substituting above values into Eq. 1, we obtain readily $R_{\max}$ =4.9067 m.

As mentioned above, the proper impedance matching between the IC chip and tag antenna is very important in RFID system. Therefore the effects of match loop sizes on input impedance of tag antenna are analyzed. The match loop proposed in our work can be considered as the deformation of T-shape match circuit. The parameters relevant to the match loop are LW, WL, L1, L2, W1 and W2 (see Fig. 3). Figs. 8~13 depict the influences of these parameters on input impedances, respectively. The parameter LW determines the width of connected line between radiated body and ground plate. So it has a great influence on input impedance, as illustrated in Fig. 14. The input impedance decreases greatly as the parameter LW increases. However we can find from Fig. 15 that the input impedance is not almost affected by the parameter LW. When the parameters L1 and L2 raise and thus the circumferences of the loop grow larger, the values of input reactance exhibit the great rising trend and yet the quantities of input resistance increase slowly. As the parameter W1 increases and the empty part in match loop become smaller, the input impedance decreases heavily. However the input impedance rises slowly when increasing the parameter W2 and hence the area of match loop.

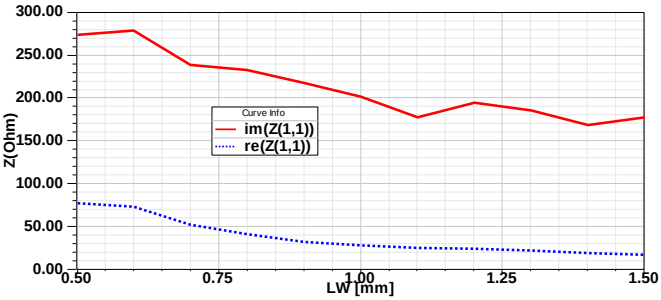

Fig. 8. Effect of parameter LW on input impedance

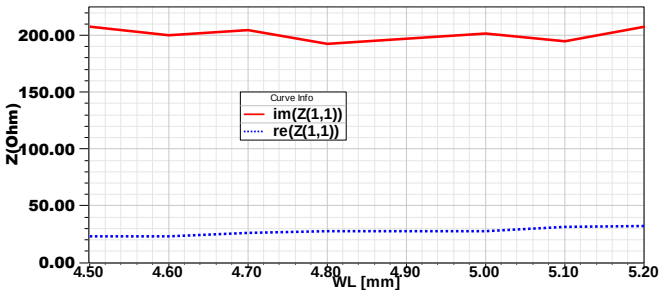

Fig. 9. Influence of parameter WL on input impedance

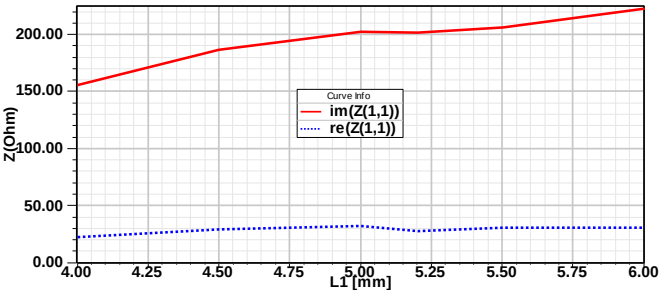

Fig. 10. Effect of parameter L1 on input impedance

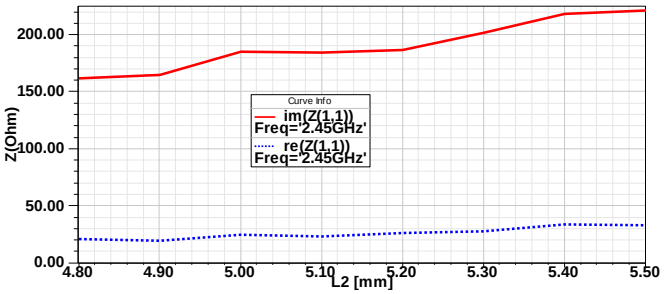

Fig. 11. Influence of parameter L2 on input impedance

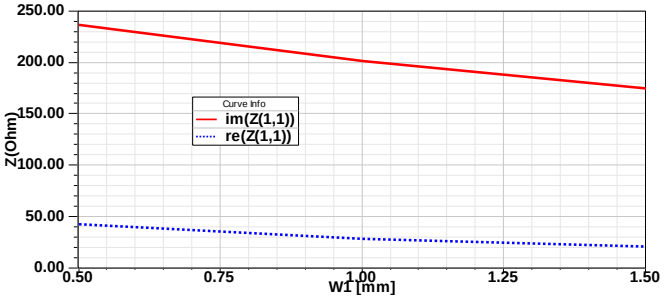

Fig. 12. Effect of parameter W1 on input impedance

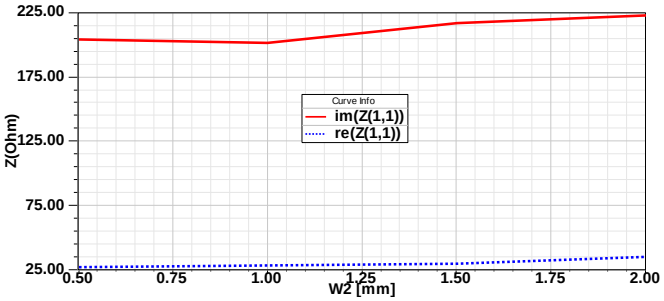

Fig. 13. Influence of parameter W2 on input impedance.

3. Summary

On the basic of Sierpinski fractal structure and mirror image technology, a loaded match loop monopole antenna at 2.45 GHz for RFID applications is designed in the present paper. Simulation results demonstrate that the designed RFID tag antenna has excellent performances and may satisfy the requirements of RFID applications. It can be applied in distribution logistics, electronic toll collection, animal tracking, and so on.

Acknowledgements

The work was supported by the Fujian Province Education Department under grant JK2012040, the National Project of Innovative Entrepreneurship of Undergraduate (201310399002), and the Key Discipline of Electronic Science and Technology.

References

[1] K. V. Seshagiri Rao, P. V. Nikitin, and S. F. Lam, “Antenna design for UHF RFID tags: a review and a practical application,” IEEE Trans. Antennas. Propag., vol. 53, no. 12, pp. 3870-3876, Dec. 2005.

[2] R. Siragusa, P. L. Auger, and S. Tedjini, “Tunable Near-Field Focused Circular Phase-Array Antenna for 5.8-GHz RFID Applications,” IEEE Antennas Wirel. Propag. Lett., Vol. 10, pp. 33–36, 2011.

[3] Y. S. Chen, S. Y. Chen, and H. J. Li, “A Novel Dual-Antenna Structure for UHF RFID Tags,” IEEE Trans. Antennas. Propag., Vol. 59, No. 11, pp. 3950–3960, Nov. 2011.

[4] E. A. Soliman, M. O. Sallam, W. D. Raedt, and Guy A. E. Vandenbosch, “Miniaturized RFID Tag Antenna Operating at 915 MHz,” IEEE Antennas Wirel. Propag. Lett., Vol. 11, pp. 1068–1071, 2012.

[5] D. H. Werner, R. L. Haup, and P. L. Werne, “Fractal Antenna Engineering: The Theory and Design of Fractal Antenna Arrays,” IEEE Antennas. Propag. Magazine, Vol. 41, No. 5, pp. 37–59, Oct. I999.

[6] D. H. Werner, and S. Ganguly, “An overview of fractal antenna engineering research,” IEEE Antennas Propag. Mag., vol. 45, no. 1, pp. 38–57, 2003.

Design of a broadband circularly polarized microstrip antenna

Xing Jiang[1], Jinhong Yan[1], Lin Peng[1]

[1]School of Information and Communication, Guilin University of Electronic Technology, Guilin, China
*Jinhong Yan, E-mail: yjh_jennifer@163.com

Abstract

A broadband circularly polarized microstrip antenna is constructed by using dual elliptical slots coupling fed. Two open stubs are connected to the feeding line and coupling to a square patch to realize the proposed circularly polarized antenna. Two rectangular slits are etched on the ground plane for impedance matching improvement. Multi-layer structure is used, and the CP performance is improved by increasing the size of reflector. The antenna is simulated by the electromagnetic simulation software CST. The simulation results show that the impedance bandwidth achieves 40% and the 3dB axial-ratio bandwidth is 42.6%.

1. Introduction

Rapidly development in the wireless communication system urgently requires wideband circularly polarized (CP) microstrip antenna. In order to product circularly polarization characteristics, two orthogonal linearly polarized elements with equal amplitude and 90° phase difference should be excited. The conventional single-feed single-patch microstrip CP antenna typically has a relatively narrow axial-ratio bandwidth. The dual-feed microstrip CP antenna has wider impedance and axial-ratio bandwidths. But, compared to single-feed type, an external polarizer such as Wilkinson power divider is used to generate circularly polarization, which results larger footprint on the substrate.

In recent years, many efforts have been made to design CP antenna with wide impedance and axial-ratio bandwidths. A CP square slot antenna fed by a coplanar waveguide (CPW) is designed with two inverted-L grounded strips and a widened tuning stub. The CP square slot antenna get an axial-ratio (AR) of less than 3dB larger than 25% and the impedance bandwidth is 52% [1]. In [2], an L-slot CP antenna single feed by L-shaped feed line is designed. Wideband CP is obtained by truncating one of the corners of the antenna element. An overlapped bandwidth of 46.5% is achieved with an AR<3dB and return loss<-10dB. A microstrip-fed symmetric-slot antenna for broadband CP radiation is presented in [3]. The antenna consists of a microstrip feed line and a wide symmetrical slot along the diagonal axis. The antenna gets a wider AR bandwidth of 50%. Many other slot antennas with different patterned slot in the metallic ground plan are designed. A compact broadband circularly polarized elliptical slots antenna for C-band applications is presented in [4]. The antenna operates the frequency band between 4.3-8GHz (60%) for VSWR < 2 and exhibits a 40% CP bandwidth. But all these antennas are bidirectional, [5] place a simple reflector underneath the bidirectional antenna without changing its structural dimension to obtain unidirectional radiation patterns with a great increased gain.

In this paper, a broadband circularly polarized microstrip antenna is presented. The proposed antenna is fed by a microstrip line with two perpendicular stubs coupling to a square patch through dual elliptical slots to excite two orthogonal E vectors. To get unidirectional radiation patterns and increase the gain, multilayer structure is used. The dual elliptical slot antenna operates over the frequency of 3.6-5.4GHz with circular polarization from 3.4-5.3GHz. The gain of the antenna is about 8dB. And the proposed antenna has wide-angle circular polarization performance.

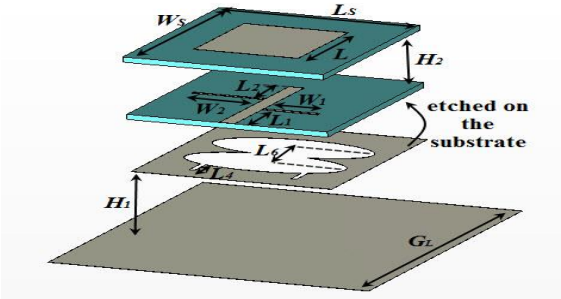

Figure 1: Geometry of the proposed CP antenna.

2. Antenna Geometry

The geometry of the proposed antenna is show in Figure 1.As shown in the figure, the proposed antenna consists of a radiation layer, a slot layer and a reflector. The antenna is printed on microwave substrate with a dielectric constant (ε_r) of 4.4 and a thickness of 1 mm. The radiation layer is a square patch printed on the substrate. The patch has a length (L) of 13mm. The slot layer is composed of a microstrip feedline and a dual elliptical slot loaded ground plane (GND). The proposed antenna feedline is a 50Ω microstrip with a width of W_f. Two open subs are attached perpendicularly to the feedline to product circular polarization. Each sub has different width. The conducting ground plane on the other side of the substrate has the same size as the substrate. Two linked elliptical slots are etched at the ground plane. By removing two rectangular slits at the ground structure, the electromagnetic coupling between the feedline and the ground plane is improved, and the impedance bandwidth is increased without any change of

size. Two elliptical slots have identical size. The distance between the centers of two ellipses is L_6. L_6 should be less than7.9 mm to insure the two slots overlapped. The radiation layer is H_2 mm higher than the slot layer. This creates an effect similar to the stacked patch antenna, which uses two patches of slightly different resonant frequency to achieve a larger bandwidth [6]. To suppress the backward radiation and hence to increase the antenna gain, the simplest way is to place a G_L-wide square reflector at distance of $H_1=\lambda_0/4$ below the ground plane of the main radiator, where λ_0 is the free-space wavelength at 4.5GHz. This leads to H_1 =15.6 mm. In general, the smaller is the value of G_L, the smaller is the 3-dB AR bandwidth. As long as G_L is greater than $5\lambda_0/8$, a CP band with an AR of less than 3 dB can still be obtained [7]. G_L = 40 mm is selected.

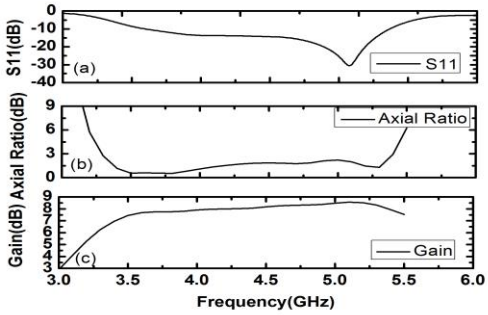

Figure 2: (a) the return loss, (b) axial ratio and (c) gain of the antenna

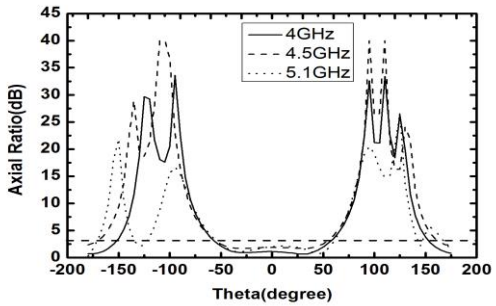

Figure 3: the wide-angle performance at 4GHz, 4.5GHz and 5.1GHz.

3. Results and Discussions

3.1. Simulated results

The proposed broadband CP microstrip antenna is simulated using electromagnetic simulation software CST Microwave Studio. The return loss, axial-ratio and the peak gains of the antenna is shown in Figure 2. The antenna obtains a simulated impedance bandwidth of 40 % (3.6GHz-5.4GHz). And a simulated 3-dB AR bandwidth 42.6 % (3.4GHz-5.3GHz) is achieved. The antenna obtains a maximum gain of 8.5dB at 5.1GHz. The wide-angle AR of the antenna is shown in Figure 3.

The simulated patterns are shown in Figure 4. The CP radiation patterns are simulated at three different frequencies: 4GHz, 4.5GHz and 5.1GHz in the *xy*-plane and *yz*-plane. As shown in Figure 4, the proposed antenna is a unidirectional antenna and generate a right-hand circular polarization in the +z-direction. The cross polarization is left-hand circular polarization.

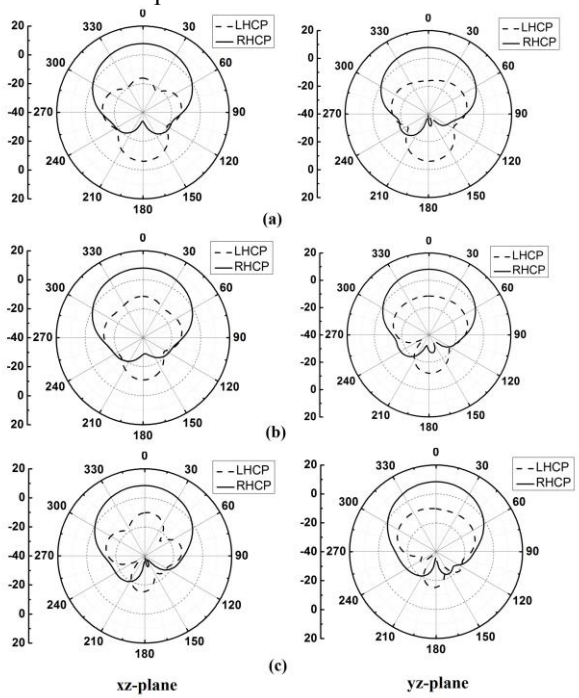

Figure 4: simulated patterns at (a) 4GHz and (b) 4.5GHz and (c) 5.1GHz

3.2. Parametric analysis

Some crucial parameters of the structure that have great impact to antenna performances of the impedance matching and AR are investigated in this subsection. The studies are performed by simulation software CST Microwave Studio.

3.2.1. Varying the patch length (L)

Figure 5 shows the impact of L on antenna performances. The patch length L basically determines the lower resonant of the antenna. When the patch length is increased from 5-20mm, it is observed that lower resonance shift from higher frequency to lower frequency. The axial-ratio of the antenna is getting smaller when the patch length increases from 5-13mm, but deteriorated when the patch length gets 20mm. L=13 mm is selected to get a good CP antenna performance.

3.2.2. Varying the position of the stubs (L_1, L_2)

The stubs are embedded in the feedline to excite two orthogonal E vectors. The parameters of the stubs play an important role in the circular polarization characteristics of presented design.

Figure 6 shows the performance of the antenna when the position of stub in the right side of the feedline is varied. With L_1 changing, the feedline structure is changed. It is observed that the higher resonant frequency of the antenna shift from lower frequency to higher frequency when L_1 increases from 6-8 mm. On the other hand, the AR bandwidth is getting larger when L_1 varies. Figure 7 shows the performance of the antenna when the position of the stub, which attached along the left side of the feedline, is varied. The matching frequency is almost the same when L_2 varies

from 3-5mm. However, it has a significant effect on the AR bandwidth. The axial-ratio of the antenna gets smaller with L_2 increasing.

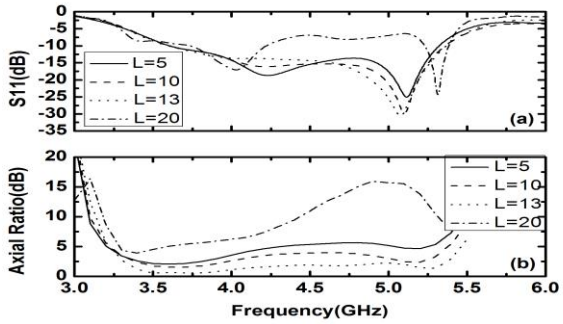

Figure 5: simulated results for proposed antenna with different values of L: (a) return loss, (b) axial ratio.

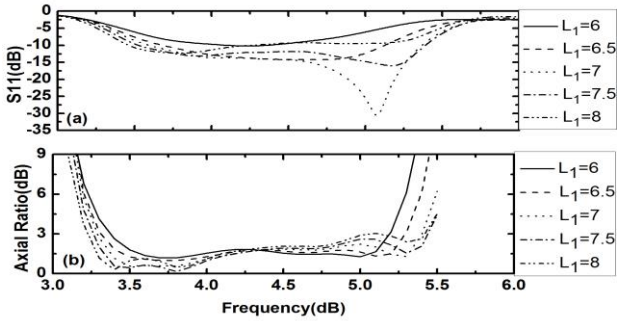

Figure 6: simulated results for proposed antenna with different values of L_1: (a) return loss, (b) axial ratio.

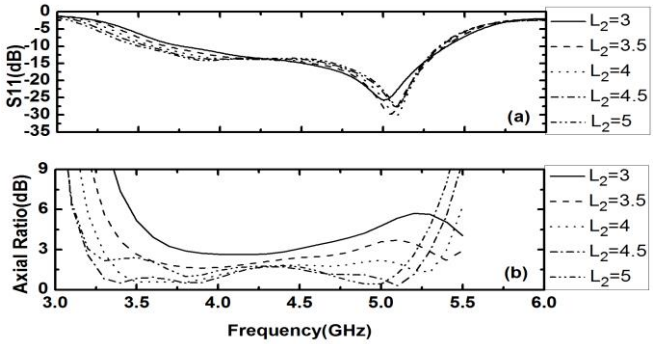

Figure 7: simulated results for proposed antenna with different values of L_2: (a) return loss, (b) axial ratio.

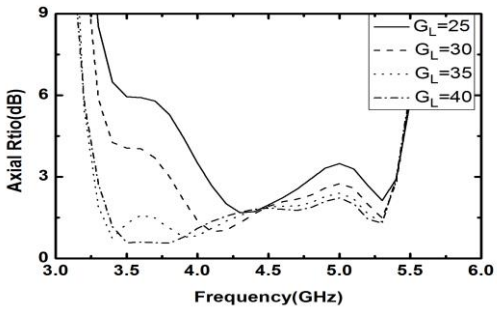

Figure 8: simulated axial ratios for proposed antenna with different values of G_L.

3.2.3. Varying the reflector length (G_L)

Figure 8 demonstrates the antenna performance for different the reflector length G_L. It observed that the larger the reflector, the wider the 3-dB AR bandwidth will be. When G_L = 40 mm is selected (which is only slightly larger than$5\lambda_0/8$), a best CP performance is achieved. Moreover, the backward radiation is decreased when the reflector length increases.

4. Conclusion

In this paper, a novel design of a broadband circularly polarized microstrip antenna coupled by a dual elliptical slot is proposed. The impedance bandwidth and the 3-dB axial-ratio bandwidth are improved by the addition of two stubs in the feedline structure and removal of two rectangular slits from the ground plane. To suppress the backward radiation and hence to increase the antenna gain, a simple reflector is used. The simulated results show that the obtained impedance bandwidth is 40%, the axial-ratio bandwidth is 42.6%, and the peak gain of the antenna is 8.5dB. The proposed antenna shows wide bandwidth and good performances, and it would be a good candidate for microwave systems require wide CP band

Acknowledgements

This work was supported by the National Natural Science Foundation of China (Grant NO. 61371056 and Grant NO. 61401110), and Innovation Project of GUET Graduate Education (Grant No. GDYCSZ201414)

References

[1] Sze J Y, Chang C C. Circularly polarized square slot antenna with a pair of inverted-L grounded strips [J]. *Antennas and Wireless Propagation Letters*, IEEE, 2008, 7: 149-151.

[2] Yang S L S, Kishk A A, Lee K F. Wideband circularly polarized antenna with L-shaped slot [J]. *Antennas and Propagation*, IEEE Transactions on, 2008, 56(6): 1780-1783.

[3] Nasimuddin ; Zhi Ning Chen ; Xianming Qing. Wideband circularly polarized slot antenna [C]. //*Microwave Conference (EuMC), 2012 42nd European.* IEEE, 2012: 830 – 833.

[4] Mohammadi S, Nourinia J, Ghobadi C, et al. Compact broadband circularly polarized slot antenna using two linked elliptical slots for C-band applications[J]. 2013.

[5] Pan S P, Sze J Y, Tu P J. Circularly polarized square slot antenna with a largely enhanced axial-ratio bandwidth[J]. *Antennas and Wireless Propagation Letters*, IEEE, 2012, 11: 969-972.

[6] Targonski S D, Pozar D M. Design of wideband circularly polarized aperture-coupled microstrip antennas [J]. *Antennas and Propagation*, IEEE Transactions on, 1993, 41(2): 214-220.

[7] Sze J Y, Pan S P. Design of broadband circularly polarized square slot antenna with a compact size [J]. *Progress In Electromagnetics Research*, 2011, 120: 513-533.

A Bandwidth-extended Electrically Small Dipole Antenna Based on Composite Right/Left Handed (CRLH) Transmission Line

Weiping Cao[1], Beibei Li[1], Xinhua Yu[1], Yannan Jiang[1]

[1]Key Laboratory of Cognitive Radio and Information Processing, Guilin University of Electric Technology, Ministry of Education, Guilin 541004,China
*corresponding author, E-mail: guetbeibeili@126.com

Abstract

A bandwidth-extended electrically small dipole antenna based on composite right/left handed (CRLH) transmission line is presented. The proposed structure is realized by a periodic ladder network of four unit cells having air-gaps and wires. Simulated results show that, adjusting the gaps and wires without any additional matching network, a 6.36% impedance bandwidth can be achieved when the length of the antenna is 50.4mm, and well-behaved radiation patterns have been displayed.

1. Introduction

In the past few years, metamaterial technology has become a hot research field regarding small antennas, due to the characteristic of miniaturization. In 2006, P.S.Hall introduced the concept of planar type left-handed (LH) dipole antenna [1]. The electric length of the left-handed dipole antenna can be shorted to $0.2\lambda_0$. Furthermore, Chenbin Lin designed a small monopole antenna based on periodic CRLH transmission line by coaxial structure in 2008 [2]. These indicated that a reduced-size dipole antenna can be realized. However, these small dipole antennas typically have narrow bandwidth. Therefore, we present a bandwidth-extended electrically small dipole antenna based on composite right/left handed (CRLH) transmission line in this letter. Adjusting the gaps and wires without any additional matching network, a 6.36% impedance bandwidth of the proposed dipole antenna can be achieved when the length of the antenna is 50.4mm, and well-behaved radiation patterns have been displayed.

2. Analysis and design

Figure1 shows the geometry of the proposed dipole antenna based on CRLH transmission line, which consists of unit cells in series [1, 2]. As seen in Figure 1, the air-gaps g, are added to one of the cylindrical conductors to make series capacitance C_L, the wires b, are placed in the middle connecting the two cylindrical conductors to make the shunt inductance L_L, forming the unit cells of CRLH transmission line. This results in different amplitudes of the out-of-phase currents

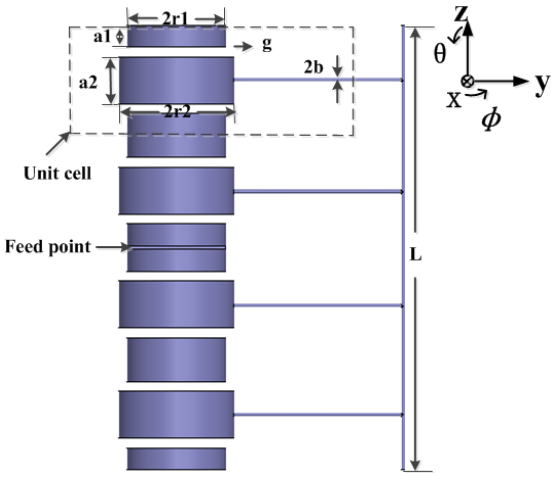

Figure 1: Configuration of the electrically small dipole antenna.

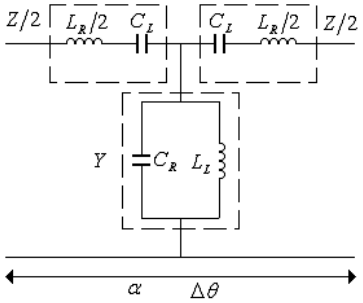

Figure 2: The equivalent circuit model of the lossless unit cell of the CRLH dipole.

I_1 and I_2 on the parallel cylindrical conductors, which produces radiation [3]. The geometrical parameters of the proposed electrically small dipole antenna based on periodic CRLH transmission line are: $r1 = 5.7mm$, $r2 = 6.6mm$, $a1 = 2.5mm$, $a2 = 5.3mm$, $g = 1.1mm$, $b = 0.2mm$, $d = 18.5mm$ .Calculations are carried out by HFSS when each parameter of the structure is changed. It is not difficult to get the equivalent model of the proposed lossless unit cell shown in Figure 2. The series capacitance C_L and shunt inductance L_L act as an LH transmission line, while C_R and L_R are distributed capacitance and inductance,

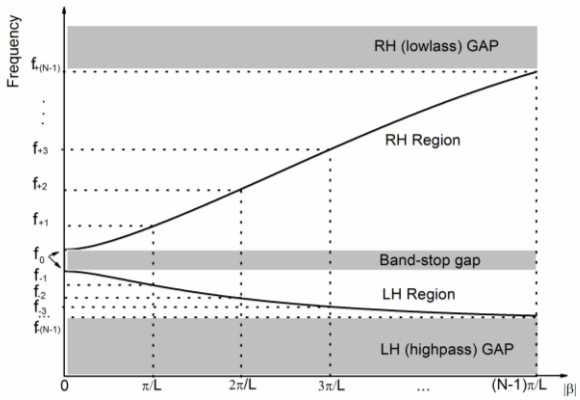

Figure 3: Dispersion relation of the CRLH TL versus resonant modes.

which act as a right-handed (RH) transmission line. The β diagram of unit cell can be determined by the following equation [4]

$$\beta(\omega) = \frac{1}{p}\cos^{-1}(1+\frac{ZY}{2})$$
$$= \frac{1}{p}\cos^{-1}\{1-[\omega^2 L_R C_R + \frac{2}{\omega^2 L_L C_L} - (\frac{L_R}{L_L}+\frac{2C_R}{C_L})]\} \quad (1)$$

Where p is the length of unit cell, Z is the series impedance and Y is the shunt admittance of the unit cell. Figure 3 describes the relationship of the resonance frequencies and phase constant. When CRLH transmission line is open-ended, it can produce waves and become a resonator according to the open boundary conditions. For the CRLH transmission line resonator, since it can have $\beta = 0$ at transition frequency and $\beta < 0$ in the LH range, the resonance mode can be zero and negative, respectively [5],

$$\beta_n L = n\pi \quad (n = 0, \pm 1, \pm 2, \cdots) \quad (2)$$

where L is physical length of the resonator and n is the resonance mode. For a periodic CRLH transmission line resonator consisting of N unit cells, the length of the resonator L and the period p are related by $L = Np$, and the resonance frequencies can be obtained by

$$\beta_n = n\pi p/L = n\pi/N \quad (n = 0, \pm 1, \pm 2, \cdots) \quad (3)$$

Because of the dispersion relation and bandwidth limited by the LH high-pass and RH low-pass cutoff frequencies, a CRLH transmission line resonator exhibits a finite number $(2N-1)$ of resonance frequencies.

3. Discussion

In this paper, the proposed dipole antenna based on CRLH transmission line consists of four unit cell, $N = 4$, the resonance modes n can be $0, \pm 1, \pm 2, \pm 3$ according to equation (3). However, a dipole antenna usually achieves its

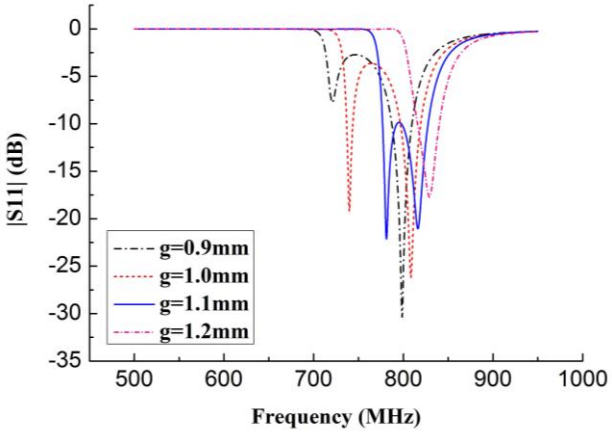

Figure 4: Simulated reflection characteristics versus frequency at $g = 0.9 \sim 1.2mm$

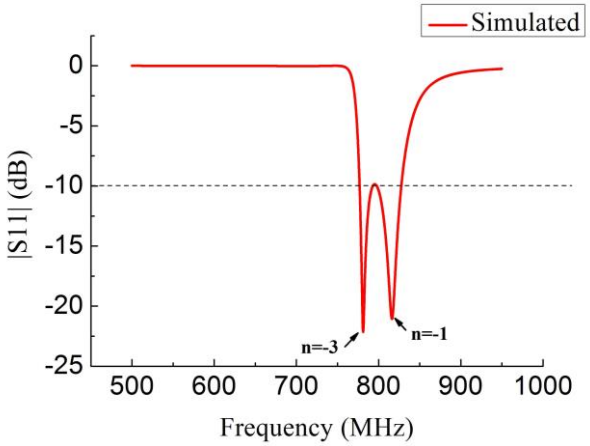

Figure 5: Simulated values of refection characteristic at $g = 1.1mm, d = 18.5mm$

resonances at odd modes and anti-resonances at even modes, the summation of I_1 and I_2 of $n = -2$ mode becomes small at the position of 0 mm, and impedance has open circuit at feed point. It results that the anti-resonance of $n = -2$ mode does not exist in the return-loss characteristic [3]. Therefore, the proposed dipole antenna based on CRLH transmission line consisting of four unit cell can only operate at two resonance modes: $n = -1$ and $n = -3$ in the LH region. According to equation (1) and Figure 3, we ensure that the dispersion property is dominated by C_L and L_L , which means that the frequencies of the two resonance modes is also determined by the value of air-gaps and wires . Hence, by adjusting the air-gaps and the length of wires to appropriate value, the two resonances can be suitably coupled with each other, and the dipole can match to about $50\,\Omega$ simultaneity at both LH modes, $n = -1$ and $n = -3$, and the wider bandwidth of an electrically small antenna based on CRLH transmission line can be achieved.

Figure 4 shows that the reflection characteristics of the electrically dipole antenna based on CRLH transmission line with different air-gaps. In the simulation, with the increasing of air-gaps, the reduced operating frequency can be observed.

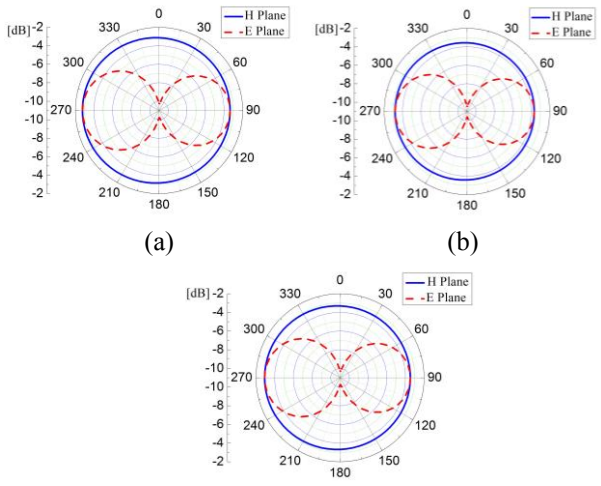

(a) (b)

(c)

Figure 6: Simulated radiation pattern. (a) Simulated result at $f_{-1} = 816.5MHz$. (b) Simulated result at $f_{-3} = 781.2MHz$. (c)Simulated result at 802.3MHz.

From the Figure 4, we can know that only one resonance mode $n = -1$ was observed when g = 1.2mm, whereas two resonance modes $n = -1$ and $n = -3$ was observed when g changes between 0.9 and 1.1mm , and when g = 1.1mm the impedance is matched well. Figure 5 shows that the dipole antenna is well matched from 776.9 MHz to 827.6 MHz with an impedance bandwidth of 6.36%. Figure 6 (a) and (b) respectively show the simulated values of radiation pattern at 816.5MHz for $n = -1$ and 781.2MHz for $n = -3$. The gain of center frequency at 802.3 MHz is -2.92 dB and its simulated radiation pattern is shown in Figure 6(c).

4. Conclusions

A bandwidth-extended electrically small dipole antenna based on periodic CRLH transmission line has been proposed in this letter. The simulated results show that, it has a 6.36% relative bandwidth, and exhibits a typical vertically polarized radiation pattern of a dipole antenna. The research for periodic CRLH transmission line structure provides a very good approach to broaden the bandwidth of the electrically small dipole antenna.

Acknowledgements

This work was supported by the National Natural Science Funds (Grant Nos.6136115, 61161002） , the Innovation Project Of GUET Graduate Education (GDYCSZ201459) and the Natural Science Foundation of Guangxi under Grant (2014GXNSFAA118283).

References

[1] H. Iizuka, Peter. S. Hall, Alejandro Lucas Borja ,“Dipole Antenna With Left-Handed Loading,” IEEE Antennas and Wirless Propagation Letters , VOL. 5, 2006.S.V. Patankar, *Numerical Heat Transfer and* Fluid Flow, Hemisphere Publishers, New York, 1980.

[2] C. Lin, H. Arai, T. Suda, “A Small Monopole Antenna Based on Composite Right/Left-Handed Transmission Line by Coaxial Structure ” , Proceedings of iWAT2008, Chiba, Japan.

[3] Q. Liu, “Antennas using left-handed transmission lines,” Ph.D. dissertation, Dept. Electrical, Electronic and Computer Eng., Birmingham Univ., Birmingham, MA, 2009, pp.84.

[4] C. Caloz, A. Sanada, and T. Itoh, “A novel composite right-/left handed coupled-line directional coupler with arbitrary coupling level and broad bandwidth,” IEEE Trans. Microw. Theory Tech., vol. 52, no.3, pp. 980-992, 2004.

[5] C. Caloz and T. Itoh, Electromagnetic Metamaterials: Transmission Line Theory and Microwave Applications, John Wiley & Sons, Incorporated Publication, 2006, pp. 249-252.

A Wide-Band Wide-Coverage Printed Dipole Antenna for Spectrum Monitoring Applications

Yufeng Yu[1*], Xiaoyi He[1], Yufeng Wang[1]

[1] No.36 Research Institute of CETC, Jiaxing, China
*corresponding author, E-mail: yuyufeng.10@gmail.com

Abstract

A wide-band wide-coverage antenna with a stable unidirectional radiation pattern is proposed in this paper. The antenna is composed of a driven dipole, a parasitic dipole, a printed balun and a metal ground. The driven and parasitic dipoles contribute three resonances, which result in a wide impedance bandwidth (VSWR≤ 3) of 100%. The parasitic dipole also leads to stable unidirectional radiation over the frequency band from 3 GHz to 8.5 GHz, in which the broadside gain is around 7.8 dBi and the half-power beamwidth in *H* plane is wider than 91°.

1. Introduction

Wide-band wide-Coverage antennas with stable unidirectional radiation patterns are urgently required in spectrum monitoring systems [1]. Log-periodic [2], horn [3] and Vivaldi [4] antennas are typically wide-band antennas; however, they are bulky in size and not suitable for high-integration systems. A printed dipole antenna with adjusted integrated balun proposed in [5] is compact in size; however, the bandwidth (RL>10 dB) of 40% is not sufficient for many spectrum monitoring systems. A cavity-backed elliptical printed dipole antenna [6] achieves an impedance bandwidth of 129.7% for VSWR≤ 2; however, H plane beam widths are narrow, especially at higher frequencies.

In this paper, a wide-band wide-coverage printed dipole antenna is proposed. A parasitic dipole is added above the driven dipole, which not only greatly broadens the impedance bandwidth but also stabilize the radiation patterns. The proposed antenna achieves an operating frequency band from 3 GHz to 8.5 GHz (96%), in which the antenna exhibits a VSWR lower than 3, a broadside gain between 7.35 dBi to 8.3 dBi and a half-power beam width (HPBW) in *H* planes between 91° to 126°. The proposed antenna is a good candidate for spectrum monitoring applications.

2. Antenna Configuration

The configuration of the proposed antenna is depicted in Figure. 1. The antenna is composed of a driven dipole, a parasitic dipole, a printed balun and a metal ground. The driven dipole is located above the metal ground with a height of h_1. The parasitic dipole is placed above the driven dipole with a height of h_2 to enhance the impedance bandwidth and stabilize the radiation patterns in the upper frequency band. A printed balun which is vertically placed between the driven dipole and the metal ground provides a transition from a microstrip line to a parallel stripline [5]. It consists of a 50-Ω microstrip line and a slot line which are printed on the front and back sides of a substrate, respectively. The parallel stripline is soldered to the two arms of the driven dipole to feed it. The feeding position is with a distance of d_0 away from the center of the dipole in the *y* direction to avoid an asymmetric H plane radiation pattern at the. An SMA connector is placed under the metal ground to feed the antenna with its inner conductor soldered to the 50-Ω microstrip line and outer conductor soldered to the metal ground.

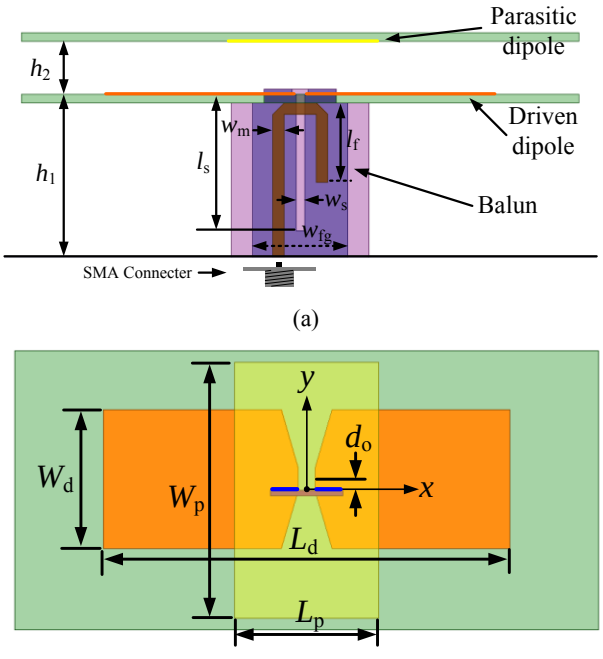

Figure 1: Antenna configuration: (a) side view and (b) top view.

The size of the metal ground is 120 mm × 70 mm. The substrate of Rogers RO 4350B with a dielectric constant of 3.48 and a thickness of 0.508 mm is used for the printed dipoles and balun in this paper. Detailed dimensions of the antenna shown in Figure 1 are as follows: L_d=36.5 mm, W_d=12.5 mm, L_p=13 mm, W_p=23 mm, d_0=1 mm, h_1=15 mm, h_2=4 mm, w_{fg}=8 mm, w_m=1.1 mm, l_f=7.5 mm, w_s=0.5 mm, l_s=12 mm.

3. Analysis and Parametric Studies

Usually a half-wavelength dipole operating at its fundamental mode has very limited impedance bandwidth. In our design, a parasitic dipole is added above the driven dipole to enhance the impedance bandwidth. Figure 2 shows simulated VSWRs versus the length of the parasitic dipole (L_p). Each VSWR shoes three resonances. It is seen that as L_p increases, the second resonance moves to lower frequencies while the first resonance keeps stable. Obviously the second resonance is contributed by the parasitic dipole and the first and third resonances are contributed by the driven dipole. With a fine tuning of the parameters of the parasitic dipole (L_p, W_p and h_2), the three resonances properly connect to each other and a wide impedance bandwidth is achieved. For L_p=13 mm, VSWR$\leqslant$ 2.8 is obtained in the frequency range of 3 GHz to 9 GHz.

Another important effect of the parasitic dipole is to stabilize the radiation patterns, especially at higher frequencies. Simulated radiation pattern comparisons at 8.5 GHz with and without the parasitic dipole are shown in Figure 3. It is clearly seen that the broadside gain is greatly enhanced with the parasitic dipole (from 1.3 dBi to 8.6 dBi). Without the parasitic dipole, the height of the driven dipole from the metal ground h_1 is about 1.2 wavelengths at 8.5 GHz, which means the reflected wave from the metal ground is almost out of phase with the direct wave, thus a radiation null at broadside direction occurs. When the parasitic dipole is added, it acts as a director which enables a directional radiation without the metal ground. The front-to-back ratio is about 8.7 dB, which means the reflected wave is extremely small compared with the direct wave. In this case, the reflected wave has little effect on the total radiation and thus a good broadside radiation is achieved.

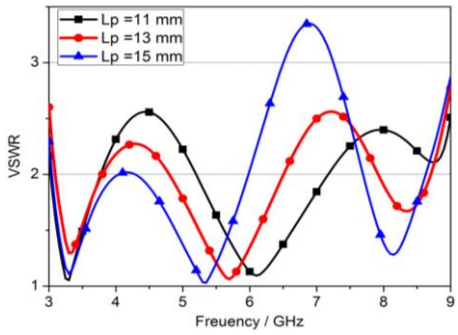

Figure 2: Simulated VSWRs of the proposed antenna versus L_p.

4. Results and Discussions

The proposed antenna is simulated and optimized using HFSS v13. Simulated VSWR is depicted in Figure 3. The relative impedance bandwidth for VSWR$\leq$ 3 is 100% (3 GHz to 9 GHz). Three resonances can be seen from the VSWR result. It is worth noting that the first and third resonance is contributed by the driven dipole and the second resonance is contributed by the parasitic dipole. The antenna cannot achieve such a wide bandwidth without the parasitic dipole.

Figure 3 also shows the simulated broadside gain. It is seen that from 3 GHz to 8.5 GHz, the antenna exhibits a stable gain between 7.35 dBi to 8.3 dBi. The gain decreases rapidly above 8.5 GHz because the grating lobe occurs.

Simulated radiation patterns in H (y-z) and E (x-z) planes at 3 GHz, 5.5 GHz and 8.5 GHz are plotted in Figure 4. It is seen that stable unidirectional radiation patterns are obtained over the wide frequency range. At the three frequencies, HPBWs in H planes are 91°, 107° and 126°, while in E planes the results are 55°, 70° and 45°.

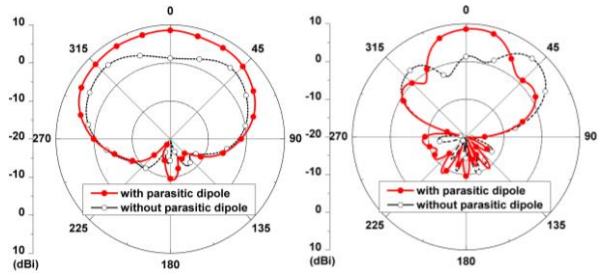

(a) (b)

Figure 3: Simulated radiation patterns at 8.5 GHz with and without the parasitic dipole: (a) H plane and (b) E plane.

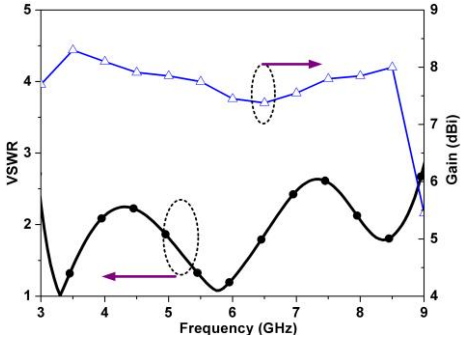

Figure 4: Simulated VSWR and gain results.

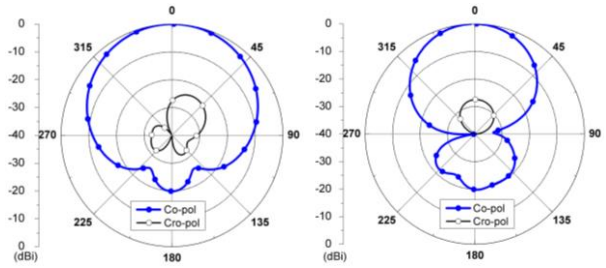

H plane E plane

(a)

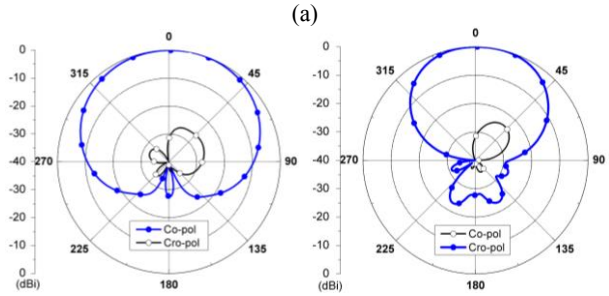

H plane E plane

(b)

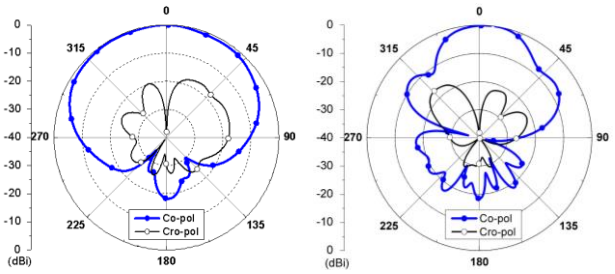

H plane E plane

(c)

Figure 5: Simulated radiation patterns: (a) 3 GHz, (b) 5.5 GHz and (c) 8.5 GHz.

5. Conclusions

A Wide-band wide-coverage dipole printed antenna is developed in this paper. A parasitic dipole is introduced above the driven dipole to broaden the impedance bandwidth and stabilize the radiation patterns. Simulated results show that the antenna achieves a bandwidth of 96%, in which VSWR is below 3, broadside gain is around 7.8 dBi and HPBW is wider than 91°. The proposed antenna is suitable for spectrum monitoring applications.

References

[1] H. Nguyen, N. Nguyen, G. Zheng, Z. Han and R. Zheng, Binary blind identification of wireless transmission technologies for wide-band spectrum monitoring, Global Telecommunications Conference, 2011.

[2] D. E. Isbell, Log periodic dipole arrays. *IRE Trans. Antennas Propagat*., vol. 8, pp. 260–267, 1960.

[3] C. A. Balanis, Antenna theory: analysis and design, 3rd ed, New York: Wiley, 2005, pp739-809.

[4] M. Chiappe and G. Gragnani, Vivaldi antennas for microwave imaging: theoretical analysis and design considerations. *IEEE Transactions on Instrumentation and Measurement*, vol. 55, no. 2, pp. 1885-1891, 2006.

[5] R. L. Li, T. Wu, B. Pan, K. Lim, J. Laskar, and M. M. Tentzeris, Equivalent-circuit analysis of a broadband printed dipole with adjusted integrated balun and array for base station applications," *IEEE Trans. Antennas Propag*., vol. 57, pp. 2180-2184, July 2009.

[6] Z. Tu, D. F. Zhou, G. Q. Zhang, F. X., X. Lei, and D. W. Zhang, A wideband cavity-Backed elliptical printed dipole antenna with enhanced radiation patterns, *IEEE Antennas Wireless Propag. Lett*., vol. 12, pp. 1610-1613, 2013.

Transmission Line Model for Compact Differential Dual-band Antenna with Stacked Patches

Liping Han, Gaofei Wu, Liyun Yan, Runbo Ma, and Wenmei Zhang

College of Physics and Electronics Engineering, Shanxi University, Taiyuan, China
*corresponding author, E-mail: hlp@sxu.edu.cn

Abstract

The transmission line model for a compact differential dual-band antenna with stacked configuration is presented in this paper. The coupling admittance between stacked patches is calculated when the antenna is fed from the upper patch. To validate the transmission line model, two compact differential dual-band antennas are designed. The simulated results indicate that the proposed transmission line model is suitable for analyzing compact differential dual-band antennas with stacked configuration.

1. Introduction

With the rapid development of wireless communication technology, compact and multi-band antennas for mobile terminals are demanded. Also, increasing demand in the wireless communication market has led to the need for compact and fully integrated radio frequency front-end products, where differential signals are preferable. Recently, some compact differential dual-band antennas have been reported.

The transmission line model is often used to predict the input characteristic of rectangular patch antenna due to its accuracy and numerical efficiency. Pues, H. proposed the transmission line model for the rectangular antenna fed by a coaxial probe and a microstrip line [1]. Gao, Wei presented the transmission line model for the aperture-coupled microstrip antenna with parasitic elements [2]. Jaisson, D presented the transmission line model for the rectangular antenna fed by proximity coupling [3]. Recently, Loizou, L. proposed a transmission line model for the capacitively loaded inverted-F antenna [4], and Ruyle, J.E. presented a wideband transmission line model for a slot antenna [5].

The aim of this paper is to provide the transmission line model for a compact differential dual-band antenna with stacked patches. The formulas for calculating the resistor and capacitor of via hole between stacked patches are provided when the antenna is fed from the upper patch. Two examples of compact differential dual-band antennas are designed to validate the transmission line model. The simulated results indicate the validation of the transmission line model for the compact differential dual-band antenna.

2. Transmission line model for antenna

2.1. Structure of antenna

The geometry of the compact differential dual-band antenna with stacked patches is shown in Fig. 1 [6]. The top layer is substrate 1 with patch 1, the middle layer is substrate 2 with patch 2, and the bottom layer is the ground plane. Patches 1 and 2 are connected through two via holes. The minimization is realized by arranging the radiating element with half guided wavelength at the first resonant frequency on two stacked layers. The antenna is designed to work at 2.4 and 5.2 GHz bands, and is simulated with CST Microwave Studio.

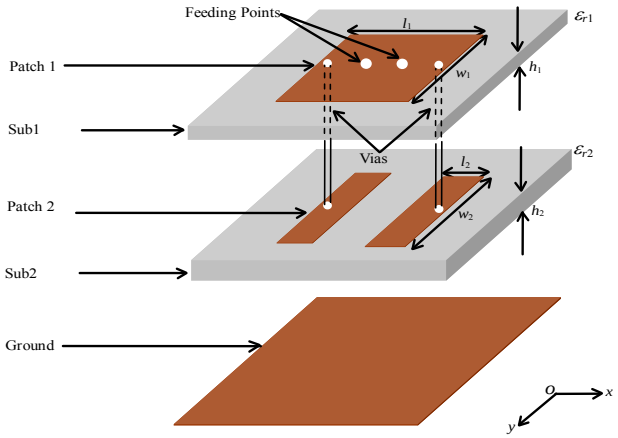

Figure 1: Geometry of antenna.

2.2. Transmission line model of antenna

Fig. 2 shows the transmission line model for the compact differential antenna. Each patch of the antenna is modeled as a section of transmission line terminated by two radiating slots, and via hole between stacked patches is represented by a parallel RLC circuit. Here, $Y_0^{\,i}$ and $Y_s^{\,i}$ denote the characteristics admittance and radiation admittance of patch i, R_v, L_v, and C_v denote the resistor, inductor and capacitor of via hole between stacked patches, L_f denotes the inductance of feeding probe.

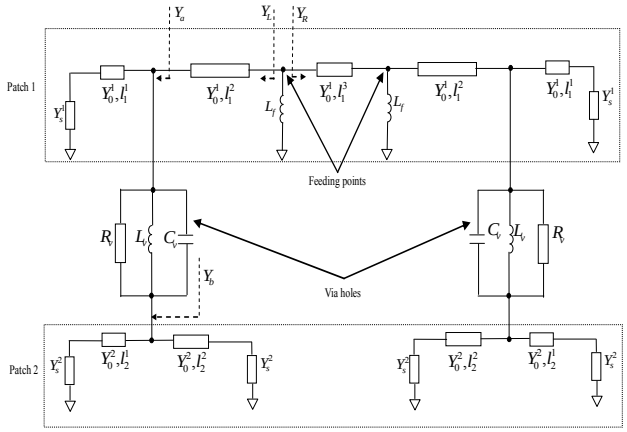

Figure 2: Transmission line model for antenna.

2.3. Determination of model parameters

The characteristic admittance (Y_0^i) of stacked patches can be calculated as follows [7]

$$Y_0^i = \frac{\sqrt{\varepsilon_e^i}}{377}\left\{\frac{w_i}{h_i}+0.883+0.165\frac{\varepsilon_e^i-1}{(\varepsilon_e^i)^2}+\frac{\varepsilon_e^i+1}{\pi\varepsilon_e^i}\left[\ln\left(\frac{w_i}{h_i}+1.88\right)+0.758\right]\right\} \quad (1)$$

where w_i is the width of patch i, and h_i and ε_e^i are the thickness and effective permittivity of substrate i, respectively.

The radiation admittance (Y_s^i) is composed of radiation conductance (G_s^i) and radiation susceptance (B_s^i), which can be computed by [8]

$$G_s^i = \frac{1}{90}\left(\frac{w_i}{\lambda_0}\right)^2 \quad (2)$$

$$B_s^i = Y_0^i \tan(\beta_i \Delta l_i) \quad (3)$$

where λ_0 is the wavelength in free space, and β_i and Δl_i are the phase propagation constant and excess length of patch i, respectively.

The inductance of the feeding probe (L_f) and the via hole (L_v) can be calculated by [9]

$$L = \frac{377h}{2\pi c_0}\ln\left(\frac{c_0}{\pi f_r d\sqrt{\varepsilon_e}}\right) \quad (4)$$

where c_0 is the speed of light, f_r is the resonant frequency of the antenna, and h and d are the thickness and diameter of feeding probe (or via hole), respectively.

The resistor and capacitor of via hole (R_v and C_v) are calculated using the coupling admittance between stacked patches. The conventional stacked antenna is fed by a feeding probe which is connected to the lower patch, and Edimo, M. gives the formula for the coupling admittance between stacked patches [10]

$$Y = -2j\omega\varepsilon_e\varepsilon_0\frac{2\pi w_1\Delta l_2}{d_2(l_2)^2(k^2-k_0^2)}j_0\left(\frac{\pi\Delta l_1}{2l_2}\right)j_0^2\left(\frac{\pi\Delta l_2}{2l_2}\right)\cos\left[\frac{\pi}{2l_2}(l_1+\Delta l_1)\right] \quad (5)$$

where d_2 is the distance between stacked patches, k is wavenumber, k_0 is the cutoff wavenumber of fundamental mode, and $j_0(\ )$ is zero-order Bessel function. However, when a coaxial probe feeds the upper patch, the coupling between stacked patches is weaker than that of the conventional stacked antenna. We can modify the coupling coefficient with 3.94 instead of 2, and the formula for the coupling admittance can be expressed as

$$Y = -3.94j\omega\varepsilon_e\varepsilon_0\frac{2\pi w_1\Delta l_2}{d_2(l_2)^2(k^2-k_0^2)}j_0\left(\frac{\pi\Delta l_1}{2l_2}\right)j_0^2\left(\frac{\pi\Delta l_2}{2l_2}\right)\cos\left[\frac{\pi}{2l_2}(l_1+\Delta l_1)\right] \quad (6)$$

2.4. Input impedance of antenna

According to Fig. 2, the input impedance of the antenna can be written as

$$Z_{in} = 2\left[j\omega L_f + (Y_L+Y_R)^{-1}\right] \quad (7)$$

where Y_L and Y_R are the feeding point admittances defined in Fig. 2. We can determine Y_L and Y_R

$$Y_L = Y_0^1\left[\frac{Y_a + jY_0^1 tg(\beta_1 l_1^2)}{Y_0^1 + jY_a tg(\beta_1 l_1^2)}\right] \quad (8)$$

$$Y_R = -jY_0^1 ctg(\beta_1 l_1^3/2) \quad (9)$$

For Y_a shown in Fig. 2, we obtain

$$Y_a = Y_0^1\left[\frac{Y_s^1 + jY_0^1 tg(\beta_1 l_1^1)}{Y_0^1 + jY_s^1 tg(\beta_1 l_1^1)}\right] + \left(\frac{1}{Y_v}+\frac{1}{Y_b}\right)^{-1} \quad (10)$$

where Y_v is the admittance of via hole, and Y_b is given by

$$Y_b = Y_0^2\left[\frac{Y_s^2 + jY_0^2 tg(\beta_2 l_2^1)}{Y_0^2 + jY_s^2 tg(\beta_2 l_2^1)}\right] + Y_0^2\left[\frac{Y_s^2 + jY_0^2 tg(\beta_2 l_2^2)}{Y_0^2 + jY_s^2 tg(\beta_2 l_2^2)}\right] \quad (11)$$

2.5. Sensitivity analysis of antenna using the model

The sensitivity analysis of the antenna is made using the transmission line model. When the dimensions of one patch are analyzed, those of the other patch remain unchanged. The odd-mode reflection coefficient for different patch 1 is shown in Fig. 3. It can be seen that as l_1 increases the first resonant frequency (f_1) decreases, but the second resonant frequency (f_2) decreases significantly. Also, as w_1 increases, both f_1 and f_2 decrease slightly. Fig. 4 shows the odd-mode reflection coefficient for different patch 2. It is evident that as l_2 increases, f_1 decreases while f_2 changes slightly. The effect of w_2 on the resonant frequencies is similar to that of w_1. From Figs. 3 and 4, we can see that l_1 and l_2 affect the resonant frequencies more significantly than w_1 and w_2. In other words, the f_1 is controlled by the lengths of stacked patches, and the f_2 is mainly determined by the length of patch 1.

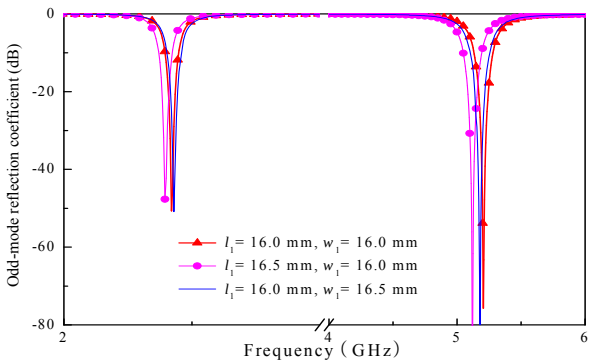

Figure 3: Odd-mode reflection coefficient for different patch 1.

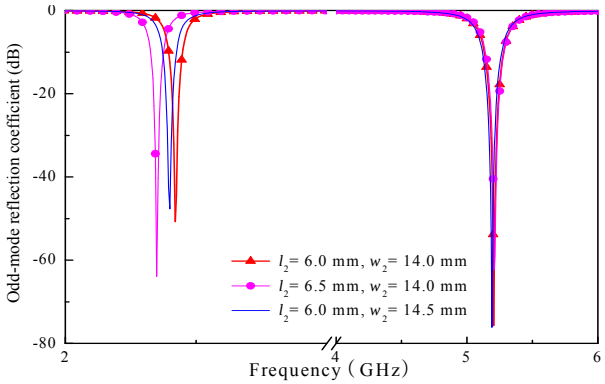

Figure 4: Odd-mode reflection coefficient for different patch 2.

3. Validation of transmission line model

To validate the transmission line model for compact differential dual-band antenna, two antennas (antenna 1 and antenna 2) are designed on Rogers 4350B substrate with relative permittivity of 3.48. When the center of the ground plane is chosen as the origin of coordinates, the x-coordinate of feeding points and via holes is denoted by $\pm x_f$ and $\pm x_v$. The dimensions of antenna 1 are, h_1=0.8mm, h_2=1.6mm, l_1=w_1=16mm, l_2=6mm, w_2=16mm, x_f=1.3mm and x_v=7.5mm, respectively. The dimensions of antenna 2 are, h_1= 0.8mm, h_2=1.6mm, l_1=16mm, w_1=17mm, l_2=2mm, w_2=12.2mm, x_f=2mm and x_v=8mm. Both antennas have a compact size of less than $0.27\lambda_1 \times 0.27\lambda_1$($\lambda_1$ is the guided wavelength at f_1).

Figs. 5 and 6 show the simulated and modeled odd-mode reflection coefficient of antennas 1 and 2, respectively. Good agreement between the simulated and modeled results is obtained. It can be seen that, for antenna 1 and antenna 2, the TLM predicts two resonant frequencies at 2.42/5.2GHz and 3.5/5.78GHz, which are close to the resonant frequencies obtained from the simulation. We can see that the maximum difference between the modeled and simulated results is less than 1%.

The simulated radiation patterns at f_1 and f_2 of both antennas are shown in Figs. 7 and 8. It can be seen that good radiations in E- and H-planes are obtained.

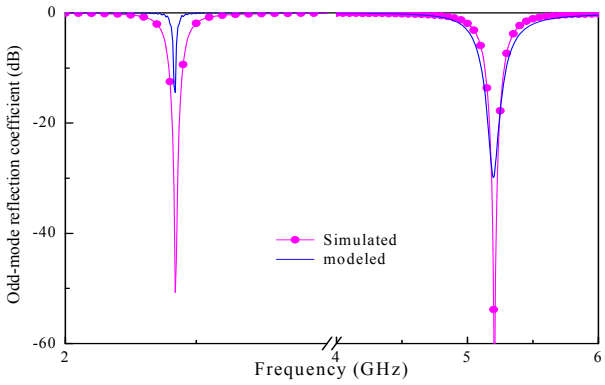

Figure 5: Simulated and modeled odd-mode reflection coefficient of antenna 1.

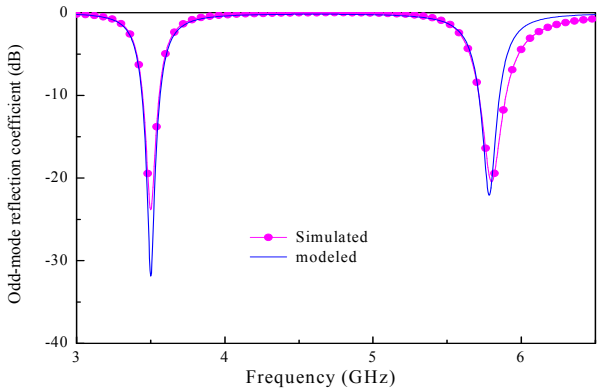

Figure 6: Simulated and modeled odd-mode reflection coefficient of antenna 2.

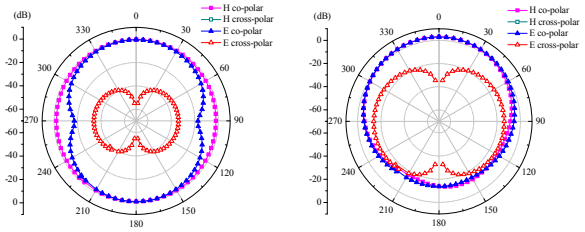

(a) At f_1 (b) At f_2

Figure 7: Simulated radiation patterns of antenna 1.

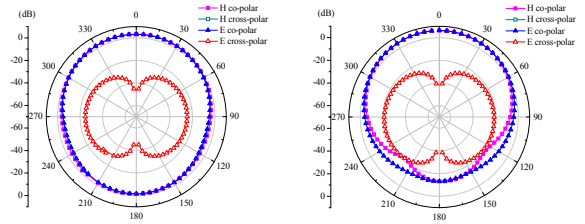

(a) At f_1 (b) At f_2

Figure 8: Simulated radiation patterns of antenna 2.

4. Conclusions

In this paper, a transmission line model for compact differential dual-band antenna with stacked configuration is demonstrated. Each patch of the antenna is modeled as a section of transmission line terminated by two radiating slots; via hole between stacked patches is represented by a resistor, an inductance and a capacitor in parallel. In particular, the formula for the resistor and capacitor of via hole between stacked patches is provided when the antenna is fed from the upper patch. The validation of the model is verified by the simulated results. Also, Good radiation performances have been achieved at both bands.

Acknowledgements

This work is supported by the National Science Foundation of China (61172045, 61271160), the National Fundamental Fund of Personal Training (J1210036) and the Natural Science Foundation of Shanxi province (2012011013-3).

References

[1] H. Pues, and A. van de Capelle, Accurate transmission-line model for the rectangular microstrip antenna, *IEE Proc. Microw. Optics Antennas* 131(6): 334-340, 1984.

[2] G. Wei, Q. Zhu, Transmission-line model analysis of aperture-coupled microstrip antenna with parasitic elements, *ICMMT2002*, Beijing, China, pp. 397 – 400, 2002.

[3] J.E. Ruyle, J.T. Bernhard, A wideband transmission line model for a slot antenna, *IEEE Trans. Antennas Propag.* 61(3): 1407-1419, 2013.

[4] D. Jaisson, Simple model for computing the input impedance of a rectangular patch antenna with electromagnetic coupling, *IEE Proc. Microw. Antennas Propag.* 152(6): 476-480, 2005.

[5] L. Loizou, J. Buckley, B. O'Flynn, J. Barton, C. O'Mathuna, A transmission line model for the capacitively loaded inverted-F antenna (CLIFA), *Proc. EuCAP2014*, Hague, Netherland, pp. 1387−1390, 2014.

[6] L.P. Han, W.M. Zhang, X.W. Chen, G.R. Han, R.B. Ma, Design of compact differential dual-frequency antenna with stacked patches, *IEEE Trans. Antennas Propag.* 58(4): 1387-1392, 2010.

[7] S. S. Zhong, *Theory and Applications for Microstrip Antennas*, Xidian University Press, Xian, 1991.

[8] J. R. Jame, P.S. Hall, *Microstrip antenna design handbook*, Artech House Inc., Norwood, 2000.

[9] J.J. Wang, Y.P. Zhang, Kai Meng Chua, A.C.W. Lu, Circuit model of microstrip patch antenna on ceramic land grid array package for antenna-chip codesign of highly integrated RF transceivers, *IEEE Trans. Antennas Propag.* 53(12): 3877-3883, 2005.

[10] M. Edimo, K. Mahdjoubi, A. Sharaiha, C. Terret, Simple circuit model for coax-fed stacked rectangular microstrip patch antenna, *IEE Proc-Microw. Antennas Propag.* 145(3): 268-272, 1998.

A Radome Used for Circular Polarized Spherical Conformal Antenna Array

Xing Jiang[1], Yingchao Huang[1], Lin Peng[1]

[1]School of Information and Communication, Guilin University of Electronic Technology, Guilin, China
*Yingchao Huang, E-mail: 599319505@qq.com

Abstract

A novel radome used for circularly polarized conformal antenna array in the C-band (4.5-5.1GHz) is presented in this paper. The structure of the radome is hemispherical and B-sandwich type. In order to study the impacts of the radome on antenna performances, characteristics including axial ratio, main beam direction and the 3 dB beam widths were analyzed. The simulation results show that the antenna covered by the radome has reached the following guidelines: during the whole bandwidth the gain is larger than 8.5 dB, the axial ratio of main lobe direction is lower than 2.5 dB, the 3 dB angular widths is larger than 55 degree and the deflection of main beam direction is smaller than 5 degrees.

1. Introduction

Radomes are often used to protect antennas from severe environmental effects in many practical applications. However, the performances of antennas are also degraded by the radomes. Thus, in order to reduce the adverse effect, it is interest to study the characteristics of antennas in the presence of various radomes. Therefore, the investigation on what the effects of a dielectric radome are and on how these effects can be minimized has received much attention in the last several decades. For instance, a high performance radome covering a circularly polarized, high gain, light weight, wide band conical horn antenna [1], a novel circularly polarized metamaterial based antenna radome [2], a dielectric hemisphere covering the slot antennas [3], and a spherical shell radome covering a uniform circular aperture [4] have been investigated.

2. The theory and design

The conventional way to solve the problemS of antenna and radome are by regarding the antenna feed, the antenna and the radome as a unit, and calculating the electromagnetic field boundary value of this unit. However, this method just suit for a few simple and ordinary structures, and has very limit for our research. As in this research, we adopted a radome with a hemi spherical structure since it is used for a hemispherical antenna array, moreover, due to circular polarization, phase of the antenna and symmetry architecture of the antenna array must also be considered. Because the radius of curvature is bigger than 1.5, we adapt a method called 'Optical Ray Approximation', which has a good performance at the analysis of electromagnetic radiation.

Though the design of a radome includes structural strength and electrical performance, we just describe the latter in this paper. At the same time, for the distance between antenna and radome is longer than several wavelengths, the electromagnetic radiation is simplified to a plan wave incident on the multilayer infinite plane.

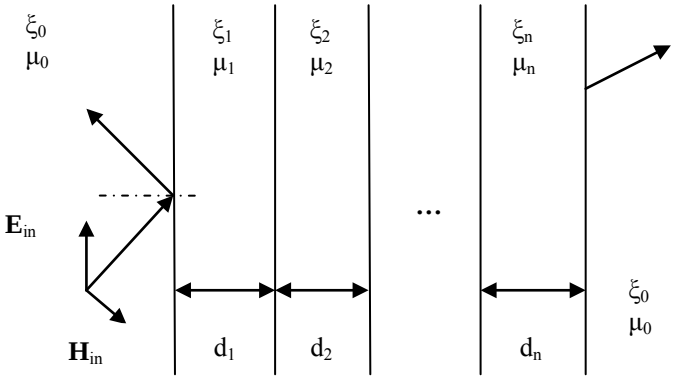

Figure 1: plan wave incident on the multilayer infinite plane

Figure 1 illustrates the transmission characteristics of a plan wave incident on a multilayer infinite plane structure from free space at θ angle. The permitivity of layers were ξ_1, ξ_2, …, ξ_n, the magnetic permeability were μ_1, μ_2, …, μ_n, the thickness were d_1, d_2, …, d_n.

Any polarized electromagnetic waves can be decomposed as a vertical polarized wave which perpendicular to the incidence plan and a horizontal polarized wave which parallel to the incidence plan. If the wave incident on an N layers infinite plane at θ angle, the electric field E_{in} and magnetic field H_{in} can be presented as follows [5]:

$$\begin{pmatrix} E_{in} \\ H_{in} \end{pmatrix} = \prod_{i=1}^{N} \begin{pmatrix} \cos\alpha_i & (j/M_i)\sin\alpha_i \\ jM_i \sin\alpha_i & \cos\alpha_i \end{pmatrix} \begin{pmatrix} 1 \\ 1 \end{pmatrix} \quad (1)$$

Where α_i is the phase angle and M_i is the admittance of the i layer which may be presented as follows:

$$\alpha_i = (2\pi d_i/\lambda)\left((\xi_i/\xi_0)(1 - j\tan\delta_i) - \sin^2\theta\right)^{1/2} \quad (2)$$

$$M_i = \begin{cases} M_{\perp i} = \left(\xi_i \mu_0 / \xi_0 \mu_i - \sin^2\theta\right)^{1/2} / \cos\theta \\ (vertical\ polarization) \\ M_{//i} = \left(\xi_i \mu_0 \cos\theta / \xi_0 \mu_i\right) / \left(\xi_i \mu_0 / \xi_0 \mu_i - \sin^2\theta\right)^{1/2} \\ (horizontal\ polarization) \end{cases} \quad (3)$$

Where λ the wavelength in vacuum, δ_i is the loss angle of the i layer.

A B-sandwich dielectric material is adopted for its wide bandwidth, which has three layers and a central symmetrical structure [5]. What's more, since the permittivity of the two outer layers is smaller than the inner's, there's a lot of choice for the thickness of the inner layer. The outer layer thickness of the classic B-sandwich dielectric material may be presented as follows:

$$d = \lambda \Big/ \left(4\sqrt{(\xi_s/\xi_0) - \sin^2\theta}\right) \quad (4)$$

The permittivity relationship of the outer layer and inner layer is presented as follow: $\xi_c = \xi_s^2$, where ξ_c is the permittivity of the inner layer and ξ_s is the permittivity of the outer layer.

If the permittivity of the outer layer is too small, there will be a significant reduction in working bandwidth. In order to reduce the influence to the antenna, we studied a novel B-sandwich dielectric material. For the loss tangent $\tan\delta$ changes with the frequency, also has a great effect to the power pattern at SHF bands, we take it into account when calculating the thickness. The optimized thickness is given as follow:

$$d = \lambda \Big/ \left(4\sqrt{\left(\left(\xi_s\left(1 - j\tan\delta_s\right)/\xi_0\right) - \sin^2\theta\right)}\right) \quad (5)$$

Where δ_s is loss angle of the outer layer.

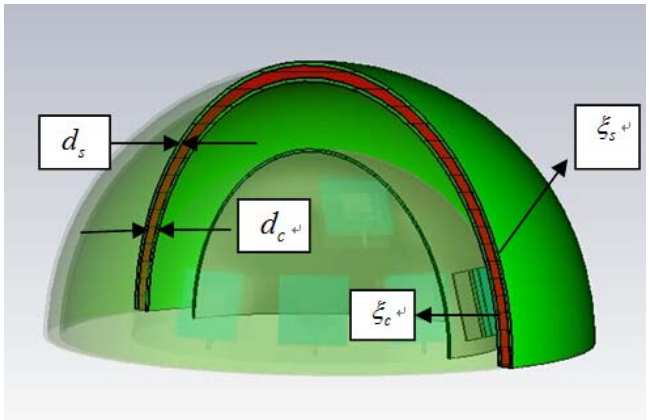

Figure 2 the model of the antenna array covered by the radome

The simulation model of the spherical conformal antenna array covered by the radome is given in figure 2. The antenna located at the radome central and the radome radius is 190 mm, the thickness of outer layer d_s and inner layer d_c were 3 mm and 9 mm, the permittivity of outer layer ξ_s and inner layer ξ_c were 2.5 and 6.5.

3. Numerical results

The model has been performed using the Microwave Studio of CST and the optimized result is presented as follows.

Simulation for main lobe direction, angular width 3dB, axial ratio, gain and VSWR were performed for the cases without & with the radome for comparison. From the simulations, radiation plot is affected by the radome and the main lobe direction is deflected (fig. 3). The difference introduced by the radome is less than 5 degrees within the band which is allowable for the antenna array.

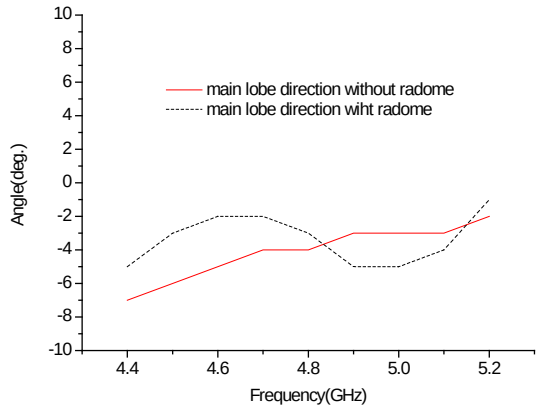

Figure 3 Comparison of main lobe direction without & with radome

3 dB pattern width and gain comparisons are shown in figure 4 and figure 5, respectively. Some differences are observed for the cases with and without radome. As shown in the figures, the pattern width is narrowed by the radome, while the largest gain shifted to higher frequencies. The disturbance is due to phase center shift produced by the introduction of radome but this has been improved through proper optimization as also can be done with the use of dielectric lens for correction of phase center [6].

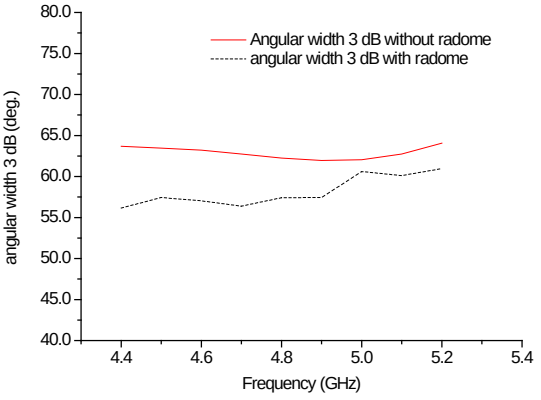

Figure 4 Comparison of angular width 3dB without & with radome

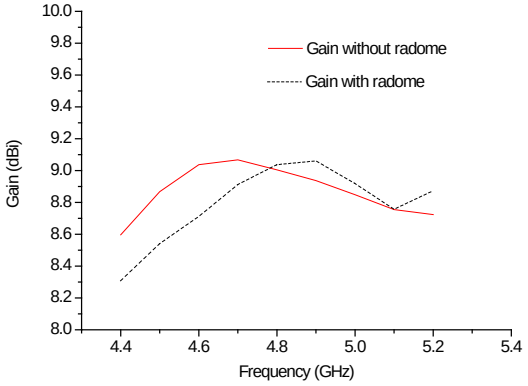

Figure 5 Comparison of gain without & with radome

Figure 6 and figure 7 show the comparison result of axial ratio and VSWR. The introduction of radome has little effect on axial ratio and VSWR and no obvious differences observed after the introduction of radome. The figures show that circular polarization bandwidth with axial ratio < 3 dB are range from 4.4GHz to 5.2GHz, and the impedance bandwidth with VSWR<1.3 are 800MHz. And, the circular polarization band and impedance band are coincidence.

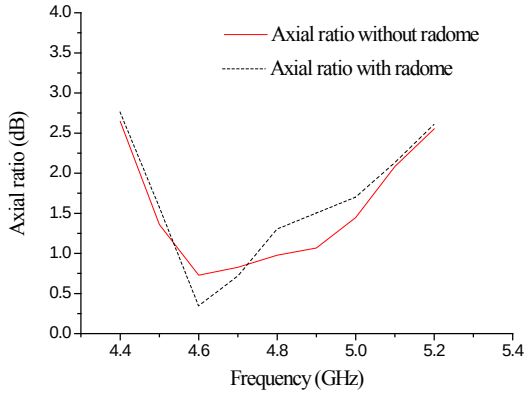

Figure 6 Comparison of axial ratio without & with radome

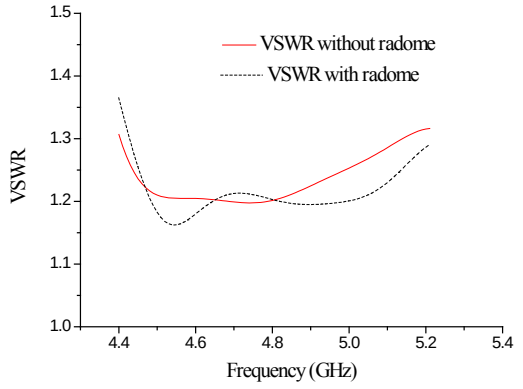

Figure 7 Comparison of VSWR without & with radome

4. Conclusion

In this paper, a novel radome is presented for spherical conformal structure. In order to reduce the adverse effects of radome to the hemispherical structure, an improved B-sandwich dielectric material was adopted as radome. Simulation results show that the radome has small influences to the performances of the antenna array and suitable for many applications. Further investigations are being conducted by our team.

Acknowledgements

This work was supported by the National Natural Science Foundation of China (Grant NO. 61371056), Guangxi Key Lab of Wireless Wideband Communication & Signal Processing (Grant No. GXKL0614103), and Innovation Project of GUET Graduate Education (Grant No. GDYCSZ201414).

References

[1] S. h. Hasan, *Design & measurements techniques for circularly polarized, dual fed, high gain, lightweight, wideband conical horn antenna with suppressed side lobes & high performance radome for space applications*, Antennas Propagation and EM Theory, 9th International Symposium on IEEE, 2010.

[2] H. S. Su, H. C. Huang, K. H. Lin, C. Y. Wu, H. H. Lin, *Gain-enhanced metamaterial radome for circularly-polarized antenna*, Antennas and Propagation Society International Symposium, 2010 IEEE.

[3] A. A. Kishk, G. Zhou, A. W. Glisson, *Analysis of dielectric-resonator antennas with emphasis on hemispherical structures*, IEEE Antennas and Propagation Magazine, 36(2): 20-31, 1994.

[4] P. S. Kooi, M. S. Leong, T. S. Yeo, X.Ma, *An analysis of a circular aperture antenna covered with a dielectric hemi-spherical shell radome over ground plane*, Antennas and Propagation Society International Symposium, 3: 1442-1445, 1995.

[5] D. X. Wang, *broadband modified B sandwich as radome's layer structure*, Journal of Electronics, 16: 232-237, 1994. (In Chinese)

[6] N. Y. Joshi, HKB. Pandya, P. K. Atrey, *Gaussian optics lens antenna (GOLA) system for plasma diagnostics*, Recent Advances in Microwave Theory and Applications, 2008. International Conference on microwave, IEEE, 2008: 457-459.

Optics and Photonics

Generation of Multiple Excitons in Ag_2S Quantum Dots: Single High-Energy *versus* Multiple-Photon Excitation

Jingya Sun,1 Weili Yu,2 Anwar Usman,1 Tayirjan T. Isimjan,1 Silvano DGobbo,1 Erkki Alarousu,1 Kazuhiro Takanabe,2 and Omar F. Mohammed*1

1Solar and Photovoltaic Engineering Research Center, Division of Physical Sciences and Engineering, King Abdullah University of Science and Technology, Thuwal 23955-6900, Saudi Arabia
2KAUST Catalysis Center, Division of Physical Sciences and Engineering, King Abdullah University of Science and Technology (KAUST), Thuwal 23955-6900, Saudi Arabia
*corresponding author, E-mail: omar.abdelsaboor@kaust.edu.sa, omar3070@caltech.edu (O.F.M.)

Abstract

In the theory of a conventional solar cell, each photon is only able to excite one electron across the band gap of the semiconductor, and any excess energy in that photon is dissipated as heat. Carrier multiplication is the phenomenon wherein the absorption of a single photon leads to the excitation of multiple electrons from the valence band to conduction band. In a material with carrier multiplication, high-energy photons excite on average more than one electron across the band gap, and so in principle the solar cell can produce more useful work. We explored the carrier multiplications generated by single high-energy and multiple photon absorption in Ag2S quantum dots (QDs) using femtosecond broadband transient absorption spectroscopy. We found that, irrespective of the size of the QDs and how the multiple excitons are generated in the Ag2S QDs, two distinct characteristic time constants of 9.6–10.2 ps and 135–175 ps are obtained for the non-radiative Auger recombination of the multiple excitons, indicating the existence of two binding excitons, namely tightly bound and weakly bound excitons. More importantly, the lifetimes of multiple-excitons in Ag2S QDs were about one and two orders of magnitude longer than those of comparable size PbS QDs and single-walled carbon nanotubes, respectively. This result is significant because it suggests that, by utilizing an appropriate electron acceptor, there is a higher possibility to extract multiple electron-hole pairs in Ag2S QDs, which should improve the performance of QD-based solar cell devices. Additionally, upon single high-energy photon excitation, we measured a MEG threshold of 2.3 Eg, suggesting that the MEG process in Ag2S QDs has a photon energy threshold close to the theoretical energy conservation limit.

1. Introduction

Flexible solar panels made from semiconductor quantum dots have great potential to be useful light-harvesting materials, opening up an optimistic view to utilize this new technology in third-generation photovoltaic devices.[1,2] Several theoretical and experimental investigations have also been devoted to the fundamental mechanism for understanding and finally controlling the MEG process in many semiconductor QDs. As an advance in this area, we propose the use of Ag2S QDs as a new material system for multiple exciton generation and solar cells applications because they have very high photo-stability, low toxicity, and low threshold photon energy for electron multiplication and long lifetimes of the generated multiple electron-hole pairs.

A practical way to generate multiple excitons in QDs is to photoexcite them with high pump fluence. In this case, the QDs absorb more than one photon, generating more than a single exciton per QD. The presence of multiple excitons in QDs, no matter whether they are generated by one or several photon(s), is usually indicated by their distinct non-radiative Auger recombination. In this case, a fast electron-hole recombination is typically observed, leaving only one exciton per individual QD, which is governed by a slow radiative decay due to electron-hole recombination. Thus, by analyzing the relative contributions of fast and slow components, the MEG threshold and the quantum efficiency can be directly determined. Among time-resolved spectroscopic techniques, the best technique to monitor the MEG process is transient absorption (TA) spectroscopy with broadband capability that allows a broad-spectral range to be covered even in the near-infrared (IR) where the first exciton absorption peak is located.

2. Discussion

In this letter, we report the carrier dynamics and MEG efficiency in Ag2S QDs with bandgaps in the range of 1.55 - 1.07 eV, using femtosecond transient absorption spectroscopy with broadband capability. The time-resolved data clearly show the existence of two types of electron-hole pairs regardless of the method of generation (single- or

multiple-photon excitation), namely tightly bound and weakly bound excitons, and they can be distinguished by the distance of the charge carrier from the hole and the strength of the Coulomb interaction. Moreover, the ratio between the two types of multiple excitons can be controlled by the solvent polarity, pump fluence and QD size as well. In addition to this observation, we found that the threshold photon energy for MEG of Ag2S QDs with the band gap of 1.23 eV is 2.3 Eg, with a quantum efficiency of 173% per single-absorbed photon at a pump photoexcitation of 3.2 times the band gap. The advantages of QD-sensitized solar cells are their adjustable band gap energy through the control of the size of the QDs, their high extinction coefficient, and their shape, composition, and low cost.[3]

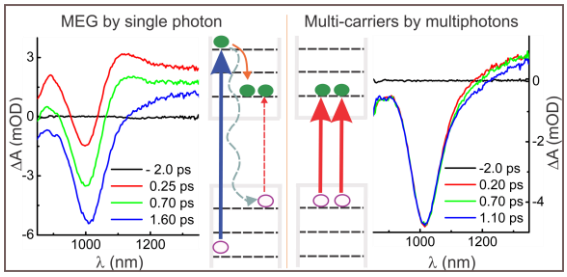

Figure 1: MEG by single high-energy photon and multi-carriers by multiphotons.

3. Conclusions

In conclusion, we measured the carrier dynamics and multiple exciton generation in Ag2S QDs using femtosecond broadband transient absorption spectroscopy. We found that multiple excitons in the QDs can be generated either by multi-photon excitation at high pump fluence or by single high-energy photon excitation. Irrespective how the multiple excitons are generated in the Ag2S QDs, the existence of two relaxation decays of the Auger recombination are evident, indicating the existence of two binding excitons, a tightly bound exciton and a weakly bound exciton. With single photon excitation, the MEG efficiency is 173% (under an excitation energy of 3.2 Eg), and the MEG threshold is 2.3 Eg, suggesting that the MEG process in Ag2S QDs has a threshold photon energy close to the theoretical energy conservation limit.

References

[1] Kamat, P. V.; Tvrdy, K.; Baker, D. R.; Radich, J. G. *Chem. Rev.*, 110, 6664-6688, 2010.

[2] Kamat, P. V. *J. Phys. Chem. Lett.*, 4, 908-918, 2013.

[3] J. Sun, W. Yu, A. Usman, T. T. Isimjan, S. D. Gobbo, E. Alarousu, K. Takanabe, O. F. Mohammed. *The J. Phys. Chem. Lett.*, 5, 659-665, 2014.

Low-Light Detection: Learning from Mammalian Evolution

Thanh Xuan Hoang[1*], Sara Nicole Nagelberg[2], Wensheng Chen[1,3], Mathias Kolle[2], and George Barbastathis[1,2]

[1]Singapore–MIT Alliance for Research and Technology (SMART) Centre, Singapore 138602, Singapore
[2]Department of Mechanical Engineering, Massachusetts Institute of Technology, Cambridge, Massachusetts 02139, USA
[3]Department of Mechanical Engineering, National University of Singapore, Singapore 117575 , Singapore
*corresponding author, E-mail: hoangxuan@smart.mit.edu

Abstract

In this summary paper, we present optical properties of a two-layer sphere with different configurations which mimic the nuclear architecture of photoreceptor cells in retinas of nocturnal and diurnal mammals. We show that the concentric sphere can act like a lens with a high numerical aperture and focus light into an ultralong photonic jet. Our analytical model of light scattering by the concentric sphere is applicable to a beam with any state of polarization, such as linear, circular, radial, azimuthal polarization.

1. Introduction

Through its evolution, animal has been known to be able to adapt to its living environment. Recently, researchers studied the retina of the eyes of nocturnal and diurnal mammals and found that there is a fundamental difference between the nuclear architecture of photoreceptor cells. The nocturnal mammals see at light intensities a million times lower than those available during the daily time, and their photoreceptors possess a light sensitivity down to a level of a few photons [1]. The light sensivity of the nocturnal mammals comes from the unique inverted nuclear architecture of its photoreceptor cells. Contrary to the nocturnal mammals, the photoreceptor cells of the diurnal mammals has a conventional architecture. A single nuclei with a conventional architecture can be represented by a two-layer sphere which has a core with a lower refractive index in comparison with the refractive index of of the shell. Contrary to the conventional architecture, the core of the inverted architecture has a higher refractive index in comparison with the refractive index of its shell as shown in Fig. 1. In this paper, we study the lensing properties of nuclei which may shed light on understanding the amazing ability of the eyes of nocturnal mammals.

In the last ten years, we have witnessed numerous studies about photonic jets formed at the shadow-side surfaces of micron-scale, circular dielectric cylinders illuminated by a plane wave [2]. The photonic jet has potentional applications in ultramicroscopy, nanolithography [2, 3]. In this paper, we discuss and present a rigorous analytical modeling of illuminating a two-layer sphere by a beam with any state of polarization.

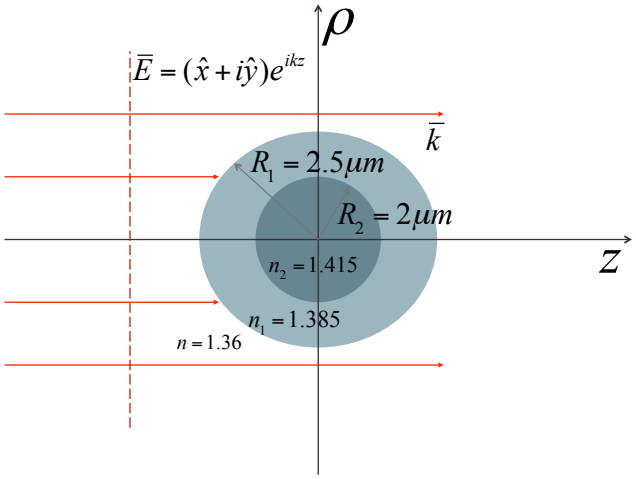

Figure 1: Nuclear architecture of a photoreceptor cell.

2. Theory

It is known that the electrtic field can be expressed in terms of electric Π_e and magnetic Π_m Debye potentials as follows:

$$E_r = \frac{i}{\omega\varepsilon}\left(\frac{\partial^2}{\partial r^2} r\Pi_e + k^2 r\Pi_e\right),$$
$$E_\theta = \frac{i}{\omega\varepsilon}\frac{1}{r}\frac{\partial^2}{\partial r\partial\theta} r\Pi_e + \frac{1}{\sin\theta}\frac{\partial}{\partial\phi}\Pi_m,$$
$$E_\phi = \frac{i}{\omega\varepsilon}\frac{1}{r\sin\theta}\frac{\partial^2}{\partial r\partial\phi} r\Pi_e - \frac{\partial}{\partial\theta}\Pi_m. \qquad (1)$$

The Debye potentials can be expressed in terms of plane wave or multipole expansions. In this paper, we use the multipole expansions. We can express the scalar Debye potentials in terms of scalar multipole fields as follows [4]:

$$\Pi_e = -i\omega\varepsilon\sum_{l=1}^{\infty}\sum_{m=-l}^{l} p_{El}^m f_l(kr) Y_l^m(\theta,\phi),$$
$$\Pi_m = ik\sum_{l=1}^{\infty}\sum_{m=-l}^{l} p_{Ml}^m f_l(kr) Y_l^m(\theta,\phi). \qquad (2)$$

In Eq. (2), p_{El}^m and p_{Ml}^m are multipole strenghts which specify the beam and are determined by the source and boundary conditions. $f_l(kr)$ can be the spherical Bessel $j_l(kr)$,

the first kind $h_l^{(1)}(kr)$ or the second kind $h_l^{(2)}(kr)$ of Hankel functions. The choice of $f_l(kr)$ depends on the electric field representing a converging beam ($h_l^{(2)}(kr)$), a diverging beam ($h_l^{(1)}(kr)$), or a beam propagating in a source-free region ($j_l(kr)$) [5].

For a plane wave with circular polarization approaching the concentric sphere as shown in Fig. 1, the incident electric field can be expressed as $E^{inc} = (\hat{x} + i\hat{y})e^{ikr\cos\theta}$. We can show that the incident field can be written as follows:

$$\Pi_e^{inc} = -i\omega\varepsilon \sum_{l=1}^{\infty}\sum_{m=-l}^{l} p_{El}^m j_l(kr) Y_l^m(\theta,\phi),$$

$$\Pi_m^{inc} = ik \sum_{l=1}^{\infty}\sum_{m=-l}^{l} p_{Ml}^m j_l(kr) Y_l^m(\theta,\phi), \qquad (3)$$

where

$$p_{El}^m = p_{El}^1 \delta_m^1, \qquad p_{Ml}^m = p_{Ml}^1 \delta_m^1,$$

and

$$p_{El}^1 = i p_{Ml}^1 \text{ and } \quad p_{Ml}^1 = \frac{2}{k} i^l \sqrt{\frac{\pi(2l+1)}{l(l+1)}}. \qquad (4)$$

For a tightly focused polarized beam, we can calculate rigorously the multipole strengths p_{El}^m and p_{Ml}^m using a far-field matching method as presented in [4]. We then can express the scalar Debye potentials which describe the scattering field as follows:

$$\Pi_e^s = -i\omega\varepsilon \sum_{l=1}^{\infty}\sum_{m=-l}^{l} a_l p_{El}^m h_l^{(1)}(kr) Y_l^m(\theta,\phi), \qquad (5)$$

$$\Pi_m^s = ik \sum_{l=1}^{\infty}\sum_{m=-l}^{l} b_l p_{Ml}^m h_l^{(1)}(kr) Y_l^m(\theta,\phi), \qquad (6)$$

where we choose $f_l(kr) = h_l^{(1)}(kr)$ due to the fact that the scattering field is leaving the sphere. The electric field in the shell contains both converging and diverging fields, and hence we can obtain the Debye potentials representing the electric field in the shell from Eqs. (5) and (6) by replacing $a_l h_l^{(1)}(kr)$ and $b_l h_l^{(1)}(kr)$ by $[a_{1l} h_l^{(1)}(k_1 r) + a_{2l} h_l^{(2)}(k_1 r)]$ and $[b_{1l} h_l^{(1)}(k_1 r) + b_{2l} h_l^{(2)}(k_1 r)]$, respectively. In the region of the core, since there is no source, any converging beam approaches the center will result in a diverging beam due to the energy flux conservation [5]. The Debye potentials in the core can be expressed as follows:

$$\Pi_e^2 = -i\omega\varepsilon \sum_{l=1}^{\infty}\sum_{m=-l}^{l} c_l p_{El}^m j_l(k_2 r) Y_l^m(\theta,\phi), \qquad (7)$$

$$\Pi_m^2 = ik \sum_{l=1}^{\infty}\sum_{m=-l}^{l} d_l p_{Ml}^m j_l(k_2 r) Y_l^m(\theta,\phi). \qquad (8)$$

The scattering coefficients $(a_l, b_l, a_{1l}, b_{1l}, a_{2l}, b_{2l}, c_l, d_l)$ are derived by apply the boundary conditions at the two spherical interfaces of the concentric sphere [6]. Next section, we present an example of illuminating the concentric sphere by a plane wave with circular polarization.

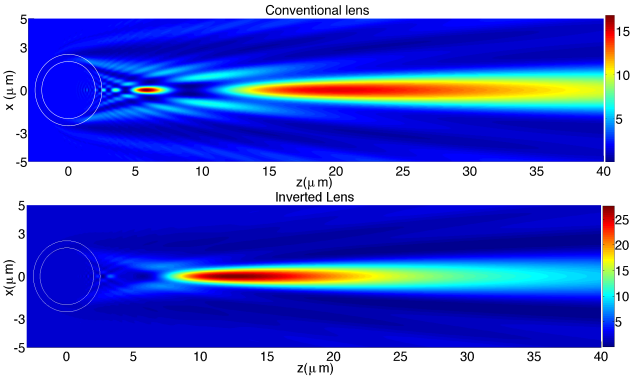

Figure 2: Lensing effects of the conventional and inverted lenses.

3. Discussion

The parameters in Fig. 1 represent the nuclear architecture of photoreceptor cells of a nocturnal mammal and we call this inverted lens. For a diurnal mammal, the nuclear architecture has a denser shell compared to its core, i.e., $n_1 = 1.415$ and $n_2 = 1.387$. In this paper, we call the nuclear architecture representing the diurnal mammal a conventional lens. To study the optical properties of these lenses, we choose the wavelenght $\lambda = 500\ nm$ since this wavelength is the most sensitive to the mammals' eyes [7]. Figure 2 shows the focusing properties of both conventional and inteverted lenses. One can oberserve that the inverted lens can focus the light more efficiently. The maximum electric intensity is much higher and the main photonic jet is tighter and nearer to the sphere compared to those of the conventional lens. In fact, the light has to pass through a layer of the retina, which consists of many nuclei distributed compactly, before being detected by sensory portions. The inverted lens with the tighter and nearer photonic jet can chanel the light from one sphere to another more efficiently, and consequently minimizes the light scattering and absorption. Hence, the inverted nuclear architecture of the photoreceptor cells helps the nocturnal mammals in detecting a low light intensity more efficiently. Figure 3 shows the electric intensity around the lenses. We can observe that the inverted lens can bend the light with a higher converging angle, i.e., we can roughly say that it has a higher numerical

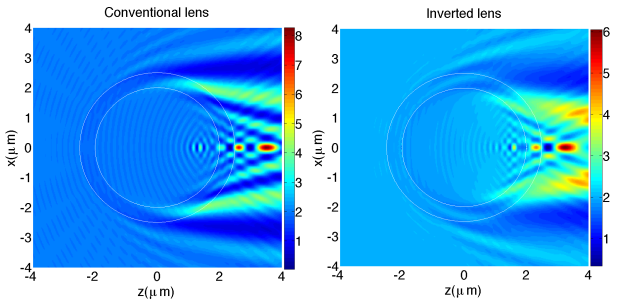

Figure 3: Lensing effects of the conventional (upper) and inverted (lower) lenses.

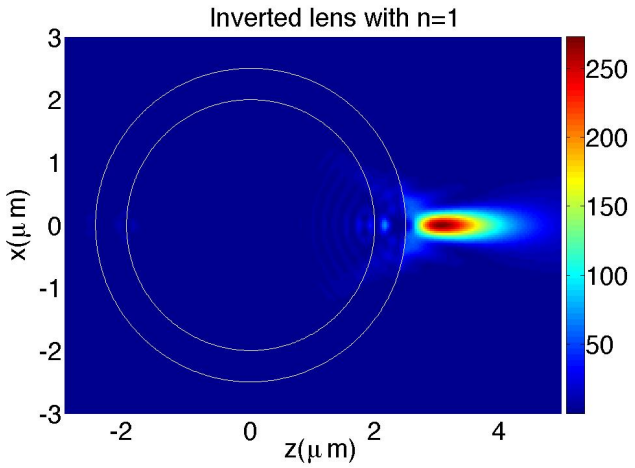

Figure 4: High numerical aperture lens with the concentric lens.

aperture compared to the conventional lens. In the context of a convex lens, this higher numerical aperture leads to the tighter spot and higher intensity at the focus of the inverted lens. Figure 4 shows the electric intensity distribution when we set the ambient refractive index in Fig. 1 to be $n = 1$. We now have a photonic jet just behind the back surface of the sphere. We no longer have an ultralong photonic jet as observed in Fig. 2. This shows that by increasing the relative refractive index of the sphere to that of the ambient environment, we can control the length and shape of the photonic jet. The inverted lens produces an ultralong photonic jet with a full width at half maximum ($FWHM$) along the longitudinal direction $L \approx 40\lambda$ in Fig. 2. However, reducing the refractive index of the ambient environment (n) reduces both the photonic jet length and its transversal dimension. When $n = 1$, the $FWHM$ of the photonic jet is now $L \approx 2\lambda$ only which is normally referred to as a photonic nanojet. The transversal size of the photonic nanojet in Fig. 4 is $\delta x \approx 320\ nm$. To obtain a photonic jet with a specific length, one may change the refractive index of the ambient environment to an appropriate value. To obtain the tightest photonic spot, one may consider to illuminate the concentric sphere with a specific wavelength which causes the optical resonance inside the shell. This phenomenon will be reported in our further paper.

4. Conclusions

This summary paper presents and discusses an analytical modeling for studying the optical scattering by a concentric sphere which represents a nuclear architecture of photoreceptor cells of mammals' eyes. Our results help to explain the ability of the nocturnal mammal in detecting a low light intensity. We also study photonic jets which have been extensively studied in the last ten years with numerous potential applications. We show that we can produce an ultralong photonic jet with appropriate parameters. Moreover, our analytical model is applicable for any beam with any state of polarization, such as linear, circular, radial, or azimuthal polarization. Hence, effects of polarization on lensing property of the photoreceptor cell can be investigated.

Acknowledgement

This research was supported by the National Research Foundation Singapore through the Singapore MIT Alliance for Research and Technology's Center for Environmental Sensing and Modeling interdisciplinary research program. The authors thank M. K. Kreysing for helpful discussions. This work was also funded partially with support from the Air Force Office of Scientific Research (AFOSR) under Award FA9550-09-0669-DOD35CAP.

References

[1] I. Solovei, M. Kreysing, C. Lanctôt, S. Kosem, L. Peichl, T. Cremer, J. Guck, and B. Joffe, Nucleararchitecture of rod photoreceptor cells adapts to vision in mammalian evolution, *Cell* 137: 356–368, 2009.

[2] Z. Chen, A. Taflove, and V. Backman, Photonic nanojet enhancement of backscattering of light by nanoparticles: a potential novel visible-light ultramicroscopy technique, *Opt. Express* 12: 1214–1220, 2004.

[3] Y. Duan, G. Barbastathis, and B. Zhang, Classical imaging theory of a microlens with super-resolution, *Opt. Lett.* 38: 2988–2990, 2013.

[4] T. X. Hoang, X. Chen, and C. J. R. Sheppard, Interpretation of the scattering mechanism for particles in a focused beam, *Phys. Rev. A* 86: 033817–033817-6, 2012.

[5] T. X. Hoang, X. Chen, and C. J. R. Sheppard, Multipole and plane wave expansions of diverging and converging fields, *Opt. Express* 22: 8949–8961, 2014.

[6] W. T. Grandy, *Scattering of Waves from Large Spheres*, Cambridge University Press, New York, 2000.

[7] M. Kreysing, L. Boyde, J. Guck, and K. J. Chalut, Physical insight into light scattering by photoreceptor cell nuclei, *Opt. Lett.* 35: 2639–2641, 2014.

Fabry-Perot interference of Terahertz Pulse radiation

Fa Tian[1], Sucheng LI[1], Weixin LU[* 1], Bo HOU[1]

[1]College of Physics, Optoelectronics and Energy, Soochow University, Suzhou 215006, China
*corresponding author, E-mail: luweixin@suda.edu.cn

Abstract

In this summary we show the setup of a THz-TDS system in our new laboratory, Wave Functional Materials Lab. The transmission of a THz pulse radiation is shown in a semiconductor thin film. The Fabry-Perot interference is demonstrated in this ultrathin film by the THz pulse radiation. The theory calculations coincide with the experimental results.

Results of the optical measurements using the stand for protection from pulsed electromagnetic interference of accelerators

I. I. Dolgov[1*], P. I. Dolgov[1], V. M. Isaev[2]

[1]"Ivan Dolgov Laboratory" LLC ("IDL" LLC), Russia

[2] "MNIIRIP" Enterprise , Russia

[*]corresponding author: idl92@rambler.ru

Abstract- The results of stands approbation for optical measurements under exposure of electron accelerators with nanosecond duration and accompanying pulsed broadband electromagnetic interference.

We have developed and successfully put to the evaluation test two stability improving methods for instrumentation optical systems (fiber-optic) used for research under the intense pulses influence of the ionizing radiation electron accelerator with the synchronous arrival of pulsed electromagnetic interference of microsecond duration. The methods presented allow measuring the phenomenon of geminate recombination, radioluminescence, change in light transmission, the coefficient of optical material reflection and other optical events.

Figure 1 shows the oscillogram #1 of electromagnetic interference in the recording devices in the operating anti-interference "RIUS-5" type acceleration installations complexes.

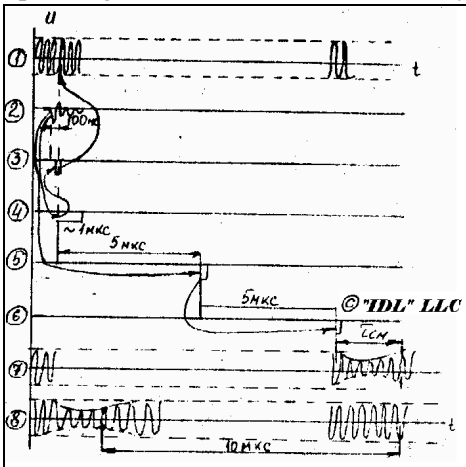

Launching system stress(V) diagram

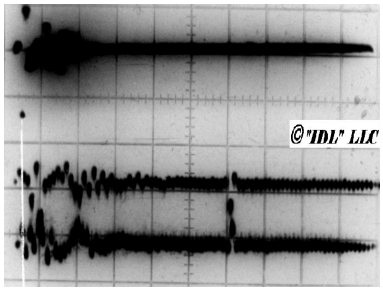

Oscillogram #1 - 2 μs/div

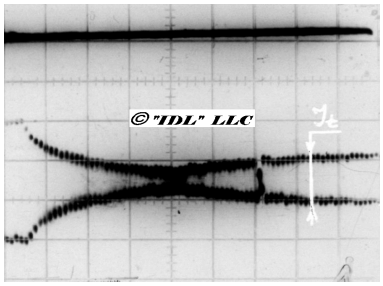

Oscillogram #2 - 0.2 μs/div

Figure 1

Oscillogram #2 shows (clear) signal delayed for 10 *μs* relative to real time of the electromagnetic interference occurrence in the recording device location. Launch of the first electrical impulses generator was carried out by the ionizing radiation pulse signal, which launches recording oscilloscope according to stress distribution launching system [1]. This scheme is essential for recording on an oscillograph with the electron-beam tube. The imperfection of such measurements scheme is a narrow optical measurements band due to high absorption in the shortwave part of the optical spectrum.

The drawback is eliminated by using our developed transportable anti-interference registration stand (TARS). External dimensions of the TARS assembled are 1.7 x 2.3 x 1.5m. This allowed it to be installed in existing metering facilities. Internal dimensions of the TARS allow locating at least four digital oscilloscopes, four photodetectors, optical emitters block and power units for them, electrical pulses generator, the optical

power splitters, launching module of recording devices, three laptops and one experimenter. The TARS is equipped with its own ventilation system, self-supporting power supply. The panel power allows you to working for straight 20 minutes in standalone mode, with the electric power of 3.5 kW, which allows for at least ten measurements per shift to be performed.

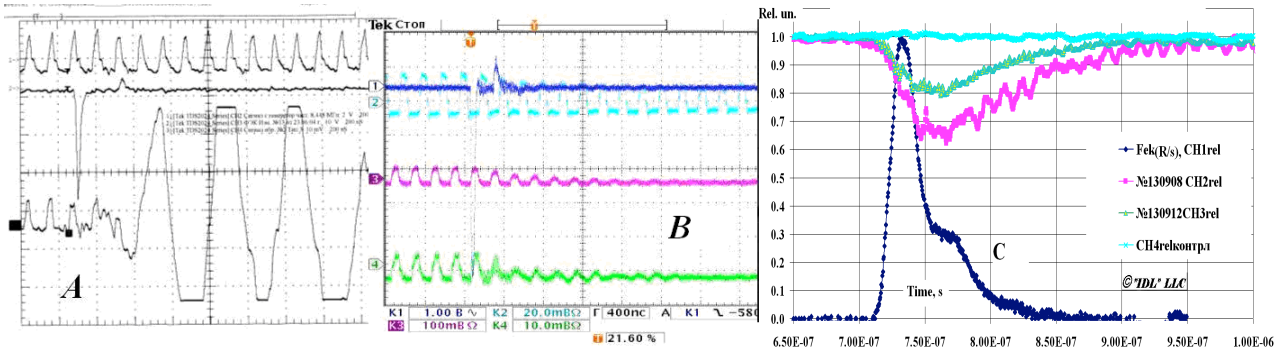

Figure 2. A: *upper signal put in* optical fibre (*OF), middle signal – the "RIUS–5" pulse shape, bottom signal – OF output signal with interference. B*: *1 – signal with "RIUS–5"; 2, 3, 4 – signals from the outputs of the same OF with optical powers of 1:10:100, respectively, at minus 60°C, measured using TARS. C:* – relative change in the optical output power of heterojunction #130908, #130912, control fiber (CH4), pulse of RIUS–5 (Fek CH1rel) with a dose rate ~ 4,25*10^8R/s.

On figure 2 *B* presents the results studies performed on three single-mode silicon-core and fluorosilicate cladding optical fibers, manufactured by MCVD method with initial optical losses of ~0.3 dB/km at a wavelength of λ = 1.55 μm and 50 m long [2]. The delay time of the onset of the absorption maximum relative to the maximum pulse accelerator RIUS–5, was ~ 0.4 ms under normal conditions and increases with decreasing temperature tests, which assumes mechanism of diffusion of the components forming the radiation color centers, at a wavelength of 1.55 μm. In Fig. *C* presents research results of the double heterostructure lasers based on GaAs at λ = 0.85 μm with the Bragg grating, the method of measurement [3]. The reduction in the output optical power may be due to a geminate recombination, changes in the quality factor of the resonator of the laser.

Developed by "IDL" LLC TARS allows investigating the optical fibers and optoelectronic components in the presence of broadband electromagnetic interference accelerators.

REFERENCES

1. Dolgov I. I. "Experimental methods of studying effects of ionizing radiation on the components of optical systems," in Proceedings of "5th National School for graduate students of young scientists and specialists in laser physics and laser technology", Sarov, April 26-29 2011, p.p. 83-89.

2. Dolgov I. I. "The methods of studies of the optical characteristics of optical materials, passive and active elements of OFC when exposed to ionizing radiation» in Proceedings of All Russian Conference, «Measuring and testing of the ASI» Russia, Moscow, 20-22 October 2009 , 87-90.

3. Van Uffen M., Fenaux Ph. Radiation Resistance of Fiberoptic Components and Predicative Models for Optical Fiber Systems in Nuclear Environments, RADECA97, Cannes, France, (1997), p.p. 445-452.

Subwavelength focusing by all dielectric graded index photonic crystal lens

Mirbek Turduev*, Melih G. Can, Khalil Dadashi, and Hamza Kurt.

Nanophotonics Research Laboratory, Department of Electrical and Electronics Engineering,
TOBB University of Economics and Technology, Ankara, Turkey.
*corresponding author, E-mail: mirbek.turduev@etu.edu.tr

Abstract

In this manuscript, we propose graded index (GRIN) medium to obtain subwavelength focusing of light by using all-dielectric materials. Continuous GRIN profile with hyperbolic secant refractive index distribution is approximated using 2D photonic crystals (PCs). Light focusing phenomenon is systematically and quantitatively analyzed at different operating frequencies and the results are numerically reported. We have obtained the full-width at half-maximum value of 0.24λ at the frequency of $a/\lambda=0.10$ with all dielectric GRIN PC structure. Subwavelength focusing of light holds great potential in nanolithography, optical sensing / imaging / microscopy, optical precision measurements and data storage.

1. Introduction

The manipulation of photons becomes dramatically rich since the introduction of photonic crystals (PC) into the literature in 1987 [1]. During the last years, the ability of controlling the flow of light further improved by introducing the idea of a graded index optics (GRIN) [2-4]. It is known that light-rays follow curved trajectories in a GRIN medium. Consequently, curving the light path gives birth to the optical effects same in conventional optical elements with curved interfaces such as focusing, diverging or collimation [4]. It is feasible to design a GRIN medium if the parameters of the two dimensional (2D) PCs are appropriately rearranged [5]. These structures are known as graded index photonic crystals (GRIN PC) and can be designed by engineering of the PC parameters, such as gradual changing of filling factor and lattice period [6]. GRIN medium can be also considered as a perfect focusing apparatus in optical systems. In this study, a novel type of GRIN PC lens structure whose refractive index distribution is adapted to the hyperbolic secant (HS) function is proposed. The analytical and numerical investigation of HS GRIN PC is provided by using Ray theory and FDTD method. The proposed GRIN PC structure provides strong focusing effect at subwavelength domain. There are recent approaches available in the literature exploring the subwavelength phenomena by utilizing nanoslit structures, metametarials, diffractive optical elements, and photonic nano-jets [7-10]. Here in this work, we show that focusing ability of GRIN PC medium pushes the limit of diffraction which is often encountered in classical optics and allows light beam to focus into an area below $\lambda<4$.

2. Focusing ability of GRIN media

In order to design GRIN media, the refractive index is modulated in the lateral y-direction according to a HS profile as in the form of $n(y)=n_0 sech(\alpha y)$, where n_0 is the refractive index at the optical axis and α is a constant parameter that affects the index gradient. One can take arbitrary values for the variable constant, in this case α is fixed to $\alpha=0.112a^{-1}$and $n_0=2.20$. Schematic view of continuous GRIN structure is depicted in Fig. 1(a).

In order to explain behavior of light waves within and without the GRIN medium, Ray theory concept is considered. We know that when the structure dimensions are much greater than the wavelength of light then the Ray theory gives an adequate approximation. Hence, we want to give a rapid insight on the modeling of light propagation through the chosen GRIN medium via Ray theory. To achieve that aim, we solved Eikonal equations [4] and the corresponding ray trajectories can be mathematically expressed by the following equations:

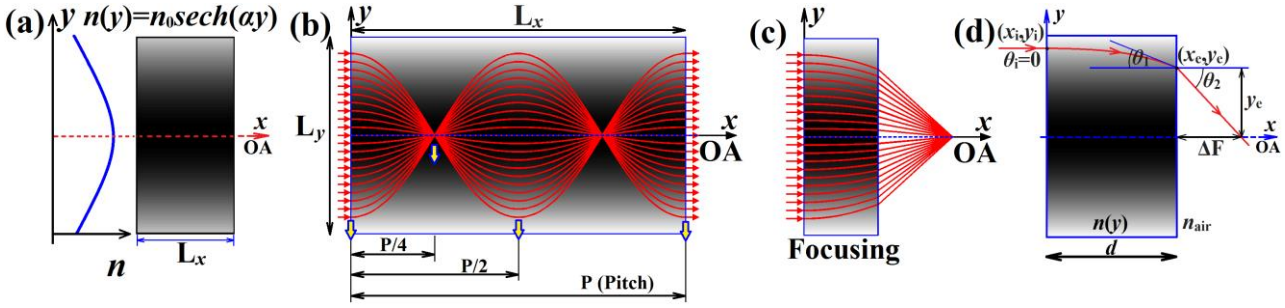

Figure 1: (a) Schematic representation of the continuous HS GRIN medium and its refractive index distribution. (b) Calculated ray trajectories in a HS profile GRIN medium with pitch size definitions and (c) the schematic view of focusing effect. (d) Detailed view of back focal length ΔF calculation.

$$y(x)=\frac{1}{\alpha}\sinh^{-1}\left(\dot{u}_0\frac{\sin(\alpha x)}{\alpha}+u_0\alpha\cos(\alpha x)\right), \quad (1)$$

$$\frac{dy(x)}{dx}=\frac{-\alpha u_0\sin(\alpha x)+\dot{u}_0\cos(\alpha x)}{\alpha\cosh\left\{\sinh^{-1}\left[u_0\alpha\cos(\alpha x)+\dot{u}_0\frac{\sin(\alpha x)}{\alpha}\right]\right\}}, \quad (2)$$

where y and dy/dx are ray position and ray slope with respect to x. The ray path formulas given in Eqs. 1 and 2 are extracted considering the initial ray position y_0 and its slope dy_0/dx at the input plane x_0=0. Figure 1(b) shows that the calculated light rays oscillate in a sinusoidal manner along the optical axis and thus, the critical parameters such as the oscillation period and the amplitude/depth of the oscillation can be calculated. The period parameter is defined as pitch (P) and given as insets in the same figure and it is defined as $P=2\pi/\alpha$. Hence, knowing the pitch enables to obtain focusing effects by appropriately arranging the length of the medium. When the length of the structure is terminated at the position of $L_x=P/4$, the rays converge and focus at the end face of structure as shown in Fig. 1(c), in which case the back focal length ΔF can be easily calculated using Snell's law as follows:

$$\Delta F=\frac{y_e\sqrt{\dot{y}(d)^2[1-n_0^2\,sech^2(\alpha y_e)]+1}}{n_0\,sech(\alpha y_e)\dot{y}(d)}, \quad (3)$$

where (x_e, y_e) is the position of the ray at the end face of the medium. According to Fig. 1(d) the length parameter d is set to x_e. The overall ray theory calculation implies that a GRIN medium can be utilized for the light converging/focusing purposes by adjusting the thickness of the GRIN structure.

3. Design concept and numerical analyses of light focusing dynamics

It is known that producing the continuous GRIN media can be considered as a challenging issue due to fabrication limitations. To overcome these difficulties, the use of PCs for the approximation of continuous GRIN media is considered to be an alternative approach. For this reason, the modulation of the lattice spacing concept is utilized [5]. To mimic GRIN media by means of PC dielectric rods, firstly, the dispersion relations of PC unit cells with different lateral sizes Δy are calculated using plane pave expansion method [11]. The corresponding group index n_g curves for each band are extracted by using the slope information of the regarding first bands. Then, the proposed structure having a specified effective refractive index profile is designed at a fixed frequency of a/λ=0.10 staying in the region where small alterations occur in the group indices. To avoid material complexity we keep refractive indices of PC rods at n=3.13. The designed medium and its imitated stair-step (discrete) version of effective index profile are presented in Figs. 2(a) and 2(b), respectively. As can be inferred from the stair-step effective index profile in Fig. 2(b), effective index changes from 1.44 to 2.20 and structure have total width of $L_y=20a$.

The designed structure is numerically modeled in 2D and its time-domain analyses are conducted by the help of finite-difference time-domain (FDTD) method [12. The medium is tested numerically at a design frequency of a/λ=0.10. As previously stated, the propagating beam oscillates along the

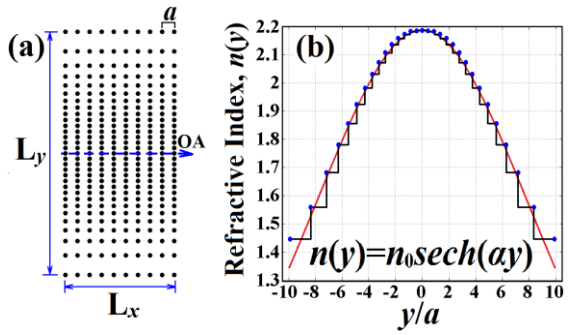

Figure 2: (a) Schematic representation designed GRIN PC media. (b) Continuous and stair-step (discrete) version of the hyperbolic secant index profile at a design frequency of a/λ=0.10.

optical axis of the GRIN medium with a period/pitch of $P=28a$. According to Fig. 1(b), to operate in focusing regime, the structural lengths L_x should satisfy the following condition:

$$L_x=\left\{L_{focus} \quad \text{if} \quad \left(\frac{m}{2}\right)P<L_x<\left(\frac{2m+1}{4}\right)P, \right. \quad (4)$$

where m is an integer and equals to m=0,1,2,3... In order to observe focusing effect, the length L_x is intentionally terminated at $L_x=9a$ and the observed spatial intensity profile at a frequency of a/λ=0.10 is shown in Fig. 3(a). The cross-sectional intensity profiles at input and at the output focal faces are obtained and superimposed in Fig. 3(b). Based on Fig. 3(b), we can surely say that the designed medium reveals subwavelength focusing with full width at the half maximum (FWHM) size of 0.24λ. The proposed GRIN PC provides focusing whose FWHM is 8.4 times narrower than that of input reference beam.

It is important to note that, we designed structure at homogenization regime where effective medium theory holds and defining of the frequency interval boundary of that regime is crucial. In other words, to ensure staying in the effective medium region the slight variation in n_g curves should be provided at certain frequency interval. In our case corresponding homogenization regime is determined within the frequencies of a/λ=[0.10-0.14]. Thus, in order to investigate focusing dynamics relating to change in

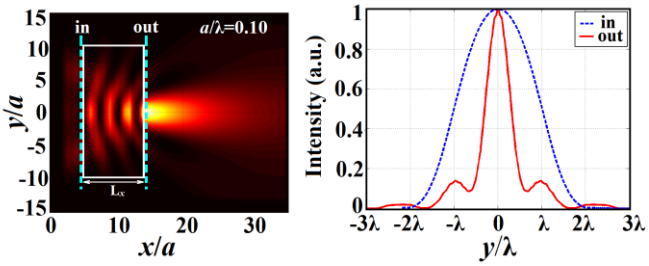

Figure 3: (a) The spatial e-field distribution of GRIN PC structure having length size equal to $L_x=9a$ at operating frequency of a/λ=0.10 and (b) cross-sectional intensity profiles of the input source and focal point at the input and output faces are given.

operating frequency and structural length we have numerically analysed the proposed structure by illuminating with light waves operating at different frequencies of a/λ=[0.10-0.14]. Moreover, we also checked FWHM variation for different structural lengths L_x. In order to finely

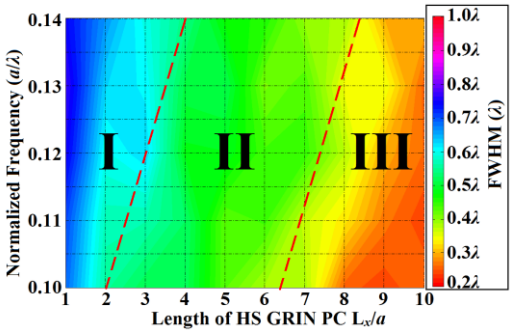

Figure 4: Energy plot of the variation of FWHMs depending on to structural length L_x and operating frequency.

exhibit the focusing ability of the design, we have gathered all data and generated energy plot of FWHM dynamics in Fig. 4. One can observe that FWHM value changes with respect to L_x at different operating frequencies. In Fig. 4 color-bar shows FWHM in terms of wavelength λ which alternates between 0.20λ and 1.0λ. The energy plot in Fig. 4 is divided to three different regions and numbered as shown. As can be seen from figure, to achieve the focusing with FWHMs changing between 0.50λ and 0.70λ at a frequencies of a/λ= [0.10-0.14] one need HS GRIN PC medium with a structural length alternating between $L_x=2a$ and $L_x=4a$. On the other hand, to reach the subwavelength value of FWHM nearly equal to 0.50λ, increasing the structural size up to $L_x=8a$ can be considered. When the length of the PC structure is getting longer than $L_x=8a$ one can observe subwavelength focusing FWHM equal to under 0.50λ. In other words, FWHM values decrease as we increase the length L_x and increase while we increase the operating frequency. In order to qualitatively present focusing property at the different operating frequencies we take cross section at the $L_x=9a$ in Fig. 4 and select operating frequencies equal to a/λ=[0.11, 0.12, 0.13, 0.14]. In this regard, extracted corresponding spatial electric fields and their cross-sectional plots are shown in Fig. 5. We can deduce from the plots that there is sub-wavelength focusing over a wide frequency region by utilizing the same inhomogeneous all-dielectric medium.

4. Conclusions

To conclude, in this work inhomogeneous GRIN medium is considered as an optical lens to induce focusing below the diffraction limit. The discrete version of continuous GRIN medium is designed by 2D PCs and time domain analyses are conducted using FDTD. The proposed GRIN PC structure provides strong subwavelength focusing effect. Also focusing analysis depending on structural length parameter and operating frequency are numerically reported. Moreover, introducing additional parametric optimizations provide us focusing effect with FWHM equal to near 0.10λ. The final results will be shared in the conference.

Acknowledgements

The authors gratefully acknowledge the financial support of the Scientific and Technological Research Council of Turkey (TUBITAK), project 110T306. HK acknowledges partial support from the Turkish Academy of Sciences.

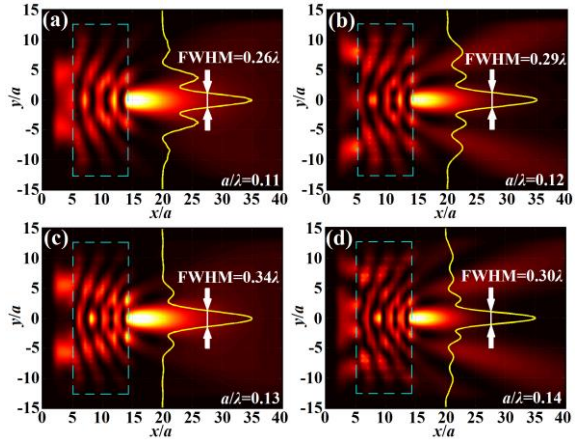

Figure 5: The spatial electric field distributions of GRIN PC structure having length size equal to $L_x=9a$ at operating frequency of (a) a/λ=0.11, (b) a/λ=0.12, (c) a/λ=0.13 and (d) a/λ=0.14.

References

[1] E. Yablonovitch, "Inhibited Spontaneous Emission in Solid-State Physics and Electronics," *Phys. Rev. Lett.*, 58: 2059-2062, 1987.

[2] R. K. Luneburg, Mathematical Theory of Optics (University of California Press, Berkeley, 1964).

[3] E. W. Marchand, Gradient Index Optics (Academic Press, New York, 1978).

[4] C. Gomez-Reino, M. V. Perez, and C. Bao, Gradient-Index Optics: Fundamentals and Applications (Springer, 2002).

[5] M. Turduev, B. Oner, I. Giden, and H. Kurt, "Mode transformation using graded photonic crystals with axial asymmetry," *J. Opt. Soc. Am. B* 30: 1569-1579, 2013.

[6] H. Kurt and D. S. Citrin, "Graded index photonic crystals," *Opt. Exp.*, 15:1240–1253, 2007.

[7] K.R. Chen, "Focusing of light beyond the diffraction limit of half the wavelength," *Opt. Lett.*, 35: 3763-3765 2010.

[8] G. Ren, C. Wang, Z. Zhao, X. Tao, X. Luo, "Off-axis characteristic of subwavelength focusing in anisotropic metamaterials," *J. Opt. Soc. Am. B* 29: 3103-3108 2012.

[9] I. Mahariq, M. Kuzuoglu, H. Tarman, and H. Kurt, "Photonic Nanojet Analysis by Spectral Element Method," 6, 6802714, 2014.

[10] D. C. O'Shea, T. J. Suleski, A. D. Kathman, D. W. Prather, *Diffractive Optics: Design, Fabrication, and Test*, SPIE Publications, 2003.

[11] S. Johnson and J. Joannopoulos, "Block-iterative frequency-domain methods for Maxwell's equations in a planewave basis," *Opt. Express*. 8: 173–190, 2001.

[12] A. Taflove, S. C. Hagness, "Computational electrodynamics," Vol. 160. Boston: Artech House, 2000.

Light Focusing by Randomly Distributed Index Gradient Medium

Zeki Hayran, Mirbek Turduev*, Ali Burak Parim, Emre Bor, and Hamza Kurt

Nanophotonics Research Laboratory
Department of Electrical and Electronics Engineering
TOBB University of Economics and Technology
*corresponding author, E-mail: mail.mirbek@gmail.com

Abstract

In this manuscript, we propose a new concept for the design of inhomogeneous refractive index profile with random distributions of elements occupying the unit cells of photonic crystals (PCs). While keeping the distances of the structure along the propagation direction constant, the positioning of PCs unit cells on the transverse direction is randomly achieved, thus disordered structures is originated from PCs. Numerous designs are randomly generated with the same Gaussian probability function in order to investigate novel optical characteristics of the medium in both frequency and time domain. Specifically we have examined similarities of transmission efficiencies and focusing abilities at low frequency regime of the designed random PC structures. Obtained results show that at low frequencies designed random PC structure can achieve strong focusing effect. Both off-centered and directional radiation patterns can be generated. The idea of merging randomness with index gradient yields rich light manipulation capabilities.

1. Introduction

The first concept of Photonic Crystals (PC) was proposed in 1987 by Yablonovic and John simultaneously to resolve the need of a characteristic material that has the ability of manipulating the propagation of light at particular wavelengths [1,2]. This approach paves the way for many studies where dielectric constant of the medium is modulated periodically and has so-called Photonic Band Gaps (PBGs) that inhibits the propagation of light waves for certain frequency intervals. The main underlying mechanism for PBG creation is the highly symmetric lattices that build multi-dimensional PCs. Later, the domain of structural form has widened thanks to the study in the field of quasi-crystals [3]. Such structures can be considered as intermediate systems between a periodic crystal and random amorphous solids. Due to the rich Fourier spectrum property of these structures, light trapping at wide band range on thin films has been studied [4].

The aim of the present work is to investigate the optical response of randomly designed structures created by Gaussian probability density functions with different standard deviations.

2. Design approach of randomly distributed PC medium

In order to construct the proposed randomly distributed PC configuration, a probability density function with a Gaussian profile is used. The PC rods are distributed in the transverse *y*-direction while keeping the distance between the rods along the propagation *x*-direction constant which is fixed to *a*, where *a* is lattice constant. Hence, the effective refractive index modulation is manipulated only in *y*-direction, *i.e.* the gradient of the dielectric filling ratio along the y-direction varies according to Gaussian distribution

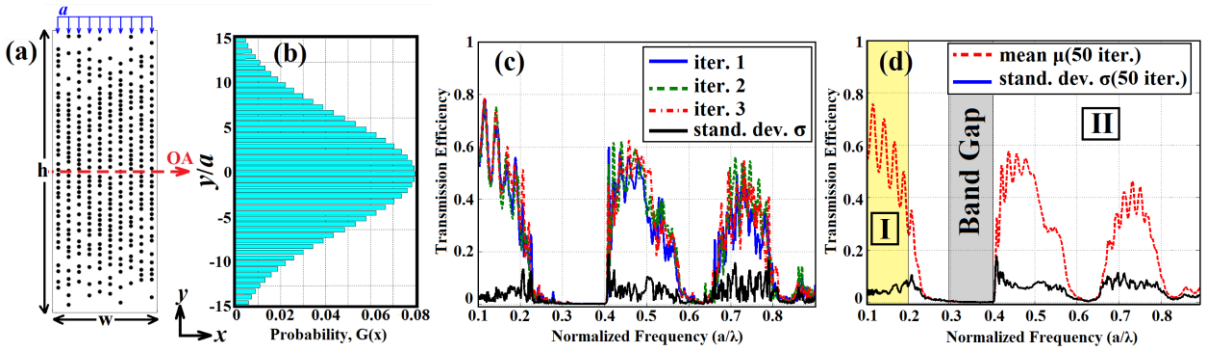

Figure. 1: (a) Schematic representation of the randomly distributed index gradient PC structure and (b) its probability distribution of the PC rods in the *y*-direction. (c) The transmission efficiencies and standard deviation of three different random structures generated with the same distribution function. Similarly, the arithmetical average of 50 different iterations and their standard deviation graph are superimposed in (d).

probability, G(y) function. Figures 1(a) and 1(b) represent the schematic view of the proposed random PC structure and the probability function G(y) graph that stipulates the positioning of the PC rods, respectively. Gaussian probability density function G(x) can be mathematically expressed by the following equation:

$$G(x) = \frac{1}{\sqrt{2\pi}\sigma} e^{-\frac{(y-\mu)^2}{2\sigma^2}}, \qquad (1)$$

where σ is the standard deviation and μ is a mean value of the distribution. As can be seen from the Fig. 1(a) and 1(b), the density of PCs tends to be higher while approaching optical axis (OA). Therefore, the distribution of the PCs along the transverse direction reveals an inhomogeneous PC medium whose effective index profile resembles a Gaussian shape.

The regarding height (h) and width (w) of the structure are equal to 30a and 10a, respectively. To avoid complexities in practical implementation of PC rods the refractive indices are kept the same and equal to n=3.13 (considered as Alumina rods). The radii of the dielectric rods fixed to r=0.2a. We should note that one can keep the unit cell size constant and randomly distribute the filling factor distribution. That aspect of the study is under investigation.

The designed random inhomogeneous medium is numerically modelled in 2D to observe the transmission response by the use of finite-difference time-domain (FDTD) method [5]. Only transverse magnetic (TM) polarization is considered. Furthermore, by assuming that every randomly generated PC structure has different time and frequency responses for propagating beams, we have calculated power transmittance for 50 different randomly generated structures; thus, it enables us to observe quantitatively the similarities and differences of the proposed design concept in the frequency domain. In order to calculate power transmission efficiency of the structure, a broad band pulse is launched at the front side of the structure. A detector is located at the end of the structure in order to measure the transmission spectra. The transmission efficiencies are calculated and normalized by taking the ratio of detected and incident power. The carefully inspection of transmission spectra for three different randomly generated structures shown in Fig. 1(c) that exhibit similar trends. At low frequencies below a/λ=0.20, there is a high transmission region which is followed by a directional band gap. The second and third high transmission intervals are observed at frequencies of a/λ=0.45-0.55 and a/λ=0.70-0.80, respectively. The transmittance value at the first frequency window oscillates between %80 and %40. On the other hand, the second and third windows display transmission efficiencies between %60 and %40. In order to measure the amount of variation in the transmission efficiency from the average of different random iteration, (different random PC structures), the standard deviation σ is calculated and its plot is depicted in the same Fig. 1(c). As can be seen, at the band gap region σ is almost zero, which means the power transmissions are nearly the same for three different random PC structures. On the other hand, standard deviation of the high transmission windows tend to be alternate around σ=0.05. Hence, we can deduce that the responses of the different random structures to propagating beam at those frequencies are almost the same. It is known that more information about a process (in our case number of randomly generated structures) gives us more certainty. In this case, to be more precise on observations another 50

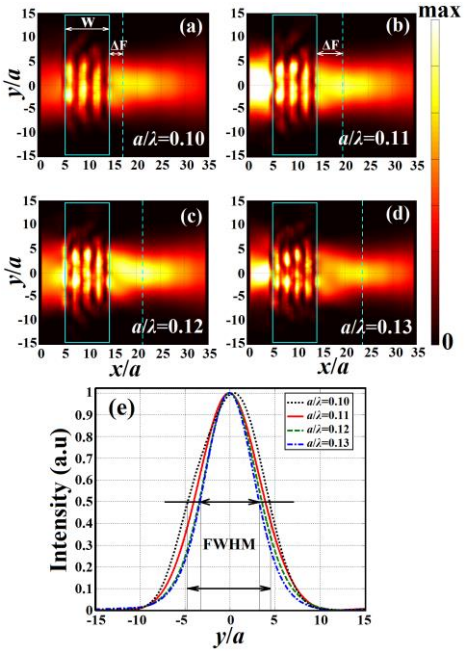

Figure 2: The spatial electric-field distributions of random GRIN-like PC medium having width equal to w=10a at the normalized frequencies of (a) a/λ=0.10, (b) a/λ=0.11, (c) a/λ=0.12 and (d) a/λ=0.13 are presented. The cross-sectional intensity profiles of the focal point for the frequencies of a/λ=[0.10,0.11,0.12,0.13] are superimposed on (e).

random PC media with the same structural parameters are investigated. The regarding average μ and standard deviation σ for 50 iterations of transmission data is obtained and superimposed in Fig. 1(d). As can be deduced form Figs. 1(c) and 1(d) increasing data samples eliminates noisy oscillations in the standard deviation graph, thus, we can say that obtained results are more reliable and reproducible.

It is crucial to note that, the design of inhomogeneous GRIN media are mostly achieved at long wavelength regimes, *i.e.* nearby the normalized frequency of a/λ=0.10 [6,7]. Therefore, for the proposed inhomogeneous PC design we expect similar focusing abilities as those in GRIN medium at operating frequencies below a/λ=0.1-0.2.

Next, FDTD method is carried out to inspect the electromagnetic wave propagation inside the proposed random PC structure within those high transmission regions which are demonstrated in Fig. 1(d). For that purpose, firstly the structure is illuminated by continuous source having a Gaussian profile at selected operating frequencies of a/λ={0.10,0.11,0.12,0.13} that lie in the first high transmission window. Then, the regarding steady state fields are extracted and shown in Figs. 2(a)-2(d). Interestingly the steady state fields prove our expectations such that incident light gets focused. On the other hand, each column of super cell has different orientation, asymmetric light propagation

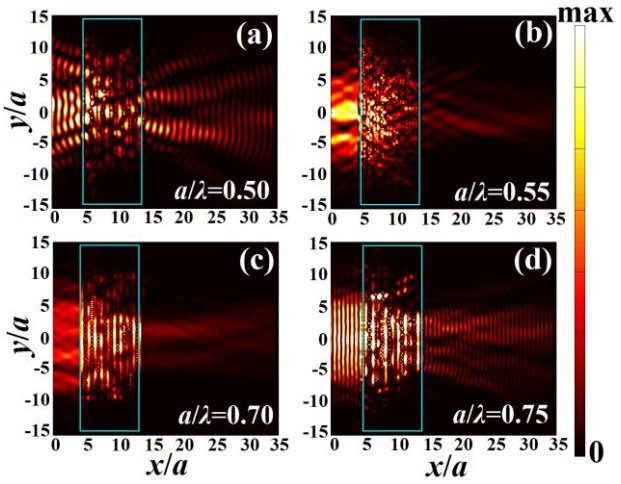

Figure 3: The spatial electric-field distributions of random GRIN-like PC medium having width equal to w=10a at the normalized frequencies of (a) a/λ=0.50, (b) a/λ=0.55, (c) a/λ=0.70 and (d) a/λ=0.75 are presented.

appears. Consequently, directional or off-centered emissions exit at the end of the structure. While the frequency is increased slowly from a/λ=0.10 up to a/λ=0.13, the focal point shifts to the right-side, *i.e.*, becomes distant from the back surface of the structure. To provide quantitative analyses of the focusing behavior at the different operating frequencies, cross-sectional intensity profiles are taken at the focal points and results are shown in Fig. 2(e). Based on the cross-sectional intensity plots, the determined full width of half maximum (FWHM) values at the focal points equal to {0.90λ, 0.87λ, 0.83λ, 0.84λ }, λ is wavelength of light in free-space. The spot size of the focused light slowly varies as we increase the frequency. It is expected to have strong focusing towards the lower edge of the first band gap. However, the focal point moves away from the structure. This behavior dictates that there is a mechanism playing role for reduction of the light focusing power.

To inspect the similar focusing characteristics at the high frequency regions, normalized values are picked up from the second and third high transmission regions a/λ =[0.50, 0.55 ,0.70, 0.75] and the results are shown in Figs. 3(a)-3(d). Strong light interaction occurs with the structure at high frequency. Complex field patterns appear at the end of the medium due to high scattering mechanism. One can utilize these results for obtaining strong focusing of light. Moreover, electric fields at high frequencies display strong localizations and back scatterings properties, so manipulation of light at those frequencies becomes more difficult yet may yield rich optical features. We will continue to explore that aspect of the study.

Illuminating the randomly designed PC structure by light waves within the cut-off frequencies (edges), operating near a/λ=0.20-0.23, a/λ=0.40-0.45 and a/λ=0.65-0.68 might arise very interesting peculiarities. Since there can be observed slow light phenomena as well as sub-wavelength focusing. We still keep working on this direction and the obtained future results will be shared in the conference. Lastly, the followed design procedure can be applied for exploring loss analysis that may arise due to undesired manufacturing problems.

3. Conclusions

To conclude, in the presented work a new concept for the design of inhomogeneous PC structure is proposed. Numerous generated PC structures are analyzed in time domain by conducting FDTD calculations. The results demonstrate wavelength scale focusing of light with tilted or off-axis radiation patterns. Moving from low frequency region towards higher bands produces complex and spectrally rich optical characteristics. Thus, it seems feasible to generate multiple focal spot segments in subwavelength region by operating at the high frequency regions. Optical microscopy, micro-particle tweezers, lithography and laser machining are some of the topics that can get benefit from the outcome of the research efforts performed with the randomly oriented index gradient medium.

Acknowledgements

The authors gratefully acknowledge the financial support of the Scientific and Technological Research Council of Turkey (TUBITAK), project 110T306. HK acknowledges partial support from the Turkish Academy of Sciences.

References

[1] Yablonovitch, E., “Inhibited spontaneous emission in solid-state physics and electronics,” *Phys. Rev. Lett.* 58-23: 2059–2062, 1987.

[2] John, S., “Strong localization of photons in certain disordered dielectric superlattices,” Phys. Rev. Lett., Vol. 58, No. 23, 2486–2489, 1987.

[3] Schechtman, D., I. Blech, D. Gratias, and J. W. Cahn, “Metallic phase with long-range orientational order and no translational symmetry,” Phys. Rev. Lett., Vol. 53, No. 20, 1951–1954, 1984.

[4] E. R. Martins, J.T. Li, Y. K. Liu, V. Depauw, Z. X. Chen, J. Y. Zhou, and T. F. Krauss, "Deterministic quasi-random nanostructures for photon control," Nature Communications, 4 (2665), (2013).

[5] F. Oskooi, D. Roundy, M. Ibanescu, P. Bermel, J. D. Joannopoulos, and S. G. Johnson, “MEEP: a flexible freesoftware package for electromagnetic simulations by the FDTD method,” Comput. Phys. Commun. 181(3), 687–702 (2010).

[6] B. Vasic, G. Isic, R. Gajic, and K. Hingerl, “Controlling electromagnetic fields with graded photonic crystals in metamaterial regime,” Opt. Express 18(19), 20321-20333 (2010).

[7] D. Yilmaz, I. H. Giden, M. Turduev, and H. Kurt, "Design of Wavelength Selective Medium by Graded Index Photonic Crystals," IEEE Journal of Quantum Electronics, 49, 477-484 (2013).

Optical Resonators Modified by Random Modulation of Refractive Index

Ali Burak Parim, Mirbek Turduev*, Zeki Hayran, Emre Bor, and Hamza Kurt

Nanophotonics Research Laboratory
Department of Electrical and Electronics Engineering
TOBB University of Economics and Technology
*corresponding author, E-mail: mail.mirbek@gmail.com

Abstract

We study a new type of optical resonator created from randomly distributed elements either in the form of air holes in dielectric background or the complementary version, *i.e.*, dielectric cylinders in air background. Finite-difference time-domain simulations demonstrate that the scattering and emission of light from randomly placed elements provides broad photonic band gap and strong localization of light. The characteristics of the resonator show dependency on the random distributions and the size of the structure. In addition to supporting localized modes, the similar type of structures hold great potential to engineer the radiation profiles of sources to induce beaming effect and manipulate out-of-plane emissions for trapping photons in solar energy and for enhancing external quantum efficiency in display applications.

1. Introduction

Compact optical resonators in terms of different shapes such as disk, ring or sphere sustain high-Q whispering gallery modes. They are frequently deployed in optical signal processing devices and bio-chemical sensing applications. Instead of having constant refractive index (such as Silicon or Silica) within the circular or spherical resonators, one can implement wavelength scale refractive index modulation by utilizing the idea behind the photonic crystal concepts [1-4].

Circular photonic crystals whose structural formation follows certain mathematical expression and do not possess translational symmetry have been studied for defect-free high-Q resonators, light localizations and low-threshold laser applications [5-7]. Sometimes, researchers pay attention to explore optical characteristics of biologically inspired structures such as sun-flowers, wings of butterflies and compound eyes of insects [8-11].

While studies on periodic and quasi-periodic photonic structures continue, there are interests for non-periodic disordered structures. Thanks to a recent study, a high resolution spectroscopy is designed by adding an intentionally controllable disorder to a structure [12]. Random lasers with disordered media and high-Q cavity with random localized disorder are recently introduced to the literature [13-14].

In the present work, we merge the idea of circular photonic crystals with randomly modulated index variation. It is expected to get benefits of both disordered media and circular resonators. One can also apply the idea of randomly created circular photonic crystals to photonic crystal fibers. Rich dispersion characteristics may arise. However, that aspect of the work is kept outside of the present study. Lastly, photonic nanojets generated by cylindrical resonators can be engineered with the proposed designs [15].

2. Design and analysis of the proposed random circular media

To design the proposed randomly distributed PC configuration, a joint probability density function with a Gaussian profile is employed. The distribution of the photonic crystal (PC) rods (in air background) or air holes (in dielectric background) locations in the 2D (*x*-*y*) plane are randomly assigned according to the Gaussian

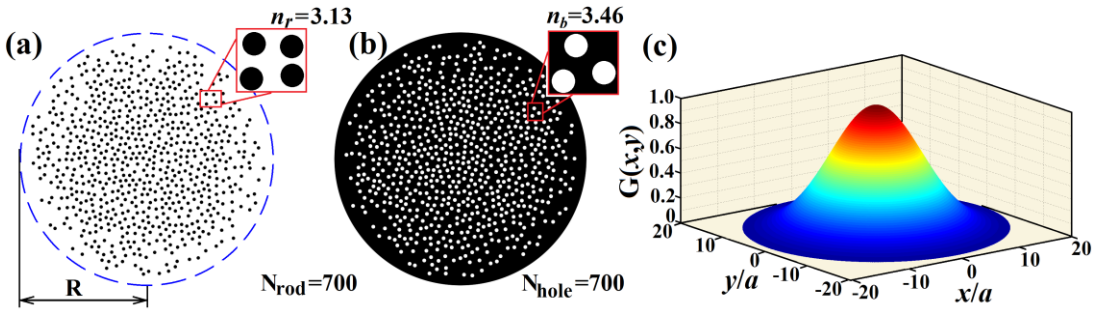

Figure 1. Schematic representations of randomly generated circular photonic crystals, (a) dielectric rods in air background and (b) air holes in dielectric background. (c) probability distribution of the elements constituting the structure in two dimensions (x, y).

density function $G(x,y)$. The corresponding mean values (μ_x, μ_y) of the marginal density functions ($G_x(x)$, $G_y(y)$) along the x and y-axis are fixed to zero, *i.e.* to the center of the circular medium. In this regard, the effective refractive index is modulated radially and the dielectric filling ratio from the center to the outer edge varies according to Gaussian distribution probability G(x,y) function. It is important to note that, to avoid overlapping problem, a minimum distance which is equal to 0.30a is considered. Figures 1(a) and 1(b) represent the schematic view of the proposed circular random PC structures that are rods in air background and holes in dielelectric background, respectively.

The regarding probability function G(x,y) that determines the radial location of the PCs is also depicted in Fig. 1(c) and its mathematical expression is given as follows:

$$G(x,y)=\frac{1}{2\pi\sigma^2}e^{-\frac{\left[(x-\mu_x)^2+(y-\mu_y)^2\right]}{2\sigma^2}}, \qquad (1)$$

where, $\sigma=\sigma_x=\sigma_y=0.35$ is the standard deviation, $\mu_x=\mu_y=0$ are a mean values of the Gaussian 2D distribution, and $(x,y)=(R\cos\theta,\ R\sin\theta)$. In order to distribute PC rods/air holes in radial direction, θ angle is generated randomly with uniform distribution. One can observe from Figs. 1(a)-1(c) that, the distribution density of PCs is likely to decrease in a Gaussian manner while moving from the center to outer edge. Therefore, utilizing Gaussian distribution on circular PC structure reveals an inhomogeneous PC medium whose radial effective index profile resembles a 2D Gaussian shape.

The structural radii of the circular designs in Figs. 1(a) and 1(b) are fixed to radial boundary equal to R=20a. We fix the number of elements (PC rods/air holes) as $N_{rod}=N_{hole}=700$ and randomly assign the locations of the each element. The reason of fixing the number of elements to 700 is to cover the circular area with radius R=20a with a filling ratio of 40%. The regarding refractive indices of PC rods are $n_r=3.13$ while dielectric background of the complementary design is $n_b=3.46$ as shown as an inset in Figs. 1(a) and 1(b), respectively. The radii of the dielectric rods/air holes fixed to $r=0.30a$.

The proposed random PC circular medium is numerically designed in 2D to analyze the transmission response utilizing the finite-difference time-domain (FDTD) method [16]. In simulations both transverse magnetic (TM) and transverse electric (TE) polarizations are considered due to the fact that wide photonic band gaps can produce polarization independent band gaps.

In order to calculate power transmission efficiency of the structure, a broad band pulse is launched at the front/left side of the structure. A detector is located at the right side of the structure in order to measure the transmission spectra. The transmission efficiencies are calculated and normalized by taking the ratio of detected and incident power. Calculated and extracted transmission efficiencies for PC rods and dielectric with air holes structures are plotted in Figs. 2(a) and 2(b), respectively. Looking for superimposed graphs in Fig. 2(a), one can observe the discrepancy

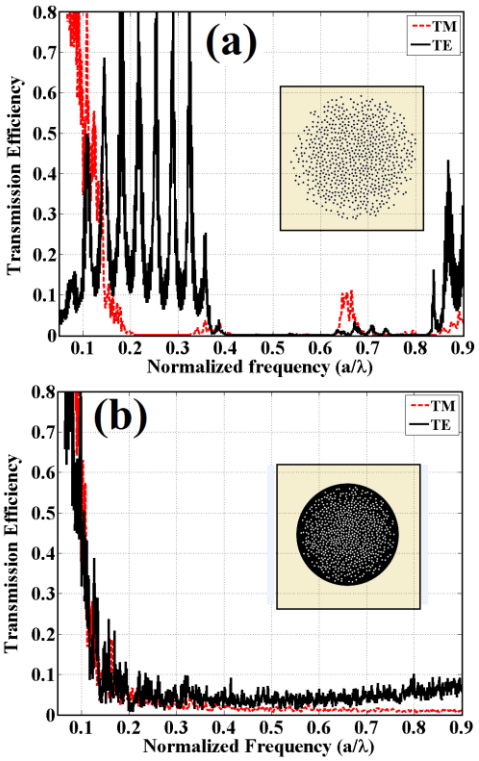

Figure 2: Transmission Efficiencies for TM and TE polarizations for both PC rod and air hole structures, respectively.

between efficiencies of TM and TE polarizations.

While analyzing PC rods circular structure, one can deduce that at frequencies below $a/\lambda=0.20$ and $a/\lambda=0.40$, there are high transmission regions which are followed by a directional band gap for TM and TE polarizations, respectively. The second transmission interval appears at frequencies $a/\lambda=0.65$-0.68 where low transmission efficiency around 0.1 can be observed for TM polarization. On the other hand, in the case of TE polarization there is no indication of any strong transmittance until frequency reaches $a/\lambda=0.85$.

Interestingly the frequency response of the dielectric background circular structure is quite different. In this case TE and TM polarizations are almost overlapped with each other over a broad band. In general it can be seen that the transmission is very low for both polarization in Fig. 2(b). Transmittance is decreasing while frequency increases until frequency reaches $a/\lambda=0.20$. One can alter the size of the structure, radii of air holes or standard deviation of Gaussian distribution to get richer spectral features. In order to get more certain information and characterize randomly generated structures more accurately we have simulated 50 different randomly generated PC structures. Next, as a result of FDTD simulations we have explored that the responses of them for propagating broad band pulse are almost the same.

In order to quickly reveal the photons propagation characteristics, we excite the structures at the center with a point source whose normalized frequency is equal to $a/\lambda=0.48$. Both TE and TM cases are studied. Certain locations act as local defect regions and light energy

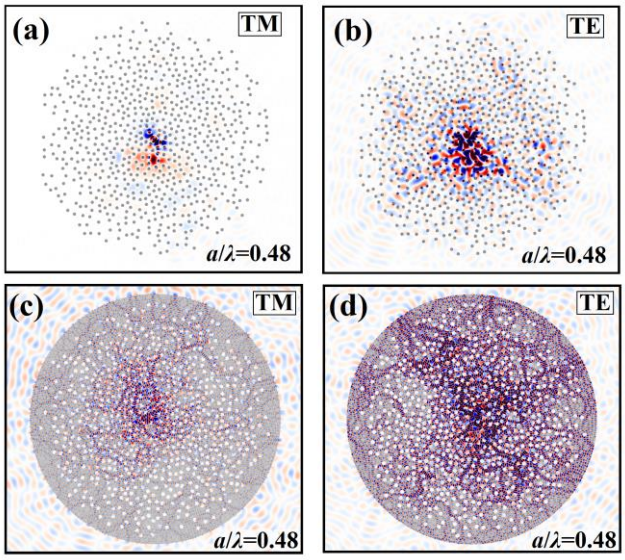

Figure 3. Snap-shots field distributions of (a) electric and (b) magnetic components of random circular photonic crystals (rods in air background) at frequency of a/λ=0.48. Similarly, at the same frequency, field distributions of (c) electric and (d) magnetic components of circular structure with air holes on dielectric background are depicted.

increased at these places. Due to the lack of the rotational and translational symmetries, the emission profile is not symmetric and multi-focus actions appear at the close proximity of the circumferences of the structures. The preliminary data encourages us to continue exploring the proposed structures for light localization, beam shaping and high-Q factors.

3. Conclusions

Wavelength scale multi-focusing towards sub-wavelength domain can provide super-resolution and non-destructive probes which are especially important for biomedical imaging applications. In addition to that goal, it is desired to manipulate the depth of field and include non-diffraction and beaming of light for the strongly focused beams [17]. All these potential properties of random circular resonator are under investigations and the findings of the study will be shared in the conference.

Acknowledgements

The authors gratefully acknowledge the financial support of the Scientific and Technological Research Council of Turkey (TUBITAK), project 110T306. HK acknowledges partial support from the Turkish Academy of Sciences.

References

[1] K. J. Vahala, "Optical microcavities," *Nature*, 424, 839–846 (2003).

[2] J. Scheuer and A. Yariv, "Optical annular resonators based on radial Bragg and photonic crystal reflectors," *Opt. Express* 11, 2736−2746 (2003).

[3] J. Scheuer and A. Yariv, "Circular photonic crystal resonators," *Phys. Rev*. E 70, 036603 (2004).

[4] E. Yablonovitch, "Inhibited Spontaneous Emission in Solidstate Physics and Electronics", *Phys. Rev. Lett*. 58, 2059-2062 (1987).

[5] W. Zhong and X. Zhang, "Localized modes in defect-free two-dimensional circular photonic crystals," *Phys. Rev. A* 81, 013805 (2010).

[6] P.T. Lee, T.W. Lu, J.H. Fan, and F.M. Tsai, "High quality factor microcavity lasers realized by circular photonic crystal with isotropic photonic band gap effect," *Appl. Phys. Lett.* 90, 151125 (2007).

[7] S. Xiao and M. Qiu, "High-Q microcavities realized in a circular photonic crystal slab," *Photonics and Nanostructures – Fundamentals and Applications*, 3, 134–138 (2005).

[8] X-H. Sun, Y-L. Wu, W. Liu, Y. Hao, and L-D. Jiang, "Luneburg lens composed of sunflower-type graded photonic crystals," *Opt. Commun*. 315, 367–373 (2014).

[9] M. Srinivasarao, "Nano-Optics in the biological world: beetles, butterflies, bird, and moths," *Chem. Rev.* 99, 1935–1961 (1999).

[10] P. Vukusic, and J. R. Sambles, "Photonic structures in biology," *Nature*, 424, 852–855 (2003).

[11] A. R. Parker, and H. E. Townley, "Biomimetics of photonic nanostructures," *Nat. Nanotech*. 2, 347–353 (2007).

[12] B. Redding, S. F. Liew, R. Sarma, and H. Cao, "Compact spectrometer based on a disordered photonic chip," *Nature Photonics*, 7(9), 746-751 (2013).

[13] N. M. Lawandy, "Disordered media: Coherent random lasing," *Nature Physics* 6, 246 - 248 (2010).

[14] K. Chung, T. J. Karle, R. Rajasekharan, C. Martijn de Sterke, and S. Tomljenovic-Hanic, "High-Q Defect-Free 2D Photonic Crystal Cavity from Random Localised Disorder", *Crystals* 4, 342-350 (2014).

[15] I. Mahariq, M. Kuzuoglu, H. Tarman, and H. Kurt, "Photonic Nanojet Analysis by Spectral Element Method," 6, 6802714, (2014).

[16] F. Oskooi, D. Roundy, M. Ibanescu, P. Bermel, J. D. Joannopoulos, and S. G. Johnson, "MEEP: a flexible freesoftware package for electromagnetic simulations by the FDTD method," *Comput. Phys. Commun.* 181(3), 687–702 (2010).

[17] H.F. Wang, L.P. Shi, G.Q. Yuan, X.S. Miao, W.L. Tan, and C.T. Chong, "Sub wavelength and super-resolution nondiffraction beam," *Appl. Phys. Lett*. 89, 171102 (2006).

Novel properties of Maxwell's fish eye as an optical microresonator

Khalil Dadashi[1,2*], Mirbek Turduev[1], Hamza Kurt[1], and Ramazan Esen[2]

[1]Nanophotonics Research Laboratory, Department of Electrical and Electronics Engineering
TOBB University of Economics and Technology, Ankara, 06560 Turkey
[2]Physics Department, Faculty of Science and Letters, Cukurova University, Adana, 01330, Turkey
*corresponding author, E-mail: kh.dadashi@gmail.com

Abstract

Whispering gallery modes (WGMs) in Maxwell`s fish eye (MFE) as a graded index medium have interesting spectral and optical transport properties. We employ the finite-difference time-domain (FDTD) method to numerically study of these properties. In comparison to conventional microdisc, mode splitting and high quality factor have been achieved. Due to rapid advances in nanofabrication methods, it seems that MFE can be one of the key optical elements in the future photonic circuits.

1. Introduction

Spherical dielectric microresonators (or microcavities) are optical elements that have attracted a lot of attention during past two decades due to their ability to exhibit novel resonance properties [1]. It means that they can select narrow segment of the incident beam for further manipulation and processing purposes [1, 2]. If a spherical or cylindrical resonator is appropriately illuminated, its natural oscillations can appear in the spectral domain. These optical oscillations are known as whispering gallery modes (WGMs) [3]. In general, the WGMs in dielectric optical resonator are function of the morphology, meaning geometry and refractive index of the resonator. Furthermore, the surrounding medium plays important role [2, 4]. Recently the spherical and circular structures coupled to straight waveguide have been studied widely as optical microresonators. The morphology dependence of these structures encouraged us to examine more complex spherical/cylindrical dielectric aiming to obtain higher quality factor, $Q = f/\Delta f$ (where f is the resonance frequency and Δf is the resonance line width) and rich optical properties [5]. As a result, the idea of using MFE resonator coupled to an optical waveguide was introduced by authors in Ref. [6] and both analytical and numerical results confirmed each other.

The generally used form of MFE is a spherically symmetric, inhomogeneous medium which is bounded with a perfectly electrical conductor boundary [7]. The refractive index of MFE varies according to a reverse quadratic function of a distance [6,7]:

$$n(r) = n_0/(1+(r/R)^2), \qquad (1)$$

where, n_0 is the refractive index in the origin, R is the physical radius of MFE, and the radius r is measured in the spherical coordinate system, $r = (x^2 + y^2 + z^2)^{1/2}$.

A brief introduction to studies of different aspects and novel properties of MFE in photonics and wave optics can be found in Ref. [6]. In principle MFE has unlimited resolution, so it can be used not only for achieving the perfect image without employing metamaterials but also for enhancing the resolution in the frame work of wave optics [8]. On the other hand, the analytical and numerical studies of MFE microresonator show that it can be used as key element for recent establishment of photonic molecule concept [6]. In this work, we studied the spectral properties, Q factor and free spectral range (FSR) of WGMs in a 2D MFE and compared the results with 2D conventional microdisc ones.

2. Numerical Simulations with FDTD method

Let us consider a simple 2D model of disc and MFE microresonators as shown in Figs. 1(a), 1(b). We will consider optical wave propagating in the $x-y$ plane, Fig. 1(a), with electric field intensity vector polarized perpendicular to the plane (TE modes). The conventional disc has constant refractive index $n_0/2$, radius R and the MFE has refractive index n_0 in the center decreasing to $n_0/2$ at the rim according to Eq. (1) and its radius is R as shown in Figs. 1(a), 1(b). They are closely coupled to a straight dielectric waveguide. A Gaussian source with broad band width is located in ports P_1 to excite the systems and the transmissions of waveguides are monitored in ports P_2. The locations of ports are shown in Fig. 1(a).

Simulations were performed for solving of the Maxwell`s equations by Yee algorithm and FDTD method [9], using a freely available software package [10]. The parameter n_0 in the refractive indices of the disc and MFE is set to 3.4641. The radius for both microresonators is set to $R = 12a$. Here a is defined as $\Delta x = \Delta y = a/20$, where Δx and Δy are the grid sizes of the 2D Yee lattice in FDTD

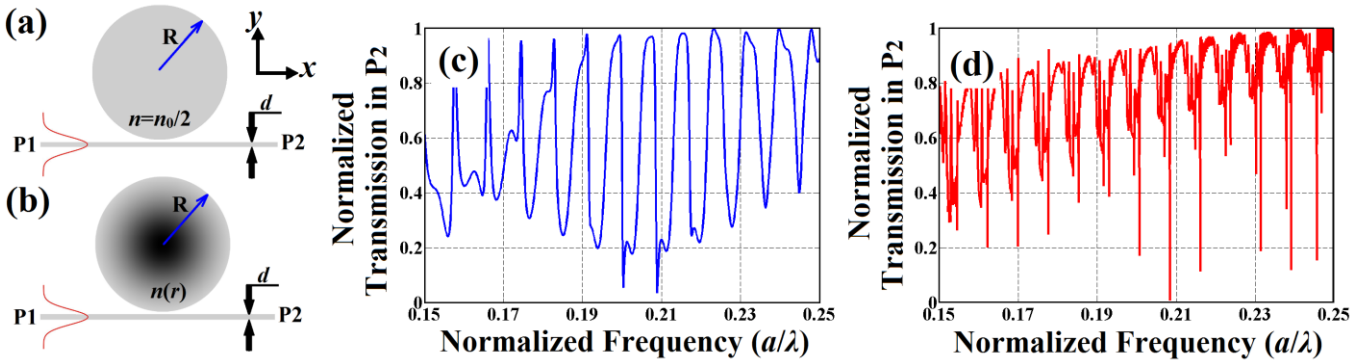

Figure 1: (a) Schematic representations of the (a) conventional microdisc and (b) 2D MFE. Normalized transmission spectra of the (c) conventional microdisc and (d) 2D MFE.

method [9]. The linear waveguides refractive index is $n_0/2$ and their widths are $d = a$. There is not any gap between waveguides and microresonators. The perfect matched layer (PML) boundary condition [9] has been used around the simulation domain. The normalized transmission spectrums of the waveguides coupled to disc and MFE are shown in Figs. 1(c), 1(d). The time steps for all simulations are $7000\Delta t$.

3. Discussion

In this work, the FDTD method is used to investigate the effect of radial variation of refractive index on the resonance frequencies of spherical microresonators. Resonances in microspheres/microcylinders can be excited under various conditions. A popular method is the excitation mechanism by evanescent coupling. In this technique, the resonator is placed close to linear waveguide or optical fiber. A schematic setup has been showed in Ref. [6] and a simple simulation domain is represented in Fig. 1(a).

The results of numerical simulations for calculating of the transmission spectrums measured in Port 2 (Figs. 1(a), 1(b)) have been represented in Figs. 1(c) and 1(d). We see from these figures that MFE refractive index, Eq. (1), has two effects: The resonances of disc have been shifted, when it has been changed to graded index medium one. These shifts are clearly shown in Table 1, as well. On the other hand, the 2D MFE microresonator displays mode splitting in the vicinity of its resonances.

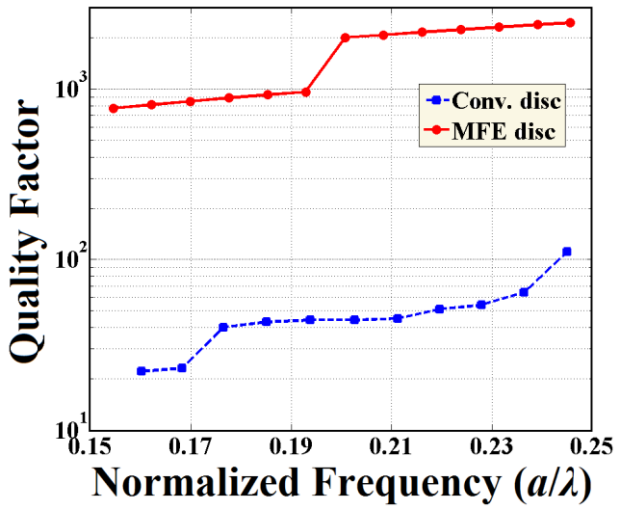

Figure 2. Calculated quality factor, Q, for the conventional microdisc and the 2D MFE.

Table 1: Calculated quality factor and free spectral range for conventional microdisc and 2D MFE.

Conv. Disc			MFE		
Freq.	Q	FSR	Freq.	Q	FSR
0.1601	22	0.0081	0.1545	811	0.0077
0.1682	23	0.0083	0.1622	850	0.0077
0.1765	40	0.0085	0.1699	888	0.0077
0.1850	43	0.0088	0.1776	926	0.0077
0.1938	44	0.0088	0.1853	965	0.0076
0.2026	44	0.0086	0.1929	965	0.0078
0.2112	45	0.0084	0.2007	2084	0.0077
0.2196	51	0.0083	0.2084	2161	0.0077
0.2279	54	0.0085	0.2161	2238	0.0076
0.2364	64	0.0085	0.2238	2314	0.0076
0.2449	111		0.2314	2391	0.0142
			0.2456	2456	

Fig. 2 represents the Q factor for all resonances of conventional disc and major resonances of MFE. Clearly, there is notable increase in magnitude of Q in MFE. Table1 contain Q factors for these two cases. The free space between consecutive resonances is known as free spectral range (FSR) [5]. The information in Table 1 shows that the FSRs for two structures are very close to each other.

Figure 3 shows the FDTD simulation results for four different time steps, when the MFE is excited by the major resonance mode labeled with $a/\lambda = 0.2314$ where $\lambda = \lambda_0/n(r)$ [6]. The snapshots show the intensity of transverse electric fields (TE modes). Forming the WGMs

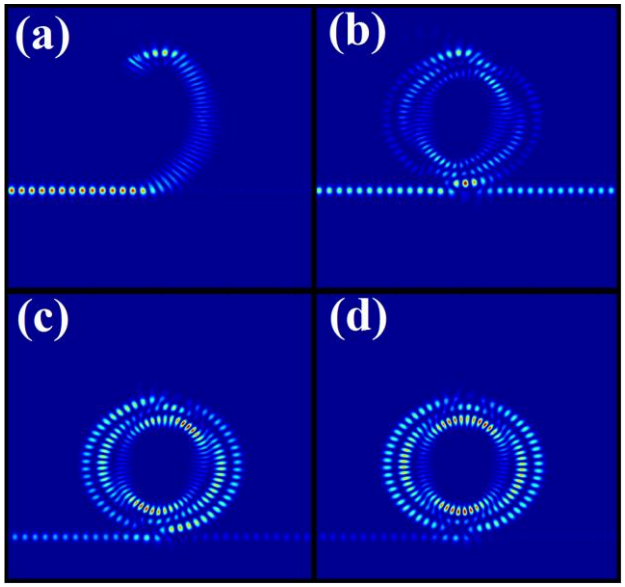

Figure 3. Snap shots of the TE modes at different (a) $200\Delta t$, (b) $1000\Delta t$, (c) $3000\Delta t$ and (d) $7000\Delta t$ time instants.

has been depicted for time steps $200\Delta t$, $1000\Delta t$, $3000\Delta t$ and $7000\Delta t$ respectively.

4. Conclusions

We derive analytical formulation for the solutions of Helmholtz equation in an inhomogeneous optical resonator whose refractive index expression follows a special formula, *i.e.,* Maxwell fish eye [6]. We continue on the same problem to highlight the rich optical properties of MFE resonator compared to more conventional ones, such as disc resonator.

Acknowledgements

The authors gratefully acknowledge the financial support of the Scientific and Technological Research Council of Turkey (TUBITAK), project 110T306. H. Kurt acknowledges partial support from the Turkish Academy of Sciences.

References

[1] K. J. Vahala, Optical Microcavities, *Nature* 424: 839-846, 2003.

[2] G. Adamovsky, S. Wrbanek, Coupling of low-order LP modes propagating in cylindrical waveguides into whispering gallery modes in microspheres, *Optics Express*, 21: 2279-2286, 2013.

[3] A. B. Matsko and V. S. Ilchenko, Optical resonators with whispering-gallery modes—part I: basics, *IEEE J. Sel. Top. Quantum Electron.* 12: 3–14, 2006.

[4] G. Schweiger and M. Horn, Effect of changes in size and index of refraction on the resonance wavelength of microspheres, *J. Opt. Soc. Am. B* 23: 212–217, 2006.

[5] I. Chremmos, O. Schwelb, N. Uzunoglu, *Photonic Microresonator Research and Applications*, Springer, 2010.

[6] K. Dadashi, H. Kurt, K. Ustun, R. Esen, Graded Index Optical Microresonators: Analytical and Numerical Analyses, *J. Opt. Soc. Am. B* 31: 2239–2245, 2014.

[7] J. Liu, R. Mendis, and D. M. Mittleman, A Maxwell's fish eye lens for the terahertz region, *Appl. Phys. Lett.* 103: 031104, 2013.

[8] U. Leonhardt, Perfect imaging without negative refraction, *New J. Phys.* 11: 093040-093051, 2009.

[9] A. Taflove, S. C. Hagness, *Computational Electrodynamics The Finite-Difference Time- Domain Method*, Third Edition, Artech House, 2005.

[10] A. F. Oskooi, D. Roundy, M. Ibanescu, P. Bermel, J. D. Joannopoulos, and S. G. Johnson, MEEP: A flexible free-software package for electromagnetic simulations by the FDTD method, *Computer Physics Communications* 181: 687–702, 2010.

Anomalous optical forces on radially anisotropic nanowires

H. L. Chen[1] and L. Gao[1,2*]

1 College of Physics, Optoelectronics and Energy of Soochow University, Collaborative Innovation Center of Suzhou Nano Science and Technology, Soochow University, Suzhou 215006, China and

2 Jiangsu Key Laboratory of Thin Films, Soochow University, Suzhou 215006, China

Abstract

We establish full-wave electromagnetic scattering theory to study radially anisotropic nanowire. In certain conditions, the theoretical predictions can be derived that the electromagnetic scattering includes non-Rayleigh vanishing and diverging. Therefore, the anisotropic nanowires can be hardly visible or exhibit superscattering. Based on that, we will have further research about the optical forces. The optical forces do not always obtain the Rayleigh's law due to the special optical properties of the radially anisotropic nanowire, it may have unusual optical forces. To verify our predictions, both numerical results with Maxwell stress tensor integration techniques and numerical simulations are performed. These results may be helpful to the potential applications in the field of nanotechnology.

* E-mail:leigao@suda.edu.cn

I. INTRODUCTION

The light-matter interaction has been studied for many years. Nowadays, optical pulling force of small particles with a forward propagating beam have received much attention [1–3]. The small particles such as silicon sphere, present both magnetic and electric dipolar responses, thus the optical force was addressed. Understanding the optical force is fundamental because it is important in applications, such as optical tweezers [4, 5] and the study of optical traps [6]. Scientists have developed a theory about optical force on small magnetodielectric particles [7, 8]. In recent years, the optical forces focused on small solid sphere [9, 10] and coated sphere [11] with a forward propagating beam have received much attention. However, most of the theories on optical force have only discussed the isotropic particles.

Recently, a lot of theories have been developed to deal with the scattering problems of anisotropic materials [12–16]. The anisotropic materials have their novel optical properties. A static electric field controls the optical properties of gold nanoparticles coated with anisotropic nematic liquid crystal [17]. For instance, in the core-shell nanosphere, the fields can be further enhanced by adjusting the spherical anisotropy in the core [18]. What's more, in the cell membranes containing mobile charges and in the phospholipid vesicle system, we can find the anisotropy [19–21]. Recently, Cheng et al. used split-ring resonators to design radially anisotropic zero-index metamaterial in two dimensions to verify the peculiar phenomena experimentally [22, 23]. They have fabricated the radially anisotropic metamaterial, and the experimental results have demonstrated the spacial power combination with high efficiency.

In this paper, we consider the radially anisotropic nanowires with an incident plane wave to study the optical force based on Mie scattering theory and Maxwell stress tensor formulation. Under certain conditions, the anomalous optical force behaviors are derived. We verify the results both analytically and numerically. This paper is organized as follows. In section II, we study the scattering theory for the anisotropic cylinder. In section III, some numerical

results of optical force in the long-wavelength region are shown. Conclusions and discussions are given in section IV.

II. SCATTERING THEORY FOR ANISOTROPIC CYLINDER

We consider a radially anisotropic cylinder of radius a made of the material with relative permittivity tensor $\overleftrightarrow{\varepsilon} = \varepsilon_r \hat{r}\hat{r} + \varepsilon_t \hat{\theta}\hat{\theta} + \varepsilon_z \hat{z}\hat{z}$ and relative permeability $\overleftrightarrow{\mu} = \mu_r \hat{r}\hat{r} + \mu_t \hat{\theta}\hat{\theta} + \mu_z \hat{z}\hat{z}$ embedded into surrounding media with the relative permittivity ε_1 and relative permeability μ_1.

Based on the Maxwell equations, when a transverse-magnetic(TM) incident wave which is defined by a wave vector k, with its magnetic field polarized along the z director, impinges on the anisotropic cylinder, the magnetic fields inside and outside of the anisotropic cylinder are expressed as,

$$\begin{aligned} H_z^{in} &= \sum_{n=-\infty}^{+\infty} \mathrm{i}^n c_n J_{n'}\left(k_2 r\right) e^{\mathrm{i}n\theta}, \qquad r < a, \\ H_z^{out} &= \sum_{n=-\infty}^{\infty} \mathrm{i}^n \left[J_n\left(k_1 r\right) + b_n H_n\left(k_1 r\right)\right] e^{\mathrm{i}n\theta}, \qquad r > a, \end{aligned} \tag{1}$$

where $n' = |n| \sqrt{\varepsilon_t}/\sqrt{\varepsilon_r}$, $k_1 = \sqrt{\varepsilon_1}\sqrt{\mu_1}k_0$, $k_2 = \sqrt{\varepsilon_t}\sqrt{\mu_z}k_0$ and $k_0 = \omega/c$. In addition, $J_n(\cdots)$ and $H_n(\cdots)$ are the nth-order Bessel and Hankel functions.

After some algebraic manipulations according to the boundary conditions, we can derive the scattering coefficient b_n [24],

$$b_n = -\frac{\sqrt{\varepsilon_t}\sqrt{\mu_1} J'_{|n|}\left(k_1 a\right) J_{n'}\left(k_2 a\right) - \sqrt{\mu_z}\sqrt{\varepsilon_1} J_{|n|}\left(k_1 a\right) J'_{n'}\left(k_2 a\right)}{\sqrt{\varepsilon_t}\sqrt{\mu_1} H'_{|n|}\left(k_1 a\right) J_{n'}\left(k_2 a\right) - \sqrt{\mu_z}\sqrt{\varepsilon_1} H_{|n|}\left(k_1 a\right) J'_{n'}\left(k_2 a\right)}. \tag{2}$$

The total time-average optical force on the dipolar cylinder is the integration over any surface S with unit normal $\hat{n}$,

$$\langle F \rangle = \frac{1}{8\pi} \mathrm{Re}[\oint_S d\vec{S} \cdot \overleftrightarrow{T}], \tag{3}$$

the bracket $\langle\rangle$ corresponds to the time average over an optical cycle, and $\overleftrightarrow{T}$ is the Maxwell stress tensor. Re means the real part of a complex number. The optical force concludes the pure electric dipole F_e , the pure magnetic dipole F_m and the electric-magnetic dipolar interaction component F_{e-m}, which can be expressed as,

$$\langle F\rangle = \langle F_e\rangle + \langle F_m\rangle + \langle F_{e-m}\rangle = \frac{k_0}{2}\mathrm{Im}[\alpha_e + \alpha_m] - \frac{k_0^4}{3}(\mathrm{Re}[\alpha_e]\mathrm{Re}[\alpha_m] + \mathrm{Im}[\alpha_e]\mathrm{Im}[\alpha_m]), \quad (4)$$

where α_e and α_m represent the electric and magnetic polarizabilities of the infinite cylinders, which can be expressed as [25],

$$\alpha_e = i\frac{2}{\pi k_1^2}b_1, \quad \alpha_m = i\frac{1}{\pi k_1^2}b_0. \quad (5)$$

III. NUMERICAL RESULTS OF OPTICAL FORCE IN THE LONG-WAVELENGTH REGION

In this section, we consider the long-wavelength limit case, that is, $k_1 a = \sqrt{\varepsilon_1}\sqrt{\mu_1}\omega a/c = \sqrt{\varepsilon_1}\sqrt{\mu_1}q \ll 1$ and $k_2 a = \sqrt{\varepsilon_t}\sqrt{\mu_z}\omega a/c = \sqrt{\varepsilon_t}\sqrt{\mu_z}q \ll 1$. In this condition, the Mie coefficients b_1 and b_0 are given by,

$$b_1 = -\frac{C_1 q^\nu + C_2 q^{\nu+2}}{iC_3 q^{\nu-2} + iC_4 q^\nu + C_1 q^\nu + C_2 q^{\nu+2}}, \quad (6)$$

$$b_0 = -\frac{D_1 q + D_2 q^3}{iD_3 q^{-1} + D_1 q + D_2 q^3}, \quad (7)$$

where $\nu = \sqrt{\varepsilon_t}/\sqrt{\varepsilon_r}$ and the parameters are written as,

$$\begin{aligned}
C_1 &= \frac{1}{2}\left(\frac{\sqrt{\varepsilon_r}}{\sqrt{\varepsilon_1}} - \frac{\sqrt{\varepsilon_1}}{\sqrt{\varepsilon_t}}\right), \quad C_2 = \frac{\sqrt{\varepsilon_1}\sqrt{\varepsilon_r}\mu_z}{4} + \frac{\varepsilon_1^{3/2}\mu_1}{16\sqrt{\varepsilon_t}} - \frac{\sqrt{\varepsilon_1}\sqrt{\varepsilon_r}\mu_1}{16} - \frac{\sqrt{\varepsilon_1}\sqrt{\varepsilon_r}\mu_z + \sqrt{\varepsilon_r}\varepsilon_t\mu_z/\sqrt{\varepsilon_1}}{8(\sqrt{\varepsilon_t}/\sqrt{\varepsilon_r}+1)}, \\
C_3 &= \frac{2}{\pi}\left(\frac{\sqrt{\varepsilon_r}}{\varepsilon_1^{3/2}\mu_1} + \frac{1}{\sqrt{\varepsilon_1}\sqrt{\varepsilon_t}\mu_1}\right), \quad C_4 = -\frac{\sqrt{\varepsilon_r}\mu_z}{\pi\sqrt{\varepsilon_1}\mu_1} - \frac{\mu_z\sqrt{\varepsilon_t}/(\mu_1\sqrt{\varepsilon_1}) - \sqrt{\varepsilon_r}\varepsilon_t\mu_z/(\mu_1\varepsilon^{3/2})}{2\pi(\sqrt{\varepsilon_t}/\sqrt{\varepsilon_r}+1)}, \\
D_1 &= \frac{1}{2}\left(-\sqrt{\varepsilon_t}\sqrt{\mu_1} + \frac{\mu_z\sqrt{\varepsilon_t}}{\sqrt{\mu_1}}\right), \\
D_2 &= \frac{1}{16}\left(\varepsilon_1\mu_1^{3/2}\sqrt{\varepsilon_t} - \frac{\mu_z^2\varepsilon_t^{3/2}}{\sqrt{\mu_1}}\right) + \frac{1}{8}\left(\varepsilon_t^{3/2}\mu_z\sqrt{\mu_1} - \varepsilon_1\mu_z\sqrt{\varepsilon_t}\sqrt{\mu_1}\right), \quad D_3 = \frac{2\sqrt{\varepsilon_t}}{\pi\varepsilon_1\sqrt{\mu_1}}.
\end{aligned}$$

For simplification, we consider the radially anisotropic nanowire surrounded by the surrounding media with permittivity $\varepsilon_1 = 1$ and permeability $\mu_1 = 1$.

(1) It is normal Rayleigh case. For ordinary small cylinder, the Mie coefficients can be reduced to,

$$b_1 \sim \frac{C_1 q^{\nu}}{iC_3 q^{\nu-2} + C_1 q^{\nu}}, \quad b_0 \sim \frac{D_1 q}{iD_3 q^{-1} + D_1 q}. \tag{8}$$

Then, the electric polarization can be written as,

$$\mathrm{Re}[\alpha_m] \sim a^2, \quad \mathrm{Im}[\alpha_m] \sim a^4 k_1^2, \quad \mathrm{Re}[\alpha_e] \sim a^2, \quad \mathrm{Im}[\alpha_e] \sim a^4 k_1^2, \tag{9}$$

where Im means the imaginary part of a complex number. Therefore, the optical force on the anisotropic nanowire can be expressed as,

$$F \sim a^4 k_1^3. \tag{10}$$

In this case, the property of the optical force for the anisotropic nanowire is similar to that of the isotropic nanowire. We plot the numerical results of optical force as a function of k_1 in Fig. 1 with the isotropic nanowires. In this figure, we find the slope of the line is 3. With the great progress of the metamaterials, the materials with the negative permittivity or/and negative permeability have been verified to exist in scientific community. Anomalous behavior for the optical force may arise with the values of these materials.

(2) If the conditions $\sqrt{\varepsilon_r}\sqrt{\varepsilon_t} = 1$ and $\mu_z = 1$ are satisfied, then it is non-Rayleigh vanishing scattering, which would result in better transparency than the isotropic nanowires. The electric and magnetic polarizabilities can be written as,

$$\mathrm{Re}[\alpha_m] \sim a^4 k_1^2, \quad \mathrm{Im}[\alpha_m] \sim a^8 k_1^6, \quad \mathrm{Re}[\alpha_e] \sim a^4 k_1^2, \quad \mathrm{Im}[\alpha_e] \sim a^8 k_1^6. \tag{11}$$

Therefore, the optical force on the anisotropic nanowire can be expressed as,

$$F \sim a^8 k_1^7, \tag{12}$$

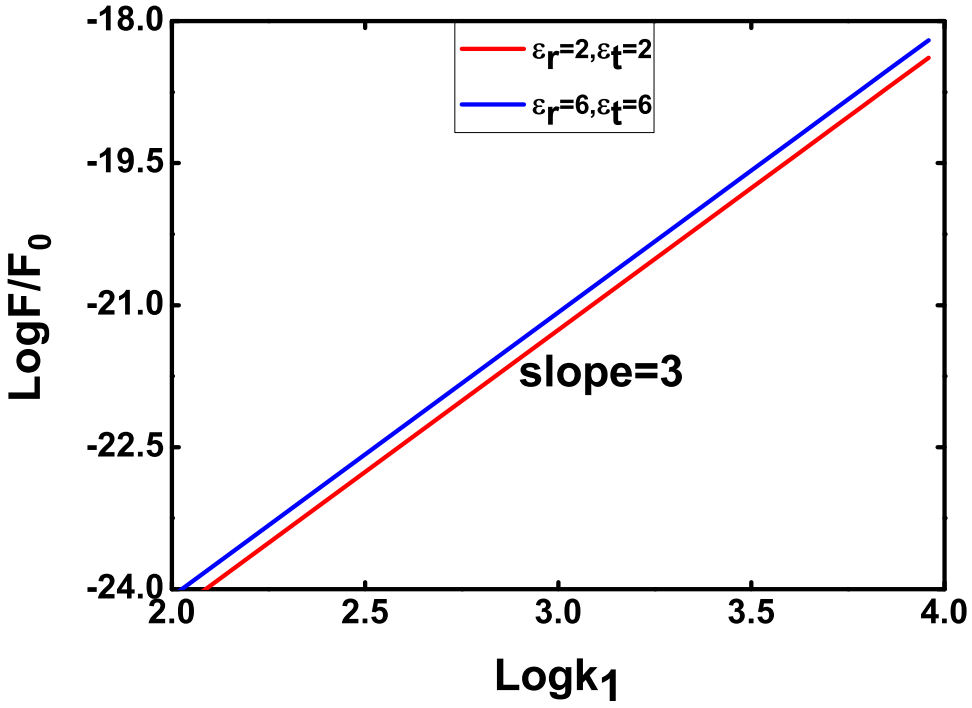

FIG. 1: Log-log plot of optical force dependence vs k_1 with $a = 100nm$ for $\mu_z = 2$.

which is different from the property of the optical force in the normal Rayleigh case. The optical force exhibits a fast decrease with decreasing k_1 and obeys unusual relation $F \sim k_1^7$, as shown in Fig. 2. Physically, in the long-wavelength limit, the anisotropic nanowire can be regarded as an isotropic one with the effective permittivity $\varepsilon_{eff} = \sqrt{\varepsilon_r}\sqrt{\varepsilon_t} = 1$ and the effective permeability $\mu_{eff} = 1$ [26]. That is to say, the anisotropic nanowire behaves as an isotropic nanowire made of vacuum approximately.

(3) In the end, we consider the following condition, $\sqrt{\varepsilon_r}\sqrt{\varepsilon_t} = -1$. Under this condition, the nanowires exhibit superscattering. In this case, the electric polarization is more important than the magnetic polarization, thus we only consider the electric polarization. The optical

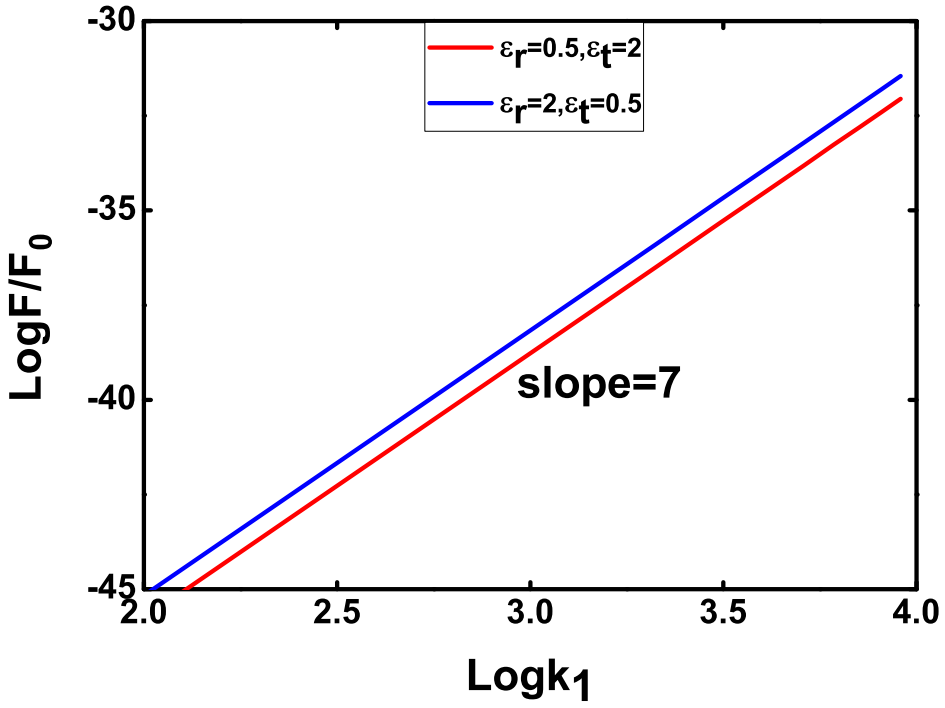

FIG. 2: Log-log plot of optical force dependence vs k_1 with $a = 100nm$ for $\mu_z = 1$.

force on the anisotropic cylinder can be expressed as,

$$F \sim k_1^{-1}. \tag{13}$$

This optical force in this case is much larger than that in Rayleigh case for the nanowires. It can be found that the optical force exhibits a rapid increase with decreasing k_1. In Fig. 3, we plot the optical force as a function of wave number k_1 by using the generalized Mie theory and Maxwell stress tensor integration method. Hence, those anomalous behaviors are consistent with our analytical predictions.

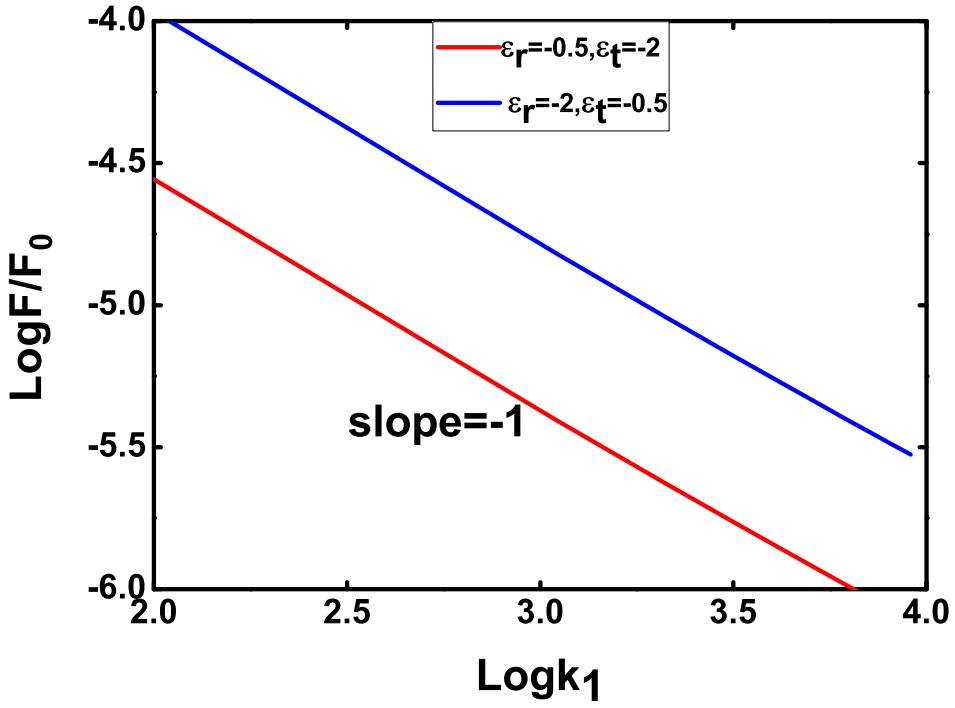

FIG. 3: Log-log plot of optical force dependence vs k_1 with $a = 100nm$ for $\mu_z = 1$.

IV. CONCLUSIONS

In this paper, we have studied the optical forces on anisotropic nanowire based on the Mie theory and Maxwell stress tensor integration method. Under certain conditions, the optical force can exhibit non-Rayleigh behavior $F \sim a^8 k_1^7$ and $F \sim k_1^{-1}$ instead of the normal Rayleigh case $F \sim a^4 k_1^3$. Under the conditions $\sqrt{\varepsilon_r}\sqrt{\varepsilon_t} = 1$ and $\mu_z = 1$, the optical force exhibits a fast decrease with decreasing k_1. On the other hand, in the condition of $\sqrt{\varepsilon_r}\sqrt{\varepsilon_t} = -1$, the optical force is much larger than the one in the Rayleigh case.

Some comments are in order. The unusual behaviors of the anisotropic nanowires are derived for the nondissipative case. If the absorptive terms are smaller than the critical ones,

dependent on the size a and the wave number k_1, we can still possibly observe the unusual behavior, as shown in our preliminary studies. As a consequence, the material of much small absorption or realistic materials can realize the unusual optical force experimentally. These results may be helpful to the potential applications in the field of nanotechnology.

ACKNOWLEDGMENT

This work was supported by the National Natural Science Foundation of China (No. 11374223), the National Basic Research Program (No. 2012CB921501), the Ph. D. Programs Foundation of Ministry of Education of China (No. 20123201110010), and the Project Funded by the Priority Academic Program Development of Jiangsu Higher Education Institutions.

---

[1] Q. Lin, J. Rosenberg, X.S. Jiang, K.J. Vahala, O. Painter, Mechanical Oscillation and Cooling Actuated by the Optical Gradient Force. Phys. Rev. Lett. 103, 103601(2009)

[2] V. Ginis, P. Tassin, C.M. Soukoulis, I. Veretennicoff, Enhancing Optical Gradient Forces with Metamaterials. Phys. Rev. Lett.110, 057401(2013)

[3] M. Li, Wolfram H.P. Pernice, H.X. Tang, Reactive Cavity Optical Force on Microdisk-Coupled Nanomechanical Beam Waveguides. Phys. Rev. Lett. 103, 223901(2009)

[4] A. Ashkin, J.M. Dziedzic, J.E. Bjorkholm, S. Chu, Observation of a single-beam gradient force optical trap for dielectric particles. Opt. Lett. 11, 288-290 (1986)

[5] D.G. Grier, A revolution in optical manipulation. Nature 424, 810-816 (2003)

[6] G.K. Campbell, A.E. Leanhardt, J. Mun, M. Boyd, E.W. Streed, W. Ketterle, D.E. Pritchard, Photon recoil momentum in dispersive media. Phys. Rev. Lett. 94, 170403 (2005)

[7] P.C. Chaumet, A. Rahmani, Electromagnetic force and torque on magnetic and negative-index scatterers. Opt. Express 17, 2224-2234 (2009)

[8] M.N. Vesperinas, J.J. Saenz, R.G. Medina, L. Chantada, Optical forces on small magnetodielectric particles. Opt. Express 18, 11428-11443 (2010)

[9] J. Chen, J. Ng, Z.F. Lin, C.T. Chan, Optical pulling force. Nat. Photon. 5, 531-534 (2011)

[10] A. Novitsky, C.W. Qiu, H. Wang, Single gradientless light beam drags particles as tractor beams. Phys. Rev. Lett. 107, 203601 (2011)

[11] N. Wang, W.L. Lu, J. Ng, Z.F. Lin, Optimized optical "tractor beam" for core-shell nanoparticles. Opt. Lett. 39, 2399-2402 (2014)

[12] J.C. Monzon, N.J. Damaskos, Two-dimensional scattering by a homogeneous anisotropic rod. IEEE TransAntennas Propag, 34(10), 1243 (1986)

[13] B. Beker, K.R. Umashankar, A. Taflove, Numerical analysis and validation of the combined field surface integral equations for electromagnetic scattering by arbitrary shaped two-dimensional anisotropic objects. IEEE Trans Antennas Propagat 37(12), 1573 (1989)

[14] C.W. Qiu, L.W. Li, H. Yao, S. Zouhdi, Properties of Faraday chiral media: Green dyadic and negative refraction. Phys Rev B 74(11), 115110(2006)

[15] H.L. Chen, L. Gao, Tunablity of the unconventional Fano resonances in coated nanowires with radial anisotropy. Opt. Express 21, 23619-23630(2013)

[16] Y. X. Ni, L. Gao, A. E. Miroshnichenko, and C. W. Qiu, Non-Rayleigh scattering behavior for anisotropic Rayleigh particles. Opt. Lett. 37, 3390-3392 (2012)

[17] S.Y. Park, D. Stroud, Splitting of surface plasmon frequencies of metal particles in a nematic liquid crystal. Appl. Phys. Lett. 85, 2920 (2004)

[18] Y.X. Ni, D.L. Gao, Z.F. Sang, L. Gao, C.W. Qiu, Infuence of spherical anisotropy on the optical properties of plasmon resonant metallic nanoparticles. Appl Phys A, 102, 673 (2011)

[19] L. Gao, T.H. Fung, K.W. Yu, C.W. Qiu, Electromagnetic transparency by coated spheres with radial anisotropy. Phys. Rev. E, 78, 046609(2008)

[20] T. Ambjornsson, G. Mukhopadhyay, S.P. Apell, M. Kall, Resonant coupling between localized plasmons and anisotropic molecular coatings in ellipsoidal metal nanoparticles. Phys. Rev. B

73, 085412(2006)

[21] B. Lange and S. R. Aragon, Mie scattering from thin anisotropic spherical shells. J. Chem. Phys. 92, 4643(1990)

[22] Q. Cheng, W.X. Jiang, T.J. Cui, Spatial power combination for omnidirectional radiation via anisotropic metamaterials. Phys. Rev. Lett. 108, 213903(2012)

[23] Y. Yuan, N. Wang, J.H. Lim, On the omnidirectional radiation via radially anisotropic zero-index metamaterials. Europhys. Lett. 100, 34005 (2012)

[24] H.L. Chen, L. Gao, Anomalous electromagnetic scattering from radially anisotropic nanowires. Phys. Rev. A 86, 033825 (2012)

[25] J.M. Aunon, M. Nieto-Vesperinas, Optical forces from evanescent Bessel beams, multiple reflections, and Kerker conditions in magnetodielectric spheres and cylinders. J. Opt. Soc. Am. A, 31, 9(2014)

[26] Y. Wu, J.S. Li, Z.Q. Zhang, C.T. Chan, Effective medium theory for magnetodielectric composites: Beyond the long-wavelength limit. Phys. Rev. B 74, 085111 (2006)

Adaptive Optical Control in Disordered Medium

Chin-Jung Chuang[1*], Wen-Cheng Chang [1]

[1] Department of Opto-electronic Engineering, National Dong Hwa University, Hualien, Taiwan
*corresponding author, E-mail: cjc@ndhu.edu.tw

Abstract

Materials such as teeth, milk or human tissue are opaque. We have shown that coherent light can be focused through them. The principle can be applied in therapy, like Laser Acupuncture and Hair Regrowth. Because by low-level laser focusing on subcutaneous tissue is maybe with a therapeutic effect. The two different optimization algorithms are programed. To approach the actual situation, we add a noise to the algorithms.

1. Introduction

Materials such as teeth, milk, white paint or human tissue are opaque because of random scattering of light. These materials distort the incident wavefront lead to diffusion of the emitted light [1]. The coherent light can be focused through these opaque material by retarding phase of the incident light have been shown [2]. Figure 1 shows the principle of inverse wave diffusion. A plane wave is focused through this scattering sample, most of the light does not reach specified target and form a random speckle (Fig. 1.a). When the incident wavefront is matched with the scattering sample, the transmitted light focuses in the target area (Fig. 1.b).

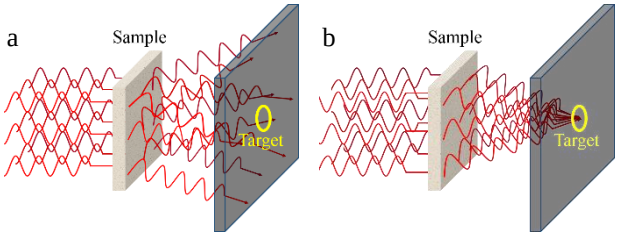

Figure 1: The principle of inverse wave diffusion. (Adapted from [2].)

The principle of inverse wave diffusion can be applied in many research area, for example, fluorescence excitation or photodynamic therapy. Among photodynamic therapy, include Laser Acupuncture [3] and Hair Regrowth [4]. By low-level laser focusing on subcutaneous tissue is maybe with a therapeutic effect [5]. Though this is not yet established, it is observed and deserve to be researched.

2. Algorithms

The algorithms discussed in this paper are all of the pixels must retard appropriate phase. The important elements of the algorithms are pixel, incident light, phase retardation, strongly scattering sample, and target area. The incident light is divided into N pixel, and the phase retardation is set for each of the pixel individually to a value between $-\pi$ and π. The transmitted field, E_{ij}, is a $i \times j$ matrix ($i \times j = N$.). E_{ij} is defined as:

$$E_{ij} = A_0 \times \exp[i(\phi_{ij} + t_{ij})]. \quad (1)$$

Where the A_0 and ϕ_{ij} are the amplitude and phase of the incident light, respectively. Phase retardation in the scattering material, t_{ij}, is an unknown matrix of the sample. The ϕ_{ij} and t_{ij} are all $i \times j$ matrix. In addition, so as to calculate conveniently, we set $A_0 = 1$ in this paper.

The optimization algorithms are programed. Initially, setting the incident phase, ϕ_{ij}, is a zero matrix and the matrix is substituted into Eq. (1).Then, taking a fast Fourier transform and the absolute value to E_{ij} in sequence can get the intensity of the target area, I_0. Time to get an intensity is defined as a single iteration, T_i. Subsequently, we change the phase retardation from $-\pi$ to π and get the intensity of the target area, I_t, respectively. And so on, until finally we find the inverse phase of the sample. When the phase retardation is close to the inverse phase, the target intensity will approach N because of the transmitted light with the same phase.

Now, we will introduce two algorithms which are the stepwise and continuous sequential algorithm in this paper. These algorithms referring to [6] are simple and intuitive. The following is discussed.

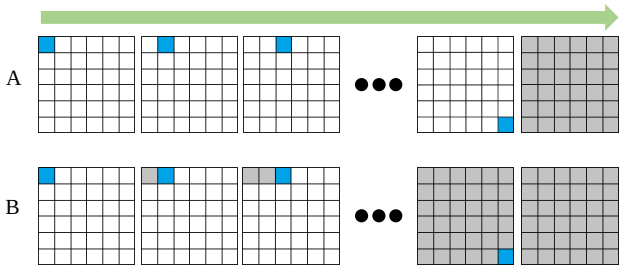

Figure 2: The principle of the two sequential algorithm.(Adapted from [6].) (blue: scanning, grey: saving)

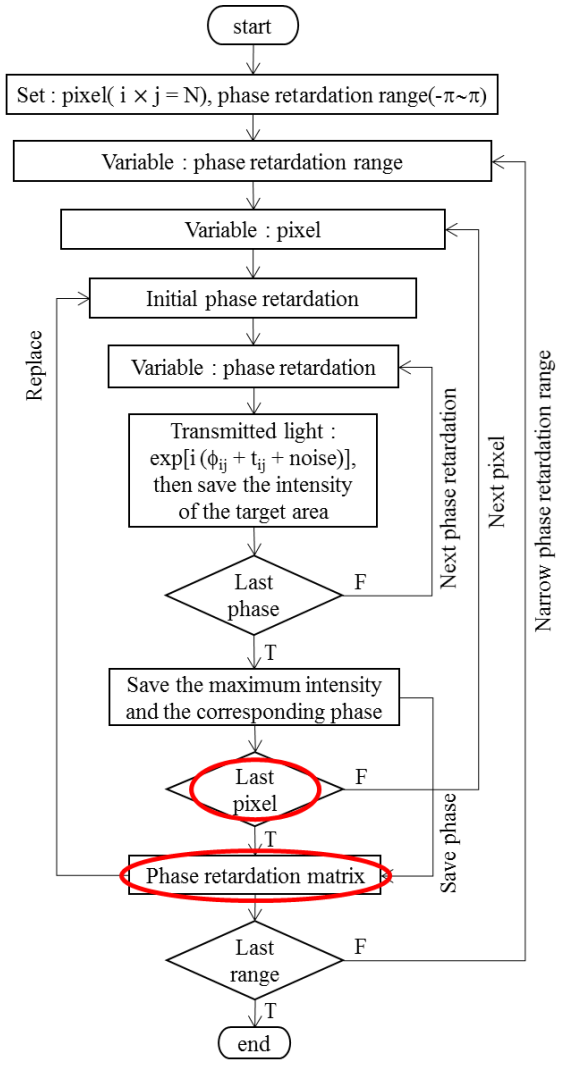

Figure 3: The flowchart of the algorithm.

2.1. The stepwise sequential algorithm

The principle of the stepwise sequential algorithm is like Fig. 2.A. The main idea is written. Initially, we find the phase retardation from $-\pi$ to π and read the maximum intensity of each of the N pixels in sequence. When the next pixel is scanned, the phase retardation of the others is reset to initial value. We wait until all of the pixels are scanned, then save the maximum intensity and the corresponding phase. If the maximum intensity do not converge on N, we will replace the initial phase retardation with the phase we get just and narrow the phase retardation range.

2.2. The continuous sequential algorithm

The continuous sequential algorithm is similar to the stepwise sequential algorithm. The different of these two algorithms is that whether the phase retardation is reset to the initial value or not. The principle of the continuous one is like Fig. 2.B.

3. Simulations

The software used to simulate these algorithms is MATLAB because of being convenient to calculate matrix.
In the beginning, some parameter set are N pixels, dividing phase retardation into M value, narrowing phase retardation range with L times, a $i \times j$ matrix of the phase of the incident light, ϕ_{ij}, a $i \times j$ matrix of the phase retardation, t_{ij}. The target of the algorithms are $\phi_{ij} \approx t_{ij}$.

3.1. Flowchart

Figure 3 is the flowchart of the stepwise sequential algorithm, and the step with red circle in it are changed is the flowchart of the continuous sequential algorithm.

4. Discussion

4.1. Non optimization

The setting of the phase retardation in the scattering material, t_{ij}, will be discussed. We use the syntax 'rand(i, j)*2*pi' to set it, because different materials will be simulated. In order to know what the target intensity range is, the following experiment is done.
From one pixel to ten thousand pixels, take several values and substitute into Eq. (1). Each of them is executed 1000 times, the average of the target intensity is taken and the two standard deviations (95%) is painted, it is like Fig. 4. Figure 4 can show that the more the pixels are, the stronger the average target intensity will be, but it is nonlinear and the slope decrease progressively. This can show the more the pixels are, the easier we observe the convergent figure. Because of the ratio of the target intensity.
Furthermore, we find that the target intensity may be lower than 1 in the two standard deviations (95%). This part do not correspond to our setting, and the target intensity must be sifted initially.

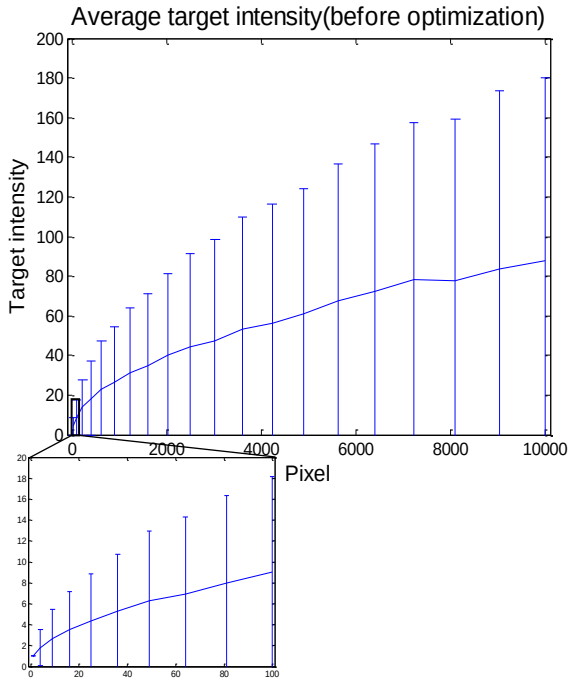

Figure 4: The average target intensity before optimization.

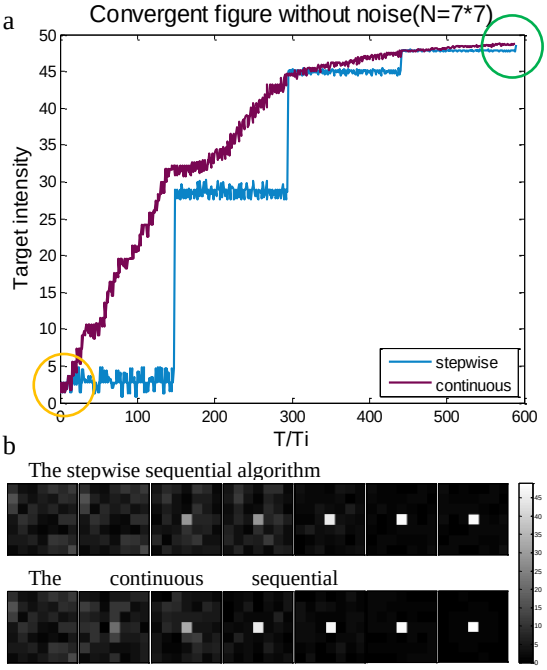

Figure 5: (a) The convergent figure of the target intensity without noise. (b) The diagram of the intensity of the two algorithms.

4.2. Ideal situation

4.2.1. Convergence

First, we will discuss the convergence and the diagram of the intensity of the two algorithms.

Figure 5.a is the convergent figure of the target intensity without noise, we set N=7 × 7, M=3, L=4, number of the iteration for x axis and the target intensity for y axis. The figure shows the intensity with a plane wave transmit is in yellow circle, the convergent intensity is close to N in green circle. Because the intensity of each pixel is set in 1 initially, when the phase of all pixels are same and the intensity will be N. The stepwise one is like stairs and the continuous one is continuous curve. In Fig. 5.b, the diagram of the intensity of the two algorithms can show clearly. The different of the two can be seen in the middle.

4.3. Effect of noise

4.3.1. Convergence

To approach the actual situation, we add a noise phase to ϕ_{ij} in Eq. 1. The noise is the percentage of 2π, so we also use the syntax 'rand(i, j)*2*pi' to set it. In Fig. 6, zero percent, five percent, fifty percent and 10×10 pixels are set. The figure shows the convergent intensity decreases with the increase of noise. When the noise increases to fifty percent, which is true or false will not be recognized and the target intensity will approximate to the initial intensity.

Furthermore, we can see that the convergence of the continuous sequential algorithm is higher than the stepwise one in the 5% noise. This will be discussed in the after paragraph.

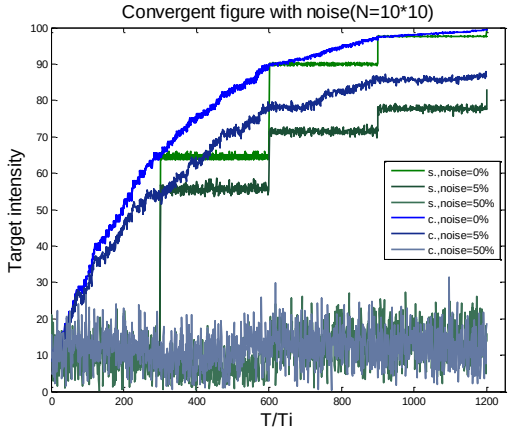

Figure 6: The convergent figure of the target intensity with noise (0%, 5%, 50%) of the two algorithms.

4.3.2. Different noise ratio

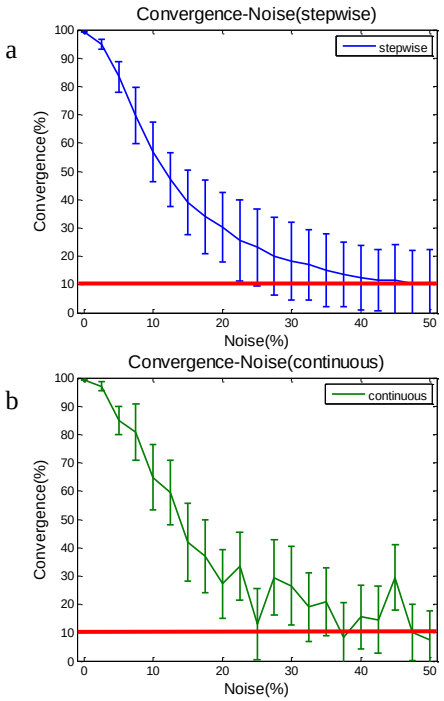

Figure 7: (a) The relationship between convergence and noise of the stepwise sequential algorithm. (b) The relationship between convergence and noise of the continuous sequential algorithm.

The convergence of the two algorithms with different noise ratio will be discussed. In the beginning, we set pixel 10×10 and the noise ratio at intervals of 2.5 from 0 to 50. Each of them is executed 100 times, the average of the convergence is taken and the two standard deviations (95%) is painted, it is like Fig. 7.
The convergence ratio is defined:

$$\text{convergence} = \frac{\text{TI}}{\text{MTI}} \times 100\% \qquad (2)$$

Where the TI is the target intensity and the MTI is the maximum of the target intensity without noise.
Figure 7 can show that the more the noise ratio is, the lower the convergence will be and it is nonlinear. The two standard deviations (95%) is smaller than others when the noise is under 5%. Then, we take the average target intensity of the 10×10 pixels from fig. 4 and print it by red line in fig.7. After printing the red line, we can see that the convergence of the two algorithms will not be enhanced when the noise ratio increase to about 25%. In addition, the convergence of the stepwise sequential algorithm is steadier than the continuous one. A number of the saving times may be a cause.

4.3.3. Different pixels

First, we set the noise ratio 5%, because it is easy to be observed from the front discussion. The relationship between convergence and pixel of the two algorithms is printed like fig. 8. Figure 8 shows the more the number of the pixel is, the lower the convergence is and it is fast. This can be seen the two algorithms are all not applied to a lot of pixels.

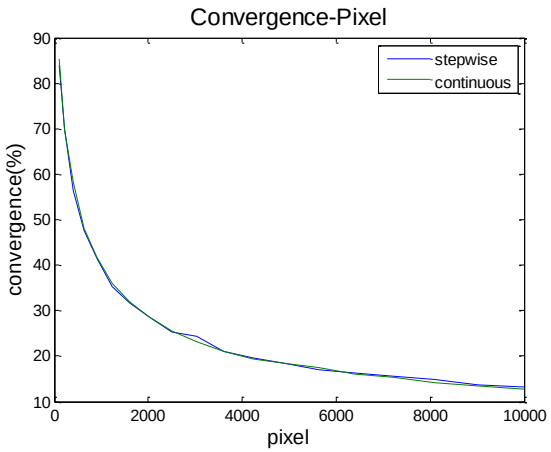

Figure 8: The relationship between convergence and pixel of the two algorithms with noise 5%.

4.3.4. Algorithms compared

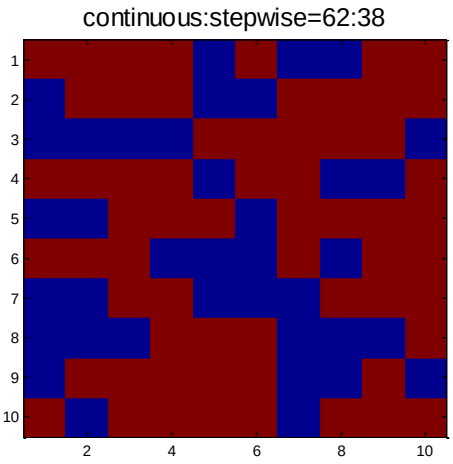

Figure 9: The two algorithms are compared. (Red: continuous, blue: stepwise)

Which algorithm is better of two will be discussed. We execute the two algorithms 100 times and record the result of them in fig.9. It can be seen the probability the continuous sequential algorithm is better than the stepwise one is approximately sixty percent. So, the level of resisting noise of the continuous one is better than the stepwise one.

5. Conclusions

The two algorithms in convergent figure are similitude. Advantages of them are steady and intuitive. And there are two disadvantages of them. First, the convergent speed is too slow to be used in a large number of pixels. Second drawback is the poor ability of resisting noise. In an ideal situation, the target intensity of these algorithms will converge to N. When a noise phase is added, the target intensity will not be enhanced in approximate twenty five percent.

In addition to the two algorithms, there are some algorithms can be tried such as genetic algorithm or partitioning algorithm.

Acknowledgements

This work is sponsored by Taiwaness Ministry of Science and Technology. Grant no: (102-2218-E-259 -005 – and 103-2221-E-259 -008 –) and Chinese Academy of Sciences Visiting Program for Taiwan Youth (Grant no. 2013TW2GB0002)

References

[1] *Waves and Imaging through Complex Media*, Softcover reprint of the original 1st ed. ed.: Kluwer, 2001.

[2] I. M. Vellekoop, and A. P. Mosk, "Focusing coherent light through opaque strongly scattering media," *Optics Letters*, vol. 32, no. 16, pp. 2309-2311, Aug, 2007.

[3] P. Whittaker, "Laser acupuncture: past, present, and future," *Lasers in Medical Science*, vol. 19, no. 2, pp. 69-80, Oct, 2004.

[4] M. Leavitt, G. Charles, E. Heyman, and D. Michaels, "HairMax LaserComb (R) Laser Phototherapy Device in the Treatment of Male Androgenetic Alopecia, A Randomized, Double-Blind, Sham Device-Controlled, Multicentre Trial," *Clinical Drug Investigation*, vol. 29, no. 5, pp. 283-292, 2009.

[5] H. Chung, T. H. Dai, S. K. Sharma, Y. Y. Huang, J. D. Carroll, and M. R. Hamblin, "The Nuts and Bolts of Low-level Laser (Light) Therapy," *Annals of Biomedical Engineering*, vol. 40, no. 2, pp. 516-533, Feb, 2012.

[6] I. M. Vellekoop, and A. P. Mosk, "Phase control algorithms for focusing light through turbid media," *Optics Communications*, vol. 281, no. 11, pp. 3071-3080, Jun, 2008.

Influence of optical gyrotropy on two-wave mixing at dynamic hologram in photorefractive crystal

Mariya Asalkhanova[1], Roman Romashko[1,2]

[1]Institute of Automation and Control Processes, FEB RAS, Vladivostok, Russian Federation
[2]School of Natural Sciences, Far-Eastern Federal University, Vladivostok, Russian Federation

In this paper the theoretical analyze of the gyrotropy influence on the efficiency of record of dynamic hologram in the photorefractive crystals (PRC) [1] is presented. The study is based on the modeling of two-wave mixing of a reference beam and a phase-modulated object beam in the cubic PRC (CdTe и BTO) [2, 3]. As estimation parameter of the interaction efficiency the object beam intensity modulation depth is used. Dependence of modulation depth on the interaction length is studied.

The object beam propagates along crystallographic axis [100] and has linear polarization tilted by 45 deg to incidence plane. The reference beam with circular polarization propagates along axis [001]. The intensity ratio of beams is equal 10. The wavelength of laser radiation for CdTe is 1064 nm, for $Bi_{12}TiO_{20}$ (BTO) – 633 nm. The specific optical rotation power of photorefractive crystals is 6.3 deg per mm which is artificially "switched on" in naturally optically non-active CdTe crystal and "switched off" in optically active BTO crystal.

Figures 1, 2 demonstrate the numerically calculated dependences of the object beam intensity modulation after interaction with the reference beam in PRC on crystal length.

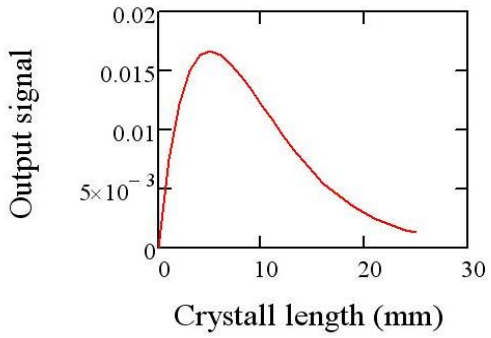

Fig.1. The dependence of the amplitude of intensity modulation in crystal CdTe without gyrotropy.

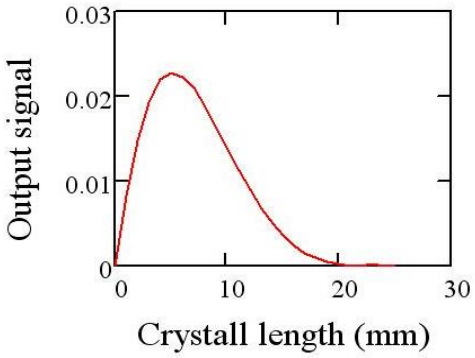

Fig.2. The dependence of the amplitude of intensity modulation in crystal CdTe with gyrotropy.

The output signal in CdTe crystal without gyrotropy reaches maximum (0.018) at the interaction length of 6 mm. If gyrotropy is "switched on" in this crystal the maximum of output signal observed at the same length becomes equal to 0.023. In the case of optically non-active BTO crystal the maximum of intensity modulation depth reaches 0.04 at interaction length equal 20 mm, while for gyrotropic PRC almost the same level of the output signal (0.037) is reached at 9 mm of crystal.

The obtained results can be used for design novel adaptive interferometry systems based on dynamic holograms recording in the PRC.

Acknowledgements

The research was funded by Russian Scientific Foundation (project 14-12-01122)

References

[1] V.V. Shepelevich, Y. Hu, A. Firsov, E. Shamonina, K.H. Ringhofer, Gain optimization with respect to the thickness of a sillenite crystal. Applied Physics B, 68(5), 923-929, 1999

[2] B.I. Sturman, E.V. Podivilov, K.H. Ringhofer, E. Shamonina, V.P. Kamenov, E. Nippolainen, A.A. Kamshilin, Theory of photorefractive vectorial wave coupling in cubic crystals, Physical Review E, 60(3), 3332, 1999

[3] R.V. Romashko, Y.N. Kulchin, A.A. Kamshilin, Optimal geometry for fast and efficient hologram recording in photorefractive crystal, Optical Review, 14(4), 176-179, 2007

Metamaterials, Plasmonics, Photonic Crystals and Complex Media

Non-reciprocal composite right/left-handed transmission line on ferrite YIG

Tao Zhou[1], Martine Le Berre[2], Francis Calmon[2],Guo hua Liu[1], Zhi hua Dong[1],Hua jie Ke[1], Zhiqun Cheng[1], Lingling Sun[1]

[1]Microelectronics CAD Center, Hangzhou Dianzi University, Hangzhou, China
[2]Université de Lyon, Institut des Nanotechnologies de Lyon, INLUMR5270, CNRS, INSA de Lyon, France
*corresponding author, E-mail: zhou.tao@hdu.edu.cn

Abstract

The modelling of composite right/left-handed transmission line and the corresponding theory have been studied. Then a parametric study of this components on ferrite has been driven. Both experimental and simulated scattering parameters are shown, and the corresponding propagation constants are given, that enables to identify the different frequency bands: left-handed band, right-handed band and bandgap. This non-reciprocal metamaterials has potential to be used in radio frequency integrated circuits.

1. Introduction

Recently, there has been a great deal of interest in the composite right/left-handed transmission lines (CRLH TLs) metamaterials (MTMs) [1-5], which introduced by Caloz and E leftheriades. The CRLH-TL can be realized by using traditional right-handed (RH) transmission lines loaded with series interdigital capacitors (IDCs) and shunt inductors. Many applications with these structures like couplers, impedance transformers, oscillator, innovative filters, antennas and others have been reported [6-11].

There are mainly two approaches for designing left-handed(LH) metamaterials, resonant approach and transmission line approach [1,3, 5]. For resonant approach, the LH metamaterials are based on cascaded unit-cell combining a SRR (negative permeability) with a metal wire (negative permittivity). Because SRR-based metamaterials have only LH properties around the resonance, it has several drawbacks such as narrow bandwidth, high lossy, and highly dispersive [3].

For engineering applications, to overcome the weaknesses of resonant approach based LH metamaterials, a non resonant LH metamaterial can be realized by transmission line approach [1], which are based on the dual configuration of a conventional RH transmission line. In this work, the theory of transmission line approach of metamaterials will be introduced first. Then, the coplanar CRLH MTMs on YIG with interdigital capacitors, and the CRLH MTMs on YIG with or without applied fields will be studied.

2. Transmission line approach of CRLH MTMs

In reality, a purely LH TL does not exist because of unavoidable RH parasitic series inductances and shunt capacitances effects, will unavoidably occur due to currents flowing in the conductors and voltage gradients developing between the conductors and the ground planes, therefore, the concept of CRLH MTMs, introduced by Caloz et al, present the most general form of a LH TL. The CRLH consists of a series inductance, series capacitance, shunt inductance and shunt capacitance. The Equivalent circuit of a loss-less CRLH TL is shown in Figure 1.

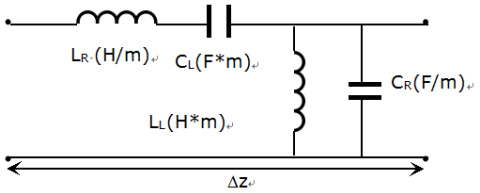

Figure 1: Equivalent circuit of the CRLH TL.

3. CRLH on ferrite YIG with applied field

A CRLH MTM on YIG substrate is shown in Figure 2. the MTM is integrated with interdigital capacitors. The equivalent circuit of the CRLH MTM on YIG substrate is shown in Figure 3. It's composed of CPW on YIG substrate, shunt capacitors and shunt inductors, series capacitors and series inductors.

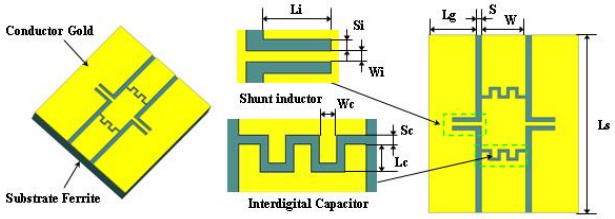

Figure 2: CRLH MTM on ferrite YIG.

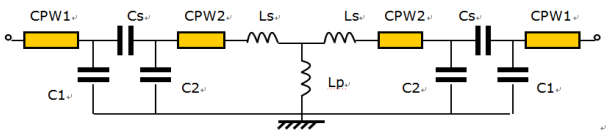

Figure 3: Equivalent circuit of the CRLH on YIG.

The CRLH MTM on ferrite YIG with applied field 140 kA/m will be studied. For the samples with 1-unit cell under field, the gyroresonance and frequencies slightly higher than the gyroresonance (6-9 GHz under applied field 140 kA/m), where the tensor of permeability has negative terms. As a consequence, the bandwidth of bandgap decreases with field compared to without field. The nonreciprocal effect due to the negative permeability terms can be observed whether in the left-handed band, in the bandgap or in the crystal band depending on the sample geometry.

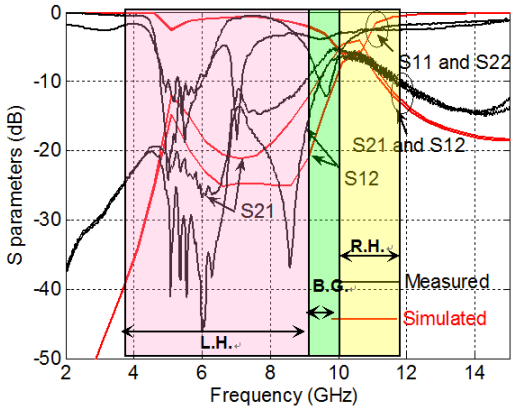

Figure 4: Measured and simulated S parameters of CRLH MTM on YIG with applied field 140 kA/m.

Figure 4 shows that, the gyroresonance frequency is around 5.5 GHz, the difference between S_{21} and S_{12} is about 8 dB around 6 GHz, and 22dB around 8.2 GHz. Figure 5 indicates that, for 1-unit CRLH MTM on YIG with applied field 140 kA/m, unit length 4195 µm, IDC finger length 75µm, inductor length 650 µm, the difference between $\beta^{+}d$ and $\beta^{-}d$ is about 2 rad around 7 GHz, a LH band is obtained at frequency band 4- 9GHz.

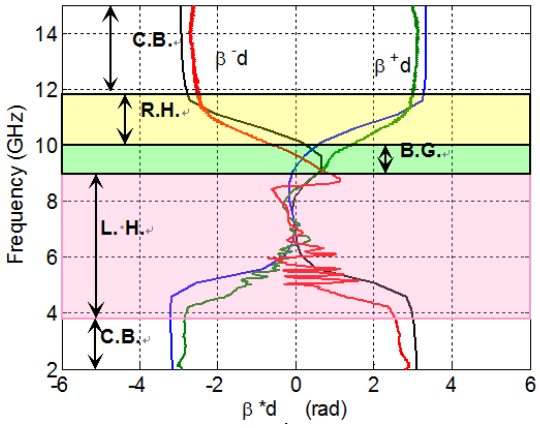

Figure 5: Propagation constants of CRLH MTM on YIG with applied field 140 kA/m.

4. Conclusions

The non-reciprocal CRLH transmission line metamaterial on ferrite YIG has been studied. Both experimental and simulated scattering parameters are shown, and the corresponding propagation constants are given. On YIG substrate with field, there is a nonreciprocal behaviour, due to the anisotropy of the permeability tensor of ferrite. Depending on the geometry of the components, the nonreciprocity due to the negative permeability terms is located whether in the left-handed band, in the bandgap or in the crystal band. Just above the gyroresonance frequency, the terms of permeability tensor are negative. As a consequence, the resonance frequency which is the closest to the gyroresonance frequency, but higher to it, is shifted to higher frequency compared to YIG without applied field.

References

[1] A.-B. Zhang, C.-D. Kim, E. Yamada, F.G. Smith, The numerical investigation on the turbulent heat transfer, *Int. J. Heat Mass Transfer* 12: 345−365, 2010.

[2] S.V. Patankar, *Numerical Heat Transfer and Fluid Flow*, Hemisphere Publishers, New York, 1980.

[3] W.M. Kays, M.E. Crawford, *Heat transfer*, Wiley, New York, pp.256-258, 1990.

[4] Y. Kawaguchi, T. Tsukahara, M. Motozawa, Experimental and numerical investigations of turbulent drag reduction phenomena by additives, *Proc. ASCHT09*, Jeju, Korea, pp. 23−32, 2009.

[1] C. Caloz, T. Itoh, *Electromagnetic metamaterials: transmission line theory and microwave applications,* Wiley-IEEE Press, 2005.

[2] G. V. Eleftheriades, A. K. Iyer, P. C. Kremer, Planar negative refractive index media using periodically LC loaded transmission lines, *IEEE Transactions on Microwave Theory and Techniques*, Volume 50, 12:2702 - 2712, 2002.

[3] A.Lai, C.Caloz , T.Itoh, "Composite right/left-handed transmission line metamaterials", *IEEE microwave magazine*,34 - 50, 2004..

[4] A. Grbic, G. V. Eleftheriades, Overcoming the diffraction limit with a planar left-handed transmission-line lens, *Phys. Rev. Lett.*, 92, 117403, 2004 .

[5] T. J.Cui, F.Ma H, R.Liu, B.Zhao, Q.Cheng, J. Y.Chin, "A symmetrical circuit model describing all kinds of circuit metamaterials", *Progress In Electromagnetics Research B*, 5:63-76, 2008.

[6] D. R.Smith, J. B.Pendry, "Wiltshire M. C. K. Metamaterials and negative refractive index", *Science*, 305: pp. 788-792 No. 5685, 2004.

[7] G.V.Eleftheriades, A.K.Iyer, P.C.Kremer, "Planar negative refractive index media using periodically L-C loaded transmission lines", *IEEE Transactions on microwave theory and techniques*, Vol. 50, 12:2702-2712, 2002. .

[8] Y. S. Wu, X.Q. Lin, A compact tunable bandpass filter with high selectivity and low insertion loss using novel CRLH cell, *Journal of Electromagnetic Waves and Applications*, Volume 27, Issue 12, 2013.

[9] C.A.Allen, K.M.K.H.Leong, T.Itoh, "Dual-mode composite-right/left-handed transmission line ring resonator", *Electronics Letters*, Vol. 42, 2:96-97 2006.

[10] Y. Y. Peng, X. P. Yu, J. M. Gu, W. M. Lim, An area-efficient CRLH (composite right/left-handed)-TL approach to the design of rotary traveling-wave oscillator, *Microwave and Wireless Components Letters, IEEE*, Volume 23, Issue 10, 2013.

[11] C. Wang, Y. Shi, S. Liu, Ultra-wideband bandpass filter using simplified dual composite right/left-handed transmission line structure, *Microwave and Optical Technology Letters*, Volume 55, 5:1165−1167, 2013 .

AES 2014, Advanced Electromagnetic Symposium
7-10 December 2014, Hangzhou

Otto configuration for the TM and TE surface plasmon detection in doped graphene at terahertz frequencies

F. Ramos-Mendieta,[1] J. Gaspar-Armenta[1] and M. Palomino-Ovando[2]

[1]Departamento de Investigación en Física, Universidad de Sonora
Apartado Postal 5-088, Hermosillo, Sonora, 83190 México
[2]Facultad de Ciencias Físico-Matemáticas, Benemérita Universidad Autónoma de Puebla
Apartado Postal 1152, Puebla, Puebla, 72000 México
framos@cifus.uson.mx

Abstract

A numerical study of the surface plasmon detection in free standing doped graphene by use of the Attenuated Total Reflectance technique is presented. For TM polarization, a surface plasmon resonance and two excitations of perfect absorption are reported at 5 THz. TE surface plasmons, which can exist only in a small frequency range, are also excitable by this technique. It is demonstrated for both polarizations that the effects of wave interference can produce total absorption in the Otto structure with graphene as component. For graphene doping levels as high as 0.8 eV and 1.2 eV have been used for calculations.

1. Introduction

During the past few years doped graphene has attracted a great deal of research interest. The reason is the expectation of graphene as a promising new material for opto-electronic applications such as photovoltaic devices, optical sensing and metamaterials.[1-2] In particular the extraordinary optical properties of graphene are related to its complex dynamic conductivity with interband and intraband contributions.[3] The interesting point is that, depending on the frequency and doping level, the imaginary part of this conductivity can take positive and negative values allowing the occurrence of transverse magnetic (TM) and transverse electric (TE) surface plasmons, respectively.[4,5]

Surface plasmons (SPs) are plasma excitations that propagate along the surface of a metallic slabs or along the graphene sheet. They are accompanied by evanescent fields that decay exponentially in the perpendicular direction to the surface. In doped graphene TM SPs have been widely studied and experimentally detected.[6-8] This is not the case of TE SPs for which only a few theoretical reports have been published.[9] It is convenient to highlight the physical difference between TM and TE SPs. While TM SPs are excitations of charge density that oscillates in the perpendicular direction to the graphene sheet, the TE SPs are modes not accompanied by surface charge. They are localized currents that oscillate in the graphene plane on the perpendicular direction to the plasmon wave vector. Another important difference is the dispersion relation. For the TM polarization the function $\omega(k_x)$ behaves in similar way to that of the ordinary plasmons in metals. However, the dispersion relation of TE SPs in graphene is very special; it practically overlays the light-line of the host medium. This line separates the frequency regions where the wave equation supports solutions of oscillatory or evanescent character.

In this paper I present a theoretical study of the SP detection in doped free-standing graphene by use of the prism-based Otto configuration. We shall demonstrate that once the TM SP is excited it is stable within a short range of variations of d (d is the air gap between the prism and the graphene sheet) but in general the angular position and frequency of the reflection dips are strongly dependent on this parameter. The conditions for complete absorption are discussed. For the TE polarization we present only preliminary results.

2. Basic Equations

For calculations the graphene conductivity derived within the random-phase approximation at zero temperature is used.[10] It is written as

$$\sigma(\omega)=\frac{i}{\pi}\frac{e^2}{\hbar}\left[\frac{\mu}{\hbar(\omega+i\tau^{-1})}-\frac{1}{4}\ln\left(\frac{2\mu+\hbar(\omega+i\tau^{-1})}{2\mu-\hbar(\omega+i\tau^{-1})}\right)\right], \quad (1)$$

where τ is the phenomenological relaxation time, e is the charge of an electron, $\hbar$ is the reduced Planck's constant and μ is the chemical potential. The first (second) term in this equation corresponds to the intraband (interband) contribution. For high doped graphene, in the limit of low energies ($\hbar\omega << \mu$) Eq. (1) reduces to the Drude-like formula

$$\sigma_{\text{intra}}=i\frac{e^2\mu}{\pi\hbar^2(\omega+i\tau^{-1})}. \quad (2)$$

The relaxation time τ takes into account losses due to electron-impurity, electron-defect, and electron-phonon scattering. It takes the value $\tau = 6.4\times10^{-13}$s when the electron mobility and doping level are μ_0 = 10000 cm^2/Vs and μ = 0.64 eV, respectively. The results presented in this papers were obtained by use of Eq. (2).

In order to obtain the reflection spectra I resolve the system of coupled equations that results from the ordinary boundary conditions that the fields satisfy at each interface of the Otto system:

$$n_1/n_2/\text{graphene}/n_3.$$

By considering the graphene as a zero thickness layer of conductivity σ one of the boundary conditions at the n_1/graphene/n_2 interface for TM waves of fields $\vec{E} = (E_x, 0, E_z)$ and $\vec{H} = (0, H_y, 0)$, leads to the next relation between the magnetic fields on both sides of the graphene sheet

$$H_{2y} - H_{3y} = \sigma E_{2x}. \tag{3}$$

A similar equation for TE polarization is obtained.

From the system of 4 coupled equations written for the Otto system it is easy to obtain the reflection coefficient to obtain the attenuated TM reflectance. In terms of the partial reflection coefficients, one at the interface n_1/n_2,

$$r_{12} = \frac{q_{z2}\varepsilon_{pr} - q_{zp}}{q_{z2}\varepsilon_{pr} + q_{zp}}, \tag{4}$$

and the other one at the interface including graphene

$$r_{23} = \frac{q_{zt} - q_{z2}\varepsilon_{tr} - \dfrac{q_{z2}q_{zt}\sigma}{\varepsilon_0\omega}}{q_{zt} + q_{z2}\varepsilon_{tr} + \dfrac{q_{z2}q_{zt}\sigma}{\varepsilon_0\omega}}, \tag{5}$$

the reflection of the total system is written as

$$r = -\frac{r_{12} + r_{23}e^{2i\varphi}}{1 + r_{12}r_{23}e^{2i\varphi}}, \tag{6}$$

where $\varepsilon_p = \varepsilon_0\varepsilon_{pr}$ and $\varepsilon_t = \varepsilon_0\varepsilon_{tr}$, $q_z = \sqrt{q_0^2 - q_x^2}$ and $\varphi = q_{z2}d$, with d the thickness of the layer n_2. Again, similar analysis can be made for TE waves.

3. Results.

Figure 1 shows the dispersion relation of the TM SPs and two series of reflection dips corresponding to the excitation of two SPs by the ATR method. The refractive index of the prism is n_p = 4. For the first case, the reflection minima maintain the angle of incidence $\theta_i \sim$ 30.5°; they were obtained when the separation prism-graphene changes from d = 15 μm to d = 25 μm (this is almost 10 μm without significant angular variation). On the other hand, less stable is the case for μ = 1.2 eV at f = 0.8 THz where the positions of the reflection minima remain at $\theta_i \sim$ 32.2° in a shorter separation range, from d = 13 μm to d = 17 μm, approximately.

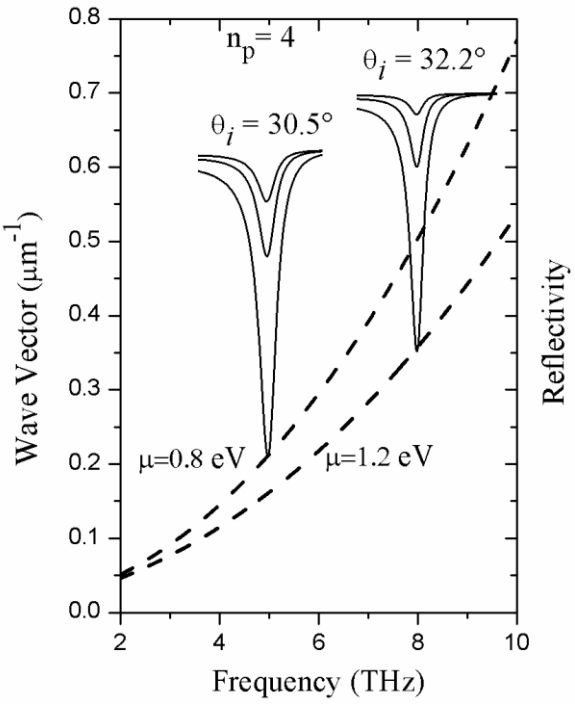

Figure 1. Dispersion relation and attenuated reflectivity of TM SPs. The reflectivity is graphed in arbitrary scale with the deepest dip resting on the corresponding mode in the dispersion curve. The collision time is τ = 1 ps. For μ = 0.8 eV the three reflectivity profiles are for d = 15, 18 and 25 μm and for μ = 1.2 eV the separations are d = 13, 15 and 17 μm. The shorter the separation the deeper the reflection dip.

The intrinsic interference effects of the Otto configuration generate the conditions for the total absorption phenomenon in which graphene dissipates completely the incident energy. Figure 2 presents two peaks of zero reflection. They occur at the angles of incidence $\theta_2 \sim$ 34.8° and $\theta_3 \sim$ 78°. The first minimum at $\theta_1 \sim$ 30.5° is associated to the SP excitation satisfying the dispersion relation. The other two dips of

total absorption result from a complex mechanism involving a) the SP resonance, b) interference effects and c) the graphene losses.

For the case of SPs of TE polarization I have found reflection minima in a very short window for the angle of incidence ($\Delta\theta_i < 10^{-3}$ degrees) beyond the critical angle $\theta_c = \sin^{-1}(n_2/n_1)$. The reflection dips can be associated to the SP excitation and they are strongly dependent on the prism-graphene separation. For TE polarization graphene with doped levels μ = 0.2 eV and μ = 0.3 eV has been used in calculations.

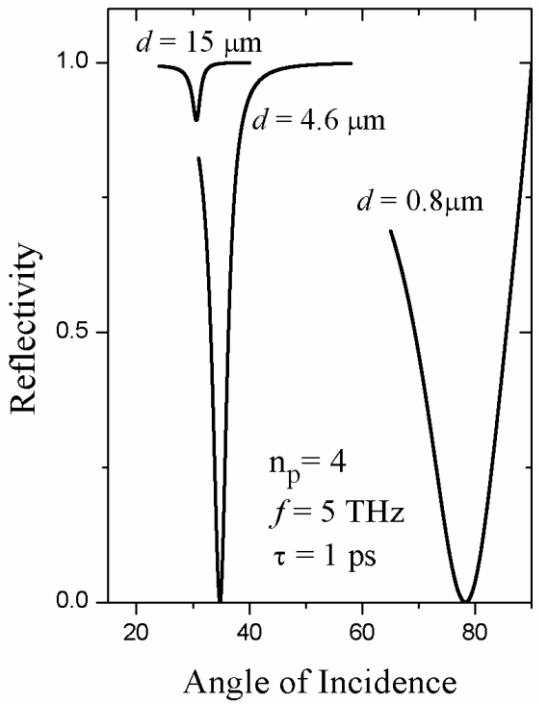

Figure 2. Attenuated reflectivity due to the SP excitation and perfect absorption of TM waves. The chemical potential is μ = 0.8 eV. The half-width of the reflection dip at θ_i~78° is twelve times the half-width of the dip at θ_i ~34.8°. Significant wave guidance is not expected at θ_i~78°.

4. Conclusions

The Attenuated Total Reflectance is a technique useful to detect SPs in doped graphene. This paper presents numerical evidences of photon-plasmon coupling for waves of TM polarization. Structural conditions to obtain total absorption are also discussed. In particular two excitations of perfect absorption were found for these waves. On the other hand, TE SPs were also studied. They are very special modes that can be detected in an ultra-tiny angular region beyond the critical angle where evanescent fields are already available.

Acknowledgements

This work was supported by SESIC México, PROMEP, Grant FOFM-2008.

References

[1] F. Schedin, E. Lidorikis, A. Lombardo, V. G. Kravets, A. K. Geim, A. N. Grigorenko, K. S. Novoselov and A. C. Ferrari, *ACS Nano* **4**, 5617 (2010).

[2] N. Papasimakis, Z. Luo, Z. X. Shen, F. De Angelis, E. Di Fabrizio, A. E. Nikolenko and N. I. Zheludev, *Opt. Express* **18**, 8353 (2010).

[3] G. W. Hanson, *J. Appl. Phys.* **103**, 064302 (2008).

[4] O. Vafek, *Phys. Rev. Lett.* **97**, 266406 (2006).

[5] M. Jablan, H. Buljan and M. Soljacic, *Phys. Rev. B* **80**, 245435 (2009).

[6]L. Ju, B. Geng, J. Horng, C. Girit, M. Martin, Z. Hao, H. A. Bechtel, X. Liang, A. Zettl, Y. R. Shen and F. Wang, *Nat. Nanotechnol.* **6**, 630 (2011).

[7]Z. Fei, G. O. Andreev, W. Bao, L. M. Zhang, A. S. McLeod, C. Wang, M. K. Stewart, Z. Zhao, G. Dominguez, M. Thiemens, M. M. Fogler, M. J. Tauber, A. H. Castro-Nieto, C. N. Lau, F. Keilmann and D. N. Basov, *Nano Lett.* **11**, 4701 (2011).

[8]Z. Fei, A. S. Rodin, G. O. Andreev, W. Bao, A. S. McLeod, M. Wagner, L. M. Zhang, Z. Zhao, M. Thiemens, G. Dominguez, M. M. Fogler, A. H. Castro-Nieto, C. N. Lau, F. Keilmann and D. N. Basov, *Nature* **487**, 82 (2012).

[9] S. A. Mikhailov and K. Ziegler, *Phys. Rev. Lett.* **99**, 016803 (2007).

[10] B. Wunsch, T. Tauber, F. Sols and F. Guinea, *New J. Phys.* **8**, 318 (2006).

Preparation and characterization of zinc oxide nanoparticles

Kitsakorn Locharoenrat

Department of Physics, Faculty of Science, King Mongkut's Institute of Technology Ladkrabang, Bangkok 10520, Thailand
T: +66-2329-8000. Fax: +66-2329-8412.
klkitsak@kmitl.ac.th

Abstract

Zinc oxide nanoparticles are prepared using the pulsed laser ablation (Nd:YAG laser at a central wavelength of 1064 nm with the pulse energy of 100 milli-joule) of the zinc metal plate immersed in a solution of sodium dodecyl sulfate at the ambient temperature. The absorbance of the produced nanoparticles with the laser fluence dependent shows the single and sharp peak around 375 nm, indicating that the nanoparticles have a narrow size (50 – 55 nm) with almost spherical shape.

1. Introduction

Recently, nanomaterials are important for many applications in different areas, such as electronic & optic nanodevices, biosensor, solar cells, and chemical catalysts, partly due to their size-dependent physical and chemical properties [1-6]. For example, the broad range of optically active compound semiconductor nanomaterials is interesting served as the building blocks for miniaturized photonic and optoelectronic nanodevices. Efforts will be made to assemble the nanostructures into useful architectures and practical nanodevices. Furthermore, one quite promising candidate is nanowire photovoltaics. Organic/inorganic photovoltaic nanodevices are subject of intense research for low cost solar energy conversion. However such nanodevices are restricted by in efficient charge transport. This is because highly discontinuous topologies of donor acceptor interface. Substituting the disordered inorganic phase with an aligned nanowires array is then suggested to improve charge collection and improve the power conversion efficiencies.

So far, second-harmonic generation (SHG) has been studied in the past decades as it is used to optically probe the electronic properties of nanoparticles when one varied dimension, geometry, constituent, or even the spatial organization [4-7]. The aims of the nanoparticles studies have varied from determining the electron dephasing in order to gain insight into a contribution of surface enhanced Raman scattering and measuring a potential for plasmonic applications such as in the optical switching systems. It is taken for granted that symmetry do not allow a generation of second-harmonic beam in the centrosymmetric nanoparticle systems. Even as the asymmetric nanoparticles are arranged so that the overall array has inversion symmetry, SHG is completely inhibited along the illumination direction. This quenching of SHG along such direction is true for both surface SHG and bulk SHG contributions. With this reason, the potential of SHG to probe the electron dynamics in metal nanopartilces has been discounted. Recently, it has been suggested that organizing the asymmetric nanoparticles in a diffraction grating will offer a spatial separation of nanoparticle-generated SH light from both the incident fundamental beam and the substrate-generated SH light. However, asymmetric nanoparticles are not strictly necessary. Then, there are extensive researches on the development of new approaches to produce such nano-sized materials.

Nanomaterials including metallic nanoparticles have been synthesized using traditional methods, such as physical and chemical methods [8-20]. For instance, self-assembly is an attractive alternative to nanolithography partly due to a high throughput and low cost. Self assembled nanostructures are expected to show intrinsic bistability in the transport characteristics that will be exploited to realize a non-volatile quantum dot memory also signatures of Coulomb blockade and Coulomb staircase (at room temperature) in quantum dots and quantum wires holding out the promise that these kind structures is suggested to find applications in single-electron-transistors including the other novel nanodevices. Nevertheless, there are some drawbacks, such as such as technical simplicity, low production yields, and contamination by a chemical reagent.

With a benefit of the pulsed-laser more recently, we currently report on a formation of the zinc oxide nanoparticles using the laser ablation technique. We have suggested that the pulsed laser ablation in the solution media will be an alternative for production of the size-selected nanoparticles. These nanoparticles are expected to be a potential candidate for photocatayst and semiconductor nanomaterials. Also, the second-harmonic generation may be used to study the coherent nonlinear optical responses in symmetric and the asymmetric for metallic nanoparticles.

2. Experimental

A zinc metal plate (purity of 99.99%) was placed in the quartz cell filled with 5 ml, 1 milli-molar of an aqueous solution of the sodium dodecyl sulfate as a surfactant at the room temperature (Fig. 1). The laser light with a fundamental photon energy of 1.17 eV was originated by a Nd:YAG laser with the pulse energy set at 100 milli-joule per pulse. The beam was focused onto the surface of the target with 2 – 3 mm in diameter of spot size. The liquid thickness was 1 mm beyond the target surface. The solution was stirred slowly during the ablation. The ablation times were varied from 10 to 20 min. The big particles and the free sodium dodecyl sulfate particles exisitng as the residues were finally removed from the solution using a centrifugal pump.

The optical properties and morphology of the prepared zinc oxide nanoparticles were investigated as follows. For the transmission electron microscope (TEM) observation, a drop of the solution of the zinc oxide nanoparticles was kept onto the copper grid and left in a vacuum oven at 50 ^{0}C for 6 h. The produced specimen was then cleaned by distilled water in order to remove the free sodium dodecyl sulfate particles and put onto a sample stage of TEM. On the other hand, the crystal structure of the zinc phase was examined by X-ray diffraction (XRD) using the CuKα radiation. Finally, the absorption spectrum of the prepared solutions was recorded by UV-Visible spectrophotometer in wavelength of 400 – 1100 nm.

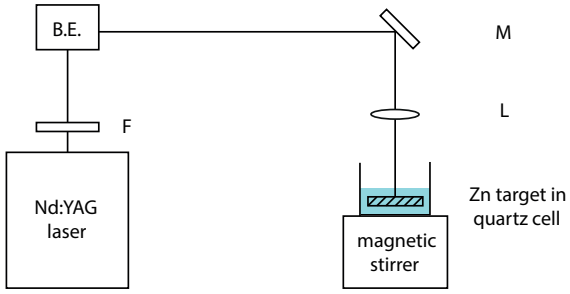

Figure 1: Block diagram of the experimental setup for producing the zinc oxide nanoparticles. The B.E., F, M, and L stand for beam elevator, filter, mirror, and lens, respectively.

3. Results & Discussion

The TEM image at a high magnification in Fig. 2 displays the uniform zinc oxide nanoparticles in the spherical shape.

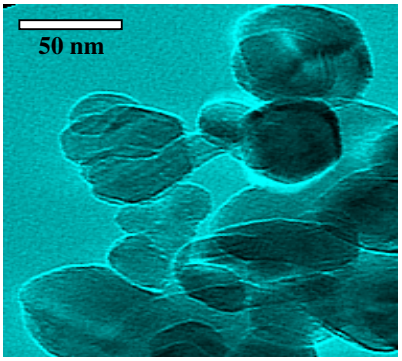

Figure 2: TEM image of the zinc oxide nanoparticles at a high magnification.

Distributions of the zinc oxide nanoparticles are estimated and shown in Fig. 3. The average diameter of the zinc oxide nanoparticles is estimated to be about 50 - 55 nm.

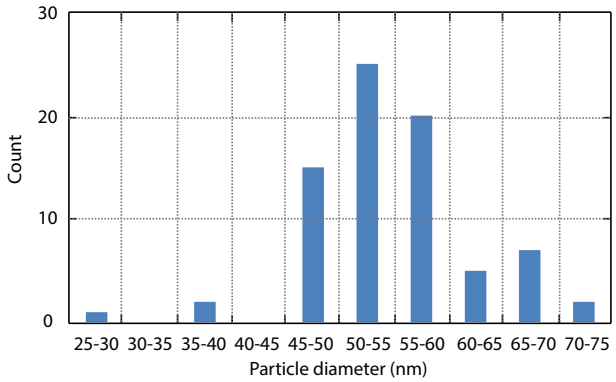

Figure 3: Distribution diagram of the zinc oxide nanoparticles.

The X-ray diffraction (XRD) pattern (not shown) consists of a dominant peak at $2\theta = 35^0$. This confirms a characteristic of the hexagonal phase zinc oxide structures.

Figure 4 shows the typical optical absorption spectra of the zinc oxide nanoparticles with the different ablation times of 10, 15, and 20 min.

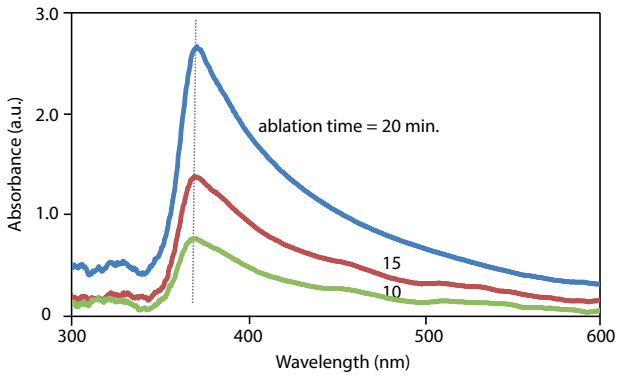

Figure 4: Measured absorption spectra of the zinc oxide nanoparticles as with various ablation times.

The spectra have a sharp peak of absorbance of all nanoparticles centered at 375 nm, corresponding to a band gap of zinc oxide (3.3 eV) [21-22]. Because the zinc oxide nanoparticles prepared in the present conditions have nearly spherical shapes as seen in Fig. 2, the polarization dependence of the resonance at 3.3 eV is also not observable in Fig. 4. Moreover, the prominent single peak is consistent with the fact that the nanoparticles present in the solution are almost spherical in shape. On the other hand, the band gaps are independent of the ablation time. This identical band gap irrespective of the ablation time indicates that the sizes of the zinc oxide nanoparticles are barely affected by the ablation time. By contrast, the absorbance of the zinc oxide nanoparticles tends to increase with the ablation time. Namely, the absorbance of 0.8, 1.5, and 2.8 corresponds to the ablation time of 10, 15, and 20 min. Since the sizes of the zinc oxide nanoparticles are independent of the ablation time, the change in the absorbance indicates that the density of the nanoparticles increases with the ablation time. These spectra are suggested that the zinc oxide nanoparticles are potentially useful for photocatalyst and semiconductor nanomaterials.

Now we discuss one possible mechanism of a generation of the zinc oxide nanoparticles in the liquid environment. When the laser pulse with a high energy hits on the surface of the zinc metal plate, it vaporizes the zinc atoms, reacting with the dissolved oxygen in the aqueous solution of sodium dodecyl sulfate containing water in order to form the zinc oxide nanoparticles. Large numbers of the zinc oxide nanoparticles arrange themselves in a specific geometry and they are covered by a layer of sodium dodecyl sulfate in order to prevent them from further coalescence and agglomeration and to limit the growth of the particles. This offers novel methods to produce the metallic oxide nanoparticles by further adding the amount of dissolved oxygen into the solution. To avoid the dissolved oxygen, one may fill the inert gas, such as argon into the solution in order to form the pure metallic nanoparticles.

4. Conclusions

We have produced the zinc oxide nanoparticles in the sodium dodecyl sulfate solution as a surfactant using the laser ablation technique at the room temperature. The produced zinc oxide nanoparticles have the spherical shapes. The typical diameters of the zinc oxide nanoparticles are about 50 - 55 nm. The absorbance of the zinc oxide nanoparticles increases with the laser fluence. The single sharp peak of the absorbance centered at 375 nm reveals that the nanparticles have a narrow size with nearly spherical shape.

Acknowledgement

This work is supported by King Mongkut's Institute of Technology Ladkrabang, Bangkok 10520, Thailand [grant number KREF 015603].

References

[1] G. Guerrero, J.G. Alauzun, M. Granier, D. Laurencin, P.H. Mutin, Phosphonate coupling molecules for the control of surface/interface properties and the synthesis of nanomaterials, *Dalton Trans.* 42:12569–12585, 2013.

[2] K. Janani, C.P. Kala, R.M. Hariharan, S. Sivasathya, D.J. Thiruvadigal, Electron transport of zigzag graphene nanoribbon based biosensor - A future perspective towards biosensor and biomedical applications, *Austin J. Nanomed. Nanotechnol*. 2: 1–5, 2014.

[3] C.-P. Li, S. Fan, C. Yin, N. Zhang, S. Du, H. Zhao, Carboxylic silica nanosheet–platinum nanoparticle modified glass carbon electrodes for pesticide detection, *Anal. Methods* 6:1914–1921, 2014.

[4] Y. Ogata, G. Mizutani, Control of Cross-sections and optical nonlinearity of Pt nanowires and the roughness effect, *Phys. Research Intl.* 2012: 969835/1-11, 2012.

[5] T. Iwai, G. Mizutani, Optical second harmonic spectroscopy of reconstructed Au(100) and (111) surfaces, *Phys. Rev. B* 72: 233406-1-4, 2005.

[6] K. Locharoenrat, A. Sugawara, S. Takase, H. Sano, G. Mizutani, Shadow deposition of copper nanowires on the faceted NaCl(110) template, *Surf. Sci*. 601: 4449-4453, 2007.

[7] N.A. Tuan, G. Mizutani, Metal-interface second harmonic generation from Pt/Cu bimetallic nanowire arrays on NaCl(110) faceted templates, *e-J. Surf. Sci. Nanotech.* 7: 831-5, 2009.

[8] S.E. Lohse, J.A. Dahl, J.E. Hutchison, Direct synthesis of large water-soluble functionalized gold nanoparticles using bunte salts as ligand precursors, *Langmuir* 26:7504–7511, 2010.

[9] S. Iravani, Green synthesis of metal nanoparticles using plants, *Green Chem*. 13: 2638–2650, 2011.

[10] C. Gutierrez-Wing, J.J. Velazquez-Salazar, M. Jose-Yacaman, Procedures for the synthesis and capping of metal nanoparticles, *Methods Mol. Biol.* 906: 3–19, 2012.

[11] S.Y. Li, M. Wang, Branched metal nanoparticles: A review of wet-chemical synthesis and biomedical applications, *Nano Life* 2: 1230002–23, 2012.

[12] S. Sinha, S.K. Chatterjee, J. Ghosh, A.K. Meikap, Semiconducting selenium nanoparticles: Structural, electrical characterization, and formation of a back-to-back Schottky diode device, *J. Appl. Phys*. 113: 1237041–8, 2013.

[13] H. Kawasaki, Surfactant-free solution-based synthesis of metallic nanoparticles toward efficient use of the nanoparticles' surfaces and their application in catalysis and chemo-/biosensing, *Nanotech. Rev*. 2: 5–25, 2013.

[14] M.A. Mahmoud , D. O'Neil, M.A. El-Sayed, Hollow and solid metallic nanoparticles in sensing and in nanocatalysis, *Chem. Mater.* 26: 44–58, 2014.

[15] J. Xu, J. Sun, Y. Wang, J. Sheng, F. Wang, M. Sun, Application of iron magnetic nanoparticles in protein immobilization, *Molecules* 19: 11465-11486, 2014.

[16] B. Swathy, A review on metallic silver nanoparticles, *IOSR J. Pharm.* 4: 38-44, 2014.

[17] C.N.R. Rao, S.R.C. Vivekchand, K. Biswas, A. Govindaraj, Synthesis of inorganic nanomaterials, *Dalton Trans*. 11: 3728–3749, 2007.

[18] G.M. Herrera, A.C. Padilla, S.P. Hernandez-Rivera, Surface enhanced raman scattering (SERS) studies of gold and silver nanoparticles prepared by laser ablation, *Nanomaterials* 3: 158-172, 2013.

[19] A.M. Atta, H.A. Al-Lohedan, A.O. Ezzat, Synthesis of silver nanoparticles by green method stabilized to synthetic human stomach fluid, *Molecules* 19: 6737-6753, 2014.

[20] P. Saravanan, R. Gopalan, V. Chandrasekaran, Synthesis and characterisation of nanomaterials, *Defence Sci. J.* 58: 504-516, 2008.

[21] C. Jagadish, S. Pearton, *Zinc Oxide Bulk, Thin Films and Nanostructures: Processing, Properties and Applications*, Elsevier, Amsterdam, 2007.

[22] X.W. Sun, Y. Yang**,** *ZnO Nanostructures and Their Applications*, Pan Stanford, Singapore, 2012.

Nano-beam cavity design with randomly located reflectors

Melih G. Can[1,*], Bilgehan B. Oner[1], Hamza Kurt[1]

[1]Nanophotonics Research Laboratory, Department of Electrical and Electronics Engineering,
TOBB University of Economics and Technology, Ankara, Turkey
*corresponding author, E-mail: m.can@etu.edu.tr

Abstract

In this study, nano-beam cavity design is investigated by incorporating randomly placed holes acting as reflectors around the defect region. The cavity structure is symmetric; the two opposite sides the defect areas are taken the same in order to keep the interference effect reciprocal. Various cases such as number of holes and locations of them are systematically studied. Due to variations of the lengths and related effective indices the reflectivity value varies. The structural parameters affecting the reflectivity parameter yields unique trends. The design is implemented by finite-difference time-domain method and results are interpreted by means of ABCD matrix technique. The leading mechanisms governing high-quality factor are explored. The work may lead new way to create and implement high Q defect structures with compact and unique configuration.

1. Introduction and Design

Photonic crystal (PC) nanobeam cavities and waveguides have recently become one of the extensively studied one dimensional counterpart of multi-dimensional photonic structures [1-5]. High-quality factors are usually desired in many applications such as optical sensors, modulators, switches, opto-mechanics and nonlinear optics. As a result, integrated nature of nanobeam cavities with ultra-high quality factors make them valuable photonic platform for these different applications.

Periodically located 1D PC is basically an optical filter, i.e., pass band and band gaps appear in the transmission spectrum. Inserting a defect region by means of breaking the periodicity generates a cavity whose resonances appear inside the photonic band gap. Aperiodic designs such as quasi-periodic, Fibonacci or Cantor dielectric structures are attractive media to investigate the properties of photon propagation through the structures as well [6, 7]. In the present study we generate randomly located 1D PC structure with judicious manipulation of the above-mentioned simple nano-beam cavity design.

In Figure 1, a conventional cavity and proposed random cavity design for a particular case are shown. The homogenous waveguide is composed on high refractive index material (Silicon, n=3.46) and the white circular regions correspond to air holes with constant radii of 0.30a. In the numerical simulations, a is the unit distance. The width of the waveguide is 1.0a. For regular case where central holes are separated by 1.20a distance, air holes are periodically placed with a separation of a. Finite Difference Time Domain method is utilized for simulations, and related computational screen resolution is chosen as *20* that gives 0.05a step value for following iteration in the numerical analyses [8].

For a random design, for every iteration air holes are shifted by 0.10a right or left side with respect to the previous position and we avoid overlapping of air holes. All possible scenarios are considered. One side of the structure is divided into different parts depending on the number of holes.

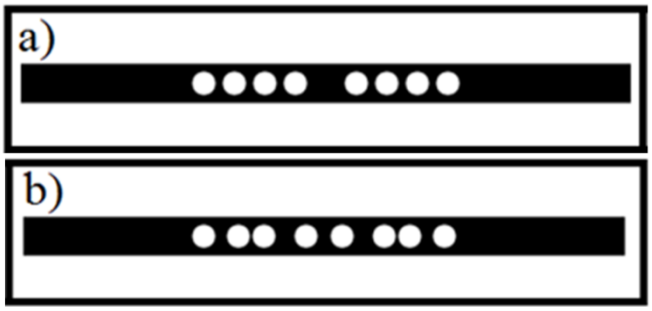

Figure 1. (a) Conventional nano-beam cavity structure with defect region at the middle of the slab and (b) randomly located holes generating a cavity structure.

Effective medium theory is used to calculate effective indices of the each part for every different design, because of the fact that cavities resonance wavelength are larger than the periodicity of photonic lattice, a. Symbolizing refractive indices of the air holes and dielectric slab with n_a and n_s respectively, the effective medium theory gives us :

$$n_{eff}^2 = \frac{n_a^2(1+f)+n_s^2(1-f)}{n_a^2(1-f)+n_s^2(1+f)} n_s^2 . \qquad (1)$$

In Eq. 1, f denotes filling fraction of the medium while silicon waveguide is the host medium.

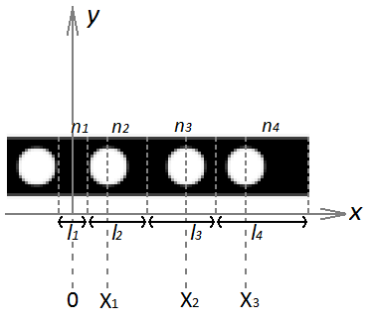

Figure 2. An example of 1D randomly located PC structure. x=0 is the midpoint of each configuration. Left side is axially symmetric with respect to the right side.

Design parameters of the structure are shared in Fig. 2. $x = X_i$ notations signify the center positions of air holes. For different random design these values randomly vary. l_i represents the length of each section. For each iteration, changing X_i variables are used to calculate l_i values.

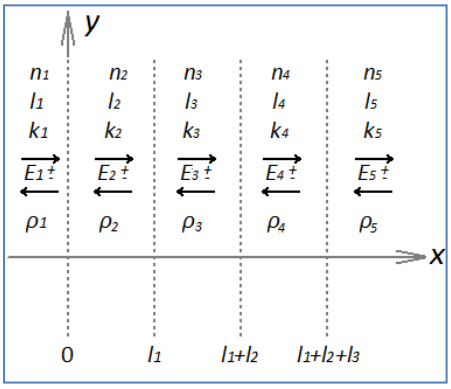

Figure 3. Dielectric multi-layers and related parameters used in ABCD matrix formulation.

Thus, effective refractive indices are calculated utilizing Eq. 1 and l_i values. Propagation vectors k_i are obtained with respect to effective refractive indices of each segment. One should note that it is assumed there is no propagation on the y direction thus k_y is taken to be zero. Wave propagation vector in the designed structure, $k = k_x$ corresponds to the normal incidence case. Accordingly, the reflected and transmitted electric fields in each region and related parameters are represented in Figure 3. For a multiple dielectric slab structure, the reflection coefficient becomes:

$$\rho_i = \frac{n_{i-1} - n_i}{n_{i-1} + n_i}. \qquad (2)$$

Backward and forward propagating electric field relation between the two following layer becomes:

$$\begin{bmatrix} E_i + \\ E_i - \end{bmatrix} = \frac{1}{\tau_i} M_i \begin{bmatrix} E_{i+1} + \\ E_{i+1} - \end{bmatrix}, \qquad (3)$$

where,

$$M_i = \begin{bmatrix} e^{jk_{i+1}l_{i+1}} & \rho_i ie^{-jk_{i+1}l_{i+1}} \\ \rho_i ie^{jk_{i+1}l_{i+1}} & e^{-jk_{i+1}l_{i+1}} \end{bmatrix}, \qquad (4)$$

and $\tau_i = 1 + \rho_i$ [9]. If we assume $\frac{1}{\tau_i} M_i = T_i$, then the total ABCD transfer matrix is given by,

$$\prod_{i=1}^{4} T_i = \begin{bmatrix} A & B \\ C & D \end{bmatrix}. \qquad (5)$$

Calculated total transfer matrix is shared in Eq. 5. However, this calculation is limited with the shared design. At the right-hand side of the structure, to have a specified defect length first air hole center (denoted as X_i) is fixed at a certain value. Locations of the rest of the air holes are changed. For increasing number of air holes transfer matrix should be extended with inclusion of new dielectric slabs. Another assumption in the formulation is absence of backward propagating wave at the right-most medium of the structure. The condition is satisfied with perfectly matched layers at the borders of the structure [8].

2. Results and Discussion

For the considered cases in the design, the radii of air holes are 0.30*a*. Defect length at the middle of the structure is fixed to 1.20*a*. We should note that the defect region can be adjusted to other value, larger or smaller. However, the resonance modes will change accordingly. Scanning parameter space starts with the nearest possible position of the air holes. Firstly, each hole is 0.70*a* away from the former hole (this case holds another periodicity). There is a 0.10*a* step not to have an overlap, then right most air hole shifts to the right and design extends to the right with 0.10*a* steps.

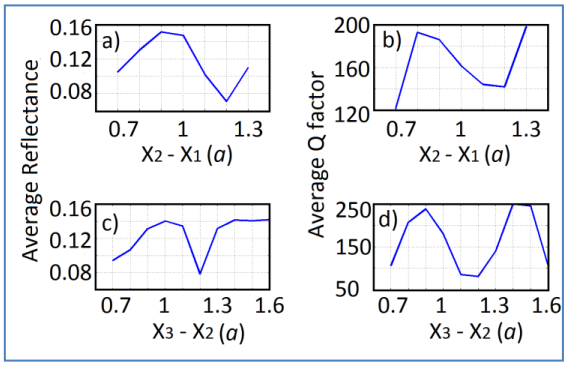

Figure 4. (a) Average reflectance of all different designs while $(X_2 - X_1)$ varies and (b) for the same parameters average Q factors of all designs. (c) Average reflectance of all different designs while $(X_3 - X_2)$ varies and (d) for the same parameters, average Q factors of all designs are plotted.

Figure 4 represent high correlation between reflectance values and the Q factors (average values are provided). For a particular case of two consecutive air holes, there exist many different random designs. Average total reflectance variations, utilizing Eq. 5, and average Q factor variations follows almost similar trend. That means when reflectance reach maximum and minimum values, Q factor oscillates in a similar manner. To the best of the knowledge, this is the first time that such an approach is considered for designing nanobeam cavities. The methodology can lead a novel way to generate high Q designs with manipulating filling fraction of the separated slabs in a random manner.

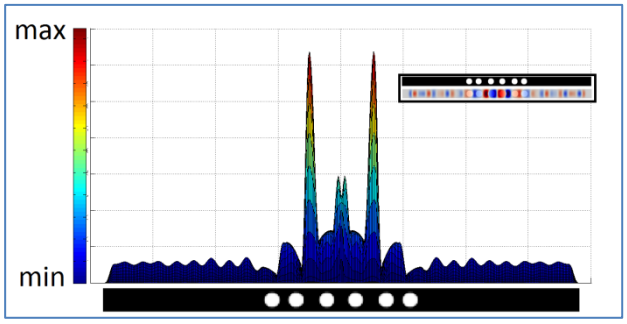

Figure 5. Total energy distribution on the structure for a particular case. Electric field distribution snapshot is also inset.

Increasing the number of randomly placed holes can yield large Q values as shown in Figs. 4(c) and 4(d). We reported the average Q-values in the results. The maximum value of Q-factor for four numbers of mirror air holes reaches 3000 which is two times higher than the regular case. Loss dependency and compact form properties of randomly designed nanobeam cavity will be investigated. Superior performances of random designed nanobeam cavities compared to regular designs deserve full and further investigation. The findings covering all these aspect will be shared during the conference.

In figure 5, total energy distribution of a particular design is plotted. One can clearly understand the cavity mechanism of the structure. Light localizes at different areas with different amount of energy. It is the idea behind the present research that the randomness can create countless different structure and promising for superior switching, sensing and low-threshold laser applications.

3. Conclusions

In the present study, we investigated fully random 1D PC nano-cavity structures. The regions surrounding the cavity section are divided into dielectric slabs and multi-layer dielectric medium approach is implemented to analyze the reflectance and quality factor.

Effective medium theory is assumed to be valid for the structure. From design to design the resonance frequencies of the cavities vary and stay within a/λ = 0.20-0.30 interval, where λ represents vacuum wavelength. The dispersion graphs of the each parts of a particular case are investigated (not shared) in order to check the correctness of the approach and close agreement between them are observed. However, for resonance modes whose wavelengths become comparable to the unit distance, then homogenization region is left and effective medium theory produces invalid results.

Finally, we point out the appearance of strong correlation between reflection coefficient and Q factors. Random structures could constitute higher Q factor and this property becomes more significant with the increasing number of air holes. On the other hand, susceptibilities of the each kind of designs to fabrication failures are numerically investigated and further studies are required in order to reach full conclusion.

Acknowledgements

The authors gratefully acknowledge the financial support of the Scientific and Technological Research Council of Turkey (TUBITAK), project 110T306. HK acknowledges partial support from the Turkish Academy of Sciences.

References

[1] J. P. Zhang, D. Y. Chu, S. L. Wu, W. G. Bi, R. C. Tiberio, R. M. Joseph, A. Taflove, C. W. Tu and S. T. Ho, "Nanofabrication of 1-D photonic bandgap structures along a photonic wire," IEEE Photon. Technol. Letters, vol. 8, no. 4, pp. 491-493, 1996.

[2] P. Lalane and J. P. Hugonin, "Bloch-wave engineering for high Qs small V's microcavities," IEEE J. Quantum Electronics, vol. 39, pp. 1430-1438, 2003.

[3] C. Sauvan, G. Lecamp, P. Lalane and J. P. Hugonin, "Modal –reflectivity enhancement by geometry tuning in Photonic crystal microcavities," Opt. Express, vol. 13, pp. 245-255, 2005.

[4] M. G. Can, B. B. Oner, and H. Kurt, "Polarization Independent Photonic Crystal Fabry-Perot Cavity," IEEE Photon. Technol. Letters, *accepted for publication*, DOI: 10.1109/LPT.2014.2359733, 2014.

[5] M. G. Can, B. B. Oner, and H. Kurt, "Polarization independent nanobeam cavity tuning using annular photonic crystals," SPIE Photonics Europe, International Society for Optics and Photonics, 2014.

[6] R. Verma, V. Banerjee, and P. Senthilkumaran, "Fractal signatures in the aperiodic Fibonacci grating," Opt. Lett. 39, pp. 2557-2560, 2014.

[7] Y. Bouazzi, et. al., "Numerical Investigation on the Spectral Properties of One-Dimensional Triadic-Cantor Quasi-Periodic Structure," Progress In Electromagnetics Research M, 36, pp. 1-7, 2014.

[8] A. Taflove and Susan C. Hagness, *Computational Electromagnetics: The Finite-Difference Time-Domain Method*, Artech House, Norwood, 2000.

[9] S. J. Orfanidis, *Electromagnetic Waves and Antennas*, New Brunswick, NJ: Rutger University, 2002.

Mimicking electromagnetically induced transparency in integrated plasmonics with radiative and subradiant resonators

Ting Wang , Yusheng Zhang and Zhanghua Han

Centre for Terahertz Research, China Jiliang University, Hangzhou , China
*Zhanghua Han, E-mail: han@cjlu.edu.cn

Abstract

We propose the use of radiative and subradiant resonators coupled to a metal-insulator-metal waveguide to represent the three-level energy diagram in conventional atomic systems and demonstrate a new realization of on-chip plasmonic analogue of electromagnetically-induced transparency (EIT) in integrated plasmonics. The radiative resonator is achieved with the help of aperture-coupling while evanescent coupling is relied for the subradiant resonator. Numerical simulation results demonstrate well-pronounced intermediate transmission peak through the bus waveguide and also show that the EIT effect can be easily controlled by the relative position of the two Fabry-Perot resonators.

• Introduction

Electromagnetically induced transparency (EIT) is a quantum interference phenomenon which can be observed in atomic systems when a strong external optical field is applied [1] to the medium. The sharp transparency window with narrow spectral width in the absorption band, accompanied with extraordinarily steep dispersion, is important to achieve a dramatic group-velocity reduction in the propagating light and to realize a variety of novel effects [2]. A great many interesting potential applications based on EIT have appeared in a wide range of fields, such as slow light, enhanced optical nonlinearities and optical information storage [3,4]. However, the realization of EIT in atom systems needs extreme experimental conditions like cryogenic conditions and gaseous medium,restricting thepractical applications of EIT. Recently, mimicking EIT in classical configurations has attracted tremendous attention and various schemes have been proposed and demonstrated to display the EIT-like spectral responses [5], e.g. coupled-resonator-induced transparency [6,7], plasmon-induced transparency (PIT) [8, 9], metamaterial-induced transparency [10-16]. Among those reported schemes, the PIT in integrated plasmonics is of special interest for high intensity photonic integrationdue to the possibility of realizing devices with ultra small footprint, thanks to the subwavelength confinement ability provided by plasmonic waveguides [8].

As we have pointed out in [8], the phenomenon of EIT can be considered using two alternative ways: as resulting from the destructive interference between two pathways involving the bare, dipole-allowed and metastable, states or, equivalently, the doublet of dressed states (created by the strong pump radiation) representing two closely spaced resonances decaying to the same continuum [1]. Figure 1 illustrates schematically the energy level diagrams of the two cases in atomic systems. In a typical three-level atomic system as shown in Fig. 1(a), dipole allowed transitions make both the ground state $|1\rangle$ and metastable state $|2\rangle$ coupled to the excited state $|3\rangle$ via the applied field while transition between $|1\rangle$ and $|2\rangle$ is forbidden. There are two different transition pathways $|1\rangle \rightarrow |3\rangle$ and $|1\rangle \rightarrow |3\rangle \rightarrow |2\rangle \rightarrow |3\rangle$ with which an atom in the ground state can experience the transition to the excited state. Equivalently, the excited state $|3\rangle$ shown as the dashed line in Fig. 1(b) will split into two dressed states $|\pm\rangle = (|3\rangle \pm |2\rangle)/\sqrt{2}$ when a strong electromagnetic filed was applied. So the atoms in the ground state can be excited to either $|+\rangle$ or $|-\rangle$ [3]. Although these two physical pictures are equivalent to each other when dealing with the EITphenomenon in atomic systems, their realization with classical systems depends on the EIT mechanism that is imitated [17]. The first picture suggests employing radiative and subradiant elements that are mutually coupled. Alternatively viewed, the EIT is achieved due to the cancellation of opposite contributions from two detuned resonances, which are equally spaced but with opposite signs of detuning from the probe frequency. In metamaterial-induced transparency, examples of the first picture can be found as metamaterials with the unit cell composed of bright and dark elements [10, 11, 14, 16] which have been widely investigated in recent years in different regions of the electromagnetic spectrum. Detuned dipoles [17] appear recently as the realization of metamaterial-induced transparency following the second picture. In coupled-resonator-induced transparencywith dielectric waveguides one can find cascaded ring resonators on the same side of the bus waveguide [6] as the representative for the first case and detuned ring resonators [18, 19] for the second. In integrated plasmonics circuit which has the potential to realize ultra compact devices, detuned resonators [8,9] have been investigated to realize PIT representing the second picture in Fig. 1, however, it is rarely reported to use the first picture to achieve the same functionality.

In this paper we propose to use mutually coupled radiative and subradiant resonators representing the three-level energy diagram atomic systems to realize the analogue of EIT in integrated plasmonics. Both the bus waveguide and the resonators are in the form of metal-insulator-metal (MIM) waveguides. An aperture between the bus waveguide and the radiative resonator is used to provide the high coupling, as is also required between the bright element and free space in metamaterial-induced transparency. Evanescent coupling is relied between the radiative and subradiant resonators. Numerical results show that well-pronounced EIT-like transmission can be demonstrated with this structure, and the transmission height can be controlled by changing the coupling strength between the two resonators when the aperture dimension is kept unchanged.

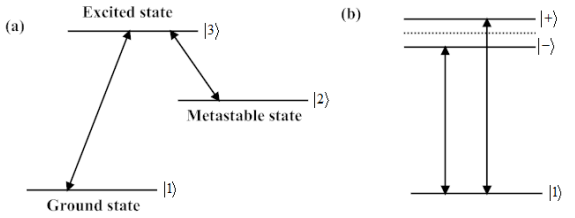

Fig. 1. Energy level diagrams in atomic systems when EIT can be observed. (a)A three-level atomic system where the transition between the continuum and the metastable state is prohibited; (b). The doublet of dressed states equivalent to (a) when a strong optical field is applied to the transition between the excited state and metastable state.

- **Radiative and subradiant resonators in MIM waveguides**

Unlike the case when two detuned aperture-coupled Fabry-Perot (FP) resonators are placed on the opposite side of the bus waveguide [8], which is shown in Fig. 2(a) and corresponds to two dressed states in Fig. 1(b), we use two Fabry-Perot resonators on the same side of the bus waveguide to represent the picture of Fig. 1(a). Figure 2(b) illustrates the geometry of the structure investigated in this paper. Both the bus waveguide and the two resonators are in the form of MIM waveguide with the same cross section, which is composed of a thin SiO_2layer embedded in the Ag background. The permittivity of Ag is described by the Drude model $\varepsilon_{Ag} = \varepsilon_\infty - \omega_p^2/(\omega^2 + j\gamma\omega)$, where ε_∞ represents the permittivity at infinite angular frequency and is chosen as 3.7, ω_p is the bulk plasma frequency with the value of *9.1eV* andγisthe oscillation damping of electrons and the value is *0.018eV* [8]. The width of SiO_2 is 100nm and its index is assumed to be 1.45. The two resonators are separated by a distance *t*.The first(1st) resonator with length L_1 is side-coupled to the bus waveguide with an aperture whose width *d* is constantly kept as 50nm throughout this paper. The aperture will ensure a strong coupling between the resonator and the bus waveguide [20], making the resonator behave as a radiative resonator like the bright element in metamaterial-induced transparency. The gap between the 1st resonator and the bus waveguide is 50nm, fully realizable with current nanofabrication techniques. The second(2nd) resonator with length L_2 is evanescently coupled to the 1st resonator, with a weaker coupling than that between the 1st resonator and the bus waveguide. Since the metal walls are optically thick and the 2nd resonator can only be coupled to the bus waveguide via the first resonator, it works as the "dark"subradiant resonator. The bus waveguide, the 1st resonator and the 2nd resonator serve as the ground state $|1\rangle$, the excited state $|3\rangle$ and the metastable state $|2\rangle$ shown in Fig. 1(a) respectively.

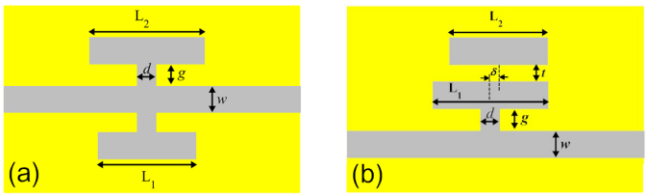

Fig. 2. Schematics of the structures (a) two aperture-coupled FP resonators are placed on the opposite side of the bus waveguide representing the dressed states in Fig. 1(b); (b) two resonators are on the same side of the waveguide representing the three-level diagram in Fig. 1(a).

The eigen plasmonic mode of the bus waveguide is used from the left port to excite the structure and the transmission is calculated using the power arriving at the exit port normalized to the incident power. The finite element method is used for the numerical simulations and by scanning the wavelength of the incident light, the transmission spectrum can be obtained.

- **Results and discussion**

First we give the result when the centers of the two resonators match each other along the propagation direction of the bus waveguide, i.e. the lateral shift δ shown in Fig. 2(b) equals to 0. In all the simulations L_1 is set to be 600nm while L_2 is 550nm giving rise to the excitation of the 2nd order FP resonator mode whose magnetic field is symmetric along the central plane of FP resonators. Note that the 1st resonator is 50nm longer than the 2nd one to have the same resonant wavelength due to a negative role that the aperture plays in the overall optical path of the resonator. The black line in Fig. 3(a) shows the transmission spectrum when the distance *t* between the two resonators is 50nm and one can see a well-pronounced intermediate transmission peak with the valueas high as 0.74at the wavelength of 1035nm between two transmission dips, demonstrating a well-known feature of the EIT-like effect. The distribution of the magnetic field are presented in Figs. 3(b)~(d) for the wavelengths of the two transmission dips(λ_1=1023nm and λ_2=1053nm) and the transmission peak(λ_3=1035nm). It is quite distinct that at the two transmission dips both the two resonators are strongly excited. However at 1023nm the magnetic fields in the two resonators are in-phase while at 1053nm they are out-of-phase. Notably, at the transmission peak only one FP resonator is excited while the field in the other resonator is much weaker. This phenomenon is quite

different with that demonstrated in plasmon-induced transparency with detuned resonators [8], where at the two transmission dips only one resonator is excited while at the transmission peak both resonators are excited with the phase opposite. As we mentioned before, the phenomenon of EIT in atomic systems can be considered using two alternative but equivalent ways shown in Fig. 1. In a similar way we can explain the magnetic field distribution shown in Fig. 3. Although the geometry represents the diagram shown in Fig. 1(a), the mutual coupling between the two FP resonators will result in a splitting of the original resonance into two super resonances like the picture shown in Fig. 1(b). Each dip in the transmission spectrum corresponds to a super resonance. Since the splitting of the original resonance is correlated with the coupling, the difference in the wavelength between the two transmission dips is a sign of the coupling strength between the two resonators. Similar to the two super waveguide modes when two straight waveguides are placed in parallel and coupled to each other, at one super resonance the fields at the two resonators are in-phase while at the other they are out-of-phase, as shown in Figs. 3(b) and (d). At the transmission peak both the super resonances are excited so that the field in one resonator is cancelled while that in the other resonator is enhanced. Different optical pathways from the bus waveguide to the two super resonances will experience a destructive interference, which cancels the original resonance effect at the transmission peak and lead to the formation of the EIT effect observed.

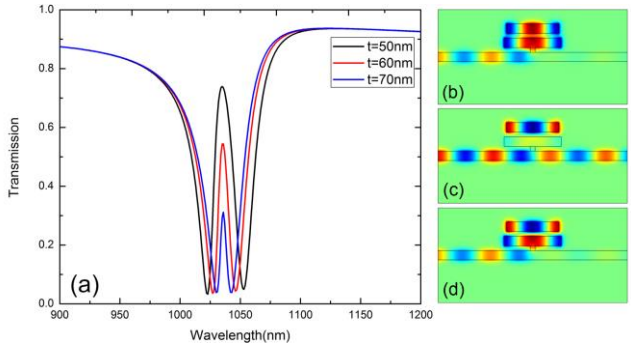

Fig.3. (a) Simulated EIT-like transmission spectra for two resonators with L_1=600nm, L_2=550nm, (b)~(d) Distribution of the real part of the magnetic field at resonance wavelengths of 1023nm, 1035nm and 1053nm when t equals to 50nm.

From the theory of EIT in atomic systems one knows that the EIT effect is related with the Rabi frequency of the control field (the frequency between $|+\rangle$ and $|-\rangle$), which reflects the coupling between the excited state and the metastable state shown in Fig. 1(a). Since the two states are represented by the two FP resonators in our proposal, one can easily control the EIT phenomenon by adjusting coupling strength between the two resonators. The easiest way is to vary the distance t between the two to control the field from one resonator penetrating the metal wall into the other. Figure 3(a) presents the transmission spectra when t is increased from 50nm to 70nm with a step of 10nm. These results clearly show that increasing t will result in a lower value of the transmission peak at the same wavelength, along with a smaller wavelength difference in the two transmission dips, which demonstrates a smaller resonance splitting due to a weaker coupling between the two resonators.

It is quite straightforward to change t to control the coupling between the two resonators. Unlike the ring resonators, the FP resonators support only standing waves at resonances, one can alternatively manipulate the overlap between the fields in the two resonators by shifting the relative position of the standing wave patterns, and then the coupling can also be changed at resonant wavelengths. If the node of the standing wave in one resonator matches spatially the antinode of the other resonator, the coupling will be the minimum. As an example, the distance t between the two resonators is kept as 60nm now while the center of the 2nd resonator is shifted by a lateral displacement δ compared to that of the 1st resonator, which is schematically shown in Fig. 2(b). Figure4(a) shows the transmission spectra when the shift δ is changed from 0nm to 50nm and 100nm. It's evidently shown that as δ increases the transmission peak drops and the wavelength difference between the two transmission dips also becomes smaller, demonstrating that the coupling between the resonators is weaker. Figures 4(b) ~ (d) give the magnetic field distribution of the transmission dips and peak when δ equals to 50nm, quite similar to the field shown in Fig. 3. The shift of the relative position between the centers of the two FP resonators provides a new means of controlling the coupling strength.

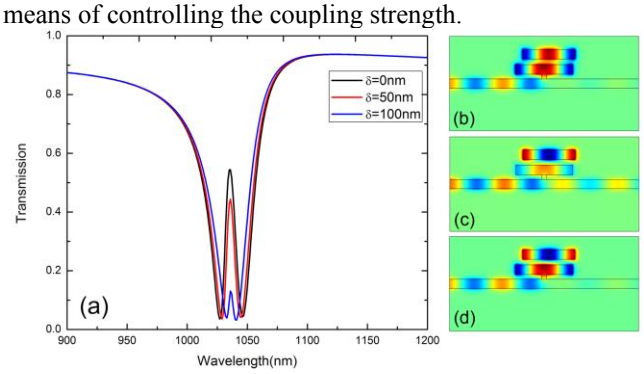

Fig. 4. EIT-like transmission spectra (a) for different lateral displacement δ calculated at t=60nm;(b) ~(d)Distribution of the real part of the magnetic field at resonance wavelengths of 1029nm, 1036nm and 1045nm with δ=50nm.

• Conclusions

In conclusion, a new scheme consisting of radiative and subradiant resonators in MIM waveguide is proposed to mimic the three-level energy diagram in atomic systems and the EIT-like spectral response in near infrared in integrated plasmonics is numerically demonstrated with this scheme. The mutual coupling of two resonators gives rise to the splitting of the original resonance into two super resonances. Different optical pathways between the bus waveguide and the two super resonances result in a transparency peak in the transmission window. The EIT-like behavior can be well engineered by changing the relative position between the radiative and subradiant resonators to tune the coupling strength between the two. This proposed new scheme

represents a great supplement to the analogue of EIT in integrated plasmonics using detuned resonators and we expect that some novel functionalitycan be further introduced into guided plasmonic circuits.

Acknowledgements

This work was supported by the National Natural Science Foundation of China (61107042).

References

- K. J.Boller, A. Imamolu, and S. Harris, Observation of electromagnetically induced transparency, *Phys. Rev. Lett.* 66: 2593-2596, 1991.
- Z. Li, Y. Ma, R. Huang, R. Singh, J. Gu, Z. Tian, J. Han, and W. Zhang, Manipulating the plasmon-induced transparency in terahertz metamaterials, *Opt. Express* 19: 8912-8919, 2011.
- M. Fleischhauer, A. Imamoglu, and J. P. Marangos, Electromagnetically induced transparency: Optics in coherent media, *Rev. Mod. Phys.*77: 633-673, 2005.
- C. Liu, Z. Dutton, C. H. Behroozi, and L. V. Hau, Observation of coherent optical information storage in an atomic medium using halted light pulses, *Nature* 409, 490-493, 2001.
- N. Papasimakis, V. A. Fedotov, N. I. Zheludev, and S. L. Prosvirnin, Metamaterial analog of electromagnetically induced transparency, *Phys. Rev. Lett.* 101: 253903, 2008.
- D. D. Smith, H. Chang, K. A. Fuller, A. Rosenberger, and R. W. Boyd, Coupled-resonator-inducedtransparency, *Phys. Rev. A* 69: 063804 , 2004.
- K. Totsuka, N. Kobayashi, and M. Tomita, Slow light in coupled-resonator-induced transparency, *Phys. Rev. Lett.* 98: 213904, 2007.
- Z. Han, and S. I. Bozhevolnyi, Plasmon-induced transparency with detuned ultracompact Fabry-Perot resonators in integrated plasmonic devices, *Opt. Express* 19: 3251-3257, 2011.
- R. D. Kekatpure, E. S. Barnard, W. Cai, and M. L. Brongersma, Phase-coupled plasmon-induced transparency, *Phys. Rev. Lett.* 104: 243902, 2010.
- S. Zhang, D. A. Genov, Y. Wang, M. Liu, and X. Zhang, Plasmon-induced transparency in metamaterials, *Phys. Rev. Lett.* 101: 47401, 2008.
- J. Zhang, S. Xiao, C. Jeppesen, A. Kristensen, and N. A. Mortensen, Electromagnetically induced transparency in metamaterials at near-infrared frequency, *Opt. Express* 18: 17187-17192, 2010.
- R. Singh, C. Rockstuhl, F. Lederer, and W. Zhang, Coupling between a dark and a bright eigenmode in a terahertz metamaterial, *Phys. Rev. B* 79: 085111, 2009.
- S.Y. Chiam, R. Singh, C. Rockstuhl, F. Lederer, W. Zhang, and A. A. Bettiol Analogue of electromagnetically induced transparency in a terahertz metamaterial, *Phys. Rev. B* 80: 153103, 2009.
- N. Liu, L. Langguth, T. Weiss, J. Kästel, M. Fleischhauer, T. Pfau, and H. Giessen, Plasmonic analogue of electromagnetically induced transparency at the Drude damping limit, *Nat. Mater.* 8: 758-762 , 2009.
- N. Liu, T. Weiss, M. Mesch, L. Langguth, U. Eigenthaler, M. Hirscher, C. Sönnic sen, and H. Giessen, Planar metamaterial analogue of electromagnetically induced transparency for plasmonic sensing, *Nano. Lett.* 10: 1103-1107, 2009.
- P. Tassin, L. Zhang, T. Koschny, E. Economou, and C. M. Soukoulis, Low-loss metamaterials based on classical electromagnetically induced transparency, *Phys. Rev. Lett.:* 102, 053901, 2009.
- S. I. Bozhevolnyi, A. B. Evlyukhin, A. Pors, M. G. Nielsen, M. Willatzen, and O. Albrektsen, Optical transparency by detuned electrical dipoles, *New J. Phys.* 13: 023034, 2011.
- Q. Xu, S.Sandhu, M. L. Povinelli, J.Shakya, S.Fan, and M.Lipson, Experimental realization of an on-chip all-optical analogue to electromagnetically induced transparency, *Phys. Rev. Lett.* 96: 123901, 2006.
- Y. Zhang, S. Darmawan, L.Y. M. Tobing, T. Mei, and D.H. Zhang, Coupled resonator-induced transparency in ring-bus-ring Mach-Zehnder interferometer, *J. Opt. Soc. Am. B* 28: 28–36, 2011.
- Z. Han, V. Van, W. N. Herman and P. T. Ho, Aperture-coupled MIM plasmonic ring resonators with sub-diffraction modal volumes, *Opt. Express* 17: 12678-12684, 2009.

Efficient and broadband Terahertz plasmonic absorbers with highly doped Si as the plasmonic material

Yusheng Zhang and Zhanghua Han

Centre for Terahertz Research, China Jiliang University, Hangzhou 310018, China
**corresponding author, E-mail: han@cjlu.edu.cn*

Abstract

The design of efficient and broadband Terahertz plasmonic absorbers with highly doped Si as the plasmonic material is proposed and the performance of these absorbers are numerically investigated. The plasmonic properties of highly doped Si are first analyzed, based on which resonant plasmonic structures consisting of a continuous layer of SiO_2 film sandwiched between the substrate and the top stripe layers both made from highly doped Si are presented. Numerical results from the reflection spectra demonstrate that these structures exhibit high absorption in the terahertz frequencies with large bandwidth and tenability, leading to a novel design of devices for absorbing terahertz radiation.

1. Introduction

Terahertz (THz) radiation, with the wavelength typically ranging from 30um to 3mm, has been one of research hot subjects in recent years, due to its potential applications in various fields, including time-domain spectroscopy, non-destructive sensing, biological imaging, etc.[1]. With the rapid progress on the research of terahertz technology applications, under some circumstance it is also required to shield some objects from THz radiation or to block the influence of THz. Thereby the demand for high-efficiency broadband THz absorber, which is important not only to academic applications but also of profound military significance, is increasing. To date most of the reported THz absorbers are based on the metamaterial(MM) concept, which are typically composed of two distinct metallic layers with a dielectric spacer[2], [3]. Although these MM absorbers demonstrate high absorption, however, most of them are suffering from inherent narrow bandwidth owing to the resonant property of the MM unit cell and the relatively low Ohmic loss of metals in the THz regime. In the visible light frequencies, one effective way of realizing high absorption is to use surface plasmons(SPs) nanostructures, due to their characteristics of subwavelength scale modal localization, large EM field enhancement and the intrinsic loss associated with the excitation of SPs[4]. The use of metallic nanostructures to enhance broadband absorption and improve performance for thin-film photovoltaic devices has been reported in the literature[5]. But in the terahertz regime, due to the properties of metals with large imaginary and negative real parts of the permittivity, regular SPPs cannot be supported and many attractive applications of plasmonics cannot be directly extended to this regime, including the plasmonic absorbers. In order to circumvent this problem, many semiconductor materials have been proposed to work as the plasmonic materials in THz because their free carrier concentrations can be steadily controlled by doping, thermal, electrical or optical excitations so that the plasma frequencies of these semiconductors can be tuned to the THz frequencies[6], [7]. Nevertheless the use of the highly doped silicon (HD-Si) as the THz plasmonic material for the application of high absorbers remains unexplored.

In this paper, the design of efficient and broadband THz plasmonic absorbers with HD-Si as the plasmonic material is proposed and the performance of these absorbers are numerically investigated. The plasmonic properties of HD-Si at different doping concentration are fist analyzed and then resonant plasmonic structures consisting of a continuous layer of SiO_2 film sandwiched between the substrate and the top stripe layers both made from HD-Si are presented, which is geometrically quite similar to the structures reported in the literature[8], [9] working in visible band. The near-zero dips in the reflection spectra from numerical simulations show that these structures exhibit high absorption in the terahertz frequencies with large bandwidth.

2. Theory and Configuration

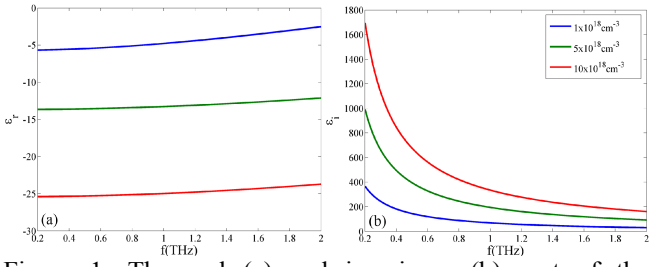

Figure 1: The real (a) and imaginary (b) part of the permittivity of HDSi obtained by the Drude model as a function of the frequency with different carrier concentrations.

The complex dielectric constant of a plasmonic material (here it is HDSi) can be characterized using the Drude model following the equation,

$$\varepsilon = \varepsilon_\infty - \frac{\omega_p^2}{\omega^2 + j\omega\gamma}, \quad (1)$$

$$\gamma = \frac{e}{m^* \mu}, \quad (2)$$

In equation (1) ε_∞ = 11.7 is the permittivity of intrinsic Si, ω the angular frequency, ω_p is the angular plasma frequency, and γ is the damping rate defined by equation (2), where e is the electron charge, m^* is the effective mass of free carriers, N is the free carrier concentration, and μ the free carrier mobility. The value of ω_p is determined by equation:

$$\omega_p^2 = \frac{e^2 N}{\varepsilon_0 m^*}, \quad (3)$$

and it is clear that the plasma frequency of a material is mainly affected by its free carrier concentration. In this paper n-type Si is chosen due to the larger mobility of electrons over holes in p-type Si and the concentration of electron is on the order of 10^{18} cm^{-3}, which is easily achievable with Si material. The mobility of electrons is also dependent on the concentration because the electron will experience more collisions with adjacent electrons when the concentration increases. To calculate the permittivity of HDSi, the following empirical formula is used[10],

$$\mu = \mu_{\min} + \frac{\mu_{\max} - \mu_{\min}}{1 + (N / N_{ref})^{\alpha}}, \quad (4)$$

where $\mu_{\min}$, $\mu_{\max}$, N_{ref}, and α are all empirical parameters.

With equations (1) ~ (4) one can calculate the permittivity of highly doped Si at different electron concentrations. Results in Fig. 1 show both the real and imaginary parts of the relative permittivity in the electron concentration range between 10^{18} cm^{-3} and 10^{19} cm^{-3}. It is quite clear from Fig. 1(a) that the HDSi demonstrates negative values in the real part of permittivity. These negative values of permittivity make it possible for the excitation of SPs in the THz frequencies on the HDSi interface with other dielectrics. The imaginary part of the HDSi dielectric constant is shown in Fig. 1(b) and is found to be much larger than the real part. As the carrier concentration increases from $1x10^{18}cm^{-3}$ to $10x10^{18}cm^{-3}$, the amplitudes of both the real part and imaginary part become bigger, due to the dependence of the plasma frequency on the carrier concentration. If one compares the plasmonic property of HDSi to that of noble metals in the optical regime, one may conclude that HDSi is not a good plasmonic material in terms of the low quality factors[11]. Although this limits the use of HDSi as the plasmonic material in the applications such like THz plasmonic antennas, the large imaginary part of the relative permittivity together with its negative real part make HDSi a good material candidate for THz absorber applications.

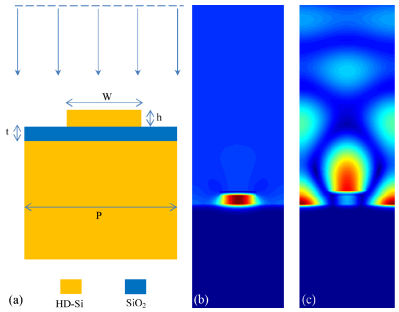

Figure 2: (a) The schematic diagram of the THz plasmonic absorber unit-cell. A continuous SiO2 film of thickness t is sandwiched between a HDSi substrate and a HDSi stripe with height h and width W. The cladding above the structure is assumed to be air, and the period of the structure is P. (b, c) The normalized distribution of magnetic field for different resonant frequency: (b) 0.95THz and (c) 1.45 THz, with the period P = 200 *um* and W = 70 *um*.

The design of our THz plasmonic absorber is schematically shown in Fig. 2(a), where a continuous SiO_2 film (n=1.45) of thickness t is sandwiched between a substrate and a top layer of one dimensional array of stripes with height h and width W, both are made from HDSi. The cladding above the structure is assumed to be air, and the period of the stripe array is P. The finite element method (FEM) together with the periodic boundary conditions are used to model the reflection of incident THz beam from the structure. Since the substrate is opaque to the THz radiation, the absorptivity of the structure can be seen from the reflection spectra straightforwardly. In the calculations the incident plane wave of the THz beam is assumed to be normal to the structure for simplicity and the electric field is set to be along the periodicity of the stripe array (TM polarized). Quite similar to the structures reported in [8], these HDSi stripes still work as gap plasmon resonators, although the gap surface plasmon mode is provided by the HDSi-SiO_2-HDSi in the THz regime instead of metal-insulator-metal structures in the optical frequencies.

3. Simulation results and discussion

The numerically calculated reflection spectra of the periodic structures shown in Fig. 2(a) are given in Fig. 3, where the height of the HDSi stripes is fixed at h = 10 *um* and the thickness of SiO_2 is set as t = 18 *um*. In Fig. 3(a), the period P is set to be 200 *um* and reflection spectra of the TM-polarized incident THz beam with five different width W of the stripes are shown as five different lines. It is quite clear that there are two resonance peaks at the lower frequency and higher frequency respectively. At the lower frequency the resonance is quite dependent on the stripe width and the longer stripe corresponds to a lower resonance. Analysis of the stripe width together with the resonance frequency make us conclude that this resonance is due to the excitation of the 1^{st} order Fabry-Perot resonator mode in the HDSi-SiO_2-HDSi structure, quite similar to the gap plasmon resonator mode reported in[8]. The mode profile of the magnetic field at the frequency of 0.95THz is shown in Fig. 2(b), which corresponds to the lower resonance frequency of the blue reflection spectra for the stripe width of 70 *um*. One can

clearly see the excitation of the 1st order Fabry-Perot resonator mode confined in the HDSi-SiO_2-HDSi structure. This mode profile confirms our conclusion about the origin of the lower resonance frequencies in Fig. 3(a). Numerical result of the mode profile shown in Fig. 2(b) also reveal that the electric field intensity within the HDSi-SiO_2-HDSi structure is about 10 times more than that of incident field, demonstrating that although the HDSi is not a good plasmonic material in the THz frequencies, the property of field enhancement associated with the excitation of SPs is still quite significant. The reflection from the all the structures at the lower resonance frequencies in Fig. 3(a) are almost zero, demonstrating the remarkable performances of the proposed structure with HDSi as perfect THz plasmonic absorbers. One can also see in Fig. 3(a) that the lower resonance frequencies shift as the stripe width changes, making it possible to realize even broader band absorption by using HDSi stripes with different widths in the same unit cell of the periodic structures. Besides the lower resonance frequencies shown in Fig. 3(a), another resonance around 1.45 THz is also present in each reflection line and this higher frequency demonstrate a Fano type resonance characteristic. Remarkably, these Fano resonances keep almost unchanged as the width of the HDSi stripe increases. Juding from the resonance properties and the mode profile shown in Fig. 2(c) at 1.45 THz for the stripe width of 70 *um*, we believe that these higher frequency resonances result from the excitation of the SPs at the HDSI-SiO2-air interface due to the existence of the periodic HDSi stripe structures working as the excitation grating. This phenomenon is quite similar to the famous Wood's anomaly[12] in the optical frequencies. Fig. 3(b) presents the reflection spectra when the width of the HDSi stripe is kept as 80*um* while the period of the structure is changing between 180 *um* and 240 *um*. One can see that the lower resonance frequency keeps unmoved due to the condition for the 1st order Fabry-Perot resonance is the same while the higher resonance frequencies experience a red-shift as the period increases. These results further confirm the origin of the high frequency resonances.

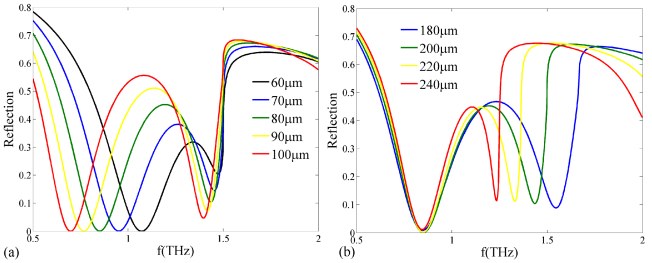

Figure 3: (a, b) Reflection spectra with different widths of highly doped silicon W and different periods of structure P with fixed h=10 um and t=18 um.

4. Conclusions

In summary, the design of a novel efficient and broadband Terahertz plasmonic absorber with HDSi as the plasmonic material is proposed and the performance of this absorber is numerically investigated. The high performances of these THz absorbers make these structures ideal for THz radiation shielding and blocking, thereby we believe the proposed THz absorbers can find broad applications in THz technology. The idea of changing the semiconductors into plasmonic materials with appropriate doping level can also be extended to other frequencies, showing high potential in military applications.

Acknowledgments

This work was supported by the National Natural Science Foundation of China (Grant No. 61107042) .

References

[1] B. Ferguson and X.-C. Zhang, "Materials for terahertz science and technology.," *Nat. Mater.*, pp. 26–33, 2002.

[2] N. Landy, S. Sajuyigbe, J. Mock, D. Smith, and W. Padilla, "Perfect Metamaterial Absorber," *Phys. Rev. Lett.*, p. 207402, 2008.

[3] H. Tao, C. Bingham, a. Strikwerda, D. Pilon, D. Shrekenhamer, N. Landy, K. Fan, X. Zhang, W. Padilla, and R. Averitt, "Highly flexible wide angle of incidence terahertz metamaterial absorber: Design, fabrication, and characterization," *Phys. Rev. B*, p. 241103, 2008.

[4] H. Raether, *Surface Plasmonson smooth and rough surfaces and on gratings*. Springer, 1998.

[5] R. a. Pala, J. White, E. Barnard, J. Liu, and M. L. Brongersma, "Design of Plasmonic Thin-Film Solar Cells with Broadband Absorption Enhancements," *Adv. Mater.*, pp. 3504–3509, 2009.

[6] S. Nashima, O. Morikawa, K. Takata, and M. Hangyo, "Measurement of optical properties of highly doped silicon by terahertz time domain reflection spectroscopy," *Appl. Phys. Lett.*, pp. 3923–3925, 2001.

[7] A. Berrier, R. Ulbricht, M. Bonn, and J. G. Rivas, "Ultrafast active control of localized surface plasmon resonances in silicon bowtie antennas," *Opt. Exp.*, pp. 23226–23235, 2010.

[8] M. G. Nielsen, D. K. Gramotnev, A. Pors, O. Albrektsen, and S. I. Bozhevolnyi, "Continuous layer gap plasmon resonators," *Opt. Exp.*, pp. 19310–19322, 2011.

[9] M. G. Nielsen, A. Pors, O. Albrektsen, and S. I. Bozhevolnyi, "Efficient absorption of visible radiation by gap plasmon resonators," *Opt. Exp.*, pp. 13311–13319, 2012.

[10] D. M. Caughey and R. E. Thomas, "Carrier mobilities in silicon empirically related to doping and field," *Proc. IEEE*, pp. 2192–2193, 1967.

[11] P. R. West, S. Ishii, G. V. Naik, N. K. Emani, V. M. Shalaev, and a. Boltasseva, "Searching for better plasmonic materials," *Laser Photon. Rev.*, pp. 795–808, 2010.

[12] R. W. Wood, "Anomalous diffraction gratings," *Phys. Rev.*, pp. 928–937, 1935.

EM diode based on two inversely configured non-reciprocal gyromagnetic gratings

Zhen Li , Rui-xin Wu , Qing-bo Li

School of Electronic Science and Engineering, Nanjing University, Nanjing 210093, China

*corresponding author, E-mail: rxwu@nju.edu.cn

Abstract

In this work, we proposed a new type of Electromagnetic (EM) diode based on non-reciprocal gyro-magnetic rods gratings and explained its unidirectional behavior by geometric optics. The grating is a line array of gyro-magnetic rods, it could reflect or steering the EM beam like negative refraction with different applied magnetic field or different injecting angle. The two gratings are reversely biased by different magnetic field and arranged asymmetrically. We demonstrated unidirectional transmission could be realized in this structure.

1. Introduction

Nonreciprocal transmission of electromagnetic wave is a very interesting and important characteristic[1-3], which is the basis of many useful components in microwave or optics engineering, among them, microwave/optics isolator is a hot pursed object. As a key component, isolator is used to eliminate the undesired backward propagation of EM waves while maintaining the forward propagation in transmission link, sometimes we could call it as electromagnetic diode. Massive efforts have been dedicated to this study for decades, and multifarious mechanism and novel devices are proposed and fabricated Except for the traditional ferrite isolators, such as fluorescent dyes with a concentration gradient[4], layered systems[5] and liquid-crystal hetero-junctions[6]. For the present, Focus is transfer to photonic crystals (PCs) based isolators.

Fundamentally, the mechanism of EM diode is related with the system symmetry including parity symmetry and time reversal symmetry. Either of the symmetry broken will lead to EM diode[7-9]. There are two means to realize the broken symmetry in PC based diodes. For parity symmetry, we could use cell component with asymmetry geometry for PCs[10], or we could adopt two dimensional photonic crystals comprising hetero-junction structure to break the spatial inversion symmetry[11,12]. For time reversal symmetry, we could use gyro-magnetic or gyro-electric material for the cell component, these materials has imaginary off-diagonal elements in permeability or permittivity matrix, the off-diagonal components determine the unpaired eigen values, this is the essential mathematics for time reversal symmetry broken[13].

Recently, a new type of EM diode was proposed which could be explained by geometric optics [14], that is by adopting properly arranged prisms, incident waves from two sides will refracted dissimilarly. Align this concept, Joo realized EM diode by using two inverted PC prisms, the prisms are right-angled and isosceles triangles, incident wave from one side will be reflected twice by the two prisms then propagate backward, while incident wave from another side will be deflected by each prism forward directly. Yangyang start from prisms of zero index material with the same shape[15], Incident from air to ZIM, EM wave will be completely reflected, while from ZIM to air, EM wave will left vertically the interface of ZIM and air, with prisms aligned in line, high efficiency unidirectional transmission can be achieved for open space.

In this article, ignited by the above idea, we proposed a new type of EM diode based on non-reciprocal gratings[16-18]. This grating formed EM diode will have more simple configuration compared to the previous concepts. The grating deflect the EM waves differently according to the incident angles, by properly collocating the gratings, which is much like the configuration of inverted bi-prism, The out-coming waves from the array will show unidirectional transmission trait. So the key points are the non-reciprocal components and their collocations. A feasible realization of this specific grating is a line array of ferromagnetic rods. For the single gyromagnetic cylinder, there exist a nonvanishing rotating dipole momentum as an analog of the Zeeman effect [19] on photonic angular momentum states (PAMSs). The collective dipole modes of the cylinder array make it could reflect or pass the EM beam non-reciprocally with inverted magnetic field or different injecting angle.

2. EM diode

2.1. EM Diode Concept

Fig. 1 (a) is the schematic of the non-reciprocal deflecting element, it is a certain grating, and it's expected to have two biasing status, and in each biasing status, it has dissimilar non-reciprocal deflection phenomenon. In one biasing status as the left two figures shown, if EM waves incident with positive angle, out-going waves will be directly reflected, if the incident angle is negative, the out –going waves will be

steering to the other side of the grating with a negative deflection angle, this is very similar with negative refraction, While in the inversing biasing status, the deflection behavior will be reversed as shown the right two figures.

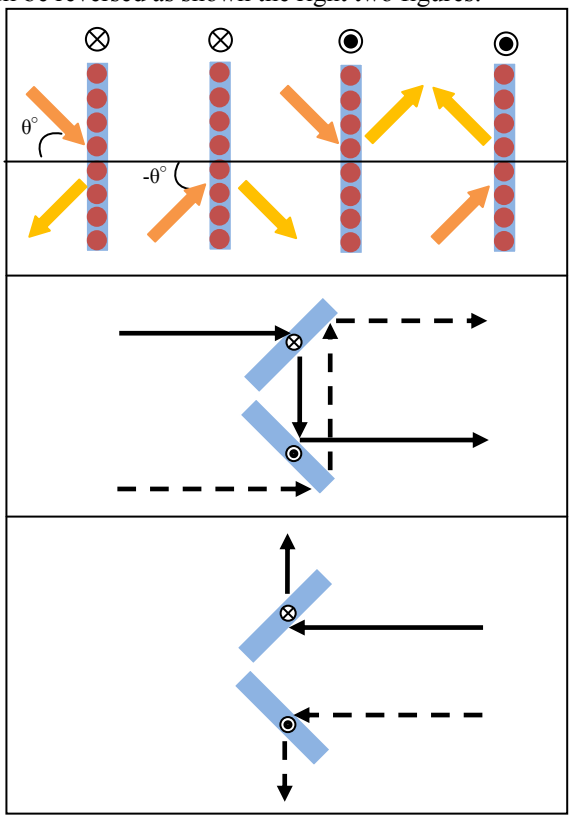

Figure 1: Schematic of the EM diode.

With two of these novel non-reciprocal gratings, EM diode could be formed, which is schematically shown in Fig. 1 (b) and (c). The two gratings are reversely biased, and arranged with inverted angles like a horn shape. The unidirectional behavior of the EM diode is illustrated in the figures according to geometry optics. Following the Snell's law, left incident ray onto each grating will be steered and projected towards the other grating, then reflected by the second grating to the forward direction as the incident ray, so EM wave could pass from left to right. While for another occasion, right incident ray onto each grating will be directly steered outwards, so no forward transmission exists, the diode is cut-off.

2.2. Realization

To realize this concept, the grating constituted by single layer of gyro-magnetic cylinders is a good candidate of the non-reciprocal grating. On one side, it has non-reciprocal diffraction trait as expected, on the other side, its non-reciprocal behavior is controlled by the external biasing magnetic field, so positive and negative magnetic field supply two types status of the grating. Here we use gyro-magnetic yttrium-iron garnet (YIG) rods for the grating. The ferrite rods are biased by applying a static magnetic field H_a along the rods' axis. In fully magnetized state, the permeability of the ferrite is a tensor in the form as Eq.1.

$$\ddot{\mu} = \begin{bmatrix} \mu_r & j\mu_\kappa & 0 \\ -j\mu_\kappa & \mu_r & 0 \\ 0 & 0 & 1 \end{bmatrix} \tag{1}$$

The tensor elements are, respectively, $\mu_r=1+[\omega_m(\omega_0-j\alpha\omega)]/[(\omega_0- j\ \alpha\omega)^2-\omega^2]$ and $\mu_\kappa=\omega_m\omega/[(\omega_0- j\ \alpha\omega)^2-\omega^2]$, where $\omega_0=\gamma H_0$ is the precession frequency and γ is the gyro-magnetic ratio. The bias magnetic field H_0 is the sum of H_a and the other fields, such as demagnetization field of ferrite rods. ω_m is the characteristic frequency related to the saturation magnetization $4\pi Ms$, and α is the damping coefficient of the ferrite. The saturation magnetization and the damping coefficient for Mg-Mn ferrite are 1884 *Gauss* and 0.01, respectively. Its relative permittivity is about $\varepsilon_r=15.26(1-j*0.0004)$. The radius of the rod is 9 mm, and the space between the centers of the adjacent rods is 24 mm. Magnetic field applied on the two gratings are reversed.

2.3. Performance

We use such designed gyro-magnetic rods chains to form the EM diode as Fig. 1. The working frequency is around 8.83 GHz. The power flow of this configuration is shown in Fig. 2. For left incident waves, after refraction and reflection on two gratings, waves could pass through the diode and propagate forward, for right incident waves, it seems like the diode block the forward transmission for the waves are deflected outwards by both of the gratings. We note that the field circulations are reversed for the two end rods of the two gratings at the center zone of the EM diode, they will interfere each other, even destroy their non-reciprocal trait, so to alleviate their influence, a buffer rod introduced into the structure between the two different gratings.

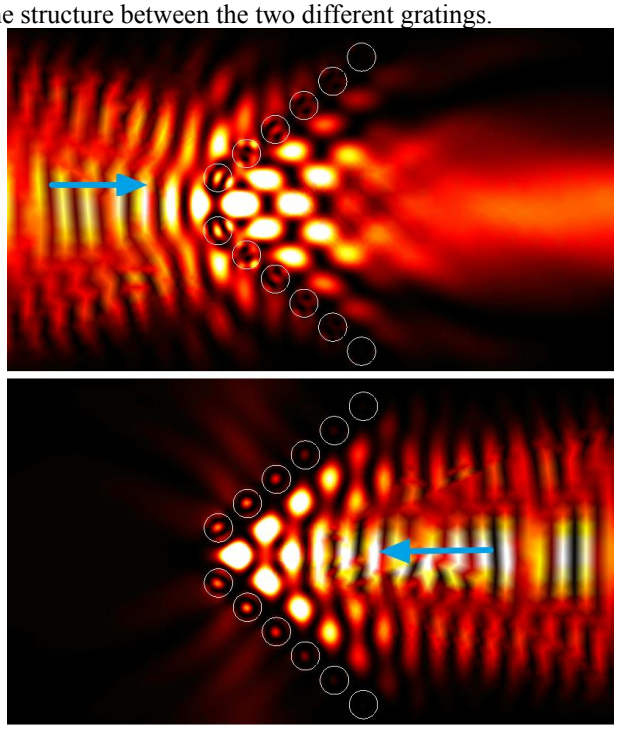

Figure 2: Power flow of the EM diode

Fig. 3 is the transmission of the diode, we can see clearly it has unidirectional transmission characteristics in the

frequency range around 8.83GHz. This verified our proposal for the new type of EM diode.

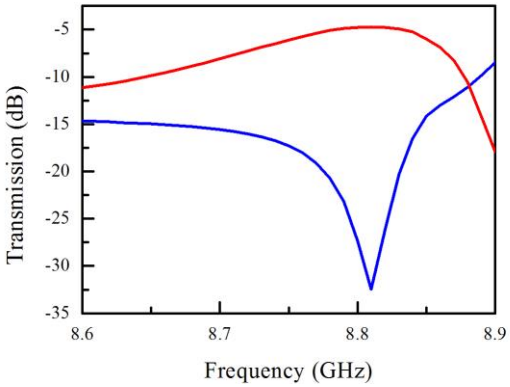

Figure 3: Transmission of the EM diode, red line is forward transmission, blue line is reverse transmission.

3. Conclusions

In this work, we proposed a new type of EM diode based on non-reciprocal gyromagnetic rods gratings. The grating is a line array of gyromagnetic rods, it could reflect or steering the EM beam like negative refraction with different applied magnetic field or different injecting angle. The two gratings are reversely biased by different magnetic field and arranged asymmetrically. We demonstrated unidirectional transmission could be realized in this structure.

Acknowledgements

This work was supported by the NSFC (61271080, 61071007, and 61001017) and RFDP (20110091110030, 20100091120045).

References

[1] R. J. Potton, Reciprocity in optics, Rep. Prog. Phys. **67**, 717–754 (2004)

[2] A. Figotin and I. Vitebsky, Nonreciprocal magnetic photonic crystals, Phys. Rev. E, 63, 066609 (2001)

[3] J. B. Khurgin, Optical isolating action in surface plasmon polaritons, Appl. Phys. Lett. **89**, 251115 (2006).

[4] S. Mujumdar and H. Ramachandran, Use of a graded gain random amplifier as an optical diode, Opt. Lett. **26**(12), 929–931 (2001).

[5] A. H. Gevorgyan, Optical diode based on a highly anisotropic layer of a helical periodic medium subjected to a magnetic field, Tech. Phys. 47(8), 1008–1013 (2002).

[6] J. Hwang, M. H. Song, B. Park, S. Nishimura, T. Toyooka, J. W. Wu, Y. Takanishi, K. Ishikawa, and H. Takezoe, Electro-tunable optical diode based on photonic bandgap liquid-crystal heterojunctions, Nat. Mater.4(5), 383–387 (2005).

[7] F. D. M. Haldane and S. Raghu, Phys. Rev. Lett. **100**, 013904(2008).

[8] K. G. Makris, R. El-Ganainy, D. N. Christodoulides, and Z. H. Musslimani, Phys. Rev. Lett. **100**, 103904 (2008).

[9] Z. Wang, Y. D. Chong, J. D. Joannopoulos, and M. Solja ˇ *ci* ´ *c*, "Reflection-free one-way edge modes in a gyromagnetic photonic crystal, Phys. Rev. Lett. **100**, 013905 (2008).

[10] C. He, M.H. Lu, X. Heng, L. Feng, and Y. F. Chen, Parity-time electromagnetic diodes in a two-dimensional nonreciprocal photonic crystal, Phys. Rev. B 83, 075117 (2011).

[11] C. Wang, C. Z. Zhou, and Z. Y. Li, On-chip optical diode based on silicon photonic crystal heterojunctions, Opt. Exp. 19, 26948 (2011)

[12] A. Cicek, M. B. Yucel, O. A. Kaya, and B. Ulug, Refraction-based photonic crystal diode, Opt. Lett, 37, (2012)

[13] Y. Poo, R. X. Wu, Z. Lin, Y. Yang, and C. T. Chan, Experimental realization of self-guiding unidirectional electromagnetic edge states, Phys. Rev. Lett. 106, 093903 (2011).

[14] J. H. Oh, H. W. Kim, P. S. Ma, H. M. Seung, and Y. Y. Kim, Inverted bi-prism phononic crystals for one-sided elastic wave transmission applications, Appl. Phys. Lett. 100, 213503 (2012)

[15] Y. Y. Fu, L. Xu, Z. H. Hang, and H. Y. Chen, Unidirectional transmission using array of zero-refractive-index metamaterials, Appl. Phys. Lett. 104, 193509 (2014)

[16] T. J. Guo, T. F. Li, M. Yang, H. X. Cui, Q. H. Guo, X. W. Cao, and J. Chen, Nonreciprocal optical diffraction by a single layer of gyromagnetic cylinders, Opt. Exp. 22 (1), 538 (2014)

[17] J. Du, Z. Lin, S. T. Chui, W. Lu, H. Li, A. Wu, Z. Sheng, J. Zi, X. Wang, S. Zou, and F. Gan, Optical beam steering based on the symmetry of resonant modes of nanoparticles, Phys. Rev. Lett. **106**, 203903 (2011).

[18] J. Du, Z. Lin, S. T. Chui, G. Dong, and W. Zhang, Nearly total omnidirectional reflection by a single layer of nanorods, Phys. Rev. Lett. **110**, 163902 (2013).

[19] J. Wang, K. H. Fung, H. Y. Dong, and N. X. Fang, Zeeman splitting of photonic angular momentum states in a gyromagnetic cylinder, Phys. Rev. B 84, 235122 (2011).

Nonreciprocal self-collimation in two-dimensional gyromagnetic photonic crystals and its applications in signal separation

Qing-Bo Li, [1,2] Zhen Li,[1] Ping Zhou,[2] and Rui-xin Wu [1*]

[1] School of Electronic Sciences and Engineering, Nanjing University, Nanjing 210093, China
[2] Huaian Key Laboratory of Information Functional Materials, School of Physics and Electronic Electrical Engineering, Huaiyin Normal University, Huaian 223300, China
*corresponding author, E-mail: rxwu@nju.edu.cn

Abstract

We investigate self-collimation properties in two-dimensional gyromagnetic photonic crystals (GPCs) fabricated by semi-cylinder rods. Nonreciprocal self-collimation transmission is found by means of band structure and equi-frequency contours (EFCs) calculations. Introducing progressively tilting flat EFC by optimizing the structure of GPC, nonreciprocal spatial wavelength division can be arrived without introducing any corrugations inside the structure. Meanwhile, the frequency range for the nonreciprocal spatial wavelength division can also be flexibly manipulated by the external static magnetic field(ESMF).

1. Introduction

Due to its unique and engineerable dispersion relations, self-collimation (SC) of photonic crystals (PhCs) have been used to implement numerous devices with outstanding performance from microwaves to optical frequency range. SC originates from a zero-curvature segment of the EFC; all modes within the flat EFC segment propagate in the same direction and have the ability of healing themselves. Thus the wave diffraction is eliminated and keeping its profile unchanged without broadening, which can be views as a boundary-less waveguide. This property allows for convenient optical applications such as bending [1], interferometer [2], filter [3], polarization splitter [4], and slow light propagation [5]. Experiments have proved the robustness of SC in a silicon platform [6、7]. Not only found in PCs, SC has also been found in low index media and metamaterials [8–10].

Nonreciprocity are of great importance in applied physics. We know that there exist three generally asymmetric systems that are possible to realize a nonreciprocal or unidirectional beam transmission: (1) a magneto-optic (MO) medium [11、12]; (2) a nonlinear medium [13、14]; and (3) a mode converter in the asymmetric structure composed of the linear and isotropic media [15、16]. Among them, GPCs have attracted a lot of attention to achieve nonreciprocity, unidirectionality, and enhancement of MO effects because of its convenient realization. For example, in presence of a static magnetic field, the GPC made of semi-cylinders rods shows unidirectional body wave due to the symmetry breaking of both parity (P) and time-reversal (T).

Wavelength division demultiplexing (WDD) has striking effects on high capacity optical communication systems. There are various techniques that can be used for designing optical WDD devices, for instance, photonic crystal superprism and superlens [17], graded index planar structures [18] and self-collimation effect [19]. This study aims at investigating the wavelength selective capabilities of the newly proposed GPCs structure. The nonreciprocal self-collimation phenomenon is introduced to design wavelength selective media. By progressively tilting flat contours, the proposed structure may operate within the frequency interval from 0.585(2πc/a) to 0.64(2πc/a) over a large bandwidth of 8.98%. And a frequency tunability can be realized by ESMF.

2. Asymmetrical GPCs and nonreciprocal transmission

Considering a gyromagnetic medium made up of ferrite semi-cylinder rods as shown in Fig. 1(a); the rods are inserted in air in square lattice with lattice constant a. The rods' axes are along the z direction and a static magnetic field also along this direction. Here, we only consider the TM polarized electromagnetic wave of which the ac electric field parallels to the z-axis. Equation 1 gives the magnetic permeability within the rods, which is a tensor.

$$\bar{\bar{\mu}}_r = \begin{pmatrix} \mu & -j\kappa & 0 \\ j\kappa & \mu & 0 \\ 0 & 0 & 1 \end{pmatrix} \tag{1}$$

The diagonal and off-diagonal elements are, respectively, $\mu = 1 + \omega_m(\omega_0 + j\alpha\omega)/((\omega_0 + j\alpha\omega)^2 - \omega^2)$ and $\kappa = \omega\omega_m/((\omega_0 + j\alpha\omega)^2 - \omega^2)$, where $\omega_0 = 2\pi\gamma H_0$ is the resonance frequency and γ is the gyro-magnetic ratio. The effective magnetic field H_0 is the sum of the applied an ESMF. $\omega_m = 4\pi M_s$ is the characteristic frequency and $4\pi M_s$ is the saturation magnetization, and α is the damping coefficient of the ferrite.

Figure. 1(a) shows the EFC of the fifth band of the GPC in Brillouin zone. We can find the EFC vary slowly, especially for the frequencies over 0.62(2πc/a). This indicates for the wide range of incident angles the refracted wave will go in same direction so that the profile of the wave will not broaden. For example, at the frequency of 0.631(2πc/a) the refracted wave will go along the y-direction for incident wave impinging from low part at the interface of GPCs and air(parallel to x-axis) in the range 0 to 30 degree with respect to x-axis, showing a typical feature of SC.

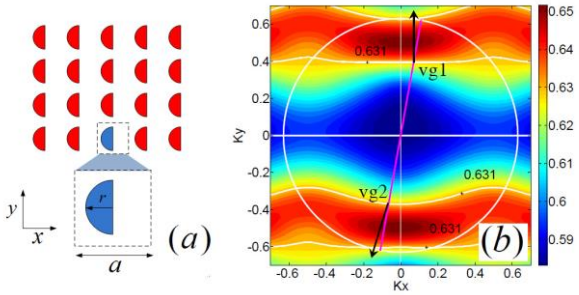

Figure1: (a) Schematic GPC consists of the semi-cylinder rods in square lattice. The lattice constant a= 10mm and radius of semi-cylinder r=3mm. (b) Equifrequency contours plot for the fifth band of the GPC. Vg1 and Vg2 show the directions of refracted waves corresponding to a pair of counter incident waves represented by pink lines, which are 19° with respect to y-axis.

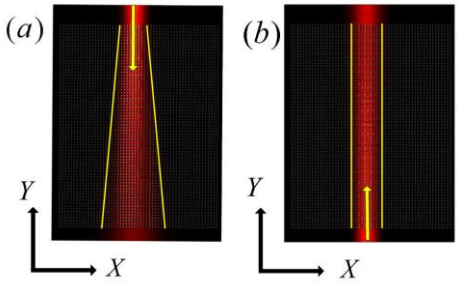

Figure2: Distribution of electric field magnitude at f =0.631 (2πc/a) simulated by COMSOL. (a) for the input wave incident from top, (b) wave incident from the bottom. The arrow represent the direction of incident wave.

Different from the conventional PCs, the EFC shown in Fig. 1(b) are asymmetric relative to the x-axis; there is a shift of contours along y-axis. Therefore, the contour shape of the same frequency shows some difference in the upper and lower parts of the EFC. As shown in Fig. 1(b), when wave impinges from upper part of GPC, then the refracted wave will slightly deviated from y-axis, showing non-reciprocal wave refraction in opposite direction of GPC. In short, the different curvature of the contours causes the effect of SC nonreciprocal. Figure 2 illustrates the distribution of electric field magnitude in the GPC when incident waves impinge on GPC above and below, respectively. It is easy to identify that field confinement along the propagation direction is better for the incident wave comes from GPC below, coincident with contours in Fig. 1(b). The results indicate the self-collimation in GPC is nonreciprocal.

3. Signal separation applications

Nonreciprocal self-collimation shown in above can be used to separate an electromagnetic (EM) signal into partial waves it contains. Figure 3(a) shows the working principle. Suppose an EM signal include the frequencies covering a band of GPC shown in Fig. 3(a). When the EM signal projects on the interface of GPC along the red line, the signal will be refracted in the GPC and many rays occur which propagates along different directions according to their frequencies. Figure 3(b) displays the details of the directions of the refracted rays. It is clear that waves with different frequencies will go along different directions. Because of the contours at these frequencies varying slowly, the refracted waves will be self-collimated. Therefore, wave beam can follow different paths (directions) inside GPC and enables the incident wave signals to resolve spatially into individual channels inside the structure.

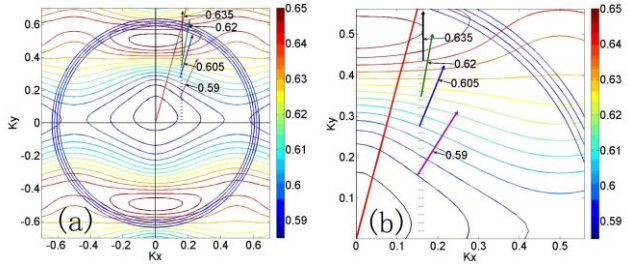

Figure 3: (a) Calculated EFC of the fifth band of square lattice GPCs and (b) detailed representation of the same band EFC. The red line shows the direction of incident wave and short arrows represent the direction of refraction waves at different frequencies.

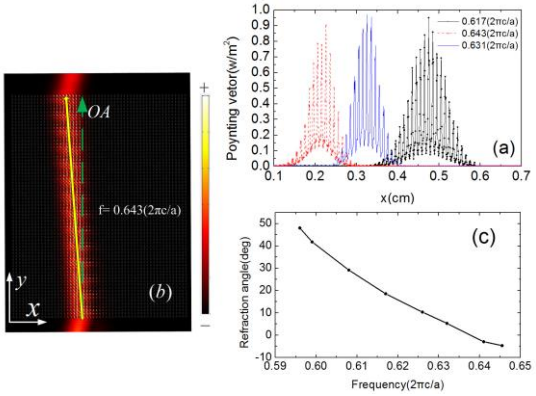

Figure 4: (a) High channel separation (low crosstalk) in the frequencies of 0.617(2πc/a), 0.631(2πc/a), and 0.643(2πc/a), respectively. (b) The spatial intensity electric field distribution of square lattice GPCs in a frequency of 0.643(2πc/a). (c) Propagation angle in terms of operating frequencies.

Figure 4 illustrates the angle resolved incident signal. A slab of GPC in the structure of Fig. 1(a) having dimension 55a x 70a is used for demonstration, where a is the lattice constant of GPC. An EM signal which covers the frequency range shown in Fig. 3(a) with same amplitude is assumed projected on the GPC. After the refracted signal goes across the GPC, the signal are separated into partial wave that can be picked up at different position along x-axis at the other end of GPC as shown in Fig. 3(a). In this way the incident

signal with different frequencies is separated into the different channels without the waveguide depending on the structural corrugations or defects. Because of the SC, the energy loss in the wave separation is lower. As shown in Fig. 3(b) the partial wave of the signal at import and out port has almost the same magnitude and the propagating wave shows a better self-collimation.

One consideration is the spatial separation of the signal in terms of their frequency. The effect of separation can be revealed from the refraction angles against the frequency. For example, when EM signal projects on GPC below with incident angle 19° [with respect to y-axis, see Fig. 3 (b)], the refraction angles as a function of frequency will be as shown in Fig. 4(c). The frequency and the angle are almost in linear relationship. This characteristic is preferred in implementation of GPCs as a frequency selective device. In the frequency range of 0.591(2πc/a)-0.640(2πc/a), the refraction angle varies 52.7°. That corresponds to an refraction angle per wavelength $\Delta\theta/\Delta\lambda = 0.09$ (deg/mm). It can facilitate the selection of different separation frequency.

4. Conclusions

We have shown within the GPC fabricated by ferrite semi-cylinder rods the self-collimated waves propagation would be happen, and self-collimated waves are nonreciprocal in counter directions due to the time and mirror symmetry breaking. A potential application of this kind of GPC is the EM signal separation. The working principle is the refracted EM signal will be separated into different wave channels according to their frequency for the signal incident at a given incident angle. An example is given and the results of signal separation is shown.

Acknowledgements

This work was supported by the NSFC (61271080, 61071007, and 61001017) and RFDP (20110091110030, 20100091120045).

References

[1] X. Yu, S. Fan, Bends and splitters for self-collimated beams in photonic crystals, Applied Physics Letters, 83: 3251–3253, 2003.

[2] D. Zhao, J. Zhang, P. Yao, X. Jiang, and X. Chen, Photonic crystal mach-zehnder interferometer based on self-collimation, Appl. Phys. Lett. , 90: 231114 ,2007.

[3] X. Chen, Z. Qiang, D. Zhao, H. Li, Y. Qiu, W. Yang, and W. Zhou, Polarization-independent drop filters based on photonic crystal self-collimation ring resonators, Opt. Express , 17:19808–19813,2009.

[4] V. Zabelin, L. Dunbar, N. Le Thomas, R. Houdre, M. Kotlyar, L. O'Faolain, and T. Krauss, Self-collimating photonic crystal polarization beam splitter, Opt. Lett. , 32: 530–532,2007.

[5] J. Arlandis, E. Centeno, R. Polles, A. Moreau, J. Campos, O. Gauthier-Lafaye, and A. Monmayrant, Mesoscopic self-collimation and slow light in all-positive index layered photonic crystals, Phys. Rev. Lett. , 108:037401, 2012.

[6] P. T. Rakich, M. R. Dahlem, S. Tandon, M. Ibanescu, M. Soljacic, G. S. Petrich, J. D. Joannopoulos, L. A. Kolodziejski, and E. P. Ippen, Achieving centimetre-scale supercollimation in a large-area two-dimensional photonic crystal, Nat. Mater. , 5:93–96, 2006.

[7] H. Li, A.Wu, W. Li, X. Lin, C. Qiu, Z. Sheng, X.Wang, S. Zou, and F. Gan, Millimeter-Scale and Large-Angle Self-Collimation in a Photonic Crystal Composed of Silicon Nanorods, IEEE Photonics J. , 5:2201306, 2013.

[8] V. Mocella, S. Cabrini, A. Chang, P. Dardano, L. Moretti, I. Rendina, D. Olynick, B. Harteneck, and S. Dhuey, Self-collimation of light over millimeter-scale distance in a quasi-zero-average-index metamaterial, Phys. Rev. Lett., 102:133902, 2009.

[9] X. Lin, X. Zhang, L. Chen, M. Soljacic, and Xunya Jiang, Super-collimation with high frequency sensitivity in 2D photonic crystals induced by saddle-type van Hove singularities, Opt. Express, 21: 30140–30147, 2013.

[10] R. Polles, E. Centeno, J. Arlandis, and A. Moreau, Self-collimation and focusing effects in zero-average index metamaterials, Opt. Express, 19: 6149–6154, 2011.

[11] C. He, M. Lu, X. Heng, L. Feng, and Y. Chen, Parity-time electromagnetic diodes in a two-dimensional nonreciprocal photonic crystal, Phys. Rev. B, 83: 075117, 2011.

[12] J. Lian, J. X. Fu, L. Gan, and Z. Y. Li, Robust and disorder-immune magnetically tunable one-way waveguides in a gyromagnetic photonic crystal, Phys. Rev. B, 85:125108, 2012.

[13] X. Hu, C. Xin, Z. Li, and Q. Gong, Ultrahigh-contrast all-optical diodes based on tunable surface plasmon polaritons, New J. Phys. ,12:023029, 2010.

[14] X. S. Lin, W. Q. Wu, H. Zhou, K. F. Zhou, and S. Lan, Enhancement of unidirectional transmission through the coupling of nonlinear photonic crystal defects, Opt. Express, 14(6):2429–2439, 2006.

[15] C. Menzel, C. Helgert, C. Rockstuhl, E. B. Kley, A. Tünnermann, T. Pertsch, and F. Lederer, Phys. Rev. Lett.,104:253902,2010.

[16] W. Ye, X. Yuan, and C. Zeng, Unidirectional transmission realized by two nonparallel gratings made of isotropic media, Optics Letters,36(15): 2842-2844, 2011.

[17] T. Matsumoto, S. Fujita and T. Baba, Wavelength demultiplexer consisting of Photonic crystal superprism and superlens, Opt. Express, 13(26): 10768-10776, 2005.

[18] H. A. B. Salameh and M. I. Irshid, Wavelength-division demultiplexing using graded-index planar structures,J. Lightw. Technol., 24(6):2401–2408, 2006.

[19] M. Turduev , I. H. Giden, H. Kurt, Extraordinary wavelength dependence of self-collimation effect in photonic crystal with low structural symmetry,

Photonics and Nanostructures-Fundamentals and Applications, 11:241-252, 2013 .

Topology-induced, strongly diamagnetic response of hollow structured metals at broadband microwave frequencies

Shahzad Anwar, Sucheng Li, Shuo Li, Qian Duan, Weixin Lu, and Bo Hou*

College of Physics, Optoelectronics and Energy, Soochow University, 1 Shizi Street, Suzhou 215006, China
*corresponding author, E-mail: houbo@suda.edu.cn

Abstract

Fractal is a type of exotic geometrical shape. By employing the H-fractal and the effective medium view, we show a broadband, strongly diamagnetic response, μ_r^{eff}~0, arising from the structured metallic plate with hollow fractal apertures and without loading high-permittivity dielectrics. In particular, such ~0 permeability is induced by the inherent topology of the fractal aperture, and is hardly achieved among other metallodielectric structures with low volumetric ratio of metal. As a demonstration, we present a design of structured metal of 64% hollowness, which gives rise to a close-to-zero effective permeability with relative bandwidth 175%.

1. Introduction

Recently, artificial magnetism without using magnetic components is receiving the intense attentions from researchers, and has been realized over the broad electromagnetic (EM) spectrum ranging from microwave to infrared and visible [1-8]. The relevant magnetic properties are readily tailored by the deterministic geometrical structures, and thus bring about many novel EM phenomena and materials, including negative refraction [1], cloaking [9], zero-index materials [10-13] and so on. For the artificial metallic structures, two typical configurations are implemented to conceive the emergent magnetism at microwave frequencies.

In the first configuration, the structures packed by subwavelength metallic elements, such as, rods and spheres, produce the moderately diamagnetic response featured by the broadband spectrum [14-17]. According to the John Lam's calculation or the Maxwell-Garnett effective medium theory, the effective relative permeability of the typical metallodielectric composites at microwave frequencies has a loose approximation, $\mu_r^{eff} \approx 1-\xi$, where ξ is the filling ratio of the metallic parts [14-17]. In a physical intuition, the metal has a good conductivity at the whole microwave regime, and excludes the EM field from its body like perfect electric conductor (PEC). Due to the exit of the magnetic field from the volume occupied by the metallic parts and the absence of the enhancement of the H-field inside the dielectric (or air) matrix, the effective permeability displays a diamagnetic response with the value comparable to the volume fraction of the dielectric (or air) host. The μ_r^{eff} expression implies a geometrical relation. If ξ is small for a structure with low metallic ratio, such as, a lattice of thin conducting wires, the system is usually regarded as nonmagnetic [17,18]. Therefore, in order to obtain the ~0 strong diamagnetism, the heavy volume of metal should be involved in the metallodielectric composites.

The second implementation is the split ring resonator (SRR) metamaterials which enable the intense magnetic effect, even the negative permeability [1,2,7]. Via inducing the resonant current circulating along the split ring made of the very thin conducting wire, a magnetic dipole can be mimicked and the desired magnetic properties can be achieved almost at will. However, the resonance nature of the SRR structure leads to the narrow band feature and constrains the potential broadband application, though the relative usage of metal is tremendously reduced in contrast to the metallodielectric system. Also, it is known that the same magnetic response can be obtained employing the all-dielectric system where the displacement current is resonant in the well-designed dielectric unit with high permittivity [19-26].

Recently, Pendry *et al*. has found that the metallic plate patterned with the subwavelength square holes of size, *d*, and lattice constant, *a*, can achieve a plasma-like dispersive permittivity and thus support the spoof surface plasmon mode [27,28]. Meanwhile, the effective relative permeability displays a nondispersive diamagnetic value, $\mu_r^{eff} = (8/\pi^2)d^2/a^2$, which is almost equal to the area fraction of the holes and consistent with the geometrical relation $1-\xi$. Inspired by this work, we introduce a deeply subwavelength aperture with fractal shape and without high-permittivity dielectric fillers to form the structured metallic plate, and show a strongly diamagnetic response of μ_r^{eff}~0. In particular, such ~0 permeability is not only much less than the area fraction of the apertures, beyond the conventional geometrical relation, but also happens at broadband microwave frequencies. The two characteristics feature our diamagnetic effect distinguishable essentially from the aforementioned two implementations. We demonstrate a numerical design of such structured metal of 64% hollow area, which gives rise to a diamagnetic permeability of value ~0.05 and relative bandwidth 175%.

2. Experiments and simulations

The fractal topology has stimulated many novel applications in electromagnetics, photonics and plasmonics in past decades [29,30]. The fractal aperture without filling high-permittivity dielectrics has been found to support the deeply subwavelength EM resonance which intensely enhances the EM energies inside the narrow aperture and hence leads to the extraordinary transmission effect [31-34]. In this work, the sample is the stainless steel plate slotted with a periodic array of the fractal apertures, illustrated schematically in Fig. 1(a). The unit cell of the array includes a five-level H-fractal slit structure, where the longest slit (the 1st level) is 10 mm and the width of each slit is 0.8 mm. Microwave spectra at normal incidence were measured by a network analyzer (Agilent N5230C) and two identical waveguide horn antennas employed as the transmitter and the receiver of EM waves. Since we are interested in the fundamental resonance of the aperture, we set the incident electric field perpendicular to the 1st level slit of the fractal pattern. On the other hand, we have done finite-difference time-domain (FDTD) simulations employing periodic boundary condition and PEC approximation to understand the measured results [35].

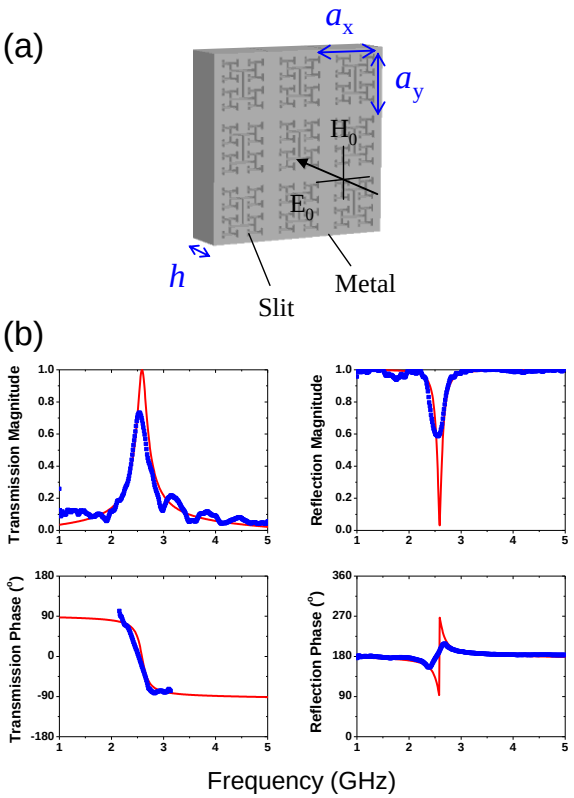

Figure 1: (a) The schematic picture where EM wave is incident normally upon the metal plate. The incident electric field is perpendicular to the 1st level slit (the vertical longest slit). The thickness of the metal plate is h=6mm, and the lattice constants of the fractal aperture array are a_x=21mm and a_y=23mm along two directions, respectively. (b) The transmission and reflection spectra including magnitude and phase (symbols for measurement and line for simulation). At the frequencies where the transmission magnitude is very low, the transmission phase becomes not well-defined and thereby is not shown.

3. Results and discussions

Figure 1(b) shows the transmission and reflection spectra of the fractal aperture array at normal incidence. Good agreement between the measurement and the simulation is seen. Note that there is a transmission resonance located at ~2.5GHz, and the resonant wavelength is much larger than both the slit width and the lattice constant. In particular, the transmission phase is zero at the resonance frequency, which implies that the wave experiences no phase change when traveling through the aperture. Our previous study has revealed the resonance comes from the cutoff of the waveguiding mode inside the fractal aperture [32].

The subwavelength feature allows us to describe the structured plate with the effective medium view. In Fig. 2(a), we have plotted the simulated reflection and transmission spectra of the structured plate of thickness h=210mm. Here the thickness is required to be not less than the lattice constant, so that the effective parameters represent precisely the EM property of the metamaterial in bulk state. From these spectra, we can retrieve the effective parameter ε_r^{eff} and μ_r^{eff} (including real and imaginary part) [36,37]. ε_r^{eff} and μ_r^{eff} here are understood as two of Cartesian components of relative permittivity and permeability tensor along the x- and y-direction, respectively, since the transmission and reflection spectra will be different upon changing the incident polarization.

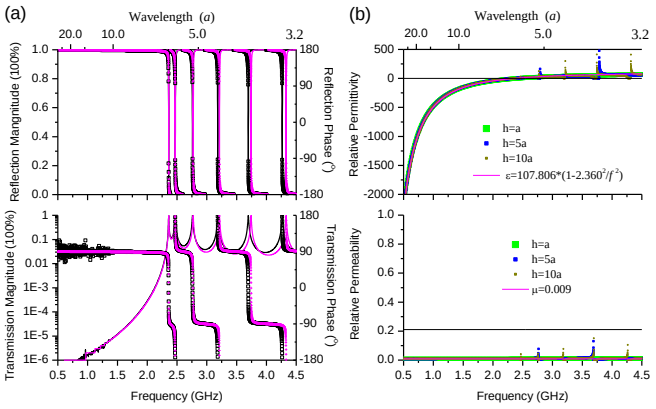

Figure 2: (a) The reflection and transmission spectra (line for magnitude and symbol for phase) of the metal plate, h=210mm, at the normal incidence from the numerical simulation (black line and black symbols) and from the effective parameter calculation (pink line and pink symbols). (b) The retrieved (symbols) and fitted (lines) effective parameters of the metal plate at different thickness, h=a, 5a, and 10a. The upper horizontal axes denote the wavelength in vacuum which has been normalized with respect to the lattice constant (a=a_x=21mm).

The retrieved effective permittivity and permeability are shown in the upper and lower panel in Fig. 2(b), respectively, for three thicknesses of plates. We examined

three thicknesses to assure the insignificant variation of effective parameters with increasing h. Their imaginary parts all are found to be zero because the PEC approximation is adopted in simulation, and are not plotted here. The spikes in the curves originate from the branch jump of complex logarithm function during the retrievement for the thick enough structure. The horizontal black lines represent ε_r=0 and μ_r=0.21 (the area fraction of fractal slits), respectively. It is found that the permittivity has the plasmon-typed behavior $1-\omega_p^2/\omega^2$, as theorized by Pendry *et al*., and that the permeability is much smaller than the area fraction of fractal slits.

We employed the permittivity of $A*\left(1-\omega_p^2/\omega^2\right)$ and a constant permeability to fit the retrieved data. The plasma frequency ω_p is determined from the cross point between the retrieved permittivity and the line ε_r=0, the parameter A and the permeability are obtained through fitting with the retrieved data at lower frequencies where the effective medium approximation is best suitable. For the plate of thickness, h=10a, we found

$$\varepsilon_r^{\ eff} = 107.806\times(1-2.360^2/f^2)$$
$$\mu_r^{\ eff} = 0.009 = 1/A, \qquad (1)$$

where the frequency, $f=\omega/2\pi$, takes the GHz unit. The fitted parameters are shown in Fig. 2(b). To verify this pair of effective parameters, we recalculated the reflection and transmission of the metal plate, h=10a, using expression (1), and compared the calculation with the simulation in Fig. 2(a). The excellent agreement at lower frequencies indicates the validity of $\varepsilon_r^{\ eff}$ and $\mu_r^{\ eff}$ in the long wavelength region.

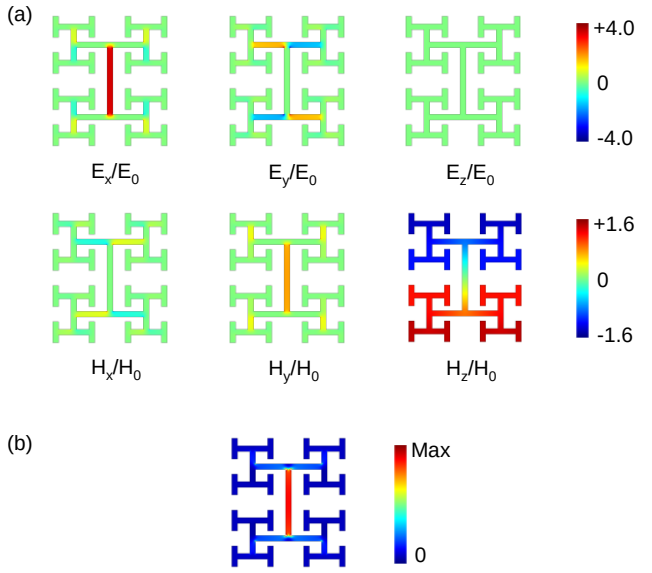

Figure 3: (a) The distributions of the electric and magnetic field components which have been normalized with respect to the incident ones, E_0 and H_0, respectively. (b) The distribution of the magnitude of the time-averaged power flow (z-component). The field maps are snapshot in the middle plane of the structured plate, h=21mm, and at the off-resonance frequency, 2.0GHz.

A microscopic origin responsible for the diamagnetic property can be qualitatively revealed by visualizing the simulated field distribution inside the aperture. In Fig. 3(a), we have plotted the electric and magnetic field components at frequency 2.0GHz for the structured plate (the similar distributions can also be obtained at other frequencies). For the electric field, the x-component is enhanced with respect to the incident one, E_0, because of the fundamental resonance effect of the fractal aperture; the y-component is spatially averaged to be zero; the z-component is forced to be zero, due to the boundary condition of PEC. For the magnetic field, the x- and z-components are spatially averaged to be zero, though the latter is slightly enhanced; the y-component is suppressed to be less than 1, which gives rise to the diamagnetism.

The quantitative calculation has found that under long wavelength approximation $\mu_r^{\ eff}=S_0^{\ 2}$, where S_0 is the overlap integral between the normally incident plane wave and the fundamental waveguiding mode inside the aperture [28, 38-40]. In fact, S_0 represents the energy exchanging channel between the free space and the structured plate, and is related physically to the distribution of the z-component of the power flow. Different drastically from the ordinarily shaped apertures (e.g., square hole), the power flow of the fractal aperture is concentrated only in the lower levels, mainly the first level slit, with negligible values in the higher level slits, as illustrated in Fig. 3(b). Therefore, the actual area for efficiently energy exchanging between the plane wave and the guided wave is much less than the nominal opening of the aperture.

With increasing the fractal levels, the proportion of the hollow area within the structured plate will increase. Being a kind of space-filling curve, the H pattern has the fractal dimension, 2, which means it may tilt completely a solid area in two-dimensional space when the fractal levels approach infinity. As a realistic design, we have added another four levels to the fractal pattern to obtain the 9 level of fractal slits in the inset of Fig. 4. To avoid the unwanted crossover between the slits, the width has been reduced to be 0.4mm, and we slightly shrink the unit cell to be 19.5mm×19.5mm, too. The hollow area portion for the 9 level fractal aperture array reaches 64%, which means the metallic portion is less than half. From the simulated transmission and reflection spectra, the effective permittivity and permeability are retrieved, as plotted in Fig. 4. It is seen that the plasma frequency appears at ~1.1GHz, the relevant wavelength being one order of magnitude larger than the array periodicity. The relative permeability is 0.05, much smaller than the area fraction of the slits. Furthermore, the diamagnetic feature persists to the frequency band from 0.1 to 1.5GHz, corresponding to the 175% relative bandwidth.

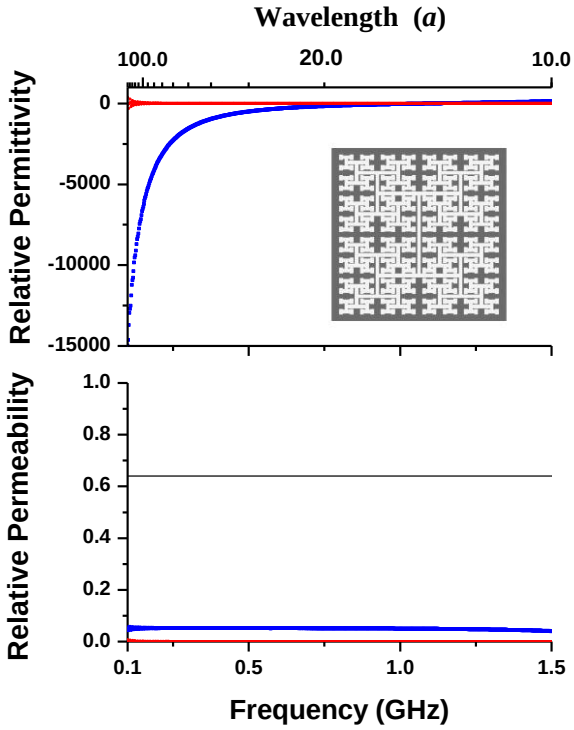

Figure 4: The retrieved effective parameters of the H fractal aperture array. The blue (red) lines denote the real (imaginary) parts of ε_r^{eff} and μ_r^{eff}, respectively. The effective relative permeability μ_r^{eff} =0.05, much smaller than the area fraction of the fractal slits, 0.64 (black line). The inset illustrates schematically a unit cell of the aperture array, where the lattice constant along the *x*- and *y*-direction is 19.5mm. The upper horizontal axis is the wavelength in vacuum which has been normalized with respect to the lattice constant.

4. Conclusions

In conclusion, we have introduced a deeply subwavelength aperture with fractal shape and without loading high-index dielectric to the structured metallic plate, and achieved a strongly diamagnetic response from the effective medium point of view. We have demonstrated a design of structured metal of 64% hollow area, which gives rise to a close-to-zero effective permeability with the 175% relative bandwidth. In particular, such ~0 permeability is beyond conventional volumetric relation of the diamagnetism in metallodielectric structures, and is related to the unique fractal topology. Our work might have some potential applications in employing metal foams to design functional materials [41,42].

Acknowledgements

This work was supported by the National Natural Science Foundation of China (Grant Nos. 11104198, 11474212), the Natural Science Foundation of Jiangsu Province (Grant No. BK20141191) and a Project Funded by the Priority Academic Program Development (PAPD) of Jiangsu Higher Education Institutions.

References

[1] D. R. Smith, J. B. Pendry, M. C. K. Wiltshire, Metamaterials and negative refractive index, *Science* 305, 788 (2004).

[2] J. B. Pendry, A. J. Holden, D. J. Robbins, and W. J. Stewart, Magnetism from conductors and enhanced nonlinear phenomena, *IEEE Trans. Microwave Theory Tech*. 47, 2075 (1999).

[3] T. J. Yen, W. J. Padilla, N. Fang, D. C. Vier, D. R. Smith et al. Terahertz magnetic response from artificial materials, *Science* 303, 1494 (2004).

[4] A. N. Grigorenko, A. K. Geim, H. F. Gleeson, Y. Zhang, A. A. Firsov *et al*. Nanofabricated media with negative permeability at visible frequencies, *Nature* 438, 335 (2005).

[5] N. Liu, L. Fu, S. Kaiser, H. Schweizer, and H. Giessen, Plasmonic building blocks for magnetic molecules in three dimensional optical metamaterials, *Adv. Mater*. 20, 3859 (2008).

[6] U. K. Chettiar, S. Xiao, A. V. Kildishev, W. Cai, H. K. Yuan, V. P. Drachey, and V. M. Shalaev, Optical metamagnetism and negative-index metamaterials, *MRS Bulletin* 33: 921-926 (2008).

[7] L. Zhou, X. Huang, Z. Yi, and S. Chui, Resonance properties of metallic ring systems, *Mater. Today* 12, 52 (2009).

[8] N. Papasimakis, S. Thongrattanasiri, N. I. Zheludev, and F. J. Garcia de Abajo, The magnetic response of graphene split-ring metamaterials, *Light: Science & Applications* 2, e78 (2013).

[9] D. Schurig, J. J. Mock, B. J. Justice, *et al*. Metamaterials electromagnetic cloak at microwave frequencies, *Science* 314, 977-980 (2006).

[10] N. Engheta, Pursuing near-zero response, *Science* 340, 286-287 (2013).

[11] S. Zhong and S. He, Ultrathin and lightweight microwave absorbers made of mu-near-zero metamaterials, *Sci. Rep*. 3, 2083 (2013).

[12] Q. Cheng, W. X. Jiang, and T. J. Cui, Spatial power combination for omnidirectional radiation via anisotropic metamaterials, *Phys. Rev. Lett*. 108, 213903 (2012).

[13] J. Luo, P. Xu, L. Gao, Y. Lai, and H. Chen, Manipulate the transmissions using index-near-zero or epsilon-near-zero metamaterials with coated defects, *Plasmonics* 7, 353-358 (2012).

[14] J. Lam, "Magnetic permeability of a simple cubic lattice of conducting magnetic spheres, *J. Appl. Phys*. 60, 4230 (1986).

[15] X. Hu, C. T. Chan, J. Zi, M. Li, and K.-M. Ho, Diamagnetic response of metallic photonic crystals at

infrared and visible frequencies, *Phys. Rev. Lett*. 96, 223901 (2006).

[16] A. K. Sarychev and V. M. Shalaev, *Electrodynamics of Metamaterials* (World Scientific, Singapore, 2007).

[17] J. Shin, J. T. Shen, and S. Fan, Three-Dimensional metamaterials with an ultrahigh effective refractive index over a broad bandwidth, *Phys. Rev. Lett*. 102, 093903 (2009).

[18] A. Pimeonov and A. Loidl, Conductivity and permittivity of two-dimensional metallic photonic crystals, *Phys. Rev. Lett*. 96, 063903 (2006).

[19] S. O'Brien and J. B. Pendry, Photonic band-gap effects and magnetic activity in dielectric composites, *J. Phys.: Cond. Matter* 14, 4035-4044 (2002).

[20] C. L. Holloway, E. F. Kuester, J. Baker-Jarvis, and P. Kabos, A double negative (DNG) composite medium composed of magnetodielectric spherical particles embeded in a matrix, *IEEE Trans. Antenn. Propag*. 51, 2596 (2003).

[21] B.-J. Seo, T. Ueda, T. Itoh, and H. Fetterman, Isotropic left handed material at optical frequency with dielectric spheres embedded in negative permittivity medium, *Appl. Phys. Lett*. 88, 161122 (2006).

[22] L. Peng, L. Ran, H. Chen, H. Zhang, J. A. Kong, and T. M. Grzegorczyk, Experimental observation of left-handed behavior in an array of standard dielectric resonators, *Phys. Rev. Lett*. 98, 157403 (2007).

[23] Q. Zhao, L. Kang, B. Du, H. Zhao, Q. Xie, X. Huang, B. Li, J. Zhou, and L. Li, Experimental demonstration of isotropic negative permeability in a three-dimensional dielectric composite, *Phys. Rev. Lett*. 101, 027402 (2008).

[24] Q. Zhao, J. Zhou, F. zhang, and D. Lippens, Mie resonance-based dielectric metamaterials, *Mater. Today* 12, 60 (2009).

[25] B.-I. Popa and S. A. Cummer, Compact dielectric particles as a building block for low-loss magnetic metamaterials, *Phys. Rev. Lett*. 100, 207401 (2008).

[26] L. Shi, T. U. Tuzer, R. Fenollosa, and F. Meseguer, A new dielectric metamaterial buiding block with a strong magnetic response in the sub-1.5-micrometer region: Silicon colloid nanocavities, *Adv. Mater*. 24, 5934-5938 (2012).

[27] J. B. Pendry, L. Martin-Moreno, F. J. Garcia-Vidal, Mimicking surface plasmons with structured surfaces, *Science* 305, 847 (2004).

[28] F. J. Garcia-Vidal, L. Martin-Moreno, and J. B. Pendry, Surfaces with holes in them: new plasmonic metamterials, *J. Opt. A: Pure Appl. Opt.* 7, S97-S101 (2005).

[29] *Frontiers in Electromagnetics*, edited by D. H. Werner and R. Mittra, (IEEE Press, Piscataway, NJ, 2000).

[30] L. Dal Negro and S. V. Boriskina, Deterministic aperiodic nanostructures for photonics and plasmonics applications, *Laser & Photon. Rev*. 6, 178-218 (2012).

[31] J. A. Matteo and L. Hesselink, Fractal extensions of near-field aperture shapes for enhanced transmission and resolution, *Opt. Express* 13, 636-647 (2005).

[32] W. J. Wen, L. Zhou, B. Hou, C. T. Chan, and P. Sheng, Resonant transmission of microwaves through subwavelength fractal slits in a metallic plate, *Phys. Rev. B* 72, 153406 (2005).

[33] M. Sun, R.-J. Liu, Z.-Y. Li, B.-Y. Cheng, D.-Z. Zhang, H. Yang, and A. Jin, Enhanced near-infrared transmission through periodic H-shaped arrays, *Physics Letters A* 365 510–513 (2007).

[34] Y. J. Bao, *et al.* Surface-plasmon-enhanced transmission through metallic film perforated with fractal-featured aperture array, *Appl. Phys. Lett*. 90, 251914 (2007).

[35] Simulations were performed using the commercial FDTD package QuickWave 2012 (http://www.qwed.com.pl).

[36] D. R. Smith, S. Schultz, P. Markos, and C. M. Soukoulis, Determination of effective permittivity and permeability of metamaterials from reflection and transmission coefficients, *Phys. Rev. B* 65, 195104 (2002).

[37] J. Baker-Jarvis, *Transmission/Reflection and short-circuit line permittivity measurements*, NIST Technical Note, National Institute of Standards and Technology, Boulder, CO (1990).

[38] X. Huang, S. Xiao, D. Ye, J. Huangfu, Z. Wang, L. Ran, and L. Zhou, Fractal plasmonic metamaterials for subwavelength imaging, *Opt. Express* 18, 10377 (2010).

[39] S. Xiao, Q. He, X. Huang, and L. Zhou, Super imaging with a plasmonic metamaterial: role of aperture shape, *Metamaterials* 5, 112-118 (2011).

[40] Q. He, S. Xiao, X. Li, and L. Zhou, Optic-null medium: realization and applicaitons, *Opt. Express* 21, 28948 (2013).

[41] T. A. Schaedler, A. J. Jacobsen, A. Torrents, A. E. Sorensen, J. Lian, J. R. Greer, L. Valdevit, W. B. Carter, Ultralight metallic microlattices, *Science* 334, 962-965 (2011).

[42] Z.-C. Shi, R.-H. Fan, K.-I. Yan, K. Sun, M. Zhang, C.-G. Wang, X.-F. Liu, and X.-H. Zhang, Preparation of iron networks hosted in porous alumina with tunable negative permittivity and permeability, *Adv. Funct. Mater*. 23, 4123-4132 (2013).

A zero –index Metamaterial Superstrate for Patch Antenna Gain Enhancement

S.M. Chaker, D. Bensafieddine, E. M. Laamari and M. Bouzouad

Telecommunications, Signal and Systems Laboratory,
BP 37G, Route de Ghardaïa, 03000, Laghouat, Algérie.
*corresponding author, E-mail: c.saleh@lagh-univ.dz

Abstract

The objective of this paper is to use a zero refractive index (n) metamaterial as single or double layer superstrate suspended above a microstrip patch antenna (MPA), operating at 43 GHZ, for the gain enhancement. A single metamaterial layer superstrate is composed of a periodic arrangement of Jerusalem cross unit-cells, and behaves as an homogeneous medium characterized by a refractive index close to zero. This metamaterial property allows gathering radiated waves from the antenna and collimates them towards the superstrate normal direction. The proposed design improves the antenna gain by 5.1 dB with single-layer superpstrate, and 7 dB with double-layer superstrate.

1. Introduction

In antenna engineering domain, researchers around the world have to resolve many fundamental challenges [1]. Antennas have to conjugate at the same time a high gain, a wide bandwidth, a diversity of polarization, and a reconfigurable (agile) radiation pattern, while remaining the most compact possible. These characteristics are often conflicting and the use of structured artificial materials bi- and three-dimensional (metamaterials and/or materials with electromagnetic/photonique bandgaps), can offer interesting solutions in this domain[2–5].

In this paper, we use a Jerusalem cross type as a metamaterial unit–cell. An array of these unit–cells is used with an optimum periodicity to design a zero refractive index metamaterial (ZIM). The ZIM material is employed as a single or a double layer superstrate (ZIM-SLS or ZIM-DLS, respectively) above a microstrip patch antenna (MPA). This metamaterial superstrate allows gathering radiated waves from the antenna and collimates them towards the superstrate normal direction. This results in the concentration of electromagnetic energy in this direction and can be effectively used for the antenna gain enhancement.

2. Metamaterial unit cell characterization

The Jerusalem cross elementary unit cell is sketched in figure 1.b. We use a dielectric substrate with a relative permittivity $\varepsilon_r = 2.2$, a thickness $d = 0.8$ mm and a metallization thickness $t = 0.035$ mm [4]. The conducting strip width w, metallization thickness t, substrate permittivity ε_r and thickness d of the unit cell shown in figure 1.a, directly govern the metamaterial electromagnetic properties. Since we have fixed some of them (t, ε_r and d), we use w as design parameter to tune the metamaterial unit cell behavior. A parametric study is used to obtain the dimensions of the metamaterial unit cell. We obtain the constitutive parameters (ε_{eff} and μ_{eff}) and the refractive index of the metamaterial, shown in figure *2*, with the Fresnel inversion method using the of the unit cell. The scattering *S* parameters are obtained by a finite difference based commercial simulation code. It can be seen from figure *4* that the Jerusalem cross based metamaterial exhibits a plasmonic-type permittivity frequency function. For frequencies greater than the plasma frequency, the relative permittivity stays between 0 and 1.

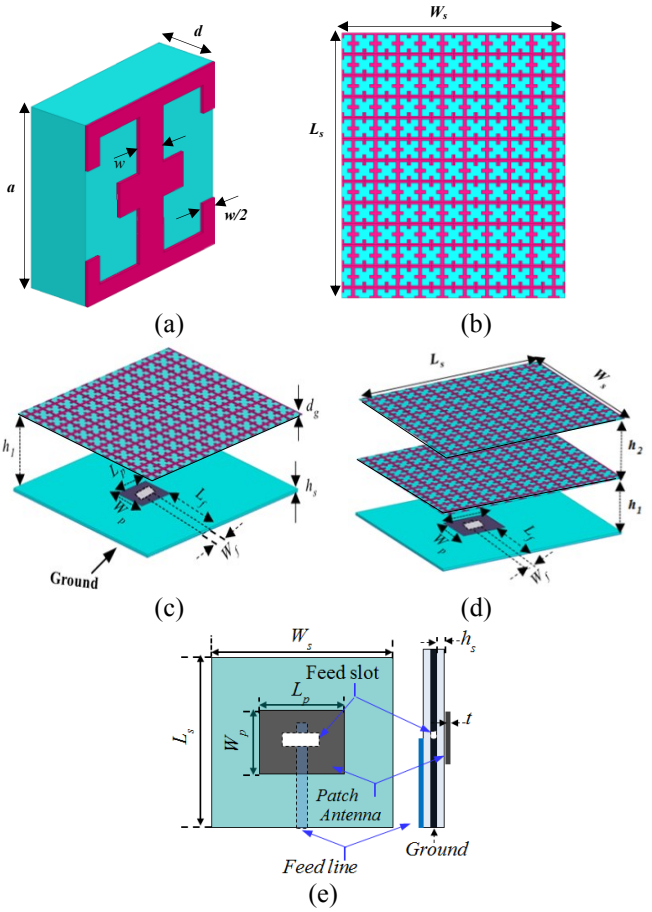

Figure 1: The proposed antenna. (a) unit- cell; (b) bottom view of ZIM superstrate layer; (c) and (d) Perspective views; (e) Antenna slot feeding details. $h = 0.8$, $W = 0.2$, $t = 0.035$, $a = 2$, $L_s = 25$, $W_s = 20$, $h_s = 0.05$, $d_g = 1.6$, $L_p = 0.257$, $W_p = 0.184$, h_1 and h_2 [units=mm].

The metamaterial presents a plasma frequency equal or a little less than 40 GHz and a very low real part (close to zero), in the operating frequency range $(40-45\ \text{GHz})$, which corresponds to the desired profile. Also, the effective permeability presents a profile close to unity. It can be seen that the constitutive parameters (ε_{eff} and μ_{eff}) have positive and close to zero imaginary parts which attests to the low-loss nature of the effective medium. From Figure *4*, it can be seen that the refractive index presents a flat profile close to zero corresponding to the desired ultra refraction $(0 < n < 1)$ [6] low dispersive behavior for the ZIM effective medium, in the operating frequency range $40-45\ \text{GHz}$. These results are obtained for conductor width $w = 0.2\ \text{mm}$.

The MSP antenna operating frequency is $43\ \text{GHz}$, consequently the corresponding wavelength in free space is 7.2 mm. Accordingly, the period a and hence the greatest dimension of the metamaterial unit cell must be much lower than the operating wavelength, to respect the homogenization criterion [7]. So it's fixed at $a = 2\ mm$ (lower than $\lambda/3 \approx 2.4$ mm).

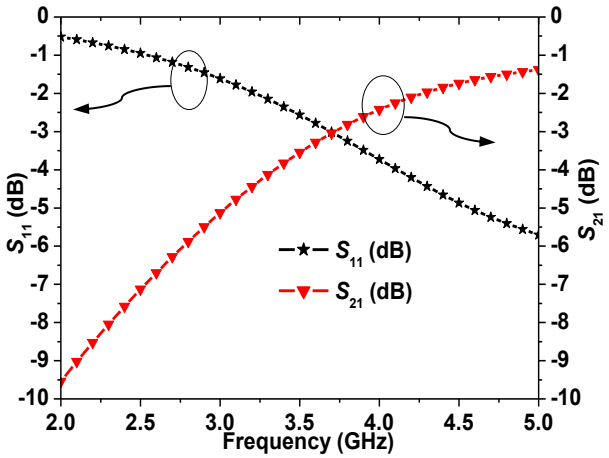

Figure 2: Scattering parameters of the metamaterial unit-cell.

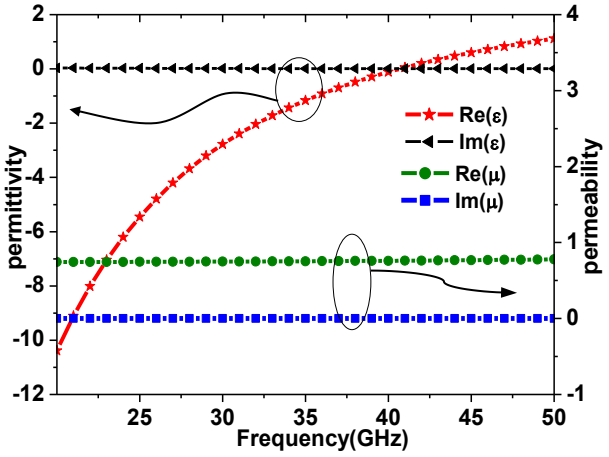

Figure 3: Effective permittivity and permeability of the Jerusalem cross type metamaterial effective medium.

The arrangement of the elementary unit cell in two directions constitutes the metamaterial grid. This metamaterial grid covers the patch antenna and its function is like a lens being able indeed to improve the antenna performances such as gain, directivity, bandwidth [6]-[8]. The unit-cell is modeled by the finite element method with unit cell boundary conditions. The scattering parameters S_{11} (dB) and S_{21} (dB) were calculated over 20-50 GHz frequency band and are shown in figure *2*.

The constitutive parameters of the the Jerusalem cross type metamaterial effective medium (ε_{eff} and μ_{eff}), shown in figure *3*, are extracted from the scattering parameters of the unit-cell using Fresnel inversion method [9]. The

figure *4* shows the metamaterial refractive index. It's clear that the refractive index real part is very close to zero over $40-45$ GHz.

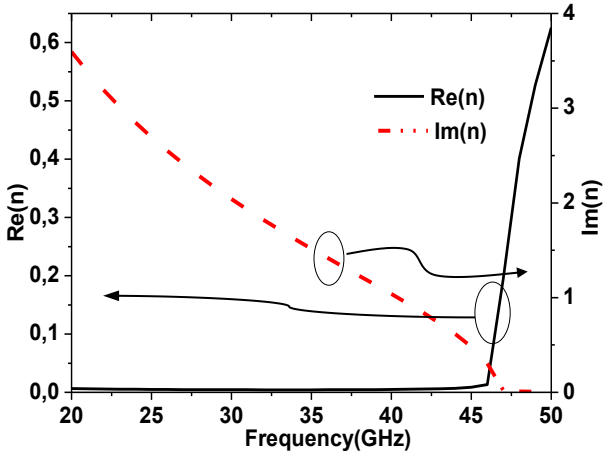

Figure 4: Refractive index of the Jerusalem cross type metamaterial effective medium.

We use the transmitted power as another parameter to appreciate the efficiency of the metamaterial lens. The transmitted power is calculated over the 20-50 GHz frequency band, and is represented in Figure 6. The incident waves travel from the face (A) (no metallized face) to the face (B) (metallized face) of the metamaterial lens, as shown in

Figure *5*. It can be seen from Figure *6*Figure *6* that the transmitted power throw the metamaterial lens is about 70%. The metamaterial lens plays a similar role as the Bragg semi-reflecting mirror.

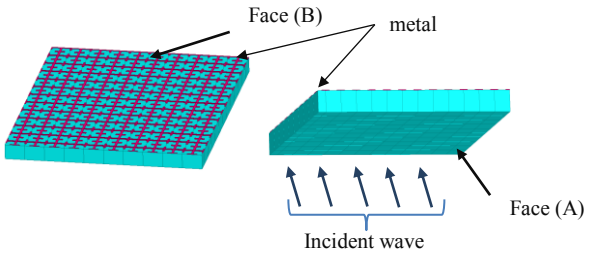

Figure 5 The metamaterial lens (a) top view; (b) bottom view.

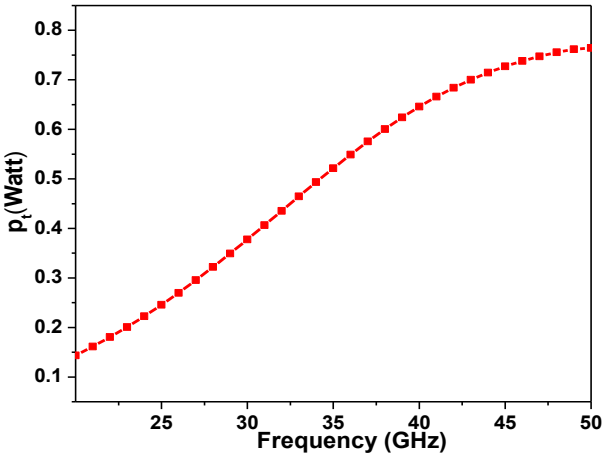

Figure 6: Transmitted power of the metamaterial unit cell.

3. High gain antenna configuration

Our designed high gain antenna is depicted in Figure *1*(c-d). The structure is formed by a slot feed microstrip patch antenna (MPA) on which the ZIM-SLS or ZIM-DLS is superposed. The patch antenna with dimension $W_p \text{x}\, L_p = (0.184 \text{ x } 0.257)$ mm , operating at 43.5 GHz , was realized on a Rogers/duroid 5880 dielectric substrate with dielectric constant $\varepsilon_r = 2.2$ and a thickness $d = 0.8$ mm. The basic building block of the metamaterial superstrate is (are) the ZIM unit-cell as displayed in figure *1*.a with geometrical parameters a w, and t. The unit-cells are arranged in an array with periodicity of $12 \text{ x } 10$, to design a layer of the ZIM superstrate, as shown in Figure 1.b. The perspective views of the proposed antenna with single and double layer superstrate are shown in Figure 1(c-d) respectively. The spacing from the radiator to the bottom of the first layer of the ZIM superstrate is h_1 and h_2 from the top of the first layer to the bottom of the second layer (in the case of the ZIM-DLS). The antenna ground plane and ZIM superstrate have dimensions of $(L_S \text{ x } W_S) = (25 \text{ x } 20)$ mm.

4. Results and discussion

From figure 7, it can be seen that d_g the thickness of the superstrate layers, h_1 the spacing between the patch antenna and the first layer and h_2 the spacing between the first and the second superstrate layer (in case of the ZIM-DLS) are key parameters in the antenna gain improvement. They can be optimized to obtain better antenna realized gain enhancement. A parametric study shows that: i) there is an optimal value for the superstrate layer thickness, that is $d_g = 1.6$ mm, for which the antenna gain is maximized, ii) for the single layer superstrate antenna (SLSA), the spacing h_1 powerfully influences the antenna gain, and iii) for the double layer superstrate antenna (DLSA), as it can be seen from figure *8*, h_1 does not affect strongly the antenna realized gain as h_2 do. Indeed, in the later case, when h_2 varies from 2.2 to 2.4 mm, by a steep 0.1 mm, the gain increases from 12 dB to 13.5 dB and then go back to 11.3 dB. The optimum values for the spacing parameters are $h_1 = 2.2$ mm and $h_2 = 2.3$ mm.

It is observed from figure 9 that the resonance of the MPA is slightly shifted to lower frequency region when loaded with the ZIM superstrate. The frequency operating band of the proposed antenna is, respectively, [41.89-43.84 GHz] and operating frequency shift by about 2 % with a ZIM-SLS, and [41.89-42.8 GHz] and operating frequency shift by about 3.6 %with a ZIM-DLS.

The maximum realized gain of the proposed antenna is found to be 12.3 dB with a ZIM-SLS and 14.2 with a ZIM-DLS. We note that the gain of the proposed antennas is constant throughout the operating frequency band, as illustrated in figure 10. If compared to the MPA on the same Rogers RT substrate, our proposed antenna design exhibits a gain enhancement, respectively, of 5.1 dB with a ZIM-SLS and 7.3 dB, with the ZIM-DLS.

The antenna radiation patterns are illustrated in figure 10-11. It is clear from the plot that loading a microstrip antenna with the ZIM based superstrate, focuses the radiation beamwidth and thereby enhances the antenna directivity. The half-power beamwidth of the antennas, at the operating frequency, in E and H-plane respectively, is observed to be 66.5º and 80.18º, for the antenna alone, 33.64º and 44.8º for the antenna with a single layer superstrate, and 33.84º and 24.89º, for a double layer, as . We observe a half-power beam width reduction of about 68%, with a ZIM-DLS, and 49% with a ZIM-SLS, in the H-plane and 50%, in the E-plane, for the two cases.

Table 1: Half power beam width θ_{-3dB}(deg) and realized gain of the patch antenna with and without ZIM superstrate.

	$\theta_{-3dB}\,(deg)$		Realized gain	B (%)
	E-Plan	H-Plan		
Antenna alone	66.5	80.1	7.2	4.6
Antenna with ZIM-SLS	33.6	44.8	12.3	4.7
Antenna with ZIM-DLS	33.8	24.9	14.2	3.0

From Table 1 and figure 11, we note that even the ZIM-DLS improves the antenna gain by about 13% more that the ZIM-SLS, and reduces the radiation pattern half power beam width to less than 25° in the H-plane: i) it decreases the bandwidth by about 36% while the ZIM-SLS doesn't affects it, ii) shifting the antenna operating frequency by about 3.6 % compared to 2 % for the ZIM-SLS, and iii) gives rise to high side lobe levels in the antenna E-Plane radiation pattern.

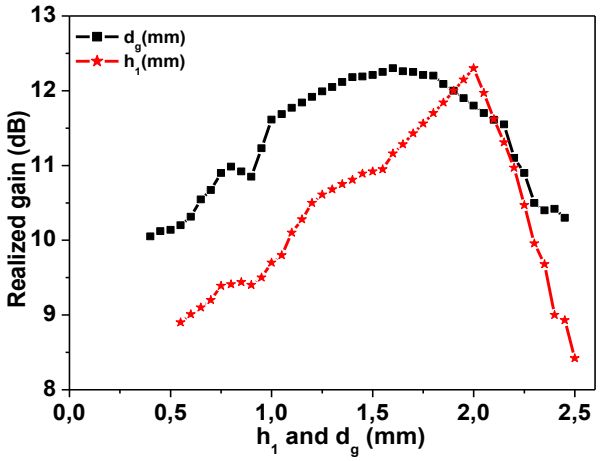

Figure 7: Realized gain of the patch antenna versus the ZIM-SLS spacing h_1 and thickness d_g.

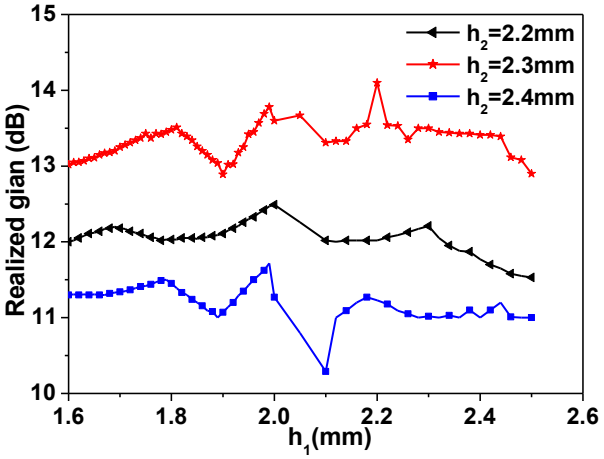

Figure 8: Realized gain of the patch antenna versus the ZIM-DLS spacing h_1 and h_2

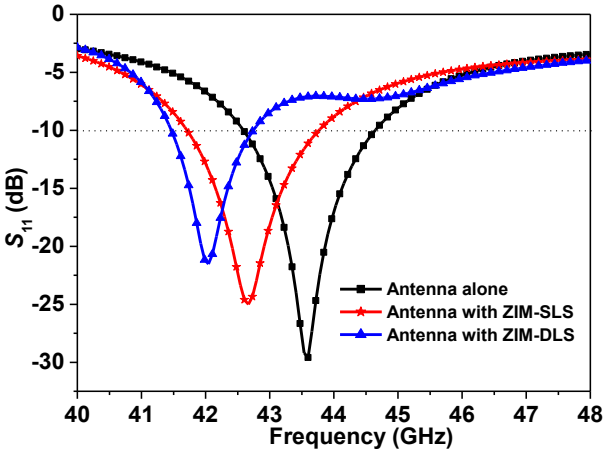

Figure 9: Reflection coefficient of the patch antenna with and without ZIM superstrate

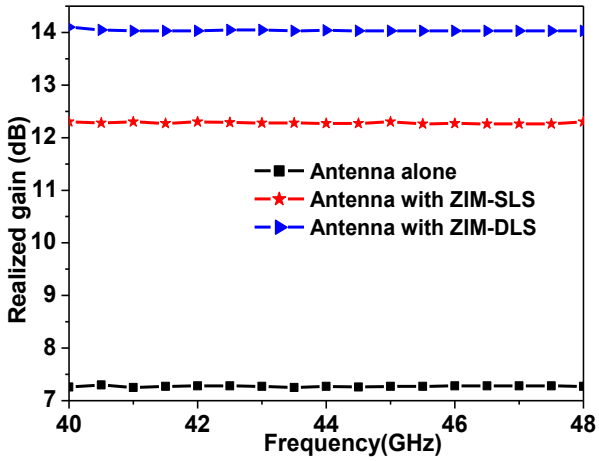

Figure 10: Realized gain of patch antenna with and without ZIM superstrate.

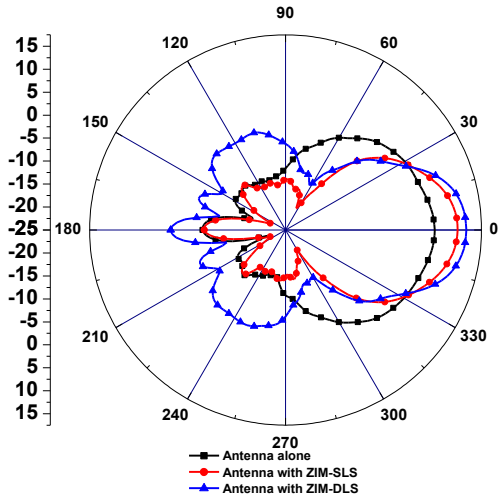

Figure 11: Radiation pattern of the patch antenna with and without ZIM superstrate: E plane ($\varphi = 90^0$).

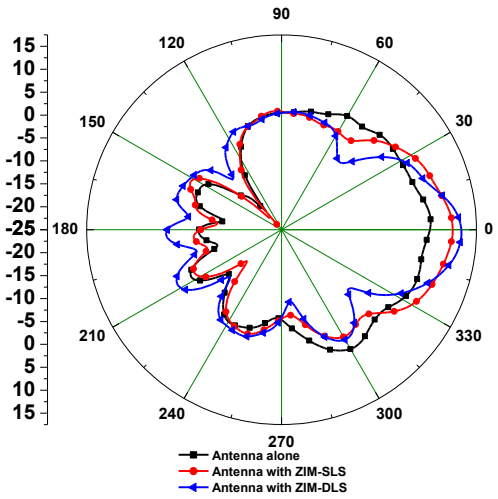

Figure 12: H plane ($\varphi = 0^0$) Radiation pattern of the patch antenna with and without ZIM superstrate: H plane ($\varphi = 0^0$).

5. Conclusion

We have proposed a high gain antenna based on a zero index metamaterial superstrate. The metamateral is designed of Jerusalem cross unit-cell. The extracted metamaterial properties indicate that, the refractive index is close to zero over 40-45 GHz. In order to verify the gain enhancement, the gain of the ZIM superstrate loaded antenna has been compared to a microstrip patch antenna resonating at same frequency. A gain enhancement up to 7 dB, and about 50% half power beam width reduction have been observed for the proposed design. The patch antenna loaded with the ZIM-DLS presents better performances over all antenna characteristics.

References

[1] B. A. Munk, "Metamaterial:Critique and Alternatives.," Wiley, New York, 2009.

[2] J. Dalin, 'Gain improvement of a microstrip patch antenna using metamaterial superstrate with the zero refractive index', International Conference on Microwave and Millimeter Wave Technology (ICMMT), May 2012, China.

[3] G. Augustin, B. P. Chacko and T. A. Denidni, 'A Zero-Index Metamaterial Unit-Cell for Antenna Gain Enhancement', Antennas and Propagation Society International Symposium (APSURSI), IEEE-AP-S, 7-13 July 2013 pp:126 – 127.

[4] M. Bouzouad. « Analyse et conception d'antennes microruban sur des substrats bandes interdites électromagnétique ». Thèse de Doctorat d'État. École nationale polytechnique d'Alger, décembre 2007.

[5] J. Cha and Y. Kuga. 'A steerable array antenna using controllable 4-bit dielectric slab phase shifters on a coplanar waveguide at 24 Ghz', Microwave and optical technology letters, Vol.49, n°12, 2007.

[6] N. Engheta, R.W.Ziolkowski, "Metamaterials physics and engineering explorations", IEEE press, 2006

[7] C.R. Simovski et al., "Homogenization of Planar Bianisotropic Arrays on the dielectric interface", Electromagnetics, 22 : p. 177-189, 2002.

[8] M. Bouzouad, B. Ouagague. *"Antennes accordables à base de métamatériaux"*.15èmesJournées Nationales Microondes,23-24-25 Mai 2007 .Toulouse.

[9] D. R. Smith "Electromagnetic parameter retrieval from inhomogeneous metamaterials" Department of Electrical and Computer Engineering, Duke University, Box 90291, Durham, North Carolina 27708, USA,PHYSICAL REVIEW E 71, 036617 2005.

Monopole antenna with metamaterials to reduce the exposure

Yenny Pinto, Xavier Begaud

[1]Institut Mines Telecom, Telecom ParisTech-LTCI CNRS UMR 5141, Paris, France
*corresponding author, E-mail: pintobal@telecom-paristech.fr

Abstract

This paper presents a simplified model of a terminal mobile where a monopole antenna is associated with three different metamaterials: Artificial Magnetic Conductor (AMC), Electromagnetic Band-Gap (EBG) and Resistive High Impedance Surface (RHIS). The objective is to evaluate what is the metamaterial which is the best solution to reduce exposure. The exposure has been evaluated using a simplified phantom model. Results show that both AMC and RHIS reduce the exposure preserving the antenna performances. A reduction of 23% in SAR 10g is obtained when the monopole is associated with an optimized RHIS structure. Two solutions, antenna without metamaterials and antenna with RHIS, are realized. The experimental results confirm the performances given by simulation (impedance matching and radiation).

1. Introduction

The reduction of human exposure to electromagnetic radiation from wireless devices is an important issue. Some studies based on the specific absorption rate (SAR) analysis show that exposure can be reduced by applying some techniques to the antenna design. A simple technique is to increase the distance between the antenna (handset, laptop) and the human organ (head, hand, etc) [1]. However, this solution is not realistic today because of the slim streamlined design of current commercial wireless devices. Other methods are focused on using an electromagnetic shield, between the antenna and the user [2]. Another technique is to suppress the current flowing in the handset box by using a ferrite sheet attached to the antenna [3]. Despite the good performance of these techniques, these are expensive and require complex manufacturing.

Recent research, focused on low cost and easy implementation solution, propose the use of metamaterials to reduce the exposure. These structures are located between the human body and the antenna. Although some solutions based on Electromagnetic Band-Gap (EBG) [4] [5] [6] or Artificial Magnetic Conductor (AMC) [7] are proposed today, this research should be driven by more detailed studies taking into account other metamaterial types like Resistive High Impedance Surface (RHIS) and for the case of the new generation of mobile handset.

The aim of this paper is to perform a detailed study with a simplified model of a current mobile phone and a simplified antenna compliant with three metamaterial structures: AMC, EBG and RHIS. These artificial materials have the capability to act as a magnetic conductor to reduce surface currents (AMC), to reduce surface waves (EBG) and to absorb currents (RHIS) [8], [9], [10]. The challenge is to show the benefits to use these structures in order to reduce the exposure without modifying the antenna performances.

2. Simplified model

The simplified model of a terminal mobile consists on a metallic plane with a monopole antenna located in three different positions (centre, middle of the edge and corner), whose size represents a current smart phone, with dimensions around 125 x 60 mm. The monopole is surrounded with the metamaterial structures (AMC, EBG and RHIS). Four cells are removed around the antenna port. The monopole antenna is designed to work à 5 GHz (IEEE 802.11n). Figure 1 shows dimensions of the different configurations.

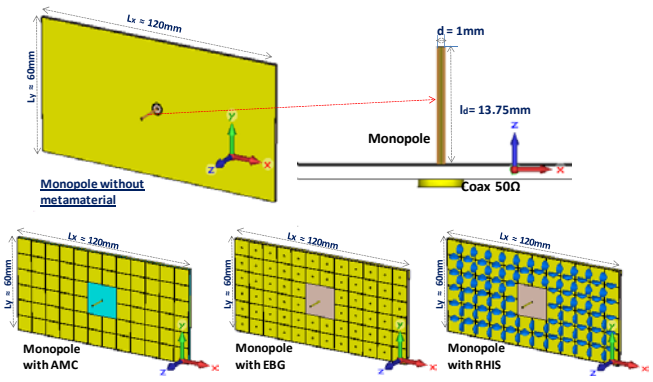

Figure 1: Monopole Antenna without and with metamaterials.

2.1. Metamaterial structures

The metamaterial structures are simulated and optimized using CST Microwave Studio™ (Frequency solver). Only one unit cell is considered because periodic boundaries are applied in simulation. Each structure consists of an infinite array of square patches above a grounded dielectric slab with thickness equals to 2.36 mm and a relative dielectric

permittivity of 2.2. The patch length is 9.7 mm and the patches gap is 0.25 mm.

The AMC bandwidth (defined as the frequency band where the phase of the reflection coefficient is between -90° and 90°) ranges from 4.42 to 5.65 GHz, where the phase difference is null at 5 GHz.

In the case of EBG structure the patches are connected to ground plane by a metallic via with 0.5 mm diameter. The band gap (defined by the bandwidth where $|S_{21}| < -20$dB) is 3.6 - 6.11 GHz.

In the RHIS structure, the squared patches (without via) are interconnected by a resistor. The optimal resistor value depends on both angle of incidence and wave polarization [11]. Three different structures are optimized to absorb incident waves at normal incidence (angle of incidence equal to 0°) and oblique incidence (60° and 85°) in TE polarization. The maximal absorption at normal incidence is obtained when the resistor R value is 377 Ω, the patch length w is 9.7mm and the gap g is 0.25 mm. In the case of oblique incidence (60°), the resistor value is 800 Ω and the patch length is 11.7 mm. For maximal absorption at 85°, the resistor value is 5600 Ω and the patch length is 12 mm.

3. Antennas performances

Antennas with and without metamaterials are simulated using CST Microwave Studio (Transient solver). All the solutions with metamaterials are compared to a reference antenna (monopole with a grounded dielectric slab without metamaterials).

Figure 2 shows the impedance matching for three different positions. In case 1, antenna at centre, solutions with AMC and three RHIS (optimized at 0 °, 60 ° and 85 ° incidence) give some shifts in frequency bandwidth (criteria: $|\Gamma| < -10$dB) but keep the antenna matched. The antenna matching is not preserved when using EBG structure, maybe the presence of the vias causes a mismatching at the input of the monopole antenna. In case 2, antenna at the middle of the edge, the impedance matching is preserved when using AMC, EBG and RHIS (optimized at 0 °). A mismatching is observed when solutions with RHIS optimized at oblique incidence (60° and 85°). In case 3, the antenna at corner, the behaviour of the reference antenna (monopole without metamaterials) is preserved by AMC and RHIS solutions.

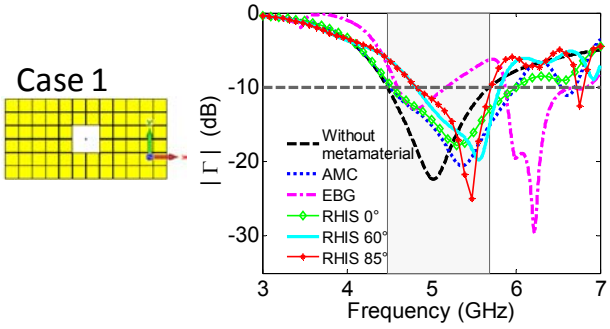

a)

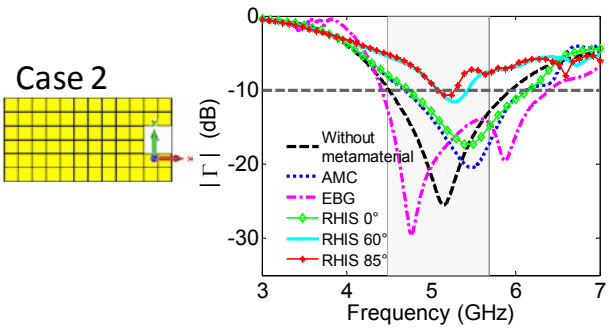

b)

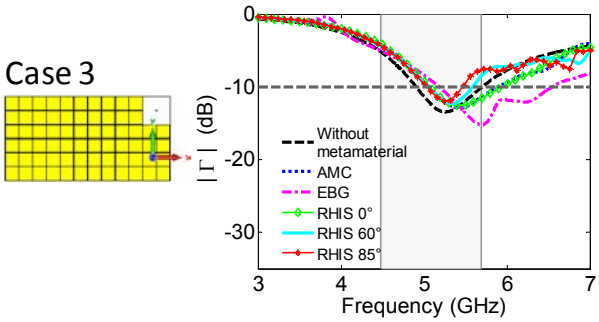

c)

Figure 2 : Impedance matching. a) Case 1: antenna at centre. b) Case 2: antenna at middle of the edge. c) Case 3: antenna at corner.

The realized gain for the three position cases is displayed in Figure 3. With the RHIS solutions, the gain changes and the total efficiency decreases due to the presence of resistors, but they remain acceptable in the operating bandwidth. The gain is increased using EBG structure in all cases. In fact, EBG structure modifies the radiation and changes the omnidirectional radiation pattern in a directive one.

In order to analyze the exposure, the best solution has to be selected. The best solution is defined as the antenna where impedance matching and omnidirectional radiation are preserved. In that case, the EBG solution has been rejected because the performances of the reference antenna are modified. AMC and RHIS solutions are selected because they preserve the antenna matched and don't significantly modify the radiation of the reference antenna.

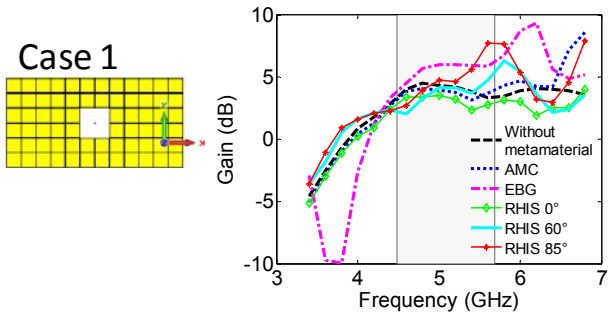

a)

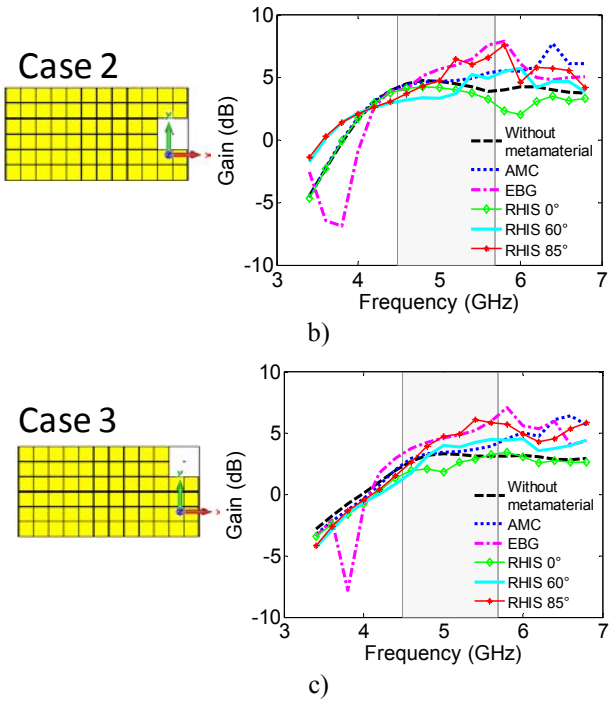

Figure 3 : Realized Gain. a) Case 1: antenna at centre. b) Case 2: antenna at middle of the edge. c) Case 3: antenna at corner.

4. Exposure Analysis

The exposure is evaluated by simulations using CST Microwave Studio. A flat phantom is illuminated by the mobile terminal antenna. The distance between the phantom and the antenna is 5 mm. The terminal is located on the center of the phantom. The model of the phantom consists on a homogeneous equivalent liquid with electrical properties: $\varepsilon_r = 39.29$, $\sigma = 3.48$ S/m and $\rho = 1030$ Kg/m^3 at 5 GHz.

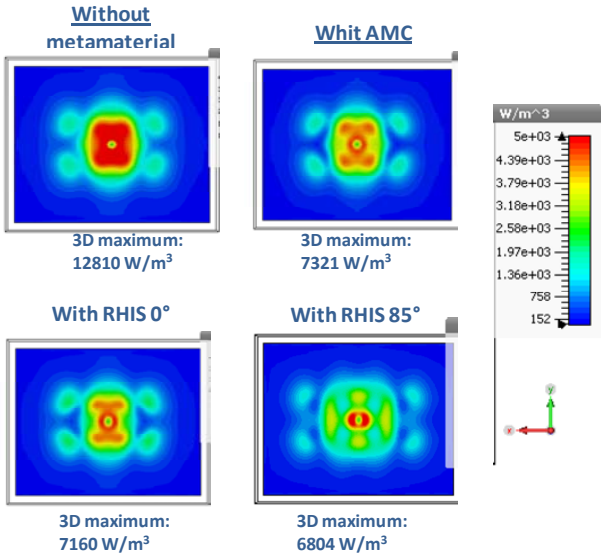

Figure 4: Spatial distribution of power loss density at 5GHz.

The power loss density is calculated for the four solutions (without metamaterial, AMC, RHIS normal incidence and RHIS oblique incidence), before calculating the SAR. Only the case 1, where the antenna is at centre has been analysed. Figure 4 shows the spatial distribution in the phantom at 5mm from the antenna. The power loss density is reduced in all metamaterial cases; however the best result is obtained when the RHIS is optimized to absorb waves at oblique incidence.

Finally, the SAR is calculated only for the best solution: the RHIS optimised for oblique incidence (85 °). The exposure reduction is evaluated through the calculation of an Exposure Index *EI* ratio by comparing the antenna with best metamaterial solution versus the antenna without metamaterial (Equation 1).

$$Ratio_{EI}(\%) = \frac{EI(w\,meta) - EI(wo\,meta)}{EI(wo\,meta)} \times 100 \quad (1)$$

In Equation 1, *EI* is the Exposure Index, 'w meta' corresponds to the solution with metamaterial and, 'wo meta' corresponds to the antenna without metamaterial. The *EI* results are displayed in Table 1. A reduction of 23.6% for Maximum SAR 10g is obtained and 6% for the Total SAR.

Table 1: Exposure index reduction

EI	Without metamaterial	With metamaterial	Ratio *EI* (%)
Total SAR (rms) [W/kg]	0.106	0.094	-11.3
Max. point SAR (rms) [W/kg]	7.07	6.84	-3.25
Maximum SAR 10g (rms) [W/kg]	1.4	1.07	-23.6

5. Validation

The two solutions used to calculate the EI are the monopole antenna without metamaterials and the monopole antenna with RHIS optimized to absorb incident waves at 85°. The objective is to confirm the performances given by simulation in terms of impedance matching and radiation patterns.

Figure 5 shows the prototype of the monopole antenna without metamaterials. The monopole antenna is placed at the center of a grounded FR-4 laminate with thickness equals to 1.6 mm and relative permittivity of 4.2.

Figure 6 shows the prototype of the monopole antenna with RHIS 85°. The RHIS structure is manufactured using the substrate Arlon Diclad 880 with thickness equals to 2.36 mm and a relative dielectric permittivity of 2.2. The resistances are the surface mounted chip resistors that are soldering between the patches. The resistance value is 5600 Ω. The prototypes size (~74 x 150 mm) is representative of a last generation mobile phone as Figures 5 and 6 shown.

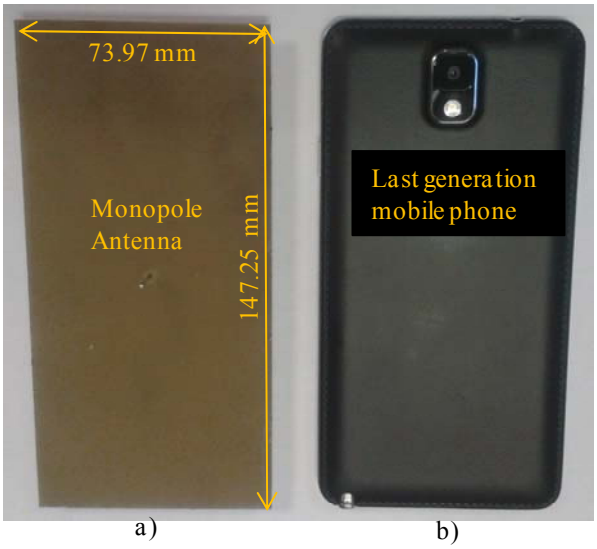

a) b)

Figure 5: a) Monopole antenna without metamaterials. b) Last generation mobile phone.

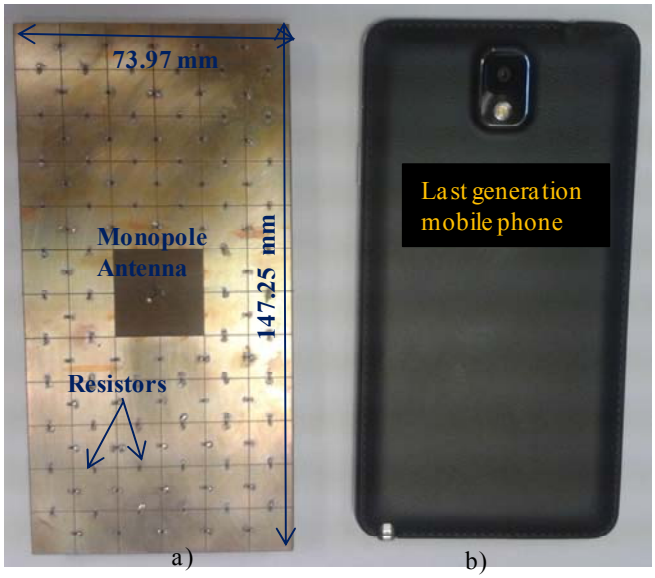

a) b)

Figure 6: a) Monopole antenna with metamaterials. b) Last generation mobile phone

First, the impedance matching is validated. Figures 7 and 8 show the simulation and measurement results. For the monopole without metamaterial (Figure 7), a very good agreement between simulation and measurement is obtained. In the case of the monopole with RHIS (Figure 8), a good agreement between simulations and measurements is observed with some little differences at low level.

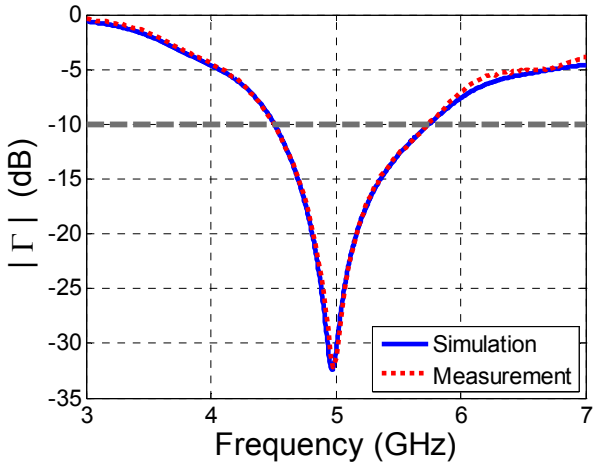

Figure 7: Impedance matching monopole antenna without metamaterials.

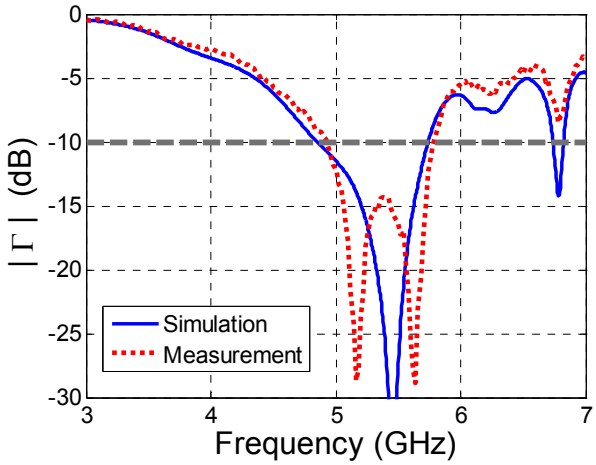

Figure 8: Impedance matching monopole antenna with RHIS 85 °.

Finally, the radiation performances are also validated by the measurement of the realized gain in two main planes. Figures 9 and 10 display the results. A very good agreement between simulations and measurements is observed in both cases.

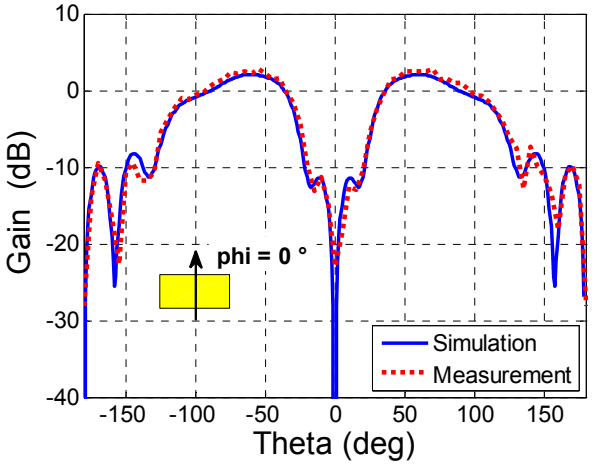

a)

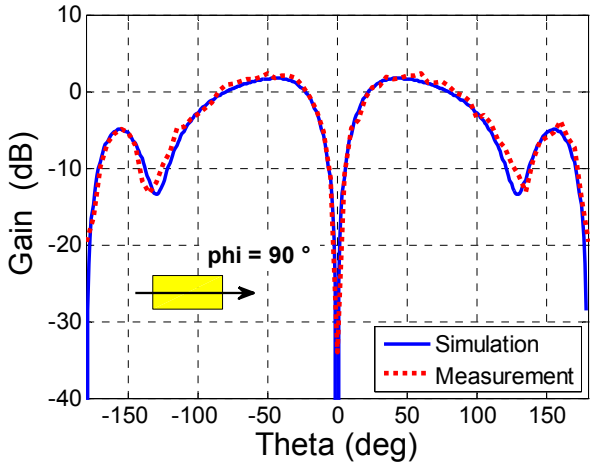

b)

Figure 9: Gain, monopole antenna without metamaterials. a) Plane phi = 0 ° b) Plane phi = 90°.

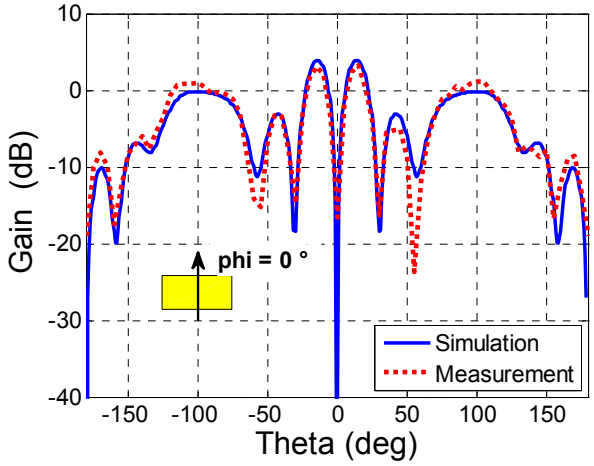

a)

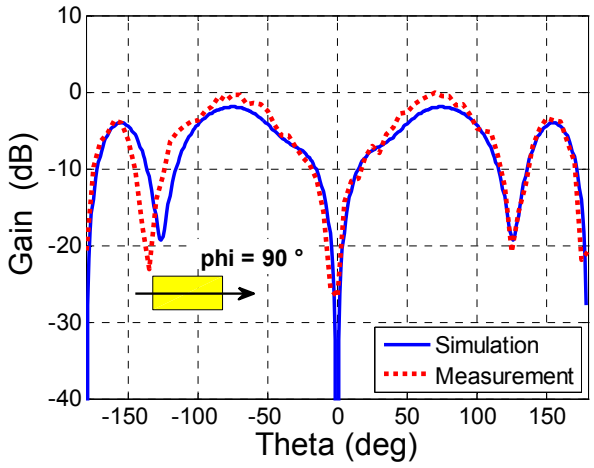

b)

Figure 10: Gain, monopole antenna with RHIS 85°. a) Plane phi = 0° b) Plane phi = 90°.

6. Conclusions

In this paper, a monopole antenna associated with three different metamaterials: Artificial Magnetic Conductor (AMC), Electromagnetic Band-Gap (EBG) and Resistive High Impedance Surface (RHIS) on a simplified model of a terminal mobile have been studied.

An appropriate metamaterial structure is a promising solution to reduce exposure preserving the antenna performances. The EBG solution has been rejected because the performances of the reference antenna are modified. The exposure can be reduced and the antenna performances are preserved using both AMC and RHIS structures. The SAR10g is reduced by 23.6% when a RHIS optimized solution is associated with a monopole. The best solution, the monopole with RHIS 85° and the reference solution, antenna without metamaterial, have been realized. A good agreement between simulations and measurements has been observed.

Acknowledgements

The research leading to these results has received funding from the European Community's Seventh Framework Program (FP7/2007-2013) under grant agreement LEXNET (Low EMF Exposure Future Networks) n° 318273.

References

[1] O. Kivekas, J. Ollikainen, T. Lehtiniemi, P. Vainikainen, "Bandwidth, SAR, and efficiency of internal mobile phone antennas", *Electromagnetic Compatibility, IEEE Transactions on*, Vol. 46, No. 1, 71-86, 2004.

[2] A. H. Kusuma, A.-F. Sheta, I. M. Elshafiey, Z. Siddiqui, M. A. S. Alkanhal, S. Aldosari, S. A. Alshebeili, S. F. Mahmoud, "A new low SAR antenna structure for wireless handset applications", *Progress In Electromagnetics Research*, Vol. 112, 23-40, 2011.

[3] M.I. Kitra, C.J. Panagamuwa, P. McEvoy, J.C. Vardaxoglou, J.R. James, "Low SAR Ferrite Handset Antenna Design", *IEEE Transactions on Antennas and Propagation*, vol. 55, no. 4, pp 1155-1164, April 2007.

[4] R. Ikeuchi, A. Hirata, "Dipole Antenna Above EBG Substrate for Local SAR Reduction", *IEEE Antennas And Wireless Propagation Letters*, Vol. 10, pp 904-906, 2011.

[5] S.I Kwak, D.U Sim, J.H Kwon, "Design of Optimized Multilayer PIFA With the EBG Structure for SAR Reduction in Mobile Applications", *Electromagnetic Compatibility, IEEE Transactions on* , vol.53, no.2, pp.325,331, May 2011.

[6] J. N. Hwang; F. C. Chen, "Reduction of the Peak SAR in the Human Head With Metamaterials", *Antennas and Propagation, IEEE Transactions on* , vol.54, no.12, pp.3763,3770, Dec. 2006.

[7] S. Lee, N. Kim, S.Y. Rhee, "Design of Novel Artificial Magnetic Conductor Reflector and Its SAR Analysis",

Progress In Electromagnetics Research Symposium Proceedings, Moscow, Russia, pp 325-328, August 2012.

[8] F. Linot, X. Begaud, M. Soiron, C. Renard, M. Labeyrie, "Characterisation of a loaded high impedance surface", *International Journal of Microwave and Wireless Technologies*, 1(9):483–487, Dec. 2009.

[9] A. C. Lepage, X. Begaud, J. Sarrazin. "Wideband directive antennas with High Impedance Surfaces (Chap. 3)", *Microwave and Millimeter Wave Circuits and Systems: Emerging Design, Technologies and Applications*, Wiley, 2012.

[10] M. Grelier, F. Linot, A. C. Lepage, X. Begaud, J. M. Le Mener, M. Soiron, "Analytical methods for AMC and EBG characterisations", *Applied Physics A,* Volume 103, Issue 3, pp 805-808, June 2011.

[11] Y. Pinto, J. Sarrazin, A.-C. Lepage, X. Begaud, N. Capet, "Resistive high-impedance surfaces (RHIS) as absorbers for oblique incidence electromagnetic waves", *Applied Physics A*, Volume 117, Issue 2, pp 693-697, November 2014.

Lattice dielectric loss in diamond and related materials at millimeter range

Boris Garin[1*], Roman Denisyuk[1], Dmitry Kalenov[1], Vladimir Parshin[2], Evgeniy Serov[2], Vadim Derkach[3], Roman Golovashchenko[3], Vadim Korzh[3], Alexander Plevako[3], Sergey Tarapov[3]

[1]Kotel'nikov Institute of Radioengineering and Electronics of Russian Academy of Sciences, Fryazino branch, Fryazino, Moscow Region, Russia
[2]Institute of Applied Physics of the Russian Academy of Sciences, Nizhny Novgorod, Russia
[3]Usikov Institute of Radiophysics and Electronics of the National Academy of Sciences of Ukraine, Kharkov, Ukraine
[*]corresponding author, e-mail: bormigar@yandex.ru

Abstract

The manifestations of the lattice dielectric losses (both intrinsic lattice loss corresponding to ideal crystal, and nonintrinsic loss due to lattice disorder, defects, etc.) are considered in some low loss diamond and related materials at the millimeter wavelengths range and very wide temperature region 1–900 K. Data on lattice loss are presented and discussed for the polycrystalline diamonds grown by the arc plasma jet technique, high purity single crystal of silicon carbide (SiC), and single crystal of semi-insulating InP. It is shown that the lattice dielectric losses essentially determine the loss in different low loss materials at the given range.

1. Introduction

Now the research of dielectric losses in low loss materials at the millimeter (MM) and terahertz (THz) ranges of electromagnetic waves is of key significance for the outlook of elemental base advance for various devices and systems of high power at the given ranges. At the present time, for example, it is most actual and critical for the problem of window materials in most powerful generators (gyrotrons) [1].

The study of the lattice loss and its lower loss limits has especial significance in the research of the problem of lowest loss.

In semiconductors with broad forbidden gap E_g the theoretical lower limit of loss is determined by the multi-phonon absorption (MPA) in corresponding ideal crystal of material [2–7]. Such a loss may be called "intrinsic" lattice loss (ILL). In many cases at the given range the main contribution to the MPA is caused by two-phonon absorption. At the MM and THz ranges, where the frequency $\omega << \omega_D$ (ω_D is the Debye frequency of crystal lattice), the so-called "difference" two-phonon processes exist. In these processes the absorption of electromagnetic quanta is followed by the excitation of one phonon of frequency ω_1 and absorption of one phonon of frequency ω_2. The frequencies must obey the condition: $\omega = \omega_1 - \omega_2$.

On the basis of theory of MPA [2,3] the general criteria of search for dielectrics with low ILL had been obtained [4,5]. The crystals with diamond structure (diamond, silicon) satisfy these criteria to the highest degree. Some crystals with zinc blende (such GaP, GaAs, InP), and sapphire adjoin to them. From analysis of restrictions from crystal space symmetry it follows that in some crystal structures (of diamond type, and some others) a small factor $\eta=(J_1/J_0)^2$ (where J_0 and J_1 are integrals of mutual overlap of electron shells of nearest and next near neighbouring atoms respectively) must be substituted to estimation of the two-phonon ILL, where $\eta \sim 10^{-2}$ [5].

In single crystals of Gold doped (compensated) Silicon (Si:Au) the extremely low loss at the frequency f~200 GHz and room temperature T=300 K was observed ($\tan\delta \sim 2\cdot10^{-6}$) [6]. It is the lowest loss that was observed in all materials at the given frequency and temperature range up now. It is the theoretical lower loss limit due to free carriers corresponding to intrinsic Silicon at room temperature, as predicted in [4,5,7].

The low losses $\tan\delta \sim 10^{-4}$ are observed at f~150 GHz and room temperature in compensated monocrystalline semiconductors of $A^{III}B^{V}$ group with zinc blende type of crystal such as GaAs, GaP, InP [8], crystal quartz, sapphire [9]. In [10–14] the quantitative theoretical estimations at the MM range was considered for the absolute values of the ILL in specific crystals, including crystals with diamond-type lattice structure (diamond, Si and Ge), and some crystals of $A^{III}B^{V}$ type, where the least loss was expected [3–5]. In particular, the quantitative estimations for the ILL at f ~ 150 GHz and T~300 K: $\tan\delta \sim 3\cdot10^{-8}$ for Diamond [13]; $\tan\delta < 10^{-6}$ for Silicon.

In the best diamonds grown by the technique of the chemical vapor deposition in microwave plasma (MPCVD) an extremely low loss at the frequencies f~200 GHz and room temperature T=300 K was observed ($\tan\delta \sim 2.5\cdot10^{-6}$) [14]. It is near to the minimal loss observed in the Si:Au. Moreover in diamonds there is a principle opportunity for further essential loss decrease [10–16]. However the production of MPCVD diamonds is very expensive. Last years another technique is under development: the growing of diamonds in the direct current arc plasma jet (APJ) [17–20]. The APJ diamonds are cheaper compared to the MPCVD diamonds. They can be applied in various elements and structures of the high power electronics at the

MM and THz ranges as a material that combines low dielectric loss, extremely high thermal conductivity, insulating property, and relative low cost. The achievable lowest losses in the APJ diamonds are too little researched.

The ILL in Diamond and Silicon are extremely low, and were not revealed experimentally up now.

In [16] the theoretical lower loss limits for different low loss materials at various frequencies at MM and THz ranges and various temperatures, and their frequency and temperature dependences were considered.

In practice, a higher level of loss is often observed, due to additional lattice loss induced by lattice disorder, defects, impurities – "nonintrinsic lattice loss" (NLL) [21,22] .

The massive samples of high purity semi-insulating (HPSI) 4H-SiC single crystal (with the hexagonal lattice of polytype "4H") have become available from the commercial firm CREE (North Caroline, USA) [23,24].

In the preset work the recent manifestations and characteristic of lattice loss in some low loss materials, APJ diamonds, high purity SiC are presented and discussed.

2. Results and discussion

In this section the data on manifestations of the dielectric loss in APJ diamonds, single crystal of high pure Silicon Carbide (SiC), and single crystal of semi-insulating (compensated) InP are presented.

2.1. Measurement techniques

2.1.1. Open resonator technique

The loss tangent tanδ and refractive index n of the sample at the short millimeter wavelength range were measured using the spectrometer based on the Fabry-Perot open resonator with a high Q-factor (Q~10^6) in IAP of RAS. Its modern configuration is presented in the Figure 1.

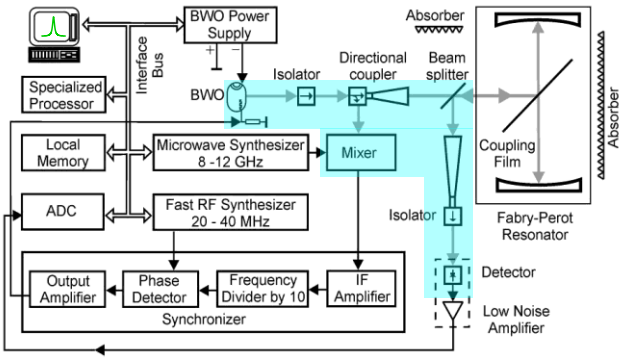

Figure 1. The configuration of the open resonator spectrometer on the base of Fabri-Perot interferometer with the set of Back-Wave Oscillators (BWO) at 36–380 GHz range, and with the phase stabilization and with "fast" digital synthesizer for resonator curve recording. This equipment was used for measurements at temperatures T =78–900 K.

The modern measurement technique is described, for example, in [14,19].

2.1.2. Disc dielectric resonator technique

The cryogenic dielectrometer with disk dielectric resonators (DDR) on whispering gallery modes (WGM) at the MM range in the Usikov IRE of NANU was for measurements at temperatures T = 0.8–300 K. The block diagram of the dielectrometer [25] is presented in the Figure 2.

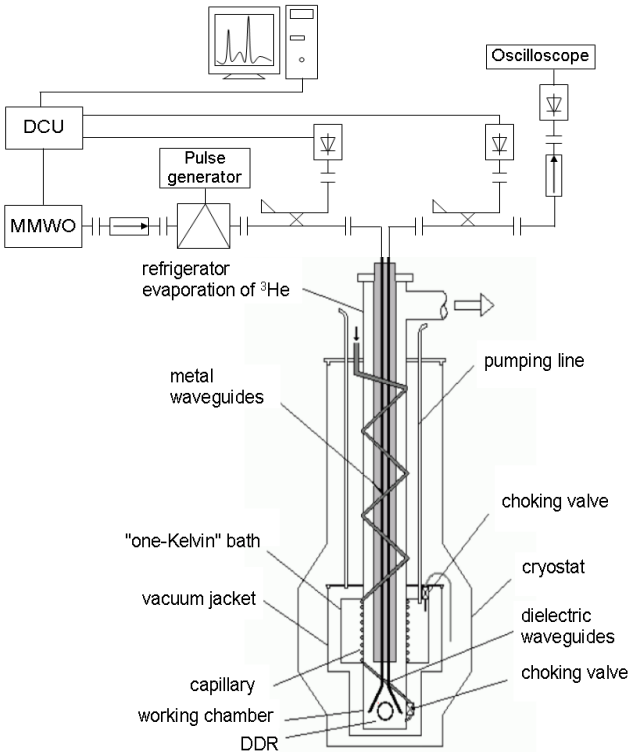

Figure 2. Block diagram of the cryogenic dielectrometer.

Main parameters: frequences 75–150 GHz; temperatures 0.8–300 K; system of cooling: "Top-loading" refrigerator with circulation of ^{4}He and ^{3}He; the volume of the working chamber: 100 cm^3.

2.2. Manifestations of lattice loss in the APJ diamonds

The losses in two samples of APJ diamonds at MM range, presented by the Beijing University of Science and Technology, were studied [18–20]. In the first sample "1", the loss tanδ was measured at room temperature and frequencies 35–201 GHz [18,19]. It was found that tanδ ~ $2\cdot10^{-4}$ at frequency f = 35 GHz, and tanδ ~ $3\cdot10^{-3}$ at f = 201 GHz. At short MM range the measuring technique at the base of high-Q open resonator was used [6] (see also the section 2.1.1). From a comparison of the measurements data on different frequencies described above it follows, that in the APJ sample 1 an essential increase tanδ with frequency (tanδ ~ f) in the MM a range is observed. It essentially differs from the frequency dependence of loss in other diamonds, in particular in MPCVD diamonds, where reduction of loss with frequency (tanδ ~1/f) in the given range was observed at f <200 GHz. In the MPCVD diamonds it caused by electric conductance in the intercrystalline (intergranular) areas [9-15]. From observable increase of loss with frequency in the investigated APJ

diamond 1 follows, that the mechanism of loss in it is another compared to the MPCVD diamonds. As theoretical interpretation of the loss in the sample 1, the mechanism of the lattice loss induced by the lattice disorder can be offered because it corresponds to dependence $\tan\delta \sim f$ [21,22]. It agrees also with smaller density (in comparison with MPCVD diamonds), corresponding to smaller value of the measured refractive index.

In another APJ diamond, sample"2", the dielectric loss was measured at various temperatures T = 300–950 K The temperature dependences were measured on two frequencies, 157 and 313 GHz. The results are presented in the Figure 3.

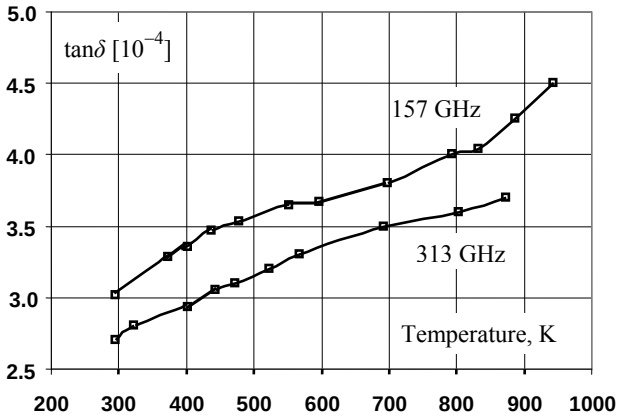

Figure 3. Temperature dependences of the dielectric loss tangent $\tan\delta$ in the APJ diamond sample 2 on two frequencies, 157 and 313 GHz.

The APJ sample 2 essentially differs on the loss temperature and frequency dependences from the MPCVD diamonds. In particular, the loss weakly depends on temperature not only at the "low" temperatures (T~300 K), but also at the "high" temperatures (T~900 K). Whereas in the MPCVD diamonds a sharp increase of loss is observed at T~500–900 K [2-4]. The decrease of loss at the increase of frequency in the sample 2 is observed as well as in the MPCVD diamonds. However it is much weaker compared to the dependence $\tan\delta \sim 1/f$ that is observed in the MPCVD diamonds at $f <$ 300 GHz [2-4] and is due to the electric conductance in the intercrystalline areas [9-15].

The sample 2 also essentially differs on the loss frequency dependence from the sample 1. In the sample 2 a decrease of loss with frequency is observed. Whereas in the sample 1 an increase with frequency is observed [6,7]. It is possible to explain these frequency and temperature dependences in the sample 2 by the combination of contributions of two loss mechanisms: a) lattice loss induced by the lattice disorder which do not depend on temperature [21,22] (and can predominate at rather low temperatures; b) the loss caused by electric conductance in the intercrystalline areas [9–15]. The received results, including much lower losses in the sample 2 show, that in this sample the concentration of lattice disorder much low, than in the APJ diamond 1.

2.3. Lattice loss in the high purity Silicon Carbide SiC

The samples of high purity semi-insulating (HPSI) massive single crystal 4H-SiC with the hexagonal lattice of polytype "4H") have become available [23,24]. Temperature dependence of dielectric loss values at f~150 GHz [24] is shown in the Figure 4.

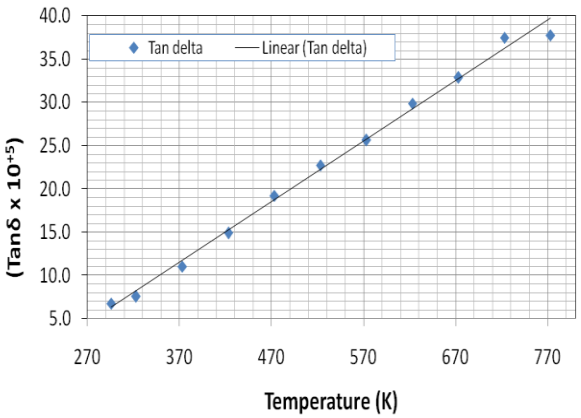

Figure 4. Loss tangent temperature dependence in high purity single crystal SiC at f~150 GHz.

Room temperature loss values and their dependence over a limited range of frequency at MM range indicate that free charge carriers are not the dominant cause of dielectric loss in this material. The observed loss temperature dependence, that is at the first approximation $\tan\delta \sim T^2$, corresponds to the two phonon ILL [16]. Moreover, the observed loss value at room temperature $\tan\delta \approx 5 \cdot 10^{-5}$ just corresponds quantitatively to the theoretical estimation for the ILL in this material at this temperature and frequency [16].

2.4. Lattice loss in InP at cryogenic temperatures

The loss in semi-insulating (compensated) crystal InP was measured at frequencies f=78 GHz and cryogenic temperatures 1–70 K by means of the dielectric disk resonator technique cryogenic complex [26].

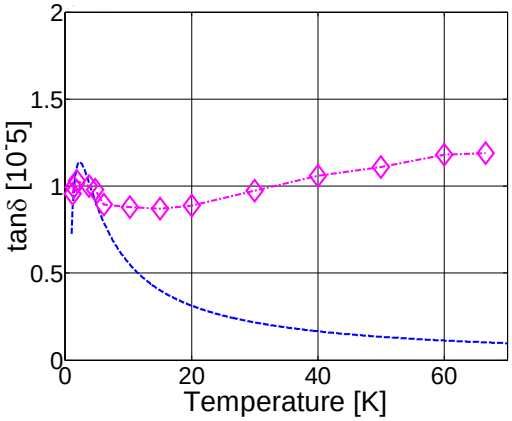

Figure 5. Loss tangent temperature dependence in the InP at f = 78 GHz and T = 1–70 The points ◊ are the experimental data The dotted line ·· is the theoretical dependence corresponding to the mechanism of Debye's relaxation.

It is visible that the loss almost does not depend on the temperature at the rather wide temperature interval. It is very specific feature corresponding to the lattice loss induced by the lattice disorder, defects, impurities – "nonintrinsic lattice loss" (NLL) following to the theory of such loss mechanism [21,22].

Some maximum of loss was observed at temperatures lower than the liquid helium temperatures, $T < 4$ K, can be fitted at the first approximation by the curve corresponding to the mechanism of Debye's relaxation. Analogous maximum was observed earlier in some MPCVD diamonds [27]. However it has not definite explanation by now.

3. Conclusions

1. The lattice dielectric losses are essential in different low loss materials including the diamond and related materials.
2. In the APJ diamonds the manifestation of nonintrinsic lattice loss due to lattice disorder and defects are observed.
3. In the single crystal of semi-insulating InP the nonintrinsic lattice loss was observed at cryogenic temperatures.
4. In the high purity single crystal of silicon carbide SiC the intrinsic lattice loss corresponding to the ideal crystal of this material was observed.

Acknowledgements

The work was supported partially by The Russian Foundation for Basic Research (project No. 14-02-90458) and National Academy of Sciences of Ukraine (project No. 10/14) in the frame of the joint Russian-Ukrainian project.

References

[1] M. Thumm. Plasma Physics and Controlled Fusion, vol. 45, pp. A143–A161, 2003.

[2] A.V. Galdetskii, B.M. Garin, Multiphonon absorption of IRE radiation in the crystals, caused by optical anharmonicity, Preprint No.17(320), Inst. of Radio Engineering & Electronics of USSR Acad. of Sci., Moscow, 1981.

[3] B.M. Garin, Proc. 19th Int. Conf. on IR and MM waves, Colchester, England, pp. 509–510, Sept. 1993.

[4] B.M. Garin, et al, Proc. 1th Ukrainian Symp. "Physics and techniques of millimeter and submillimeter radio waves", Part 1. Kharkov, Ukraine, p.86, 1991.

[5] B.M. Garin, Proc. Third Int. Conf. on Millimeter-Wave and Far-Infrared Science and Technol. Guangzhou, China, pp. 275–277, Aug.22–26, 1994.

[6] Heidinger R., Molla J., Parshin V.V., Proc. 21st Int. Conf. on Infrared & Millimeter Waves, Berlin, Germany, paper AW8, 1996.

[7] B.M. Garin, A.N. Kopnin, M.P. Parkhomenko, et al, Method for producing silicon with extremely low millimeter and submillimeter range losses, Sov. Phys. Tech. Phys. Lett., 20: 878–879, 1994.

[8] L.N. Vershinina, V.V. Meriakri, B.A. Murmuzhev, et al., High frequency properties of solid states, Kiev, p.158, 1985.

[9] V.V. Parshin, Int. J. on IR & MM Waves 15: 339–348, 1994.

[10] B.M. Garin, Proc. 5th Int. Symp. on Modern Advances in Microwave Technol., Kiev, Ukraine, 1995; Proc. 4th Int. Conf. on Millimeter-Wave and Far-Infrared Sci. and Technol., Beijing, China, Aug. 1996.

[11] B.M. Garin, A.N. Kopnin, M.P. Parkhomenko, et al., Proc. 21st Int. Conf. on Infrared & Millimeter waves. Berlin, Germany, paper CT15, July 1996.

[12] B.M. Garin, V.V. Parshin, V.G. Ral'chenko, et al., "Losses in diamond in the millimeter range", Tech. Phys. Lett., 25: 288–289, 1999.

[13] B.M. Garin, V.V. Parshin, S.E. Myasnikova, V.G. Ralchenko, Diamond and Related Materials 12: 1755–1759, 2003.

[14] V. Parshin, B. Garin, S. Myasnikova, A. Orlenekov, Dielectric losses in CVD diamonds in the millimeter-wave range at temperatures 300–900 K, Radiophysics and Quantum Electronics 47: 974–981, 2004.

[15] B.M. Garin, M.P. Parkhomenko, V.V. Parshin, S.E. Myasnikova, R. Heidinger, I. Danilov, J. Molla, V.G. Ralchenko, V.N. Derkach, S.I. Tarapov, Dielectric losses in CVD diamonds at frequencies 1kHz–200GHz and temperatures 70–800 K, Proc. Seventh Applied Diamond Conf./Third Frontier Carbon Technology Joint Conf., Tsukuba, Japan, Editors M. Murakawa, M. Miyoshi, Y. Koga, L. Schafer, and Y. Tzeng, USA, NASA, Vol. NASA/CP–2003-212319, Aug. 2003.

[16] B.M. Garin, Lower Loss Limits at Millimeter and Terahertz Ranges, *Proc. Joint 29th Int. Conf. on IR & MM Waves and 12th Int. Conf. on THz Electronics*, Karlsruhe, Germany, pp.393–394, Sept.27–Oct.1, 2004.

[17] F.X. Lu, W.Z. Tang, T.B. Huang, et al., *Diamond and Related Materials* 10: 1551, 2001.

[18] B.M. Garin, V.V. Parshin, E.A. Serov, Ch.Ch. Jia, W.Z. Tang, and F.X. Lu, Electromagnetic Properties at Millimeter Wavelength Range of Diamond Films Grown by DC arc Plasma Jet Technique, *Proc. Symp. "Progress in Electromagnetics Research" (PIERS)*, Suzhou, China, pp. 455–457, Sept. 12–16, 2011,

[19] B.M. Garin, V.V. Parshin, V.I. Polyakov, A.I. Rukovishnikov, E.A. Serov, Ch.Ch. Jia, W.Z. Tang, F.X. Lu, Dielectic Properties and Applications of CVD Diamonds in the Millimeter and Terahertz Ranges", *Recent Advances in Broadband Dielectric Spectroscopy, NATO Science for Peace and Security Series B: Physics and Biophysics*, Editor Y.P. Kalmykov, Springer Science+Business Media, Dordrecht, Netherlands, Chapter 6, pp. 79–87, 2012.

[20] B.M. Garin, V.I. Polyakov, A.I. Rukovishnikov, A.V. Khomich, V.V. Parshin, E.A. Serov, Ch.Ch. Jia, F.X. Lu, W.Z. Tang, "Dielectric Loss at Millimeter Range and Temperatures 300–950 K, and electrophysical properties in Diamonds Grown by the Arc Plasma Jet Technology", *Proc. Progress In Electromagnetics Research Symposium (PIERS)*, Guangzhou, China, pp. 2096–2099, Aug. 25–28, 2014.

[21] B.M. Garin, One-phonon dielectric loss by excitation of sound, Sov. *Phys. Solid State,* 32, pp. 1917–1920, 1990.

[22] B.M. Garin, Disorder-induced one-phonon absorption of millimeter and submillimeter waves, *Proc. Int. Conf. on MM and SubMM Waves and Applications*, San-Diego, USA, SPIE Proc. Vol.2250, p.55, Jan. 1994.

[23] J.M. Dutta and C.R. Jones, Precision Measurement of Low Loss Window Materials, *Proc. Mater. Res. Soc. Symp.*, MRS Vol. 833, Editors Yong S. Cho, D. Shiffler, C. A. Randall, H. A.C. Tillman, and T. Tsurumi, pp. 63–71, 2005.

[24] J. M. Dutta, C. R. Jones, V. V. Parshin, B. M. Garin, V.I. Polyakov, A.I. Rukovishnikov, MM-Wave Dielectric Loss and Point Defects in HPSI SiC, *Proc. 34th Int. Conf. on Infrared, Millimeter, and Terhertz Waves"*, Busan, Korea, Sept. 21–25, 2009.

[25] Golovashchenko R.V., Goroshko O.V., Derkach V.N., Korzh V.G., Tarapov S.I., Investigation of temperature and

frequency dependences of dielectric characteristics of bulk dielectrics and semiconductors. *Proc. 21st Int. Crimean Conf. "Microwave and Telecommunication Technology"*, Sevastopol, pp. 922–923, Sept. 2011.

[26] Derkach V.N., Golovashchenko R.V., Korzh V.G., Plevako A.S., Tarapov S.I., Garin B.M., Dielectric losses in diamond-like materials at the cryogenic temperatures in the millimeter waveband, *Proc. 24th Int. Crimean Conf. "Microwave & Telecommunication Technology"*, Sevastopol, Crimea, pp. 918–919, Sept. 7–13, 2014.

[27] B.M. Garin, V.I. Polyakov, A.I. Rukovishnikov, L.A. Avdeeva, V.N. Derkach, V.V. Parshin, V.G. Ralchenko, Dielectric loss and energy distribution of the shallow levels in CVD diamonds, *Diamond and Related Materials* 15: 1917–1920, 2006.

Remote Sensing, Inverse Problems, Imaging, Radar and Sensing

Analysis of GPR Antenna System Above Ground

Ji Ma, Guangyou Fang, and Yicai Ji

Key Laboratory of Electromagnetic Radiation and Sensing Technology, Chinese Academy of Sciences, Beijing, China
*corresponding author, E-mail: jima@mail.ie.ac.cn

Abstract

We demonstrate an analysis of a ground penetrating radar (GPR) antenna system by using Wavenology EM, which is an efficient electromagnetic wave simulator. The system includes three identical half ellipse antennas: one is used for transmission, and the other two are for reception. Our investigations show that the antenna system has good radiation characteristics both in frequency and time domain. Furthermore, the ground effects on the antenna performance are taken into account by the FDTD method using adaptive mesh. The detection results of targets buried in soil by means of the proposed system are presented. The received waveform shows that the system can be applied to broadband radar successfully.

1. Introduction

Modeling and simulating ground penetrating radar (GPR) [1] pose important theoretical significance for the case of different antennas, background media and underground targets. The achievements can serve as the guideline for imaging analysis and antenna design in GPR system, which can also implement quantitative analysis of electromagnetic fields.

In the numerical modeling, couplings between the GPR system and the background medium can not be neglected as the medium has a distinct impact on the signals. Since signals generated by GPR are usually transient pulse waves, the finite-difference time-domain method (FDTD) seems to be the most proper solution [2,3]. However, the application of FDTD to the problem presents some difficulties. To model the GPR system precisely, a small size of cell must be employed. Therefore, if a uniform grid is used in the whole computational domain, the memory requirements and computation time are considerable. To achieve the analysis efficiently, the whole model including the GPR and background medium is simulated by using Wavenology EM software, which has a nonuniform mesh solver and can solve multiscale problems well.

In this paper, a GPR antenna system mounted on a moving vehicle used for geophysical research is presented. By using the EM simulator Wavenology EM, the electromagnetic characteristics of the GPR system in the background have been investigated. Detection results show that the system can be applied in the engineering.

2. Modeling and simulation

One of the highlighted features of Wavenology EM is the ability to analyze antennas by the FDTD method using adaptive mesh. It provides a flexible and fast route to solving multiscale electromagnetic problems.

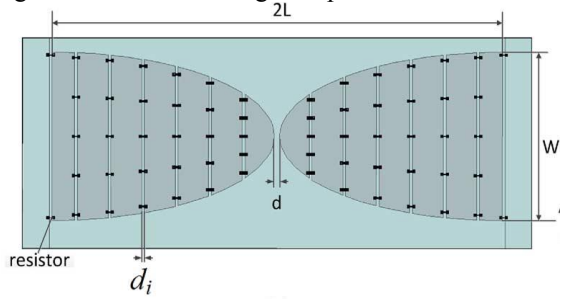

Figure 1: Geometry of the antenna

The antenna used in this study employed two arms of half elliptical shape which was divided into seven sections by equally spaced slots. From the previous work by Wu and King, each slot is loaded by five parallel resistors r^i (i=1,2,3,4,5,6), as shown in Fig. 1. Table 1 shows the value r^i.

Table 1: Values of the resistors

r^1	r^2	r^3	r^4	r^5	r^6
50Ω	60Ω	75Ω	100Ω	130Ω	220Ω

The dimensions of the antenna are as follows: 2L=336mm, W=120mm, d=4mm, and d_i=2mm. Three identical half ellipse antennas were mounted at the open side of the cavity who has a height of 22 mm, as shown in Fig. 2. It is noted that port 1 is used for transmission and the other two are for reception.

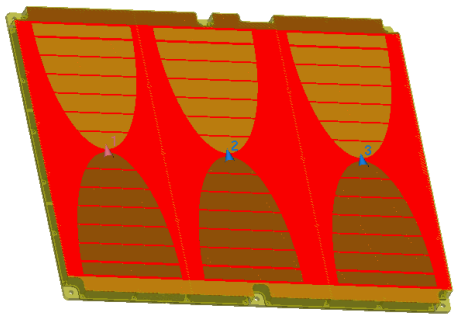

Figure 2: 3D view of the antenna system

Fig. 3 shows the position of the antenna system mounted on the vehicle, and the distance between the antenna and the ground is 30cm. The dimension of the vehicle is 1.4 ×0.8 × 0.87 m^3.

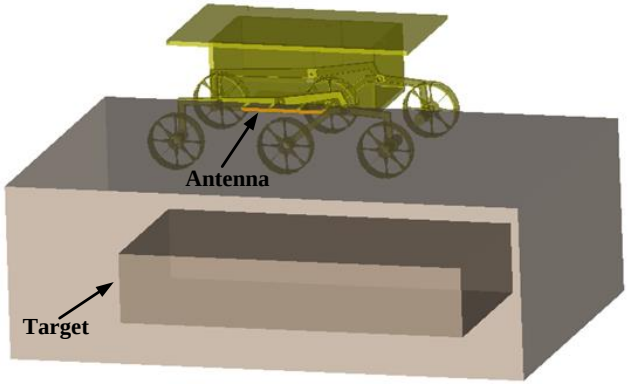

Figure 3: Antenna system mounted on the vehicle

3. Results

In this section, we demonstrate some electromagnetic characteristics and detection results for the GPR system.

Firstly, the VSWR of antennas is shown in Fig. 4 when antennas are fed by a pair of transmitting lines with characteristic impedance of 100 Ω. It can be seen that the VSWR of antenna is below 2 from 250MHz to 750 MHz and a good agreement is observed between the simulation and measurement.

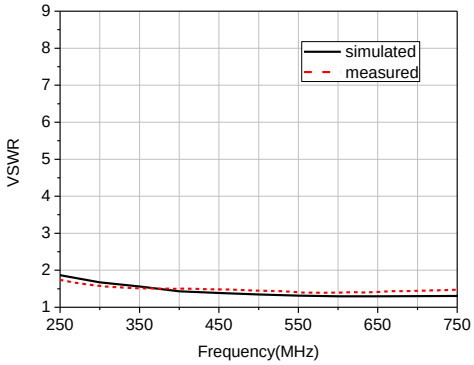

Figure 4: VSWR of antennas

Secondly, the transient waveform for the GPR system has been investigated. For the Fig. 3, the relative permittivity and electric conductivity of the soil are 6.0 and 0.001, respectively. The target is a cupreous cube whose size is 1 ×4 × 2 m^3. The distance between the top face of cube and the ground is 0.5m. The transient waveforms for the three ports are observed in Fig. 5. It can be seen that the signals from the scattering of target can be received by port 2 and 3 after 10 ns.

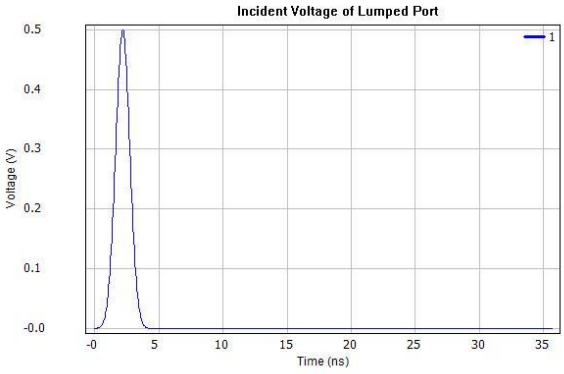

(a)

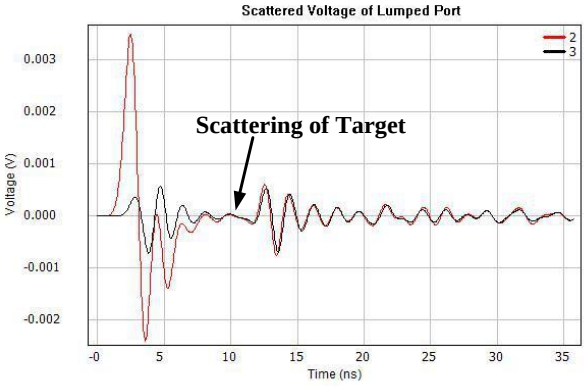

(b)

Figure 5: (a) radiated and (b) received signals

Finally, the detection results for the GPR system in an indoor scene are shown in Fig. 6.

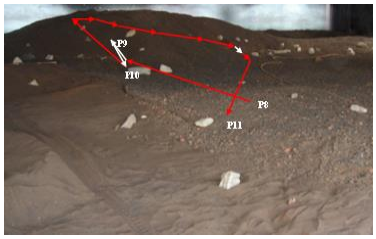

(a)

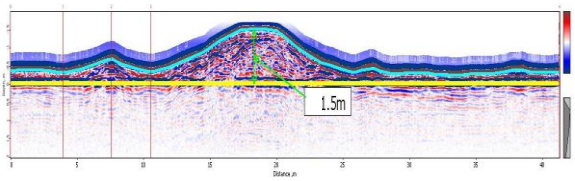

(b)

Figure 6: (a) indoor scene and (b) detection results for the GPR system

4. Conclusions

We have designed and analyzed a GPR system by using the EM simulator Wavenology. Numerical results show that the system can work well as a broadband radar. In practice, the system has been applied to the engineering widely.

References

[1] D. J. Daniels, *Ground Penetrating Radar*, 2nd ed, IEE, London, U. K., 2004.

[2] K. S. Yee, Numerical solution of initial boundary value problems involving Maxwell's equations in isotropic media, *IEEE Trans. Antennas Propagat.* 14: 302−307, 1966.

[3] A. Taflove, S. C. Hagness, *Computational Electrodynamics: The Finite-Difference Time-Domain Method*, 3rd ed, Artech House Publisher, Norwood, MA, USA, 2005.

Design of Remote Medical System Based On B/S Architecture

Zhiqun Cheng[1], Kai XU[2]

(Key Lab. of RF Circuit and System, Education Ministry, Hangzhou Dianzi University, Hangzhou Zhejiang 310018, China)

[1]E-mail: zhiqun@hdu.edu.cn [2]E-mail: 15958191648@163.com

Abstract

With the rapid development of network and information technology, telemedicine system has been widely concerned. A new type of medical system called remote medical consultation system is designed which is based on the Web technology and it is established based on the B/S model. Tornado framework and python scripting language ultimately are adopted to achieve many functions that include remote medical consultation; online instruction and online operation live and so on. Whether doctors or patients, the only thing they need to do is a Web Brower which can achieve real-time medical consultation and communication in different regions.

Keywords

Telemedicine, Web, Tornado framework

1. Introduction

Telemedicine is a very new treatment method that can achieve online therapy, which is based on network technology and combines with the medical technology [5]. With the rapid development of the information technology in twenty-first Century; it has become a trend in the future for patients to see a doctor. Telemedicine not only can implement online treatment for patients through the internet technology, but also can help medical experts to conduct online real-time communication [1]. Through the Internet and the modern network communication technology, we could send text data, voice and image data to the remote medical experts. This new method can be used to achieve the real meaning of the cross regional "face to face" consultation. The conception of the telemedicine system is first proposed by the USA, and now it has nearly half century of history [2]. So far Europe and the United States have been in the leading position in this field [3]. And it starts relatively late in China, but it has been paid more attention in recent years.

In this paper, a detailed analysis of the remote medical consultation process will be introduced at beginning. And then, design of a real-time remote medical consultation system which is based on B/S mode is described. Tornado framework is used in the system [4]. These functions which will be included the diagnosis, consultation, online operator guidance and so on can achieve in this telemedicine system.

2. Tornado Framework and B/S Model

2.1 Tornado Framework

Tornado is web framework that achieved by python and the asynchronous network library, not only because its asynchronous frame properties is very well, but also save a lot of memory in asynchronous applications without the need to open a large number of processes. The framework now has been used in many Web Pages. It can solve many problems for the Web developers and designers.

Tornado framework has obvious difference with normal mainstream Web Server framework. First, it uses the non-blocking server; this model shows that it runs very fast, it can even handle several thousands of connection per second. Especially for the real-time Web service, the tornado framework is a very good Web framework.

2.2 B/S Model

B/S is short for browser/server mode; the user only needs to install any type browser on their computer as the client running platform. All the major development, maintenance and upgrade work are all processed on the Server end, so by this way it can simplify the client software. First of all, the client input consultation system URL in the browser, and then there will be a HTTP request sent to the specified Web server. The server will analyze the URL then ultimate locate the requested location Webpage which sent by the client request. Finally, the query results will use the form of HTML pages and return to the user, the page will ultimate display in the user's browser. Since the B/S model has many advantages, such as simple operate, safety, excellent performance, and good expansibility and so on. Therefore, in practice, we usually adopt Brower/Server mode as shown in figure 1.

Figure 1: B/S Basic principle

3. Consultation Modes and Overall Function

3.1 Consultation Modes

We can regard the remote medical consultation system as a virtual health institution which base on the network. The patient's information, appointments remote operation is through the network and the information will store in the telemedicine management center, only the administrator or some doctors can check out the patients' information. Schematic of the system is shown in figure 2

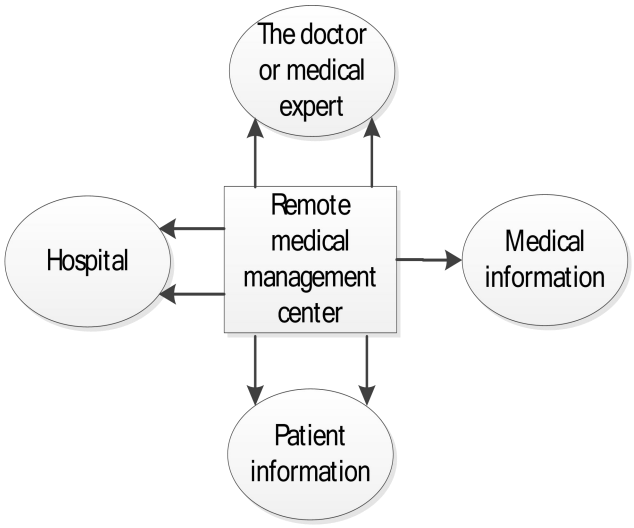

Figure 2: Schematic diagram of telemedicine system

Remote medical consultation system can be divided into two modes, one is real-time consultation and another kind is the non real-time consultation.

With regard to the non real-time consultation, the medical experts usually check the patient's case history and diagnosis through the network. In this way there is no time constrains and it also need not require the medical experts and patients online at the same time, the transmission on network performance requirements are not particularly high, so this diagnoses method has the advantage of flexibility. The patient's diagnosis result was provided by medical experts or hospitals.

But in real-time consultation system, the patients and the medical experts can communication online with "face to face" through video conference by voice mode or text mode which can get the ultimate purpose of consultation. Compare to non real-time diagnosis, this way will require much more broadband because of the high performance of the real-time consultation on the network. Even so, because of the real-time diagnosis have more interactive and can greatly improve the treatment efficiency, so it is more practical.

3.2 The Overall Functional Design

There are three different categories of user support for the register to choose, they are the patients, the doctors and the administrator. The figure 3 displays the different kinds of user's function.

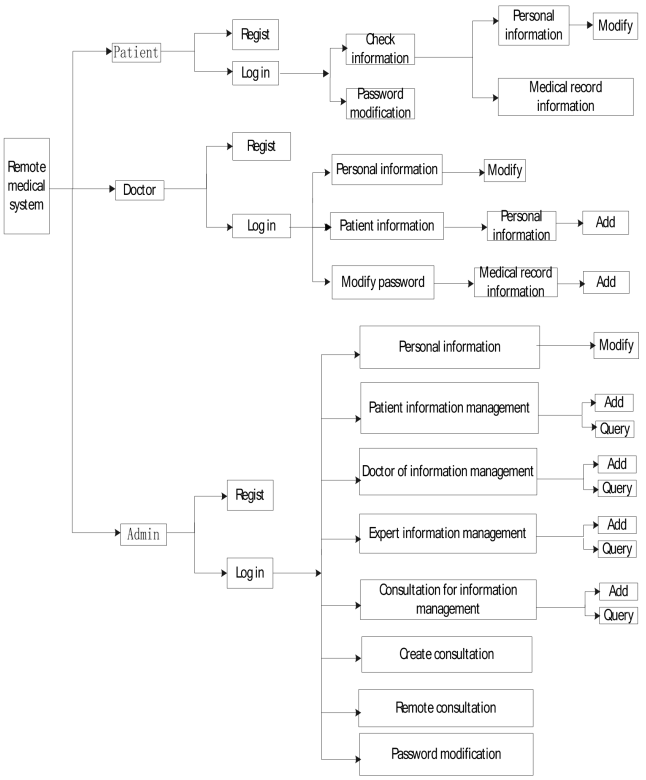

Figure 3: Schematic diagram of telemedicine system

Patients:

Firstly, the patient must register personal account and set up password, after this, the patient can enter the registered account and the corresponding password. If the account and the password are both right, then the patient will log in the system successfully. When the patients enter in the system, they can check out or modify personal information. The modified information will be saved in the database

Doctors or the medical experts:

Like the patients, the doctors or the medical experts must register their own personal account too, the registration process is the same as the front. Compare to the patient, after enter in the system, the doctors and medical experts not only can check out or modify his own personal information, but also can check out the patients information. These privileges help the doctor and medical experts know the patients' history case better. But to the doctors or the medical experts, they cannot check out information each other. If doctors and medical experts have modified their personal information, then likes the patients, all these changes will be saved in the database.

Administrator:

Administrator is only one in the remote telemedicine system. It means that nobody can go to the administrator account except himself. Administrator's account need not register by the user; it usually registers by the designer of the remote telemedicine system. The password and the account that administrator enters the system are told by designer of the system.

Compare to the patients and doctors, administrator not only can check out or modify personal information, but also

can check out the patients, and doctors information. Except for changing the patients' and doctors' information, the administrator can add and delete personal information in the database, These privileges help the administrator works better if there will be some update in the database, and can makes the system more power.

The administrator can also create the consultation which is the most important part of the system, these can make the doctors and patients to talk online and exchange views each other. Of course, the administrator can change the password which is created by the designer of the system. All of changes will save in the database.

3.3 The Remote Session Diagnosis Process

The remote session is the most important part of this website; and the following steps can make a remote medical consultation.

(1) Patient or doctor registers the username in the website. The information will save in the database center.

(2) Patient or doctor Logins in. Then, they can create the link for conference.

(3) The consultation ID number need to be inputted, 0 represents the public consultation, 1 stands for private consultation. Consultation password, user name and the nickname will display in the consultation.

(4) Other users can join the consultation; if experts from remote region want to join the consultation by putting the register account, the corresponding consultation ID number and password, clicking option of "join". In the consultation process, the experts can make real-time diagnosis on patients through voice or text.

(5) Doctors also can make discussion at the forum module of the website to further determine the treatment program for the patient. Whereas patients can also leave the doctor messages so that the doctors know the patient's situation after the consultation. Its main process is shown in figure 4:

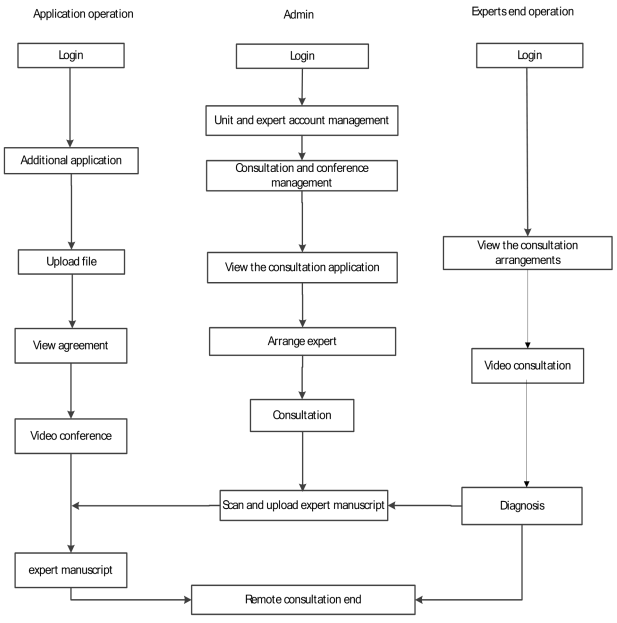

Figure 4: Remote consultation process

As we know, if we want to make a consultation with other doctors or patients, we should follow these five simple steps. The creator of the consultation has the only one conference ID and the unique password, and the creator can send message to inform other people. When other people get the message, they can put the conference ID and the right conference password, they will join in the consultation right now. That's the core of the remote telemedicine system function. And if patients have some questions to ask the doctors. They can leave message to the doctors or log in the forum to communicate with doctors or medical experts.

4. Conclusions

The remote service system of medical information technology based on tornado framework has simple and intuitive interface. It can make the patients and the doctors to operate more easily. It also has powerful function and can run stable. The system not only can help doctors and experts interactive discussions and auxiliary diagnosis for some difficult cases, but also reduce the costs. At the same time, the system will make people in remote areas to enjoy high quality medical services. The region hospitals can share information each other. All of things will help improve the hospitals' cooperation. This will be development trend for medical system. So, compared with the tradition method, this new technology will simplify the cure steps.

References

[1] Sung-M-Y; Kim-M-S; Kim-E-Jet, al.CoMed: a real-time collaborative medicine system [J]. Int-J-Med-Inf.2000Jul:57(2-3):117-26.

[2] Zach S. Telemedicine Overview and Summary Electrical and Electronics Engineers in Israel, 2010,5-6:409

[3] Dick, Richards, Steen, Elaine B. The Computer-based Patient Record, An Essential Technology for Health care [J].Washington DC: National Academy Press, 1997.

[4] Ellard D R. Telemedicine in Northern Norway [J]. J Telemedicine and Telecare. 1997, 3(1): 1—22.

[5] Berteand M, Guardo R, Roberge F. Microprocesson Application for Numerical Encoding and Teansmission [J]. Proc IEEE, 1977, 65:714-722.

An Application of Active RFID and Zigbee Systems

Horng-Lin Shieh [1*], LI YING [2], and Hung-Lun Kuo [2]

[1,3] Department of Electrical Engineering, St. John's University, New Taipei City, Taiwan

[2] School of Electrical Engineering, Zhejiang University of Water Conservancy and Electric Power, Zhejiang China

[*]corresponding author: shieh@mail.sju.edu.tw

Abstract- This study used RFID technology to assist medical care personnel with ward round and nursing, so as to increase the management efficiency and reduce the human caused careless mistakes. Using the RFID tag, ZigBee technology, and long-range wireless communication, this study built an emergency care system. The proposed system consists of active RFID-ZigBee tag, active RFID-ZigBee positioning reader (including Router) and ZigBee-RS232 wireless network module. This architecture does not require any communication cable. As long as the Router is placed in the corresponding position, the patient can be located, making the construction relatively simple.

This study used RFID, ZigBee technology and graphical man-machine interface to complete a medical care positioning system. The test results proved that the nursing personnel can reduce the careless mistakes in medical treatment by using the medical care positioning system, and they can know the real-time situation of each patient. When a patient is in an emergency, he can press the emergency signal button on the active tag to send a distress signal to the host side, so that the nursing personnel can provide rescue in time.

Acknowledgements, This paper is supported by the Ministry of Science and Technology under contract number MOST 103-2221-E-129 -001

REFERENCES

1. Shieh HL, Lin SF, Chang WS (2012) RFID medicine management system Proceeding of 2012 International Conference on Machine Learning and Cybernetics, 1890-1894.
2. Want R (2006) An Introduction to RFID Technology. IEEE Pervasive Computing, vol.5, no.1, 25-33.
3. Li Y and Zhang k (2010) Research on Application of ZigBee Technology in Flammable and Explosive Environment, Wireless Sensor Network, vol. 2, no. 6, 467-471
4. ZigBee Alliance, ZigBee Wireless Sensor Applications for Health, Wellness and Fitness, https://docs.zigbee.org/zigbee-docs/dcn/09-4962.pdf.

RDOA based Emitter Localization using Constrained Least Square Algorithm under NLOS Environment

Kyunghyun Lee[1], Jungkeun Oh[1], Kwanho You[1,*],

[1]Department of Electrical and Computer Engineering, Sungkyunkwan University, Suwon, Korea
*corresponding author, E-mail: khyou@skku.edu

Abstract

The emitter localization is a significant problem in many fields such as target tracking, wireless communication, radar and many types of mobile application. RDOA is recently used as a location determination method which utilizes range difference of signal arrival between each receiver. In RDOA localization, there are two kinds of factors which decrease the accuracy of estimation: the nonline-of-sight (NLOS) noise and measurement one. In this paper, we apply Kalman filter and constrained least square (CLS) algorithm for compensating these noises. With the proposed two algorithms, we can confirm high accuracy for localization. A simulation demonstrates the performance of our proposed algorithm.

1. Introduction

The global positioning system (GPS) is the most commonly used localization method. Since GPS signal necessarily requires a satellite signal, however, it can be easily distributed by jamming. In a few years, many localization methods using distributed signal receiver such as time of arrival (TOA), angle of arrival (AOA), received signal strength (RSS) are actively researched. RDOA, which is the localization method using range difference of signal arrival, receive great attention recently. In contrast with other localization method, RDOA technique does not require time synchronization between receivers. In this paper, we use RDOA technique for localization. In two dimensional coordinates, each RDOA indicates a hyperbola between two receivers. With using at least three receivers for localization, more than two defined hyperbolas intersect at specific spot in an ideal case. Since these hyperbolic equations are nonlinear by some noises, however, these equations do not derive one specific solution. [1]

In RDOA based localization system, the NLOS noise and measurement one are major factors which cause precision decline of estimate. In order to mitigate the NLOS problem, Venkatraman [2] proposed a probability density function based measurement noise formulation and statistical techniques to distinguish LOS and NLOS propagation. Seow [3] presented a comprehensive NLOS localization scheme and a least square estimator based on AOA and TOA.

In this paper, we propose Kalman filter based recognition algorithm to identify the data partition which contains the NLOS noise. Also we suggest CLS algorithm based localization method. CLS algorithm is the optimization method based on least square (LS) algorithm. This paper is organized as follows. In Section 2, the NLOS recognition method based on Kalman filter is determined. With using identified LOS RDOA data, we analyze CLS algorithm based location determination technique which derive the solution more precisely than standard LS algorithm in Section 3. A simulation data is presented in Section 4 to confirm the performance of proposed algorithm. Finally, we conclude this paper in Section 5.

2. Kalman filter based NLOS recognition algorithm

Before we derive location estimation of an emitter, we need to consider the NLOS noise which causes distance inaccuracy at specific receiver. In this section, we divide measured range data into some partitions depending on time interval and recognize NLOS noise contained partition in each receiver. In order to identify NLOS partition at each receiver, Kalman filter can be applied to the state of emitter location.

The state of an emitter can be determined as two dimensional coordinates as follows

$$X_{k+1} = AX_k + \Gamma w_k, \quad k = 1, \cdots, M \tag{1}$$

with

$$A = \begin{bmatrix} 1 & \Delta t \\ 0 & 1 \end{bmatrix}, \ \Gamma = \begin{bmatrix} 0 \\ \Delta t \end{bmatrix},$$

and $X_k = [p_x \ v_x]^T$ is the state vector of *x*-location at the time sample t_k . w_k is the driving noise vector with a covariance of $C = \sigma_d^2 I$. p_x and v_x are the location and velocity of *x*-direction, respectively. In this paper, there are two state vectors of *x*-location and *y*-location which can express the location and velocity of an emitter. $Y_k = [p_y \ v_y]^T$ is the state vector of *y*-location.

The measured location vector Z_k can be expressed as

$$Z_k = HX_k + u_k \tag{2}$$

where $H=[1 \quad 0]$ and u_k is the measurement noise vector with a covariance of which the covariance matrix is $R=\sigma_m^2 I$.

From equations (1) and (2), the update process of the Kalman filter is denoted as follows

$$\hat{X}_k^- = A\hat{X}_{k-1} \tag{3}$$

$$P_k^- = AP_{k-1}A^T + \Gamma C \Gamma^T \tag{4}$$

$$K_k = P_k^- H^T (HP_k^- H^T + R)^{-1} \tag{5}$$

$$\hat{X}_k = \hat{X}_k^- + K_k(Z_k - H\hat{X}_k^-) \tag{6}$$

$$P_k = P_k^- - K_k H P_k^- . \tag{7}$$

Equations (3) and (4) are the time update process. Equations (5), (6) and (7) are the measurement update process. P_k denotes the covariance matrix of a state vector X_k and Z_k is Kalman filter gain.

We compare measured range data with estimated one derived from Kalman filter for recognizing the NLOS contained partition. The measured range data $r_m(t_k)$ between an emitter and *m*-th receiver at the time sample t_k can be formulated as

$$r_m(t_k) = r_i(t_k) + \Delta r_m(t_k) + \Delta r_{nlos}(t_k) \tag{8}$$

where $r_i(t_k)$, $\Delta r_m(t_k)$ and $\Delta r_{nlos}(t_k)$ denote the real range, the measurement range error and the NLOS range error, respectively.

In this paper, we suppose that there is one receiver which always exists under LOS environment. The standard deviation of measured range data between an emitter and each receiver is compared with the range standard deviation of an LOS receiver. The standard deviation ($\hat{\sigma}_{nlos}$) of unknown range data can be expressed as

$$\hat{\sigma}_{nlos} = \sqrt{\frac{1}{M}\sum_{k=1}^{M}(r_m(t_k) - r_{Kalman}(t_k))^2} \tag{9}$$

where $r_{Kalman}(t_k)$ is the estimated range by using Kalman filter. M is the number of range data in each partition.

Similarly, the standard deviation under LOS environment σ_m can be obtained from equation (9). Then, we can recognize whether each measured range data partition of a specific receiver is under NLOS environment or not with a subsequent hypothesis test.

$$H_1(LOS\ condition):\ \hat{\sigma}_{nlos} < \varepsilon\sigma_m$$

$$H_2(NLOS\ condition):\ \hat{\sigma}_{nlos} \geq \varepsilon\sigma_m \tag{10}$$

The parameter ε is chosen experimentally. If the identified range partition is under LOS environment, we progress the localization with this LOS RDOA data in order to estimate precise location of an emitter.

3. Localization using CLS method

In this section, we formulate the location expression equation based on RDOA method and determine the localization method using CLS algorithm. Although we recognized NLOS RDOA data, however, the measured data includes some errors due to measurement noise. In order to compensate this measurement error, the CLS algorithm is applied to our localization method. The CLS algorithm is one of the mathematical optimization methods which minimize the objective function in accordance with some constraints. In this paper, Lagrange multiplier method based CLS algorithm is applied to localization problem. [4]

3.1. RDOA based emitter location formulation

In order to apply CLS algorithm, the localization equation has to be formulated using RDOA data. If we gather RDOA data from at least three location-known receivers, we can derive localization formula of an emitter. We represent the unknown location of an emitter as $\mathbf{ms} = \left[\, p_x,\ p_y \,\right]^T$ and the known location of receivers are expressed as $\mathbf{bs}_i = \left[x_i,\ y_i\right]^T$, $i = \{1,\ 2,\ \cdots,\ N\}$. The RDOA measurement value can be obtained as follows

$$\begin{aligned} r_i &= \|\mathbf{ms} - \mathbf{bs}_i\| = \sqrt{(p_x - x_i)^2 + (p_y - y_i)^2} \\ r_{i1} &= \sqrt{(p_x - x_i)^2 + (p_y - y_i)^2} \\ &\quad - \sqrt{(p_x - x_1)^2 + (p_y - y_1)^2} \end{aligned} \tag{11}$$

where r_i is the range between an emitter and *i*-th receiver. With given $N-1$ RDOA data, the location of an emitter can be acquired as following equation

$$\mathbf{Gu} = \mathbf{b} \tag{12}$$

with

$$\mathbf{G} = \begin{bmatrix} x_2 - x_1 & y_2 - y_1 & r_{21} \\ \vdots & \vdots & \vdots \\ x_N - x_1 & y_N - y_1 & r_{N1} \end{bmatrix},$$

$$\mathbf{b} = \frac{1}{2}\begin{bmatrix} (x_2 - x_1)^2 + (y_2 - y_1)^2 - r_{21}^2 \\ \vdots \\ (x_N - x_1)^2 + (y_N - y_1)^2 - r_{N1}^2 \end{bmatrix}$$

and the parameter $\mathbf{u} = \left[\, p_x,\ p_y,\ r_1 \,\right]^T$ is the solution of formulated localization equation which consists of emitter location. We can derive the LS solution using pseudoinverse. Since the LS solution contains some error, however, we have to apply the optimization method to this formulation.

3.2. CLS based localization algorithm

In this section, the error between estimated solution and true one as following equation has to be minimized.

$$J_e = (\mathbf{G}\hat{\mathbf{u}} - \mathbf{b})^T (\mathbf{G}\hat{\mathbf{u}} - \mathbf{b}) \quad (13)$$

In equation (13), the estimate of parameter vector $\mathbf{u}$ is denoted by $\hat{\mathbf{u}}$.

In this CLS problem, we solve the objective function subject to the constraint as the following equation.

$$\hat{\mathbf{u}}^T \boldsymbol{\Sigma} \hat{\mathbf{u}} = 0 \quad (14)$$

where $\boldsymbol{\Sigma} = diag(1,\ 1,\ -1)$. Equation (14) can be rewritten as $(\hat{p}_x - x_1)^2 + (\hat{p}_y - y_1)^2 = \hat{r}_1^2$, equivalently. This optimization problem which is represented as equations (13) and (14) can be solved by using Lagrange multiplier method. [4] The Lagrange function denotes as follows

$$L(\hat{\mathbf{u}}, \eta) = (\mathbf{G}\hat{\mathbf{u}} - \mathbf{b})^T (\mathbf{G}\hat{\mathbf{u}} - \mathbf{b}) + \eta \hat{\mathbf{u}}^T \boldsymbol{\Sigma} \hat{\mathbf{u}} \quad (15)$$

where η is a Lagrange multiplier. The solution of this localization problem is the value which satisfies the derivative of Lagrange function with respect to $\hat{u}$ as zero.

The estimate of $\hat{u}$ by using proposed CLS based localization algorithm is derived as follows

$$\hat{\mathbf{u}} = (\mathbf{G}^T \mathbf{G} + \eta \boldsymbol{\Sigma})^{-1} \mathbf{G}^T \mathbf{b} \quad (16)$$

with η which satisfies the following equation.

$$\sum_{i=1}^{3} \frac{\alpha_i \beta_i}{(\eta + \lambda_i)^2} = 0 \quad (17)$$

where

$$\mathbf{G}^T \mathbf{G} \boldsymbol{\Sigma} = \mathbf{Q} \boldsymbol{\Lambda} \mathbf{Q}^{-1} \quad (18)$$

$$\boldsymbol{\alpha} = \mathbf{Q}^T \boldsymbol{\Sigma} \mathbf{G}^T \mathbf{b} = \left[\alpha_1, \alpha_2, \alpha_3\right]^T$$

$$\boldsymbol{\beta} = \mathbf{Q}^{-1} \mathbf{G}^T \mathbf{b} = \left[\beta_1, \beta_2, \beta_3\right]^T$$

Equation (18) is the eigenvalue decomposition process and $\boldsymbol{\Lambda} = diag(\lambda_1, \lambda_2, \lambda_3)$ is a diagonal matrix whose diagonal elements are the corresponding eigenvalues. Equation (16) is the optimized solution which minimizes the equation (13). The first and second elements of estimated parameter vector $\hat{\mathbf{u}}$ are the x-location and y-location, respectively. We can estimate more precise location of an emitter than standard LS solution.

4. Simulation

In this section, the reliability of the proposed algorithm is confirmed through a simulation. Our simulation includes five receivers which are (0, 0) km, (0, 100) km, (100, 0) km, (100, 100) km and (50, 100) km, respectively. We divide 200 time samples by 4 partitions. The NLOS noise is assumed to follow the Gaussian distribution with a mean of 3 and a variance of 1.5. Also a mean and variance of measurement noise are supposed as 1 and 1.5, respectively. Figure 1 shows the root mean square error (RMSE) comparison between NLOS noise contained result using standard LS algorithm and NLOS noise compensated result using proposed algorithm. The performance of our proposed algorithm can be verified by figure 1.

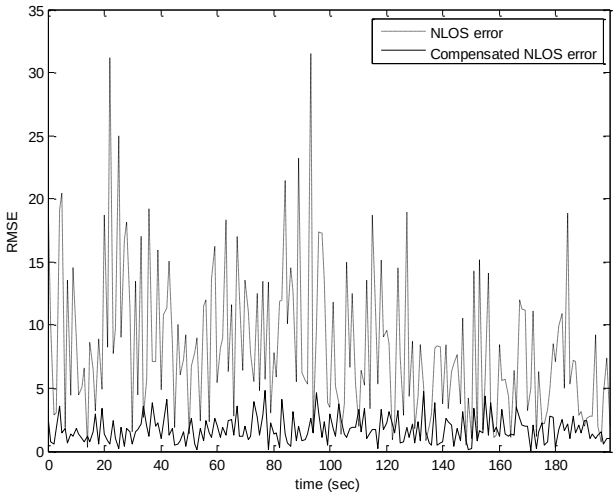

Figure 1: RMSE comparison between compensated result and uncompensated one

5. Conclusions

In this paper, we recognize the NLOS partition using Kalman filter. With the use of identified LOS data from each receiver, the Lagrange multiplier method based CLS algorithm is applied to RDOA based localization problem. We confirm a high performance of our proposed algorithm through a simulation. Although RDOA data contains NLOS noise and measurement one, we can derive precise location of emitter by using this algorithm.

Acknowledgements

This research was supported by Basic Science Research program through the National Research Foundation of Korea (NRF) funded by the Ministry of Education, Science and Technology (2013R1A1A2006728).

References

[1] K. Yang, J. An, X. Bu, and G. Sun, Constrained total least squares location algorithm using time difference of arrival measurements, *IEEE Trans. Veh. Technol.* 59: 1558−1562, 2010.

[2] S. Venkatraman and J. Caffery Jr., A statistical approach to non-line-of-sight BS identification, *Proc. 5th Int. Symp. Wirel. Pers. Multimedia Commun.*, Hawaii, USA, pp. 296−300, 2002.

[3] C. K. Seow, and S. Y Tan, Nonline-of-sight localization in multipath environments, *IEEE Trans. Mob. Comput.* 7: 647−660, 2008.

[4] K. W. Cheung, H. C. So, W. K. Ma and Y. T Chan, A constrained least squares approach to mobile positioning: algorithms and optimality, *EURASIP J. Appl. Signal Process. 2006*: 1−23, 2006.

Hybrid TDOA and AOA Localization using Weighted Least Square via RSS

Jungkeun Oh[1], Kyunghyun Lee[1], Wooram Lee[1], Kwanho You[1,*]

[1]Department of Electrical Engineering, Sungkyunkwan University, Suwon, Korea
* corresponding author, E-mail: khyou@skku.edu

Abstract

In this paper, we propose an estimation technique based on hybrid time differential-of-arrival (TDOA) and angle-of-arrival (AOA) that allows the application of weighted least squares (WLS). The accuracy of localization is a very significant problem since the measurement data can be affected by environmental noise. As a solution to this problem the received signal strength (RSS) based WLS method has been proposed and applied. This paper shows that the solution for hybrid TDOA and AOA localization error minimization has improved the estimation performance compared with typical WLS method and RSS based WLS method.

1. Introduction

This Estimating the trajectory has been used widely in military and observation industry. In the localization problem, the global positioning system (GPS) has been widely used for estimating the position of an emitter. However it would be expensive to be adopted in the mobile network because additional hardware is required in the emitters. Many researches have been performed concerning location estimation method. There are various existing location estimation approaches such as RSS, AOA, TOA, and TDOA. Among these techniques TDOA is proved to have a good accuracy [1].

The emitter position cannot be determined precisely by a geometric way. Instead, it can be estimated from a set of nonlinear equations derived from the RSS, AOA, TOA or TDOA measurements with the knowledge of the receiver location. In order to estimate the precise position of an emitter, the location determination techniques based on TOA and TDOA with least squares method [2]. The solution of the nonlinear equations can be derived directly from a least square (LS) or weighted least square (WLS). The WLS method includes an additional weight that determines how much each term in the data set influences the final estimated value. WLS approximation is applied on estimated ranges in order to estimate position, using a log normal shadowing model for path loss [3]. Cong [4] propose a hybrid TDOA and AOA location scheme which combines TDOA with AOA location.

In this paper, AOA and TDOA are two time-related parameters. In addition, various wireless location schemes using RSS have also been studied. Finally some simulation results demonstrate the effectiveness of the proposed hybrid TDOA-AOA localization algorithm using RSS ranging under the environment in which receivers with constant velocity are used.

2. System model

2.1. RSS based ranging

If In case of RSS, the range can be estimated based on the measured received signal strength between the *i-th* receiver and the emitter. Path loss can be defined as the ratio of a transmitted power to a received power, usually expressed in dB. Considering d , a distance between receiver and emitter, and d_0, a reference distance is 1m, L the total path loss is written as follows [3]:

$$L = 20\log(\frac{4\pi d_0}{\lambda}) + 10n_p \log(\frac{d}{d_0}) \quad (1)$$

where λ is the wavelength (m). n_p is the path loss exponent.

The strength of the emitter's power, cable losses, and antenna gain as well as the appropriate path loss model help in estimating the range between receiver and emitter. The measured loss varies about this mean according to a zero-mean Gaussian random variable, X_σ, with a standard deviation σ of shadowing (dB).

$$L = 20\log(\frac{4\pi d_0}{\lambda}) + 10n_p \log(\frac{d}{d_0}) + X_\sigma \quad (2)$$

The log normal shadowing model is interesting for estimation because it defines a linear relation between signal strength and the logarithm of the distance between an emitter and receiver[5].

Let's consider the log normal shadowing described by the equation (2) as a path loss model. The distance *d* follows a log-normal distribution[6].

$$\mathbf{PDF} = \frac{1}{\Gamma d\sqrt{2\pi}} \exp\left[-\frac{1}{2}\left(\frac{\log(d) - \Pi}{\Gamma} \right)^2 \right] \quad (3)$$

where

$$\Gamma = \frac{\sigma \ln 10}{10 n_p},\ \Pi = \frac{(TP - TP_0)\ln 10}{10 n_p} + \ln 10 \tag{4}$$

As d follows a log-normal distribution, the mean, median and mode of estimated distance. The mode which is one of the Maximum Likelihood method is the best estimator. The mode of estimated distance $\hat{d}_{\text{mode}}$ is given by

$$\hat{d}_{\text{mode}} = \exp\left(\Pi - \Gamma^2\right) \tag{5}$$

We use the estimated variances of mode estimators of distance given by :

$$\hat{\sigma}^2_{\text{mode}} = \hat{d}^2_{\text{mode}}(1 - \exp(-\Gamma^2)) \tag{6}$$

2.2. AOA and TDOA method

The estimation of mobile trajectory based on TDOA of the received signals has been in existence for a long time and they have executed in various approaches. The problem can be stated as following [7]

$$\begin{aligned} r_{i1} = &\sqrt{(x - x_i)^2 - (y - y_i)^2} \\ &- \sqrt{(x - x_1)^2 - (y - y_1)^2} + n_{i1}^{TDOA} \end{aligned} \tag{7}$$

where r_{i1} is the TDOA measurement from *i-th* receiver to the first receiver, (x, y) is the unknown location of emitter position, (x_i, y_i) is the known position of *i-th* receiver, (x_1, y_1) is the known position of receiver 1, and n_{i1}^{TDOA} is the TDOA measurement noise. The solution by minimizing the target function of TDOA positioning is as following

$$\hat{\mathbf{p}} = \arg\min_{\mathbf{p}} \sum \left(r_{i1} - \left\| \mathbf{p} - \mathbf{p}_i \right\| - \left\| \mathbf{p} - \mathbf{p}_1 \right\| \right)^2 \tag{8}$$

where $\mathbf{p} = \left[x,\ y\right]^T$ is the emitter's position and $\mathbf{p}_i = \left[x_i,\ y_i\right]^T$ is the position of *i-th* receiver.

As AOA localization, the mathematical model is [4]

$$\theta = \tan^{-1}\left(\frac{y - y_1}{x - x_1} \right) + n_{\theta 1}^{AOA} \tag{9}$$

The localization model is expressed as following

$$\begin{aligned} (x - x_i)\sin\theta_i = &(y - y_i)\cos\theta_i \\ &+ \sqrt{(x - x_i)^2 + (y - y_i)^2}\, n_{\theta i}^{AOA} \end{aligned} \tag{10}$$

where θ_i is the measured angle between emitter and *i-th* receiver. $n_{\theta 1}^{AOA}$ is the AOA measurement noise [8,9]. The least square solution can be obtained by minimizing the target function of AOA positioning as follows

$$\hat{\mathbf{p}} = \arg\min_{\mathbf{p}} \sum \left[-\sin\theta_i (x - x_i) + \cos\theta_i (y - y_i) \right]^2 \tag{11}$$

The positions are initially estimated from TDOA and AOA measurements; then a final position is estimated by integrating the estimated positions using least square estimation. As in equation (11), the mathematical models for TDOA and AOA are nonlinear. A tightly integrated scheme combines the TDOA and AOA measurements directly in least square estimator. After linearization with a Taylor-Series, the linearized model is as follows

$$\mathbf{p} = \begin{bmatrix} x \\ y \end{bmatrix} = \begin{bmatrix} x_0 \\ y_0 \end{bmatrix} + \left(\mathbf{A}^T \mathbf{W}^{-1} \mathbf{A} \right)^{-1} \mathbf{A}^T \mathbf{W}^{-1} \mathbf{B} \tag{12}$$

where the design matrix $\mathbf{A}$ and $\mathbf{B}$ can be defined as

$$\begin{aligned} \mathbf{A} &= \begin{bmatrix} \frac{x_0 - x_2}{r_2} & \frac{y_0 - y_2}{r_2} \\ \vdots & \vdots \\ \frac{x_i - x_2}{r_i} - \frac{x_0 - x_1}{r_1} & \frac{y_i - y_2}{r_i} - \frac{y_0 - y_1}{r_1} \\ -\sin\theta_{i1} & \cos\theta_{i1} \\ \vdots & \vdots \\ -\sin\theta_{iM} & \cos\theta_{iM} \end{bmatrix}, \\ \mathbf{B} &= \begin{bmatrix} r_{21} \\ \vdots \\ r_{i1} \\ 0 \\ \vdots \\ 0 \end{bmatrix} - \begin{bmatrix} r_{21}^0 \\ \vdots \\ r_{i1}^0 \\ -(x_0 - x_{i1})\sin\theta_{i1} + \cos(y_0 - y_{i1})\theta_{i1} \\ \vdots \\ -(x_0 - x_{iM})\sin\theta_{iM} + \cos(y_0 - y_{id})\theta_{iM} \end{bmatrix} \end{aligned} \tag{13}$$

The correlation matrix $\mathbf{W}$ is $diag\left(\mathbf{W}_{TDOA} \quad \mathbf{W}_{AOA}\right)$.

2.3. WLS estimation using RSS ranging

As the emitter gets the necessary amount of RSS ranging, it can perform the first step by estimating different ranges $\left(\hat{d}_i\right)$ with respect to the *M* discovered receivers. From the equation (6), the proposed covariance matrix $\mathbf{W}_{TDOA}$ of estimated ranges is defined by

$$\mathbf{W}_{TDOA} = \text{diag}(\hat{\sigma}^2_{\text{mode},i}),\ i = 2, \cdots, M \tag{14}$$

The correlation matrix $\mathbf{W}_{AOA}$ is

$$\mathbf{W}_{AOA} = \sigma_{AOA}^2 \begin{bmatrix} d_{\theta 1}^2 & \cdots & 0 \\ \vdots & \ddots & \vdots \\ 0 & \cdots & d_{\theta M}^2 \end{bmatrix} \quad (15)$$

σ_{AOA}^2 is the variance of the AOA observations, $d_{\theta M}^2$ is the distance between the emitter and the *M-th* receiver.

3. Discussion

In this section, we demonstrate the performance of proposed localization algorithm using RSS-WLS by some simulations. The initial locations of each receiver are (0, 0)m, (80, 800)m, (800, 180)m, and (450, 650)m. We assume the Gaussian distribution measurement noises.

As shown in figure 1, emitter moves along a curve from (0, 100)m to (800, 740)m. The thin solid line denotes a true trajectory of an emitter while the thick solid line means the estimated location of an emitter by using Hybrid TDOA and AOA algorithm.

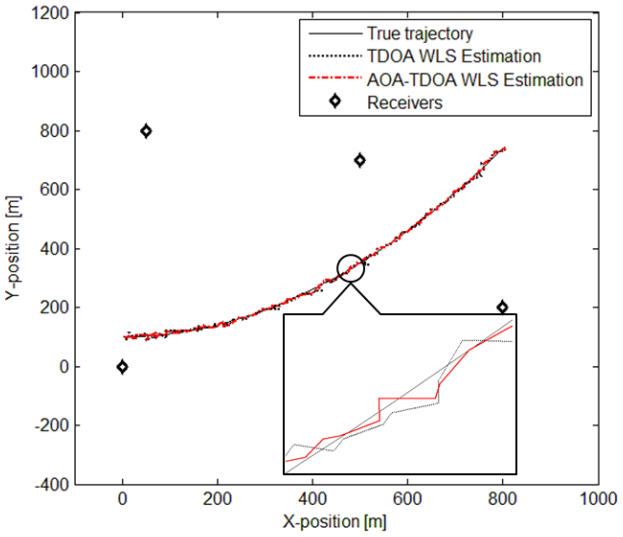

Figure 1: Trajectory comparison of Hybrid TDOA and AOA via RSS weight and TDOA via RSS weight

4. Conclusions

In this paper, the geolocation method using RSS based TDOA and AOA method is introduced. The general geolocation algorithm using TDOA signals can estimate only the emitter's position. The RSS-WLS algorithm has efficiently improved the weighted least square method. Assuming the range of log-normal shadowing model for path loss, we can estimate the weight covariance for RSS-WLS. The proposed method uses the weight covariance that follows log-normal distribution using received signal strength ranging.

Acknowledgements

This research was supported by Basic Science Research program through the National Research Foundation of Korea (NRF) funded by the Ministry of Education, Science and Technology (2013R1A1A2006728).

References

[1] B.T. Fang, "Simple solutions for hyperbolic and related position fixes," IEEE Trans. Aerospace & Electronic Systems, vol. 26, no. 5, pp. 748-753, Aug 2002.

[2] G. Shen, R Zetik, and R.S. Thoma, "Performance comparison of TOA and TDOA based location estimation algorithms in LOS environment," Proc. of the 5th Workshop on Positiong, Navigation and Communication, pp. 71-78, Mar 2008.

[3] M. Laaraiedh, S. Avrillon, and B. Uguen. "Enhancing positioning accuracy through direct position estimators based on hybrid RSS data fusion," IETR, Apr 2009.

[4] L. Cong, W. Zhuang, "Hybrid TDOA/AOA mobile user location for wideband CDMA cellular systems," IEEE Transactions on Wireless Communications, Vol.1, July 2002.

[5] K. Whitehouse, C. Karlof, and D. Culler, "A practical evaluation of radio signal strength for ranging-based localization," Mobile Computing and Communications Review, vol. 11, no. 1, Jan. 2007.

[6] M.P. McLaughlin, "A Compendium of Common Probability Distributions," Regress+ Documentation. 1999

[7] K.C. Ho, and W. Xu, "An accurate algebraic solution for moving source location using TDOA and FDOA measurements," IEEE Trans. Signal Processing, vol. 52, no. 9, pp. 2453-2463, Sep, 2004.

[8] A. Broumandan, T. Lin, J. Nielsen, and G. Lachapelle, "Practical results of hybrid AOA/TDOA geo-location estimation in CDMA wireless networks," Proc. of IEEE 68th Vehicular Technology Conference, pp. 1-5, Canada, Sep. 2008.

[9] H. J. Du and J. P. Y. Lee, "Simulation of multi-platform geolocation using a hybrid TDOA/AOA method," Technical Memorandum of Defense R&D Canada-Ottawa (TM 2004-256), Dec. 2004.

Seismic Wave Measurement using Laser Interferometer

Eunhwan OH[1], Wooram LEE[1], Minwoo LIM[1], and Kwanho YOU[1,*]

[1]Department of Electronic Engineering, Sungkyunkwan University, Suwon, Korea
*corresponding author, E-mail: khyou@skku.edu

Abstract

In this paper, we propose a seismic signal measurement method using laser interferometer. The laser interferometer is very effective in the measurement of ultra-precision displacement. However, some error factors disturb an accuracy measurement. To enhance the accuracy in length measurement, we use the adaptive fading Kalman filter. A modified energy ratio (MER) is method used to calculate the distance of epicenter. We prove the performance of the proposed seismic measurement method through some simulations.

1. Introduction

In seismology, many researchers have studied about earthquake to investigate magnitude, epicenter, tsunamis, scale and response spectrum. In the earthquake analysis, the seismic wave is mainly measured by seismometer or accelerometer. The more studies deeply progress, the more accurate measurement equipment is required. To enhance precise seismic wave measurement, we use a laser interferometer.

The laser interferometer is an ultra-precision measurement device and it is used in industry which requires small displacement [1]. However, there are some errors caused by environmental inconsistency. The environmental factors can be classified as vibration, temperature, air flows and humidity [2].

In order to solve the effect of the environmental errors, we suggest a compensation method using adaptive fading Kalman filter [3]. To determine the epicenter distance, we use a modified energy ratio (MER) method which can determine the arrival time of P and S wave. Then, the epicenter distance is calculated.

This paper is composed as follows. In Section 2, we explain how to obtain the measurement and reference value using a laser interferometer. Section 3 accounts for adaptive fading Kalman filter and how to apply heterodyne laser interferometer. Section 4 explains MER method for picking PS-time to calculate the epicenter distance. In Section 5, some simulation results prove the effectiveness of the performance. Finally, conclusion appears in Section 6.

2. Seismic wave detection using heterodyne laser interferometer

In heterodyne laser interferometer, the laser head emits two beams with different frequencies which are polarized and orthogonal to each other. Figure 1 presents a heterodyne laser interferometer system. The laser head emits two light sources which are mixed orthogonally to each other.

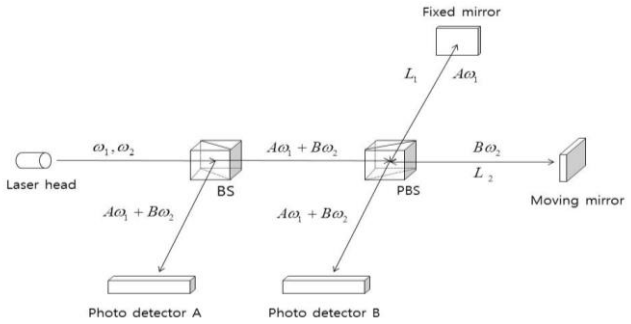

Figure 1: Heterodyne laser interferometer system

In the photo detector A, the intensity of reference electric fields is expressed as follows

$$E_{A1} = \frac{1}{\sqrt{2}} A e^{i(\omega_1 + \Phi_A)}$$
$$E_{A2} = \frac{1}{\sqrt{2}} B e^{i(\omega_2 + \Phi_B)} \quad (1)$$

where ω_1, ω_2 is the different frequencies of the laser beam, A, B are amplitudes and Φ_A and Φ_B are the initial phase. The reference signal intensity I_r is

$$I_r \propto (E_{A1} + E_{A2})(E_{A1} + E_{A2})^*$$
$$= \frac{1}{2}(A^2 + B^2) + AB\cos[\Delta\omega t + (\Phi_B - \Phi_A)] \quad (2)$$

In the photo detector B, the intensity of measurement electric fields is expressed as follows

$$E_{B1} = \frac{1}{\sqrt{2}} A e^{i(\omega_1 t + \Phi_A)}$$

$$E_{B2} = \frac{1}{\sqrt{2}} B e^{i(\omega_2 t + \Phi_B + \Delta\Phi)} \tag{3}$$

where $\Delta\Phi$ is the phase difference. The measurement signal intensity I_m is

$$\begin{aligned} I_m &\propto (E_{B1} + E_{B2})(E_{B1} + E_{B2})^* \\ &= \frac{1}{2}(A^2 + B^2) + AB\cos[\Delta\omega t + (\Phi_B - \Phi_A) + \Delta\Phi] \end{aligned} \tag{4}$$

where $\Delta\omega$ is $\omega_1 - \omega_2$. We eliminate DC component of I_r and I_m by using high pass filter. In order to obtain a phase value, we use a lock-in amplifier (LIA). Then, the value of I_x and I_y are expressed as follows

$$\begin{aligned} I_x &\propto \frac{AB}{2}\cos\Delta\Phi \\ I_y &\propto \frac{AB}{2}\sin\Delta\Phi \end{aligned} \tag{5}$$

With I_x and I_y, we can obtain $\Delta\Phi$ as follows,

$$\Delta\Phi = \tan^{-1}\left(\frac{I_y}{I_x}\right) \tag{6}$$

With the phase value, we can obtain the displacement (ΔL) between fixed mirror and moving mirror from the equation of $\Delta\Phi = 4\pi n\Delta L / \lambda$. n is a refractive index and λ is the mean of wavelength .

3. Error compensation with adaptive fading kalman filter

In this section, we show how to compensate for the errors which are caused by environmental factors using adaptive fading Kalman filter (AFKF). In the laser interferometer system, the modeling of the displacement movement of stage can be expressed as state equation and measurement equation, respectively [4]

$$\begin{aligned} &\begin{bmatrix} I_x(k+1) \\ I_y(k+1) \end{bmatrix} = \begin{bmatrix} \cos\Delta\Phi(k) & -\sin\Delta\Phi(k) \\ \sin\Delta\Phi(k) & \cos\Delta\Phi(k) \end{bmatrix} \begin{bmatrix} I_x(k) \\ I_y(k) \end{bmatrix} \\ &z(k) = \tan^{-1}\left(\frac{I_x(k)}{I_y(k)}\right) + n(k) \end{aligned} \tag{7}$$

$n(k)$ is a measurement noise and $z(k)$ is a phase value of the laser interferometer.

When measuring seismic wave, we can not predict the variation of target movement. In case a sampling time is shorter than the change of trajectory, it is supposed that the previous two sequence steps data which is ($k-1, k$) can describe a progression to the next step.

$$\begin{aligned} &\begin{bmatrix} I_x(k+1) \\ I_y(k+1) \end{bmatrix} = \begin{bmatrix} \cos\Delta\Phi_{k,k-1} & -\sin\Delta\Phi_{k,k-1} \\ \sin\Delta\Phi_{k,k-1} & \cos\Delta\Phi_{k,k-1} \end{bmatrix} \begin{bmatrix} I_x(k) \\ I_y(k) \end{bmatrix} \\ &\Delta\Phi_{k,k-1} = \Phi(k) - \Phi(k-1) \end{aligned} \tag{8}$$

The following equations are the complete set of AFKF equations for time update and measurement update process

$$\begin{aligned} \hat{x}_k^- &= f(\hat{x}_{k-1}, 0) \\ P_k^- &= \lambda_k A_K P_{k-1} A^T + W_k Q_k W_k^T \\ K_k &= P_k^- H_k^T (H_k P_k^- H_k^T + V_k R_k V_k^T)^{-1} \\ \hat{x}_k &= \hat{x}_k^- + K_k(z_k - h(\hat{x}_k^-, 0)) \\ P_k &= (I - K_k H_k) P_k^- \end{aligned} \tag{9}$$

where P_k^- and P_k represents a priori and posteriori estimate error covariance, respectively. R and Q are the covariance of process noise and the covariance of the measurement noise, respectively. K_k is a Kalman gain of $k-th$ step. And A and H are Jacobian matrix of state equation and measurement equation, respectively.

In the AFKF, the compensation accuracy can be increased by adding fading factor λ_k. The suboptimal fading factor λ_k adjusts the variance of the predicted state vector with $\lambda_k = diag(\lambda_1, \lambda_2, \lambda_3, \cdots, \lambda_m)$. If the fading factor becomes $\lambda_k \le 1$, it proceeds following a state equation (9). If not, the fading factor λ_k is updated as follows

$$\begin{aligned} \lambda_{k+1} &= \max\left\{1, \frac{\alpha \cdot tr[N_k]}{tr[M_k]}\right\} \\ N_k &= C_0 - R_k - H_k Q_k H_k^T \\ M_k &= H_k A_k P_k A_k^T H_k^T \\ C_0 &= \begin{cases} \dfrac{\phi_0 \phi_0^T}{2}, k = 0 \\ \dfrac{\lambda_k \phi_k \phi_k^T}{1+\lambda_k}, k \ge 1 \end{cases} \end{aligned} \tag{10}$$

In the equation (10), α is a positive constant, and $tr[\cdot]$ means a trace of matrix.

4. PS-time picking using MER

Seismic waves are divided as P-wave, S-wave and surface wave. To determine the distance from observatory to the epicenter, the measurement of the arrival time of the P-wave and S-wave is very important. The standard method mainly used for picking the arrival times is based on the ratio of short term average (STA) to long term average (LTA) method. However, when there are much noise in the seismogram, the MER method yields faster than STA/LTA method [5]. We use MER method for picking the arrival times of P-wave and S-wave.

MER and STA/LTA method are based on energy ratio calculations, and the difference between MER and

STA/LTA method is the size and placement of energy collecting windows at each test point.

$$f_{er}(i) = \sum_{j=i-p}^{i} sig(x_j)^2 \Big/ \sum_{j=i}^{i+p} sig(x_j)^2$$
$$f_{mer}(j) = (abs(sig(x_j)) \times f_{er})^3 \quad (11)$$

Here, f_{er} is an energy ratio, f_{mer} is a modified energy ratio, the $sig(x)$ is a seismic signal and p is the test point.

5. Simulation results

In this section, we demonstrate the performance of the AFKF and MER method. To determine the distance from an observatory to the epicenter, the laser interferometer is used as a seismometer. In this simulation, the values of laser mode are set as $\lambda = 632.991$ and $n = 1.00000002665$

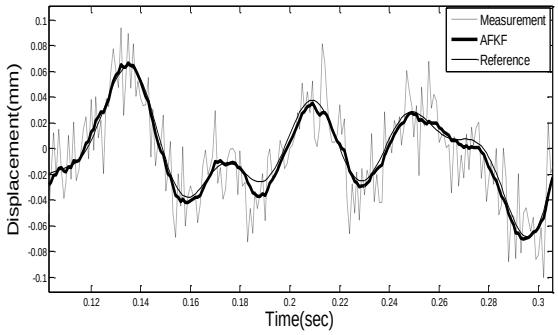

Figure 2: Error compensation based on AFKF

The seismic signal in figure 2 is magnified for visibility. The dotted line is the measurement value, the thin solid line is the reference value and the bold solid line is the compensated value. It shows that seismic wave is compensated.

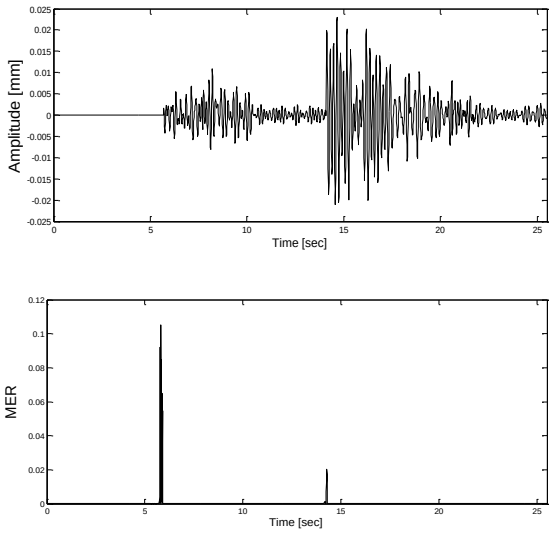

Figure 3: Modified Energy Ratio

Figure 3 shows seismic wave and MER method. Through figure 3, the performance of MER method is proved. In this simulation, we set $p = 20$. The first and second jumping points represent the arrival time of P-wave and S-wave. It shows that the arrival times of P-wave and S-wave are respectively 5.87sec and 14.3sec. The velocities of P-wave and S-wave are supposed as 8.2km/sec and 3.7km/s. The epicenter distance from an observatory can be calculated as 56.8km with the equation of $D = P_V S_V T_{PS} / (P_V - S_V)$. D is the epicenter distance, P_V is P-wave velocity, S_V is S-wave velocity and T_{PS} is P-S time.

6. Conclusion

In this paper, we suggest a seismic signal measurement method using a heterodyne laser interferometer. In heterodyne laser interferometer, some environmental factors exists such as vibration, temperature and air flow. To compensate the environment error, we used adaptive fading Kalman filter. In order to pick the arrival time of P-wave and S-wave, we used MER method and calculated the epicenter distance.

Acknowledgements

This research was supported by Basic Science Researchprogram through the National Research Foundation of Korea (NRF) funded by the Ministry of Education, Science and Technology (2013R1A1A2006728).

References

[1] H. Yeh, W. Ni, and S. Pan, "Digital closed-loop nanopositioning using rectilinear flexure stage and laser interferometer," Control Engr. Prac., Vol. 13, pp. 559-566, 2005.

[2] W. Hou and G. Wilkening, "Investigation and compensation of the nonlinearity of heterodyne interferometers," Measurement Science & Technology, Vol. 7, pp. 520-524, 1992.

[3] D. Jwo and F. Chung, "Adaptive Kalman filter for navigation sensor fusion," Sciyo Publisher, Sanghai, 2010.

[4] W. Lee, J. Lee, and K. You, "Improved measurement accuracy in heterodyne laser interferometer using WDF," Electronics Letters, Vol.45, pp. 1085 – 1087, 2009.

[5] J. Wong, L. Han, J. Bancroft, and R. Stewart, "Automatic time-picking of first arrivals on noisy microseismic data," Proc. CESG, 2009

Bioeffects of EM fields, Biological media, Medical electromagnetics

Internal Homogenization of Biological Tissues for Electromagnetic Dosimetry

Hulusi Acikgoz

Engineering Faculty, KTO Karatay University, Konya, Turkey
E-mail: hulusi.acikgoz@gmail.com

Abstract

In this paper, the internal homogenization method is introduced to determine the effective physical properties (permittivity and conductivity) of biological tissues. This method is performed on a 2D child head model obtained from MRI data. The child head model is approximated by a multilayered spherical geometry. Internal homogenization concept is compared with the original (heterogenous) model where all tissues (4 tissues) are considered and effective medium theories such as Maxwell-Garnett and Polder van Santen.

1. Introduction

Nowadays, mobile phones and wireless handy computers are widely used and there have been public concerns about their possible hazardous effect due to the emitted electromagnetic radiation. To quantify these effects, the most widely used quantity is the Specific Absorption Rate (SAR) [1]. Since SAR measurement on a living human body is difficult to experiment, dosimetry based on computer simulations is commonly used technique [2]. In numerical dosimetry, the FDTD method is a well-known method to solve Maxwell's equations but its cubic meshing scheme reduces the accuracy when complex geometries are simulated.

In this paper, the Finite Element Method (FEM) is used. However, the FEM is a time consuming technique. Furthermore, human head is a complex structure composed of several biological tissues with different thickness and physical properties. This complex and fine structure is very difficult to simulate even with high computing systems. Therefore, homogenization plays an important role to simplify the structure and then reducing the time required for the simulation. Homogenization consists of replacing the entire complex structure with a simplified model having effective physical properties. In literature, different approaches were proposed to homogenize composite materials such as metamaterials, periodic structures, etc [3]. In [4], concerning the homogenization of a multilayered structure, authors proposed to use finite difference – time domain (FDTD) grid with a coarser mesh which allows to reduce the computation. [5] developed the adjoint method combined with the FDTD method for the homogenization of human body's models. In the present work, the method called "internal homogenization" introduced by [6] is used and the obtained results are compared with those of the heterogeneous medium and results given from Maxwell-Garnett and Polder van Santen theories.

2. Homogenization

Homogenization is a term given to the treatment of inhomogeneous medium where physical properties are dependent of the space coordinates. Its aim is to find an effective medium model where physical properties do not vary within the model. In case of an external excitation, such a medium should exhibit similar behavior to the equivalent inhomogeneous medium. To calculate the effective material parameters of a heterogeneous medium, effective medium theories (EMT) are often used. In subsequent sections, the internal homogenization based on layered spherical structure and some of widely used EMT such as Maxwell-Garnett and Polder van Santen mixing theories will be presented.

2.1. Internal Homogenization Procedure

Although, the concept of "internal homogenization" was introduced to assign an effective permittivity for a single inclusion contained in a bulk material, we applied it to attribute an effective medium parameter to a simplified child head. As opposed to the internal homogenization, the external homogenization consists of assigning an effective permittivity to a distribution of inclusions in a matrix.

For simplicity, the child head model is considered to have subwavelength structure so that the quasi-static approximation can be applied. The simplified model is assumed to have multi-layered spherical geometry that is composed of 4 different tissues: skin, muscle, skull and brain.

The internal homogenization procedure is as follow: the 2D heterogeneous model is replaced by an equivalent multi-layered spherical structure (Figure 1). The radius of each tissue is calculated in accordance to its total area given by MRI data (Table 1).

Table 1: Approximated thickness of each tissue

	Skin	Muscle	Skull	Brain
Radius (m)	0.1286 (r_4)	0.1139 (r_3)	0.0686 (r_2)	0.0324 (r_1)

The homogenization is then applied to the multi-layered spherical structure. Thereafter, in order to calculate its response to an external electromagnetic excitation, the calculated effective medium parameters are presented to the 2D model of the head.

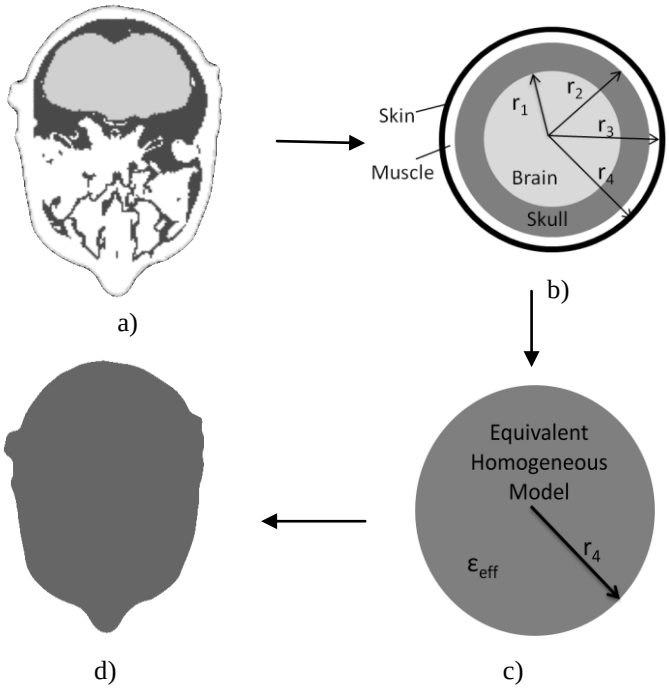

Figure 1: Internal homogenization scheme: a) heterogeneous head model, b) simplified spherical multi-layered model, c) equivalent homogeneous model with effective permittivity ε_{eff} and radius r_4 , d) homogeneous head model

The internal homogenization method is based on the equivalence of the polarizability of the multi-layered model and the equivalent homogeneous model. The homogenization procedure begins with the first two inner layers i.e. the brain and the skull tissues.
The polarizability is expressed as α_1 and α_2 for the two layered sphere (brain + skull) and the equivalent homogeneous sphere, respectively.

$$\alpha_1 = -4\pi\varepsilon_0\left(\frac{r_2^3(\varepsilon_1+2\varepsilon_2)(\varepsilon_2-\varepsilon_0)+r_1^3(\varepsilon_1-\varepsilon_2)(2\varepsilon_2+\varepsilon_0)}{2r_1^3(\varepsilon_1-\varepsilon_2)(\varepsilon_2-\varepsilon_0)+r_2^3(\varepsilon_1+2\varepsilon_2)(\varepsilon_2+2\varepsilon_0)}\right)r_2^3$$

$$\alpha_2 = 4\pi\varepsilon_0\left(\frac{\varepsilon_{12}-\varepsilon_0}{\varepsilon_{12}+2\varepsilon_0}\right)r_2^3$$

where ε_1 and ε_2 are the permittivity of the brain and the skull respectively, and r_1 , r_2 are the approximated radius of each tissue. By equating these two polarizabilities, the effective permittivity ε_{12} (for the brain and the skull) of the equivalent sphere is given by:

$$\varepsilon_{12} = \varepsilon_2\frac{r_2^3(\varepsilon_1+2\varepsilon_2)+2r_1^3(\varepsilon_1-\varepsilon_2)}{r_2^3(\varepsilon_1+2\varepsilon_2)-r_1^3(\varepsilon_1-\varepsilon_2)}$$

This calculation is repeated in an iterative manner until the effective permittivity ε_{eff} of the whole model (4 layers structure) is determined.

2.2. Maxwell-Garnett EMT

One of the most popular and widely used effective medium theories is the so called Maxwell-Garnett EMT. It dates from the beginning of the last century. It is expressed as:

$$\varepsilon_{eff} = \varepsilon_e + 3f\varepsilon_e\frac{\varepsilon_i-\varepsilon_e}{\varepsilon_i+2\varepsilon_e-f(\varepsilon_i-\varepsilon_e)}$$

The Maxwell-Garnett formula is based on the fact that the heterogeneous medium is composed of isotropic spherical inclusion with ε_i diluted in isotropic host material of permittivityε_e. The volume fraction occupied by the inclusion is f. The formula is valide for very low concentration inclusions (f<< 1). As for the internal homogenization described above this theory implies the quasi-static approximation. It has been applied for several material types including microwave absorbing material containing conducting particles [7], composite dielectric medium [8], conducting polymers [9], etc.

2.3. Polder van Santen EMT

A derivation of the Maxwell-Garnett mixing expression is Polder van Santen formula (also called Böttcher formula) that can treat a variety of mixtures. Especially it is valid for ellipsoid inclusion and for all volume fractions. For spherical inclusion the formula takes the form given below:

$$\frac{\varepsilon_{eff}-\varepsilon_e}{3\varepsilon_{eff}} = f\frac{\varepsilon_i-\varepsilon_e}{\varepsilon_i+2\varepsilon_e}$$

For dilute materials Maxwell-Garnett and Polder van Santen formulas should give the same effective medium parameters [10].

3. Results

The homogenization procedures described above is applied to a 2D child head model obtained from MRI data. The physical properties of the head tissues from 10 MHz to 3 GHz are given below (Figure 2 and 3) [11].

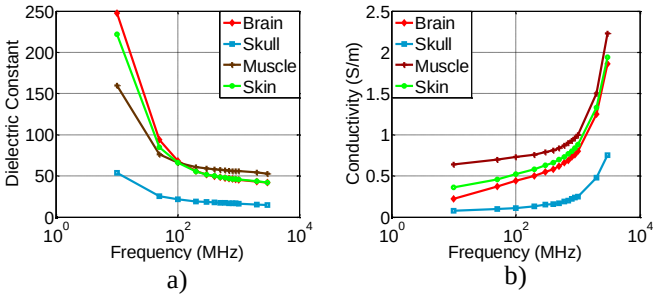

Figure 2: Tıssues parameters (10 MHz to 3 GHz): a) Dielectric Constant, b) Conductivity [11]

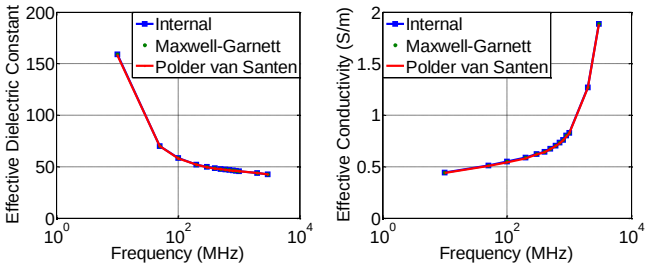

a) b)

Figure 3: Effective parameters of the homogeneous head model obtained with the three EMT (10MHz to 3 GHz): a) Effective Dielectric Constant, b) Effective Conductivity

The same procedure described in 2.1 (Figure 1) is used to obtain the effective parameters with the three different EMTs. These are given in Figure 3. One can notice that for the three methods, similar effective parameters are obtained independently of the frequency of the excitation. These results are confirmed by the fact that the filling fraction f for each tissue layer is very low especially for the three innermost layers (Table 2). Thus, the medium is considered as a dilute one.

Table 2: Filling fraction for each layer

r_1^3/r_2^3	0.1052
r_2^3/r_3^3	0.2184
r_3^3/r_4^3	0.6948

These effective properties are then used in the 2D head model where only the external boundary exists and all internal boundaries are suppressed. Thus, the computation time will be reduced due to a lower mesh number. In fact, the number of mesh when the heterogeneous model is considered is 85490, whereas after the homogenization only 6146 meshes remain due to the removal of all internal boundaries. The FEM computation is about ten times slower after the homogenization.

Validation of the internal homogenization method is carried out by computing the electric field distribution inside the original heterogeneous and the homogeneous models. The source of radiation is an infinitesimal dipole placed at 1 cm from the boundary of the skin. Figure 2 and Figure 3 show the electric field distribution at two frequencies, 100 MHz and 900 MHz, for heterogeneous and homogeneous models, respectively.

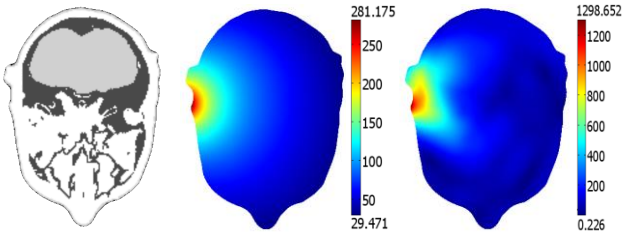

Figure 4: Heterogeneous model (left), the electric field distribution at 100 MHz (center) and 900 MHz (right)

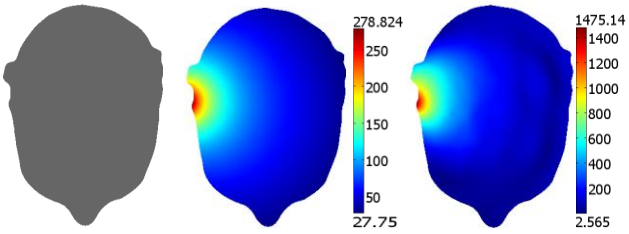

Figure 5: Homogeneous model (left), the electric field distribution at 100 MHz (center) and 900 MHz (right)

It is clearly shown that at low frequency (100 MHz) the electric field distribution is similar for both models. However, at higher frequency (900 MHz), there is a net difference between them. To quantify this difference, the relative error induced by each EMTs, internal homogenization, Maxwell-Garnett and Polder van Santen are computed. These are plotted versus the normalized electric field intensity in Figure 6 and Figure 7. On these plots, each data represent the error calculated at a specific space coordinate within the head model.

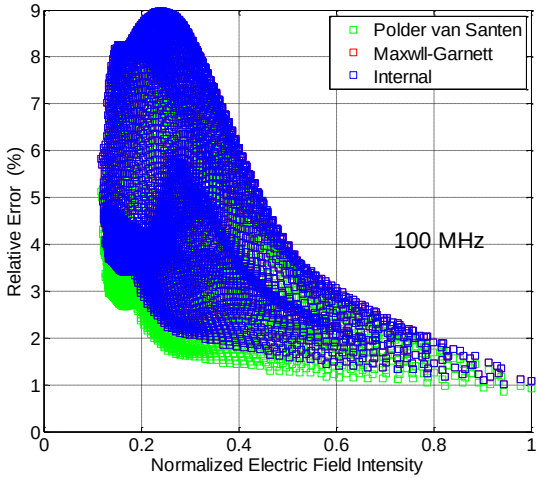

Figure 6: Error relative Normalized Electric Field Intensity at 100 MHz

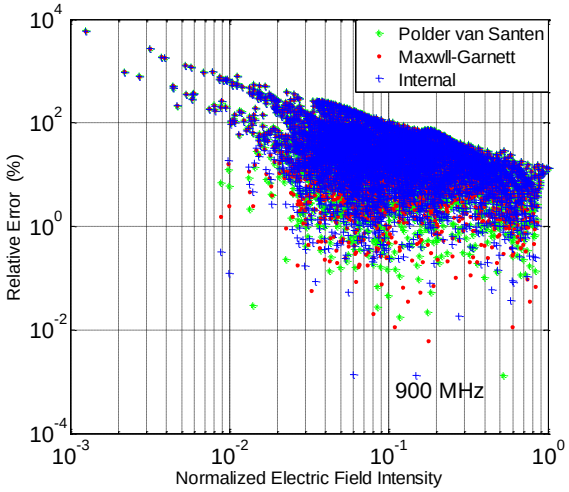

Figure 7: Error relative vs. Normalized Electric Field Intensity at 900 MHz

Figure 6 and 7 show that the error is more important at 100 MHz than at 900 MHz. Moreover, at both frequencies the higher the electric field intensity, the lower is the error. From this observation, one can state that, in the vicinity of the excitation, where the EM radiation is much likely to have damage on biological tissue, the error induced by the homogenization is less important.

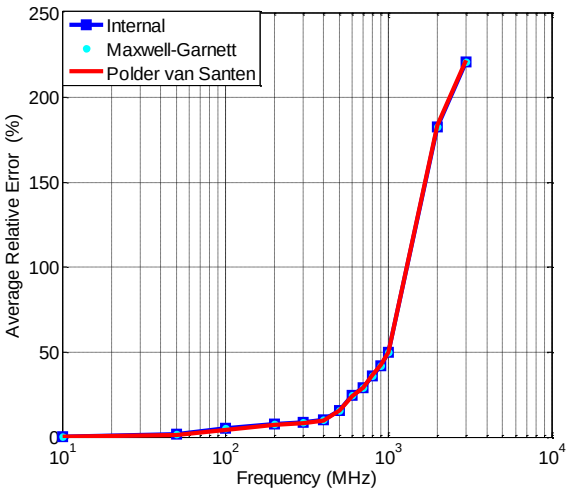

Figure 8: Average Relative Error vs. Frequency

Furthermore, to confirm the validity of the employed internal homogenization method, the average relative error is plotted versus the frequency (Figure 8). The average error remains acceptable up to 400 MHz (about 10%). Beyond this frequency, the homogenization gives inaccurate results. This important error is due on one hand to the fact that the quasi-static approximation that is made is no more valid beyond this frequency. On the other hand, the spherical multilayered structure is not fully representative of the complex head structure. At high frequencies, the EM response is more dependent on fine details of the structure.

4. Conclusions

In this paper, the concept of internal homogenization is presented and the results are compared with the heterogeneous model and Maxwell-Garnett and Polder van Santen effective medium theories. It has been shown that up to a certain frequency where the quasi-static approximation is valid, the complex multi-layered structure can be replaced by its counterpart effective medium. The internal homogenization method gives results similar to those obtained from Maxwell-Garnett and Polder van Santen EMTs.

Although, the employed method is limited in frequency, it is worth to note that most of the error is far away from the excitation and is located where the electric field intensity is weak. Thus, one can propose to use the homogenization only in the vicinity of the radiation source, inside the head, a few centimeters from the skin. Homogenization allows to diminish the number of mesh required to represent thin shells and consequently the simulation time is reduced considerably.

References

[1] IEEE, *Recommended practice for determining the peak spatial-average Specific Absorption Rate (SAR) in the human head from wireless communications devices: measurement techniques*, IEEE Standard 1528, 2003.

[2] V. Monebhurrun, *M-F. Wong ; J.* Wiart, *Numerical and Experimental Investigations of a Commercial Mobile Handset for SAR Calculations*, The 2nd International Conference on Bioinformatics and Biomedical Engineering, 2008. ICBBE 2008, 16-18 May 2008.

[3] X. Chen, T. M. Grzegorczyk, B. Wu, J. Pacheco, and J. A. Kong, *"Robust method to retrieve the constitutive effective parameters of metamaterials,"* Phys. Rev. E, vol. 70, pp. 016608-1–016608-7, 2004.

[4] A. Pradier, F. Lacroux, D. Lautru, M.F Wong,V. Fouad Hanna, J. Wiart, "*Influence of the homogenization of tissues on the electric field Calculation in Numerical Dosimetry for wireless Application*", Proceedings of the 9th European Conference on Wireless Technology, Manchester (UK), September 2006.

[5] J. Silly-Carette, D. Lautru, A. Gati, M-F. Wong, J. Wiart, V.Fouad Hanna, "*Optimisation of the homogenization of tissues using the adjoint method and the FDTD*", International Microwave Symposium Digest, 2008 IEEE MTT-S, 15-20 June 2008.

[6] U. K. Chettiar, N. Engheta, *Internal homogenization: Effective permittivity of a coated sphere*, OPTICS EXPRESS, Vol. 20, No. 21, 8 October 2012.

[7] M. Y. Koledintseva, P. C. Ravva, R. E. DuBroff, J. L. Drewniak, K. N. Rozanov, and B. Archambeault, "*Engineering of composite media for shields at microwave frequencies*," *Proc. IEEE EMC Symposium*, Vol. 1, 169–174, Chicago, IL, August 2005.

[8] P. Mallet, C. A. Guérin, and A. Sentenac, "*Maxwell-Garnett mixing rule in the presence of multiple scattering: Derivation and accuracy*", Phys. Rev. B 72, 014205, 25 July 2005

[9] O. Levy, "*Maxwell Garnett theory for mixtures of anisotropic inclusions: Application to conducting polymers*", PHYSICAL REVIEW B, vol. 56, no 13, 1 October 1997.

[10] A. Sihvola, "*Electromagnetic mixing formulas and applications"*, IEE Publishing, London, 1999

[11] Federal Communication Commission, *"Body Tissue Dielectric Parameters"*, http://transition.fcc.gov/oet/rfsafety/dielectric.html

Educational Electromagnetics

Application of LTSpice in Communication Electronic Circuit Course and Experiment Training

Guohua Liu, Zhiqun Cheng, Tao Zhou, Huajie Ke and Zhihua Dong

School of Electronic and Information, Hangzhou Dianzi University, Hangzhou, China
*corresponding author, E-mail: ghliu@hdu.edu.cn

Abstract

With the development of information computer technology, new Electronic Design Automation (EDA) tools are applied in college courses teaching. Communication electronic circuit course is an important fundamental undergraduate course for the major of electrical engineering. First, the course involves rich nonlinear electronic circuit theoretical knowledge and a large number of mathematical formulas. Most of this knowledge is difficult for students to learn. Furthermore, to improve the students' circuit design and practical ability, the course contains practice training. Compared with other electronic courses, it covers both abstract theory and experiment study.

LTSpice is a high performance free analog circuit SPICE simulator, schematic and waveform viewer. It is small and fast when simulated high frequency circuits. It is conveniently for students to view the output waveforms of the circuits. The third party SPICE model can be added to LTSpice easily.

In this paper, the application of LTSpice in communication electronic circuit course teaching including class teaching, practice training and students' after-class research. Firstly, the teacher demonstrates the waveforms of function circuit such as high frequency small signal amplifier, high frequency oscillator, amplitude modulation (AM), frequency modulation (FM), etc. The mode of classroom teaching can stimulate interest of the students in learning. Improve the efficiency of the course classroom teaching. Secondly, the students achieve several simulation experiments in practice training. The experimental contents are both basic function circuits and communication system design. For example, students are required to design a "small power FM transmitter system" and to simulate the results with LTSpice IV in communication circuit laboratory. Finally, the students are required to accomplish at least two communication design projects with the EDA software after-class time. The practice shows that all the three aspects of teaching application of LTSpice can improve the innovation thoughts and capacity of the students.

Nanoplasmonics

Two-dimensional graphene plasmons as analogue of two-dimensional hydrodynamic waves

Baile Zhang[1,2*]**, Xiao Lin**[1,3]**, and Xihang Shi**[1]

[1]Division of Physics and Applied Physics, School of Physical and Mathematical Sciences,
Nanyang Technological University, Singapore 637371, Singapore.

[2]Centre for Disruptive Photonic Technologies,
Nanyang Technological University, Singapore 637371, Singapore.

[3]State Key Laboratory of Modern Optical Instrumentation,
Department of Information Science and Electronic Engineering,
Zhejiang University, Hangzhou 310027, China.

[*]corresponding author: blzhang@ntu.edu.sg

Abstract-Intricate and intriguing hydrodynamic wave phenomena are revealed to have counterparts in graphene plasmonics, including the plasmonic splashing generated by a fast-moving electron perpendicularly impacting upon a two-dimensional graphene monolayer and the plasmonic V-shaped ship-wake generated by a swift electron moving parallel above a graphene monolayer.

Graphene plasmons, as a kind of peculiar plasmonic waves on graphene, have been drawing immense attention lately [1-12]. However, most related studies predominantly focused on very basic wave phenomena such as the measurement on wavelength and the observation on reflection and refraction [1-4], while the door to the "virgin land" of many intricate and intriguing wave phenomena (such as those fascinating hydrodynamic waves on two-dimensional liquid surface in nature [13-15]) on graphene is still missing.

In the first part, we fill this gap by investigating dynamic excitation of graphene plasmons when a monolayer graphene is perpendicularly impacted by a swift electron, as an analogue of hydrodynamic splashing. A central jet-like rise, called "Rayleigh jet" or "Worthington jet" as a hallmark in hydrodynamic splashing, is demonstrated as an excessive concentration of graphene plasmons, followed by plasmonic ripples dispersing like concentric ripples of deep-water waves. This plasmonic jet, serving as a monopole antenna, can generate radiation at atomic scale, and thus breaks the fundamental formation length limit for transition radiation, which is an important extension of Ginzburg and Frank's theory of transition radiation by squeezing the formation length down to the atomic scale. In the second part, we demonstrate a V-shaped plasmonic wave pattern when a swift electron moves parallel above a graphene monolayer, which is stationary with respect to the swift electron, as an analogue of hydrodynamic ship-wakes. The plasmonic wake angle is found to be same with the Kelvin angle and thus insensitive to the electron velocity when the electron velocity is small, and gradually transit into the Mach angle and thus decrease by increasing the electron's velocity when the electron velocity is large. Taking into account the advantages of precise spatial control and wideband excitations, the predicted electron induced radiation provides a promising light source for further graphene optics studies.

Our work is inspired by the formal similarity between the dispersions of graphene plasmons and hydrodynamic deep-water waves. Since there are so many exciting wave phenomena in hydrodynamics, our approach can be generally extended to reveal other novel plasmonic wave phenomena in the platform of

graphene.

Acknowledgements,

This work was sponsored by Nanyang Technological University for Start-Up Grants, the Singapore Ministry of Education under Grant No. Tier 1 RG27/12 and Grant No. MOE2011-T3-1-005.

REFERENCES

1. Fei, Z. *et al*. "Gate-tuning of graphene plasmons revealed by infrared nano-imaging," *Nature* **487**, 82-85, 2012.
2. Chen, J. *et al*. "Optical nano-imaging of gate-tunable graphene plasmons," *Nature* **487**, 77-81, 2012.
3. Gonzalez, P. A. *et al.* "Controlling graphene plasmons with resonant metal antennas and spatial conductivity patterns," *Science* **344**, 1369-1373, 2014.
4. Yan, H. *et al.* "Damping pathways of mid-infrared plasmons in graphene nanostructures," *Nat. Photon*. **7**, 394-399, 2013.
5. Brar, V. W., Jang, M. S., Sherrott, M., Lopez, J. J. & Atwater, H. A. "Highly confined tunable mid-infrared plasmonics in graphene nanoresonators," *Nano Lett.* **13**, 2541-2547, 2013.
6. Low, T. & Avouris, P. "Graphene plasmonics for terahertz to mid-infrared applications," *ACS Nano* **8**, 1086-1101, 2014.
7. Vakil, A. & Engheta, N. "Transformation optics using graphene," *Science* **332**, 1291-1294, 2011.
8. Grigorenko, A. N., Polini, M. & Novoselov K. S. "Graphene plasmonics," *Nat. Photon*. **6**, 749-758, 2012.
9. Jablan, M., Buljan, H. & Soljačić, M. "Plasmonics in graphene at infrared frequencies," *Phys. Rev. B* **80**, 245435, 2009.
10. Jablan, M., Buljan, H. & Soljačić, M. "Plasmons in graphene: fundamental properties and potential applications," *Proc. IEEE* **101**, 1689-1704, 2013.
11. García de Abajo, F. J. "Multiple excitation of confined graphene plasmons by single free electrons," *ACS Nano* **7**, 11409-11419, 2013.
12. Zhou, W. *et al*. "Atomically localized plasmon enhancement in monolayer graphene," *Nat. Nanotech.* **7**, 161-165, 2012.
13. Whitham, G. B. *Linear and Nonlinear Waves* (John Wiley & Sons, 1974).
14. Rein, M. "Phenomena of liquid drop impact on solid and liquid surface," *Fluid Dynamics Res.* **12**, 61-93, 1993.
15. Worthington, A. M. *A Study of Splashes* (Longmans, Green and Co., London, 1908).

Hybrid photonic-plasmonic crystals with high Q factors and its related applications on coherent fluorescence emission and chemical sensor

Lei Shi

Department of Physics, Fudan University, Shanghai,China
E-mail: lshi@fudan.edu.cn

One of the main limitations in plasmonics is its intrinsic loss. Here, we propose that by using a dielectric grating on top of a flat metal surface, leaky surface optical modes with high Q factors including plasmonic and guided modes are well supported and coupled to the free space. Both experimental and theoretical results show that the plasmonic modes have the Q factors as high as 100 and the guided modes have the Q factors as high as 160. Moreover, due to those high Q factor modes, hybrid photonic-plasmonic crystals are applied to realize directional fluorescence emission with high degree of spatial and temporal coherence as well as chemical sensor with high sensitivities and figure of merit.

References

1. Lei Shi et al. Laser & Photo. Rev. 8, 717-725, 2014
2. Lei Shi et al. Phys. Lett. A 374, 1059-1062, 2010
3. Lei Shi et al. Appl. Phys. Lett. 97, 251111, 2010
4. Xindi Yu, Lei Shi et al. Adv. Funct. Mater. 20, 1910-1916, 2010
5. Xiaowen Yuan, Lei Shi et al. Opt. Express 22, 23473, 2014

Propagation of quantum signal in plasmonic waveguides

Xi-Feng Ren, Yong-Jing Cai, Ming Li, Chang-Ling Zou, Xiao Xiong, Hua-Lin Lei, Bi-Heng Liu, Guo-Ping Guo, and Guang-Can Guo*

[1] Address: Key Lab of Quantum Information, University of Science and Technology of China, CAS, Hefei, Anhui, 230026, China

[2] Address: Synergetic Innovation Center of Quantum Information & Quantum Physics, University of Science and Technology of China, Hefei, Anhui 230026, China

[*] *Email address: renxf@ustc.edu.cn*

Abstract: Quantum photonic integrated circuit (QPIC)[1] based on dielectric waveguides has been widely used in linear optical quantum computation. Recently, surface plasmon was introduced to this area since it can confine and manipulate light beyond the diffraction limit[2]. Here, on-chip quantum interference of two single surface plasmons is realized with dielectric loaded surface plasmon polariton waveguides. The high visibility larger than 90% not only proves the Bosonic nature of single plasmons, but also is feasible for realizing basic quantum logic gates in linear optical quantum computation. The effect of intrinsic losses in plasmonic waveguides on quantum information processing is also discussed. Even though the influence is negligible in this experiment, our studies reveal that loss can reduce the quantum interference visibility dramatically in some cases, which means quantum coherence must be carefully considered when designing QPIC devices[3].

We also demonstrate for the first time the maintaining of quantum polarization entanglement in both a nanoscale dielectric tapered fibre and a plasmonic waveguide[4]. The transmitted states throughout the two waveguides have fidelities of 0.958 and 0.932 with the maximally polarization entangled state Φ+, respectively. Furthermore, the Clauser, Horne, Shimony, and Holt (CHSH) inequality tests performed, resulting in values of $2.588 \pm 0.141 > 2$; and $2.495 \pm 0.147 > 2$, respectively, demonstrate the violation of the hidden variable model. Since both of the waveguides confine the effective mode area to subwavelength scale, they may be used as near-field quantum probes in a quantum near-field micro/nano-scope, which can realize high spatial resolution, ultra-sensitive, fibre-integrated, and plasmon- enhanced detection, as well as bridge nanophotonics and quantum optics.

References:

1. A. Politi, M. J. Cryan, J. G. Rarity, S.Yu, & J. L. O'Brien, Silicaon-silicon waveguide quantum circuits, Science 320, 646-649 (2008).

2. W. H. Reinier, P. K. Leo& Z. Valery, Quantum interference in plasmonic circuits. Nat. Nanotechnol. 8, 719-722 (2013).

3. Yong-Jing Cai, Ming Li, Xi-Feng Ren**,** Chang-Ling Zou, Xiao Xiong, Hua-Lin Lei, Bi-Heng Liu, Guo-Ping Guo, and Guang-Can Guo, High-visibility on-chip quantum interference of single surface plasmons, Phys. Rev. Applied 2, 014004 (2014).

4. Ming Li, Chang-Ling Zou, Xi-Feng Ren, Xiao Xiong, Yong-Jing Cai, Guo-Ping Guo, Li-Min Tong, and Guang-Can Guo, Maintaining photonic quantum polarization entanglement in nanoscale waveguides, unpublished.

Purcell effect at silver nanowires and nanorings

Konstantin Filonenko and Vladimir G. Bordo

NanoSyd, Mads Clausen Institute,
Syddansk Universitet, Alsion 2, DK-6400 Sønderborg, Denmark
*corresponding author, E-mail: filonenko@mci.sdu.dk

Abstract

The spontaneous emission enhancement at metallic nanowires and nanorings is studied and the results are compared with each other. The maximum of the Purcell factor over the broad range of principal and minor nanoring radii values is found and plotted as a function of the distance between the emitter and the nanoring for different mode numbers.

1. Introduction

The metal nanowires (NW) and nanorings (NR) have a broad range of applications. Particularly, they can serve as essential elements of nanolaser resonant cavities [1]. Due to nanolaser small dimensions, an important role is played by the Purcell effect [2]. This is especially true, when surface plasmon polaritons (SPPs) are employed, because of their small mode volumes. The resulting spontaneous emission enhancement can lead to the thresholdless lasing. In this respect, the knowledge of the Purcell factor is important in choosing an optimal configuration of a plasmonic resonator. Therefore, we aim at calculating the Purcell factor in cylindrical NWs and in toroidal NRs and compare the results with each other. We analyze the Purcell factor dependence on geometry in more detail for the case of a nanoring, because it was not studied in literature before, although one can on the equivalent grounds consider a resonator proposed in Ref. [1], with a metal NW replaced by a metal NR.

The main goal of this study is to identify the whispering gallery modes (WGMs) of the NR, which are most strongly coupled to a two-level dipole emitter in weak regime and, thereby, may be suitable for achieving thresholdless lasing [3, 4]. The focus is laid on the case, where the principal radius R of the toroidal NR is much larger then the sum of its minor radius a and the emitter distance to the nanowire surface d, that is, $R/(a+d) >> 1$. In this case, the toroidal modes can be approximated by the cylindrical modes and the problem can be solved analytically [5]. Here we apply the results of the analytic theory to find the maximum of the Purcell factor as a function of the NR radii and represent it as a function of the emitter distance from the toroidal surface and the mode number.

When comparing the results for a NR with the corresponding results for a NW we use the model of sufficiently long NW proposed in [6].

2. Mathematical model

The emitter is located in an isotropic homogeneous medium with the dielectric permittivity ϵ_1 at a distance $d \geq 1$ nm from the metal NW (NR), which is modeled as a metal cylinder (toroid) of (minor) radius $a < 15$ nm and length $L >> 2\pi(a+d)$. Throughout our study we present the results for Ag, which the dielectric function is obtained as an interpolation of data, given in Ref. [7]. The emitter is characterized by the dipole moment oriented along one of the axes of the rectangular coordinate system. Here we consider orientations along the x - and z - axes.

In order to handle the problem analytically, we use the Hertz potentials to solve the electrodynamical problem. The analytic solution of the Helmholtz equations for the electric Hertz vector Π_j^e is used to find the electric field intensities outside ($j = 1$) and inside ($j = 2$) the cylinder (toroid). The tangential parts of these fields are matched at the cylindrical (toroidal) surface and the mode equation is found. In the considered range of parameters only the modes symmetric with respect to the cylinder axis (toroid center line) exist. In the case of the cylinder the solution is reduces to the single-mode expression with continuous dependence of the mode effective refractive index n_{eff} on the emitter transition wavelength λ, while for the toroid it is reduced to a single sum over the toroidal number $m = L/\lambda$, with each term characterized by a discrete complex frequency ω_m. The modes of the NW are found by solving the mode equation for n_{eff} numerically. The real and imaginary parts of ω_m for the NR modes are identified as the heights and widths of the resonance peaks for all relevant m values.

After the time-Fourier transform of the scattered field $E_\alpha^\alpha(\mathbf{R}_0, \mathbf{R}_0; \omega)$ for a particular orientation $\alpha = x, y, z$ of the emitter dipole moment $\vec{\mu}_\alpha = \mu\vec{e}_\alpha$ is found analytically, we use its connection with the field susceptibility tensor [6] to calculate the Purcell factor (cf. Eqs. (44) and (2.18) of Refs. [8] and [6], respectively):

$$F_\alpha = \frac{6\pi}{k_0^3 \epsilon_1^{3/2}} \mathrm{Im}\left[E_\alpha^\alpha(\mathbf{R}_0, \mathbf{R}_0; \omega)\right], \qquad (1)$$

where $k_0 = 2\pi/\lambda$ and $\omega = 2\pi c/\lambda$ denote the vacuum wavenumber and the frequency of the field time-Fourier harmonic, respectively, and λ and c are the emitter transition wavelength and the speed of light in vacuum, respectively.

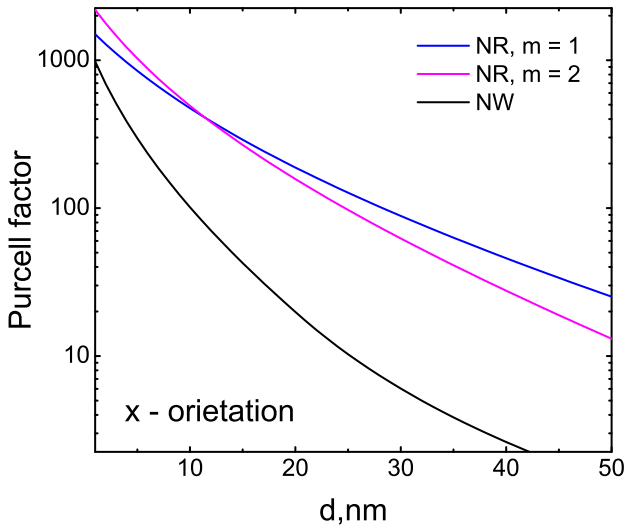

Figure 1: The Purcell factor of the x-oriented emitter at Ag NR (blue and magenta curves) and at Ag NW (black curve) maximized over the radii as a function of the distance d between the emitter and the lateral surface. The emitter transition wavelength is taken as $\lambda = 700$ nm.

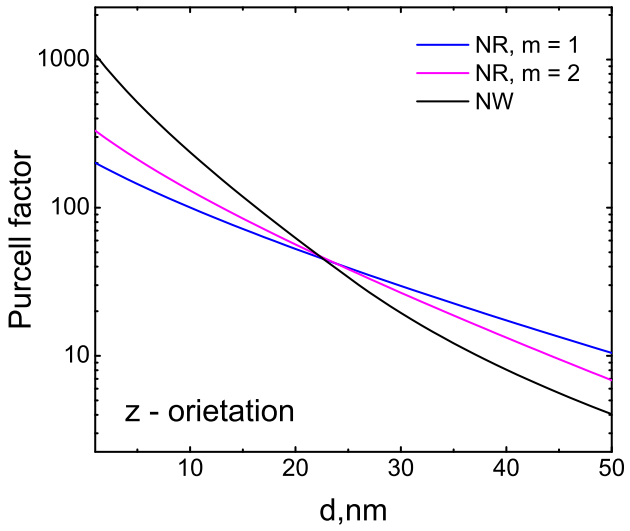

Figure 2: The Purcell factor of the z-oriented emitter at Ag NR (blue and magenta curves) and at Ag NW (black curve) maximized over the radii as a function of the distance d between the emitter and the lateral surface. The emitter transition wavelength is taken as $\lambda = 700$ nm.

3. Results and discussions

In order to compare the magnitude of the Purcell effect in metal NWs and NRs, we fix the emitter wavelength at $\lambda = 700$ nm, and find the maximum of the Purcell factor over the radii values $R = 100 - 1000$ nm and $a = 5 - 50$ nm for the fixed nanowire-emitter distances in the range $d = 1 - 50$ nm. The resulting values are plotted in Figs. 1 and 2 for the x - and the z - orientations, respectively. It is seen from Fig. 1 that the emission from the x-orientated dipole

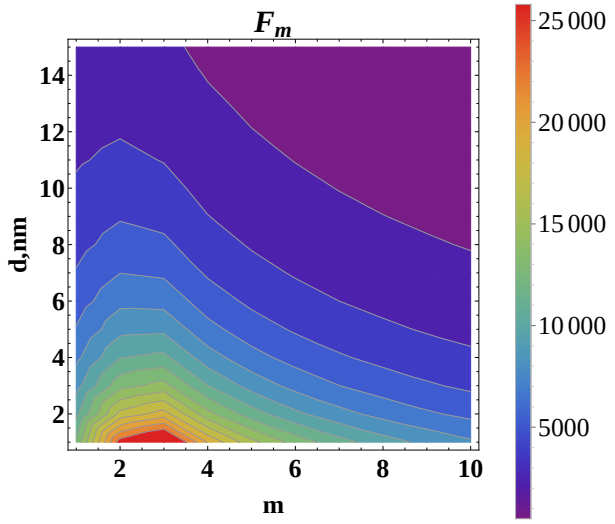

Figure 3: The Purcell factor for Ag NR as a function of the mode number m and the wire-emitter distance d maximized over the radii values.

at Ag NR (blue curve) is enhanced several times stronger than that at Ag NW. For $d < 10$ nm the WGM with $m = 3$ is enhanced stronger then the mode with $m = 2$, whereas the WGM mode with $m = 2$ dominates for $d > 11$ nm. The situation is different for the z - orientation. Below $d < 25$ nm the cylindrical mode is dominantly enhanced, and the NR mode with $m = 3$ has the smallest Purcell factor, but as d becomes larger, these modes exchange their priority: the blue curve goes above the magenta curve and the black curve goes below it.

These results are obtained for particular wavelength value $\lambda = 700$ nm. In order to find the maximum with respect to all three parameters λ, a, R we first find the resonance wavelengths as functions of a and R for each of the modes with $m = 1 - 15$ and then evaluate Purcell factor at these resonant wavelengths as a function of radii in the ranges $R = 100 - 1000$ nm and $a = 5 - 50$ nm. We find the maximum of this function for each $d = 1 - 15$ nm. The result is presented for x-orientation in Fig. 3, where the Purcell factor is plotted as a function of d for the first several modes. The figure shows that the spontaneous emission into the mode with $m = 3$ is most strongly enhanced, and rapidly weakens as the mode number grows. As our previous studies showed, the total normalized spontaneous emission rate at Ag NRs can reach the values slightly below the 30000, which is at least 10 times larger then that for Ag NWs. The previously maximum 17000-fold spontaneous emission enhancement for the mode with $m = 2$ was found for non-optimized parameter values. Now it is seen from the Fig. 3 that our optimized nanoring geometry gives us more then 25800-fold enhancement for the mode with $m = 3$.

4. Conclusion

We have calculated the dependence of the Purcell factor of a two-level emitter at Ag nanowires and nanorings and compared the results with each other. The analysis shows that for the x - orientation the enhancement is more pronounced in the case of the metal nanoring, whereas for z - orientation it is more pronounced for the metal nanowire at the small radii. We have maximized the Purcell factor on all the parameters of the problem and have found the maximum 25800-fold enhancement for the x-oriented dipole (the WGM mode with m = 3). The study shows that the photons are preferably funneled into the the lower order whispering-gallery modes in the weak coupling regime, which can be used in modeling a plasmonic nanolasers.

Acknowledgement

We are grateful to the Danish Council for Independent Research, Natural Sciences (FNU) for financial support ("Theory of Nanowire Plasmonic Lasers").

References

[1] X. Wu, Y. Xiao, C. Meng, X. Zhang, S. Yu, Y. Wang, C. Yang, X. Guo, C. Z. Ning, L. Tong, Hybrid Photon-Plasmon Nanowire Lasers, *Nano Lett.* 13: 5654–5659, 2013.

[2] E. M. Purcell, Spontaneous emission probabilities at radio frequencies, *Phys. Rev.*, 69: 681, 1946.

[3] R. F. Oulton, V. J. Sorger, T. Zentgraf, R.-M. Ma, C. Gladden, L. Dai, G. Bartal, X. Zhang, Plasmon lasers at deep subwavelength scale, *Nature*, 461: 629–632, 2009.

[4] V. G. Bordo, Lasing in nanowires: Ab initio semiclassical model, *Phys. Rev. A*, 88: 013803, 2013.

[5] K. Filonenko, V. G. Bordo, Theory of the Purcell effect at metal nanorings, submitted, 2014.

[6] V. Bordo, Purcell factor for a cylindrical nanocavity: ab initio analytical approach, *J. Opt. Soc. Am. B*, 29: 1799–1809, 2012.

[7] P. B. Johnson, R. W. Christy, Optical constants of the noble metals, *Phys. Rev. A*, 6: 4370–4379, 1972.

[8] J.M. Wylie, J.E. Sipe, Quantum electrodynamics near an interface, *Phys. Rev. A*, 30: 1185–1193, 1984.

Plasmonic properties of Au@Pd nanorods

Kitsakorn Locharoenrat[1]*, and Pattareeya Kittidachachan[1]

[1]Department of Physics, Faculty of Science, King Mongkut's Institute of Technology Ladkrabang, Bangkok 10520, Thailand
T: +66-2329-8000. Fax: +66-2329-8412.
*corresponding author, E-mail: klkitsak@kmitl.ac.th

Abstract

We focus on the plasmonic properties of the palladium-coated gold nanorods. Two characteristic plasmon bands of the palladium-coated gold nanorods have been detected in the optical absorption. One at about 525 nm, associated with the electron oscillation along the transverse direction, is independent of the palladium-shell thickness and the dielectric indices of the surrounding media. The other at about 820 – 860 nm, associated with the electron oscillation along the longitudinal direction, obviously exhibits the band shift with changes in the palladium-shell thickness and dielectric surroundings. This study shows a new way for tuning the photo-catalytic ability of nanorods, and for using them in biological-/chemical-sensors.

1. Introduction

Bimetallic nanoparticles can offer additional degrees of freedom compared with the pure elemental particles by altering their physical properties. This can enable a wide range of applications in technologies such as catalysis [1-6] and optical devices [7-11]. Like bimetallic nanoparticles, application of the bimetallic nanorods served as catalysts is one of the most active areas of nanoscience. Bimetallic nanorods having the large surface-to-volume ratio are one of the nanomaterials used to improve the selectivity and the rate of metal-catalyzed reaction. Moreover, the bimetallic nanorods served as nano-catalysts can provide a way to utilize smaller amounts of the expensive catalyst materials, by using a less expensive metal for the core material. On the other hand, the core-shell structured nano-catalysts retain the high surface plasmon resonance. These can, for instance, act as built in sensing components able to signal exposure to the biological agents and the toxic chemicals before their dosages are harmful.

So far, the bimetallic nanorods can be in alloy form or core–shell, relying on the synthesis conditions, miscibility and kinetics of reduction of metal ions. In this contribution, the authors present the optical properties of the core-shell particles where palladium wrapped gold nanorods have been obtained with various palladium-shell thicknesses and surrounding media. Palladium is unique for its catalytic property in addition to platinum. It is expected to be a highly useful industrial catalyst for producing hydrogen from methane, for reducing automobile pollutant gases, and even in the direct methanol fuel cell. Gold has also attracted much attention as a potential core for the bimetallic core-shell nanorods because of its strong optical absorption in the visible region [12-13], and catalysis properties [14-16], with the size and shape dependent properties. Furthermore, the use of gold is more economically viable than the metals that are generally used for catalysis.

2. Experimental

First, the responses of the surface plasmon resonances (SPR) were confirmed by observing the absorbance of the gold core/ palladium shell nanorods with different weight ratios of palladium and gold. The optical set-up was shown in Fig. 1. The nanorods were prepared according to Nikoobakht et. al. [17]. Their sizes and shell thicknesses are characterized by using transmission electron microscopy (TEM). Present experimental results were shown in terms of the absorbance (a.u.) with respect to the wavelength (nm). Next, optical absorption of a set of palladium-coated gold nanorods in different dielectric constant liquids was carried out as shown in Table 1. The response of SPR was also detected for the neat ethanol and toluene. Experimental data were presented in terms of the plasmon shift versus the refractive index.

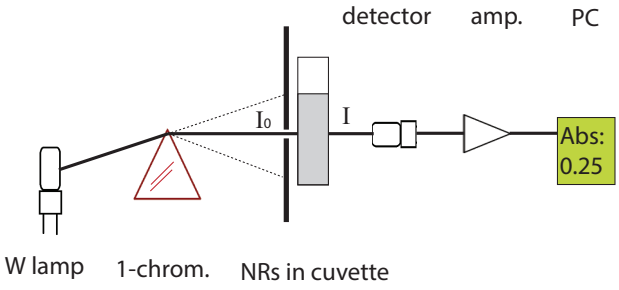

Figure 1: The optical set-up.

Table 1: Chemical media with variable refractive indices.

Ethanol fraction (%)	Toluene fraction (%)	Refractive index
100	0	1.36
67	33	1.40
50	50	1.43
33	67	1.45
0	100	1.49

3. Results and Discussion

TEM image in Fig. 2 displays the uniform palladium-coated gold nanorods. Diameter and length of the gold nanorod core are 40 $\pm$ 3 nm and 96 $\pm$ 6 nm, respectively. Thickness of a coated palladium shell was 3 $\pm$ 2 nm.

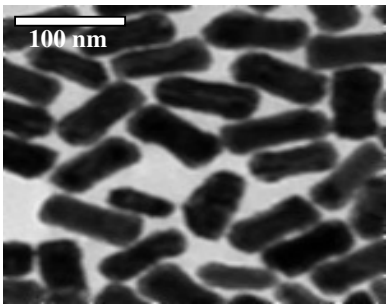

Figure 2: TEM image of the palladium-coated gold nanorods. Diameter and length of the gold nanorod core are 40 $\pm$ 3 nm and 96 $\pm$ 6 nm, respectively. Thickness of a coated palladium shell was 3 $\pm$ 2 nm.

The measured optical absorption of the palladium-coated gold nanorods with Pd/Au weight ratios of 0.04, 0.08, 0.13, and 0.21 are shown in Fig. 3.

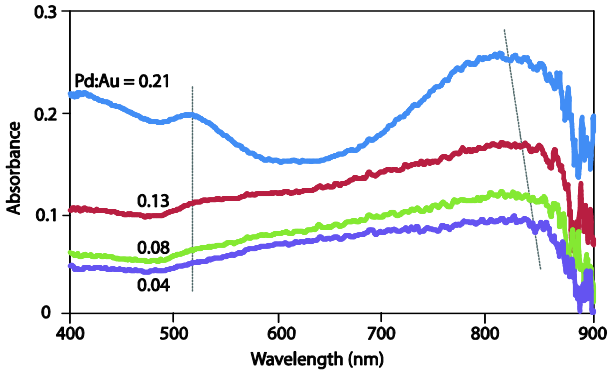

Figure 3: Measured absorption spectra of palladium-coated gold nanorods with various Pd/Au weight ratios. Left (right) peak represents TPB (LPB).

Two major plasmon peaks can be detected in all the samples. One is related to the electron oscillations perpendicular to the long axis of the rod (the transverse plasmon band, TPB), and another one is related to the conduction electron oscillations parallel to the long axis of the rod (the longitudinal plasmon band, LPB). Among the two modes, the transverse oscillations of electrons give the absorption band at a low wavelength of about 525 nm corresponding to that from the nanosphere [18]. This resonant location is independent of the palladium-shell thickness by changing Pd/Au weight ratios. Then it does not show the detectable shift when Pd/Au weight ratios increase from 0.04 to 0.21.

On the other hand, the longitudinal oscillations of electrons give the band at a high wavelength and the peak position is dependent of palladium-shell thickness. With increasing thickness of the palladium-shell, the plasmon absorption maximum shows the blue-shifted LPB corresponding to optical responses of the pure palladium nanorods due to less negative values of the real part of the permittivity of palladium as compared to gold [19]. For instance, the absorption band shifts from 860 to 820 nm when Pd/Au weight ratios increase from 0.04 to 0.21. Then, by varying the Pd/Au ratios, we can adjust a blue shift of plasmon band to be anywhere from 860 nm to 820 nm, for example right from the infrared to the near-infrared.

Furthermore, the intensity of the resonance is significantly enhanced with increasing the deposited palladium because more free electrons are involved into the plasmon. At such structure, palladium has a higher electron chemical potential (the work functions of gold and palladium are 5.3 and 5.0 electron volt, respectively [20]). Next, the surface electron density in the gold-core enhances at the expense of the electrons from the outer palladium-shell. Last, once the two metals contact each other, electrons can flow from palladium to gold until the electron chemical potential is equal. At this plasmon resonance, electric field surrounding nanorods is thus significantly disturbed, resulting in local field enhancement. Therefore, by varying the Pd/Au weight ratios we also are able to alter the intensity of the surface plasmon resonance absorbance.

In order to study the response of the plasmon peak to the refractive index of the surrounding medium, we disperse the palladium-coated gold nanorods into the organic solvents of varying refractive indices. Due to the recognizable dependence of the plasmonic sensitivity on the palladium-shell thickness, the palladium-coated gold nanorods with different palladium-shell thickness can give rise to distinct plasmon peak shift even in the same surrounding media. Figure 4 shows the peak positions of the plasmon resonance for a constant weight ratio of palladium/gold of 0.04 immersed into a series of organic dielectric media as a representative example.

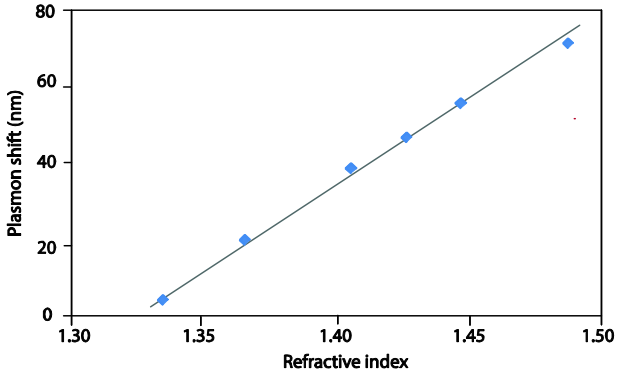

Figure 4: Peak positions of the plasmon resonance for a constant Pd/Au weight ratio of 0.04 immersed into a series of organic dielectric media. The solid line is guide to the eyes.

The peak location of transverse plasmon band (TPB) is independent of the dielectric media. The absorption peak at 525 nm (λ_1) does not change when the refractive indices of the media increase from 1.363 to 1.493 (not shown). By contrast, the peak position of the longitudinal plasmon band (LPB) at about 860 nm (λ_2) shows evident red shift with increasing the refractive indices as shown in Fig. 4. The shift magnitude of λ_2 has a relationship in the linear format with the refractive index. The host media of the high refractive indices (the dielectric constants) are effectively more polarizable and thus couple more readily with the surface plasmon electrons. The energy needed to collectively excite the electrons is then reduced. The maximum in the plasmon absorbance is then shifted to the red shift.

In summary, the deposited palladium onto the Au nanorods or changes in medium refractive index would indicate the color change (a shift in the plasmon peak position) proportional to the magnitude of the changes in the electromagnetic field around the nanorod surfaces. The UV-Vis-NIR spectra clearly represent both low and high wavelength plasmon bands due to the transverse and the longitudinal plasmon modes of the rods, respectively. The high wavelength plasmon band (λ_2) shows the band shift, whereas the low wavelength plasmon band (λ_1) remains constant with the controlled palladium-shell thickness and dielectric media. Since the palladium-coated gold nanorods have an inherent photo-sensing ability, they will be a very desirable behavior for photo-catalysis, and for SPR-based sensor platform.

4. Conclusions

We describe two observations regarding the optical properties of the gold-palladium core-shell nanorods. They possess the unique optical response with two characteristic plasmon resonance bands in the optical absorption. Unlike the resonant peak from the transverse plasmon band (TPB), the resonant peak from the longitudinal plasmon band (LPB) excitation shows a remarkable band shift with the controlled palladium-shell thickness and dielectric media. A blue-shift of the longitudinal localized surface-plasmon resonance in the UV-Vis-NIR absorption spectrum is observed by adding more palladium atoms in order to form a shell on the gold-core. This allows one to alter the plasmon resonance of the palladium-coated gold nanorods. On the other hand, since the high refractive indices of the organic solvents can screen the incident electromagnetic field, the longitudinal localized surface-plasmon resonance is even red-shifted with increasing the refractive index of the surrounding medium. Due to the excellent reproduction of the absorption response and the intense plasmon peaks, the palladium-coated gold nanorods can serve as superior candidate for chemical/biological sensing, and for photo-catalysis.

Acknowledgment

This work is supported by King Mongkut's Institute of Technology Ladkrabang, Bangkok 10520, Thailand [grant number 39/2013].

References

[1] A. Wieckowski, E.R. Savinova, C.G. Vayenas, *Catalysis and Electrocatalysis at Nanoparticle Surfaces*, Dekker, London, 2009.

[2] S.T. Christensen, H. Feng, J.L. Libera, N. Guo, J.T. Miller, P.C. Stair, J.W. Elam, Supported Ru–Pt bimetallic nanoparticle catalysts prepared by atomic layer deposition, *Nano Lett.* 10: 3047–3051, 2010.

[3] Y. Shiraishi, H. Sakamoto, Y. Sugano, S. Ichikawa, T. Hirai, Platinum nanoparticles strongly associated with graphitic carbon nitride as efficient co-catalysts for photocatalytic hydrogen evolution under visible light, *Chem. Commun.* 7: 9287–9297, 2014.

[4] R. Wang, Z. Wu, C. Chen, Z. Qin, H. Zhu, G. Wang, H. Wang, C. Wu, W. Dong, W. Fan, J. Wang, Graphene-supported Au–Pd bimetallic nanoparticles with excellent catalytic performance in selective oxidation of methanol to methyl formate, *Chem. Commun.* 49: 8250-8252, 2013.

[5] H. Liu, F. Ye, Q. Yao, H. Cao, J. Xie, J.Y. Lee, J. Yang, Stellated Ag-Pt bimetallic nanoparticles: An effective platform for catalytic activity tuning, *Sci. Rep.* 5: 3969-72, 2014.

[6] J. Liu, S. Zou, L. Xiao, J. Fan, Well-dispersed bimetallic nanoparticles confined in mesoporous metal oxides and their optimized catalytic activity for nitrobenzene hydrogenation, *Catal. Sci. Technol*. 4: 441-446, 2014.

[7] M. Grzelezak, J.P. Juste, L.M. Marzan, Optical properties of platinum-coated gold nanorods, *J. Phys. Chem. C* 111: 6183-6188, 2007.

[8] J. Suntivich, Z. Xu, C.E. Carlton, J. Kim, B. Han, S.W. Lee, N. Bonnet, N. Marzari, L.F. Allard, H.A. Gasteiger, K.H. Schifferli, Y.S. Horn, Surface composition tuning of Au–Pt bimetallic nanoparticles for enhanced carbon monoxide and methanol electro-oxidation, *J. Am. Chem. Soc.* 135: 7985–7991, 2013.

[9] Y.H. Su, W.L. Wang, Surface plasmon resonance of Au-Cu bimetallic nanoparticles predicted by a quasi-chemical model, *Nanoscale Res. Lett.* 8: 408-415, 2013.

[10] B.W. Boote, H. Byun, J.H. Kim, Silver-gold bimetallic nanoparticles and their applications as optical materials, *J. Nanosci. Nanotechnol.* 14: 1563-77, 2014.

[11] J.A. Adekoya, E.O. Dare, M.A. Mesubi, N. Revaprasadu, Synthesis of polyol based Ag/Pd nanocomposites for applications in catalysis, *J. Mater.* 2014: 184216-24, 2014.

[12] R. Guzel, Z. Ustunda, H. Eki, S. Keskin, Z.G. Durgun, A.A. Turan, A.O. Solak, Effect of Au and Au@Ag core–shell nanoparticles on the SERS of bridging organic molecules, *J. Coll. Interf. Sci.* 351: 35-42, 2010.

[13] O. Estévez-Hernández, P. Santiago-Jacinto, L. Rendón, E. Reguera, Gold nanoparticles conjugated to benzoylmercaptoacetyltriglycine and L-cysteine methylester, *J. Coll. Interf. Sci*. 350: 161-167, 2010.

[14] J. Wang, W.D. Zhang, Sputtering deposition of gold nanoparticles onto vertically aligned carbon nanotubes for electroanalysis of uric acid, *J. Electroanal. Chem*. 654: 79-84, 2011.

[15] L. Wang, P. Hoffmann, H. Heinzelmann, R. Pugin, Hierarchical positioning of gold nanoparticles into periodic arrays using block copolymer nanoring templates, *J. Coll. Interf. Sci.* 356: 496-504, 2011.

[16] I.H. Hsu, T.K. Wu, Y.C. Sun, Gold nanoparticle-based inductively coupled plasma mass spectrometry amplification and magnetic separation for the sensitive detection of a virus-specific RNA sequence, *J. Chromatography A* 1218: 1795-1801, 2011.

[17] B. Nikoobakht, Z.L. Wang, M.A. El-Sayed, Preparation and growth mechanism of gold nanorods (NRs) using seed-mediated growth method, *Chem. Mater.* 15: 1957-1962, 2003.

[18] M.L. Sandrock, F.M. Geiger, C.A. Foss, Synthesis and Second-harmonic generation studies of noncentrosymmetric gold nanostructures, *J. Phys. Chem. B* 103: 2668-2673, 1999.

[19] E.D. Palik, *Handbook of Optical Constants of Solids*, Elsevier Science, New York, 2008.

[20] J.A. Dean, *Lange's Handbook of Chemistry*, McGraw Hill, New York, 2009.

Novel thermal devices engineered with artificial materials

Yungui Ma
State Key Lab of Modern Optical Instrumentation, Centre for Optical and Electromagnetic Research, Zhejiang University, Hangzhou 310058, China
E-mail: yungui@zju.edu.cn

Extended from its electromagnetic counterpart [1,2], transformation thermodynamics applied to thermal conduction equations can map a virtual geometry into a physical thermal medium, realizing the manipulation of heat flux with almost arbitrarily desired diffusion paths, which provides unprecedented opportunities to create thermal devices unconceivable or deemed impossible before [3,4]. In this talk we report our recent work on manipulation of transient heat flux employing this technique and showed two thermal devices: a heat flux cloak and an efficient plate heater. In the cloaking device we will show that heat flux can be guided by a transformed medium to flow around a vacuum obstacle and restore its diffusion direction as if nothing inhomogeneous exists in their trajectories [5]. We will also show a first bifunctional electric-thermal cloaking device made of composite materials [6]. In the third experiment we will report an efficient plate heater that can transiently achieve a large surface of uniform temperature powered by a small thermal source [7]. Our research results are good examples of the powerful application of coordinate transformation on wave/flux manipulation and may help to broaden research in acquiring extraordinary ways to control and utilize heat energy or configure novel heat devices.

References

[1] J. Pendry, D. Schurig, and D. R. Smith, "Controlling Electromagnetic Fields," *Science*, **312**, 2006, pp. 1780-1781.
[2] U. Leonhardt, "Optical conformal mapping," *Science*, **312**, 2006, pp. 1779-1780.
[3] S. Narayana, and Y. Sato, "Heat flux manipulation with engineered thermal materials," *Phys. Rev. Lett.*, **108**, 2012, pp. 214303.
[4] S. Guenneau, C. Amra, and D. Veynante, "Transformation therdyamics: cloaking and concentrating heat flux," *Opt. Express*, **20**, 2012, pp. 8207.
[5] Y. G. Ma, L. Lan, W. Jiang, F. Sun, and S. L. He, "A transient thermal cloak experimentally realized through a rescaled diffusion equation with anisotropic thermal diffusivity," *NPG Asia Mater.*, **5**, 2013, e75.
[6] Y. G. Ma, Y. C. Liu, M. Raza, Y. Wang, ande S. L. He, "Experimental demonstration of a multiphysics cloak: Manipulating heat flux and electric current simultaneously", *Phys. Rev. Lett*. 2014. (In press)
[7] Y. C. Liu, W. Jiang, S. L. He, and Y. G. Ma, "An efficient plate heater with uniform surface temperature engineered with effective thermal materials," *Opt. Express*, **22**, 2014, 170006.

Subwavelength and Unidirectional Control of Electromagnetic Flux in Hyperbolic Mediums

Lian Shen, Runren Zhang, Zuojia Wang, Bin Zheng, and Hongsheng Chen

The Electromagnetics Academy at Zhejiang University, Zhejiang University, Hangzhou 310027, China

Abstract

We study the propagation of transverse-magnetic electromagnetic waves in the bulk and at the surface of two asymmetric hyperbolic metamaterials. We reveal that with appropriately designed material parameters, novel regimes of wave propagation emerge; in such special case, phase matching cannot be achieved unless surface voltage exists or the hyperbolic medium is regarded to be lossy. Our theoretical study also demonstrates a way to subwavelength control of electromagnetic waves without utilizing surface plasmons. Moreover, we predict that the unidirectional subwavelength scale electromagnetic flux may exist at the interface between asymmetric hyperbolic mediums, giving rise to constituting a further important step towards real world applications.

Inverse Design for Optical Devices Using Nanowire Arrays

Jingjing Zhang

Department of Photonics Engineering, Technical University of Denmark, Lyngby, 2800, Denmark
Email:jinz@fotonik.dtu.dk

With artificially designed subwavelength structures, metamaterials [1] have revolutionized the design paradigm of photonic devices and resulted in a variety of unprecedented optical effects and breakthrough applications, such as negative refraction [2], subwavelength imaging [3], and invisibility cloaking [4]. Metamaterials consisting of subwavelength spaced nanowire arrays [5, 6] are demonstrated to work over a broad range of frequency with much lower material loss, and therefore have great potential in realizing optical devices.

Here, we use inverse design to generate a variety of optical devices of predefined functions that can be achieved with metallic nanowire arrays. Evolutional optimization algorithms are applied in these inverse designs, because they are well suited for searching open ended design parameters. Two design approaches are considered. The first approach is combined with forward design schemes, such as transformation optics, to provide the initial parameters of the device for optimization. As an example, two different devices, i.e. TM polarized cloak and electromagnetic field concentrators, are designed with optimal performance, as shown in Fig. 1. In this approach, nanowires are considered as homogenized metamaterials with effective properties, which can be controlled by the spacing and radius of the nanowires. The second approach is to consider each nanowire as an individual optical scattering element, and use evolutional optimization method to directly generate the geometry and material properties of the nanowires. This method is demonstrated in designing TE polarized cloak and controlling directional emission. In all these inverse designs, we could impose constraints upon the parameters to ensure that every design searched by the algorithm could be realistically fabricated. The power of these inverse design schemes is not restricted to the specific examples we consider here. The university of these approaches allows them to be modified to design other optical devices with predefined functions.

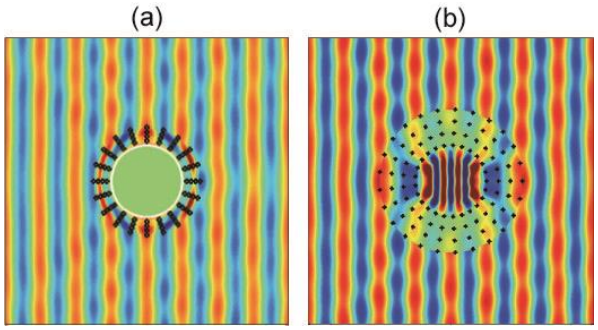

Fig1. The field distributions for a (a) cylindrical cloak (b) electromagnetic field concentrator with optimized designs under a plane wave incidence.

1. J. B. Pendry, A. J. Holden, D. J. Robbins, W. J. Stewart, IEEE Transactions on Microwave Theory and Techniques 47, 2075, (1999).
2. R. A. Shelby, D. R. Smith, S. Schultz, Science 292, 77–79, (2001).
3. J. B. Pendry, Phys. Rev. Letts. 85, 3966–3969, (2000)..
4. J. B. Pendry, D. Schurig, D. R. Smith, Science 312, 1780–1782, (2006).
5. J. Elser, R. Wangberg, V. A. Podolskiy, and E. E. Narimanov, Appl. Phys. Lett. 89, 261102 (2006).
6. J. Yao, Z. Liu, Y. Liu, Y. Wang, C. Sun, G. Bartal, A. M. Stacy, X. Zhang, Science 321, 930 (2008).

Presentation Method (Invited/Regular Oral/Poster): Invited

Material Modelling

Loss Analysis of Rotating Machines by Considering Mechanical Stress

Katsumi Yamazaki

Department of Electrical, Electronics, and Computer Engineering, Chiba Institute of Technology, Japan
E-mail: yamazaki.katsumi@it-chiba.ac.jp

Abstract

A combined stress-electromagnetic field analysis has been developed for the loss estimation of rotating machines by considering mechanical stress caused by stator shrink fittings and rotor centrifugal forces. The effects of the stress on the reluctivity and losses of machine cores are modeled by using an equivalent stress, which considers the angle between magnetic field and principal stress. The finite element mesh used for the electromagnetic field analysis is deformed due to the displacement cause by the mechanical stress. The calculated results are compared with the measured results in order to confirm the validity of the proposed method. The measured and calculated results are found to be in good agreement. Several direct and indirect effects of the mechanical stress on the machine characteristics are revealed.

1. Introduction

The mechanical stress often causes characteristics deterioration of rotating machines, i.e., increases in reluctivity and loss of machine cores [1]-[6]. Most famous effect is the increase in stator-core loss with compressive stress caused by shrink fitting. Many papers have dealt with this phenomenon. Large mechanical stress is also generated at the rotor core of high speed machines by the centrifugal forces.

In most of the previous papers, the reluctivity and the core loss are assumed to be simple functions of von Mises stress and amplitude of flux density at each point in the core [1]-[4]. However, the reluctivity and core loss depend on not only the strengths of the stress and flux density, but also their directions even in the case of isotropic magnetic materials used for rotating machines.

From these viewpoints, we have developed a combined stress-electromagnetic field (EMF) analysis that considers the angle between magnetic field and principal stress [5], [6]. In the proposed method, an equivalent stress expression, which was derived from the magneto-elastic energy [7], is introduced. In addition, the finite element mesh used for the EMF analysis is deformed due to the displacement cause by the mechanical stress.

The proposed method is applied to an induction motor (IM) and an interior permanent magnet synchronous motor (IPMSM). The calculated results are compared with the measured results in order to confirm the validity of the proposed method.

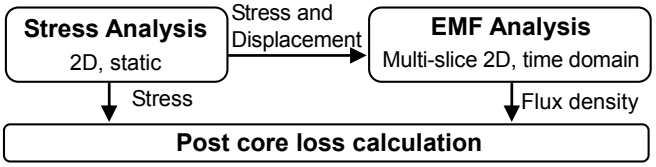

Fig. 1. Block diagram of calculation procedure.

2. Calculation method

2.1. Outline of calculation method

Fig. 1 shows the block diagram of the proposed method. The linear static finite element method (FEM) is applied to the stress analysis for the estimation of the stress and the deformation caused by the stator shrink fitting and the rotor centrifugal force. On the other hand, the nonlinear time-stepping FEM is applied to the EMF analysis in order to take into account the harmonic fields in the machines. The result of the stress analysis is given to the EMF analysis in order to modify the reluctivity, which is assumed to be a function of both the flux density and the stress at each finite element. In addition, the finite element mesh of the EMF analysis is also deformed according to the motor-shape deformation caused by the centrifugal force. Then, the loss of the core is calculated from the time-variation in the flux density in the post calculation, which is reported in [8]. This calculation is based on the one dimensional (1-D) nonlinear time-stepping FEM in order to consider the skin effect within the thickness of the electrical steel sheet used for the core. The effect of the stress distribution is also considered in this calculation.

2.2. Coupling between stress and EMF

The equations of the two dimensional (2-D) plane stress analysis are as follows

$$\frac{\partial \sigma_x}{\partial x} + \frac{\partial \tau_{xy}}{\partial y} = 0 \tag{1}$$

$$\frac{\partial \tau_{xy}}{\partial x} + \frac{\partial \sigma_y}{\partial y} = 0 \tag{2}$$

where σ_x and σ_y are the x and y components of the stress, respectively; τ_{xy} is the shearing stress.

Fig. 2 shows an example of flux density vector $\boldsymbol{B}=(B_x, B_y)$ in motor cores and principal stresses (σ_1, σ_2) calculated from σ_x, σ_y, and τ_{xy}. In the figure, the vector magnetic properties are neglected. In general, (B_x, B_y) and (σ_1, σ_2) are not parallel even in the case of isotropic magnetic materials.

Therefore, 2-D Maxwell-Ampere equation at the motor cores can be expressed, as follows:

$$\nabla \cdot \left\{ \nu\left(\sigma_1, \sigma_2, B_x, B_y\right) \nabla A_z \right\} = 0 \tag{3}$$

where A_z is the magnetic vector potential; ν is the reluctivity, which is a function of σ_1, σ_2, B_x, and B_y. Since enormous experiments are required to obtain this function, ν is simplified by using equivalent stress σ_{eq} [6], as follows:

$$\nu\left(\sigma_1, \sigma_2, B_x, B_y\right) = C_\nu\left(\sigma_{eq}, |\boldsymbol{B}|\right) \nu_{\sigma 0}\left(|\boldsymbol{B}|\right) \tag{4}$$

where $\nu_{\sigma 0}$ is the reluctivity when the mechanical stress is zero; C_ν is the reluctivity increase ratio. The 2D expression of σ_{eq} is as follows:

$$\sigma_{eq} = \left(\sigma_1 - \frac{1}{2}\sigma_2\right) h_1^2 + \left(\sigma_2 - \frac{1}{2}\sigma_1\right) h_2^2 \tag{5}$$

where $\boldsymbol{h}=(h_1,\ h_2)$ is the unit vector, which direction corresponds to that of the magnetic field. σ_{eq} is derived under the assumption that a same magneto-elastic energy leads to a same characteristics of the magnetic materials. The energy for (σ_1, σ_2) and (B_x, B_y) is equal to that for single axial stress σ_{eq}, which direction is parallel to $\boldsymbol{B}$ [7]. Therefore, ν can be expressed by using C_ν, which is determined by experiments of core materials by imposing single axial stress σ along the direction of $\boldsymbol{B}$.

Finally, the core loss is approximately calculated by using σ_{eq} and the time variation in $\boldsymbol{B}$ obtained by the EMF analysis, as follows:

$$w_c = \sum_{k=1}^{2} \left\{ C_e\left(\sigma_{eq,k}, B_{\max,k}\right) w_{e,k,\sigma 0} + C_h\left(\sigma_{eq,k}, B_{\max,k}\right) w_{h,k,\sigma 0} \right\} \tag{6}$$

where w_c is the core loss density; C_e and C_h are the increase ratios of eddy current and hysteresis losses, respectively; $\sigma_{eq,1}$ and $\sigma_{eq,2}$ are the equivalent stresses for $\boldsymbol{h}$=(1,0) and $\boldsymbol{h}$=(0,1), respectively; $B_{\max,1}$ and $B_{\max,2}$ are the amplitude of B_1 and B_2, which are the flux-density components along the principal stress axes, as shown in Fig. 2; $w_{e,k,\sigma 0}$ and $w_{h,k,\sigma 0}$ are the eddy current and hysteresis loss densities caused by B_k when the stress is zero. This expression is based on the approximation that the w_c is the sum of the losses caused by B_1 and B_2.

C_e and C_h in (6) can also be determined by experiments of core materials [1]-[5]. On the other hand, $w_{e,k,\sigma 0}$ and $w_{h,k,\sigma 0}$ are estimated by using the method reported in [5] and [8].

3. Applications

3.1. Application to an IM

First, the proposed method is applied to a 750 W class 4 pole IM. The stator housing is made by structural purpose iron, which conductivity is 8.3×10^6 S/m. The rotor conductor is an aluminum cage with one-rotor-slot-pitch skew. The rated rotational speed is 1400 rpm.

Fig. 3 shows the calculated permeability distribution under the no-load condition at the rated voltage. The result neglecting the shrink-fitting stress is also shown. It is observed that the permeability of the stator yoke considerably decreases by the stress.

Fig. 4 shows the measured and calculated total no-load losses. The calculated result by the proposed method is found to be in good agreement with the experimental result,

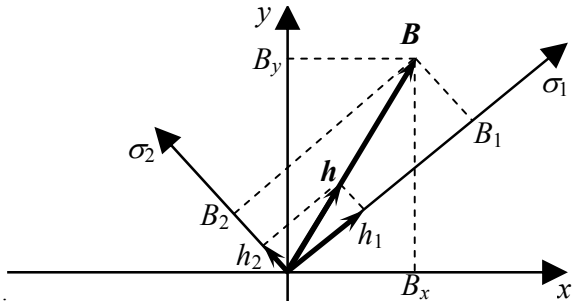

Fig. 2. Principal stress axis and flux density vector.

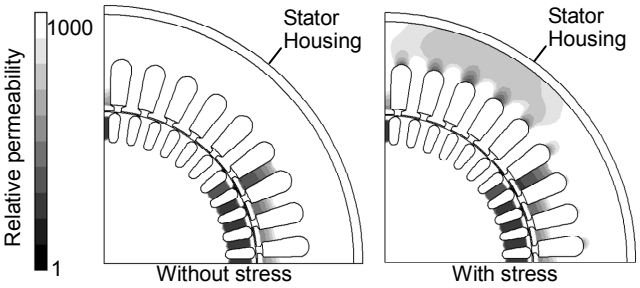

Fig. 3. Calculated permeability distributions of IM (no-load, 200 V).

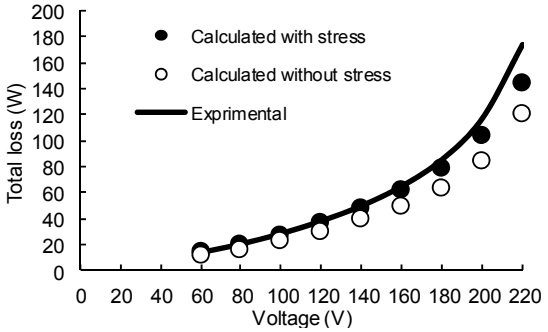

Fig. 4. Measured and calculated no-load loss of IM.

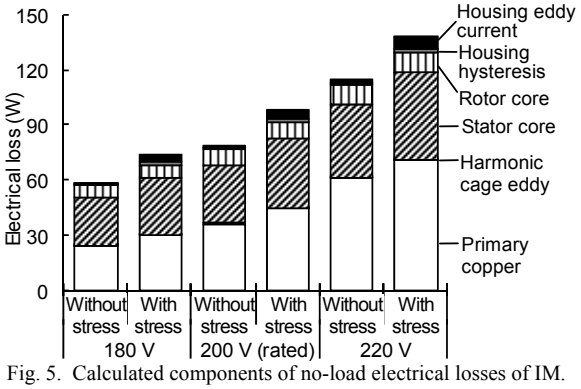

Fig. 5. Calculated components of no-load electrical losses of IM.

whereas the calculation without the shrink-fitting stress considerably underestimates the loss. Fig. 5 shows the calculated components of the no-load electrical loss. It is clarified that the result without the stress underestimates not only the stator core loss, but also the primary copper loss and housing loss, particularly the housing eddy current loss. It is considered that relatively large eddy currents are generated in the stator housing by the leakage flux from the yoke according to the decrease in the permeability by the shrink fitting stress because the hosing is made from the solid iron. This is one of the indirect effects of the mechanical stress on the loss characteristics.

3.2. Application to an IPMSM

Next, the proposed method is applied to to an 8 pole, 100 kW class IPMSM employing Nd-Fe-B magnets. The maximum rotational speed is 10000 min^{-1}. This motor is driven by a PWM inverter, which carrier frequency is 10 kHz. The stator is shrinking fitted by an aluminum housing.

Fig. 6 shows the principal stress distribution obtained by the stress analysis. Circumferential compressive stress caused by shrink fitting is observed at the stator yoke, whereas large tensile stress caused by centrifugal force is observed at the rotor surface and the rotor bridge between the inside magnet at the maximum speed.

Fig. 7 shows the displacement of the stator and rotor cores calculated by the stress analysis. The stator core is displaced to inside by the shrink fitting, whereas the rotor core is displaced to outside by the centrifugal force. The rotor-core displacement varies with rotor speed. This displacement is more than 5% of the air gap at the maximum speed.

Fig. 8 shows the experimental and calculated iron losses including the magnet eddy-current losses. The accuracy of the calculated iron loss is improved by considering the stress and the deformation. The remained calculation error is considered to be caused by the neglect of punching effect. It is observed that the rotor-core loss considerably increases at high speeds by the stress and the deformation. It is considered that there are two reasons of this increase. One is the transverse stress effect at the rotor. The harmonic rotor fluxes at the surface are nearly in the radial direction, whereas that of the tensile stress is in circumferential direction. From (5), this situation is considered to be equivalent to that the compressive stress, which strength is half of that of the transverse tensile stress, is imposed along the magnetic field direction. The other reason is the increase in the slot harmonics caused by the air-gap decrease shown in Fig. 7. The rotor-core loss increases by 6% by this effect. These effects are negligible at low speeds.

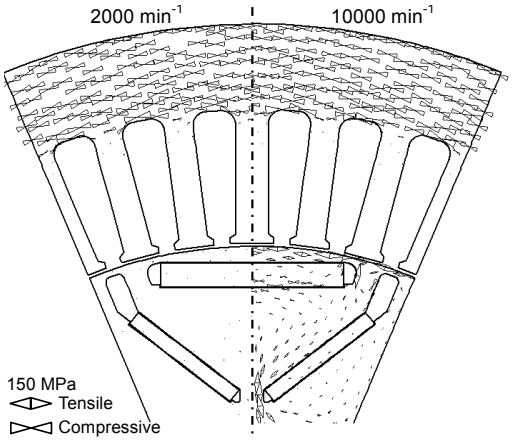

Fig. 6. Calculated principal stress distribution of IPMSM.

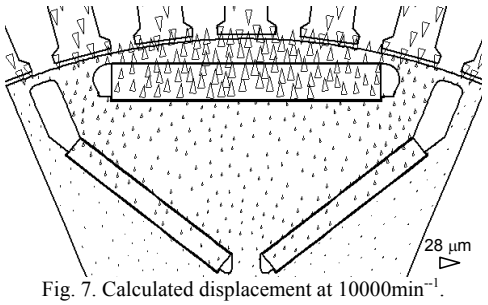

Fig. 7. Calculated displacement at 10000min^{-1}.

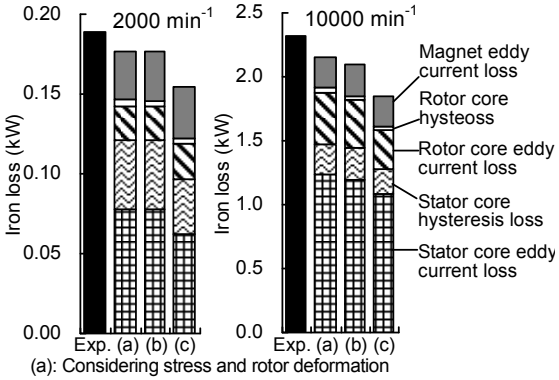

Fig. 8. Experimental and calculated iron losses of IPMSM (Armature current 300 A, Current angle 80 deg).

4. Conclusions

A combined stress-electromagnetic field analysis using an equivalent stress has been developed for the loss estimation of rotating machines by considering mechanical stress caused by stator shrink fittings and rotor centrifugal forces. The measured and calculated results are found to be in good agreement. Several direct and indirect effects of the mechanical stress on the loss are revealed.

References

[1] A. Daikoku, M. Nakano, S. Yamaguchi, Y.Tani, Y. Toide, H, Arita, T. Yoshioka, and C. Fujino, "An accurate magnetic field analysis for estimating motor characteristics taking account of stress distribution in the magnetic core," *IEEE Trans. Ind. Applicat.*, vol. 42, No. 3, pp. 668-674, 2006.

[2] D. Miyagi, N. Maeda, Y. Ozeki, K. Miki, and N. Takahashi, "Estimation of iron loss in motor core with shrink fitting using FEM analysis," *IEEE Trans. Magn*., vol. 45, no. 3, pp. 1704-1707, 2009.

[3] M. Nakano, C. Fujino, Y.Tani, A. Daikoku , Y. Toide S. Yamaguchi, H, Arita, and T. Yoshioka, "High precision calculation of iron loss by considering stress distribution of magnetic core," *IEEJ Trans. on IA*, vol. 11, no. 129, pp. 1060-1067, 2009.

[4] K. Yamazaki and Y. Kato, "Optimization of high-speed motors considering centrifugal force and core loss using combination of stress and electromagnetic field analyses*," IEEE Trans. Magn.,* vol. 49, No. 5, pp. 2181-2184, 2013.

[5] K. Yamazaki and Y. Kato, "Iron loss analysis of interior permanent magnet synchronous motors by considering mechanical stress and deformation of stators and rotors," *IEEE Trans.Magn.*, vol. 50, No. 2, 7022504, 2014.

[6] K. Yamazaki and W. Fukushima, "Loss analysis of induction motors by considering shrink fitting of stator housings," *IEEE Trans.Magn.* (in press)

[7] L. Daniel and O. Hubert, "An equivalent stress for the influence of multiaxial stress on the magnetic behavior," *J. Applied Physics*, vol. 105, 07A313, 2009.

[8] K. Yamazaki and N. Fukushima, "Iron loss model for rotating machines using direct eddy current analysis in electrical steel sheets," *IEEE Trans. Energy Conversion*, vol. 25, no. 3, pp. 633-641, 2010.

[9] N. Kurita, Y. Takahashi, K. Fujiwara, and Y. Ishihara, "Effect of stress dependence of magnetic properties on operating characteristics of permanent magnet motors," *The papers of Technical Meeting on Static Apparatus and Rotating Machinery, IEE Japan*, SA-11-79 /RM11-92, 2011.

Magneto-Electric Effect for Multiferroic Heterostructures by Monte Carlo Simulation

Zidong Wang (王子东), Malcolm J. Grimson

Department of Physics, University of Auckland, Auckland 1010, New Zealand
*corresponding author, E-mail: Zidong.Wang@auckland.ac.nz

Abstract

Magneto-electric effect in a multiferroic heterostructure, i.e. a coupled ferromagnetic-ferroelectric thin film, has been investigated through the use of Monte Carlo simulations. The classical anisotropic Heisenberg model used consists of the interaction energy, the uniaxial anisotropic energy, and the Zeeman energy. The purpose of this article is to demonstrate the dynamic response of polarization is driven by an external magnetic field, when there is a linear magneto-electric coupling at the interface between the ferromagnetic and ferroelectric components.

1. Introduction

Recently, the magneto-electric effect in thin multiferroic films has been investigated theoretically [1,2] and experimentally [3,4]. The key to understanding the nature of the magneto-electric effect is the knowledge about a coupled magnetic and electric response by elastic interaction [5]. As *Figure 1* shows, a magnetized material produces mechanical strain, due to the magnetostrictive deformation; then the strain is passed to the adjacent electric material, resulting in a polarization, due to particles' shape alteration by stress. Thus, a magnetic-mechanical effect in the ferromagnet and a mechanical-electric effect in the ferroelectric constitute the magneto-electric effect in mulitferroics.

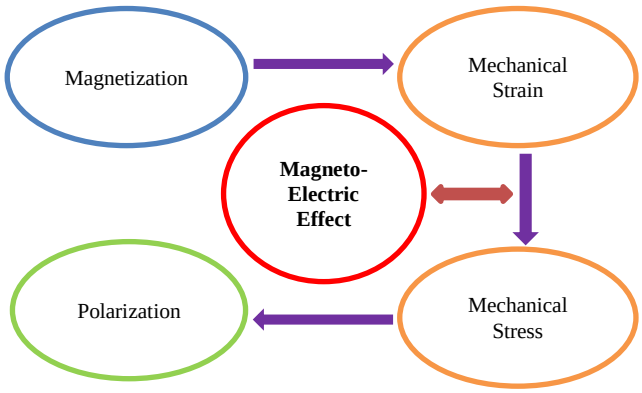

Figure 1: (colour online) Principle of the magneto-electric effect, driven by magnetic material.

The understanding of the mechanism of the magneto-electric effect is quite limited. In this work, a computational method for the magneto-electric effect in the multiferroic heterostructure sample is given in section 2, numerical results are presented in section 3 and a summary in section 4.

2. Simulation Model and Method

The composite material incorporates ferromagnetic and ferroelectric films, is called a multiferroic heterostructure. The dynamic magneto-electric effect is defined as the induced polarization of a multiferroic material in a time-dependent external magnetic field. Our numerical model clearly exhibits the aforementioned phenomenon.

2.1. Heterostructure Thin Film

Figure 2 shows a sketch of ferromagnetic and ferroelectric layers combined in a 2-D lattice. L_S represents the number of layers in the ferromagnetic film, and L is the total layer number in this sample. Each layer contains a fixed number of spins: the *blue arrows* represent the magnetic spins, and the *green arrows* represent the electric pseudo-spins. All of them have three degrees of freedom. The magneto-electric effect occurs at the interface, where g represents the magneto-electric coupling (*red line*). An external magnetic field, $B(t)$, is applied along the z-direction (*violet arrow*).

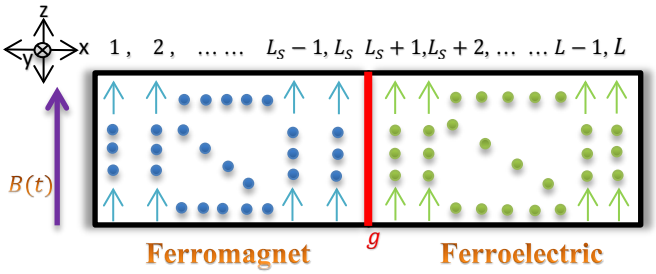

Figure 2: (colour online) Schematic of a multiferroic heterostructure thin film, blue arrows represent the magnetic spin, and green arrows represent the electric pseudo-spins. An external magnetic field is applied along the z-axis (violet arrow). The interface between ferromagnet and ferroelectric is represented by the red line.

2.2. Simulation Method

The system under consideration is operating with the classical anisotropic Heisenberg model. The following Hamiltonians have been employed for the ferromagnetic

film, H_{FM} (*Equation (1)*) [6], and the ferroelectric film, H_{FE} (*Equation (2)*) [7]:

$$H_{FM} = -J_S \sum_{<i,j>}^{N_S} \left(S_i^x S_j^x + S_i^y S_j^y + S_i^z S_j^z\right) - \mathrm{K}_S \sum_{i}^{N_S} (S_i^z)^2 \quad (1)$$

$$H_{FE} = -J_P \sum_{<i,j>}^{N_P} \left(P_i^x P_j^x + P_i^y P_j^y + P_i^z P_j^z\right) - \mathrm{K}_P \sum_{i}^{N_P} (P_i^z)^2 \quad (2)$$

Where $S_i^{x,y,z}$ and $P_i^{x,y,z}$ denote the magnetic spin and the electric pseudo-spin components at film site i with the unit size, i.e., $|S_i^{x,y,z}| = |P_i^{x,y,z}| = 1$; $S_j^{x,y,z}$ and $P_j^{x,y,z}$ denote the total strength of site i's neighbour spins and pseudo-spins, respectively; J_S and J_P are interaction strengths for the ferromagnetic film and ferroelectric film respectively; K_S and K_P are uniaxial anisotropy coefficients, both of them favour in z-direction. The Zeeman effect between magnetic spins and external magnetic field, $B(t)$, applied in z-direction are described by (*Equation (3)*):

$$E_z = -B(t) \sum_{i}^{N_S} S_i^z \quad (3)$$

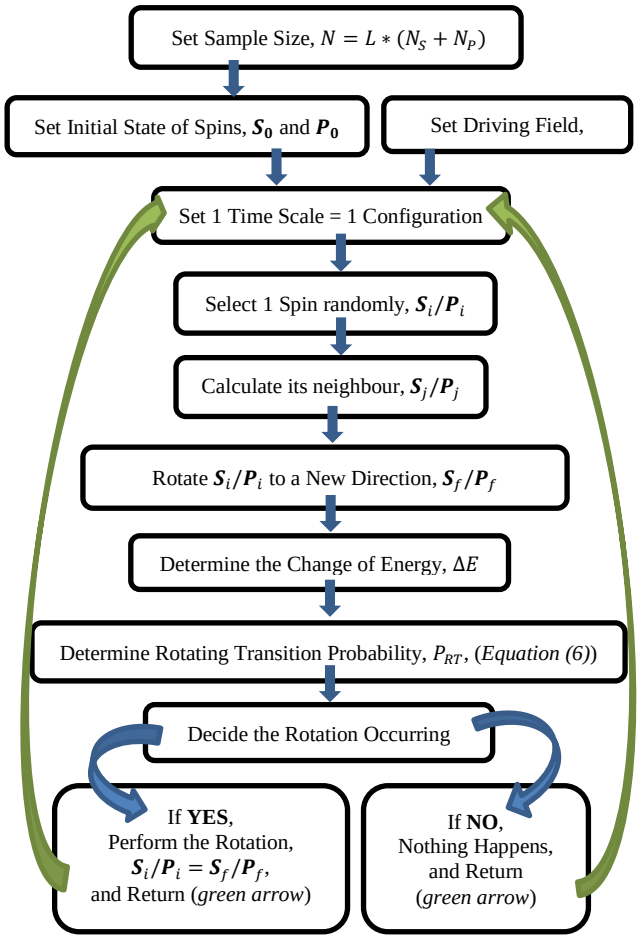

Figure 3: Steps of the Metropolis Algorithm in a dynamic Monte Carlo simulation.

Table 1. Essential Parameters for Simulation.

Ferromagnet Parameters	
Layers, L_S	3
Spins per Layer, N_S	1000
Interaction Strength, J_S	1
Uniaxial Anisotropy, K_S	0.1
Initial States, $\boldsymbol{S_0}$	Random
Ferroelectric Parameters	
Layers, L_P	6
Pseudo-Spins per Layer, N_P	1000
Interaction Strength, J_P	1
Uniaxial Anisotropy, K_P	0.1
Initial States, $\boldsymbol{P_0}$	Random
Other Parameters	
External Field Amplitude, B_0	10
External Field, $B(t)$	$B_0 sin(\omega t)$
Magneto-electric Coupling, g	Varied
Monte Carlo Steps per Spin	1000
'Inverse Temperature', β	1

The magneto-electric effect at the interface has been considered as a result of a linear coupling [1]. *Equation (4)* represents the interface energy for the spin in the last ferromagnetic layer, $\boldsymbol{S}_{N_S}$ and the pseudo-spin in the first ferroelectric layer, $\boldsymbol{P}_1$.

$$E_{ME} = g\left(S_{N_S}^x P_1^x + S_{N_S}^y P_1^y + S_{N_S}^z P_1^z\right) \quad (4)$$

Thus, the sum of the energies (*Equation (5)*) is used to determine the energy change:

$$H = H_{FM} + H_{FM} + E_z + E_{ME} \quad (5)$$

Using the Metropolis algorithm in dynamic Monte Carlo simulation [6, 7], the formula

$$P_{RT} = \exp(-\beta \Delta E) \quad (6)$$

is used to calculate the transition probability, where ΔE is the total energy change, $\beta = (k_B T)^{-1}$ is the 'inverse temperature', and k_B is the Boltzmann's constant. The entire process of the simulation method is shown in *Figure 3*.

3. Simulation Results

The numerical results of magnetic and electric responses were obtained. Essential parameters are used for the mulitiferroic thin film simulations in *Table 1*. Free boundary conditions and periodic boundary conditions have been applied in the x- and z-directions, respectively. A sequence of size $(L_S \times N_S + L_P \times N_P)$ trials comprises one Monte Carlo step per spin, is the unit of time in these simulations.

The simulation results show the z-component of mean magnetization, S_z, and polarization, P_z, per spin in each layer. *Figure 4* shows the different dynamic responses in each layer for a magneto-electric coupling, $g = 1$. In *Figure 4 (a)*-(c), responses of the magnetization in ferromagnetic layers follow an applied oscillatory driven field of angular frequency, $\omega = 2\pi/1500000$, with amplitude, $B_0 = 10$. In

the ferroelectric film, the energy transition is only executed by nearest-neighbour interactions. Thus, the amplitude of the polarization response tapers off quickly, with a longer delay time, for the further layers (*Figure 4 (d)-(i)*).

From another perspective, the hysteresis loop in each layer is shown in *Figure 5* for a magneto-electric coupling of $g = 1$. Normal symmetric hysteresis loops are formed in the ferromagnetic section of the film (*blue loops*). The electric polarization (*red loops*), indirectly driven by the external magnetic field, changes its characteristic from symmetric to asymmetric with penetration of the ferroelectric. The hysteresis curves are asymmetric loops in *Figure 5 (e)-(i)*.

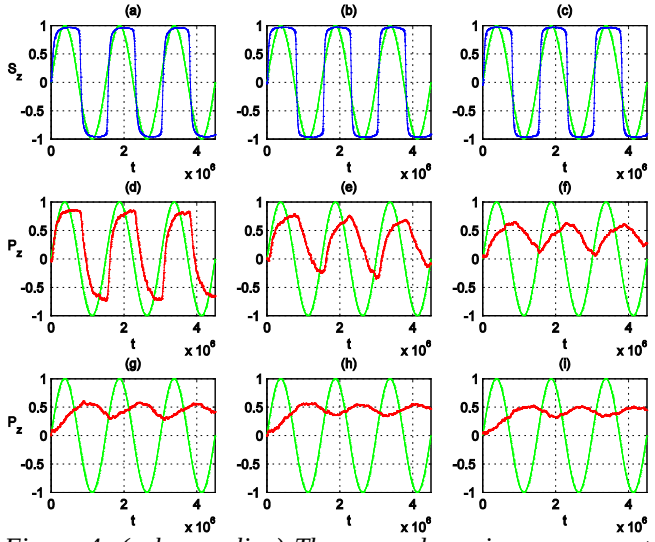

Figure 4: (colour online) The mean dynamic z-component responses in each layer, to an external sinusoidal magnetic field (green lines), with a magneto-electric coupling, $g = 1$. (a)-(c) show the magnetic responses (blue lines), S_z, in the first three ferromagnetic layers; (d)-(i) show the polarization responses (red lines), P_z, in the next six ferroelectric layers.

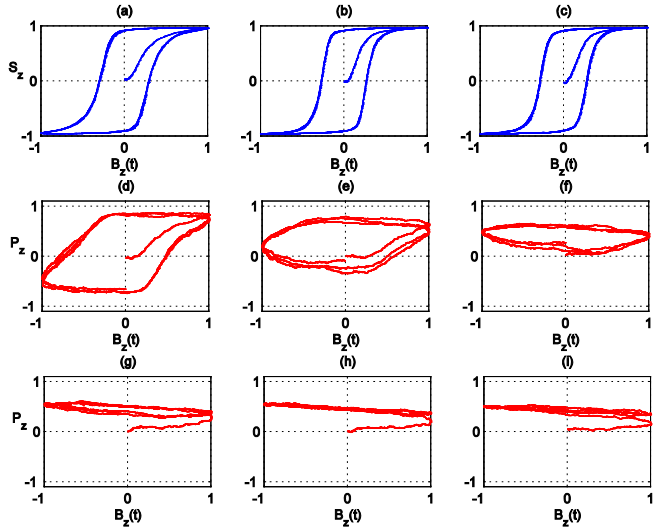

Figure 5: (colour online) The hysteresis loop in different layers which shows the mean magnetization (blue loops) and polarization (red loops) in response to the external driving magnetic field. The same data from Figure 4 is used.

Two 3-D plots of the time-dependent magnetization and polarization responses in each layer are shown in *Figure 6*, for different magneto-electric couplings, $g = 1$ and $g = 0.3$. The dynamic response for $= 1$, from the data in *Figure 4* and *5*, is given in the *top panel* of *Figure 6*. Comparison with the results in the *bottom panel* of *Figure 6* for a similar system with a different magneto-electric coupling, $g = 0.3$, shows the magneto-electric effect is varied with different magneto-electric couplings. In the *bottom panel* of *Figure 6*, a weak magneto-electric coupling gives dramatic decay of the polarization response after the interface (between the 3rd layer and the 4th layer in *Figure 6*). At the interface a small gap can be observed on each panel, which is evidence for the existence of a magneto-electric effect.

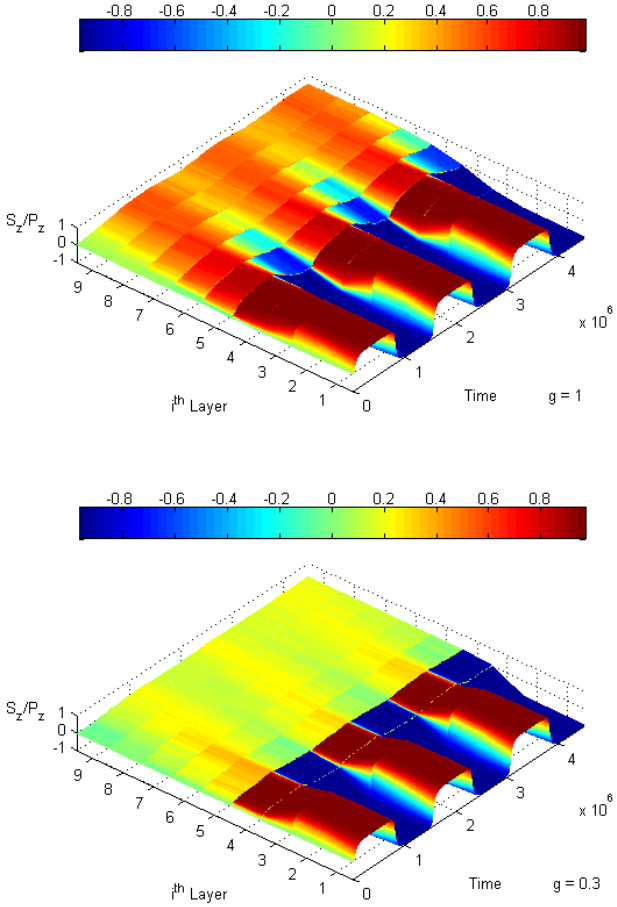

Figure 6: (colour online) 3-D plots show the dynamic magnetization/polarization responses in each layer. The top panel with a magneto-electric coupling, $g = 1$, and bottom panel $g = 0.3$.

In order to study the dependence on magneto-electric effect of the multi-ferroic film, simulations have been performed to determine the responses of magnetization and polarization for different values of the magneto-electric coupling, g. To investigate the continuous decay behaviour of polarization response in each ferroelectric layer, a close inspection of the maximal magnetization and polarization in each layer is

presented in *Figure 7* for $0.2 \leq g \leq 1$. For the sake of clarity, each result is shown for the system with a random initial state. The results in *Figure* 7 can be compared directly by different magneto-electric couplings. A faster exponential decay of the maximal polarization is observed for smaller value of coupling g. As mentioned before, the magneto-electric effect decreases as the magneto-electric coupling, decreases.

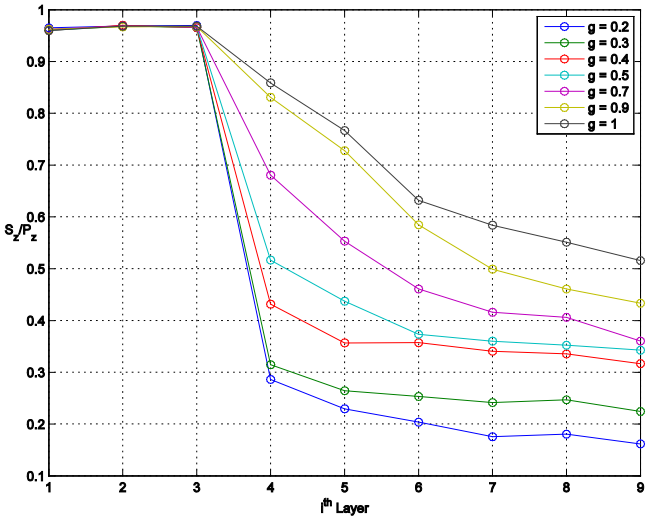

Figure 7: (colour online) Maximal magnetization and polarization in each layer, shows an exponential-like decay figure in the ferroelectric part (layer 4-9), with different values of magneto-electric coupling in the range $0.2 \leq g \leq 1$. *The lines through those points are only guide to the eye.*

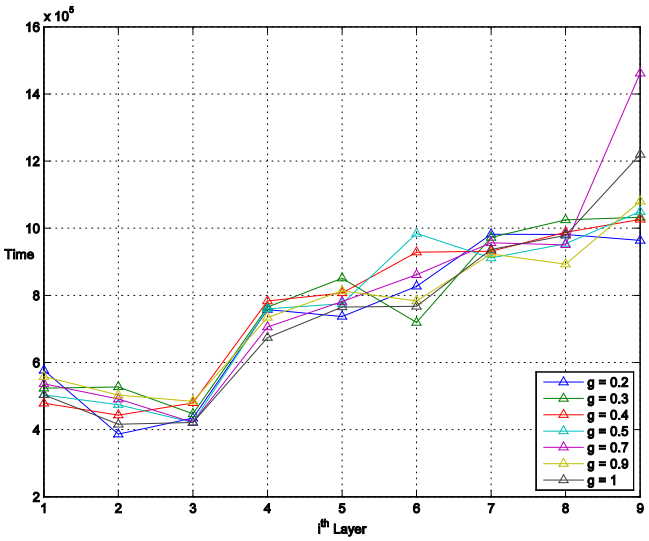

Figure 8: (colour online) The exact time when maxima response occurred in each layer, shows a linear-like delay behaviour in the ferroelectric part (layer 4-9), for different values of magneto-electric coupling in a range of $0.2 \leq g \leq 1$.

The delay behaviour of the polarization response in each ferroelectric layer is shown in *Figure 8* for $0.2 \leq g \leq 1$. The linear character of the curves (4^{th}- 8^{th} Layer on *Figure 8*) indicates that the speed of the interaction energy transition has the same rate in each ferroelectric layer. Except for the edge layer (9^{th} Layer on *Figure 8*), due to the free boundary condition. *Figure 8* further shows the curves with different colours are mixed up, which means that the time of the peak response is not related to the coupling g. In a nutshell, the delay behaviour in the ferroelectric film is independent of the magneto-electric effect.

4. Conclusions

In this paper, the magneto-electric effect has been demonstrated by the Monte Carlo method in a 2-D mulitferroic heterostructure thin film within a classical anisotropic Heisenberg model. As a proof of concept, the polarization was distinctly controlled by the external magnetic field as indicated by experiments [3,4]. The magneto-electric coupling, g, is clearly seen to be a crucial role in controlling the energy transition between the interface of ferromagnetic and ferroelectric film. For a large coupling g, the effect of response is distinctly observed. The competition between different values of the coupling g determines the magnitude of the response in system, which exhibits an exponential decay of maximal response in each ferroelectric layer. But, the relaxation time is not changed by varying the value of coupling g. As an aside, this system can also be driven by an external electric field, and shows a magnetic response in the magnetic material as well.

Acknowledgements

The authors gratefully acknowledge Bingjin Zhao and Yuhua Wang for financial support.

References

[1] L. Chotorlishvili, R. Khomeriki, A. Sukhov, S. Ruffo, J. Berakdar, "Dynamics of Localized Modes in a Composite Multiferroic Chain", *Physical Review Letters* 111, 117202, 2013.

[2] Alexander Sukhov, Chenglong Jia, Paul P Horley, Jamal Berakdar, "Polrizaiton and Magnetization Dynamics of a Field-Driven Multiferroic Structure", *J. Phys.: Condens. Matter*, 22, 352201, 2010.

[3] N, Jedrecy, H.J. von Bardeleben, V. Badjeck, D. Demaille, D. Stanescu, H. Magnan, A. Barbier, "Strong Magnetoelectric Coupling in Multiferroic Co/BaTiO3 Thin Films", *Physical Review B*, 88, 121409, 2013.

[4] I. Fina, M. Dix, J.M. Rebled, P. Gemeiner, X. Marti, F. Peiro, B. Dkhil, F. Sanchez, L. Fabrega, J. Fontcuberta, "The Direct Magnetoelectric Effect in Ferroelectric–Ferromagnetic Epitaxial Heterostructures", *Nanoscale*, 5, pp.8037-8044, 2013.

[5] Ce-Wen Nan, "Magnetoelectric Effect in Composites of Piezoelectric and Piezomagnetic Phases", *Physical Review B*, vol.50, no.9, 1994.

[6] Hyunbum Jang, Malcolm J. Grimson, “Thin Ferromagnetic Films with Competing Surfaces: A Monte Carlo Study of the Classical Heisenberg Model”, *Physical Review B,* vol.55, 12556, 1997.

[7] Hyunbum Jang, Malcolm J. Grimson, “The Competition of Bulk and Surface Fields in a Transverse Ising Model Thin Film” *J. Phys.: Condens. Matter*, 11, 5045, 1999.

A review on the homogenization model based on inclusion problems

Romain Corcolle

Laboratoire de Génie Électrique de Paris,
CNRS (UMR 8507)/SUPELEC/UPMC/Univ Paris-Sud, 11 rue Joliot Curie, 91192 Gif sur Yvette, France
E-mail: romain.corcolle@lgep.supelec.fr

Abstract

The seek for materials with better performance can be partly addressed by composite materials. Mixing several materials can lead to a new material combining the advantages of the constituents. In order to design properly composite materials, relevant modeling tools such as homogenization models are strongly needed. These models determine the macroscopic behavior of heterogeneous materials. Two main approaches exist for homogenization : full-field and mean-field approaches. The full-field approach generally relies on a Finite Element model which determines the field distribution in the composite material, the macroscopic behavior being deduced from the average of the fields. On the other hand, mean-field approach only determines a mean-field per phase information, which is considerably less consuming on the computational point of view.
This talk will focus on a mean-field homogenization model based on inclusion problems. It will be shown that this model is particularly powerful, retrieving classical homogenization models, dealing with coupled behavior, and more…

Efficient methods for macroscopic magnetization simulation described by the assembly of simplified domain structure models

Tetsuji Matsuo[1], Tomohiro Nakamura[1], Shumpei Ito[1], Takeshi Mifune[1], Chikara Kaido[2]

[1]Graduate School of Engineering, Kyoto University, Kyoto, Japan
[2]Kitakyushu National College of Technology, Kitakyushu, Japan
*corresponding author, E-mail: tmatsuo@kuee.kyoto-u.ac.jp

Abstract

This article presents two methods for the fast computation of macroscopic magnetization model called assembled domain structure model. First, an efficient method for computing the demagnetizing field is proposed. Secondly, a direct searching method of equilibrium point is developed, which greatly reduces the computation time.

1. Introduction

Macroscopic magnetic properties of iron-core material result from multiscale magnetization processes such as the microscopic domain-wall motion and the mesoscopic domain-structure transition. Recently, to construct a physical macroscopic magnetization model, several energy based multiscale approaches [1]-[4] have been developed. For example, Ref. [2] has successfully represented the macroscopic anhysteretic magnetic property of the grain oriented silicon steel sheet including the magnetoelastic property. In Refs. [3] and [4], an assembly of simple domain structure models (SDSMs) represented the macroscopic hysteretic behavior of magnetic sheets.

The SDSM [5] is a mesoscopic magnetization model of crystal-grain scale describing domain-wall motion and magnetization rotation. The assembly of SDSMs [3] is expected to constitute a physical macroscopic magnetization model based on the local energy minimization. However, the assembly of large number of SDSMs requires long computation time because of the large computational cost for obtaining the demagnetizing field and the long transient process to an equilibrium point.

This article proposes an efficient method for the computation of demagnetizing field and develops a direct searching method of equilibrium point.

2. Assembly of Domain Structure Models

2.1. Simplified domain structure model

An SDSM with two domains [5], as shown in Fig. 1(a) is used to describe behavior of a mesoscopic magnetic particle, where the magnetization is assumed uniform in each domain i (i = 1, 2). The normalized magnetization vector in domain i is given by $\boldsymbol{m}_i = (\sin\theta_i\cos\varphi_i, \sin\theta_i\sin\varphi_i, \cos\theta_i)$.

The total magnetic energy, e, is assumed to be given by the summation of Zeeman energy, the crystalline anisotropic energy, the domain-wall energy, and the magnetostatic energy as is summarized in Appendix A.1.

The magnetization is determined by finding a local energy minimum that satisfies $\partial e/\partial \boldsymbol{X} = 0$ where $\boldsymbol{X} = (\theta_1, \varphi_1, \theta_2, \varphi_2, \lambda)$ and λ is the volume ratio of domain 1. In Ref. [3], a local minimum is obtained by finding an equilibrium point of artificial state equation given as

$$\mathrm{d}\boldsymbol{X}/\mathrm{d}t = \boldsymbol{Y},$$
$$\mathrm{d}\boldsymbol{Y}/\mathrm{d}t = -\partial e/\partial \boldsymbol{X} - \beta \boldsymbol{Y} \quad (1)$$

where β is a dissipation coefficient. A local energy minimum depending on the initial condition is obtained by the numerical integration of (1) until reaching the steady state where $\mathrm{d}\boldsymbol{X}/\mathrm{d}t = \mathrm{d}\boldsymbol{Y}/\mathrm{d}t = 0$.

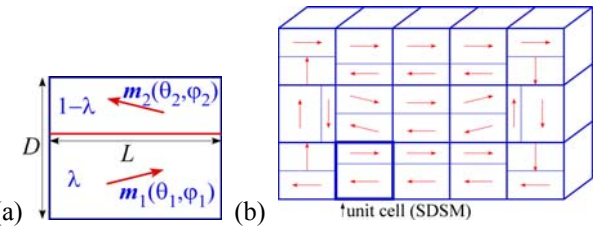

(a) (b)

Figure 1: ADSM: (a) unit cell (SDSM) and (b) assembled SDSMs (ADSM).

2.2. Assembled domain structure model

The macroscopic magnetization model is constituted by assembling the SDSMs [3], as shown in Fig. 1 (b), which is called the assembled domain structure model (ADSM). Each SDSM composing the ADSM is called a cell. The Zeeman energy, the anisotropic energy, and the domain-wall energy of cells are independently summed up to obtain the components of total energy e in the ADSM.

In the same way as in the micromagnetic simulation (see Appendix A.2), the magnetostatic energy is given as

$$e_{\mathrm{st}} = \sum_i \boldsymbol{h}_{\mathrm{st}}(i) \cdot \boldsymbol{m}(i) \quad (2)$$

where i is the cell index and $\boldsymbol{h}_{\mathrm{st}}$ is the normalized demagnetizing field; $\boldsymbol{h}_{\mathrm{st}}$ is given as

$$\boldsymbol{h}_{\mathrm{st}}(i) = \sum_{i'} \boldsymbol{s}(i-i')\boldsymbol{m}(i') \tag{3}$$

where $\boldsymbol{s}(i-i')$ is the normalized demagnetizing coefficient matrix between the cells i and i' and $\boldsymbol{m}(i)$ is the normalized magnetization of the cell i.

The state variable vector $\boldsymbol{X}$ consists of $\boldsymbol{X}(i)$ (i = 1, …) in each cell. A local energy minimum point is obtained by solving (1).

3. Efficient Computation of Demagnetizing Field

3.1. Computation using field decomposition

The convolution (3) is efficiently executed by using the fast Fourier transform (FFT) [6], which, however, often requires a large computational cost even with the use of FFT.

A simple way to reduce the convolution computation is updating the demagnetizing field only once at every p time-steps in the numerical integration of Eq. (1), where p is an integer. However, this procedure often results in the instability of numerical integration.

The demagnetizing field $\boldsymbol{h}_{\mathrm{st}}(i)$ in a cell can be divided into the two components $\boldsymbol{h}_{\mathrm{stin}}(i)$ and $\boldsymbol{h}_{\mathrm{stex}}(i)$ that are generated by the own cell i and by the other cells, respectively. They are given as

$$\boldsymbol{h}_{\mathrm{stin}}(i) = \boldsymbol{s}(0)\boldsymbol{m}(i) \tag{4}$$

$$\boldsymbol{h}_{\mathrm{stex}}(i) = \sum_{i' \neq i} \boldsymbol{s}(i-i')\boldsymbol{m}(i') = \sum_{i'} \boldsymbol{s}'(i-i')\boldsymbol{m}(i') \tag{5}$$

where

$$\boldsymbol{s}'(i) = \begin{cases} 0 & (i=0) \\ \boldsymbol{s}(i) & (i \neq 0) \end{cases}. \tag{6}$$

The components of $\boldsymbol{s}(0)$ are often large. This is why the demagnetizing field should be updated at every time-step. Compared with $\boldsymbol{s}(0)$, $\boldsymbol{s}(i)$ ($i \neq 0$) is relatively small, which implies that the $\boldsymbol{h}_{\mathrm{stex}}$ may be updated less frequently than $\boldsymbol{h}_{\mathrm{stin}}$. Consequently, it is reasonable to update $\boldsymbol{h}_{\mathrm{stin}}$ at every time-step and $\boldsymbol{h}_{\mathrm{stex}}$ at every p (≥ 2) time-steps in the numerical integration.

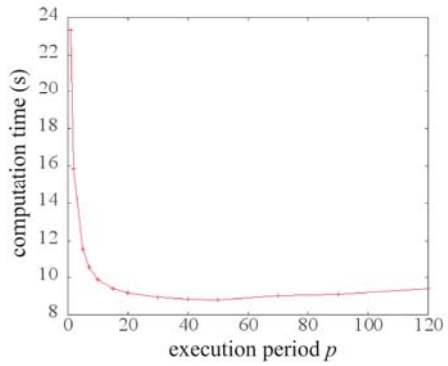

Figure 2: The relation between the execution period for the convolution and the computation time.

3.2. Computational results

A magnetic material having dimensions $l_x \times l_y \times l_z$ is analyzed with the ADSM, where l_x: l_y: l_z is set to 2: 1: 0.01. The material is divided into 32 × 16 × 1 cells. A cubic crystalline anisotropy is assumed with $\kappa = 2K / (\mu_0 M_S^2) = 0.01$.

Figure 2 shows the relation between the execution period p for the convolution and the computation time. When p = 20, the computation time is reduced by 64 % compared with that with p = 1. Figure 3 shows the MH curves along the <110> axis set along the y-direction, which are obtained with p = 1 and 20. The numerical integration is executed by the forward Euler scheme. The property obtained with p = 20 coincides with that with p = 1.

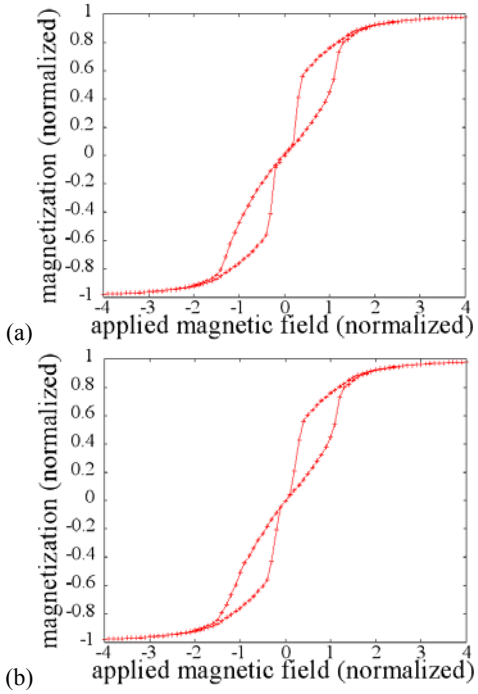

Figure 3: Simulation results with or without convolution execution reduction: (a) execution period p = 1 and (b) p = 20.

4. Direct Solution of Equilibrium Point

4.1. Direct solution using unit cell property

If the magnetization property of unit cell is known, the macroscopic magnetization property can be synthesized from the magnetizations of unit cells.

Figure 4 shows an example of the magnetization property of unit cell along the easy-axis direction. The magnetization state is classified into three types as below:

S_+: the single domain state with positive magnetization,
S_-: the single domain state with negative magnetization,
WM: the state of 180° domain-wall motion.

The three magnetization states above exist within the respective intervals of the normalized applied field h as bellow (see Appendix A.3):

$$I_{S+}: \{h \mid h_S \leq h < \infty\},$$

$$I_{S-}: \{h \mid -\infty \leq h \leq -h_S\},$$

$$I_{WM}: \{h \mid -h_{WM} \leq h \leq h_{WM}\}.$$

In the macroscopic model, by including h_{stex} into the applied field h as

$$h_{eff}(i) = h + h_{stex}(i) \quad (7)$$

the magnetization of each cell can be determined using the unit cell property, where $h_{eff}(i)$ is called effective field. When $h_{eff}(i)$ moves outside the interval of present magnetization state, the magnetization state transition occurs in cell i.

The alternating magnetization property is obtained by changing the applied field h step by step to find corresponding equilibrium point as follows.

Among all the cells where $h_{eff}(i)$ moves outside the present interval, the cell is chosen where $h_{eff}(i)$ is the most distant from the present interval. The magnetization state in the chosen cell is changed to another state so as for $h_{eff}(i)$ to be included in the corresponding interval. The magnetizations are also corrected in the cells having the 180° domain-wall motion state in accordance with the change of $h_{eff}(i)$. After the state transition and the magnetization correction, the demagnetizing field is recalculated and the procedure above is repeated until the demagnetizing field converges.

4.2. Computational results

The cells aligned one-dimensionally as in Fig. 5 are magnetized along the longitudinal direction. The normalized cell size is given by l_x: l_y: l_z = 1: 1: 0:1 with κ = 0.01. Figure 6 shows the magnetization curves obtained by the original ADSM solving Eq. (1) using 1, 8 and 128 cells, whereas the properties shown in Fig. 7 is given by the direct solution. The magnetization curve obtained by the direct method coincides with that obtained by the original ADSM in the case of single cell. In the case of 128 cells, however, the coercive force given by the direct solution is smaller than that given by the original ADSM. This suggests that the ADSM solving Eq. (1) sometimes fails to judge the convergence to an equilibrium point and wrongly stops the time-integration of Eq. (1) before escape from an unstable equilibrium point becomes evident because the escaping process may require very long transient time. The ADSM with the direct solution reconstructs the very small coercive force compared with the anisotropy field that is often observed in soft magnetic materials. Table I compares the computation time required by the both methods to obtain the MH curve, where the direct solution reduces the computation time less than 1/450 of that consumed by the ADSM solving Eq. (1) in the case of 128 cells.

5. Conclusion

First, this article presents an efficient method for the demagnetizing field computation using the decomposition into near and far fields. It is also expected that the decomposition allows the near filed to be integrated by an implicit scheme.

Second, the search of an equilibrium point is greatly accelerated by the direct solution method using the magnetization property of unit cell. If the unit cell property is unknown, the magnetization state transition should be switched based on the bifurcation point detection as was discussed in Ref. [7].

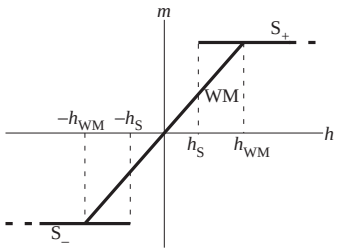

Figure 4: Magnetization property of unit cell.

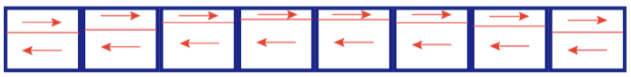

Figure 5: 1D alignment of cells.

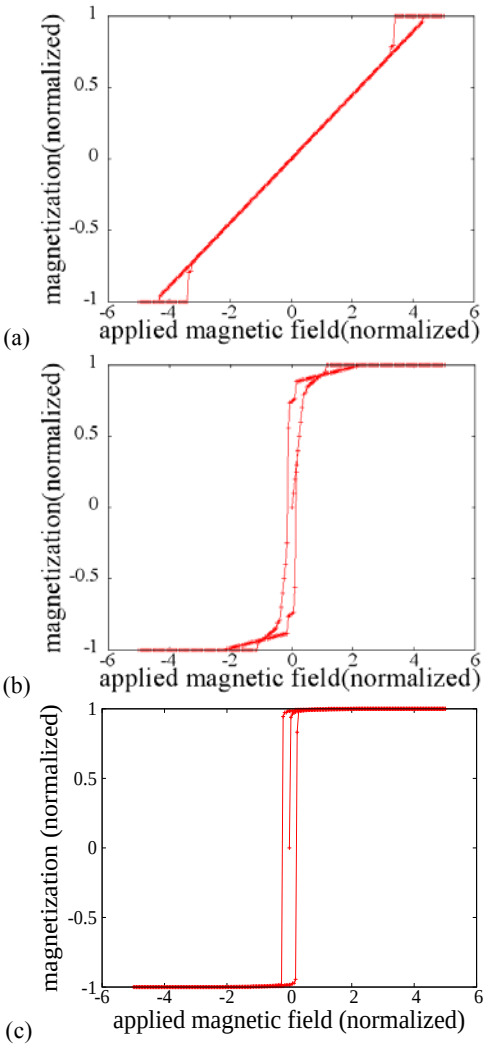

Figure 6: Simulation results of the original ADSMs with (a) 1, (b) 8, and (c) 128 cells.

Table 1: The computation time of ADSMs (sec).

# of cells	8	128
direct solution	0.702	7.64
solving Eq. (1)	134.4	3511.

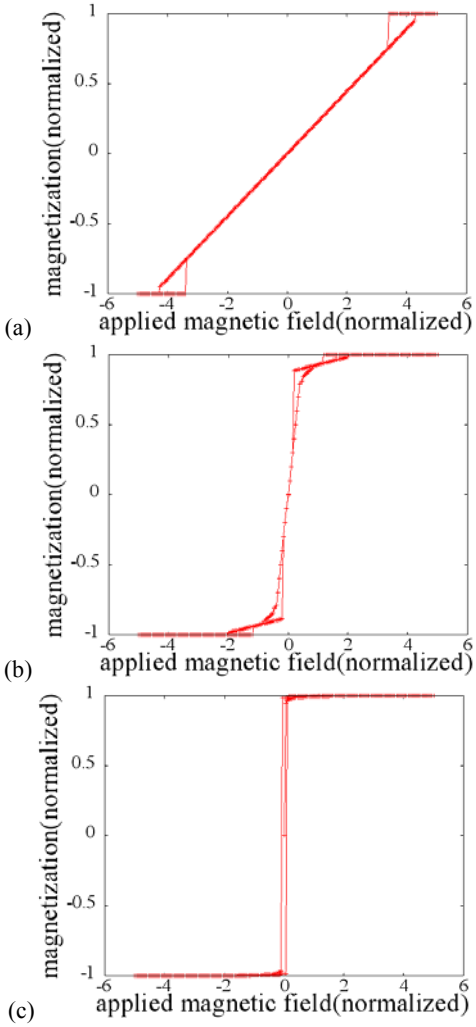

Figure 6: Simulation results of the direct method with (a) 1, (b) 8, and (c) 128 cells.

Acknowledgements

This work was supported in part by the Japan Society for the Promotion of Science, Grant-in-Aid for Scientific Research (C), Grant No. 26420232.

References

[1] O. Hubert and L. Daniel, Multiscale modeling of the magneto-mechanical behavior of grain-oriented silicon steels, *J. Mgan. Magn. Mater.* 320: 1412-1422, 2008.

[2] L. Daniel, O. Hubert, N. Buiron, and R. Billardon, Reversible magneto-elastic behavior: A multiscale approach, *J. Mech. Phys. Solids* 56: 1018-1042, 2008.

[3] M. Sudo, T. Mifune, T. Matsuo, and C. Kaido, A simplified domain structure model exhibiting pinning field, *IEEE Trans. Magn*. 49: 1829-1832, 2013.

[4] S. Ito, T. Mifune, T. Matsuo, C. Kaido, Macroscopic magnetization modeling of silicon steel sheets using the assembly of six-domain particles, *J. Appl. Phys.* (accepted for publication).

[5] T. Matsuo, Magnetization process analysis using a simplified domain structure model, *J. Appl. Phys.* 109: 07D332, 2011.

[6] N. Hayasi, K. Saito and Y. Nakatani, Calculation of demagnetizing field distribution based on fast Fourier transform of convolution, *Jpn. J. Appl. Phys.* 35: 6065-6073, 1996.

[7] T. Nakamura, S. Ito, T. Mifune, T. Matsuo, C. Kaido, Representation of magnetization process based on bifurcation property of domain structure, MMM 2014, CH-06, 2014.

Appendix A. Domain Structure Model

A.1. Simplified domain structure model

The SDSM locally minimizes the total magnetic energy, e, normalized by the crystalline anisotropy energy [5]; e is given as

$$e = e_{ap} + e_{an} + e_{w} + e_{st} \tag{A.1}$$

where e_{ap} is the Zeeman energy, e_{an} is the crystalline anisotropic energy, e_{w} is the domain-wall energy, and e_{st} is the magnetostatic energy.

The normalized crystalline anisotropic energy is given as

$$e_{an} = \lambda f_{an}(\theta_1, \varphi_1) + (1-\lambda) f_{an}(\theta_2, \varphi_2) \tag{A.2}$$

where f_{an} represents the angular dependence and λ is the volume ratio of domain 1. The Zeeman energy due to the normalized applied field, $\boldsymbol{h} = h\,(\cos\varphi_H, \sin\varphi_H, 0)$, is given as,

$$e_{ap} = -2\boldsymbol{h}\cdot[\lambda \boldsymbol{m}_1 + (1-\lambda)\boldsymbol{m}_2] \tag{A.3}$$

where $h = H_{ap} / (\kappa M_S)$, H_{ap} is the magnitude of the applied magnetic field, M_S is the magnitude of spontaneous magnetization, $\kappa = 2K / (\mu_0 M_S^2)$ and K is the anisotropy constant. A simple Bloch wall model gives the domain-wall energy as

$$e_w = w\,(1-\boldsymbol{m}_1\cdot\boldsymbol{m}_2)/2 \tag{A.4}$$

where $w = 4l_k/D$, $l_k = (A/K)^{1/2}$, A is the exchange stiffness constant and D is the width of the two domains. The SDSM assumes that the demagnetizing field is uniformly given by the multiplication of demagnetizing factors and the average magnetization. The magnetostatic energy is given as

$$e_{st} = s_x m_x^2 + s_y m_y^2 + s_z m_z^2 \tag{A.5}$$

where $(m_x, m_y, m_z) = \boldsymbol{m} = \lambda\boldsymbol{m}_1 + (1-\lambda)\boldsymbol{m}_2$, $s_x = k_x/\kappa$, $s_y = k_y/\kappa$ and $s_z = k_z/\kappa$; k_x, k_y, and k_z are the demagnetizing factors.

The total energy e becomes a local extremum when Eq. (1) is satisfied. Its solution gives a local minimum for e when all the eigenvalues of $\partial^2 e/\partial \boldsymbol{X}^2$ are positive.

A.2. Assembly of domain structure models

To obtain the energy components of the ADSM, the Zeeman energy, the anisotropic energy and the domain-wall energy of cells are independently summed up. The normalized magnetostatic energy e_{st} is computed as follows.

The demagnetizing field $\boldsymbol{H}_{\mathrm{st}}$ in the ADSM is obtained in the same way as in the micromagnetic simulation [6]; $\boldsymbol{H}_{\mathrm{st}}$ at cell i is given as

$$\boldsymbol{H}_{\mathrm{st}}(i) = -M_s \sum_{i'} \boldsymbol{N}(i-i')\boldsymbol{m}(i') \tag{A.6}$$

where i and i' are cell indexes and $\boldsymbol{N}$ is the demagnetizing coefficient matrix [3]. The magnetostatic energy E_{st} is given as

$$E_{\mathrm{st}} = -\frac{\mu_0 M_{\mathrm{S}} V}{2} \sum_i \boldsymbol{H}_{\mathrm{st}}(i) \cdot \boldsymbol{m}(i) \tag{A.7}$$

where V is the cell volume. The normalized magnetostatic energy is given by

$$e_{\mathrm{st}} = \frac{E_{\mathrm{st}}}{VK} = -\sum_i \boldsymbol{h}_{\mathrm{st}}(i) \cdot \boldsymbol{m}(i) \tag{A.8}$$

where $\boldsymbol{h}_{\mathrm{st}}$ is the normalized demagnetizing field; $\boldsymbol{h}_{\mathrm{st}}$ is given as

$$\boldsymbol{h}_{\mathrm{st}}(i) = \frac{\boldsymbol{H}_{\mathrm{st}}}{\kappa M_{\mathrm{S}}} = -\sum_{i'} \boldsymbol{s}(i-i')\boldsymbol{m}(i') \tag{A.9}$$

where $\boldsymbol{s}(i) = \boldsymbol{N}(I, J, K) / \kappa$.

A.3. Solution types in a unit cell

The uniaxial anisotropy is represented as

$$f_{\mathrm{an}}(\theta_i, \varphi_i) = \sin^2\theta_i \cos^2\varphi_i \,. \tag{A.10}$$

The cubic anisotropy is given as

$$\begin{aligned} f_{\mathrm{an}}(\theta_i, \varphi_i) &= \sin^2\theta_i \cos^2\varphi_i (1 - \cos^2\varphi_i \sin^2\theta_i) \\ &\quad + \frac{1}{4}(\cos^2\theta_i - \sin^2\theta_i \sin^2\varphi_i)^2 \end{aligned} \tag{A.11}$$

where the three easy axes are along $\boldsymbol{e}_x = (1, 0, 0)$, $\boldsymbol{e}_y+\boldsymbol{e}_z = (0, 1, 1)$, and $-\boldsymbol{e}_y+\boldsymbol{e}_z = (0, -1, 1)$ directions similarly to the grain-oriented silicon steel sheet. Both anisotropy types (A.10) and (A.11) yield the single-domain and two-domain magnetization states in a unit cell as follows.

When $\varphi_{\mathrm{H}} = 0$, the single domain state, S_+, is represented by

$$\theta_1 = \theta_2 = \pi/2 \,,\ \varphi_1 = \varphi_2 = 0 \,,\ \lambda = 1/2 \tag{A.12}$$

whereas the state of 180° domain-wall motion, S_{WM}, is represented as

$$\theta_1 = \theta_2 = \pi/2 \,,\ \varphi_1 = 0 \,,\ \varphi_2 = \pi \,,\ \lambda = \frac{1}{2}\left(1 + \frac{h}{s_x}\right) \,. \tag{A.13}$$

The state S_+ is stable when

$$h > h_{\mathrm{S}} \equiv \max\left(s_x - s_y - 1, s_x - s_z - 1, s_x - w - 1\right) \tag{A.14}$$

whereas the state S_{WM} is stable when

$$|h| < h_{\mathrm{WM}} \equiv \min\left(s_x\sqrt{\frac{1+s_y-w}{1+s_y+s_y w}}, s_x\sqrt{\frac{1+s_z-w}{1+s_z+s_z w}} \right). \tag{A.15}$$

Graphene electronics and photonics

Tunable Coplanar Waveguide Fed Ultra Wideband Terahertz Monopole Antenna Based on Graphene

Tao Zhou[1], Xin Qin, Hua-jie Ke[1], Zhi-hua Dong[1], Mian Pan[1], Guo-hua Liu[1], Hai-jun Gao[1], Jin-cai Wen[1], Zhi-qun Cheng[1], Ling-ling Sun[1]

[1]Hangzhou Dianzi University, Electronics and and Information College, Hangzhou, China
*corresponding author, E-mail: zhou.tao@hdu.edu.cn

Abstract

We propose the concept and design of a CPW-fed tunable ultra wideband terahertz monopole antenna based on graphene sheet. The surface conductivity of graphene sheet under different chemical potential is studied systematically, the frequency-reconfiguration of the antenna under chemical potential 0.25 eV and 0.5eV is studied. The proposed antenna has a characteristic of dynamic ultra wideband frequency-reconfiguration, low reflection coefficient, good omnidirectional radiation pattern and easy integration. The attractive properties of the graphene antenna can be used in sensing systems and nanoscale wireless communications.

Introduction

Graphene is a material formed by carbon atoms arranged in a flat two-dimensional hexagonal structure[1], it has attracted great interests of the research community due to its unique characteristics [2-4]. Owing to graphene supports plasmon polariton waves in the terahertz (THz) frequency range, enables the miniaturization and electrical tunability of antennas [5]. However, only few previous reviews considered the antenna applications of graphene [6-10]. Graphene was first placed as middle layer under conventional metal antenna operating at 120 GHz [9], where it was applied to permit or prevent radiation by applied electric field. Then, the first paper on graphene applied as a real radiator was published [10], where the operation frequency and the radiation property of antennas with different sizes were studied. Another concept of a THz antenna achieved by graphene sheet was proposed [6], there it was proved that the graphene antenna supported surface plasmonic resonances in THz band, and the resonant frequencies could be tuned by the chemical potentials corresponding to the applied electric fields.

In this work, a tunable ultra wideband (UWB) graphene terahertz antenna fed by coplanar waveguide (CPW) is studied systematically. First, the surface conductivities of graphene sheet under different chemical potentials are presented, the corresponding resonant frequencies, S parameters and radiation patterns in the THz range are given. We demonstrate that, beside the UWB operation frequency related to the circular graphene radiator and CPW fed, the proposed THz antenna has comparable radiation characteristics as that of the conventional metallic antennas, and frequency tunability related to the chemical potential.

1. Theorical analyses of graphene sheet

From the electromagnetic perspective, the atomic thickness allows graphene to be modeled as an equivalent surface conductivity[13-16]. The conductivity depends on the chemical potential , which related to the initial doping of the material or the applied electric field, temperature T, frequency w, and transport relaxation time t. Graphene's conductivity can be calculated by Kubo formula, Within the random-phase approximation, the conductivity can be considered in a local form with the Drude-like intraband contribution[11].

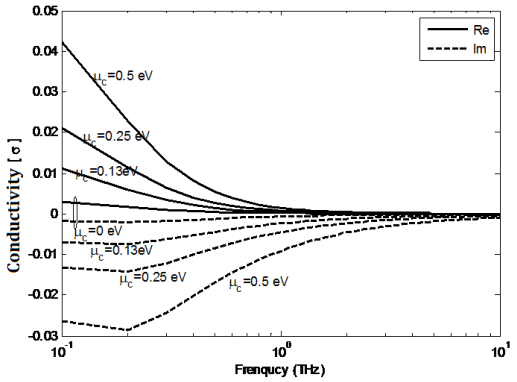

Figure 1: Equivalent conductivity under different chemical potential μ_c , T=300K, τ=1 ps.

Studies of surface conductivity with different chemical potential μ_c is shown in Figure 1. We assume T=300K, τ=1ps, at a given frequency, the real part of surface conductivity increases with the μ_c, while the imaginary part decreases with the μ_c.At the given frequency, the reactance increases with the chemical potential, while the resistance decreases with the chemical potential, thus the losses of graphene decreases and the inductive behavior increases.

The graphene antenna which we proposed has a dimension of a few micrometers, for the graphene sheet with dimension larger than 100nm, the edge effects on the graphene conductivity can be neglected [10-12]; thereby in this work, the surface conductivity model will be used to develop the graphene antenna.

2. CPW fed UWB graphene antenna

A CPW fed graphene antenna on quartz is displayed in Figure 2, it consists of conventional metallic CPW and round graphene radiator on quartz, the thickness of quartz is 50μm, the radius of the round graphene radiator is 100 μm; The CPW center strip width is 80μm, and gap width is 11.5μm. The antenna was simulated using a full-wave solver , as mentioned in section 2, the boundary conditions of graphene sheet is modeled by the surface impedance.

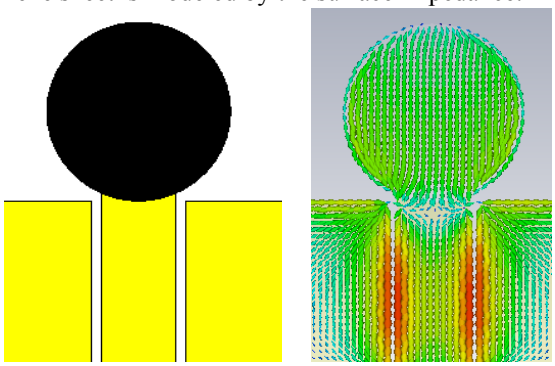

(a) (b)

Figure 2: CPW fed UWB graphene antenna and surface current distribution.

3. Discussions

The Voltage standing wave ratio (VSWR) of antenna under chemical potential 0.25 and 0.5eV are studied.The operation frequency and frequency bandwidth increase with the chemical potential, as the chemical potential increases from 0.25eV to 0.5eV, the operation frequency (VSWR<2) increases from 0.2 THz - 0.46 THz to 0.215 THz - 0.52 THz, and the corresponding frequency bandwidth increases from 0.26 THz (77%) to 0.305 THz (83%). Therefore, the Proposed antenna can be dynamically reconfigured via electric field bias.

The radiation pattern of the UWB graphene antenna at 0.35THz is studied. As expected, the radiation pattern is comparable to that of the conventional metallic antennas, the proposed antenna has almost the same radiation pattern under different chemical potentials, an omnidirectional radiation pattern is achieved, the directivity is 2.9 dBi.

4. Conclusions

We have studied a tunable graphene antenna , which fed by metallic CPW. The proposed antenna has a wide band width of more than 75%, the frequency reconfiguration of antenna under different chemical potential is studied. It presents a characteristic of dynamic reconfiguration, high miniaturization, ultra wide-band and good omnidirectional radiation. The integration of such antennas will pave the way to the devices of nanoscale wireless communications and sensing applications.

5. Acknowledgements

This work was supported by the National Natural Science Foundation of China (No.61331006, No.61001066 and No.61372021), Natural Foundation of Zhejiang Province (No.LY13F010018 and No.LQ14F010012).

References

[1] K. Geim and K. S. Novoselov, “The rise of graphene”, *Nature Materials* 6, 183-191, 2007.

[2] P. Blake, E. W. Hill1, A. H. Castro Neto, K. S. Novoselov, D. Jiang, R. Yang, T. J. Booth, and A. K. Geim, “Making graphene visible”, Appl. Phys. Lett. 91, 063124, 2007.

[3] C. Stampfer, J. Güttinger, F. Molitor, D. Graf, T. Ihn, and K. Ensslin, “Tunable Coulomb blockade in nanostructured graphene”, *Appl. Phys. Lett*. 92, 012102, 2008.

[4] A. Vakil and N. Engheta, “Transformation optics using graphene”, *Science* 10, Vol. 332, no.6035, 1291-1294, 2011.

[5] A. Cabellos, I. Llatser, E. Alarcon, A. Hsu, T. Palacios, “Use of THz Photoconductive Sources to Characterize Tunable Graphene RF Plasmonic Antennas”, *Physics optics*, 18 Feb 2014.

[6] M. Tamagnone, J. S. Gomez-Diaz,J. R. Mosig,and J. Perruisseau-Carrier, “Reconfigurable terahertz plasmonic antenna concept using a graphene stack”, *Appl. Phys. Lett.* 101, 214102, 2012.

[7] J. S. Gomez-Diaz, J. Perruisseau-Carrier, P. Sharma, and A. Ionescu, “Non-contact characterization of graphene surface impedance at micro and millimeter waves”, *J. Appl. Phys.* 111, Issue 11, 114908, 2012.

[8] H. S. Skulason, H. V. Nguyen, A. Guermoune, V. Sridharan, M. Siaj, C.Caloz, and T. Szkopek, “110 GHz measurement of large-area graphene integrated in low-loss microwave structures”, *Appl. Phys. Lett.* Vol. 99,Issue 15, 153504,2011.

[9] M. Dragoman, A. A. Muller, D. Dragoman, F. Coccetti, and R. Plana, “Terahertz antenna based on graphene”, *J. Appl. Phys.* Vol. 107, Issue 10, 104313, 2010.

[10] M.Tamagnone, J.S.Gomez-Diaz, J.R.Mosig, and J.Perruisseau-Carrier, “Analysis and design of terahertz antennas based on plasmonic resonant graphene sheets”, *J.Appl. Phys.*, Vol 112, Issue 11, 114915, 2012.

[11] I.Llaster, Christian Kremers, Albert Cabellos-Aparicio,Josep Miquel Jornet, Eduard Alarcon, Dmitry N. Chigrin, “Graphene-based nano-patch antenna for terahertz radiation”, *Photonics and Nanostructures - Fundamentals and Applications* 10,353-358, 2012.

[12] M. Jablan, H. Buljan, and M. Soljacic, “Plasmonics in graphene at infrared frequencies”, *Phys. Rev. B* 80, 245435, 2009.

[13] G. W. Hanson, “Dyadic Green's functions and guided surface waves for a surface conductivity model of graphene”, J. *Appl. Phys*. 103, 064302, 2008.

[14] M. Liu, X. Yin and X. Zhang, “Double-layer graphene optical modulator”, *Nano Letters* 12 (3), 1482-1485, 2012.

[15] G. W. Hanson, “Dyadic Green's Functions for an

Anisotropic, Non-Local Model of Biased Graphene", *IEEE Trans. Ant. Prop.* 56, 747 – 757, 2008.
[16] A. Vakil and N. Engheta, "Transformation optics using graphene."*Science*, vol. 332, no. 6035, pp. 1291–4, Jun. 2011.

Ultra-High Frequency Nano-mechanical Resonator with Graphene/Graphene Oxide Doubly Clamped Beam

Yuehang Xu*, Tengda Mei, Yan Sun

School of Electronic Engineering, University of Electronic Science and Technology of China,Chengdu, China
*corresponding author, E-mail: yuehangxu@uestc.edu.cn

Abstract

The remarkable properties of graphene have renewed interest in ultra-high frequency nano-electromechanical systems (NEMS) with extraordinary mechanical and electronic attributes. However, the resonant frequency of graphene NEMS is still under 300MHz at room temperature. To further increase the resonator frequency, this paper presents an ultra-high frequency nano-mechanical resonator by using graphene/graphene oxide (G/GO) doubly clamped beam. The calculation of resonator frequency is based on the compact model of graphene mechanical resonator including electro-mechanical coupling effects. The results show that the resonator frequency of G/GO nanomechanical resonator can reach up to 350.2MHz.

1. Introduction

Ultra-high frequency nano-mechanical resonators have broad application prospects in high quality factors microwave devices, high sensitivity sensor, single molecule detector and macroscopic quantum effect detection [1-6]. Due to the properties of nano-scale physical size, two-dimensional plane physical structure, excellent mechanical and electric properties, graphene based nano-mechanical resonator has incomparable advantages compared with conventional bulk materials in fabrication, and activation and readout method [7-9]. Recently, the emerging of electric readout methods has decreased the complexity of readout technique dramatically and thus enables the integrated of NEMS into integrated circuits (ICs) [10-12]. Since the first demonstration of graphene mechanical resonator, 2D-materials (i.e black phosphorus crystal, MoS_2) based mechanical resonators have attracted widely attention [13-16]. However, due to the atomic thickness of 2D-materials, the frequency is still much lower than that made of SiC beam even if 2D-materials has much higher Young's modulus [5]. Though the carbon nanotube based nano-mechanical resonator has reported over few GHz resonant frequency [17]. However, the consistence in carbon nanotube fabricaton is still far away to massive production. As a result, it is necessary to explore more feasible way to realize higher frequency nano-mechanical resonators with electrical readout.

In this paper, we focus on the possibility of realizing higher resonator frequency based on graphene. Taking the advantages of good mechanical and high insulate property of graphene oxide (GO), a graphene/graphene oxide (G/GO) doubly clamped beam is considered to reduce the requirement of process producing short length graphene suspended beam. In order to preserve the good electron mobility of graphene layer, which can use resonant channel transistor (RCT) based electrical readout method, single layer graphene is adopted in out scheme. The effects of thickness, width, length, Young's modulus, density and tension of beam to operation frequency are thoroughly investigated. The analysis is based on RF compact model of graphene RCT of local gate graphene RCTs.

2. Device Fabrication

The GO is fabricated with Hummer method, and the graphene is produced with CVD on copper foil. First, the GO thin film is transferred on the SiO_2 (300nm)/Si (400μm) by spinning GO solvent. Then the single layer graphene is transferred on the GO thin film. In order to get narrow and high quality of G/GO beam, a PMMA/SU-8 combined lithography method is used to etch the required beam size as shown in Fig.1. The Cr/Au is evaporated to clamp the G/GO beam as electrodes by thermal evaporation. Finally, the suspended G/GO is realized by etching the SiO_2 using BOE. Fig.2 shows the SEM picture of suspended G (single layer)/GO (9nm) clamped on two electrodes by using back-gate structure.

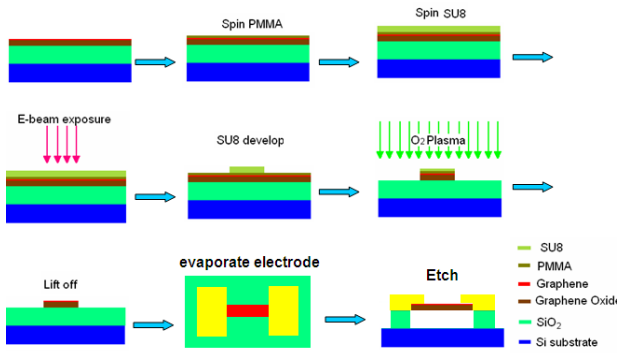

Fig. 1 Fabrication process of G/GO mechanical resonator

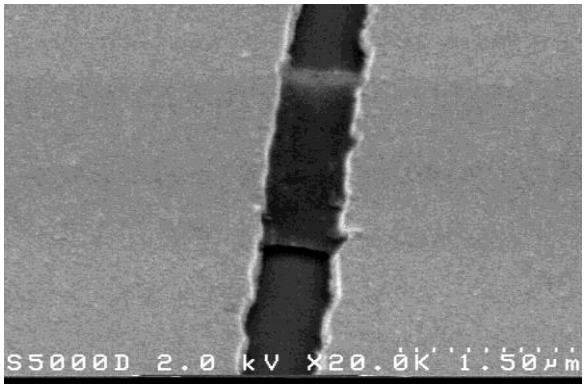

Fig. 2 SEM picture of suspended G (single layer)/GO (9nm)

3. Compact model

Compact model of RCT is not only useful to provide the basis to improve the process and device structure, but also dispensable for the design of graphene NEMS ICs. As the resonant frequency of graphene mechanical resonators goes up to more than hundreds MHz, the compact RF models of RCT becomes more important for the reality application of graphene NEMS due to the effects of parasitic parameters. To minimize the parasitic coupling between gate and source/drain electrodes, local gate structure (Fig.3) is used in our modeling and further analyze of G/GO resonator.

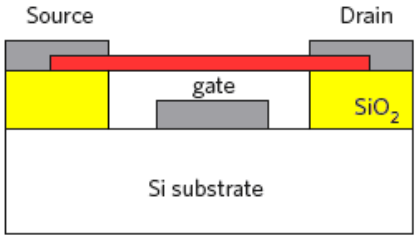

Fig.3 Cross section of local gate structure Graphene Mechanical resonator

The actuation is realized by electrostatic force with a time (t) -varying RF signal v_{gs}= v_{in} cos(ωt) (input RF signal) and DC voltage V_g (DC bias) applied to gate

$$\begin{aligned} F &= 1/2\frac{\partial C_g}{\partial z}(V_g + v_{in}\cos\omega t)^2 \\ &\cong \frac{\varepsilon_0 A}{2z_0^{\,2}}V_g^{\,2} + \frac{\varepsilon_0 A}{z_0^{\,2}}V_g v_{in}\cos\omega t \\ &= F_s + F_d\cos\omega t \end{aligned} \tag{1}$$

where $z=z_0-\Delta z$ is distance between gate and graphene, z_0 is equilibrium distance between gate and graphene, Δz is the beam deflection, C_g is gate-channel capacitance, ω is the angular frequency of input signal, ε_0 is the permittivity of vacuum, A is the effective channel area (intersection area of graphene and gate electrode), and F_s and $F_d$cos(ωt) are the constant and time-varying components of force, which gives static tension (T) and cause sinusoidal deflection of beam resonator, respectively. The fundamental resonant frequency f_r for doubly clamped beam under tension T can be expressed as

$$f_r = \sqrt{(a(\frac{E}{\rho})^{1/2}\frac{d}{L^2})^2 + \frac{0.57a^2T}{\rho L^2 wd}} \tag{2}$$

where E is the Yong's modulus, for graphene flake at low temperature E=0.9×1012Pa, ρ_G=2200 kg/m3 is the mass density, d, w, and L are the thickness, width, and length of the suspended graphene sheet, respectively, and the clamping coefficient a =1.03 for doubly clamped beams. To accurate modeling of the tension dependent resonant frequency, a quadratic function of gate bias V_{gs} is proposed to describe the tension T of graphene membrane

$$T = pV_{gs}^{\,4} - \lambda V_{gs}^{\,2} + T_0 \tag{3}$$

where T_0 is the initial tension in graphene membrane when no gate bias is applied, the p and λ temperature depended parameters.

The relation between resonant frequency f_r and gate bias V_{gs} showed in Eq.4. The calculated result and the measured data are shown in Fig.4.

$$f_r = \sqrt{\left(a\left(\frac{E}{\rho}\right)^{1/2}\frac{d}{L^2}\right)^2 + \frac{0.57a^2\left(pV_{gs}^{\,4} - \lambda V_{gs}^{\,2} + T_0\right)}{\rho L^2 wd}} \tag{4}$$

As the gate voltage change from 0 to -10 V, the resonate frequency range of the transferred device is 57.5 MHz ~ 88.25 MHz at room temperature.

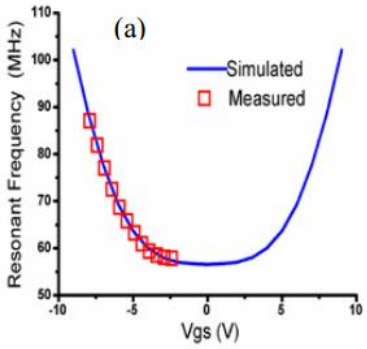

Fig.4 The relation between gate bias and resonant frequency

Considering the local gate graphene mechanical resonator as a field effect transistor, called RCT, the transistor theory can be used in our modeling. Based on drift-diffusion transport assumption, the current in channel can be written as

$$I_d = \frac{w}{L}\int_0^L en(x)v(x,E)dx \tag{5}$$

where the $n(x)$ is relationship between carrier oncentration and location

$$n(x) = \sqrt{n_0^2 + \left(C_{tot}\left(V_{gs} - V(x) - V_{gs0}\right)/e\right)^2} \tag{6}$$

and the mobility-field relation

$$v(E) = \mu E(x)/\left(1 + \frac{\mu_0 E(x)}{v_{sat}}\right) \tag{7}$$

where $V(x)$ is the potential in channel, which can be found with self–consistent method or an approximate solution. E(x)

is the electrical field in channel which equals to *dV(x)/dx*, v_{sat} is the saturation velocity of carriers, depends on the phonon scattering in graphene.

The intrinsic capacitances of MOS structure can be written as:

$$C_{gs} = \frac{dQ_{ch}}{dV_{gs}}|_{Vds=const} \qquad C_{gd} = \frac{dQ_{ch}}{dV_{ds}}|_{Vgs=const} \tag{8}$$

Q_{ch} is the overall net channel charge, which can be expressed as

$$Q_{ch} = ew\int_0^L [p(x)-n(x)]dx = \frac{1}{2}C_q V_c \tag{9}$$

Besides the intrinsic capacitance, the direct coupling of signal between gate and drain is existed. This coupling between pads can be regard as a parasitic capacitance C_{pgd}. The classical small signal equivalent circuit topology of MOS structure (shown in Fig.5) is used in our paper. Table II. shows the calculated parameters of small signal model by fitting the measured S-parameters for the device.

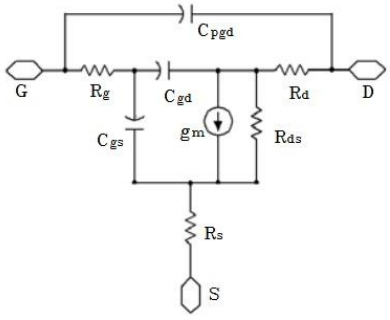

Fig.5. RF equivalent circuit of graphene RCT

In order to combine electromechanical model and electrical model to get the RF model of RCT, the drain-source *RF* current induced by field effect and mechanical vibration is deduced with[18]

$$I_{ds}^{RF} = v_{gs}g_m \exp(j\omega\tau) + v_{gs}V_g \frac{\Delta z}{z_0} g_m \exp(j\omega\tau) \tag{10}$$

Substitute Eq.(2) and Eq.(5) into Eq.(16), we can obtain

$$I_{ds}^{RF} = v_{gs}g_m \exp(j\omega\tau)\times \left[1+\frac{V_g^2 v_{gs}\varepsilon_0 A}{0.735Lwd\rho(2\pi f_r)^2 z_0^3}\left|\frac{1}{\left(1-\left(\frac{f}{f_r}\right)^2+j\frac{1}{Q}\frac{f}{f_r}\right)}\right|\right] \tag{11}$$

Let

$$g_{total} = g_m \times \left[1+\frac{V_g^2 v_{gs}\varepsilon_0 A}{0.735Lwd\rho(2\pi f_r)^2 z_0^3}\left|\frac{1}{\left(1-\left(\frac{f}{f_r}\right)^2+j\frac{1}{Q}\frac{f}{f_r}\right)}\right|\right] \tag{12}$$

Replacing g_m with g_{total}, we could get the final model of RCTs.

The compact model has been implemented into commercial SPICE-like high–frequency simulation software Agilent Advanced Design System (ADS) [19]. And the RCTs fabricated by exfoliation and transfer are used for validation purpose. The comparison of measured and simulated S_{21} is shown in Fig 6.

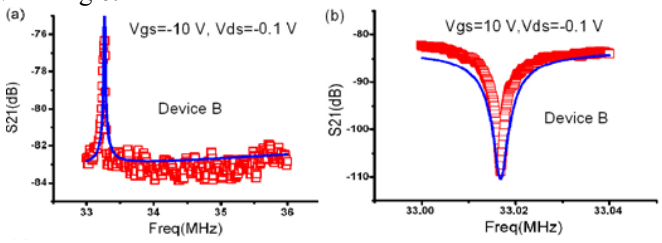

Fig.6 The comparison of measured S_{21} (square) and simulated S_{21} (solid line)

Fig.6 (a) is the measured S parameter of direct exfoliation device at V_{gs}=-10V, V_{ds}=-0.1V with -45 dBm input power. A clear peak appears around 33 MHz. The peak magnitude is as high as 13 dB above the background. Fig.6 (b) is the measured S parameter of direct exfoliation device under V_{gs}=10V, V_{ds}=-0.1V with -55 dBm input power to acquire high Q factor. A large dip (more than 20 dB) indicates that the two currents offset with each other at this condition. The Q factor of direct exfoliation device is ~ 10000 (due to the low temperature measurement and low input power level).

To explore the bias (V_{gs}) dependence of RCT, the calculated is shown in Fig.7. Fig.7 is the S_{21} of direct exfoliation RCT at V_{ds}=0.1V, P_{in}= -45 dBm, V_{gs}= -15V~15V. It clearly shows that a negative V_{gs} brings a peak, the resonant peak shift obviously with the increasing V_{gs}.

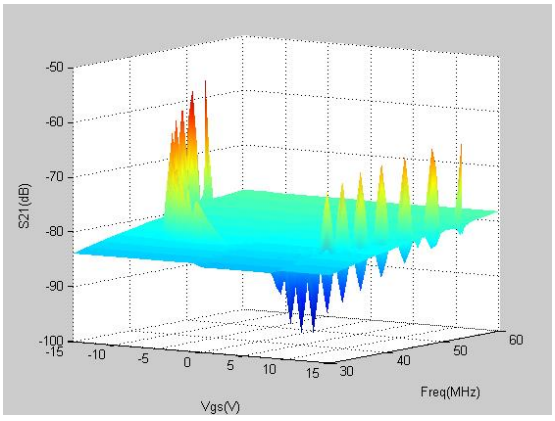

Fig.7. The mega sweep of bias-dependent resonator frequency.

4. Optimization of G/GO Mechanical Resonator

After getting the reasonable compact model, here we start the analysis of the factors which may affect the resonant frequency for optimization of graphene resonators. To simplify the analysis, we assume that the thickness of graphene do not change the mechanical and electronic properties.

Fig.8 shows the beam width (W) dependence of resonant frequency of graphene mechanical resonator.

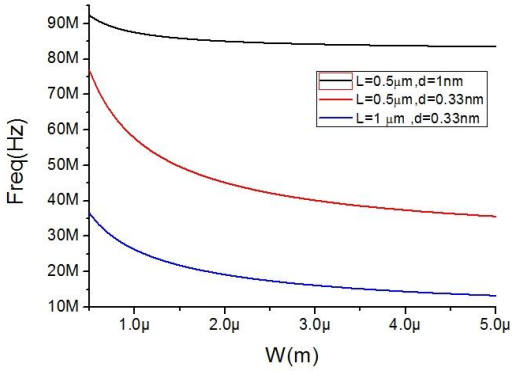

Fig. 8 Curve of resonant frequency vs. beam width

We can see that the change of frequency with W is very clear at beam length L=0.5μm for single layer graphene. However, for multi-layer (~3) graphene, the variation is very small. And as the increase of L, i.e. L=1μm，the variation becomes easy for single layer graphene. Fig.9 shows the variation of resonant frequency with beam length. We can see that the d do not change the resonant frequency much when L>2μm. However, when L<1μm, the thickness of beam is largely affect the resonant frequency.

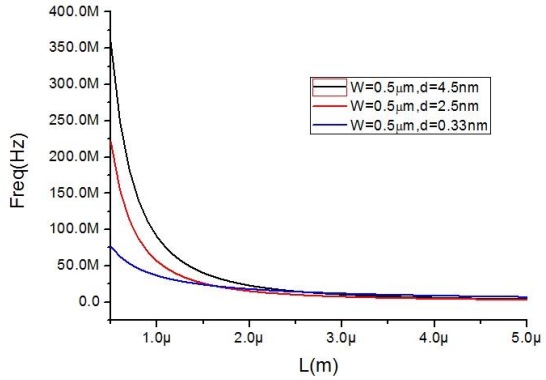

Fig.9 Curve of resonant frequency vs. beam length

Fig.10 shows the curve of resonant frequency vs. beam thickness d at L=0.5μm, W=1μm. The frequency is quite linear with d, which means that we can increase the resonant frequency by increase the thickness of beam.

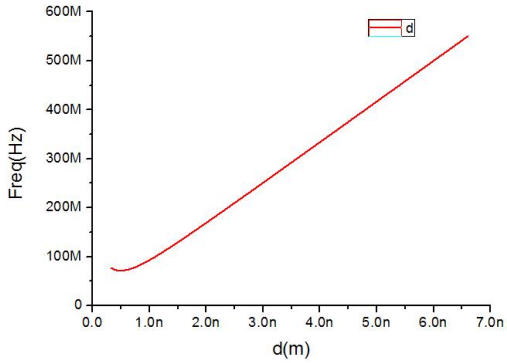

Fig. 10 Curve of resonant frequency vs. beam thickness L=0.5um， W=1um

Fig.11 shows the variation of resonant frequency beam at different material density and tension. We can see that increase of material density will decrease the resonant frequency (Fig.11 (a)). And the increase of the tension will definitely increase the resonant frequency (Fig.11 (b)).

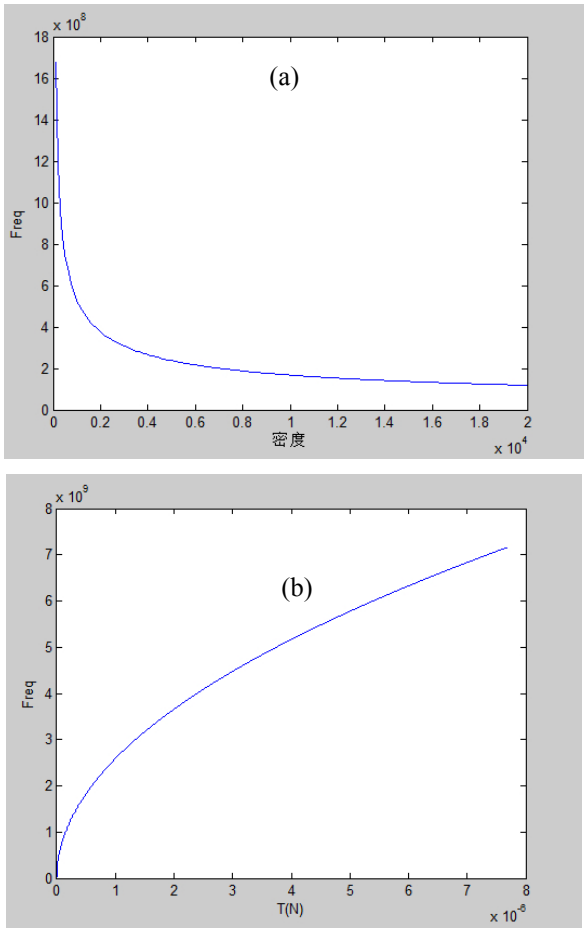

Fig.11 Curve of resonant frequency vs. beam material density and tension

From the analysis, we can see that the feasible way to increase the resonant frequency, except for at the cost of shorten the beam length in process, is to increase the thickness of beam without decreasing the Young's modulus and increase the material density. As a result, we choose G/GO composite material beam to realize our nano-mechanical resonator. The density of GO is similar with graphene $\rho_{GO}=\rho_G=2200kg/m^3$ and thus we consider the density of G/GO $\rho_{G/GO}=2200kg/m^3$. Because the Young's modulus of GO $E_{GO}=0.185\times10^{12}$Pa, the Young's modulus of G/GO can be calculated by

$$E_c=\frac{E_1+E_2}{8}+\frac{3}{2}\frac{E_1E_2}{(E_1+E_2)}=0.375\times10^{12}\,\text{Pa} \qquad (13)$$

Here we choose the common photolithograph process with a minimum resolution of 1μm to fabricate our devices. Fig.12 shows the simulated results of transmission response of G/GO graphene nano-mechanical resonator with L=1μm, W=1μm, and d_{GO}=25nm at room temperature. The bias is V_{gs}=-8V， V_{ds}=-0.2V. The results show that the resonant frequency is 350.2MHz. Higher frequency can be achieved by decrease the beam length. The local gate process can be realized by using the same method described in [18].

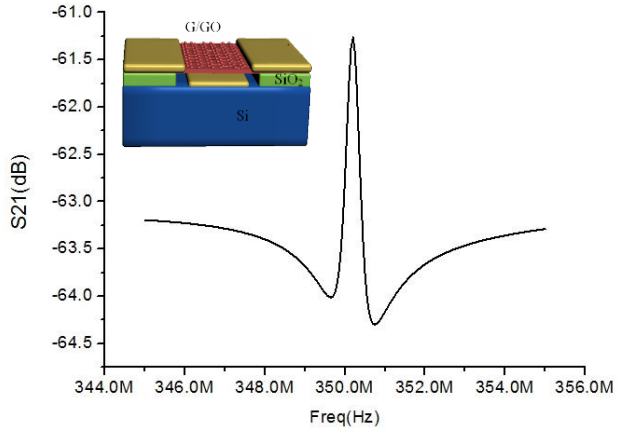

Fig.12 Simulated transmission response (S_{21}) of local gate G/GO nano-mechanical resonator

5. Conclusions

To increase the resonant frequency of nano-mechanical, a graphene/graphene oxide (G/GO) based nano-mechanical resonator is investigated. The fabrication result shows the feasible of process in realize suspended G/GO beam less than 1μm. The local gate structure G/GO nano-mechanical resonator is analyzed and the results show that this structure can realize higher than 300MHz frequency at room temperature with a gate length of 1μm. The future work will discuss the fabrication of local gate G/GO graphene and Q factors. These results also provide a new idea to realize ultra higher frequency nano-mechanical resonator with 2-D high strength materials based composite materials, like fluorographene.

References

[1] H. G. Craighead. Nanoelectromechanical systems, *Science*, 2000, 290(24): 1532-1535.

[2] A. N. Cleland and M. L. Roukes. A nanometre-scale mechanical electrometer, *Nature*, 1998, 39: 160-162.

[3] A. K. Naik, M. S. Hanay, W. K. Hiebert, et al. Towards single-molecule nanomechanical mass spectrometry. *Nature Nanotechnology* , 2008,4 : 445-450.

[4] C. T.-C Nguyen, L. P. B. Katehi, and G. M. Rebeiz. Micromachined devices for wireless communications. *Proc. IEEE*, 1998, 86: 1756-1768.

[5] X. M. H. Huang, C.A. Zorman, M. Mehregany, M.L. Roukes, *Nature*, 2003, 421: 496.

[6] X. L. Feng, C.J. White, A. Hajimiri, M.L. Roukes. A self-sustaining ultrahigh-frequency nanoelectromechanical oscillator, *Nature Nanotechnology* . 2008 3: 342-346.

[7] K. S. Novoselov, et al. Electric Field Effect in Atomically Thin Carbon Films, *Science*, 2004, 306:666.

[8] J. Scott Bunch, Arend M. van der Zande, et al. Electromechanical Resonators from Graphene Sheets. *Science*, 2007, 315:490-493

[9] C. Lee, X. D. Wei, J. W. Kysar, and J. Hone. Measurement of the elastic properties and intrinsic strength of monolayer Graphene. *Science*, 2008, 321: 385-388.

[10] Changyao Chen, Sami Rosenblatt, et al. Performance of Monolayer Graphene Nanomechanical Resonators with Electrical Readout. *Nature Nanotech.* 2009, 4: 861-867.

[11] Yuehang Xu, Changyao Chen, et al., RF Electrical Transduction of Graphene Mechanical Resonators. *Applied Physics Letters*, 2010,97(24): 3111

[12] C. Chen, L. Sunwoo, et al. Graphene mechanical oscillators with tunable frequency， *Nature Nanotech.* 8, 923–927 (2013).

[13] Sunwoo Lee, Changyao Chen, Vikram V. Deshpande, Gwan-Hyoung Lee, et al., Electrically integrated SU-8 clamped graphene drum resonators for strain engineering, *Appl. Phys. Lett.*,2013,102:153101

[14] Sunwoo Lee,Vivekananda P. Adiga, Robert A. Barton, Arend M. van der Zande, Gwan-Hyoung Lee, B. Rob Ilic, Alexander Gondarenko, Jeevak M. Parpia, Harold G. Craighead, and James Hone, Graphene Metallization of High-Stress Silicon Nitride Resonators for Electrical Integration, *Nano Lett.* 2013, 13, 4275−4279

[15] Zenghui Wang, Hao Jia, Xuqian Zheng, Rui Yang, Zefang Wang,Guojun Ye, Chen X. H., Jie Shan, Philip Feng, Black Phosphorus Nanoelectromechanical Resonators Vibrating at Very High Frequencies, *Nanoscale*, Oct. 2014

[16] Jaesung Lee, Zenghui Wang, Keliang He, Jie Shan, Philip X.-L. Feng Air damping of atomically thin MoS2 nanomechanical resonators , *Applied Physics Letters*, 2014,105(2):023104-023104-5.

[17] Garcia-Sanchez D, Van der Zande A M, Paulo A. S, et al. Mechanical Detection of Carbon Nanotube Resonator Vibrations *Nano Lett.* 2008(8): 1399-1403

[18] Y. Xu, Y.Guo, Y.Wu, R. Xu and B. Yan, Electrical Read out of Nano-electromechanical system signal by Using Graphene Resonant Channel Transistor, *Acta Physica Sinica*, Vol.61(1): 010701,2012

[19] Yuehang Xu, Oupeng Li, Ruimin Xu, Graphene Resonant Channel Transistor, April 17,2013, *IEEE MTT-S International Wireless Symposium (IWS 2013)*,Beijing

Enhanced light-matter interaction in graphene

Sanshui Xiao[1,2]

[1]*DTU Fotonik, Department of Photonics Engineering, Technical University of Denmark, 2800, Kgs. Lyngby, Denmark.*

[2]*Center for Nanostructured Graphene (CNG), Technical University of Denmark, DK-2800 Kgs. Lyngby, Denmark.*

mail:saxi@fotonik.dtu.dk, website: http://www.fotonik.dtu.dk/sem

Graphene has attracted lots of attention due to its remarkable electronic and optical properties, thus providing great promise in photonics and optoelectronics. However, the performance of these devices is generally limited by the relatively weak light-matter interaction in graphene. The combination of graphene with noble-metal nanostructures is currently being explored for strong light-graphene interaction. We introduce a novel hybrid graphene-metal system for studying light-matter interactions with gold-void nanostructures exhibiting resonances in the visible range [1]. The hybrid system is further explored for sensing of Rhodamine 6G molecules with respect to the strong surface-enhanced Raman scattering. The interaction between graphene plasmon (supported by nanodot and antidot arrays) and the substrate phonons [2] is also experimentally demonstrated and structural control is used to map out the hybridization of plasmons and phonons, where the graphene is structured by the nanosphere lithography with structural control down to the sub-100 nanometer regime, see Fig. 1.

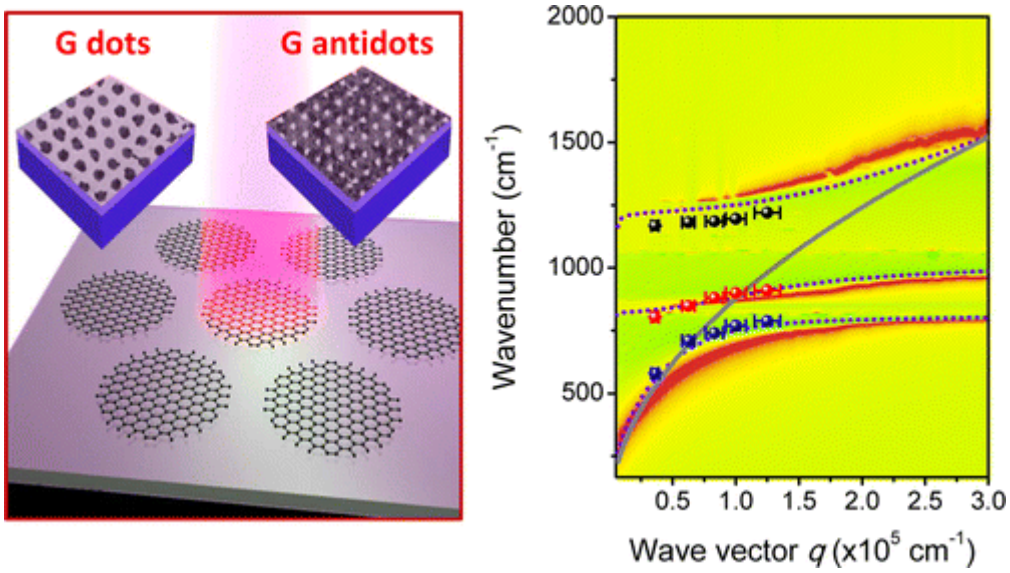

Fig. 1. Plasmon-phonon interaction in graphene nanostructures

References:

[1]. X. Zhu, W. Wang, W. Yan, M.B. Larsen, P. Bøggild, T. G. Pedersen, S. Xiao, J. Zi, and N. A. Mortensen, *Nano Lett.*, 14, 2907 (2014).

[2]. X. Zhu, L. Shi, M.S. Schmidt, A. Boisen, O. Hansen, J. Zi, S. Xiao, and N. A. Mortensen, *Nano Lett.* 13, 4690 (2013).

Antenna Arrays: CEM Modeling and Array Signal Processing

Dual Frequency Reflectarray Using Square Ring with Four Branches

Tao Zhou[1], Xi-Wang Dai[1], Zhi-hua Dong[1], Mian Pan[1], Guo-hua Liu[1], Hua-jie Ke[1], Hai-jun Gao[1], Jin-cai Wen[1], Zhi-qun Cheng[1], Ling-ling Sun[1]

[1]Hangzhou Dianzi University, Electronics and and Information College, Hangzhou, China
*corresponding author, E-mail: zhou.tao@hdu.edu.cn

Abstract

A novel reflectarray, based on square ring with four branches, is proposed for dual frequency operation. The cell element consists of a square ring with four perturbation branch structure, showing a dual-band characteristic due to the change of the current distribution. A crossed-dipole is applied on the front of cell element for adjusting the phase of reflection coefficient. The reflectarray can control reflected beams independently at dual frequencies with different polarizations. Prototypes of this reflectarray are present and studied, which validate the effectiveness of the reflectarray.

1. Introduction

Microstrip reflectarray, integrated with the advantages of reflectors and phased arrays, is proposed for replacing conventional parabolic reflector antennas[1]. A microstrip reflectarray consists of an array of microstrip patch elements, and reflects a beam in a specified direction when illuminated by a primary source. It has been widely applied to radar and space communication systems, and wireless communication systems. It has advantages such as low cost, low profile, low mass and volume, easy manufacturing, and scannable beam compared to conventional parabolic reflectors[2]. In the wireless communication system, microstrip reflectarray can be mounted on ceiling of tall buildings or embedded into walls to reflect beams covering different areas, especially those blind areas to the primary source. However, microstrip reflectarray has the disadvantage of narrow band, which has limited its application in communication systems[3,4]. To combat its shortcoming, different kinds of dual band reflectarrays are proposed. Different dimensions of resonance structure are fabricated on the same one layer and multi-layer configuration reflectarray are proposed for dual band application[5-7].

In this work, a novel reflectarray cell element is proposed for dual band application, which is composed of crossed-dipole elements and frequency selective surface using the structure of square ring with four branches. The FSS configuration is on surface of one layer, and can be easily fabricated. With the four perturbation branch structure, the current distribution of square ring is changed and a dual-band characteristic is shown. A crossed-dipole is placed on the opposite size of dielectric with FSS structure. This reflectarray scatters only the desired frequency but is transparent to the electromagnetic waves at other frequencies. A progressive phase distribution is achieved for the reflected wave at both frequencies by adjusting the resonant length of the crossed-dipole in each elementary cell of reflectarray. With the crossed-dipole, it can control independently the direction of both horizontally and vertically polarized reflect beams. The dual-band reflectarray can be designed to scatter low frequency beam with horizontal polarization, and to scatter high frequency beam with vertical polarization. Using this method, a 5*3 reflectarray of variable size crossed-dipole and squaring ring with four branches is presented. The properties of the new reflectarray is discussed and analyzed, which shows its effectiveness in the design of reflection beams properties for two different working frequencies with different polarizations, respectively.

2. Cell structure

An FSS consisted of a square ring with four branches is a surface which exhibits different reflection and/or transmission properties as a function of frequency. The square ring and the four branches structure compose the multi-resonance structure, which shows the dual band characteristic. The cell element structure is shown in Figure 1. The period in both x and y directions is D=7mm and the circumference of the square ring is 12mm. The branch has a 0.2mm width and 2mm length, while the gap between the branch and the nearest edge of the square ring is 0.1mm. The structure is attached on the surface of a dielectric substrate with a thickness of h=1.5mm and relative permittivity of 2.55.

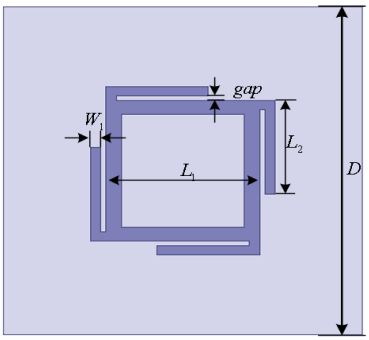

Figure 1: Cell structure.

3. Design of Dual-band Reflectarray

In order to reflect the incident wave in desired direction, the proper phase shifts of the individual element are necessary. The configuration of a dual-band reflectarray is shown in Figure 2.

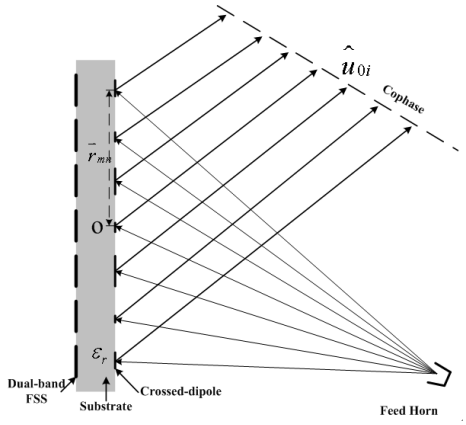

Figure 2: Configuration of dual frequency reflectarray.

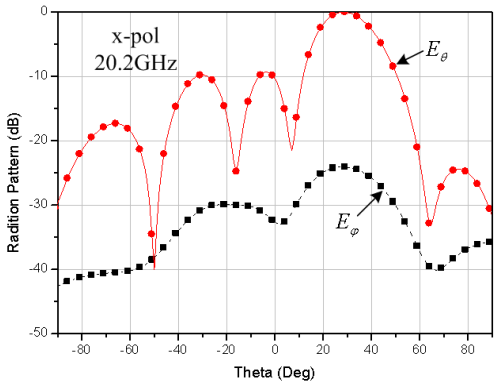

(a)

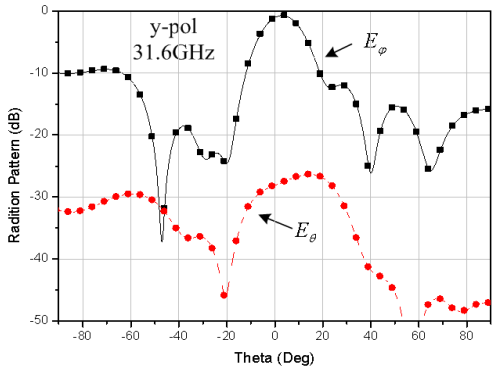

(b)

Figure 3: Radiation patterns of the dual frequency reflectarray.

For the dual band reflectarray, the perpendicular property of the crossed-dipole can be designed for each working frequency respectively. The dimension of crossed-dipole needs to be changed in order to obtain the required phase. With the square ring with four branches structure backed, the length of crossed-dipole can be adjusted to analysis the property of element. The compensated phase curve can be calculated with the infinite periodic array method. After obtaining the phased curve, the resonant length of the mn_{th} element is determined to produce a phase shift ϕ_{mni} in the field scattered from element.

In the design, the incident plane waves come from different directions for dual resonance frequencies with different polarizations. The far field radiation patterns of the dual frequency reflectarray are performed, which are shown in Figure 3. We note here that the x-polarized scattered wave at f_{01}=20.2GHz has maximum scattering toward the direction (θ_{o1}, ϕ_{o1})=(30°, 0°), and the y-polarized scattered wave at f_{02}=31.6GHz has maximum scattering toward the direction (θ_{o2}, ϕ_{o2})=(0°, 0°). Both results demonstrate the effectiveness of the present idea, which agrees with the design requirement.

4. Conclusions

This paper presents a novel dual frequency reflectarray for beam control of reflected waves. The cell element has the structure of square ring with four branches, which shows the dual band property. With the crossed dipole on the opposite surface of cell element, the reflectarray can control the reflected beam to propagate at the desired direction for two resonance frequencies with different polarization. A reflectarray operated at 20.2GHz and 31.6GHz was designed, the analysis was performed to confirm the effectiveness of this configuration.

5. Acknowledgements

This work was supported by the National Natural Science Foundation of China (No.61331006, No.61001066 and No.61372021), Natural Foundation of Zhejiang Province (No.LY13F010018 and No.LQ14F010012).

References

[1] J. Huang, "Analysis of a microstrip reflectarray antenna for microspacecraft applications," *TDA Progress Report* 42-120,153-173, 1995.

[2] John Huang and José A. Encinar, "Reflectarray antenna," *John Wiley & Sons, Inc.*, Hoboken, New Jersey, 2008.

[3] L. Li et al., "Microstrip reflectarray using crossed-dipole with frequency selective surface of loops," *ISAP2008*, TP-C05, 1645278.

[4] Long Li et al. "Frequency Selective Reflectarray Using Crossed-Dipole Elements With Square Loops for Wireless Communication Applications" *IEEE Transactions on Antennas and Propagation*, Vol. 59 , Issue: 1 ,pp 89 - 99 , 2011.

[5] Furuno,T. et al. "Dual frequency selective reflectarray for propagation improvement," *2010 International Workshop on Antenna Technology (iWAT)*, pp,1 − 4, March 2010.

[6] Chaharmir, M.R. Shaker, J. ; Cuhaci, M. ; Ittipiboon, A. "Broadband reflectarray antenna with double cross loops" *Electronics Letters*, Vol. 42 , Issue: 2 pp: 65 - 66

2006.

[7] Sean V. Hum, Michael Okoniewski, Robert J. Davies, "Realizing an Electronically Tunable Reflectarray Using Varactor Diode-Tuned Elements," *IEEE Microwave and Wireless Components Letters*, Vol. 15, No. 6, 2005.

Millimeter-Wave Cavity-Backed Antenna Arrays with Overlapped Aperture

Jiang Qi and Shi-Wei Qu
School of Electronic Engineering, University of Electronic Science and Technology of China (UESTC)
2006 Xiyuan Avenue, Western High-Tech Zone
Chengdu 611731, Sichuan Province, China

***Abstract*-In the paper one of the key problems of cavity-backed antennas, i.e. the conflict between electrically large dimensions and applications to beam scanning antenna arrays, is addressed by partially overlapping the cavity aperture without performance degradation. An 8-element E-plane linear cavity-backed antenna array and a 4 × 8 planar one are given based on the proposed idea. They can feature realized gains of 19.8 and 25.5dBi, respectively, as well as a maximum aperture efficiency of over 100% across a frequency bandwidth of 79.3%, from 17. 8 to 41.6 GHz.**

I. INTRODUCTION

In recent decades, wideband wireless systems have been widely applied in many fields such as ground-penetrating radars, biomedical imaging systems, communication systems etc [1]. In many cases, these systems require antennas can be available over a large frequency band with low standing-wave ratio (SWR) and unidirectional patterns. Microstrip antennas can only present stable and unidirectional patterns with 70% bandwidth at most [2]. Comparatively, bowtie antenna with slot loading can present large impedance bandwidth, but the patterns are distorted over a bandwidth of one octave [3]. To achieve a unidirectional antenna for wideband applications, cavity-backed antennas are utilized and presented in many papers [4]-[7] due to their unidirectional patterns, wideband characteristics and high efficiency. In [4], a cavity-backed dipole antenna has been designed and can achieve a broad-band SWR response, unidirectional radiation patterns, and almost constant gain (10.5±1dBi) over an operating bandwidth of 1.8:1. In [7], a cup-shaped cavity-backed rounded triangular bowtie antenna has been presented. By optimizing dimensions of the cavity and the bowtie antenna, an SWR≤ 2 bandwidth of over 120%, a broadside gain of 8.5- 15.9 dBi are achieved.

Although the cavity-backed antenna has many advantages as above mentioned, they are rarely used as an element in the antenna array because of several main limitations. Firstly, the diameter of most cavity-backed antennas is larger than half or even a wavelength. For example, the cavity diameter of the one in [7] is approximately 0.99 λ_m (λ_m is the free-space wavelength at the lower edge of the frequency band for VSWR ≤ 2). If it is used as an array element, the inter-element distance is too large to maintain the radiation patterns stable in higher frequency band, which limits the operating bandwidth of the cavity-backed antenna arrays. In addition, as another problem, installation of the cavity-backed antenna array is difficult due to the vertical feeding baluns relative to the ground plane. Due to the issues mentioned above, for the array applications, the key problems of the cavity-backed elements that need to be solved are reducing the cavity sizes and properly designing the array aperture and the feeding network.

In this paper, an 8-element linear array with cavity-backed elements is proposed. The overlapped elliptical cavities can effectively reduce the inter-element distance and the array overall dimensions, but does not impact the array performance. The dipole exciters as well as a parallel fed network are printed in the two sides of the substrate, and then the substrate can be conveniently installed as the given method. Then, a 4×8 planar array is also proposed in this paper. Simulations show that a bandwidth of over 79.3% for SWR < 2, a broadside gain of 19.1 – 25.5 dBi are achieved by the planar array.

II. LINEAR ARRAY WITH 8 CAVITY-BACKED ELEMENTS

A. Array Geometry

Fig. 1 shows geometry of the proposed cavity-backed antenna array. It is composed of 8 cavity-backed dipole elements arranged along the E-plane direction and a parallel feeding network. Due to electrically large dimensions of the cavity, an overlapped cavity aperture is employed in this design to suppress grating lobes of the array factor. Investigations show that the mutual coupling is hardly changed after overlapping. Meanwhile, dipole exciters are used along with a simple balun from a 50Ω microstrip line to a double-side parallel strip line. Both the dipoles and the balun are printed onto a substrate, and the cavities can be cut into two metal blocks along the central line. Then installations can be easily implemented by clipping the substrate between the two blocks, forming a robust array structure. Dimensions of the cavity and the inter-element spacing are a = 5 mm, b = 4 mm and d = 7 mm ($0.7\lambda_0$ corresponding to the free-space wavelength at the center frequency), respectively.

B. Results of Linear Array

The operating frequency of the proposed linear array is centered at 30GHz. Simulations show that the array can be matched well in a large frequency band from 17.8 to 41.6GHz, corresponding to a fractional bandwidth of 79.3%, although only a simple feeding network with 7 branch-line power

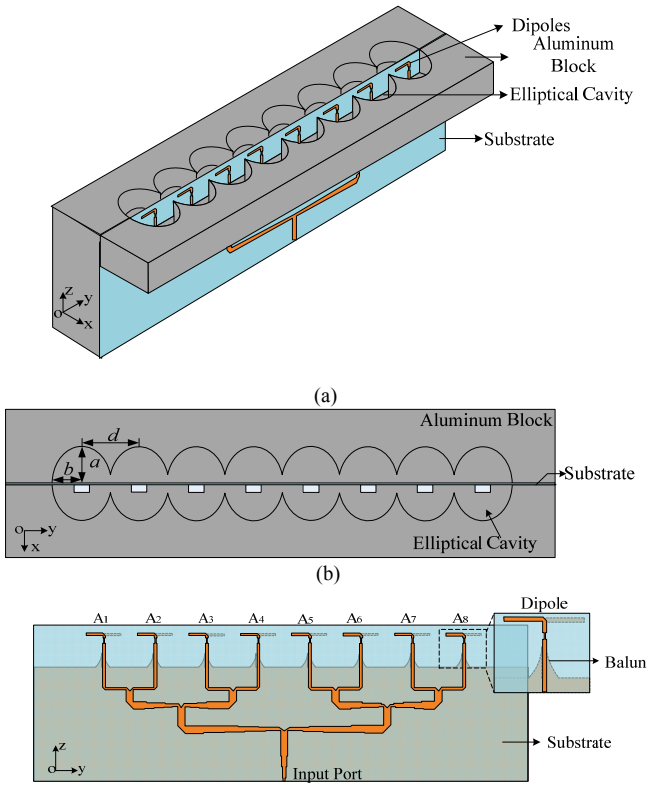

Fig.1 Geometries of the proposed 8-element cavity-backed linear array. (a) 3-D view. (b) Top view. (c) The substrate.

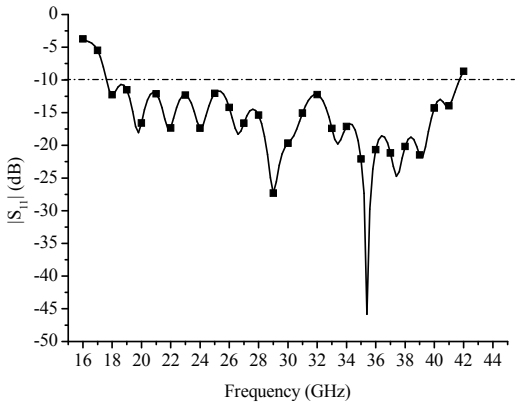

Fig.2 Simulated S parameter of the proposed 8-element cavity-backed linear array.

dividers are employed. It is worth being noted that the aperture efficiency can be over 100% in lower frequency band below 23GHz, as shown in Fig. 3, because the electric fields outside the physical aperture of the array still positively contribute to the broadside radiation [5]-[7], which is one of the key advantages of cavity-backed antennas. The aperture efficiency can still be over 80% as frequency goes up to 39.5GHz. The realized gain of the array across the whole

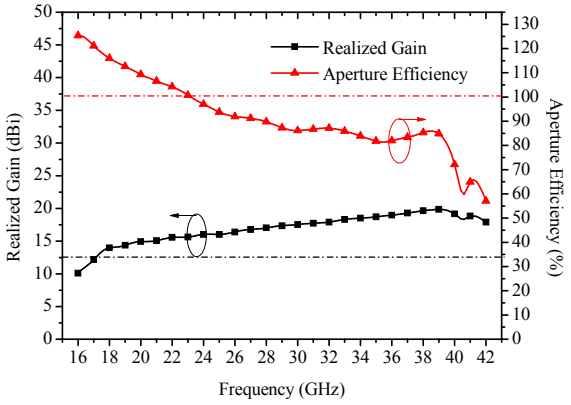

Fig.3 Simulated realized gain and aperture efficiency of the proposed 8-element cavity-backed linear array.

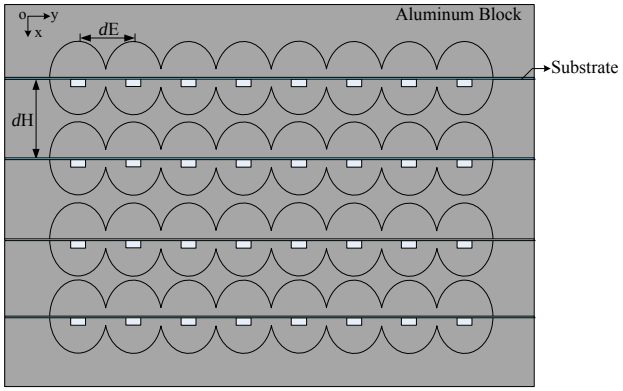

Fig.4 The proposed 4× 8 planar array.

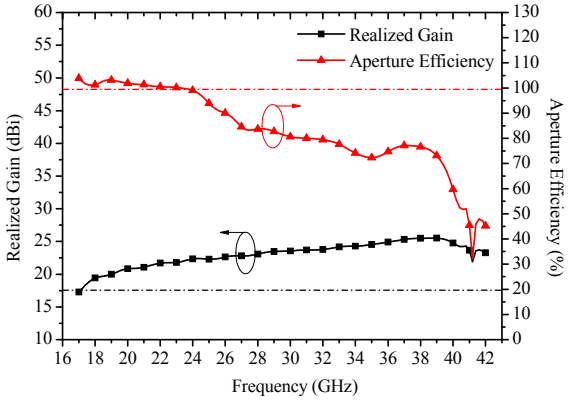

Fig.5 Simulated realized gain and aperture efficiency of the 4×8 planar array.

frequency band is gradually increased from 12.5 to 19.8dBi with a peak at 39GHz.

III. Planar Array with 4 × 8 Cavity-Backed Elements

For a higher gain, a larger aperture with more cavity-backed elements is necessary. A linear array topology is certainly

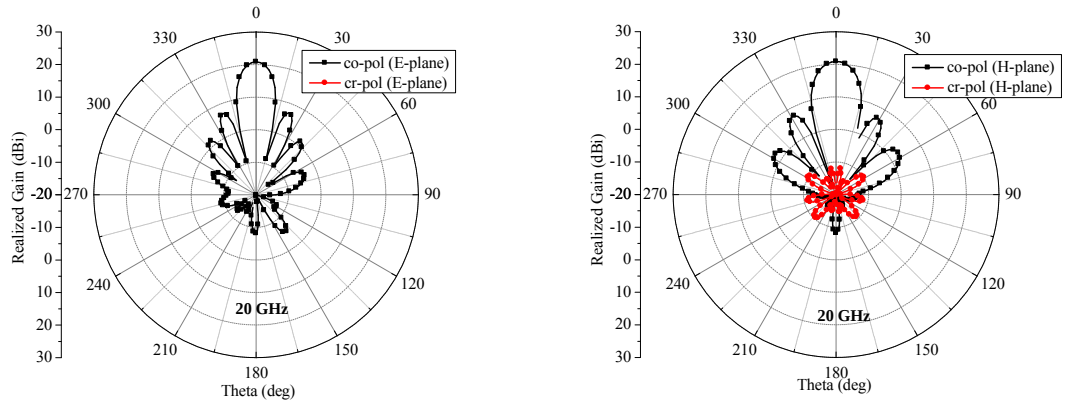

(a)

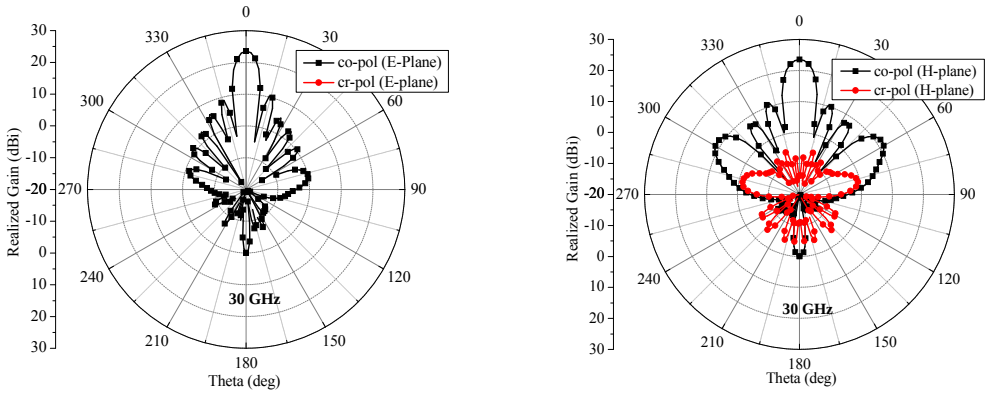

(b)

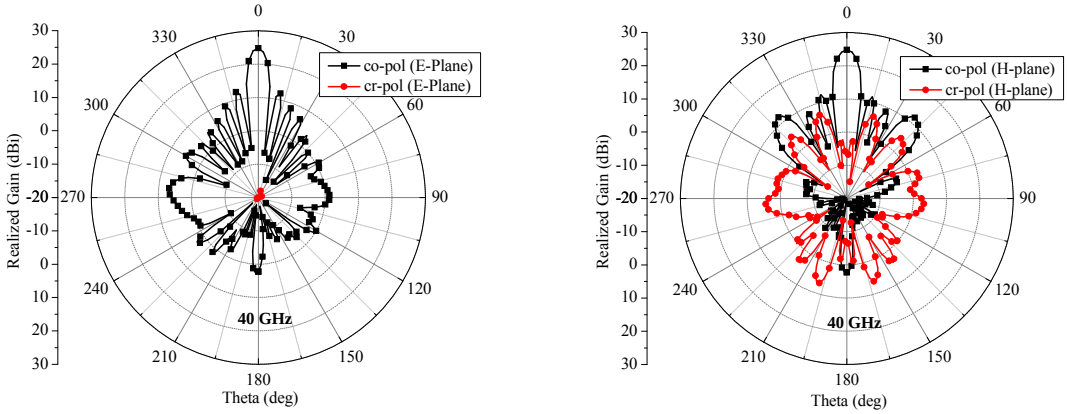

(c)

Fig.6 Simulated radiation patterns in the E and H planes at (a) 20, (b) 30, and (c) 40GHz.

suitable, but in this design a planar array is designed from the viewpoints of radiation patterns. Fig. 5 shows geometry of the planar array, constructed by arranging 4 linear arrays in Section II along the x axis. The inter-element distances along the x- and y-axis directions are denoted by d_E and d_H, respectively (d_E = d =7mm and d_H = 11mm).

Fig. 5 shows the realized gain and aperture efficiency of the planar array. The gain is over 19 dBi across the whole frequency band with a peak 25.5 dBi at 39GHz, and the corresponding aperture efficiency is over 45%. Note that the aperture efficiency is still over 100% below 24GHz and over 70% below 39.4GHz. Fig. 6 gives the simulated radiation patterns in the E and H planes at 20, 30, and 40GHz. The side lobe level are always below -11dB in both planes, but two large side lobes can be observed in the H plane as frequency goes beyond 30GHz due to the large element spacing. Meanwhile, the E-plane cross polarization (cr-pol) is always over -45dB in the whole frequency band, and the H-plane cr-pol is relatively larger but still below -30 dB in an angle range of the main beam.

IV. CONCLUSION

Applications of the cavity-backed dipoles to antenna arrays are investigated in this paper. By partially overlapping the cavity aperture, the antenna array can be designed more compact than ever, and then the grating lobes can be voided in the corresponding plane. Two cavity-backed antenna arrays in this work, i.e., a linear and a planar array, can present a maximum aperture efficiency of over 100% and a realized gain of 19.8 and 25.5dBi, respectively, across the whole frequency band from 17.8 to 41.6GHz.

ACKNOWLEDGMENT

This work was supported in part by the National Science Foundation of China under grants No. 61101036, and in part by the Specialized Research Fund for the Doctoral Program of Higher Education under grant number 20110185120002.

REFERENCES

[1] B. Allen, M. Dohler, E. E. Okon, W. Q. Malik, A. K. Brown, and D. J. Edwards, *Ultra-Wideband Antennas and Propagation*. New York: Wiley, 2007.

[2] X. N. Low, Z. N. Chen, and W. K. Toh, "Ultrawideband Suspended Plate Antenna With Enhanced Impedance and Radiation Performance," IEEE *Trans. Antennas Propag*., vol. 56, pp. 2490-2495, Aug. 2008.

[3] A. A. Lestari, A. G. Yaravoy, and L. P. Ligthart, "RC-loaded bow-tie antenna for improved pulse radiation," *IEEE Trans. Antennas Propag*., vol. 52, pp. 2555-2563, Oct. 2004..

[4] J. L. Wong and H. E. King, "A cavity-backed dipole antenna with widebandwidth characteristics," *IEEE Trans. Antenna Propag.*, vol. 21, no. 5, pp. 725–727, Sept. 1973.

[5] S.-W. Qu, C. H. Chan, and Q. Xue, "Ultrawideband Composite Cavity-Backed Folded Sectorial Bowtie Antenna With Stable Pattern and High Gain," *IEEE Trans. Antennas Propag*., vol. 57, no. 8, pp. 2478-2483, Aug. 2009.

[6] S.-W. Qu, J.-L. Li, Q. Xue, and C. H. Chan, "Wideband cavity-backed bowtie antenna with pattern improvement," *IEEE Trans. Antennas Propag*., vol. 56, no. 12, pp. 3850–3854, Dec. 2008.

[7] S.-W. Qu, C. H. Chan, and Q. Xue, "Ultrawideband Composite Cavity-Backed Rounded Triangular Bowtie Antenna With Stable Patterns," *J. of Electromagn. Waves and Appl.*, v5-7ol. 23, pp. 685-695, 2009.

A Design of UHF-RFID Reader Antenna with Circular Polarization

Yanzhong Yu, Zhengbao Rao, Min Hu

1.College of Physics & Information Engineering, Quanzhou Normal University, Fujian, 362000, China;
2. Key Laboratory of Information Functional Materials for Fujian Higher Education, Fujian, 362000, China.
*corresponding author, E-mail: yuyanzhong059368@gmail.com

Abstract

A UHF-RFID reader antenna with circular polarization is designed in the present paper. In order to achieve the requirements of RFID reader applications, three measures are adopted. First way is to use a modified Minkowski fractal as radiating element for compacting dimension and broadening bandwidth. The second is to utilize the square truncation to obtain the circular polarization. In order to promote the gain of the proposed antenna, the slot-opened technology is employed lastly. The proposed design is analyzed and optimized by using HFSS. The numerical results demonstrate that performances of the optimized antenna are acceptable for practical RFID applications. The optimized antenna has the advantages of simplicity, miniaturization, and easy fabrication.

1. Introduction

Radio frequency identification (RFID) is a wireless non-contact technology that uses radio frequency electromagnetic fields to exchange information, for the purposes of automatically identifying and tracking tags attached to objects [1]. It is composed of a tag for transmitting product information and a reader for receiving data. With the rapid development of Internet of Things (IoT), recently much attention has been paid to RFID technology since it is one of key technologies in (IoT). At present, a large number of practical RFID applications in every trade can be found readily, e.g., distribution logistics, electronic toll collection, carton tracking, and parking lot access [2].

In whole RFID domain, the UHF-RFID system is the most popular owing to its low cost and high performances. Therefore the antenna presented in this paper is operated in UHF bands (920.5–924.5 MHz). In design RFID reader antenna, the property of circular polarization is required to guarantee the reliability of communicating between reader and tag, because the tag attached to the product is usually arbitrarily oriented and its antenna is almost linearly polarized [3]. Consequently, circular polarization plays a very important performance in the design of reader antenna. According to polarized theory, to let antenna emit CP wave, the key is to stimulate two linearly polarized waves with orthogonal polarization, and their amplitudes are equal and their phase differences are 90 degree. In order to design CP reader antennas, several suggestions have been proposed, such as corner-truncated patch antennas, dual-fed or hybrid-fed exciting antennas, slot-opened patch antennas, and CPW slotted patch antennas.

A design a fractal-like CP antenna for RFID reader applications is described in this article. For the purpose of compacting dimensions and extending bandwidth, the modified Minkowski fractal concept is adopted. To achieve circular polarization, a corner-truncated patch is utilized owing to its simplicity and easy fabrication. And a ground plane with opening slot is employed to improve the gain of the designed antenna. The simulated results show that the optimized antenna exhibits acceptable performances in terms of return loss, total gain, AR, and impedance matching.

2. Antenna configuration

The fractal structures can be employed to design antennas for size compactness and multiband operation [4], such as Koch fractal antenna, Sierpinski triangle fractal, and Hilbert fractal antenna. In our paper the modified Minkowski fractal is used to design a CP reader antenna for RFID applications. The generation procedure for the Minkowski fractal is given in Fig. 1, in which it is reconstructed by replacing the central zone with indentation length by indentation width. Here we define an indentation factor (IF) as the ratio of indentation width to indentation length [5]. Apparently the internal structure of Minkowski fractal is determined by IF. It was found that the Minkowski fractal patch antenna exhibits good characteristics of size reduction and resonating frequency decline, But when the order of iteration increases over two, the complexity of fractal structure and the difficulty of manufacturing ascend sharply. Therefore the iteration order of Minkowski fractal is usually no more than two. In our design we take the iteration order equals to one. The configuration of the designed antenna is illustrated in Fig. 2, in which it consists of three layers. The radiating square patch, which is a modified Minkowski fractal with two square truncations at diagonal corners for implementing CP performance, is placed on the top layer. The FR4_epoxy with relative dielectric constant of $\varepsilon_r = 3.6$, loss tangent of $\tan\delta = 0.017$, is considered as substrate and is placed at the middle layer. The bottom layer is a ground plane opened with cross-shaped grooves for improving the gain of the

designed antenna. It is back fed by the coaxial cable (50 Ω). The advantages of the designed antenna are simpler structure, lower cost and easier fabrication when compared with other reader antennas [6]. The initial sizes for the designed antenna are listed in Table 1, in which L6 denotes the spacing between feeding point and the origin of antenna model, and L7 represents the width of the slot on the ground plane.

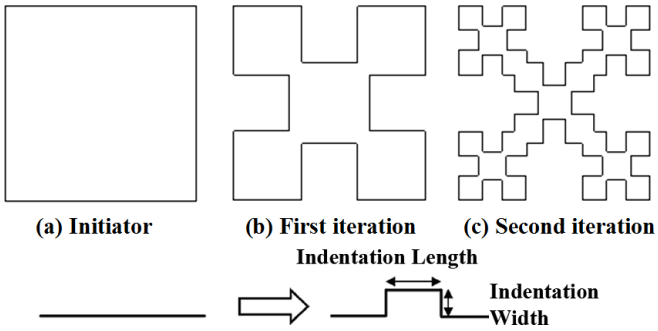

Fig. 1. Geometries of Minkowski fractal (0~2 order)

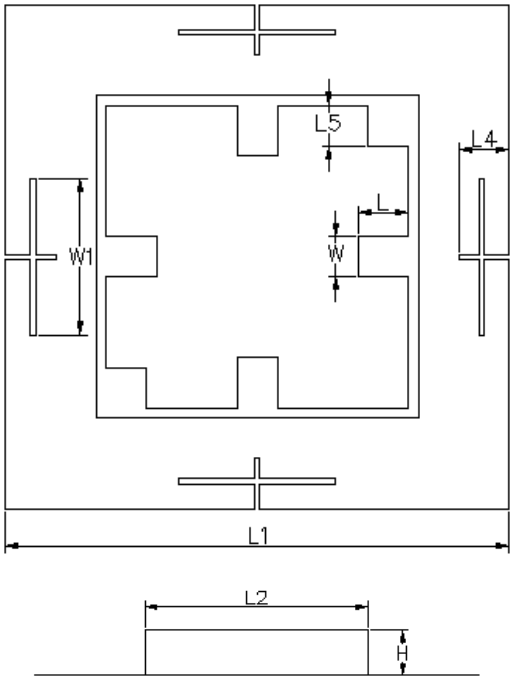

Fig. 2. Configuration of the proposed antenna

Table 1. Initial sizes of the proposed antenna (mm)

Parameter	L	L1	L2	L3	L4	L5
Value	10	112	75	73	10	7
Parameter	L6	L7	W	W1	H	
Value	17	1	10	40	4.5	

3. Analyses and optimization

The initial antenna is calculated by HFSS. Fig. 3 shows the simulated return loss of initial antenna. It is evident that the simulated result exhibits an impedance bandwidth (S11<=-10 dB) of 34 MHz (3.6%) that satisfies the requirements of broadband basically. However, the central frequency point is located at 928 MHz (S11=-24.3 dB) that is out of range of 920~925 MHz. The input impedance as a function of frequency is illustrated in Fig. 4. The input impedance at desired frequency point of 920 MHz is Zreader=(66.6+j7.1) Ω, which does not proper mach to 50 Ω. From Figs. 3 and 4, it can be seen that the simulated results do not achieve the requirements of RFID reader applications. In order to facilitate the design and optimization processes for engineers, the parametric study should be conducted.

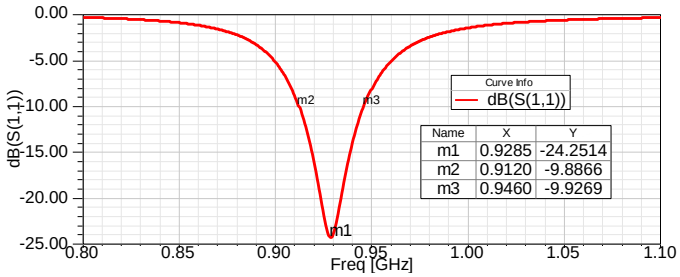

Fig. 3. Retrun Loss of initial antenna

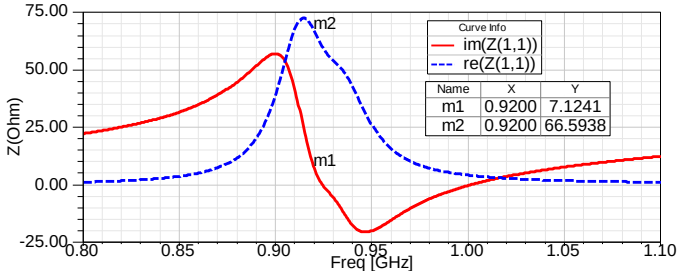

Fig. 4. Input impedance of initial antenna

Parametric investigation can obtain more helpful information to quicken the process of antenna design and optimization. To better understand the effect of the parameters on the performances of proposed antenna, only one parameter is tuned, while others remain unchanged. The influence of indentation width L on return loss and input impedance is depicted in Fig. 5, respectively. It is found that within 0.8 ~1.1 GHz the resonating frequency drops gradually and return loss S11 reduces with the increase of indentation width L. The real part of input impedance decreases slowly from 66.6 Ω to 45.9 Ω as L increases from 10 mm to 12 mm. Nevertheless, the imaginary part waves from 7.1 Ω (inductive) to -11.8 Ω (capacitive).

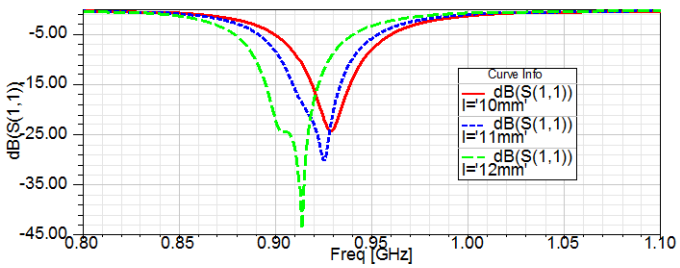

(a) Return loss

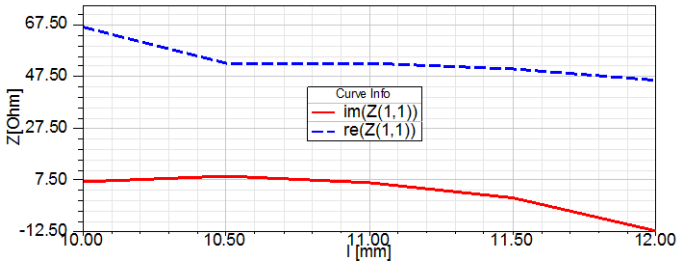

(b) Input impedance

Fig. 5. Effect of parameter L on the antenna performances.

Other parameters, such as patch length L3, length of square truncation L5, substrate thickness H, and so on, may be analyzed similarly. These results will not be covered here due to the lack of space. It is found by parametric analyses that parameters L and L5 have a great effect on the resonating frequency, and the return loss is affected heavily by the parameters L3, L6 and H, and the input impedance is determined chiefly by the parameters L, L5, L6, and H. By repeating optimization, the optimal sizes for the proposed antenna are obtained ultimately. They
L3=73.2 mm, L5=7.5 mm, L6=18 mm,
other sizes are the same as the initiation.
optimized antenna are depicted in Fig. 6
of return loss S11<=-10 dB must be
applications. It may be observed clearly f
the optimized antenna exhibits a bandwid
of 901 ~ 941 MHz (4.3%) with central
MHz. In general, the coaxial cable with i
50 Ω is used as the feed line of reader
employed to back feed the designed ant
(b) one can get the input impedance at res
of 920 MHz is Z_{reader}=(57.9-j2.6) Ω, whi
impedance value of 50 Ω. This indicates that there exist a proper impedance matching between the optimized antenna and coaxial cable. Gain is a very important index in measuring antenna performances. At 920 MHz, Fig. 6 (c) displays the 2D radiation patterns in the x-z and y-z planes. It can be discerned that the patterns in x-z plane and y-z plane overlap nearly and the maximum gain of G=1.12 dB locates at the direction of $\theta=0^\circ$, $\varphi=0^\circ$. On the upper half plane the optimized antenna exhibits a spherical radiation and has an excellent symmetry. Additionally, AR is a key index that represents a CP degree and not less than 0 dB, i.e., AR>=0 dB. When AR=0 dB, it means the antenna works at pure CP state. In practical applications, the range of 0<=AR<=3 dB is acceptable for the CP antenna. The AR versus frequency of the optimized antenna is depicted in Fig. 6 (d). It is seen that the AR equals to 1.16 dB at the central frequency of 920 MHz. In short, the performances of the optimized antenna can meet the requirements of RFID system.

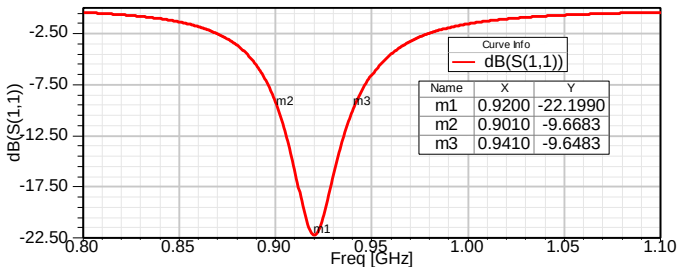

(a) Return loss S11 versus frequency

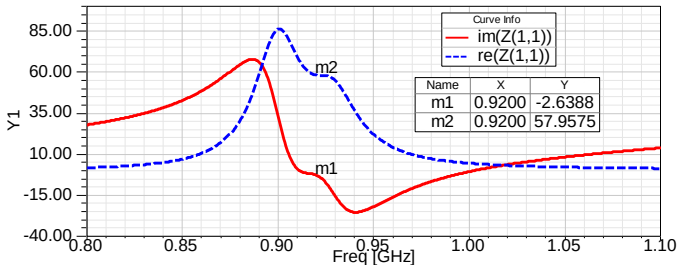

(b) Input impedance versus frequency

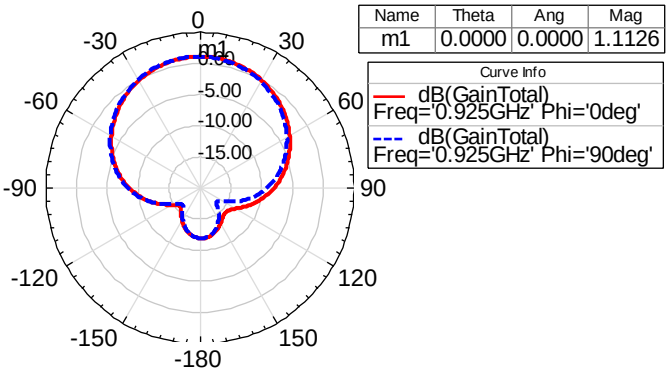

(c) 2D radiation patterns in X-Y and Y-Z planes

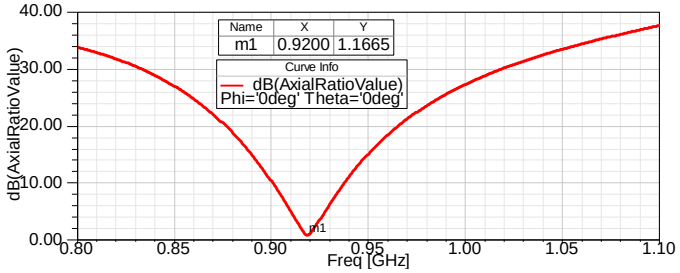

(d) AR versus frequency

Fig. 6. Simulated results of the optimized antenna

Acknowledgements

This work was supported by Fujian Province Education Department under grant JK2012040, the National Project of Innovative Entrepreneurship of Undergraduate (201310399002), and the Key Discipline of Electronic Science and Technology.

References

[1] Z. N. Chen, X. Qing, and H. L. Chung, "A universal UHF RFID reader antenna," IEEE Trans. Microw. Theory Tech., Vol. 57, No. 5, pp. 1275–1282, May 2009.

[2] C. Raviteja, C. Varadhan, M. Kanagasabai, A. K. Sarma, and S. Velan, "A Fractal-Based Circularly Polarized UHF RFID Reader Antenna," IEEE Antennas Wirel. Propag. Lett., Vol. 13, pp. 499-502, 2014.

[3] H. L. Chung, X. Qing, and Z. N. Chen, "A broadband circularly polarized stacked probe-fed patch antenna for UHF RFID applications," Int. J. Antennas Propag., vol. 2007, 2007, Art. ID 76793, 8 pp.

[4] D. H. Werner, R. L. Haup, and P. L. Werne, "Fractal Antenna Engineering: The Theory and Design of Fractal Antenna Arrays," IEEE Antennas. Propag. Magazine, Vol. 41, No. 5, pp. 37-59, Oct. I999.

[5] Sayantan Dhar, Rowdra Ghatak, Bhaskar Gupta, and Dipak Ranjan Poddar, "A Wideband Minkowski Fractal Dielectric Resonator Antenna," IEEE Trans. Antennas Propag., vol. 61, no. 6, pp. 2895–2903, June 2013.

[6] R. Siragusa, P. L. Auger, and S. Tedjini, "Tunable Near-Field Focused Circular Phase-Array Antenna for 5.8-GHz RFID Applications," IEEE Antennas Wirel. Propag. Lett., Vol. 10, pp. 33-36, 2011.

Teaching and Training Electromagnetics around the world : what 's new

A software tool for electromagnetic optimization teaching

Laurent Santandrea

LGEP-CNRS, France
*corresponding author, E-mail: santandrea@lgep.supelec.fr

Abstract

Optimization still to be an interest for electromagnetic device design and still requires an appropriate teaching in electromagnetic cursus. In this aim the Master PIE (Physique et Ingénierie de l'Energie) of the Université Paris-Sud have developped specific lectures and pratical tutorials. In this work we propose to describe one of pratical tutorials, based on the use of a computer tool (OSD). Though a Graphical user interface proposes different optimization problems (analytical problems or practical electomagnetic problems) and differents methods to solve them. Students are first encouraged to describe and to look critically each of proposed problems. In the second part they have to explore the different algorithms to solve each of them, and to appreciate advantages and drawbacks of each optimization technique. In this paper we try to present this tool and to show its upgrade to current problems as multiobjective or discrete optimization for electromagnetic devices.

Computational Electromagnetic Methods and Their Applications

Study of High-Degree Stability for Marching-on-in-Degree Time Domain Technique

Ming-Da Zhu[1], and Wen-Yan Yin[2,3]

[1]Department of Electronics and Communication Engineering, Donghua University, Shanghai 201620, China
[2] Centre for Optical and EM Research (COER), State Key Lab of MOI, Zhejiang Provincial Key Lab of Sensing Technologies, Zhejiang University, Hangzhou 310058, China
[3] Centre for Microwave and RF Technologies (CMRFT), Key Lab of Ministry of Education for Design and EMC of High-Speed Electronic Systems, School of Electronic Information and Electrical Engineering, Shanghai Jiao Tong University, Shanghai 200240, China
*corresponding author, E-mail: mingda.zhu@dhu.edu.cn

Abstract

The marching-on-in-degree (MOD) method has been presented earlier to solve time domain integral equations to for transient electromagnetic scattering phenomena. This is accomplished by expanding the transient responses by a set of associated Laguerre polynomials, and recursively solving the matrix equation in the degree-marching manner. Although the MOD scheme is assumed to be stable compared with marching-on-in-time one (MOT), there is few numerical or theoretical investigation on the recursive operations of MOD, which may result in instability for MOD schemes with high degree of associated Laguerre polynomials.

In this paper, the high-degree stability is studied for MOD method in the time domain integral equations. Results in this paper suggest that, the inaccurate numerical quadratures of high-degree associated Laguerre polynomials yield instable MOD solvers. Hence, a modified MOD technique for time-domain magnetic field integral equations (TD-MFIE) is proposed to solve this instability. Some numerical results are presented to illustrate the validity of these claims in solution of transient scattering problems.

Metal-nonmetal oscillations in doped blue phosphorene:a first-principles study

Weiyang Yu[1,2], Zhili Zhu[1], Chong Li[1], Chunyao Niu[1], Junhyung Cho[3], Yu Jia[1]*

[1]International Laboratory for Quantum Functional Materials of Henan and School of Physics and Engineering, Zhengzhou University, Zhengzhou 450001, China

[2]School of Physics and Chemistry, Henan Polytechnic University, Jiaozuo 454000, China

[3]Department of Physics and Research Institute for Natural Sciences, Hanyang University, 17 Haengdang-Dong, Seongdong-Ku, Seoul 133-791, Korea

*corresponding author, E-mail: jiayu@zzu.edu.cn

Abstract

Based on density functional theory(DFT), we have investigated systematically the geometry structure and electronic properties of non-metallic atom doped blue phosphorene, such as B-, C-, N-, O-, Al-, Si- and S-doped blue phosphorene systems. An intriguing general rule of metal-nonmetal oscillations has been obtained that the dopant atom from group-IVA and VIA leads to metal properties, while dopant atom from group-IIIA and VA gives rise to semiconductor properties, which is different from traditional *n* or *p* doping effect in bulk case. Then the underlying mechanism was investigated with the electronic filling analysis.

1. Introduction

The discovery of graphene laid the foundations for many new areas of research. One of the most important foundation is the intensive investigation of two-dimensional (2D) atomic-layer systems, including graphene itself[1], transition metal dichalcogenides (TMDCs)[2], silicene[3] and germanane[4], as candidate materials for future electronics applications[5-7]. Most recently, a new 2D few-layer black phosphorus (BP) have been successfully fabricated by exfoliation[8] ,which has drawn immediately attention to the society of material science[9-11]. Monolayer BP (known as black phosphorene) is, besides graphene, the only stable elemental 2D material that can be mechanical exfoliated. Black phosphorene has been theoretically predicted to be direct gap or nearly direct gap semiconductors with energy gaps ranging from 2 eV to 0.8 eV[9] .It was reported that FET devices have been made using few-layer black phosphorene as the channel, and high carrier mobility up to 10^3 $cm^2/V{\cdot}s$ and an on/off ratio up to 10^4 was achieved for the black phosphorene transistors at room temperature, which make black phosphorene an attractive material for future nanoelectronic applications[12]. Blue phosphorene, the allotrope of black phosphorene, has the same stability in room temperature as black phosphorene, and its band gap is larger than black phosphorene[13]. The application of blue phosphorene is more widely.

In 2D materials, doping is an essential approach which can tune the electronic structure and thus the variation broadens the range of applications of the doping material. For graphene, both experimental and first-principles studies have shown that carrier concentration can be modulated by substitutional doping[14], or charge transfer doping from adsorbed atoms, molecules, and clusters[15-20]. If charge transfers from the dopant atom to the graphene, the Dirac point will shift to an energy below the Fermi level of pristine graphene, known as *n* doping. This will lead to electrons being the majority charge carrier in graphene. Conversely, charge transferred from graphene to the dopant atom will shift the Dirac point above the Fermi level of pristine graphene, known as *p* doping. In this case, holes will be the majority charge carrier[21].

For blue phosphorene, we notice that all studies on phosphorene in literatures did not concern on the doping effects such as the effects of defects and impurities except for Sun et al predicted phosphorene a potential superconductor by electron-doped[22]. However, for the design of realistic devices, the effects of defects and impurities have to be taken into account. Here we present the theoretical discovery of a new category of monolayer doping system of metal-nonmetal oscillating with different dopant atoms from group-IIIA, IVA, VA and VIA, respectively. Dopant atoms from group-IVA and VIA lead to metal properties, while Dopant atoms from group-IIIA and VA give rise to semiconductor properties. The present results are different from traditional *n*- or *p* doping effect in other 2D semiconducting materials.

2. Computational details

The present calculations have been performed by Vienna ab initio simulation package (VASP) code[23] while the exchange-correlation effect were described by the Perdew-Burke-Ernzerhof based on the general gradient approximations (GGA-PBE)[24]. The projector augmented wave (PAW) method[25] in its implementation was used to describe the electron-ion interaction. The kinetic energy cutoff for the plane wave basis set was chosen to be 500 eV, while the Brillouin zone was sampled with 4×5×1 k-points (Γ point centered) generated by the Monkhorst–Pack

scheme[26]. A vacuum layer more than 10Å was introduced to simulate the monolayer blue phosphorene. The structures are fully relaxed until the force on each atom less than 0.01 eV/Å. Band structure calculations was performed using the tetrahedron method with the Blöchl corrections[27].

3. Results and discussion

3.1. Geometry structure

Figure 1 gives the top and side view of the structures of blue phosphorene supercell with doping atoms, in which a single dopant atom binds to a phosphorus monovacancy. Throughout the paper we will refer to this structure as the substitutional configuration, and the dopant atom is indicated with red solid atoms. For blue phosphorene unit cell, the relaxed lattice constants are $a_1=a_2=3.33$Å. The structures of 2×2 doped blue phosphorene supercells are also optimized, and the obtained bond lengths are $d_1=d_2=2.28$Å, and bond angles are $\theta_1=120.0^o$, $\theta_2=60.0^o$. The present calculations are in good agreement with experiment and other theoretical results[13], which indicates that the calculation is accurate.

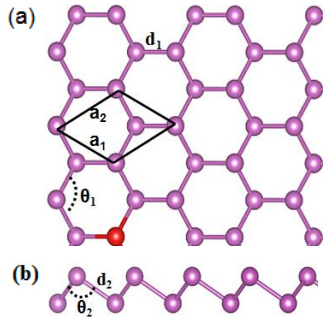

FIG. 1. (Color online) (a) Top and (b) side view of blue phosphorene supercell with substitutional X-atom, giving a clear indication with red atom.

3.2. Electronic structures

The band structures of B-, C-, N- and O-doped blue phosphorene are calculated and presented in Fig. 2 (a). It is clear in Fig. 2 (a) that for group-IIIA and -VA doping (X=B and N), the systems present semiconducting properties with band gap of 1.18 and 0.83 eV, respectively, which is smaller than the band gap of pure blue phosphorene (1.82eV). When doping atoms are from group-IVA and -VIA, the systems appear metallic properties without band gap [see Fig. 2 (b)]. For comparison, the band structure of pure phosphorene was also shown in Fig. 2 (b). From electronic filling analysis we can see that the degenerated band near Fermi level is a little split for N-doped phosphorene because of the symmetry of the pure is destroyed. But the destruction is so little that the band structure near Fermi level is still keep the original appearance for the same s^2p^3 orbital in group-VA. As for C-doped system, the degenerated band is totally split, and the VB is half filled for the lack of one electron and the energy level decreases, which results in the band crossing the Fermi level and performing metal property. While for B-doped system, the degenerated band is split to a large extent for less of a pair electrons and the Fermi level decreases to cause a large energy gap, leading to semiconductor. For O-doped system, the CB is half filled for the excess of one electron and the energy level increases leading to the CB cross the Fermi level.

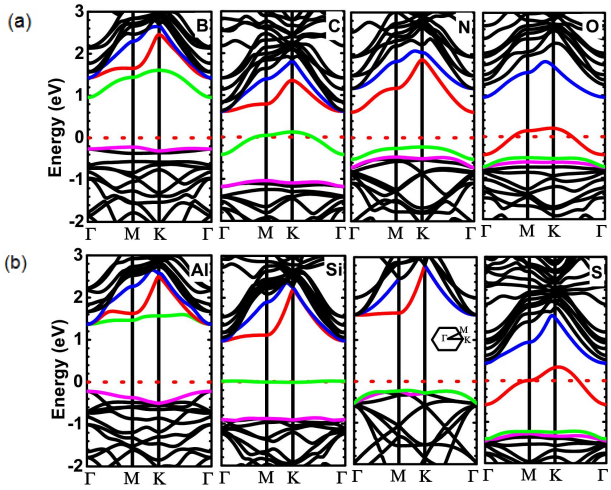

FIG. 2. (Color online) Band structures of (a) B-, C-, N- and O-doped blue phosphorene and (b) Al-, Si- and S-doped blue phosphorene, respectively, along with the band structure of pure phosphorene, and insert map is the path of integration. The Fermi level is at zero energy and marked by a horizontal dotted line.

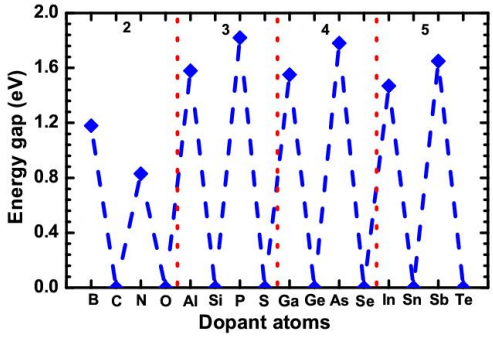

FIG. 3. (Color online) Energy gap of all the IIIA, IVA, VA and VIA family doping systems. The different period, 2, 3, 4 and 5, is separated with red upright dot line.

3.3. Metal-nonmetal oscillating

To investigate whether above conclusion is universal, we calculate the other doping systems extensively. The Energy gap was plotted in Fig. 3. It is obvious that the energy gap is of an oscillating distribution with different elementary group. There exhibits no energy gap if the dopant atoms root in group-IVA and -VIA, such as C, O, Si, S, Ge, Se, Sn and Te doping systems. While dopant atoms from group-IIIA and -VA, the doping systems exist energy gap, see B, N, Al, Ga, As, In and Sb doping

systems. The interesting results show that different from traditional *n* or *p* doping effect in other semiconducting materials, group-IVA and VIA doping gives metal and group-IIIA and -VA doping gives semiconductor in 2D blue phosphorene.

4. Conclusions

In summary, a series doped systems of group-IIIA, -IVA, -VA and -VIA atoms in 2D blue phosphorene have been investigated by first-principles calculations. It is found that different from traditional *n* or *p* doping effect in semiconducting materials, there is a metal-nonmetal oscillating that the group-IVA and VIA doping gives rise to metal properties, while the group-IIIA and -VA doping leads to nonmetal. The underlying mechanism have been investigated with the electronic filling analysis. The present metal-nonmetal oscillations shown here not only facilitate a deep understanding of blue phosphorene with defect or impurity, but also provide an intriguing route to add functionalities or to tune response of devices based on blue phosphorene materials, and attract more experimentalists to develop new phosphorene-based nanoelectronic device. Experimentally, doping could be achieved by artificially creating defects or monovacancies in blue phosphorene and impurity state could be probed with photoemission spectroscopy or other techniques.

Acknowledgements

This work was supported by the National Basic Research Program of China (Grant No. 2012CB921300), the National Natural Science Foundation of China (Grant Nos. 11274280 and 11304288). The calculations were performed on the High Performance Clusters of Zhengzhou University.

References

[1] A. K. Geim and I. V. Grigorieva, Van der Waals heterostructures, *Nature* 499: 419−425, 2013.

[2] Q. H. Wang, K. Kalantar-Zadeh, A. Kis, J. N. Coleman, and M. S. Strano, Low frequency electronic Noise in single-layer MoS2 transistors, *Nat. Nanotechnol.* 7: 699−712, 2012.

[3] P. Vogt, P. D. Padova, C. Quaresima, J. Avila, E. Frantzeskakis, M. C. Asensio, A. Resta, B. Ealet, and G. L. Lay, Silicene: compelling experimental evidence for graphenelike two-dimensional silicon, *Phy. Rev. Lett.* 108: 155501−1, 2012.

[4] E. Bianco, S. Butler, S. Jiang, O. D. Restrepo, W. Windl, and J. E. Goldberger, Stability and exfoliation of germanane: a germanium graphane analogue. *ACS Nano* 7: 4414−21, 2013.

[5] H. Wang, L. Yu, Y. H. Lee, Y. Shi, A. Hsu, M. L. Chin, L. J. Li, M. Dubey, J. Kong, and T. Palacios, Integrated circuits based on bilayer MoS_2 transistors, *Nano Lett.* 12: 4674−4680, 2012.

[6] I. Popov, G. Seifert, and D. Tománek, Designing electrical contacts to MoS_2 monolayers: a computational study, *Phys. Rev. Lett.* 108, 156802−1, 2012.

[7] S. Z. Butler, S. M. Hollen, L. Cao, Y. Cui, J. A. Gupta, H. R. Gutierrez, T. F. Heinz, S. S. Hong, J. Huang, A. F. Ismach, E. Johnston-Halperin, M. Kuno, V. V. Plashnitsa, R. D. Robinson, R. S. Ruoff, S. Salahuddin, J. Shan, L. Shi, M. G. Spencer, M. Terrones, W. Windl, and J. E. Goldberger, Progress, challenges, and opportunities in two-Dimensional materials beyond Graphene, *ACS Nano* 7: 2898−2906, 2013.

[8] E. S. Reich, Phosphorene excites materials scientists *Nature* 506:19, 2014.

[9] V. Tran, R. Soklaski, Y. F. Liang, and L. Yang, Layer-controlled band gap and anisotropic excitons in few-layer black phosphorus, *Phys. Rev. B* 89: 235319−1, 2014.

[10] R. X. Fei and L. Yang, Strain-engineering the anisotropic electrical conductance of few-Layer black phosphorus, *Nano Lett.* 14: 2884−2889, 2014.

[11] V. Tran and L. Yang, Scaling laws for the band gap and optical response of phosphorene nanoribbons, *Phys. Rev. B* 89: 245407−1, 2014.

[12] M. Buscema, D. J. Groenendijk, S. I. Blanter, G. A. Steele, H. S. J. van der Zant, A. Castellanos-Gomez, Fast and broadband photoresponse of few-Layer black phosphorus field-Effect transistors, *Nano Lett.* 14: 3347−3352, 2014.

[13] Z. Zhu and D. Tomanek, Semiconducting layered blue phosphorus: a computational study, arXiv:1403.1300, 2014.

[14] H. Liu, Y. Liu, and D. Zhu,. Chemical doping of graphene, *J. Mater. Chem.* 21: 3335−3345, 2011.

[15] F. Alzina, H. Tao, J. Moser, Y. García, A. Bachtold, and C. M. Sotomayor-Torres, Probing the electron-phonon coupling in ozone-doped graphene by Raman spectroscopy, *Phys. Rev. B* 82: 075422−1, 2010.

[16] W. J. Zhao, P. H. Tan, J. Zhang, and J. Liu, Charge transfer and optical phonon mixing in few-layer graphene chemically doped with sulfuric acid, *Phys. Rev. B* 82: 245423−1, 2010.

[17] N. Jung, B. Kim, A. C. Crowther, N. Kim, C. Nuckolls, and L. Brus, Optical reflectivity and Raman scattering in few-layer-thick graphene highly doped by K and Rb, *ACS Nano* 5: 5708−5716, 2011.

[18] Z. Zhang, H. Huang, X. Yang, and L. Zang, Tailoring electronic properties of graphene by π–π stacking with aromatic molecules, *J. Phys. Chem. Lett.* 2: 2897−2905, 2011.

[19] H. Medina, Y. C. Lin, D. Obergfell, and P. W. Chiu, Tuning of charge densities in graphene by molecule doping, *Adv. Funct. Mater.* 21: 2687–2692, 2011.

[20] M. K. Srivastava, Y. Wang, A. F. Kemper, and H. P. Cheng, Density functional study of gold and iron clusters on perfect and defected graphene, *Phys. Rev. B* 85: 165444−1, 2012.

[21] L. Tsetseris, B. Wang, and S. T. Pantelides, Substitutional doping of graphene: the role of carbon divacancies, *Phys. Rev. B* 89: 035411−1, 2014.

[22] D. F. Shao, W. J. Lu, H. Y. Lv, and Y. P. Sun, Electron-doped phosphorene: a potential monolayer superconductorar, Xiv: 1405.0092, 2014.

[23] G. Kresse and J. Furthmüller, Efficient iterative

schemes for ab initio total-energy calculations using a plane-wave basis set, *Phys. Rev. B* 54: 11169−1, 1996.
[24] J. P. Perdew, K. Burke, M. Ernzerhof, Generalized gradient approximation made simple, *Phys. Rev. Lett.* 78: 1396-1, 1997.
[25] G. Kresse and D. Joubert, From ultrasoft pseudopotentials to the projector augmented-wave method, *Phys. Rev. B* 59: 1758−1, 1999.
[26] H. J. Monkhorst and J. D. Pack, Special points for Brillouin-zone integrations, *Phys. Rev. B* 13: 5188−1, 1976.
[27] P. E. Blöchl, O. Jepsen, and O. K. Andersen, Improved tetrahedron method for Brillouin-zone integrations, *Phys. Rev. B* 49: 16223−1, 1994.

Plasma Sheath Multipath analysis and Its Effect on GNSS Navigation

Du Yongxing[1], Xi Xiaoli [2], Song Zhongguo[2] liu Jiangfan[2],

[1]Inner Mongolia University of Science & Technology, Inner Mongolia, China
[2]Xi'An University of Technology, Xi'An, China
*corresponding author, E-mail: xixiaoli@xaut.edu.cn

Abstract

When hypersonic vehicle reenters the Earth's atmosphere, the plasma sheath will be generated by its collision with ambient air that would affect Global Navigation Satellite System (GNSS). In order to understand such effects, the transmission coefficient of the plasma sheath has been investigated using the numerical method before. But this is found to be insufficient, for besides the attenuation on the signal energy, the multipath effect between the plasma sheath and the vehicle surface is also a serious factor which may result in errors in pseudorange measurement and carrier phase measurement of GNSS receiver, and finally affect the positioning accuracy. The multipath of the plasma sheath is analyzed by finite-difference time-domain (FDTD) method combined with further signal processing and a simulation platform is established to verify this effects on positioning performance. Simulation results indicate the degradation of positioning performance when these multipath signals were present, causing position error with several meters to tens of meters.

Index Terms: **Plasma sheath, finite-difference time-domain (FDTD) , Multipath, navigation signal.**

1. Introduction

During a hypersonic vehicle's reentry into the Earth's atmosphere, the plasma sheath formed may lead to an interruption of communication, telemetry or satellite navigation, namely "Blackout Phenomenon" [1-2]. A variety of numerical analytical methods have been developed to solve the wave propagation in plasma, among which the finite difference time-domain (FDTD) method has become popular due to its simplicity and wideband capability [3]–[6]. The research in [6] shows that the electromagnetic (EM) wave attenuation by the plasma sheath are severely on the navigation frequency band. In this paper, a further signal processing has been carried out based on the calculation results of FDTD to evaluate the plasma sheath impact on performance of received GNSS signal from different aspects, such as pseudorange error, carrier phase error and positioning accuracy and so on. Besides the attenuation on the signal energy, the multipath effect between the plasma sheath and the vehicle surface will also lead to poor positioning accuracy and lower receiver sensitivity. Simulation results indicate that even if the GNSS signal can pass through the plasma sheath(with attenuation less than 30dB), the multipath effect caused by multi- reflections between the plasma sheath and the vehicle surface will lead position error with several meters to tens of meters, which should be avoided when designing the navigation strategy of vehicle with high speed.

In this paper, The simulation model of plasma sheath is introduced, then the transmission coefficient is investigated using FDTD method, which is used for further signal processing of an antenna array placed on the surface of the aircraft to analyze the multipath effect of the plasma sheath. Finally, the simulation results and the conclusion are given in the end.

2. Simulation Methodology

The electron distribution of the plasma sheath is blunt wedge-shaped shown in Fig.1. Due to the wide, flat top surface of the vehicle, the plasma density doesn't change much along the depth direction. Therefore, a 2D FDTD model assuming homogeneity in the third dimension could be used to simulate the EM wave propagation. The vehicle surface can be considered as perfect electric conductor (PEC) boundary, which also terminates the simulation domain at the bottom. The other three boundaries are covered by the Perfectly Matched Layer (PML) absorbing boundary condition (ABC) [7, 8].

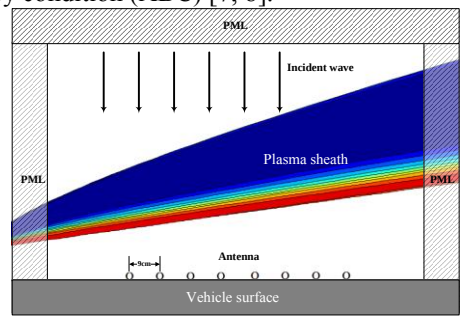

Figure 1: Computation model, color map shows the electron distribution of the plasma sheath

A uniform linear sensor array (ULA) is placed on the surface to detection the power of multipath signals in different incident angle. However, multipath propagation is usually fully correlated of sensor array processing, When all incidence signals are coherent, a preprocessing technique such as the spatial smoothing (SS) can be adapted to

decorrelate of the coherence of signals [9].

2.1. FDTD

The complex permittivity of the plasma sheath generated by the collision of the hypersonic vehicle with the ambient air is frequency dependent and can be represented by

$$\varepsilon(\omega)=\varepsilon_0\left[1+\frac{\omega_p^{\ 2}}{\omega(j\nu-\omega)}\right]=\varepsilon_0\left(1+\chi(\omega)\right) \quad (1)$$

where ε_0 is the vacuum permittivity, ω_p is the plasma frequency, given by

$$\omega_p=\sqrt{\frac{e^2 n_e}{\varepsilon_0 m_e}} \quad (2)$$

where n_e is the electron density, m_e is the electron mass, and e is the electron charge. In (1), ν is the collision frequency, given by

$$\upsilon=3\times10^8\frac{\rho}{\rho_0}\ T \quad \text{Hz} \quad (3)$$

where ρ/ρ_0 is the density ration and T is the temperature in Kelvin [1].

In time domain, the constitutive relation between D and E fields can be written in a convolution form, given by

$$\vec{D}(t)=\varepsilon_\infty\varepsilon_0\vec{E}(t)+\varepsilon_0\int_0^t\vec{E}(t-\tau)\chi(\tau)d\tau \quad (4)$$

Discretized representation of this constitutive relation in the FDTD implementation can be derived by the piecewise linear recursive convolution (*PLRC*) method [8]. Following the same procedure as in [10], the update equation for the electric field is written as

$$\begin{aligned}E_\eta\big|^{n+1}=&\frac{1-\xi^0}{1+\chi^0-\xi^0}E_\eta\big|^n\\&+\frac{\Delta t}{\varepsilon_0\left(1+\chi^0-\xi^0\right)}\left(\nabla\times H\right)_\eta\Big|^{n+1/2}\\&+\frac{1}{1+\chi^0-\xi^0}\psi_\eta\big|^n\end{aligned} \quad (5)$$

here, $\psi_\eta^{\ n}\ (\eta=x,y)$ is an auxiliary variable, given by

$$\psi_\eta^n=\left(\Delta\chi^0-\Delta\xi^0\right)E_\eta^n+\Delta\xi^0E_\eta^{n-1}+\exp(-\nu\Delta t)\psi_\eta^{n-1}$$

In (5)

$$\chi^0=\frac{\omega_p^{\ 2}}{\nu}\Delta t-\frac{\omega_p^{\ 2}}{\nu^2}\left[1-\exp\left(-\nu\Delta t\right)\right]$$

$$\xi^0=\frac{\omega_p^{\ 2}}{2\nu}\Delta t+\frac{\omega_p^{\ 2}}{\nu^3\Delta t}\left[-1+\left(1+\nu\Delta t\right)\exp\left(-\nu\Delta t\right)\right]\exp\left(-\nu\Delta t\right)$$

$$\Delta\chi^0=-\frac{\omega_p^{\ 2}}{\nu^2}\left[1-\exp\left(-\nu\Delta t\right)\right]\left(1-\exp\left(-\nu\Delta t\right)\right)$$

$$\Delta\xi^0=\frac{\omega_p^{\ 2}}{\nu^3\Delta t}\left[-1+\left(1+\nu\Delta t\right)\exp\left(-\nu\Delta t\right)\right]\left(1-\exp\left(-\nu\Delta t\right)\right)$$

The PML ABC is implemented using the stretched-coordinate PML (SC-PML) based on the bilinear transform method, details of which can be found in [8].

2.2. Estimation of Multipath Signals

The coherent of multipath signals may lead to mistakes in the estimation of multipath numbers and power. The decorrelation technique is adapted to recover the rank of the correlation matrix of those multipath signals, and then the power and arriving direction of each multipath signal are estimated. The procedures are listed as follows:

(1) Estimate the correlation matrix $\hat{\mathbf{R}}_{\mathbf{xx}}$ of the received signals by

$$\hat{\mathbf{R}}_{\mathbf{xx}}=\frac{1}{P}\sum_{p=0}^{P-1}\mathbf{X_p}\mathbf{X_p^H} \quad (6)$$

where $\mathbf{X_p}=\left[x_{1p},\ \cdots\ x_{Mp}\right]^T$ is a vector of $(M\times1)$ at the p^{th} snapshot, and M is the element number of the antenna array. The $(\cdot)^H$ and $(\cdot)^T$ superscripts denote the conjugate transpose and transpose operator, respectively.

(2) Find the eigendecomposition of the correlation matrix

$$\hat{\mathbf{R}}_{\mathbf{xx}}=\mathbf{V}\mathbf{\Lambda}\mathbf{V}^H \quad (7)$$

where $\mathbf{\Lambda}=diag\left\{\lambda_1,\cdots,\lambda_M\right\}$, $\lambda_1\geq\cdots\geq\lambda_M=\lambda_{\min}$ are the eigenvalues of the matrix. $\hat{\mathbf{R}}_{\mathbf{xx}}$, $\mathbf{V}=\left[\mathbf{q_1},\cdots,\mathbf{q_M}\right]$ is the matrix composed by the corresponding eigenvectors.

(3) Estimate the number of sources $\hat{K}$ by looking for how many times the smaller eigenvalues $\lambda_{\min}$ is repeated (L)

$$\hat{K}=M-L \quad (8)$$

The eigenvectors corresponding to the L smaller eigenvalues spanned to the noise space:

$$\mathbf{V_n}=\left[\mathbf{q}_{\hat{k}+1},\mathbf{q}_{\hat{k}+2},\ \cdots\ \mathbf{q}_M\right].$$

(4) Plot the space spectrum as a function of θ

$$\hat{P}(\theta)=\frac{\mathbf{a}^H(\theta)\mathbf{a}(\theta)}{\mathbf{a}^H(\theta)\mathbf{V}_n\mathbf{V}_n^H\mathbf{a}(\theta)} \quad (9)$$

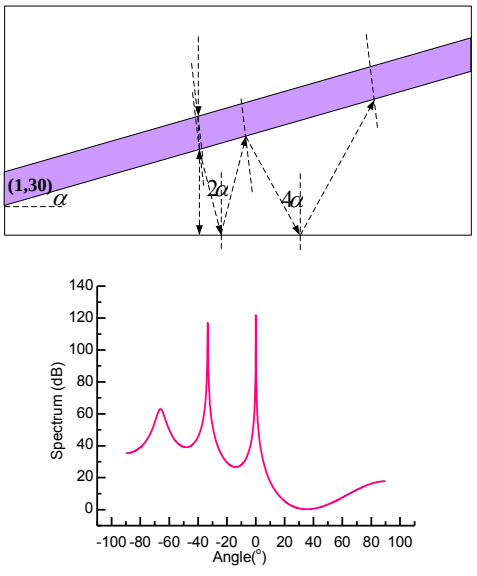

Figure 2: The multipath direction estimation with an incidence angle of 16.7° to the aircraft surface, the result of which is compared with ray-tracing method.

where $\mathbf{a}(\theta)$ is the steering vector of antenna array. the estimated results were compared with ray-tracing method for example in Fig. 2.

3. Discussion

Now we move on to a real plasma sheath model when the hypersonic aircraft are re-entering the earth's atmosphere. Fig. 3 shows the electron and temperature distribution of the hypersonic reentry plasma sheath of cross-sectional plane, which was obtained by hypersonic flow field numerical simulation.

Fig. 4 shows transmission coefficient of eight element uniform linear receiver array. It is clearly seen that the attenuation at GPS carrier frequency (1.575GHz) is about 2~7dB, which is acceptable for all ordinary GPS receiver. Fig. 5 indicates that there are serious multipath signals, which are 5~8dB lower than directive wave, and would lead to the acquisition, tracking and positioning errors of GPS receiver.

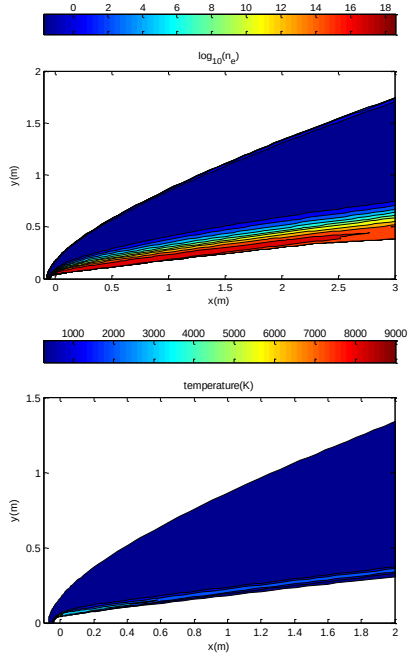

Figure 3: Electron distribution and temperature density distribution of the plasma sheath.

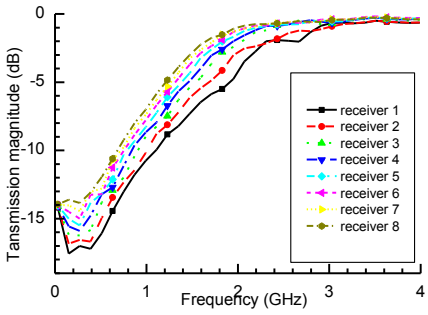

Figure 4: Transmission coefficient of eight element uniform linear receiver array

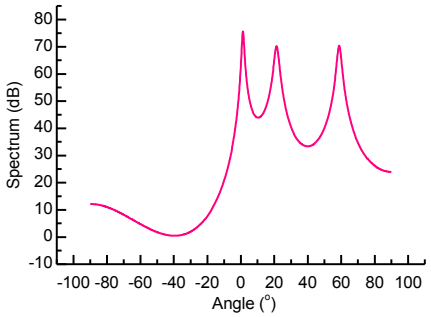

Figure 5: The estimated multipath effect of the plasma sheath.

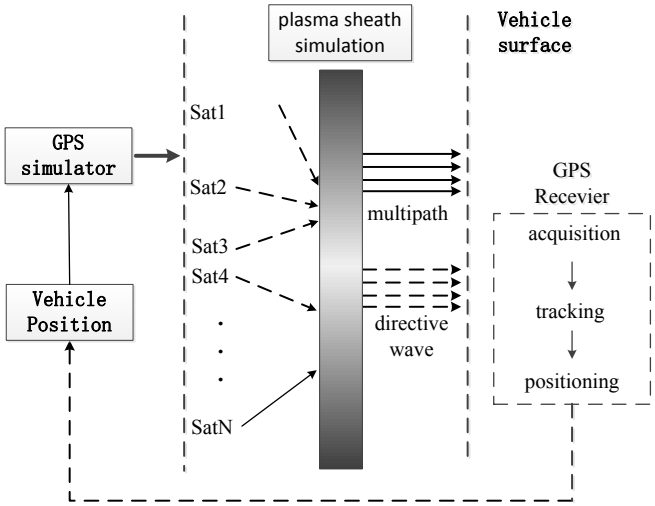

Figure 6: The simulation platform to verify multipath effect of the plasma sheath.

Fig. 6 is a simulation platform consisting of GPS signal simulator and GPS software receiver, which is established to verify this effects on positioning performance. Simulation results indicate the degradation of positioning performance when multipath signals were present, causing position error with several meters to tens of meters, shown in Table 1.

Table 1: Positioning Error Caused by Plasma sheath with multipath effect considered (The positioning error of GPS receiver itself is less than 1m)

Average Ne [/m^3]	Plasma Sheath Thickness[cm]	Average Positioning Error [m]
10^{12}	50	1.574
10^{13}	50	4.850
10^{14}	50	17.564
10^{15}	50	12.553
10^{16}	50	Positioning Failure

4. Conclusions

The multipath effect of the plasma sheath to GNSS has been investigated using a numerical method combined with further signal processing, and a simulation platform is established to verify this effects on positioning performance. Simulation results indicate the degradation of positioning

performance when these multipath signals were present, causing position error with several meters to tens of meters even with little attenuations. This phenomenon should be avoided when designing the navigation strategy of a hypersonic vehicle.

Acknowledgements

This work was supported in part by National Key Laboratory Foundation of China under Grant 9140C530404130C53003 and in part by Outstanding Ph.D. Thesis Research Foundation of Xi'an University of Technology.

References

[1] R. A. Hartunian, G. E. Stewart, S. D. Fergason, T. J. Curtiss, and R. W. Seibold, “Causes and mitigation of radio frequency (RF) blackout during reentry of reusable launch vehicles,” Aerosp. Corp., El Segundo, CA, Contractor Rep. ATR-2007(5309)-1, 2007.

[2] E. D. Gilllman, J. E. Foster, and I. M. Blankson, “Review of leading approaches for mitigating hypersonic vehicle communications blackout and a method of ceramic particulate injection via cathode spot arcs for blackout mitigation,” NASA,Washington, DC, NASA/TM-2010-216220, 2010.

[3] D. K. Kalluri, V. R. Goteti, and A. M. Sessler, “WKB solution for wave propagation in a time-varying magnetoplasma medium: Longitudinal propagation,” IEEE Trans. Plasma Sci., vol. 21, no. 1, pp. 70–76, Feb. 1993.

[4] T. T. Huang, H. L. Joo, D. K. Kalluri, and K. M. Groves, “Wave propagation in a transient plasma—Development of a Green’s function,” IEEE Trans. Plasma Sci., vol. 26, no. 1, pp. 19–25, Feb. 1998.

[5] R. J. Luebbers, F. Hunsberger, and K. S. Kunz, “A frequency-dependent finite-difference time-domain formulation for transient propagation in plasma,” IEEE Trans. Antennas Propag., vol. 39, no. 1, pp. 29–34, Jan. 1991.

[6] J. Liu, X. Xi, G. Wan, and L. Wang, "Simulation of Electromagnetic Wave Propagation Through Plasma Sheath Using the Moving-Window Finite-Difference Time-Domain Method," IEEE Trans. Plasma Sci., vol. 39, no. 3, pp. 852-855, Mar. 2011.

[7] J. P. Berenger, "A perfectly matched layer for the absorption of electromagnetic waves," J. Comput. Phys., vol. 114, no. 2, pp. 185-200, 1994.

[8] X. Xi, R. Luo, J. Liu, J. Zhang, and Y. Liu, "Combined Piecewise Linear Recursive Convolution-Bilinear Transform Implementation of the CFS-PML for Unmagnetized Plasma," IEEE Microw. Wireless Compon. Lett., vol. 21, no. 6, pp. 277-279, Jun. 2011.

[9] S.U. Pillai and B.H. Kwon, “Forward/backward spatial smoothing techniques for coherent signals identification,” IEEE Trans. Acoust., Speech, Signal Process., vol. 37, no. 1, pp. 8-15, 1989.

[10] D. F. Kelley and R. J. Luebbers, "Piecewise linear recursive convolution for dispersive media using FDTD," IEEE Trans. Antennas Propag., vol. 44, no. 6, pp. 792-797, Jun. 1996.

Extrapolation of Wideband Electromagnetic Response from Limited Frequency- and Time-Domain Data

Chu-Ming Gong[1], Wei-Lin Xiong[1]*, Jie-Fang Su[1], He-Nan Li[1] and Ming-Da Zhu[1]

[1]Department of Electronics and Communication Engineering, Donghua University, Shanghai 201620, China
*corresponding author, E-mail: weilin.xiong@outlook.com

Abstract

It has been shown that a wideband electromagnetic response can be extrapolated from limited early-time and low-frequency data by fitting a set of orthogonal functions and its Fourier transform. The extrapolation technique substantially reduces the computational demands. However, since the problem is often ill-conditioned, the solution of the extrapolation is very sensitive to noise in the known part of the electromagnetic response.

In this paper, a novel extrapolation technique which using limited frequency- and time-domain information is presented. The wideband response is expressed as linear combination of associated Laguerre functions. A regularization method along with proper interpolation of the initial data is introduced to solve the ill-conditioned problem, which make the extrapolation technique much less sensitive to noise in the known part of the response. Some numerical results are presented to illustrate the performances of the proposed method in extrapolation of wideband electromagnetic problems.

The Modeling and Simulation of Plasma Sheath effect on GNSS system

Song Zhongguo[1], Xi Xiaoli [1], liu Jiangfan[1], Du Yongxing[2]

[1]Xi'An University of Technology, Xi'An, China
[2]Inner Mongolia University of Science & Technology, Inner Mongolia, China
*corresponding author, E-mail: xixiaoli@xaut.edu.cn

Abstract

Plasma sheath can potentially degrade Global Navigation Satellite System (GNSS) through signal attenuation as well as phase noise when a hypersonic vehicle reenters the Earth's atmosphere. Modeling and simulation method of GNSS system disturbed by plasma sheath is introduced in this paper by means of electromagnetic wave propagation theory combined with the satellite signal simulation technique. The transmission function of the plasma sheath with stratified model are derived utilizing scattering matrix method. The effects of the plasma sheath on GPS signal reception and positioning performance are examined. Experimental results are presented and discussed, partly supporting the validity of the analytical method proposed.

***Index Terms*: *Plasma sheath, Transmission function, GPS, Carrier-to-noise ratio, Positioning accuracy*.**

1. Introduction

When a hypersonic vehicle reenters the Earth's atmosphere, plasma sheath generated by its collision with atmosphere affects the electromagnetic (EM) wave propagation by altering the phase, amplitude, direction, and power spectral density [1,2]. Moreover, there exists serious EM attenuation on the satellite navigation frequency band as noted in [3], therefore, the influence of the plasma sheath to localization system or heading reference units should be assessed through hardware-in-the-loop simulation. A ground system enables the assessment by providing simulated navigation data contaminated by plasma, during which the data required to be obtained nearly real-time.

A variety of analytical methods have been developed to solve the wave propagation in plasma in literature [3–7]. Nevertheless, the massive computational resources required, especially with the non-uniform plasma model, severely limit the practical application in the communication system emulation. The scattering matrix method (SMM) presented in [8] dealing with non-uniform, collisional and magnetized plasma with stratified model, required little computational resources and time consumption. But only vertical incidence on the plasma layer is presented.

In this paper, the transmission function $h(t)$ in plasma environments is derived for GPS signals on the basis of SMM. The influence of the plasma sheath to GPS system has been simulated, which is rarely discussed due to the difficulty to directly introduce those numerical results of plasma effect into navigation signal processing. Some experimental results are presented and partly support the validity of proposed method.

2. The Equivalent Transmission Function of Plasma Sheath

In order to establish the satellite navigation signal model modulated by plasma, the time domain transmission function $h_{rf}(t)$ in the radio frequency (RF) should be extracted first, then the modulated signal $y_{rf}(t)$ can be described as convolution of $h_{rf}(t)$ and incident signal $f_{rf}(t)$:

$$y_r(t) = f_r(t) * h_r(t), \tag{1}$$

2.1. $h_{rf}(t)$ and $h_{if}(t)$

Although $h_{rf}(t)$ can be directly obtained through SMM, due to the RF (Radio frequency) model will significantly increase the amount of calculation, therefore it should be down converted to IF (intermediate frequency) or baseband by:

$$\begin{aligned} y_{rf}(t)\cos(\omega_{LO}t) &= f_{rf}(t) * h_{rf}(t)\cos(\omega_{LO}t) \\ &= f_{rf}(t) * h_{rf}(t)\left(\frac{e^{j\omega_{LO}t} + e^{-j\omega_{LO}t}}{2}\right) \end{aligned} \tag{2}$$

where ω_{LO} is local oscillation frequency. After filtering out high-frequency component, IF signal $y_{if}(t)$ become

$$y_{if}(t) = \frac{1}{2} f_{rf}(t) * h_{rf}(t) e^{-j\omega_{LO}t}, \tag{3}$$

Then define IF transmission function as:

$$h_{if}(t) = h_{rf}(t) \bullet \left(\frac{e^{-jw_{LO}t}}{2}\right), \tag{4}$$

After a bit of algebraic manipulation, the equivalent IF signal modulated by plasma expressed by:

$$y_{if}(t) = 2\left[f_{if}(t) * h_{if}(t) \right], \tag{5}$$

where $f_{if}(t)$ has the same form of $y_{if}(t)$ in (3).

The $h_{rf}(t)$ and $h_{if}(t)$ can be extracted with the processing

flow shown in Fig.1, considering reducing of the Gibbs phenomenon by inserting points at borders of data sets [9].

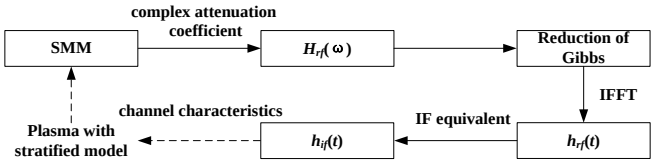

Figure 1: The derivation flow of $h_{rf}(t)$ and $h_{if}(t)$ based on the scattering matrix method.

2.2. SMM

The plasma model analyzed in this paper is steady-state, non-uniform, collisional and non-magnetized, due to the expressions are tediously long for magnetized model with EM waves inclined incidence. The stratified model of which is shown in Fig. 2, where the plasma sheath is divided into *n* layers with different electron density of each layer. The complex dielectric constant and the transmission coefficient in the *m*th layer is expressed as:

$$\varepsilon_r^{(m)} = 1 - \frac{\omega_{p,m}^2}{\omega(\omega - j\nu)}, \tag{6}$$

$$k^{(m)} = \frac{\omega}{c}\sqrt{\varepsilon_r^{(m)}}, \tag{7}$$

where $\omega_{p,m}$ is the plasma frequency of the *m*th layer, ν is the collision frequency, ω is the plane wave frequency, c is the speed of light in free space and $\mu_r = 1$.

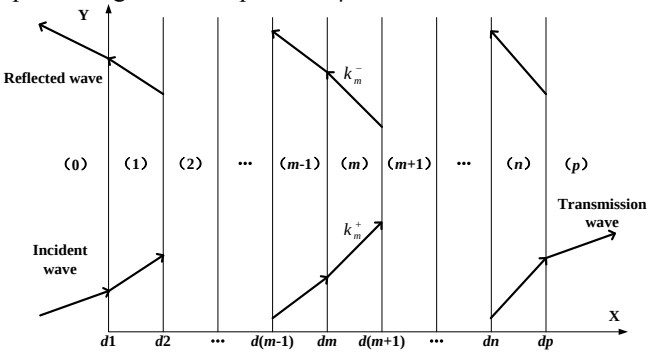

Figure 2: The stratified model of plasma sheath with EM wave inclined incidence.

As for GPS system, the problem can then be described as analyzing the electromagnetic scattering of layered plasma medium with right-hand circularly polarized wave incidence.

Considering the horizontal polarized situation first, we assume the plane wave with electric vector polarized in direction *z*, the incident field in direction k_m^+ and reflective field k_m^- can be written respectively as:

$$\begin{aligned}\vec{E}_m^+ &= B_m Z_m H_0 \left(-\hat{x}\sin\theta_m + \hat{y}\cos\theta_m\right) \\ &\quad \cdot e^{-jk^{(m)}\left(x\cos\theta_m + y\sin\theta_m\right)} \\ \vec{H}_m^+ &= \hat{z} B_m H_0 e^{-jk^{(m)}\left(x\cos\theta_m + y\sin\theta_m\right)}\end{aligned}, \tag{8}$$

$$\begin{aligned}\vec{E}_m^- &= C_m Z_m H_0 \left(-\hat{x}\sin\theta_m - \hat{y}\cos\theta_m\right) \\ &\quad \cdot e^{-jk^{(m)}\left(-x\cos\theta_m + y\sin\theta_m\right)} \\ \vec{H}_m^- &= \hat{z} C_m H_0 e^{-jk^{(m)}\left(-x\cos\theta_m + y\sin\theta_m\right)}\end{aligned}, \tag{9}$$

where θ_m is the angle between the k_m^+ and X-axis, Z_m is the wave impedance of plasma layer, B_m and C_m are the unknown complex scattering coefficients of *m*th layer to be determined.

The total reflection coefficient and transmission coefficient are defined as *A* and *D* respectively. Match tangential field components of both electric field and magnetic field. Firstly, according to the boundary condition in layer zero:

$$\begin{aligned}&Z_0 H_0 \hat{y}\cos\theta_0 - A Z_0 H_0 \hat{y}\cos\theta_0 \\ &= B_1 Z_1 H_0 \hat{y}\cos\theta_1 - C_1 Z_1 H_0 \hat{y}\cos\theta_1\end{aligned}, \tag{10}$$

$$H_0\hat{z} + A H_0 \hat{z} = B_1 H_0 \hat{z} + C_1 H_0 \hat{z}, \tag{11}$$

the following equation is obtained:

$$\begin{pmatrix} B_1 \\ C_1 \end{pmatrix} = S_1 \begin{pmatrix} A \\ 1 \end{pmatrix}, \tag{12}$$

where

$$S_1 = \frac{1}{2k^{(0)}\cos\theta_1}\begin{pmatrix} k^{(0)}\cos\theta_1 - k^{(1)}\cos\theta_0 & k^{(0)}\cos\theta_1 + k^{(1)}\cos\theta_0 \\ k^{(0)}\cos\theta_1 + k^{(1)}\cos\theta_0 & k^{(0)}\cos\theta_1 - k^{(1)}\cos\theta_0 \end{pmatrix} \tag{13}$$

To match boundary condition at the *m*th interface similarly:

$$\begin{pmatrix} B_m \\ C_m \end{pmatrix} = S_m \begin{pmatrix} B_{m-1} \\ C_{m-1} \end{pmatrix}, \tag{14}$$

where S_m is the scattering matrix defined as:

$$\begin{aligned}S_m = &\begin{pmatrix} e^{-jk^{(m)}d_m\cos\theta_m} & e^{jk^{(m)}d_m\cos\theta_m} \\ k^{(m-1)}\cos\theta_m e^{-jk^{(m)}d_m\cos\theta_m} & -k^{(m-1)}\cos\theta_m e^{jk^{(m)}d_m\cos\theta_m} \end{pmatrix}^{-1} \\ &\bullet \begin{pmatrix} e^{-jk^{(m-1)}d_m\cos\theta_{m-1}} & e^{jk^{(m-1)}d_m\cos\theta_{m-1}} \\ k^{(m)}\cos\theta_{m-1} e^{-jk^{(m-1)}d_m\cos\theta_{m-1}} & -k^{(m)}\cos\theta_{m-1} e^{jk^{(m-1)}d_m\cos\theta_{m-1}} \end{pmatrix}\end{aligned} \tag{15}$$

Finally, the boundary condition at *p*th layer results in the following matrix equation:

$$V_p = \frac{1}{2k^{(p)}\cos\theta_n}\begin{pmatrix} \left(k^{(p)}\cos\theta_n + k^{(n)}\cos\theta_p\right)e^{j\left(k^{(n)}\cos\theta_n - k^{(p)}\cos\theta_p\right)d_p} \\ \left(k^{(p)}\cos\theta_n - k^{(n)}\cos\theta_p\right)e^{-j\left(k^{(n)}\cos\theta_n + k^{(p)}\cos\theta_p\right)d_p} \end{pmatrix} \tag{16}$$

Substitute (12) and (14) into (16) to form:

$$S_g = \left(\prod_{m=n}^{2} S_m\right) S_1, \tag{17}$$

the S_g can be writen as S_g=(S_{g1} S_{g2}), where S_{g1} S_{g2} is the first and last column vector of S_g, which can be expressed by

$$\begin{pmatrix} A \\ D \end{pmatrix} = -\left(S_{g1}, -V_p\right)^{-1} \bullet S_{g2}, \tag{18}$$

Similarly, The scattering matrix for vertical polarized situation is represented by (19), (20) and (21), then reflection coefficient and transmission coefficient can also be obtained.

$$S_1 = \frac{1}{2k^{(1)}\cos\theta_1} \cdot \begin{pmatrix} k^{(1)}\cos\theta_1 - k^{(0)}\cos\theta_0 & k^{(1)}\cos\theta_1 + k^{(0)}\cos\theta_0 \\ k^{(1)}\cos\theta_1 + k^{(0)}\cos\theta_0 & k^{(1)}\cos\theta_1 - k^{(0)}\cos\theta_0 \end{pmatrix}, \tag{19}$$

$$S_m = \begin{pmatrix} e^{-jk^{(m)}d_m\cos\theta_m} & e^{jk^{(m)}d_m\cos\theta_m} \\ k^{(m)}\cos\theta_m e^{-jk^{(m)}d_m\cos\theta_m} & -k^{(m)}\cos\theta_m e^{jk^{(m)}d_m\cos\theta_m} \end{pmatrix}^{-1} \cdot \begin{pmatrix} e^{-jk^{(m-1)}d_m\cos\theta_{m-1}} & e^{jk^{(m-1)}d_m\cos\theta_{m-1}} \\ k^{(m-1)}\cos\theta_{m-1}e^{-jk^{(m-1)}d_m\cos\theta_{m-1}} & -k^{(m-1)}\cos\theta_{m-1}e^{jk^{(m-1)}d_m\cos\theta_{m-1}} \end{pmatrix}, \tag{20}$$

$$V_p = \frac{1}{2k^{(n)}\cos\theta_n} \cdot \begin{pmatrix} \left(k^{(n)}\cos\theta_n + k^{(p)}\cos\theta_p\right)e^{j\left(k^{(n)}\cos\theta_n - k^{(p)}\cos\theta_p\right)d_p} \\ \left(k^{(n)}\cos\theta_n - k^{(p)}\cos\theta_p\right)e^{-j\left(k^{(n)}\cos\theta_n + k^{(p)}\cos\theta_p\right)d_p} \end{pmatrix}, \tag{21}$$

Note that the derivation process above is similar with [8], but considering inclined incidence, which is desired in the positioning performance simulation with several GPS satellite signals incoming from various directions.

The influence of plasma electron density and thickness on the transmission characteristics of EM wave are simulated, and the transmission coefficient amplitude, phase and group delay are shown in Fig.3. Similarly, the effects of plasma collision frequency are presented in Fig.4. Those results indicate rather significant impacts to phase and amplitude on satellite navigation frequencies band of about 1~2GHz.

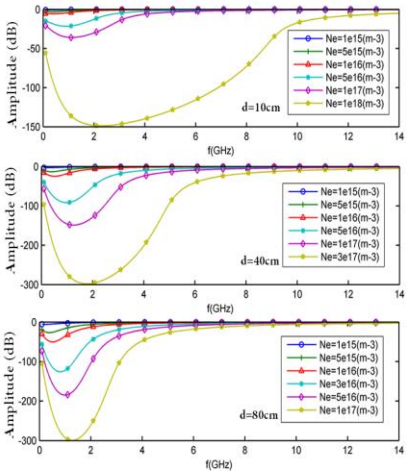

(a)

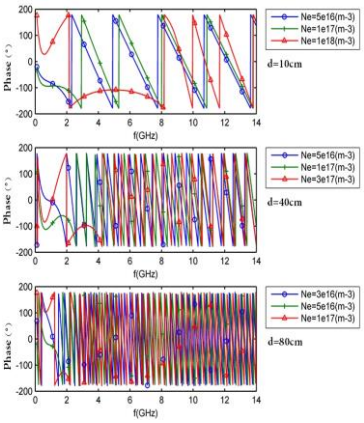

(b)

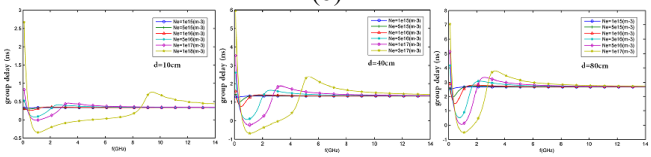

(c)

Figure 3: The transmission coefficient amplitude, phase and group delay with plasma sheath thickness d=10cm, 40cm, 80cm. The electron density of each layer obeys the exponential distribution, and the *Ne* represents the mean electron density.

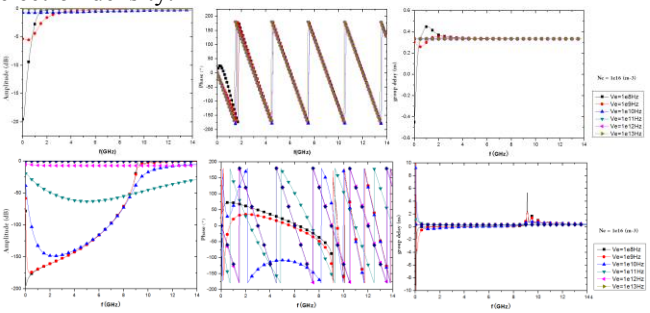

Figure 4: The influence of plasma collision frequency *ve* with plasma electron density $N_e = 10^{16}(\mathrm{m}^{-3})$ and $10^{18}(\mathrm{m}^{-3})$.

Throughout the derivation above, this method involves only the manipulation of 2×2 matrices. Therefore, the required results can be obtained very quickly thus suitable for real-time applications.

3. Simulation Methodology

A simulation platform for GPS system was established to investigate effects of the plasma sheath on signal reception and positioning performance. The platform meanly consists of a GPS simulator, a GPS receiver and the plasma sheath simulation unit shown in Fig.5.

We limit our discussion within the GPS L1 band and C/A code, then the IF signal of the satellite after down-conversion can be expressed by

$$x^i(n) = \sqrt{P_C^i}\left(C^i(n)D^i(n)\right)\sin\left(\omega_{if}n\right), \tag{22}$$

where superscript *i* stand for the index of visible satellites, $P_C{}^i$ is the mean power of the received signal determined by the pseudo-distance, $C^i(n)$ is the C/A code, $D^i(n)$ is the navigation message and ω_{if} is the intermediate frequency.

The received IF satellite signals disturbed by plasma sheath can be expressed as:

$$y_{if}(n) = \sum_{i=1}^{N} x^{i}(n) * h_{if}^{i}(n), \qquad (23)$$

where N is the number of visible satellites. The simulated signal will then processed with GPS IF receiver to resolving the positioning.

In Fig.6, a simulation result of the GPS L1 positioning error is presented and indicates that plasma will degrade the positioning accuracy, particularly increasing the standard deviation. Table 1 shows the carrier-to-noise ratio (CNR) of each visible satellite, the satellite PRN8 and PRN10 disappeared due to the low incidence angle relative to the top surface of the plasma sheath.

The mean positioning error and standard deviation are simulated with Monte Carlo method, and the results are presented in Table 2 and Table 3.

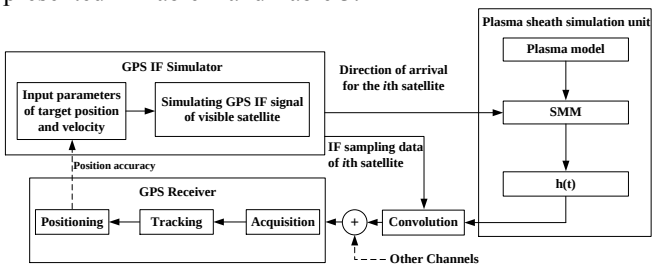

Figure 5: The simulation flow chart.

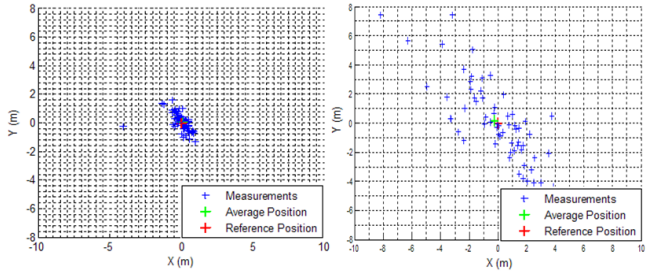

(a) (b)

Figure 6: A case of the positioning error caused by plasma sheath: (a) without plasma; (b) plasma with Ne=10^{16}m^{-3}, ve=10^{8}Hz and d=10cm.

Table 1: The carrier-to-noise ratio of each visible satellite.

CNR (dBHz)	PRN2	PRN5	PRN8	PRN10	PRN26	PRN29
Without plasma	44.1	44.4	42.7	42.8	44.6	44.2
10^{15}m^{-3}(40cm)	43.1	43.5	--	--	43.8	43.2
10^{15}m^{-3}(80cm)	42	42.6	--	--	43	42.2
10^{16}m^{-3}(10cm)	40.6	41.7	--	--	42.3	41.1

Table 2: The positioning error caused by plasma with different electron density and thickness.

	Max Error	Mean Error	Std Error
Without plasma	2.20 m	0.02 m	0.84 m
10^{15}m^{-3}(40cm)	7.41 m	0.41 m	2.10 m
10^{15}m^{-3}(80cm)	7.80 m	0.10 m	2.54 m
10^{16}m^{-3}(10cm)	10.85 m	0.69 m	3.20 m

Table 3: The positioning error caused by plasma with different plasma collision frequency.

Ne=10^{15}m^{-3},d=10cm	Max Error	Mean Error	Std Error
ve=10^{7}Hz,	15.8 m	10.1 m	3.00 m
ve=10^{8}Hz	4.44 m	2.02 m	1.02 m
ve=10^{9}Hz	2.39 m	0.26 m	0.88 m
ve=10^{10}Hz	2.40 m	0.20 m	0.88 m
ve=10^{11}Hz	2.49 m	0.22 m	0.83 m
ve=10^{12}Hz	2.21 m	0.03 m	0.85 m

4. Experiment

Experiments have been carried out to assess the proposed analytical technique with the experimental setup shown in Fig.7. The transmitting antenna connected to a RF GPS simulator and the receive antenna connected to a RF GPS

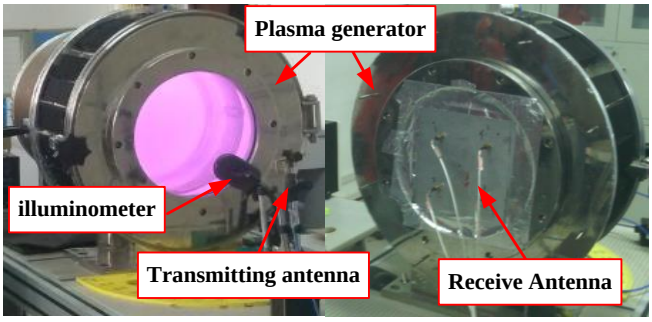

Figure 7: Experimental setup of the plasma impact on GPS system, which mainly consists of a plasma generator, a GPS simulator and a GPS receiver. The illuminometer is used to calibrate the readout of the plasma generator.

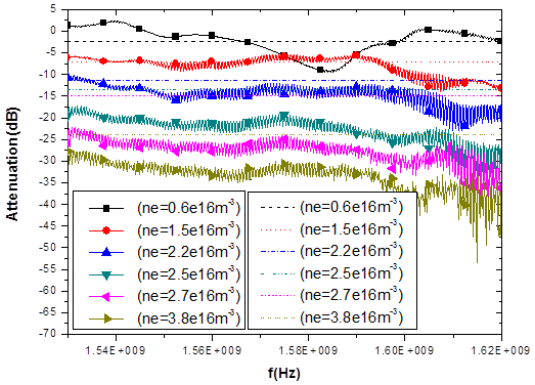

Figure 8: The attenuation of experiment compared with the theoretical simulated result.

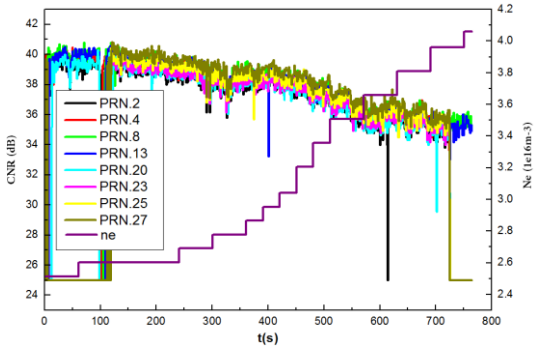

Figure 9: The carrier-to-noise ratio of a set of experiment data.

receiver. Due to the uncertainty performance of RF front-end, the experiment is only a qualitative test. The experimental results are presented in Fig.8, which correlate well with simulation data. In Fig.9, the CNR of experiment is presented with an average value of around 40dBHz which consistent with the simulation value, and partly support the validity of proposed the method.

5. Conclusions

This paper provides a modeling and simulation method of GNSS system disturbed by plasma sheath. The effects of the plasma sheath on GPS signal reception and positioning performance are investigated. Simulated and experimental results are presented and discussed, partly supporting the validity of the analytical method proposed.

The plasma sheath discussed in this paper is cold plasma and the analytical method remain based on a static model.

Acknowledgements

This work was supported in part by the Ph.D. research startup foundation of Xi'an University of Technology under Grant 105-211411

References

[1] S. G. Ohler, B. E. Gilchrist, and A. D. Gallimore, "Electromagnetic signal modification in a localized high-speed plasma thruster," IEEE Transactions on Plasma Science, vol.27, pp.587-594, 1999.

[2] T. C. Lin and L. K. Sproul, "Influence of re-entry turbulent plasma fluctuation on EM wave propagation," Computers & Fluids.vol.35, pp.703-711, 2006.

[3] J. Liu, X. Xi, G. Wan, and L. Wang, "Simulation of Electromagnetic Wave Propagation Through Plasma Sheath Using the Moving-Window Finite-Difference Time-Domain Method, " IEEE Transactions on Plasma Science, vol. 39, no. 3, pp. 852-855, Mar. 2011.

[4] M. Laroussi, J. R. Roth, et al. "Numerical Calculation of the Reflection, Absorption, and Transmission of Microwaves by a Nonuniform Plasma Slab, ". IEEE T Plasma Sci., 21(4), 366-372 (1993).

[5] A, Rokhlenko, "The reflection of electromagnetic waves by a conducting surface shielded with a plasma layer," IEEE Transactions on Plasma Science, vol.24, no.1, pp.182-186, Feb. 1996.

[6] D. L. Tang, A. P. Sun, X. M. Qiu, P. K. Chu, "Interaction of electromagnetic waves with a magnetized nonuniform plasma slab," IEEE Transactions on Plasma Science, vol.31, no.3, pp.405-410, June. 2003.

[7] B. Jazi, Z. Rahmani, B. Shokri, "Reflection and Absorption of Electromagnetic Wave Propagation in an Inhomogeneous Dissipative Magnetized Plasma Slab," IEEE Transactions on Plasma Science, vol.41, no.2, pp.290-295, Feb. 2013.

[8] B. J. Hu, G. Wei, and S. L. Lai, "SMM Analysis of Reflection, Absorption, and Transmission from Nonuniform Magnetized Plasma Slab," IEEE Transactions on Plasma Science, vol. 27, no. 4, 1131-1136, 1999.

[9] F. De Ridder, R. Pintelon, J. Schoukens, and A. Verheyden, "Reduction of the Gibbs phenomenon applied on non-harmonic time base distortions," IEEE Transactions on Instrumentation and Measurement. vol. 54, pp 1118-1125, 2005.

A Polynomial Interpolation Method of MoM Matrices for Analyzing Multilayer Structure in Frequency Sweeps

Zhen-Lei Wang, Wei-Dong Li, Zhe Song, Zhang-Cheng Hao

***Abstract* — A polynomial interpolation method is presented for accelerating impedance MoM matrix filling in frequency sweeping from multilayer microstrip structure. In this method, frequency samples are expressed into analytical forms in terms of roots of Chebyshev polynomial, for enhancing the interpolation accuracy. The interpolated matrix element is a product of the normalized frequency and the remaining part after factoring out the dominant phase term from the original matrix element so that its frequency behavior can be captured by polynomials. Numerical examples show that the method is capable of fast generating the MoM matrices and accurate solutions over frequency band.**

Index Terms—**Impedance matrix, multilayer Green function, dominant phase term, frequency sample optimization**

I. INTRODUCTION

THEmethod of moments (MoM) has been proven to be an effective numerical method for analyzing electromagnetic (EM) radiation and scattering problems. In the MoM, the time and memory costs of the impedance matrix filling are essentially proportional to its dimension, respectively. For the frequency responses over a frequency band, the matrix needs to be recomputed at each point of frequency, which requires $O(N^2)$ memory and Quantity time, where *N* is the number of unknowns. In such case, CPU time for calculating the impedance matrix dominates the overall solution time. Some fast algorithms for calculating MoM matrix have been developed to reduce the CPU time, such as polynomial interpolation scheme with frequency samples [1-5]. The performance of the polynomial interpolation methods applied to planar microstrip structures needs to be further investigated.

In this conference paper, a Chebyshev polynomials interpolation scheme [1] is investigated for fast generating the impedance matrix over a frequency band arising from multilayer microstrip structure. Besides the phase term, the matrix element from such structure consists of the linear and inverse terms of frequency. In this method, after the dominant phase term is extracted [2-5] and the frequency scale is multiplied, the frequency behavior of the modified matrix element can be captured by polynomial interpolation method.

This work was supported by the NNISRP 201110046 and the DPHEC 20120092110012.

The authors are with the State Key Laboratory of Millimeter Waves, School of Information Science and Engineering, Southeast University, Nanjing, 210096, P. R. China.

Especially, the frequency samples optimized will make matrix error norm stay at the low level. For reducing the computation of matrix at the frequency samples, a triangle-triangle approach is employed preferably to the traditional RWG-RWG approach [6]. Both approaches yield the same accurate impedance matrix.

II. GREEN'S FUNCTION OF MULTILAYER STRUCTURE

The critical factor for the efficient and accurate MoM analysis is the evaluation of multilayer medium's Green's function, which are expressed in terms of the Sommerfeld integrals (SIs) [7]. Because SIs are time-consuming to evaluate, the discrete complex image method (DCIM) was developed to compute the complete set of integral equation kernels for planar multilayers Spectral domain Green's function can be written into a simple form as

$$\tilde{G} = A\frac{F}{2jk_{zm}} \tag{1}$$

where A is dependent on dielectric and the primary field term is extracted from F .

The spatial form of the Green's function [8, 9] consist of quasi-static term, surface wave term, and discrete complex image term [10, 11]. Its tangential component can be written in concise form

$$\begin{cases} \mathrm{G}_{xx}^{A}(\rho) = \dfrac{A}{4\pi}\left(F_{st}\cdot\dfrac{e^{-jk_0\rho}}{\rho} - 2\pi j\sum_i \mathrm{Re}\,s_i H_0^{(2)}(\mathrm{k}_{\rho i}\rho)\mathrm{k}_{\rho i} + \sum_{i=1}^{N_c} a_i\dfrac{e^{-jk_0 r_i}}{r_i}\right) \\ r_i^2 = \rho^2 + b_i^2 \end{cases} \tag{7}$$

where $\mathrm{G}_{xx}^{A}(\rho)$ is the vector potential for single dielectric and $\mathrm{Re}\,s_i$ is the residue for the pole k_{ri} , $H_0^{(2)}$ denotes the zeroth-order Hankel function of the second kind and the N_c is the number of complex image. The notations a_i and b_i are the magnitude and phase of the *ith* complex image, respectively, which are solved by the GPOF method [12]. The scalar potential $G_\phi(\rho)$ has the similar expression. The mixed potentials of Green's function is linear combination of the dyadic vector from $\bar{\bar{\mathrm{G}}}^{A}(\rho)$ and $G_\phi(\rho)$. By applying the Galerkin's procedure, the matrix element at each frequency within the frequency band $[f_l, f_h]$ can be obtained as

$$Z_{mn} = j\eta_0\left(k_0\int_{T_m}\int_{T_n}\vec{f}_m(\vec{r})\cdot\bar{\bar{G}}^A(\vec{r}\,|\,\vec{r}')\cdot\vec{f}_n(\vec{r}')ds'ds + \frac{1}{k_0}\int_{T_m}\vec{f}_m(\vec{r})\cdot\nabla_s\int_{T_n}G^{\phi}(\vec{r}\,|\,\vec{r}')\nabla'_s\cdot\vec{f}_n(\vec{r}')ds'ds\right) \quad (8)$$

A. Polynomial interpolation scheme

The impedance matrix element is not very sensitive to frequency and it can be explicitly expressed as a function of frequency. Hence, some polynomial interpolation algorithms can be used to reduce the CPU time for calculating the matrix in frequency sweeping case.

A modified version of matrix element employed here is

$$\tilde{Z}_{mn} = Z_{mn} f_r e^{j2\pi f_r \rho_{mn}} \quad (9)$$

where $f_r = f / f_h$ is the normalized frequency varies from f_l / f_h to 1, and ρ_{mn} is the distance between the RWG elements of source and field point. Seen from (8), Z_{mn} contains the linear and inverse terms of f_r , and is not suited for polynomial interpolation. Seen from (9), the factor $\frac{1}{f_r}$ in scalar potential can be counteracted. Hence, $\tilde{Z}_{mn}$ may be more suitable for the polynomial interpolation than Z_{mn}.

The polynomial interpolation formula for each f_r in $[f_l / f_r, 1]$ is expressed as

$$\tilde{Z}_{mn}(f_r) = \sum_{i=0}^{3}\tilde{Z}_{mn}(x_i)\gamma_i(f_r) \quad (10)$$

where

$$\gamma_i(f_r) = \prod_{j=0, j\neq i}^{j=3}\left(\frac{f_r - x_j}{x_i - x_j}\right) \quad (11)$$

B. Triangle-triangle approach to impedance matrix

An efficient triangle-triangle approach for calculating impedance matrix is used here, which reduces the time cost of calculating matrix to 1/9 from point view of theoretic analysis. The triangle-triangle interaction in the vector potential of (8) can be transformed as

$$\begin{aligned}&\int_{T_m}ds\int_{T_n}ds'(r-r_p)\cdot(r'-r'_q)G^A_{xx}(\rho)\\ &=\int_{T_m}ds\int_{T_n}ds'(r-r_o)\cdot(r'-r'_o)G^A_{xx}(\rho)\\ &+(r_o-r_p)\int_{T_m}ds\int_{T_n}ds'(r'-r'_o)G^A_{xx}(\rho)\\ &+(r'_o-r'_q)\int_{T_m}ds\int_{T_n}ds'(r-r_o)G^A_{xx}(\rho)\\ &+(r_o-r_p)\cdot(r'_o-r'_q)\int_{T_m}ds\int_{T_n}ds'G^A_{xx}(\rho)\end{aligned} \quad (13)$$

where r_o is the barycentric point of the triangle.

In this triangle-triangle approach, the integrals in (13) can be used without repeat computation when *p* and *q* change from 1 to 3, respectively. It is readily seen that the approach reduces the computation complexity to about 1/9 of that of the RWG-RWG approach.

III. Examples and Discussion

In this section, the method is validated in comparison with the direct MoM. All simulations are performed on a Xeon PC with 2.5GHz processor and 24 GB RAM.

A circular patch antenna on a dielectric substrate is investigated as shown in Fig.1, the substrate thickness is 1.5748 mm and the relative permittivity ε_r is 2.2. The number of unknowns for this problem is 1798 when it is modeled by the RWG basic functions. The antenna has its first resonant frequency at 10 GHz, and the interpolation scheme is implemented from 6 to 11 GHz with 4 samples in each frequency sub-band of 2.5 GHz. The frequency step size of $\Delta f = 0.1$GHz is used. In Fig.2-4, the results show agreement compared to the direct computation.

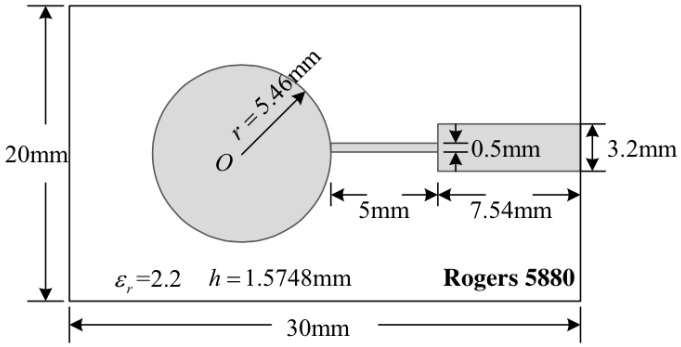

Fig. 1. Size of the circular patch antenna, h=1.5748 mm.

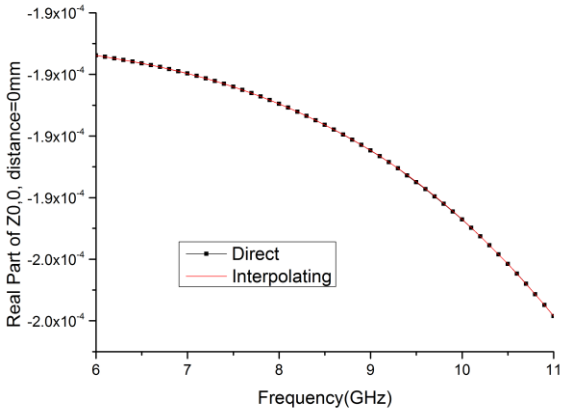

(a)

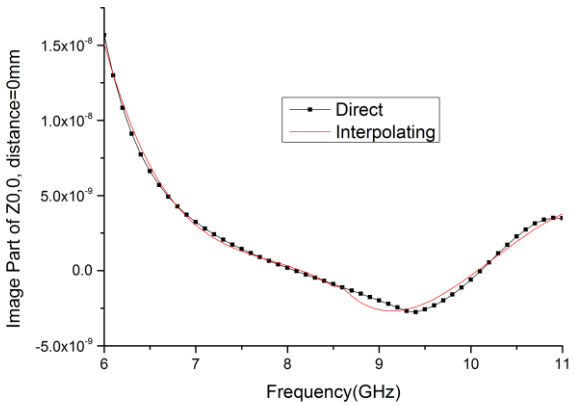

(b)

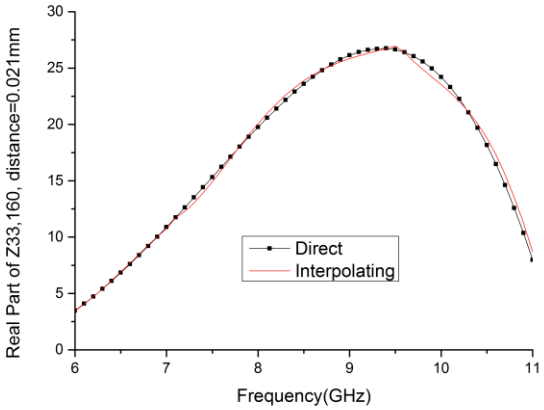

(a)

Fig.2. Impedance matrix element $Z_{0\&0}$, distance=0mm. (a) Real Part. (b) Image Part.

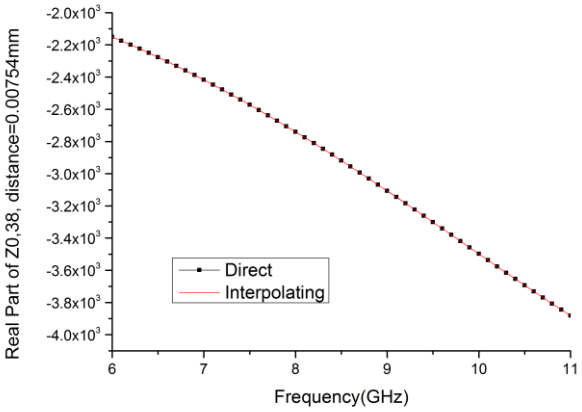

(a)

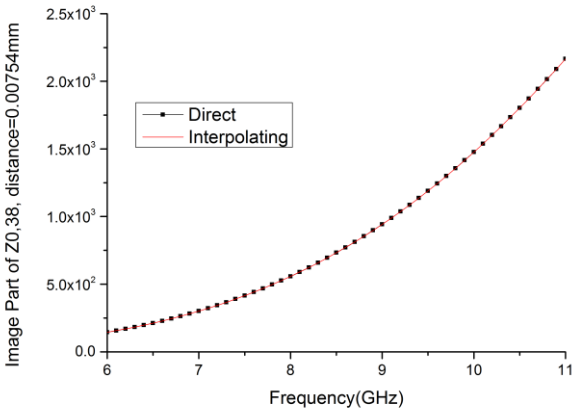

(b)

Fig.3. Impedance matrix element $Z_{0\&38}$, distance=0.00754mm. (a) Real Part. (b) Image Part.

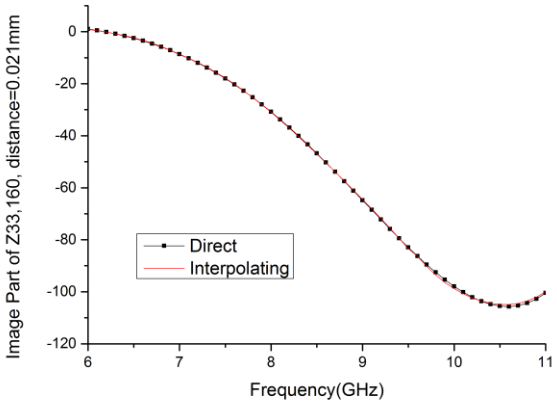

(b)

Fig.4. Impedance matrix element $Z_{33\&160}$, distance=0.021mm. (a) Real Part. (b) Image Part.

For the near region, where the distance between the basic and testing functions is relatively small. The interpolation of real part of the impedance matrix element is effective but the imaginary part has some deviation from 9 to 10 GHz because the order of magnitude is much small (below 10^{-8}). Next, in the intermediate region, we observe the matrix elements all have large order of magnitude (the majority are larger than 10^{3}) so that the effect of interpolation is ideal. The surface wave term become a growing part of the Green's function when on the far region and the element also at low level (around 10), which lead to the interpolation of matrix element have a little offset but still can keep up with the changes of frequency.

IV. Conclusion

In this conference paper, we have presented an improved interpolation technique for impedance matrix over frequency band arising from planar multilayer structure. MoM matrices associated with extraction of remaining phase term and frequency samples optimization, and have presented an efficient triangle-triangle approach for the filling of impedance matrix.

ACKNOWLEDGMENT

The authors would like to thank Dr. Chun Cai at Shenzhen Academy of Metrology and Quality Inspection for his help, which lead to a great improvement on this paper.

REFERENCES

[1] W.-D. Li, H.-X. Zhou, J. Hu, Z. Song, and W. Hong, "Accuracy Improvement of Cubic Polynomial Inter/Extrapolation of MoM Matrices by Optimizing Frequency Samples," *IEEE Antennas & Wireless propagation letters*, Vol.10, pp. 888-891, 2011.

[2] E.H.Newman,"Generation of wide-band data from the method of moments by interpolating the impedance matrix,"*IEEE Trans.Antennas Propagat*., vol.36, no.12, pp.1820-1824, Dec.1988.

[3] J.Yeo and R. Mittra, "An algorithm for interpolating the frequency variations of method-of-moments matrices arising in the analysis of planar microstrip structures," *IEEE Trans.Microw.Theory Tech*., vol.51, no.3, pp.1018-1025, Mar.2003.

[4] A.S.Barlevy and Y.Rahmat-Samii, "Characterization of electromagnetic band-gaps composed of multiple periodic tripods with interconnecting vias: Concept, analysis, and design, *IEEE Trans Antennas Propagat"* vol.49, no.3, pp.343-353, Mar.2001.

[5] W.-D. Li, H.-X. Zhou, W. Hong, and T. Weiland, "An accurate interpolation scheme with derivative term for generating MoM matrices in frequency sweeps," *IEEE Trans. Antennas Propag*., vol. 57, no. 8, pp. 2376-2385, Aug. 2009.

[6] Y. Zhang, M. Taylor, and T. K. Sarkai, "Parallel in-core and out-of-core solution of electrically large problems using the RWG basis functions," *IEEE Antennas Propagt, Mag*., vol. 50, no. 5, pp.84-94, Oct. 2008.

[7] F. Ling, J.-M.Jin, "Discrete Complex Image Method for Green's Functions of General Multilayer Media," *IEEE Microwave and Guided Wave Letters*, vol. 10, no. 10, OCT. 2000.

[8] Z. Song, H.–X. Zhou, J. Hu, W.–D. Li, W. Hong, "Accurate location of all surface wave modes for Green's functions of a layered medium by consecutive perturbations," Science China Information Sciences. 2010, 53:2363-2376.

[9] Z. Song, H.–X. Zhou, J. Hu, W. Hong, "Accurate evaluation of Green's functions in a layered medium by SDP-FLAM," Science in China Series F: Information Sciences. 2009, 52: 867-875. Information Sciences. 2010, 53:2363-2376.

[10] F.Ling "Fast electromagnetic modeling of multilayer microstrip antennas and circuits [D]" [PH. D. Dissertation]. University of Illinois at Urbana-Champaign: Department of Electrical and Computer Engineering.

[11] D. G.Fang. Antenna Theory and Microstrip Antennas [M]. UK: Taylor and Francis; 2009.

[12] Y.Hua, T.K..Sarkar, Generalized pencil-of-function method for extracting poles of an EM system from its transient response [J]. *IEEE Trans. Antennas Propag*. 1989; 37(2):229-234.

Accurate Prediction of Shielding Effectiveness of Coated Cabin Using Conformal FDTD Method

Jian Wang[1,*] and Wen-Yan Yin[2]

[1]School of Information Science and Engineering, Ningbo University, Ningbo, 315211, China
[2] Center for Optical and EM Research, State Key Lab of MOI, Department of Optical Engineering, Zhe Jiang University, Hangzhou, 310058, China
*corresponding author, E-mail: wangjian1@nbu.edu.cn

Abstract

A modified fourth-order finite-difference time-domain (FDTD (2, 4)) conformal technique is proposed for characterizing shielding effectiveness of an arbitrary three-dimensional coated cabin. This conformal scheme has higher accuracy than that of the conventional FDTD and FDTD (2, 4) methods, in which coarse meshes are normally used and staircase errors will be introduced in modeling curved PEC objects. In our numerical treatment, only two integration loops of Faraday's law are used for updating magnetic field components, while the updating equations of electric field components are not changed as in normal FDTD method. It is numerically demonstrated that high accuracy and low dispersion errors can be achieved in computing shielding effectiveness of some typical cabin structures.

1. Introduction

It is known that deckhouses are typical structures on ship platform, and their shielding performance is usually described in term of shielding effectiveness (SE) [1-2]. As we know, the finite-difference time-domain (FDTD) method is very efficient for investigating the interaction of an electromagnetic pulse with various conductive composites. Unfortunately, in practical applications, coatings, slots, and even a panel window must be introduced in these deckhouses which will lead to much more confusion in implementing FDTD method, especially in modeling some curved structures due to the consideration of staircase problems. We know that several efficient interface treatment techniques have been implemented to model these structures so as to reduce staircase error and computer recourses in the past few years [3-6]. However, most of previous techniques are still based on the conventional FDTD method, which are limited in solving electrically large problems [7-8]. In this paper, a new interface treatment technique is proposed to reduce staircase error and computer recourses based on the FDTD (2, 4) scheme, which includes an effective parameter technique for coating medium and a stable high-order conformal technique for PEC objects. The first one adopts an average dielectric constant derived by the linear averages of different dielectric regions in one spatial discrete cell. Then, such a new dielectric constant is introduced to further modify the electric updating equations. The PEC conformal technique proposed in this paper, different from the traditional one [10], needs the Faraday's law of two integral loops to modify the updating equations of the magnetic fields. The hybrid method considers both the dielectric and PEC boundary information so that it is suitable to solve the electromagnetic analysis of coating objects.

The paper is organized as follows. Section 2 describes the procedure for constructing the hybrid conformal technique based on the FDTD (2, 4) method. Next, some typical numerical examples are presented in Section 3 to demonstrate both the efficiency and the versatility of the proposed technique when applied to electrically large and complex objects. Finally, some conclusions and observations are included in Section 4.

2. Interface Treatment Technique in FDTD (2, 4)

In the proposed method, we combine the PEC and the dielectric conformal techniques and both ones are extended to high-order form so as to match the FDTD (2, 4) updating equations.

2.1. Dielectric Interface Treatment Technique for Coating Objects

The conformal meshes on the interface of the PEC backing material, coating medium and free space are shown in Fig. 1(a). In [3], some effective parameters are introduced to modify the electric field update equations. We now extend this idea to FDTD (2, 4) method so as to decrease the dispersive error. Based on the scheme in [4], a linear average technique, as shown in Fig. 1(b), is given by

$$e_x^{eff}(i+1/2, j, k) = e_1, \tag{1}$$

$$e_x^{eff}(i+1/2, j+1, k) = e_0, \tag{2}$$

$$e_y^{eff}(i, j+1/2, k) = (y_1 e_1 + y_2 e_0)/\mathrm{D}y, \tag{3}$$

$$e_y^{eff}(i+1, j+1/2, k) = (y_3 e_1 + y_4 e_0)/(y_3 + y_4), \tag{4}$$

where Δx and Δy are the step sizes along the x- and y-directions, respectively. ε_1 is the relative permittivity of the coating material. The conductivity can be similarly treated

on the conformal meshes. Then, these effective parameters are used to modify the *E*-field update equations of FDTD (2, 4) method in [10].

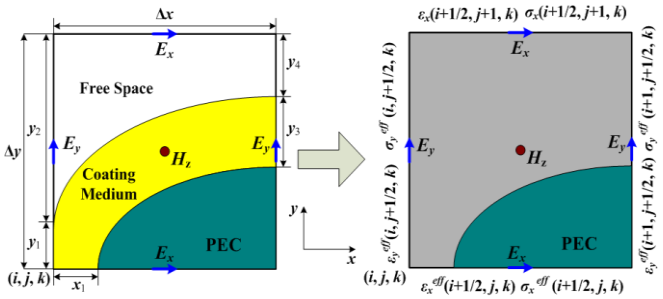

(a) (b)

Figiure 1: The proposed dielectric interface treatment technique. (a) The distorted meshes on the interface; (b). The modified meshes on the interface.

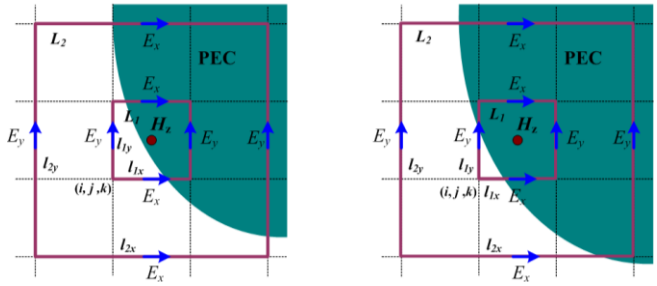

(a) (b)

Figure 2: The proposed high-order conformal technique. (a) Stable conformal meshes; (b) Unstable conformal meshes.

2.2. High-Order Conformal Technique for PEC Objects

As the conformal scheme shown in [4], in our high-order conformal technique, the *E*-field is updated in the same way as in the conventional FDTD (2, 4) method and the *H*-field update equations are modified by Faraday's Law as follows

$$\frac{1}{m}\frac{\partial}{\partial t}\iint_S \mathbf{H}\cdot d\mathbf{s} = -\oint_L \mathbf{E}\cdot d\mathbf{l} \tag{5}$$

where *S* and *L* denote, respectively, the area and the boundary of each distorted cell in two integration loops as shown in Fig. 2(a). The integral path of the *E*-field is detoured along the distorted loop.

Then, the update equation of the magnetic field component H_z is obtained by

$$H_z\big|_{i,j,k}^{n+1/2} = H_z\big|_{i,j,k}^{n-1/2} + \frac{\Delta t}{m}\sum_{v=1}^{2}\frac{a_v}{S_z^{(v)}(i,j,k)}\left\{E_x\big|_{i+1/2,j+v,k}^{n}\cdot l_{vx}\big|_{i,j+1,k} - E_x\big|_{i+1/2,j-v+1,k}^{n}\cdot l_{vx}\big|_{i,j,k} - E_y\big|_{i+v,j+1/2,k}^{n}\cdot l_{vy}\big|_{i+1,j,k} + E_y\big|_{i-v+1,j+1/2,k}^{n}\cdot l_{vy}\big|_{i,j,k}\right\}, \tag{6}$$

where $\alpha_1 = 9/8$ and $\alpha_2 = -1/8$. As we know, if the area of irregular mesh is very small, as shown in Fig. 2(b), this mesh is unstable. Thus, in order to obtain stability and accurate numerical results, we set

$$S_v^{(1)}(i,j,k) = \begin{cases} S_v^{(1)}(i,j,k), & S_v^{(1)}(i,j,k) \ge S_{1v}^{eff}(i,j,k); \\ S_{1v}^{eff}(i,j,k), & \xi\Delta S \le S_v^{(1)}(i,j,k) \le S_{1v}^{eff}(i,j,k); \\ 0, & S^{(1)}(i,j,k) \le \xi\Delta S. \end{cases} \tag{7}$$

where $v=x$, y and z , and $S^{(1)}(i, j, k)$ and ΔS are the areas of the inner irregular and regular cells, respectively. Here, ξ is chosen to be 0.05 and the stable area S^{eff} is given by

$$S_{1x}^{eff} = \max\left(l_{1y}\big|_{i,j,k}\cdot\Delta z,\ l_{1y}\big|_{i,j,k+1}\cdot\Delta z,\ l_{1z}\big|_{i,j,k}\cdot\Delta y,\ l_{1y}\big|_{i,j+1,k}\cdot\Delta y\right) \tag{8}$$

$$S_{1y}^{eff} = \max\left(l_{1x}\big|_{i,j,k}\cdot\Delta z,\ l_{1x}\big|_{i,j,k+1}\cdot\Delta z,\ l_{1z}\big|_{i,j,k}\cdot\Delta x,\ l_{1z}\big|_{i+1,j,k}\cdot\Delta x\right) \tag{9}$$

$$S_{1z}^{eff} = \max\left(l_{1x}\big|_{i,j,k}\cdot\Delta y,\ l_{1x}\big|_{i,j+1,k}\cdot\Delta y,\ l_{1y}\big|_{i,j,k}\cdot\Delta x,\ l_{1y}\big|_{i+1,j,k}\cdot\Delta x\right) \tag{10}$$

.

It is noted that the updating equations of electric field need no modification on the regular or irregular cells except for the dielectric constant shown in Figs. 1(a) and (b).

3. Numerical Results and Discussion

To verify the accuracy and efficiency of our proposed technique, a coating deckhouse on the ship platform is considered. The structure walls are modeled with the thickness of 4 cm. The geometry of this model is shown in Fig. 3 and the ground plane is set to be PEC and the radius of the cylinder structure is 2 m. The thickness of coating material is 2 mm. This coating is assumed to be nonmagnetic and characterized by a relative permittivity ε_r=4 and conductivity σ=30 S/m. In our computation, the CFL number of our scheme is 0.4 and the cell size is 2 cm.

Fig. 4(a) shows the SE results in the center of the deckhouse with and without coatings. The incident wave is propagating along the *y*-direction. It can be found that our method agrees well with the CST results and SE of the structure with coatings is 5dB lower than the case without coatings.

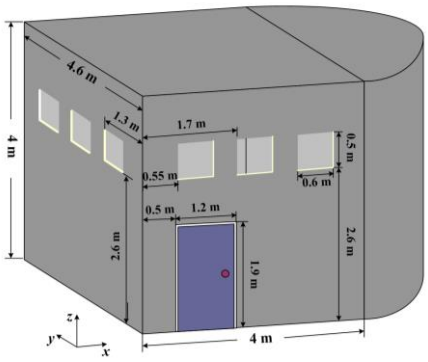

Figure 3: Geometry of a deckhouse shielding model on a ship.

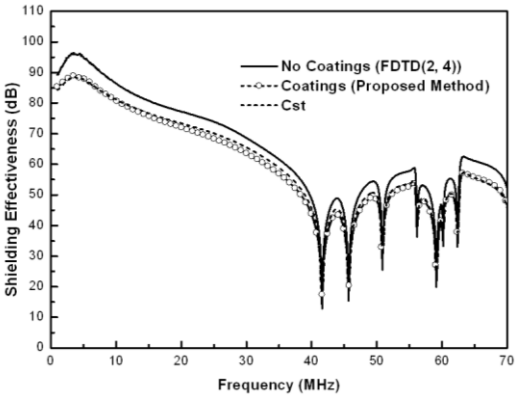

(a)

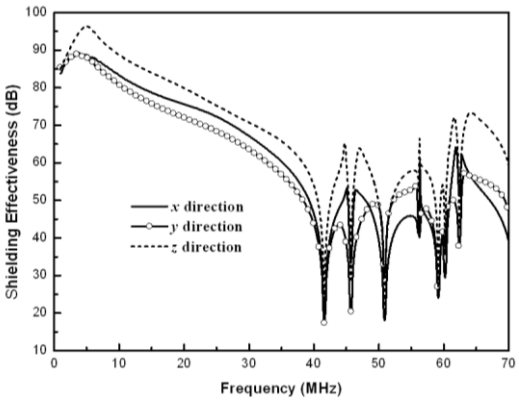

(b)

Figure 4: (a) The SE results in the center of the structure and (b) The SE results of illuminated by the incident wave propagating along with different directions.

Fig. 4(b) shows the SE of the structure illuminated by the incident wave propagating along with different directions. It can be seen that the shielding effectiveness results obtained by the incident wave propagating along with the *y*-directions are lower than that obtained by the others. Physically, much more energy can couple into the enclosure when the incident wave propagates along with the *y*-direction.

4. Conclusions

In this paper, a new interface treatment technique is proposed to predict the shielding effectiveness of coating structures in ship platform, in which we introduce some effective dielectric parameters obtained by using linear average concept to modify the update equations of electric fields. In addition, a high-order conformal technique using Faraday's Law in two integral loops to modify the H field update equations. We observe that the proposed method has low numerical dispersion error, and can achieve high accuracy even using large space cells.

Acknowledgements

This work is supported by the National Natural Science Foundation under Grant 61301049 of China. The authors also appreciate the financial supports by the Natural Science Foundation of Ningbo City under Grant 2013A610119 and the foundation from the Zhejiang education department under Grant Y201327381.

References

[1] V. Rajamani, C. F. Bunting, M. D. Deshpande, and Z. A. Khan, Validation of Modal/MoM in shielding effectiveness studies of rectangular enclosures with apertures, *IEEE Trans. Electromagn. Compat*., 48(2): 348-353, 2006.

[2] Q. -F. Liu, W. -Y. Yin, J. -F. Mao, and Z. -Z. Chen, Accurate characterization of shielding effectiveness of metallic enclosure with thin wires and thin slots[J]. *IEEE Trans. Electromagn. Compat*., 51(2): 293–300, 2009.

[3] J. Z. Lei, C. H. Liang, W. Ding, and Y. Zhang, Study on MPI-Based parallel modified conformal FDTD for 3-D electrically large coated targets by using effective parameters, *IEEE Antennas and Wireless Propagat. Lett.*, 7: 175–178, 2008.

[4] W. Yu and R. Mittra, A conformal finite difference time domain technique for modeling curved dielectric surfaces, *IEEE Microw. Wireless Compon. Lett.*, 11(1): 25–27, 2001.

[5] T. Xiao, and Q. H. Liu, A 3-D Enlarged Cell Technique (ECT) for the Conformal FDTD Method, *Trans. Antenna Propagat.,* 56: 765–773, 2008.

[6] J. Dai, Z. Chen, D. Su, and X. Z, Stability analysis and improvement of the conformal ADI-FDTD methods, *IEEE Trans. Antennas Propagat*., 59(6): pp.2248–2258, 2011.

[7] S. Benkler, N. Chavannes, and N. Kuste, A new 3-D conformal PEC FDTD scheme with user-defined geometric precision and derived stability criterion, *IEEE Trans. Antennas Propagat*., 54(6): 1843–1849, 2006.

[8] E. Neufeld, N. Chavannes, T. Samaras, and N. Kuster, Novel conformal technique to reduce staircasing artifacts at material boundaries for FDTD modeling of the bioheat equation, *Phys. Med. Biol*., 52: 4371–4381, 2007.

[9] S. Dey and R. Mittra, A locally conformal finite-difference time-domain (FDTD) algorithm for modeling three-dimensional perfectly conducting objects, *IEEE Microw. Guided Wave Lett*., 7: 273–275, 1997.

[10] J. Fang, Time domain finite difference computation for Maxwell's equations, Ph.D. dissertation, Univ. California at Berkeley, CA, 1989.

A Compact Circularly-Polarized Patch Antenna With Dual-band For GNSS Applications

Yang Hailong, Xi Xiaoli, Song Zhongguo, Liu Jiangfan, Shi Xiaomin

Xi'An University of Technology, Xi'an, China
*corresponding author, E-mail: xixiaoli@xaut.edu.cn

Abstract

A Compact Circularly-Polarized (CP) Patch antenna is designed and simulated in this paper. The antenna with a four-layer structure is presented. The structure consists of two metallic patches, a feeding network, and a ground plane. This compact dual-band antenna is designed for GPS, GLONASS, BDS-2 and GALILEO operation at (1164-1230 MHz) and (1559-1610 MHz) bands. A Stacked Patch is employed for the dual-band. The right-hand circularly polarized (RHCP) field property is achieved by connecting two ports of the Wilkinson power divider which have a 0-90 degree phase shift. The antenna has a small size of 50mm* 50mm. Analysis and design are conducted with the Ansoft HFSS. Simulation results are presented and discussed.

Index Terms: **Right-hand circularly polarized (RHCP), Antenna, Aperture-Stacked, Dual -band.**

1. Introduction

With the rapid development of global navigation satellite system (GNSS) such as GPS, GLONASS, BDS and GALILEO in the last decades [1-3], more frequency bands will be available for global positioning applications. As an important part of the GNSS, antenna design is of primary importance where dual-band antennas are especially desirable for multi-mode navigation. Nowadays, microstrip patch antennas have been enjoying proliferated use in many circularly-polarized applications due to their lightweight, low cost, ease of production and other characteristics [4]. However, most of them cover only a single frequency [5-7] or dual-band only for GPS applications [8, 9]. The antenna proposed in [10] is able to operate at GPS, GLONASS, and BDS-2 bands, however, its size is rather large, besides the feeding grid and the structure are very complex. In addition, the BDS-2 (B2), GPS (L2, L5), GLONASS (G2), and GALILEO (E5a, E5b) have not been covered.

In this paper, in order to reduce the size and the number of the feeding points, we divided the GNSS bands into two bands as shown in the table.1. A novel compact dual-feed circularly polarized antenna is designed for GNSS dual-band, i.e., 1164-1300 MHz and 1559-1610 MHz. A Stacked Patch is employed to realize the dual-band. The feeding network of power divider is employed for CP radiation. Simulation results are presented and discussed.

2. Antenna Description

The design goal for our antenna is to cover the entire GPS, GLONASS, BDS-2 and GALILEO bands. Since the operation frequencies of the above systems are close to each other, we divide them into a lower band (1164-1300 MHz) and a higher band (1559-1610 MHz) as listed in Table 1. Such a small dual-band GNSS antenna is suitable for portable GNSS applications, especially for multi-mode navigation. Fig.1 shows the layered structure (l1=50mm being their side lengths) of the antenna geometry. As seen here, the proposed antenna consists of two metallic patches located on the top of the stacked dielectric substrates. The layer descriptions are listed in Table2. Fig.2 shows the top view of the two metallic patches. The top parasitic patches (see Fig.2 (a)) around the top patch helps increasing the bandwidth of the high-frequency impedance. The two ports of Wilkinson power divider are connected to the 50 coaxial cables placed close to the top patch (see Fig.2 (b)). The feeding network-Wilkinson power divider is printed on the plane of the third substrate. The proposed antenna utilizes a 0-90 degrees Wilkinson power divider (see Fig.3) to achieve good RHCP. The right-handed and left-handed transmission lines are printed on the one port of the Wilkinson power divider. It can effectively reduce the size and broaden phase frequency characteristics of the power splitter [11]. The Wilkinson power divider is printed within FR-4 substrate with thickness of 1mm and relative permittivity of 2.65 due to its low cost. The bottom of the antenna and feeding circuitry shares the same ground.

Table 1: The desired frequency bands of the antenna.

Lower band (1164-1300MHz) Higher band (1559-1610MHz)	Frequency band	Frequency rang
Lower band	GPS L5	1176±12MHz
Lower band	GPS L2/L2C	1227±12MHz
Lower band	GLONASS G2	1252±7MHz
Lower band	GALILEO E5a/b	1192±15MHz
Lower band	BDS-2 B2	1207±10MHz
Lower band	BDS-2 B3	1268±10MHz
Higher band	GPS L1	1575±10MHz
Higher band	GLONASS G1	1609±7MHz
Higher band	BDS-2 B1	1561±2MHz

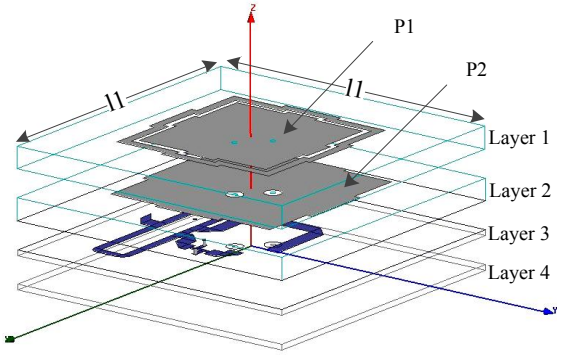

Figure 1: The geometry of the explode antenna.

Table 2: The layers describe of the antenna.

Layer	ε_r	h (mm)	Top	Bottom
1	9.6	4	P1	No patch
2	9.6	4	P2	GND
3	2.65	1	GND	Power divider
4	2.65	1	No patch	GND

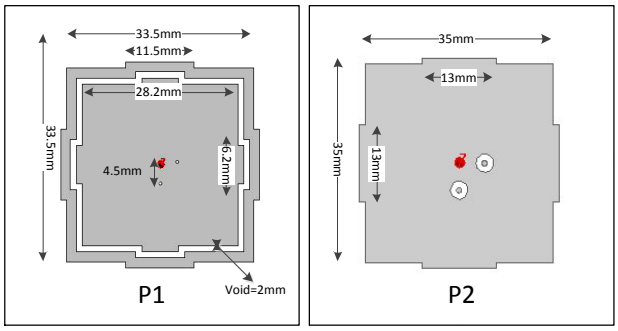

(a) (b)

Figure 2: Two metallic patches size of the antenna located on the top of substrates (ε_r =9.6).

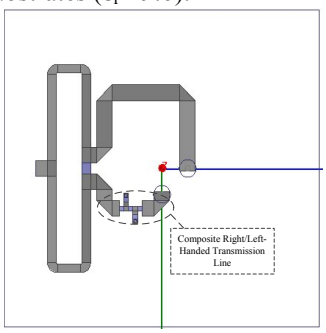

Figure 3: The feeding network of the proposed antenna located on the bottom of layer3 substrates (ε_r =2.65).

3. Simulation Results

All the parameters have been optimised by using commercial software Ansoft HFSS 13.0 Microwave Studio. Parametric study has been carried out towards the design goal as listed in Table1. Fig.4 and Fig.5 show the magnetic field distributions at the two center frequencies of the two desired bands, i.e., 1.22 GHz and 1.57 GHz, respectively. As expected, when operating at the higher band, the magnetic field is concentrated within the top patch dielectric substrate. When operating at the lower band, the magnetic fields are concentrated within the second patch dielectric substrate.

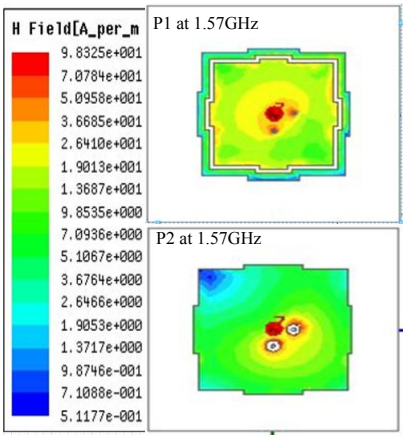

Figure 4: Magnetic field distributions at frequency of 1.57GHz

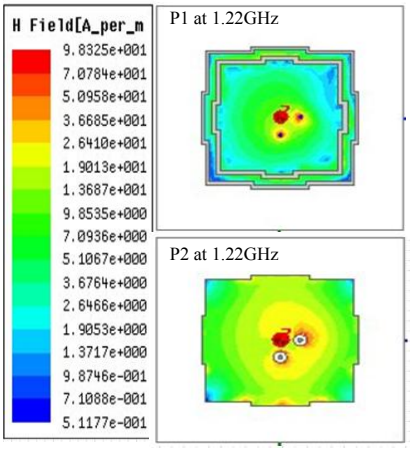

Figure 5: Magnetic field distributions at frequency of 1.22GHz.

The simulated return loss is shown in Fig.6 for different values of the patch P1. It can be seen that the length of the top patch P1 (Lp1) can influence the return loss of the higher band. Fig.7 illustrates the length of the layer2 patch P2 (Lp2) can influence the return loss of the lower band. Matching at the upper frequency is therefore realized by appropriate choice of Lp1 and Lp2. The appropriate value of Lp1 and Lp2 are selected as 28.2 mm and 35mm. Fig.8 shows the return loss of the proposed antenna optimized. As seen here, the frequency band (-10dB) is from 1.16 GHz to 1.30 GHz and 1.50 GHz to 1.70 GHz, respectively. It covers the GPS (L1, L2, L5), GLONASS (L1, L2), BDS-2(B1, B2, B3) and GALILEO (E5a, E5b) bands.

Fig.9 shows the VSWR of the whole band. As seen here, the VSWR < 2:1 band is from 1.1 GHz to 1.3 GHz and 1.5 GHz to 1.7GHz. It has a good matching for the working bands of the GNSS.

Fig.10 shows the simulated axial ratio from 0.8GHz to 1.8GHz. As seen here, the most of axial ratio values of the higher and lower bands are below 5. Fig.11 and Fig.12 illustrate the simulated axial ratio at 1.22 GHz in XOZ-plane (φ=0°, θ: -180°~180°) and 1.57 GHz in XOZ-plane (φ=0°, θ: -180°~180°). It is observed that the axial ratio is

lower than 3dB for -90° < θ < 90° at 1.22 GHz, while at 1.57 GHz, a 5dB bandwidth is achieved for -75° < θ < 75°.

Fig.13 and Fig.14 show the simulated normalized E-plane (φ=0°) RHCP radiation pattern at 1.22 and 1.57 GHz, respectively. It is found that the RHCP antenna gain is around 4 dBi at 1.22 GHz and 0.2 dBi at 1.57 GHz.

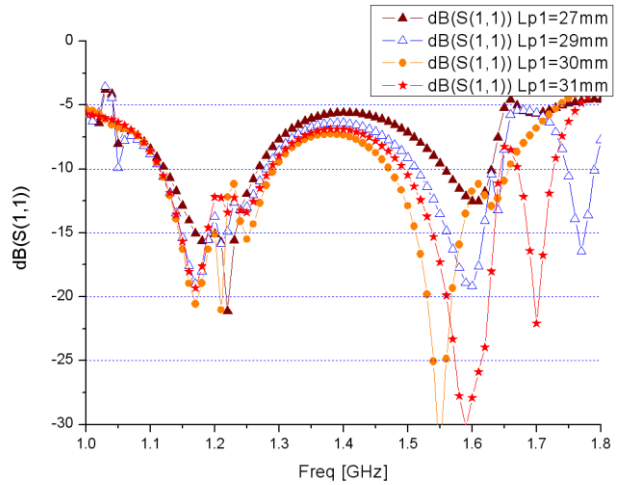

Figure 6: Simulated results of the return loss S11 for the proposed antenna with different length of top patch Lp1.

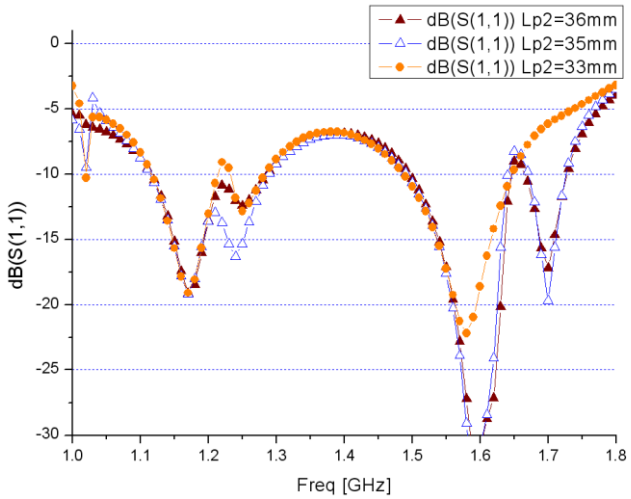

Figure 7: Simulated results of the return loss S11 for the proposed antenna with different length of layer 2 patch Lp2.

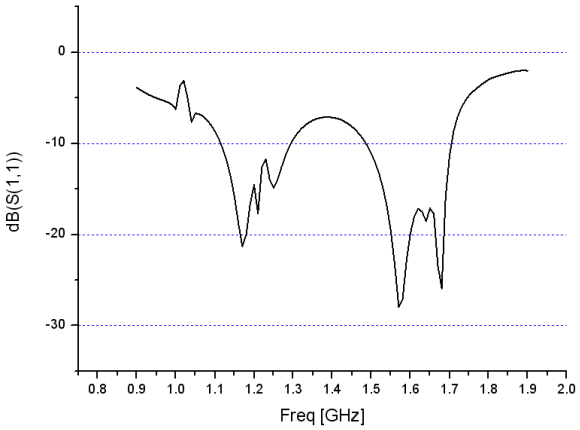

Figure 8: Simulated results of the return loss S11 for the proposed antenna.

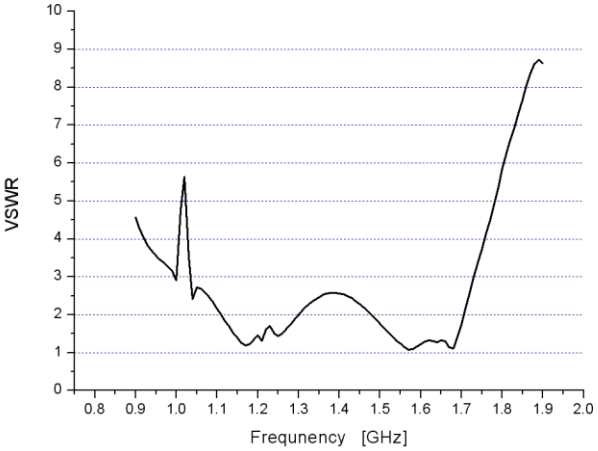

Figure 9: Simulated results of the VSWR for the proposed antenna.

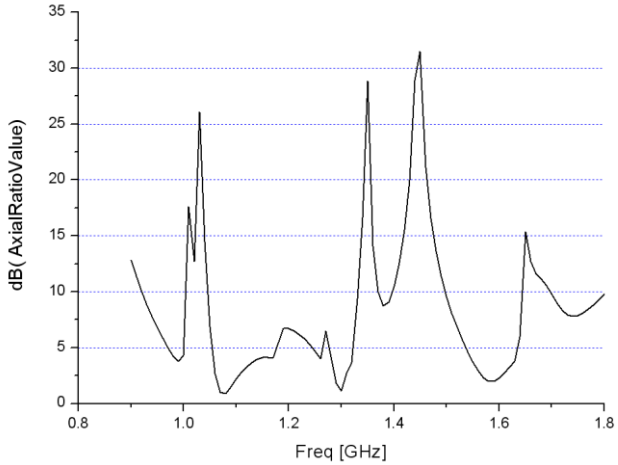

Figure 10: Simulated axial-ratio for the proposed antenna.

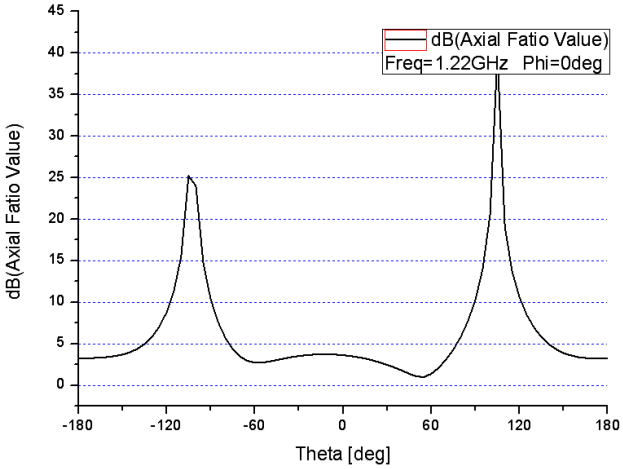

Figure 11: Simulated axial-ratio for the proposed antenna at 1.22GHz.

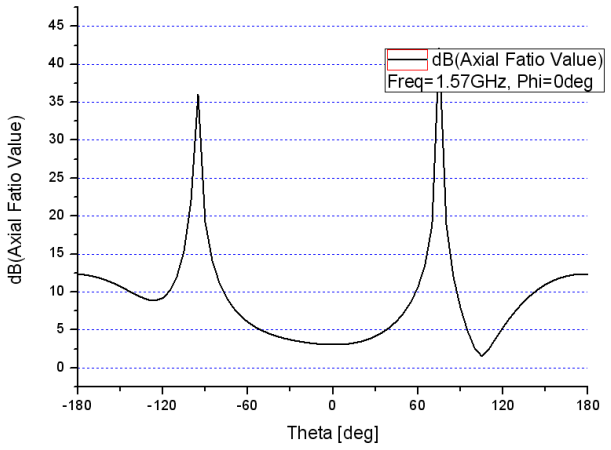

Figure 12: Simulated axial-ratio for the proposed antenna at 1.57GHz.

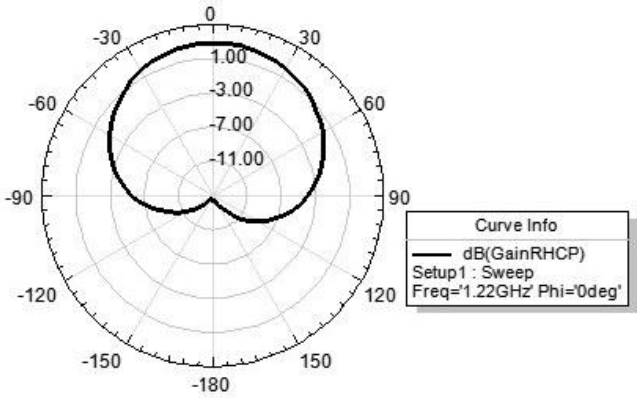

Figure 13: Simulated radiation patterns for RHCP and LHCP for the proposed antenna at 1.22 GHz.

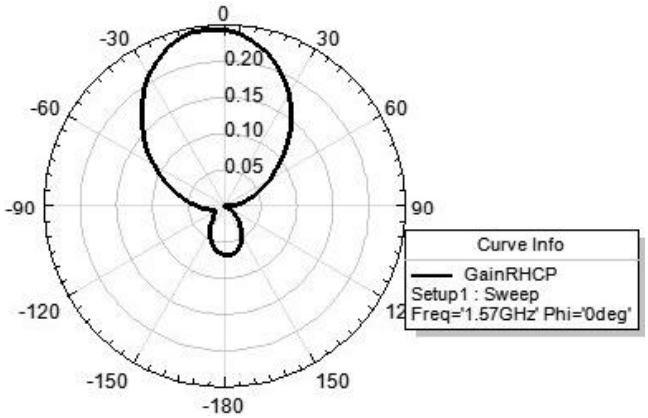

Figure 14: Simulated radiation patterns for RHCP and LHCP for the proposed antenna at 1.57GHz.

4. Conclusions

A compact CP microstrip antenna with a four-layer structure is presented. The structure consists of two metallic patches, a feeding network, and a ground plane. The parasitic patches of the top increase impedance bandwidth of the high frequency. At the same time, both the impedance bandwidth (below -10dB return loss) and the axial ratio bandwidth cover the entire GPS, CLONASS, BDS, and GALILEO bands. The proposed antenna is a very good candidate for multi-mode GNSS navigations.

References

[1] T. Zhi-Hong and C. Qing-Xin, "Compact circular polarized antenna for GPS and CNSS applications," in Microwave Conference Proceedings (APMC), 2010 Asia-Pacific, Yokohama, pp. 622-625, 2010

[2] P. Misra and P. Enge, "Global Positioning System: Signals, Measurements, and Performance," Lincoln, MA, USA: Ganga-Jamuna Press, 2010.

[3] N. Samam a, Global Positioning: "Technologies and Performance," New York, NY, USA: Wiley, 2008

[4] Wen-Shyang C., Chun-Kun W., Kin-Lu W, "Novel compact circularly polarized square microstrip antenna," Antennas and Propagation, IEEE Transactions on, 2001,49(3):340-342.7-10 Dec. 2010.

[5] L. Boccia, G. Amendola, and G. D. Massa, "A shorted elliptical patch antenna for GPS applications," IEEE Antennas Wireless Propag. Lett., vol. 2, pp. 6–8, 2003.

[6] L. Boccia, G. Amendola, and G. D. Massa, "Performance evaluation of shorted annular patch antennas for high-precision GPS systems," Microw. Antennas Propag., vol. 1, pp. 465–471, Apr. 2007.

[7] O. Leisten, J. C.Vardaxoglou, P. McEvoy, R. Seager, and A Wignfield, "Miniaturized dielectrically-loaded quadrifilar antenna for global navigation positioning system (GPS)," Electron. Lett., vol. 37, no. 22, pp. 1321–1322, Oct. 2001.

[8] O. P. Falade, M. U. Rehman, Y. Gao, X. D. Chen, and C. G. Parini, "Single feed stacked circular polarized antenna for triple band GPS receivers," IEEE Trans. Antennas Propag., vol. 60, no. 10, pp. 4479–4484, Oct. 2012.

[9] L. Yoonjae, S. Ganguly and R. Mittra, "Multi-band L5-capable GPS antenna with reduced backlobes," in Antennas and Propagation Society International Symposium, 2005 IEEE, pp. 438-441 Vol. 1A, 2005

[10] L. Jianxing, S. Hongyu, L. Hang, and Z. Anxue, "Quad-Band Probe-Fed Stacked Annular Patch Antenna for GNSS Applications," Antennas and Wireless Propagation Letters, IEEE, vol. 13, pp. 372-375, 2014

[11] Genc A, Baktur R. Dual- and Triple-Band Wilkinson Power Dividers Based on Composite Right- and Left-Handed Transmission Lines[J]. Components, Packaging and Manufacturing Technology, IEEE Transactions on, 2011,1(3):327-334.

An Efficient Macromodeling Methodology for Transient Simulation of Signal Integrity Problems

Ashish Sarvaiya*[,1], Sanjeev Gupta[2],

[1]Government Engineering College, Bhavnagar, Gujarat, India
[2]Dhirubhai Ambani Institute of Information and Communication Technology, Gandhinagar, Gujarat, India
*corresponding author, E-mail: aks.sarvaiya@gmail.com

Abstract

This paper proposes an efficient macromodeling methodology for transient simulation of Signal Integrity (SI) problems. Tabulated frequency domain data in the form of admittance matrix is obtained through Finite Integration Technique (FIT). Vector Fitting Method (VFM) is used here to construct a macromodel from tabulated frequency domain data. Resulting pole residue macromodel is directly embedded into HSPICE or compatible circuit solvers. In this paper, a systematic macromodeling methodology is discussed and a simple procedure of embedding the macromodel into circuit solver is described. Single ended via connected with two microstrip lines example show the validity of the proposed methodology.

1. Introduction

The development of an accurate and efficient macromodeling methodology becomes necessary for transient simulation of Signal Integrity (SI) problems. In signal & power integrity applications, typical networks are high speed interconnects, electrically long transmission line, Printed Circuit Board with a variety of interconnect discontinuities such as pins and vias and packaging networks. The multi port frequency dependent network's equivalent circuit representation is highly desirable for circuit solvers [1]. In spite the CPU expenses and convergence issues of full wave method; the full wave method can be used to extract the network property, such as its Y-parameters, Z-parameters, or S-parameters [2]. Thereafter, the macromodeling techniques [3]–[4] can be used to construct macromodel from the given tabulated frequency domain data characterizing the network property of the system. A technique for constructing multiport macromodel using a fast implementation of the vector fitting method is discussed in [5]. Vector Fitting Method (VFM) is a robust and well known rational function approximation method which is used in this paper. We have used VF technique for constructing a macromodel for a given networks.

In this paper, an efficient methodology is proposed for transient simulation of Signal Integrity (SI) problems. Tabulated frequency domain data in the form of admittance matrix is obtained through Finite Integration Technique (FIT). Vector fitting technique is then used to construct the macromodel. Thereafter resulting pole residue macromodel is directly embedded using foster pole- residue form in circuit solver. Automated netlist file is generated and embedded into commercial HSPICE or compatible circuit solver. In this paper, systematic methodology is discussed and details of embedding the macromodel into circuit solver are described. As a test case, single ended via connected with two microstrip lines is presented which validating that the proposed approach is applicable for Signal Integrity (SI) problems.

2. Methods for extracting Y-parameters and vector fitting technique

2.1 Admittance Parameters Extraction

The Finite Integration Technique (FIT) provides a dual grid discretization scheme applicable to various electromagnetic problems. FIT uses discretize set of *Maxwell's Grid Equations* (MGEs) [6]:

$$\mathrm{Ce} = -\frac{\mathrm{d}}{\mathrm{dt}}\mathrm{b}, \quad \check{\mathrm{C}}\mathrm{h} = \frac{\mathrm{d}}{\mathrm{dt}}\mathrm{d} + \mathrm{j},$$
$$\tilde{\mathrm{S}}\mathrm{d} = \mathrm{q}, \quad \mathrm{Sb} = 0, \qquad (1)$$

Where topological matrix C and $\tilde{C}$ as the discrete equivalent of the analytical curl operator and discrete divergence operators S and $\tilde{S}$. Solution of the discretized set of *Maxwell's Grid Equations* can be obtained by the transient solver. The time derivatives by central differences yields explicit update formulation for the loss-free case [6]:

$$\mathrm{e}^{\mathrm{n}+1/2} = \mathrm{e}^{\mathrm{n}-1/2} + \Delta\mathrm{t}\,\mathrm{M}\,\bar{\varepsilon}^{-1}\left[\tilde{\mathrm{C}}\,\mathrm{M}\,\bar{\mu}^{-1} + \mathrm{j}_{\mathrm{S}}^{\mathrm{n}}\right],$$
$$\mathrm{b}^{\mathrm{n}+1} = \mathrm{b}^{\mathrm{n}} - \Delta\mathrm{t}\mathrm{C}\mathrm{e}^{\mathrm{n}+1/2}, \qquad (2)$$

A method for the calculation of admittance matrix where the admittance matrix Y(s) can alternatively be transformed from its scattering (S)-parameters is efficient and used in this paper [7]. The S-parameters can also be obtained

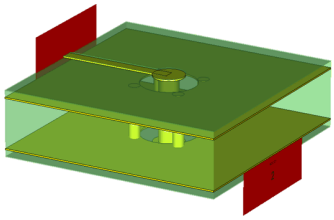

Figure 1: Model of Single ended via connecting with two microstrip lines

through measurement e.g. vector network analyzer. Y–parameter matrix of Np-port subnetwork can be shown as following:

$$Y_{ij}(s) = \begin{bmatrix} Y_{11}(w_k) & \cdots & Y_{1n}(w_k) \\ \dots & \dots & \dots \\ Y_{n1}(w_k) & \cdots & Y_{nn}(w_k) \end{bmatrix} \quad (3)$$

Where $w_k = 2\pi f_k, k = 1,2,..K$, are discrete frequency points within the desired band.

2.2 Vector fitting Technique

In Vector Fitting Method, the objective is to identify a rational approximation of the each elements of (4) that approximates a given broad band frequency response $Y_{ij}(s)$ as closely as possible

$$Y_{ij}(s) = \sum_{n=1}^{N} \frac{r_{n,ij}}{s-q_n} + d_{ij} + se_{ij}, \quad (4)$$

Where $\{r_{n,ij}\}$ and $\{q_n\}$ denote, respectively, the residues and poles, both of which are complex, in general and while the terms $\{d_{ij}\}$ and $\{e_{ij}\}$ are real constants, i, j = 1, 2, …, N_p.

Vector fitting is an iterative procedure for solving (4). Each iteration consists of a pole identification step followed by a residue identification step with known pole. The pole identification step requires in each iteration to solve in the least squares (LS) sense equation

$$W(s) = \sigma(s) \cdot Y_{ij}(s) = \sum_{n=1}^{N} \frac{\hat{r}_{n,ij}}{s-\tilde{q}_n} + \hat{d}_{ij} + s\hat{e}_{ij}, \quad (5)$$

$$\text{Where } \sigma(s) = 1 + \sum_{n=1}^{N} \frac{\tilde{r}_n}{s-\tilde{q}_n} \quad (6)$$

Substituting (6) into (5) and for a given sample points M_f, following linear equation in compact form can be derived:

$$A_f \cdot u = b_f, \quad (7)$$

Solving the least squares problem of (8), the coefficients of $\sigma(s)$ and product of $\sigma(s).Y_{ij}(s)$ are obtained.

The second step is the calculation of the residues of $Y_{ij}(s)$. An iterative process is used to enhance accuracy, and $Y_{ij}(s)$ converges to an optimized rational function fit.

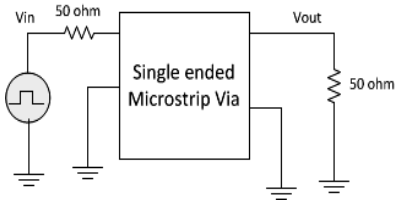

Figure 2 : Schematic circuit diagram of the test model; Two-port network having source and load elements.

3. Embedding the macromodel into circuit simulator

3.1. Foster Pole-Residue Representation

Once the macromodel of the given network is created as described in preceding section, for embedding macromodel into HSPICE or compatible circuit solvers, following syntaxes in *Foster Pole-Residue form* is used.

Gain E(s) form [8]:
Exxx n+ n- FOSTER in+ in- k0 k1+ (Re {A1}, Im {A1})/ (Re {p1}, Im {p1}) + (Re {A2}, Im {A2})/ (Re {p2}, Im {p2}) + (Re {A3}, Im {A3})/ (Re {p3}, Im {p3}) + ... …… (8)

A pole-residue pair is represented by four numbers - real and imaginary part of the residue, then real and imaginary part of the pole. We must make sure that Re $[p_i]$ <0; otherwise, the simulations will certainly diverge. For example, to represent G(s) in the forms of equations (8),

$$G(s) = 0.001 + 1 \times 10^{-12}s + \frac{0.0008}{s+1\times10^{10}} + \frac{(0.001-j0.006)}{s-(-1\times10^{8}+j1.8\times10^{10})} + \frac{(0.001+j0.006)}{s-(-1\times10^{8}-j1.8\times10^{10})} \quad (9)$$

We will input in the net list file as:
G1 1 0 FOSTER 2 0 0.001 1e-12+ (0.0004, 0)/ (-1e10, 0) (0.001, -0.006)/ (-1e8, 1.8e10)

The netlist file can be prepared as per above procedure for each elements of (4). This net list file can be easily inserted into HSPICE or its compatible software for the transient simulation.

4. Numerical results

The printed circuit boards (PCBs) may contain large number of discontinuities, and their presence causes signal distortion problems. For this reason an accurate modeling of discontinuities at PCB level is essential for signal integrity (SI) analysis. A proposed methodology is validated for a simple via hole connecting with microstripes in multilayer PCB.

A single ended via connected with two microstrip lines is shown in Fig.1. Y-parameter matrix of this network

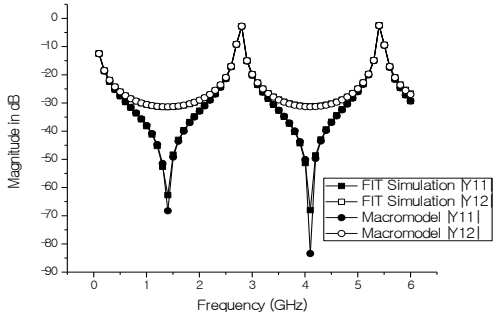

(a)

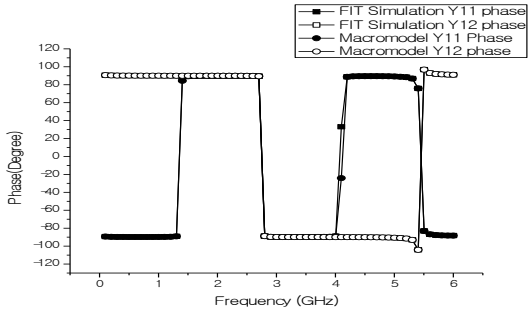

(b)

Figure 3: Y parameters of the Single ended via simulated by FIT in CST MWS and Vector Fitting method. (a) Magnitude. (b) Phase

is extracted by Finite Integration Technique (FIT) using CST Microwave Studio (MWS). The model network is having input and output port, port 1 and port 2 respectively. In FIT, for transient simulation, gaussian pulse source and ABC boundary condition are used. Each elements of Y-parameter matrix is approximated with vector fitting method. 50 poles including 10 real and 40 complex conjugates poles are extracted to match the parameters of the test network up to 6 GHz. Good agreements can be observed in Fig. 3 between the FIT simulated Y parameters and the macromodel Y parameters based on the vector fitting method. Thereafter, for embedding the macromodel into circuit solvers, netlist file which is the equivalent sub circuit in time domain, is automatically created and inserted into HSPICE or equivalent circuit simulator by the proposed approach in this paper. Obtained time domain model is used to perform the transient analysis of simple via hole in multilayer PCBs. The schematic circuit is having 50 ohm source and 50 ohm load impedance at port 1 and 2 respectively as shown in Fig. 2. The circuit is excited at port 1 by a pulse having a rise/fall time of 0.02 ns and a pulse width of 4 ns and transient simulation is performed. Transient simulation results are shown in Fig. 4. Result indicates that the line is ringing with overshoots.

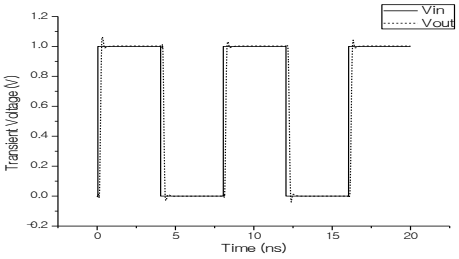

Figure 4: Transient voltage waveforms: (a) at port 1 denoted as Vin and at port 2 denoted as Vout.

5. Conclusion

This paper proposes an efficient macromodeling methodology for transient simulation of Signal Integrity (SI) problems. In this paper, systematic methodology is discussed and details of embedding the macromodel into circuit solver are described. Single ended via connected with two microstrip lines test case is presented which demonstrating that the proposed approach is suitable for a transmission lines, high speed interconnects as well on board discontinues such as via holes. Passivity checking is also vital for transient simulation to be converged. Accuracy and robustness of any rational function fitting process is strongly dependent on the quality of the input data hence in future, pre processing of input data through data processing technique can be performed to remain data to be stable, passive and causal. In future, proposed method can be applied to perform the transient simulation of variety of EMC-EMI, Signal Integrity and Power Integrity problems.

References

[1] G. Antonini, "SPICE equivalent circuits of frequency-domain responses," *IEEE Trans.Electommagnetic Compatibility*, vol. 45, pp. 502–512, August 2003.

[2] E.X.Liu, E.P.Li, L.W.Li and Z. Shen, " Finite-Difference Time-Domain macromodel for Simulation of electromagnetic interference at high speed interconnects*",IEEE Trans.Magnetics,*vol.41, no.65-71, January 2005

[3] R. Achar and M. S. Nakhla, "Simulation of high-speed interconnects,"*Proc. IEEE*, vol. 89, no. 5, pp. 693–728, May 2001.

[4] B. Gustavsen and A. Semlyen, "Rational approximation of frequency domain responses by vector fitting," *IEEE Trans. Power Del.*, vol. 14,no. 3, pp. 1052–1061, Jul. 1999.

[5] D. Deschrijver, M. Mrozowski, T. Dhaene, and D. De Zutter, "Macromodeling of multiport systems using a fast implementation of the vector fitting method," *IEEE Microw. Wireless Compon. Lett.*, vol. 18, no. 6, pp. 383–385, Jun. 2008.

[6] CST MWSR Manual, CST Studio Suite, 2012

[7] T. Mangold and P. Russer, "Full-wave modeling and automatic equivalent-circuit generation of millimeter-wave planar and multilayer structures,"IEEE Trans. Microwave Theory Tech., vol. 47, no. 6, pp. 851–858,Jun. 1999.

[8] Star-HSPice Manual, Avant Corporation, 1998.

Electromagnetic and Light Scattering

Scattering of cylindrical vector beams by a multilayered sphere

Renxian Li, Chunying Ding, Ruiping Yang

School of Physics and Optoelectronic Engineering, Xidian University, Xi'an 710071, China

Abstract

The scattering of a cylindrical vector beam by a multilayered sphere is investigated. An analytical formula for the calculation of beam shape coefficients of a cylindrical vector beam is first derived using Integral Localized Approximation. After the verification of beam shape coefficients by the comparison of the reconstructed field and the original field obtained from the definition, the far-field scattered intensity is evaluated, and the rainbow produced by cylindrical vector beams is also studied.

1. Introduction

Cylindrical Vector Beams (CVBs), which are solutions of vector wave equation in the paraxial limit, have cylindrical symmetry in both amplitude and polarization. The special features of CVBs have attracted considerable interest for a variety of novel applications, including lithography, particle acceleration, material processing, high-resolution metrology, atom guiding, optical trapping and manipulation. For instance, a radially polarized beam focused by a high numerical aperture objective has a peak at the focus, and can trap a high-index particle. On the contrary, an azimuthally polarized beam has null central intensity, and can trap low-index particle. These two kinds of beams can be experimentally switched.

CVBs can be generated by many methods, which are categorized as active or passive depending on whether amplifying media is used. The simplest method is to convert an incident Gaussian beam to a radially polarized beam using a radial polarizer. However this method does not produce very high purity transverse modes. More efficient methods use interferometry. Since a CVB can be expressed as the linear superposition of two Hermite-Gaussian or Laguerre-Gaussian beams with different orientations of polarization. Another efficient method is based on optical fiber. This technique takes advantage of the similarity between the polarization properties of the modes that propagate inside a step-index optical fiber and CVBs. When TE_{01} or TM_{10} is excited in the fibre, it excites a CVB in free space.

Up to now, researches mainly focus on the focusing properties and the applications of CVBs. In fact, most applications of CVBs involves the scattering of CVB by a particle. This paper is devoted to the interaction of CVBs with a multilayered sphere. The incident beam is expanded using Beam Shape Coefficients (BSCs) and vector spherical harmonic functions. The far-field scattered intensity, including rainbow intensity, will be discussed.

2. Theoretical background

Cylindrical vector beams are solutions of vector wave equation

$$\nabla \times \nabla \times \vec{E} + k^2 \vec{E} = 0 \tag{1}$$

where $k = 2\pi/\lambda$ is wavenumber with λ being the wavelength. In the paraxial approximation, the radially and azimuthally polarized vector Bessel-Gaussian beams, two kinds of typical CVBs, can be expressed as

$$\vec{E}_{rad} = E_0 \frac{\rho}{w_0} e^{-\frac{\rho^2}{w_0^2}} e^{i(\omega t - kz)} \hat{e}_\rho \tag{2}$$

$$\vec{E}_{azi} = E_0 \frac{\rho}{w_0} e^{-\frac{\rho^2}{w_0^2}} e^{i(\omega t - kz)} \hat{e}_\phi \tag{3}$$

where ρ and ϕ are respectively the radial and azimuthal coordinates, $\hat{e}_\rho$ and $\hat{e}_\phi$ are unit vectors in ρ and ϕ directions, and the subscripts rad and azi denote the polarization state. w_0 is the width of beam waist, and E_0 is a constant. Fig. 1(a) and 1(b) respectively give the intensity distribution of radially and azimuthally polarized Bessel-Gaussian beam in the plane $z = 0$. Note that the longitudial component of CVB is negligible under the condition of paraxial approximation. A general CVB can be considered as a linear superposition of a radially polarized CVB and an azimuthally polarized one.

Using ILA, we can obtain the analytical formula for CVBs. For example, BSCs for a radially polarized Bessel-Gaussian beams can be written as

$$\begin{aligned} g_{n,TM}^{m,rad} &= \frac{1}{2} Z_n^m \overline{\Omega}_n e^{im\phi_0} \left[2\rho_n J_m(-2i\rho_n\rho_0)\right. \\ &+ \left. i\rho_0 (J_{m-1}(-2i\rho_n\rho_0) - J_{m+1}(-2i\rho_n\rho_0))\right] \end{aligned} \tag{4}$$

Once BSCs is obtained, the far-field scattered intensities can be given directly according to GLMT

$$I_1 = |S_1(\theta)|^2, \quad I_2 = |S_2(\theta)|^2 \tag{5}$$

with

$$\begin{aligned} S_1 &= \sum_{n=1}^{\infty} \sum_{m=-n}^{+n} \frac{2n+1}{n(n+1)} \left[m a_n g_{n,TM}^m \pi_n^{|m|}(\cos\theta) \right. \\ &+ \left. i b_n g_{n,TE}^m \tau_n^{|m|}(\cos\theta) \right] \exp(im\varphi) \end{aligned} \tag{6}$$

$$\begin{aligned} S_2 &= \sum_{n=1}^{\infty} \sum_{m=-n}^{+n} \frac{2n+1}{n(n+1)} \left[a_n g_{n,TM}^m \tau_n^{|m|}(\cos\theta) \right. \\ &+ \left. i m b_n g_{n,TE}^m \pi_n^{|m|}(\cos\theta) \right] \exp(im\varphi) \end{aligned} \tag{7}$$

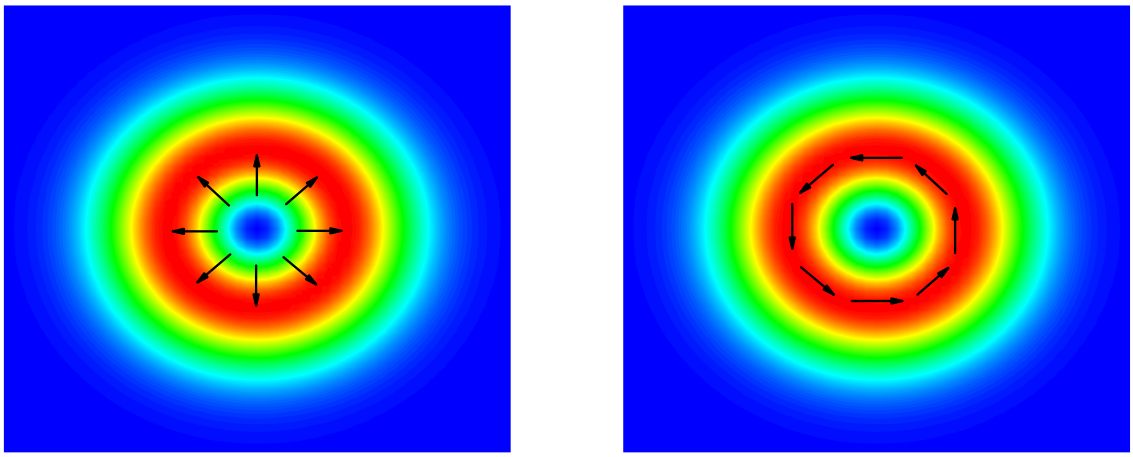

(a) Radially polarized CVB (b) Azimuthally polarized CVB

Figure 1: Intensity distribution of CVB. The arrows indicate the direction of polarization.

$$\pi_n^m(\cos\theta) = \frac{dP_n^m(\cos\theta)}{d\theta} \quad (8)$$

$$\tau_n^m(\cos\theta) = m\frac{P_n^m(\cos\theta)}{\sin\theta} \quad (9)$$

Where a_n and b_n are the traditional Mie scattering coefficients, and can be expanded using Debye series

$$\left.\begin{matrix} a_n \\ b_n \end{matrix}\right\} = \frac{1}{2}\left[1 - R_n^{212} - \sum_{p=1}^{\infty} T_n^{21}\left(R_n^{121}\right)^{p-1} T_n^{12}\right] \quad (10)$$

with

$$T_n^{21} = \frac{m_1}{m_2}\frac{2i}{D_n} \quad (11)$$

$$R_n^{212} = \frac{\alpha\xi_n^{(2)'}(\kappa_2)\xi_n^{(2)}(\kappa_1) - \beta\xi_n^{(2)}(\kappa_2)\xi_n^{(2)'}(\kappa_1)}{D_n} \quad (12)$$

$$T_n^{12} = \frac{2i}{D_n} \quad (13)$$

$$R_n^{121} = \frac{\alpha\xi_n^{(1)'}(\kappa_2)\xi_n^{(1)}(\kappa_1) - \beta\xi_n^{(1)}(\kappa_2)\xi_n^{(1)'}(\kappa_1)}{D_n} \quad (14)$$

$$D_n = -\alpha\xi_n^{(1)'}(\kappa_2)\xi_n^{(2)}(\kappa_1) + \beta\xi_n^{(1)}(\kappa_2)\xi_n^{(2)'}(\kappa_1) \quad (15)$$

$$\kappa_j = m_j ka \quad (16)$$

$$\alpha = \begin{cases} 1, & \text{for TE} \\ \frac{m_1}{m_2}, & \text{for TM} \end{cases}, \beta = \begin{cases} \frac{m_1}{m_2}, & \text{for TE} \\ 1, & \text{for TM} \end{cases} \quad (17)$$

where the prime indicates the derivative of the function with respect to its argument. $\xi_n^{(1)}(\cdot)$ and $\xi_n^{(2)}(\cdot)$ are respectively the spherical Riccati-Hankel functions of first and second kinds. For convenience, we note $p = -1$ and $p = 0$ respectively for the diffraction and direct reflection in this paper. In our previous work, we have theoretically and numerically proved that when p ranges from 1 to ∞, Eq. (10) is identical to the traditional Mie scattering coefficients.

2.1. Numerical results and discussions

This section is devoted to numerical results and discussions. In our calculation, we assume the incident beam is azimuthally polarized, and the wavelength of incident beam is $\lambda = 632.8\ nm$. The radius and refractive index of the particle is respectively $a = 100\ \mu m$ and $m_1 = 1.33$. The refractive index of surrounding media is $m_2 = 1.0$. The radius of beam waist is $w_0 = 100\ \mu m$.

Fig. 2 gives the first and second rainbows produced by an azimuthally polarized CVB calculated by generalized Lorenz-mie theory. To clarify the physical mechanism of such rainbows, the contributions of single scattering processes are simulated. Fig. 3 gives the first rainbow ($p = 2$) and second one ($p = 3$). The interference result of first and second rainbows is also given in Fig. 4.

3. Conclusion

In this paper, a rigorous theory of the interaction of CVBs and a sphere is given. In the theory, the BSCs is calculated using integral localized approximation, and the scattering coefficients is expanded by Debye series. Rainbow intensity is calculated. In this detailed abstract, limited numerical results are given, and more results and discussions will be added in the whole manuscript.

Acknowledgement

The authors acknowledge support from the Natural Science Foundation of China (Grant No. 61101068), and the Fundamental Research Funds for the Central Universities.

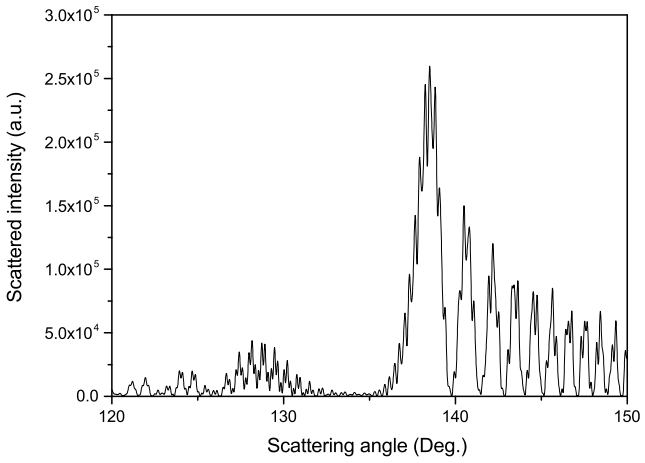

Figure 2: First and second rainbows produced by an azimuthally polarized CVB.

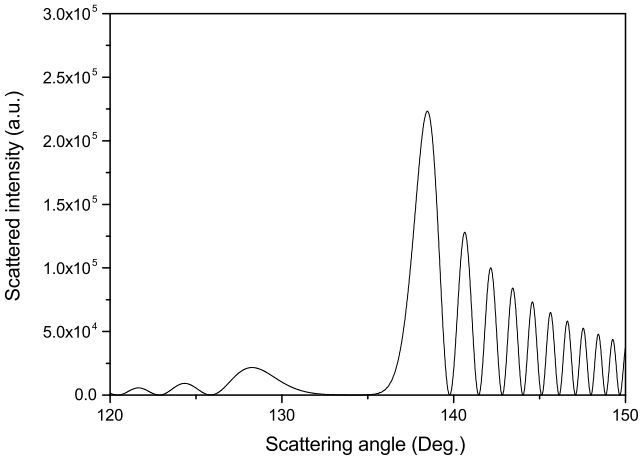

Figure 4: Interference of first and second rainbows produced by an azimuthally polarized CVB.

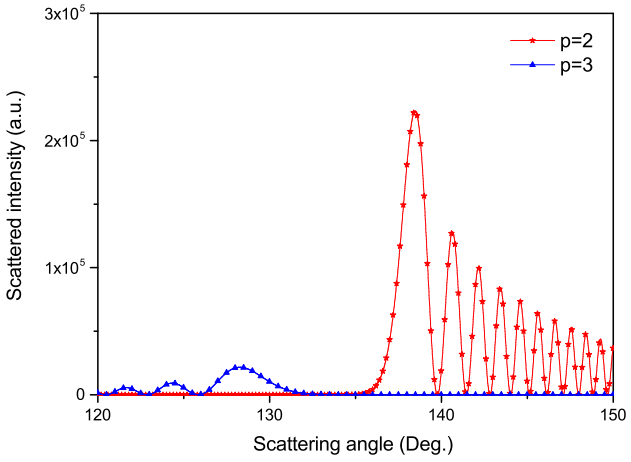

Figure 3: First and second rainbows produced by an azimuthally polarized CVB ($p = 2$ and 3).

Study of UPML absorbing boundary condition for the five-step LOD-FDTD method

Li-Xia Yang, Xue-Jian Feng

Department of Communication Engineering, Jiangsu University, Zhenjiang, China;
*corresponding author, E-mail:lixiayang@yeah.net

Abstract

In this paper, the uniaxial anisotropic perfectly matched layer (UPML) absorbing boundary condition in unconditionally stable five-step locally one-dimensional finite-difference time-domain (LOD5-FDTD) method are deduced. Efficiency parameters of the UPML absorbing boundary condition (ABC) are obtained through a series of test. In addition, target field phase distribution of a sinusoidal source is analyzed, which further illustrate the stability and efficiency of the UPML absorbing boundary condition.

1. Introduction

The three-dimensional five-step LOD-FDTD (LOD5-FDTD) method [1] is an unconditionally stable method whose time step is not restricted by the Courant-Friedrich-Lewy (CFL) stability condition [2]. It is worth mentioning that the LOD5-FDTD method has second order accuracy in time domain and it gives less numerical dispersion than the ADI-FDTD [3-4], two-step LOD-FDTD [5], three-step LOD-FDTD [6] method.

In order to apply to free-space simulation, the LOD-FDTD method should have an efficiency absorbing layer in the computation boundary. In [7-8], the split-field perfectly matched layer (PML) and convolution PML have been applied to LOD-FDTD method. The Mur's and uniaxial anisotropic PML (UPML) absorbing boundary condition [9] have been implemented within the two-dimensional LOD-FDTD method [10].But the numerical examples illustrate that the UPML-ABC exhibit vary bad absorbing effect when utilized in the LOD-FDTD method. In this paper, the UPML-ABC has been applied into the LOD5-FDTD method. Optimized parameters of the UPML-ABC have been obtained through a series of numerical experiment. On the basis of the optimized parameters, the reflection error and target field phase distribution of the simulation experiments show that the UPML-ABC can be used in the LOD5-FDTD method.

2. Formulation

In the UPML medium, the Maxwell's curl equations in frequency domain can be written as follows

$$\nabla \times \vec{H} = j\omega\varepsilon_0\varepsilon_r \overline{\overline{\varepsilon}}\, \vec{E} \tag{1}$$

$$\nabla \times \vec{E} = -j\omega\mu_0\mu_r \overline{\overline{\mu}}\, \vec{H} \tag{2}$$

Where ε_r and μ_r are the relative permittivity and permeability of the isotropic space, and $\overline{\overline{\varepsilon}}$, $\overline{\overline{\mu}}$ are relative permittivity and permeability tensors, respectively, which can be written as

$$\overline{\overline{\varepsilon}} = \overline{\overline{\mu}} = \begin{bmatrix} \dfrac{s_y s_z}{s_x} & 0 & 0 \\ 0 & \dfrac{s_x s_z}{s_y} & 0 \\ 0 & 0 & \dfrac{s_x s_y}{s_z} \end{bmatrix}$$

$$s_Q = \kappa_Q + \frac{\sigma_Q}{j\omega\varepsilon_0},\ Q = x, y, z \tag{3}$$

Where κ_Q and σ_Q are the attenuation factor and conductivity, respectively.

For the UPML medium, the LOD5-FDTD method for the first sub-step in frequency domain is as follows

$$-\frac{2}{3} j\omega\varepsilon_1 \frac{s_x s_z}{s_y} E_y = \frac{\partial H_z^n}{\partial x} + \frac{\partial H_z^{n+1/6}}{\partial x} \tag{4}$$

$$\frac{2}{3} j\omega\varepsilon_1 \frac{s_x s_y}{s_z} E_z = \frac{\partial H_y^n}{\partial x} + \frac{\partial H_y^{n+1/6}}{\partial x} \tag{5}$$

$$\frac{2}{3} j\omega\mu_1 \frac{s_x s_z}{s_y} H_y = \frac{\partial E_z^n}{\partial x} + \frac{\partial E_z^{n+1/6}}{\partial x} \tag{6}$$

$$-\frac{2}{3} j\omega\mu_1 \frac{s_x s_y}{s_z} H_z = \frac{\partial E_y^n}{\partial x} + \frac{\partial E_y^{n+1/6}}{\partial x} \tag{7}$$

Where $\varepsilon_1 = \varepsilon_0\varepsilon_r$, $\mu_1 = \mu_0\mu_r$ .With the following six auxiliary variables:

$$D_x = \frac{2}{3}\varepsilon_1 \frac{s_z}{s_x} E_x,\ D_y = \frac{2}{3}\varepsilon_1 \frac{s_x}{s_y} E_y,\ D_z = \frac{2}{3}\varepsilon_1 \frac{s_y}{s_z} E_z \tag{8}$$

$$B_x = \frac{2}{3}\mu_1 \frac{s_z}{s_x} H_x,\ B_y = \frac{2}{3}\mu_1 \frac{s_x}{s_y} H_y,\ B_z = \frac{2}{3}\mu_1 \frac{s_y}{s_z} H_z \quad (9)$$

Then, by substituting (8),(9) in (4-7) and converting the expression from frequency domain to time domain via $j\omega \to \partial / \partial t$, we obtain:

$$\frac{\partial E_z^n}{\partial x} + \frac{\partial E_z^{n+1/6}}{\partial x} = \frac{2}{3}\frac{\partial}{\partial t}(s_z B_y) \quad (10)$$

$$\frac{\partial E_y^n}{\partial x} + \frac{\partial E_y^{n+1/6}}{\partial x} = \frac{2}{3}\frac{\partial}{\partial t}(-s_x B_z) \quad (11)$$

$$\frac{\partial H_z^n}{\partial x} + \frac{\partial H_z^{n+1/6}}{\partial x} = \frac{2}{3}\frac{\partial}{\partial t}(-s_z D_y) \quad (12)$$

$$\frac{\partial H_y^n}{\partial x} + \frac{\partial H_y^{n+1/6}}{\partial x} = \frac{2}{3}\frac{\partial}{\partial t}(s_x D_z) \quad (13)$$

By using central difference scheme for time and spatial derivative, we can solve the electric and magnetic field components of the UPML. And the field components could be updated in the following order

$$E \Rightarrow B \Rightarrow H \Rightarrow D \Rightarrow E \quad (14)$$

Similarly, for the other four sub-steps, the updating electric and magnetic field component can be derived.

3. Numerical results

In this section, there are two numerical simulations test have provided to validate the proposed methods.

In the first test, a point electric dipole source is located at the center of the computation region. The structure of the computation region is $40\times40\times40$ cells and the UPML has 10 cells along x, y and z direction. The spatial step is $\Delta x = \Delta y = \Delta z = 5cm$ and the observation point is located in $Ez(0,10\Delta y,0)$. A Gaussian pulse $P(t) = 10^{-10}\exp\left[-((t-3T)/T)^2\right]$ $T = 2ns$ is used as the excitation source. For the purpose of comparison, a reference solution having zero ABC artifacts was computed by using a large domain. The relative reflection error is defined as:

$$\delta = 20\log_{10}\left(\frac{|E_z - E_{ref}|}{\max|E_{ref}|}\right) \quad (15)$$

where E_{ref} is electric field at the observation point for a lager domain without reflection.

And CFL number (S) is defined as the ratio of the time step size (Δt) to the CFL limit (Δt_{CFL}):

$$S = \frac{\Delta t}{\Delta t_{CFL}} \quad (16)$$

In order to obtain better absorption effect, the UPML-ABC parameters for implicit LOD5-FDTD method is given as:

$$\sigma_{\max} \approx \frac{m-2.3}{\left(150\pi\Delta\sqrt{\varepsilon_r}\right)}, \kappa = 20 \quad (17)$$

But for the traditional explicit FDTD method the parameters were given in [9].

Figure 1 shows the electric field component E_z against time at the observation point for both of the computation field and reference filed. It is clearly seen that the computation results quite agree with the reference solutions in the Figure. And the relative error with different S at the observation point is shown in figure 2, which illustrate the stability and good absorbing performance of the proposed method.

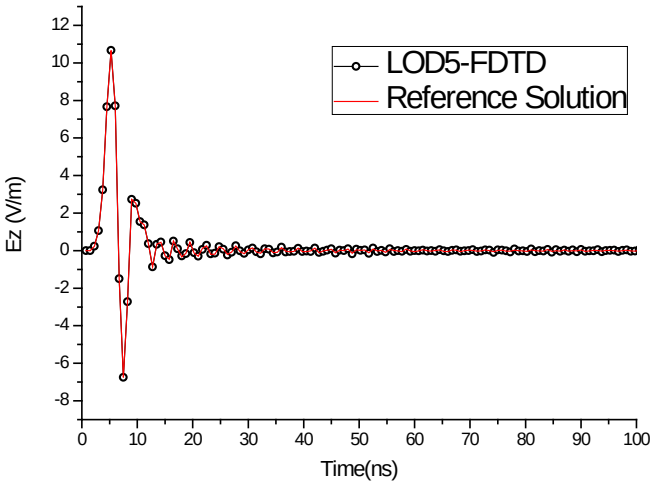

Figure 1: E_z against time at the observation point where $S = 9$.

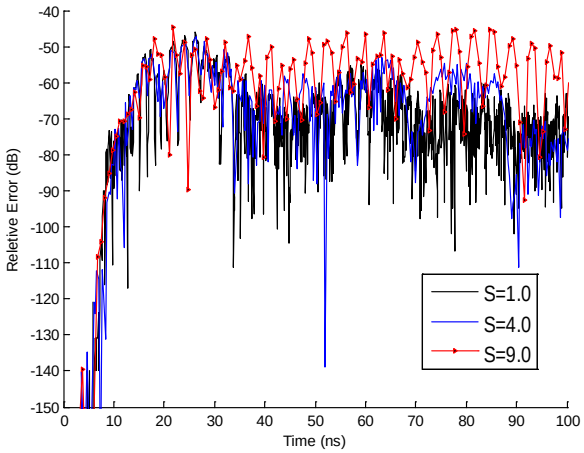

Figure 2: The relative error against time at the observation point.

Next, target field phase distribution of a sinusoidal source is analyzed with UPML-ABC. The computation region is of $160\times160\times160$ cells, and the sinusoidal source is located at $(0,0,0)$. And the computation region is surrounded by additional 10-cell UPML absorbing layers. Excitation source expression is as follows:

$$\boldsymbol{P}(t) = \hat{e}_z \sin(\omega t), \omega = 2\pi c \qquad (18)$$

LOD5-FDTD cell size is $\Delta x = \Delta y = \Delta z = 5\text{cm}$. Figure 3 shows the radiation phase distribution of E_z component at the *xoy* plane. The CFL number *S* is *4.0*. It is clearly seen that the presented UPML has efficiency absorbing performance for LOD5-FDTD method.

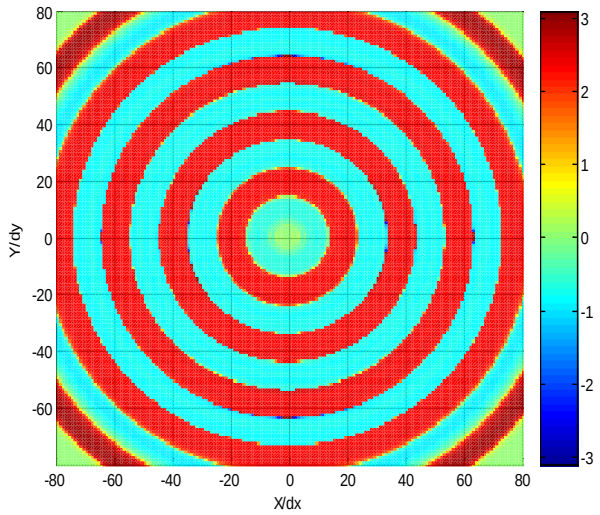

Figure 3: The radiation phase distribution of E_z at z=0 plane.

4. Conclusions

The uniaxial anisotropic perfectly matched layer (UPML) absorbing boundary condition (ABC) in unconditionally stable five-step locally one-dimensional finite-difference time-domain (LOD5-FDTD) method is presented. The numeric results show the stability and efficiency of the proposed method with the proposed UPML-ABC parameters.

Acknowledgements

This work is supported by the National Natural Science Foundation of China under Grant (No.61072002); Elitist of Liu-Da Summit Project in Jiangsu Province at 2011 under Grant (No. 2011-DZXX-031); and graduate research innovation (KYXX_0034).

Reference

[1] A. K. Saxena, K. V. Srivastava, “A Three-Dimensional Unconditionally Stable Five-Step LOD-FDTD Method,” *IEEE Trans. Antennas Propagation.*, vol. 62, no.3, pp. 1321-1329, Mar.2014。

[2] R. Courant, K. Friedrichs, and H. Lewy, “On the partial difference equations of mathematical physics,” *IBMJ.*, vol. 11, pp. 215–234, Mar.1967.

[3] T. Namiki, “A new FDTD algorithm based on alternating-direction implicit method,” *IEEE Trans.Microw.Theory.Tech.*, vol.47, no.10, pp.2003-2007, Oct.1999.

[4] F. Zheng, Z. Chen, and J. Zhang, “A finite-difference time-domain method without the Courant stability conditions,” *IEEE Microw. Guided Wave Lett.*, vol.9.11,pp. 441-443,Nov.1999.

[5] E. L. Tan, “Unconditionally stable LOD-FDTD method for 3-D Maxwell’s equations,” *IEEE Microwave and Wireless Components Letters.*, vol. 17, no.2, pp. 85-87, Feb.2007.

[6] I. Ahmed, E. k. Chua, E. P. Li, and Z. Chen, “Development of the three dimensional unconditionally stable LOD-FDTD method,” *IEEE Trans. Antenna Propag.*, vol.56, no. 11. pp. 3596-3600, Nov. 2008.

[7] V.E.do Nascimento, B. H. V. Borges, and F. L. Teixeira, “Split-Field PML Implementations for the Unconditionally Stable LOD-FDTD Method,” IEEE Microwave and Wireless Components Letters, vol. 16, no.7, pp.398-400, Jul.2006.

[8] I.Ahmed, E. Li, K.Krohne, “Convolutional Perfectly Matched Layer for an Unconditionally Stable LOD-FDTD Method,” IEEE Microwave and Wireless Components Letters, vol. 17, no. 12, pp. 816-819, Dec.2007.

[9] S. D. Gedney, “An Anisotropic Perfectly Matched Layer-Absorbing Medium for the Truncation of FDTD lattices,” *IEEE Trans. Antennas Propagation.*, vol. 44, no. 12, pp. 1630-1639, Dec.1996

[10] F. Liang, G. Wang, “Study of Mur’s and UPML Absorbing Boundary Condition for the LOD-FDTD Method,” *ICMMT*, v 2, p 947-949, 2008

An efficient implementation of NPML for truncating anisotropic media

Lijuan Shi[1], Lixia Yang[2], Zhichao Cai[2]

[1] School of Science, Jiangsu University, Zhenjiang, China
[2] Department of Communication Engineering, Jiangsu University, Zhenjiang, China
*corresponding author, E-mail: lixiayang@yeah.net

Abstract

In this paper, an efficient implementation of the modified nearly perfectly matched layer (NPML) absorbing boundary conditions (ABCs) for truncating anisotropic media is presented. The primary advantage of the proposed formulation is the simplicity in the FDTD implementations. The complex coordinate stretching in the NPML scheme and the spatial interpolation method are employed in the technique. Numerical results show that the presented scheme has good absorbing performance for anisotropic mediums.

1. Introduction

The finite-difference time-domain method (FDTD) [1] is widely regarded as one of the most popular computational electromagnetic simulation techniques. Nevertheless, to handle open region problems using the FDTD method, efficient and accurate absorbing boundary conditions (ABCs) are required to truncate the computational domains. Since the Mur ABC was proposed in 1981, a number of high effective absorbing boundary condition has been introduced to achieve this goal.

Cummer has introduced an unsplit-field PML formulation named as Nearly Perfectly Matched Layer (NPML) [2]. The NPML has been proven to be fundamentally equivalent to the original PML in Cartesian coordinates [3,4]. The main advantage of the NPML is the simplicity in the FDTD implementations because it does not involve Berenger's field splitting technique. Ramadan introduced the NPML for truncating linear and nonlinear dispersive FDTD grids [5,6]. The NPML is also applied to truncate plasma FDTD domains [7]. In this work, based on the nearly perfectly matched layer (NPML) theory, the implementation of the NPML for truncating anisotropic media FDTD domains will be investigated.

2. Formulation

For a homogeneous anisotropic medium, the Maxwell's equations can be written as

$$\nabla \times \boldsymbol{H} = \overline{\overline{\varepsilon}} \cdot \frac{\partial \boldsymbol{E}}{\partial t} + \overline{\overline{\sigma}} \cdot \boldsymbol{E} \tag{1}$$

$$\nabla \times \boldsymbol{E} = -\overline{\overline{\mu}} \cdot \frac{\partial \boldsymbol{H}}{\partial t} - \overline{\overline{\sigma}}_m \cdot \boldsymbol{H}\,, \tag{2}$$

where $\boldsymbol{E}$ is electric field strength, $\boldsymbol{H}$ is magnetic field strength, and $\overline{\overline{\boldsymbol{\varepsilon}}}$, $\overline{\overline{\boldsymbol{\sigma}}}$, $\overline{\overline{\boldsymbol{\mu}}}$, $\overline{\overline{\boldsymbol{\sigma}}}_m$ are, respectively, permittivity, conductivity , permeability and magnetic conductivity tensor. Here, consider the two-dimensional TM polarization wave as an example. The fields are invariant in the z direction $\partial/\partial z = 0$. Thus, the Maxwell equations are reduced to three partial differential equations as below

$$\left.\begin{aligned} &\frac{\partial H_y}{\partial x} - \frac{\partial H_x}{\partial y} = \varepsilon_{33}\frac{\partial E_z}{\partial t} + \sigma_{33}E_z \\ &\begin{bmatrix} \dfrac{\partial E_z}{\partial y} \\ -\dfrac{\partial E_z}{\partial x} \end{bmatrix} = -\boldsymbol{\mu}_{TM}\begin{bmatrix} \dfrac{\partial H_x}{\partial t} \\ \dfrac{\partial H_y}{\partial t} \end{bmatrix} - \boldsymbol{\sigma}_{\boldsymbol{m}TM}\begin{bmatrix} H_x \\ H_y \end{bmatrix} \end{aligned}\right\}, \tag{3}$$

where

$$\boldsymbol{\mu}_{TM} = \begin{bmatrix} \mu_{11} & \mu_{12} \\ \mu_{21} & \mu_{22} \end{bmatrix}, \boldsymbol{\sigma}_{\boldsymbol{m}TM} = \begin{bmatrix} \sigma_{m11} & \sigma_{m12} \\ \sigma_{m21} & \sigma_{m22} \end{bmatrix}. \tag{4}$$

Using the central difference approximation, Equation (3) can be discretized as

$$\left.\begin{aligned} &\frac{\partial H_y}{\partial x}\Big|_{i,j}^{n+1/2} - \frac{\partial H_x}{\partial y}\Big|_{i,j}^{n+1/2} = \left(\frac{\varepsilon_{33}}{\Delta t} + \frac{\sigma_{33}}{2}\right)\left(E_z\Big|_{i,j}^{n+1} + E_z\Big|_{i,j}^{n}\right) \\ &\begin{bmatrix} H_x\Big|_{i,j}^{n+1/2} \\ H_y\Big|_{i,j}^{n+1/2} \end{bmatrix} = \nu_m\begin{bmatrix} H_x\Big|_{i,j}^{n-1/2} \\ H_y\Big|_{i,j}^{n-1/2} \end{bmatrix} - \kappa_m\begin{bmatrix} \dfrac{\partial E_z}{\partial y}\Big|_{i,j}^{n} \\ -\dfrac{\partial E_z}{\partial x}\Big|_{i,j}^{n} \end{bmatrix} \end{aligned}\right\}, \tag{5}$$

where

$$\left.\begin{aligned} \kappa_m &= \left(\frac{\boldsymbol{\mu}_{TM}}{\Delta t} + \frac{\boldsymbol{\sigma}_{\boldsymbol{m}TM}}{2}\right)^{-1} = \begin{bmatrix} \kappa_{m11} & \kappa_{m12} \\ \kappa_{m21} & \kappa_{m22} \end{bmatrix} \\ \nu_m &= \kappa_m \cdot \left(\frac{\boldsymbol{\mu}_{TM}}{\Delta t} - \frac{\boldsymbol{\sigma}_{\boldsymbol{m}TM}}{2}\right) = \begin{bmatrix} \nu_{m11} & \nu_{m12} \\ \nu_{m21} & \nu_{m22} \end{bmatrix} \end{aligned}\right\}. \tag{6}$$

Using the stretched coordinate NPML formulations [2] and redefining some variables, the space partial derivative of field components in equation (5) can be written as

$$\frac{\partial E_\alpha}{\partial \beta}=\frac{\partial}{\partial \beta}\left(\frac{1}{1+\sigma_\beta/j\omega}E_\alpha\right)=\frac{\partial \tilde{E}_{\alpha\beta}}{\partial \beta}$$
$$\frac{\partial H_\alpha}{\partial \beta}=\frac{\partial}{\partial \beta}\left(\frac{1}{1+\sigma_\beta/j\omega}H_\alpha\right)=\frac{\partial \tilde{H}_{\alpha\beta}}{\partial \beta} \quad , \tag{7}$$

where

$$\alpha\in\{x,y,z\},\quad \beta\in\{x,y,z\},\ \text{and}\ \alpha\neq\beta\ . \tag{8}$$

Substituting equation (7) into equation (5), we obtain

$$\left.\begin{aligned}\frac{\partial \tilde{H}_{yx}}{\partial x}\Big|_{i,j}^{n+1/2}-\frac{\partial \tilde{H}_{xy}}{\partial y}\Big|_{i,j}^{n+1/2}&=\left(\frac{\varepsilon_{33}}{\Delta t}+\frac{\sigma_{33}}{2}\right)\left(E_z\Big|_{i,j}^{n+1}+E_z\Big|_{i,j}^{n}\right)\\ \begin{bmatrix}H_x\big|_{i,j}^{n+1/2}\\ H_y\big|_{i,j}^{n+1/2}\end{bmatrix}&=\nu_m\begin{bmatrix}H_x\big|_{i,j}^{n-1/2}\\ H_y\big|_{i,j}^{n-1/2}\end{bmatrix}-\kappa_m\begin{bmatrix}\frac{\partial \tilde{E}_{zy}}{\partial y}\big|_{i,j}^{n}\\ -\frac{\partial \tilde{E}_{zx}}{\partial x}\big|_{i,j}^{n}\end{bmatrix}\end{aligned}\right\} \tag{9}$$

Here we will limit ourselves to consideration of the H_x component in equation (9). To implement this equation we must consider the actual locations of H_x in the Yee cell. We can obtain

$$H_x\Big|_{i,j+\frac{1}{2}}^{n+1/2}=\left[\nu_{m11}H_x+\nu_{m12}H_y\right]_{i,j+\frac{1}{2}}^{n-1/2}-\left[\kappa_{m11}\frac{\partial \tilde{E}_{zy}}{\partial y}-\kappa_{m12}\frac{\partial \tilde{E}_{zx}}{\partial x}\right]_{i,j+\frac{1}{2}}^{n} \tag{10}$$

Since the value of $H_y\Big|_{i,j+\frac{1}{2}}^{n-1/2}$ and $\frac{\partial \tilde{E}_{zx}}{\partial x}\Big|_{i,j+\frac{1}{2}}^{n}$ in (10) are not available at the location $\left(i,j+\frac{1}{2}\right)$, they must be interpolated from four neighboring quantities [8]. They can be approximated by

$$H_y\Big|_{i,j+\frac{1}{2}}^{n-1/2}=\frac{1}{4}\left[H_y\Big|_{i+\frac{1}{2},j+1}^{n-1/2}+H_y\Big|_{i+\frac{1}{2},j}^{n-1/2}+H_y\Big|_{i-\frac{1}{2},j}^{n-1/2}+H_y\Big|_{i-\frac{1}{2},j+1}^{n-1/2}\right] \tag{11}$$

$$\frac{\partial E_{zx}}{\partial x}\Big|_{i,j+\frac{1}{2}}^{n}=\frac{1}{4\Delta x}\left[E_{zx}\Big|_{i+1,j+1}^{n}+E_{zx}\Big|_{i+1,j}^{n}-E_{zx}\Big|_{i-1,j}^{n}-E_{zx}\Big|_{i-1,j+1}^{n}\right] \tag{12}$$

Finally, we obtain the update equations of H_x as below

$$\begin{aligned}H_x\Big|_{i,j+\frac{1}{2}}^{n+1/2}&=\nu_{m11}H_x\Big|_{i,j+\frac{1}{2}}^{n-1/2}-\frac{\kappa_{m11}}{\Delta y}\left[E_{zy}\Big|_{i,j+1}^{n}-E_{zy}\Big|_{i,j}^{n}\right]\\&+\frac{\kappa_{m12}}{4\Delta x}\left[E_{zx}\Big|_{i+1,j+1}^{n}+E_{zx}\Big|_{i+1,j}^{n}-E_{zx}\Big|_{i-1,j}^{n}-E_{zx}\Big|_{i-1,j+1}^{n}\right]\\&+\frac{\nu_{m12}}{4}\left[H_y\Big|_{i+\frac{1}{2},j+1}^{n-1/2}+H_y\Big|_{i+\frac{1}{2},j}^{n-1/2}+H_y\Big|_{i-\frac{1}{2},j}^{n-1/2}+H_y\Big|_{i-\frac{1}{2},j+1}^{n-1/2}\right]\end{aligned} \tag{13}$$

Similar derivations hold for the H_y and E_z components. According to equation (7) and using the relation $j\omega\rightarrow\partial/\partial t$, the stretched field component $\tilde{H}_{yx}\Big|_{i+\frac{1}{2},j}^{n+1/2}$ can be discretized into the following form

$$\tilde{H}_{yx}\Big|_{i+\frac{1}{2},j}^{n+1/2}=\frac{\left(1-\frac{\sigma_x\Delta t}{2}\right)\tilde{H}_{yx}\Big|_{i+\frac{1}{2},j}^{n-1/2}+H_y\Big|_{i+\frac{1}{2},j}^{n+1/2}-H_y\Big|_{i+\frac{1}{2},j}^{n-1/2}}{1+\frac{\sigma_x\Delta t}{2}} \tag{14}$$

Similarly, the update equations can be obtained for $\tilde{H}_{xy}\Big|_{i,j+\frac{1}{2}}^{n+1/2}$, $\tilde{E}_{zy}\Big|_{i,j}^{n}$ and $\tilde{E}_{zx}\Big|_{i,j}^{n}$.

Finally, the proposed algorithm should be implemented in the following order:

$$\tilde{E}_{\alpha\beta}\Rightarrow H\Rightarrow\tilde{H}_{\alpha\beta}\Rightarrow E\Rightarrow\tilde{E}_{\alpha\beta} \tag{15}$$

3. Numerical verification

In this section, to validate the proposed algorithm for truncating 2-D anisotropic medium, the radiation of an electric dipole is calculated. The cross section of the computational region is shown in Figure 1.

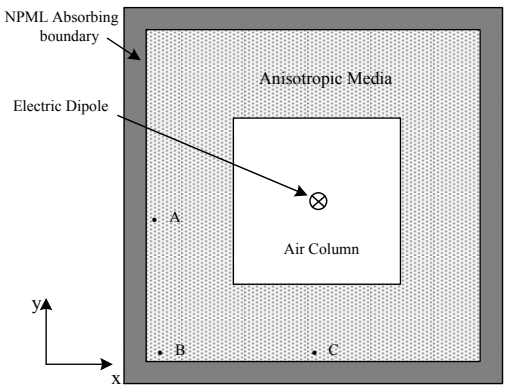

Figure 1: The cross-section diagram of absorbing boundary performance verification model.

The electric dipole is located at the center of the region. The innermost layer is the air square column, containing 20×20 FDTD cells. The middle layer is filled with anisotropic media. There are 40×40 FDTD cells altogether in the two regions.

The six sides of the computational region are all truncated by 6-cell NPML absorbing boundary. The FDTD cell size is $\Delta x = \Delta y = 0.25\text{mm}$. The time step is $\Delta t = \Delta x / 2c_0$, where c_0 is the speed of light. The permittivity tensor of anisotropic media is set as $\overline{\overline{\varepsilon}} = \varepsilon_0 \begin{pmatrix} 2.05 & 0.0866 & 0.0 \\ 0.0866 & 2.15 & 0.0 \\ 0.0 & 0.0 & 0.0 \end{pmatrix}$. Here we select three representative field-observation points. The field-observation point A $(-18\Delta x, 0)$,B $(-18\Delta x, -18\Delta y)$ and C $(0, -18\Delta y)$ are all in the xoy plane. In this example, the electric field of the electric dipole is a differentiated Gaussian pulse expressed by

$$P(t) = 10^6 \cdot \frac{t - t_0}{\tau} \cdot \exp\left[-\frac{4\pi (t - t_0)^2}{\tau^2} \right], \qquad (16)$$

where parameters of the pulse are $\tau = 40\Delta t$ and $t_0 = 0.8\tau$.

For the purpose of comparison, a reference field was computed by using a larger domain with the size of 800×800 FDTD cells, in which the size of the air square column remains unchanged. The computational domain is also terminated by 6-cell NPML absorbing boundary. The three field-observation points are at the same position as in the test grid. There are no reflections from the NPML absorbing layers during the time-stepping span of interest as the reference grid domain is enough large. The reflection coefficient is defined as $R_{dB} = 20\log_{10}\left| F\left\{E_z^R(t) - E_z^T(t)\right\} \Big/ F\left\{E_z^R(t)\right\} \right|$, where $F\{\square\}$ is the Fourier transform operation, $E_z^T(t)$ and $E_z^R(t)$ are the fields computed using the test and the larger domains, respectively [5,6]. Numerical results of reflection coefficient at points A, B and C are shown in Figure 6, which indicates good absorbing performance of the proposed method.

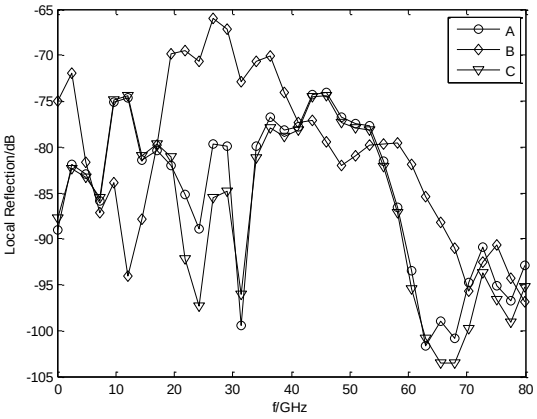

Figure 2: The local reflection at point A, point B, point C.

4. Conclusions

Based on the nearly perfectly matched layer (NPML) theory, a finite-difference time-domain (FDTD) absorbing boundary condition (ABC) is presented for truncating anisotropic medium. In the proposed technique, the complex coordinate stretching in the NPML scheme and the spatial interpolation method are employed. The radiation fields of an electric dipole in anisotropic media are calculated using the presented ABC. The results are numerically verified by the comparison with the reference solutions.

Acknowledgements

This work is supported by the National Natural Science Foundation of China under Grant (No.61072002); Elitist of Liu-Da Summit Project in Jiangsu Province at 2011 under Grant (No. 2011-DZXX-031).

References

[1] A Taflove, S.C. Hagness, *Computational Electrodynamics: The Finite-difference Time-domain Method*, Artech House, Norwood, 2005.

[2] S.A. Cummer, A simple , nearly perfectly matched layer for general electromagnetic media, *IEEE Microwave Wireless Components Letters* 13: 128-130, 2003.

[3] W.-Y Hu, S.A. Cummer, The nearly perfectly matched layer is a perfectly matched layer, *IEEE Microwave Wireless Components Letters* 3: 137-140, 2004.

[4] J.P. Berenger, On the reflection from cummer's nearly perfectly matched layer, *IEEE Microwave Wireless Components Letters* 14: 334-336, 2004.

[5] O. Ramadan, Unconditionally Stable Nearly PML Algorithm for Linear Dispersive Media, *IEEE Microwave Wireless Components Letters* 15: 490-492, 2005.

[6] O. Ramadan, On the Accuracy of the Nearly PML for Nonlinear FDTD Domains, *IEEE Microwave Wireless Components Letters* 16: 101-103, 2006.

[7] Z.-W. Zheng, L.-X. Yang Lixia, Z.-C. Cai, Novel PML absorbing boundary condition of magnetized plasma, *Journal of Jiangsu University* 34: 156-160, 2013.(in Chinese)

[8] J. Schneider, S. Hudson, The finite-difference time-domain method applied to anisotropic material, *IEEE Trans. Antennas and Propaga.* 41: 994-999, 1993.

Electromagnetic scattering from a gyrotropic anisotropic sphere in an off-axis obliquely incident Gaussian beam

Ying-ying Tian, You-lin Geng

Institute of Antenna and Microwaves, Hangzhou Dianzi University, Hangzhou 310018, China

Abstract

An analytical solution to the scattering of an off-axis Gaussian beam obliquely incident by a gyrotropic anisotropic sphere is obtained in the particle-centered system. The incident off-axis Gaussian beam is expanded in terms of spherical vector wave function. The internal electromagnetic fields of the gyrotropic anisotropic sphere are proposed in the matrix form of the spherical vector wave functions. Utilizing the continuous tangential boundary conditions, both the scattered and the internal field coefficients are derived analytically. Numerical calculations are presented. The influences of the beam width and the permittivity tensors on the scattered field distribution are analyzed. The correctness of the theory is verified by comparing our numerical results with the results that the plane wave scattering by a gyrotropic anisotropic sphere.

Key words: Gaussian beams; spherical vector wave functions; electromagnetic scattering

1. INTRODUCTION

Due to increasing applications of anisotropic media and laser sources in radar detection and near-field measurement, the study of this paper is of great urgency to exploit the potential of both the scattered field and internal field in the gyrotropic sphere[1,2,3]. Based on the local approximation to the off-axis beam shape coefficients and the coordinate rotation theory, the off-axis obliquely incident Gaussian beam is expanded with the spherical vector wave functions in the primary coordinate of the gyrotropic anisotropic sphere. The internal fields can be expanded by the spherical vector wave functions. Utilizing the continuous tangential boundary conditions, both the scattered and the internal fields coefficients are derived analytically. A special case is between this paper with a plane wave where the beam width $\omega_0 = 20\lambda$, and they are agree with very well. A time dependence of the form $\exp(-i\omega t)$ is assumed for all the EM fields but is ignored throughout the treatment.

2. THEORETICAL FORMULATIONS

The formula of the incident Gaussian beam can be found in the reference [2]. The internal electromagnetic fields are proposed in the matrix form of the spherical vector wave functions and can be found in the reference [1].

3. NUMERICAL CALCULATIONS

Calculations were performed for an x' polarized off-axis Gaussian beam obliquely

incident on a center-located gyrotropic anisotropic sphere of radius a, with Euler angles α, β and γ. The beam is assumed to have an electric-field amplitude equal to unity in the beam waist center located at (x_0, y_0, z_0) in the particle-centered system $oxyz$. The RCS distributions for the far scattered field are presented in the particle-centered system.

Because this are no numerical results for the gyrotropic anisotropic sphere scattering by an off-axis Gauss beam, to verify the correctness of our theory and numerical results, we give two figures, there are Fig. 1 and Fig. 2. In Fig. 1, the beam waist radius $\omega_0 = 20\lambda$. Fig. 1 is the numerical results between this paper and the plane wave scattering by a lossless gyrotropic anisotropic sphere where the electrical size is $k_0 a = 0.75\pi$ and $\varepsilon_g = 0$, $\varepsilon_s = 2.0\varepsilon_0$, $\varepsilon_s\varepsilon_t = 2.4\varepsilon_0$, $\mu_g = 0$, $\mu_s = 2\mu_0$, $\mu_s\mu_t$ is equal μ_0, $0.4\mu_0$ and $1.6\mu_0$, and $(x_0, y_0, z_0) = (0,0,0)\lambda$, $\alpha = \beta = \gamma = 0^o$. Fig.2 are RCS of the *E*-plane and *H*-plane made for an off-axis Gaussian beam obliquely incident on a titanium dioxide sphere $\varepsilon_s = 7.197\varepsilon_0, \varepsilon_s\varepsilon_t = 5.913\varepsilon_0$. The permeability and permittivity tensor elements are assumed to be $\mu_s = \mu_0$, $\mu_t = 1, \mu_s\mu_g = 0$ and $\varepsilon_s\varepsilon_g = 0, \omega_0 = 3.0\lambda$ where the electrical dimension is chosen as the $k_0 a = 2\pi$. The obliquely incident angle and the beam waist positioning are taken arbitrarily, that is, $(x_0, y_0, z_0) = (1.0,1.0,0.5)\lambda$, $\alpha = 8^\circ, \beta = 6^\circ, \gamma = 5^\circ$. From Fig. 1 and Fig. 2, it is shown that when the beam waist radius is very large, the numerical results of this paper are coincided with that of the plane wave, and it is shown that the theory and Fortran programs for this paper are correct.

From this, we give some other numerical results of a generous gyrotropic anisotropic sphere by an off-axis Gaussian beam, they are shown in Fig. 3 and Fig. 4.

The effects of the beam width on the RCS in the *E*-planes are shown by Fig. 3. The permeability and permittivity tensor elements are assumed to be $\mu_s = (2+i)\mu_0$, $\mu_t\mu_s = (1+0.5i)\mu_0$, $\mu_s\mu_g = 0.8\mu_0$ and $\varepsilon_s = (1.5+0.1i)\varepsilon_0$, $\varepsilon_s\varepsilon_t = (3+2i)\varepsilon_0$, $\varepsilon_s\varepsilon_g = 0.8\varepsilon_0$, where the electrical dimension is $k_0 a = 2\pi, \alpha = \beta = \gamma = 0^o$, $(x_0, y_0, z_0) = (0,0,1.0)\lambda$. It is obvious that the RCS for Gaussian beams is smaller than that for a plane wave because of the influence of the beam shape coefficients. As the beam width increases, the RCS approaches that for plane wave incidence. As expected, our results in the case of Gaussian beam incidence with a relatively large waist radius of $\omega_0 = 20\lambda$ are in excellent agreement with the results in the case of plane wave incidence.

Fig. 4 are RCS of the *E*-plane and *H*-plane made for an off-axis Gaussian beam obliquely incident on the sphere. The permeability and permittivity tensor elements are assumed to be $\mu_s = \mu_0$, $\mu_t = 1$, $\mu_s\mu_g = 0.1\mu_0$ and $\varepsilon_s = 2.25\varepsilon_0$, $\varepsilon_s\varepsilon_t = 2.3\varepsilon_0$, $\varepsilon_s\varepsilon_g = 0.1\varepsilon_0$, $\omega_0 = 3.0\lambda$ where the electrical dimension is chosen as the $k_0 a = 2\pi$. The obliquely incident angle and the beam waist positioning are taken arbitrarily, that is, $(x_0, y_0, z_0) = (1.0,1.0,0.5)\lambda$, $\alpha = 6^\circ, \beta = 8^\circ, \gamma = 5^\circ$. It is shown that both the

intensity and the angular distribution of the RCS are influenced by the permittvity tensors.

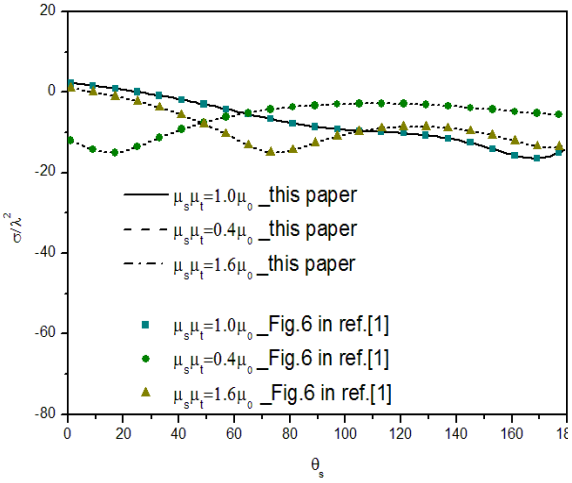

Fig. 1 Results of lossless gyrotropic anisotropic sphere compared with those in [1].

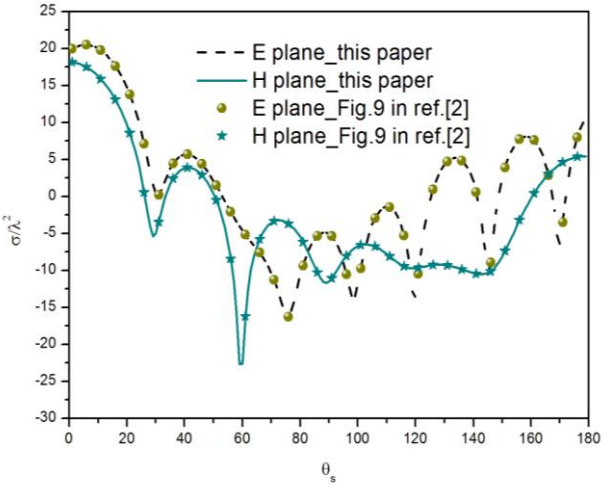

Fig. 2 Results made for an off-axis Gaussian beam obliquely incident on a titanium dioxide sphere.

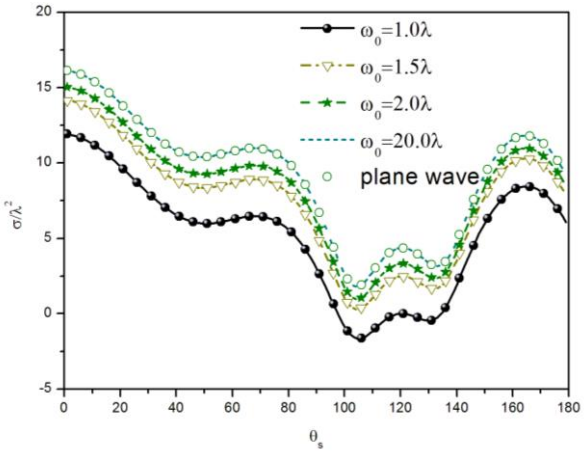

Fig. 3 Effects of the beam width on RCS.

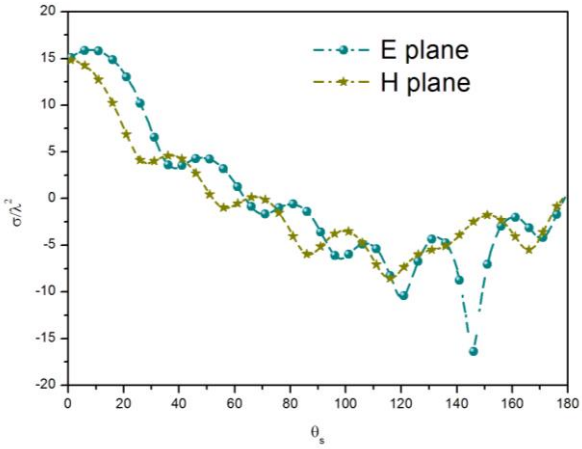

Fig. 4 Results made for an off-axis Gaussian beam obliquely incident on the sphere.

4.CONCLUSIONS

Numerical results show that with the beam waist radius increasing, the distribution of the RCS is increasing.

REFERENCES

[1] J. L.-W. Li, W.-L.Ong and K. H. -R. Zheng, "Anisotropic scattering effects of a gyrotropic sphere characterized using the T-matrix method," Phys. Rev. E, vol.85, no.3, pp.036601, 2012.

[2] Q. K. Yuan, Z. S Wu, and Z. J. Li , "Electromagnetic scattering for a uniaxial anisotropic sphere in an off-axis obliquely incident Gaussian beam," J. Opt. Soc. Am. A, vol.27, no. 6, pp.1457-1465, June 2010.

[3] Z. S Wu, Z. J. Li, H. Li, Q. K. Yuan, and H. Y. Li , "Off-Axis Gaussian Beam Scattering by an Anisotropic Coated Sphere," IEEE Transactions on antennas and Propagation, vol.59, no.12, pp.4740-4748, 2011.

Broadband low-loss and small units left-handed metamaterials composed of slotted “工” shaped

Dong Huai-Jing[1] Geng You-Lin[1] He Zheng-Rui[1]
[1] (Hangzhou Dianzi University, Institue of Antenna and Microwaves, Hangzhou 310018, China)
*corresponding author, E-mail: gengyoulin@aliyun.com

Abstract

A method of designing a single side left-handed structure based on the integration of electric resonator and magnetic resonator is proposed in this paper. The left-handed units are formed by slotted “工” shaped placed on one side of the substrate, and then make them arranged in periodic structures. The results of HFSS software simulation and a series of effective electromagnetic parameters extraction show that the left-handed structure exhibits negative effective permittivity and permeability simultaneously in a frequency range from 8.65 GHz to 14.17 GHz. Its relative bandwidth reaches 48.4%, and the unit electrical length and loss are less than the same type of structures. This new structure lays a foundation for left-handed metamaterials widely used.

1. Introduction

In 1986, veselogo firstly proposed the left-handed materials[1], and indicated that this structure had negative permittivity and permeability in some certain electromagnetic spectrum, it behaved some marvelous effect, such as negative refraction[2], perfect Lens[3], reversed Doppler effect[4], etc. Due to its excellent electromagnetic characteristics, The left-handed materials has many wide and important applications in the optical imaging[3], antenna system, microwave component, electromagnetic stealth fields and so on. However, the theory of left-handed materials was firstly proposed by Smith[5] until 30 years later. He proposed the structure combined by split ring resonators (SRR) and continuous rods (ROD). The study of left-handed materials entered a fast track of growth since then.

In recent ten years, the left-handed material develops quickly. Different design types were raised. Generally, it can be divided into two types by the direction of the incident electromagnetic wave, one form is the incident electromagnetic wave parallels to the dielectric substrate, such as the “H” shaped structure, symmetrical ring structure[6], “巨”shaped structure, Omega structure[7] and so on; Another form is the incident electromagnetic wave perpendiculars to the dielectric substrate, such as the structure of metal wires, the net structure[8], the grid shaped structure[9] and so on. However, compared to the paralleled incident structure, the perpendicular incident structure has previous disadvantages, it cause the shielding effect easily, higher absorption and so on, which should be avoided completely in the practical environment. According to the structure types, the paralleled incident structure can be divided into two types: single side and double sides. Because of the double sides structure need to be etched on the both sides of the dielectric substrate, which makes harder to produce and a bigger loss as well, it is not the best practical structure. So, at present time the study of the single side paralleled incident left-handed material structure is the main direction. Many types of single side structure have been coming at present time. Such as the left-handed material with the cross metal wire structure of Nasrin[10], the left-handed material combined of magnetic resonator and the plane of the short metal wire by Chen Chun-hui, and the cross ring structure by Yang Chen, the double S structure by Sun Yong-zhi. However, there are series problems in these structures, like complex structure, narrow bandwidth, large loss and volume, which seriously limit the application and development of left-handed materials. So the design of single side left-handed unit with simple structure, wide band and low loss has been the focus of study in this field.

This paper presents a slotted “工”shaped left-handed materials. It is a one side structure and the electric and magnetic resonators are integrated on the same side of the medium substrate. The structure was simulated using the commercial electromagnetic software HFSS. And the equivalent parameters can be extracted by NRW algorithm[11、12]. The result shows that in the band from 8.65 to 14.17GHz, the effective permittivity and permeability are simultaneously negative. The relative bandwidth up to 48.4 percent, the center frequency of unit length is only 0.058, it truly realized the design of broadband and low consumption of small units of left-handed materials.

2. Design and simulation analysis of unit

To realize left-handed properties, the permittivity and permeability should simultaneously negative. According to the Left-handed medium transmission line theory, when the parallel inductance and capacitance in series appear on the direction of electromagnetic wave propagation at the same time, we can got the left-handed characteristics. And the more simple and direct to produce the parallel inductance and capacitance in series, the larger bandwidth left-handed properties get as long as the smaller loss and the smaller

volume. According to this theory, this paper designs a kind of left unit structure integrated by electric and magnetic resonator. As shown in Fig.1 (a), a "工" shaped metal structure with prominent ends and the middle slit etched on the FR4 substrate whose thickness is 0.5mm and dielectric constant is 4.4. Among them, short horizontal metal line length is 1.4mm, long vertical metal line length is 3.16mm, the width of all metal is 0.12mm,the thickness of which is 0.035mm. The gap size on the long vertical metal line is 1.5 × 0.05mm.

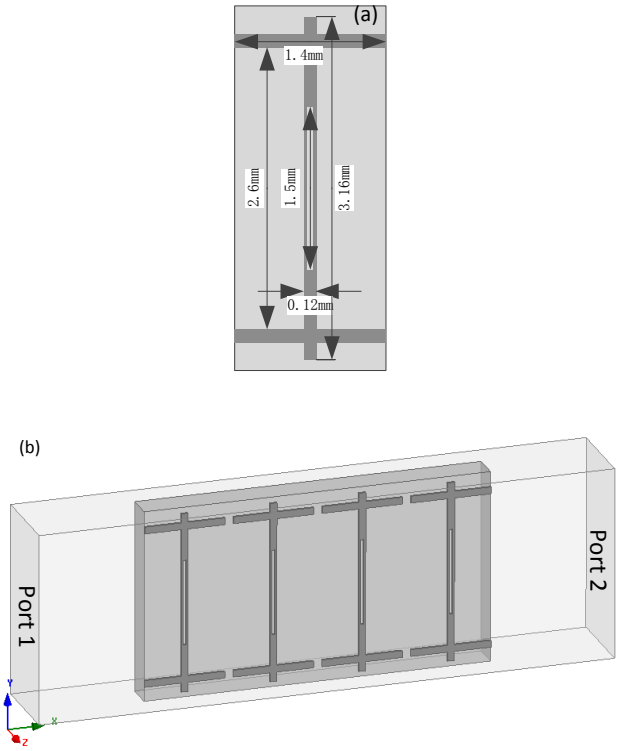

Figure 1: (a) The size of unit structure;
(b) The software simulation model

In order to verify the structure has left-handed characteristic, we use the high frequency simulation software Ansoft HFSS to simulate and optimize the structure. As shown in Fig. 1 (b), there is a simulated model which consists of four units placed in the center of waveguide. The distance between Units is 0.15mm.The waveguide wall is composed of two pairs of ideal electrical wall (PEC) and ideal magnetic wall (PMC), the distance between the up and down PEC is 3.36mm, the distance between the before and after PMC is 1.524mm. The electromagnetic waves communicate from port 1 to the port 2 along the +x direction. After this, the simulated model in waveguide can simulate the reflection and transmission properties of the electromagnetic plane wave from the port 1 to Port 2 through the left hand medium. The simulation analysis can help us get the reflection and transmission coefficients of amplitude and phase variation with frequency curve of the two port waveguide. As shown in Fig. 2, the amplitude and phase in two frequency point 8.65GHz and 14.17GHz has a sudden change at the same time and the band between is pass band. In addition to, we can extract the left hand equivalent permittivity, permeability, refractive index through the NRW algorithm. And then we can determine the characteristics of the left hand in the end. As shown in Fig. 3, the simulated structure arrays have negative equivalent permittivity, permeability and refractive index at the same time in the range of 8.65-14.17GHz, Which reflect the left-handed property of the deformation "工" shaped structure. And in the range of 8.65-14.17GHz the amplitude of S21 is more than -0.6dB. This shows that the transmission loss less than 0.15dB per unit.

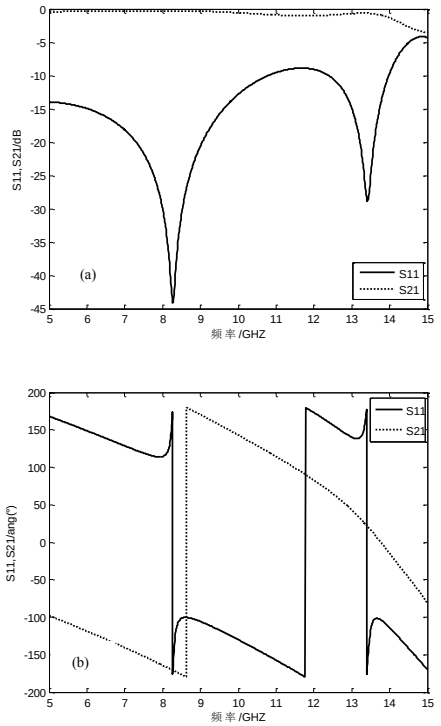

Figure 2: (a) The amplitude of S parameters;
(b) The phase of S parameters

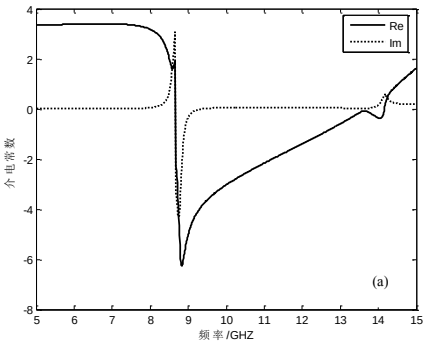

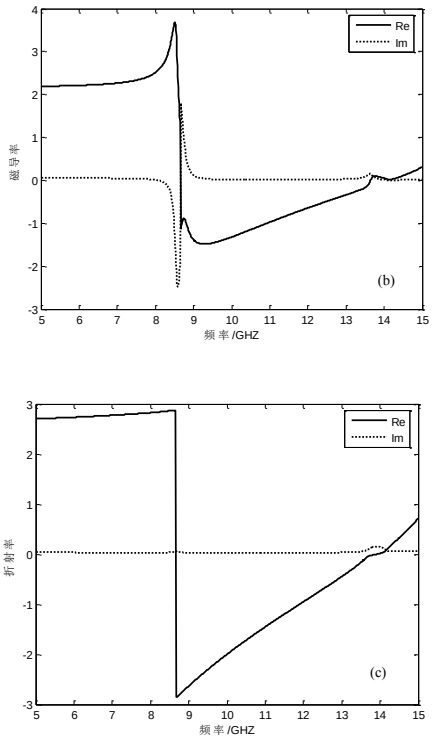

Figure 3: (a) The equivalent permittivity;
(b) The effective permeability;
(c) The refractive index

3. Conclusions

According to the transmission line theory, this paper puts forward a new left-handed structure-slotted "工" shaped structure. The software simulation proved that: the structure has left hand characteristic in 8.65-14.17GHz. The absolute bandwidth is 5.52GHz. The relative bandwidth is 48.4%. At the center frequency, the electric unit of length is about 0.058, and transmission loss of the average unit is below 0.15dB. Compared with other structures, the structure not only reduces the loss, but also reduces the anisotropy which caused by the too big electrical size. At the same time, it also greatly expand the bandwidth of left-handed materials. Which bring it broad prospects in application.

References

[1]. Veselago V G， The electrodynamics of substances with simultaneously negative values of ε and μ, Sov. Phys. Usp. 10:509-514,1968

[2]. Shelby R A, Smith D R, Schultz S, Experimental verification of a negative index of refraction, Science 292 :77-79,2001

[3]. Pendry J B,Holden A J, Robbins D J, Magnetism from conductors and enhanced nonlinear phenomena, IEEE Trans.Microwave Theory Tech 47: 2075-2084, 2000

[4]. Seddon N, Bearpark T, Observation of the inverse Doppler Effect, Science 302: 1537-1540, 2003

[5]. Smith D R, Padilla W J, Vier D C, Nemat-Nasser S C, Schultz S, Composite medium with simultaneously negative permeability and permittivity, Phys. Rev. Lett. 84: 4184-4187, 2000

[6]. Grzegorczyk T M, Moss C D, Lu Jie, Chen X D, Pacheco J Jr, Kong J A, Properties of left-handed metamaterials: transmission, backward phase, negative refraction, and focusing, IEEE Trans. Microwave Theory Tech 53: 2956-2957, 2005

[7]. Ran L, Huangfu J, Chen H, Li Y, Zhang X, Chen K, Kong J A, Microwave solid-state left-handed material with a broad bandwidth and an ultralow loss, Phys. Rev. B 70: 73101-73102, 2004

[8]. Kafesaki M, Tsiapa I, Katsarakis N, Koschny T, Left-handed metamaterials: The fishnet structures Fundamentals and Applications, Phys. Rev. B 75: 235114:1-9, 2007

[9]. Zhou J F, Zhang L, Tuttle G, Koschny T, Soukoulis C M, Negative index materials using simple short wire pairs, Phys. Rev. B 73: 041101-041105, 2006

[10]. Nasrin A, Keyvan Forooraghi, Zahra Atlasbaf, A Wideband Uniplanar Polarization Independent Left-Handed Metamaterial, IEEE Antennas and Wireless Propagation Letters 10: 524-527, 2011

[11]. Zilokowski E W, Design, fabrication, and testing of double negative metamaterials, IEEE Trans. Antenna. Propag. 51: 1516-1529, 2003

[12]. Chen H S, Zhang J J, Bai Y, Luo Y, Ran L X, Jiang Q, Kong J A, Experimental retrieval of the effective parameters of metamaterials based on a waveguide method, Opt. Express 14: 12944-12949, 2006

Analytical solution to electromagnetic scattering by a gyrotropic anisotropic spherical shell

Youlin Geng

Institue of Antenna and Microwaves, Hangzhou Dianzi University, Hangzhou, China
E-mail: gengyoulin@aliyun.com

Abstract

Based on the spherical vector wave function in homogeneous gyrotropic anisotropic medium, and the first and second Bessel function satisfying the same different equation and recursive formula, the electromagnetic filed in gyrotropic anisotropic medium can be expressed as the addition of the first and the second spherical vector wave function in gyrotropic medium, and the electromagnetic fields in the inner and outer space can be expressed as the spherical vector wave function in free space. Applying the continue boundary conditions in the surface of the gyrotropic anisotropic spherical shell, the expansion coefficients of electromagnetic fields in gyrotropic anisotropic medium, inter fields in free space, and the scattering fields in free space can be obtained. Analytical solution of a plane wave scattering by a gyrotropic anisotropic spherical shell can be derived. one special case of numerical results is given between this paper and the mode expansion with T-matrix where the inner radius approaches 0.

1. Introduction

Considerable attentions have been paid to the interaction of electromagnetic fields with anisotropic medium [1-5] during the past decades. Primarily, this increasing interest in anisotropic media is due to the potential application in the fields of antennas, radar cross sections and microwave/millimeter wave communication system.

In recent years, electromagnetic scattering by optically anisotropic magnetic particles [6], gyrotropic particles [7], gyrotropic particles [8] and a radially multilayered gyroelectric sphere [9] have been studied based on the vector spherical wave functions (SVWFs) combined with T-matrix method.

On the base of the expansion of the plane wave factors in terms of SVWFs in isotropic medium[10] and the Fourier transform, SVWFs in source-free uniaxial, plasma, ferrite and gyrotropic anisotropic medium are derived and a plane wave scattering by anisotropic spherical medium have been done[11-15] by the author and co-workers. But SVWFs solution to the scattering by a gyrotropic anisotropic spherical shell has not been worked out, this paper discusses this problem, that is, the SVWFs solution to electromagnetic scattering of a plane wave by a gyrotropic anisotropic shell.

Because the first and second SVWFs in gyrotropic anisotropic medium satisfy the same differential equations and recursive formula, electromagnetic fields in a gyrotropic anisotropic spherical shell can be expressed as the addition of the first and the second SVWFs in gyrotropic anisotropic media. Applying continue boundary conditions at the surface of the gyrotropic anisotropic spherical shell, the field expansion coefficients of electromagnetic fields in terms of SVWFs in the gyrotropic spherical shell and free space can be derived. Numerical results for the very general gyrotropic anisotropic shell are obtained and those in special cases are compared between the present method where the inner radius approaches 0 and homogeneous gyrotropic anisotropic sphere[8].

2. Electromagnetic fields in homogeneous gyrotropic media

Fig. 1 shows the cross section of a gyrotropic anisotropic spherical shell. The outer and inner radii of the gyrotropic anisotropic shell are a_1 and a_2, respectively. In this paper, the region 1 is gyrotropic anisotropic medium, where their permittivity and permeability tensor are $\bar{\varepsilon}$ and $\bar{\mu}$, the region 0 and region 2 are free space whose permittivity and permeability are ε_0 and μ_0. This structure is illuminated by a plane wave (which have a unity amplitude of the electric component, with the polarization along +x-direction and propagation in the +z-direction).

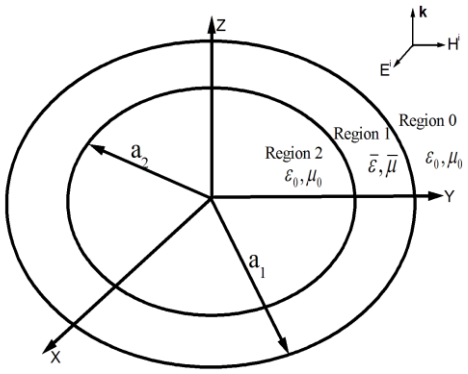

Fig. 1 The geometry of scattering by a gyrotropic spherical shell

From the Source-free Maxwell' equations, the vector wave equation for the electric field in a gyrotropic anisotropic medium (region 1) can be written in the following form [14,15]

$$\nabla\times(\bar{\mu}^{-1}\cdot\nabla\times\boldsymbol{E})-\omega^2\bar{\varepsilon}\cdot\boldsymbol{E}=0 \qquad (1)$$

where the permittivity tensor $\bar{\varepsilon}$ and permeability tensor $\bar{\mu}$ can be written as [8,14,15]

$$\bar{\varepsilon}=\begin{bmatrix}\varepsilon_t & -i\varepsilon_g & 0\\ i\varepsilon_g & \varepsilon_t & 0\\ 0 & 0 & \varepsilon_z\end{bmatrix} \qquad (2a)$$

$$\bar{\mu}=\begin{bmatrix}\mu_t & -i\mu_g & 0\\ i\mu_g & \mu_t & 0\\ 0 & 0 & \mu_z\end{bmatrix} \qquad (2b)$$

Using the Fourier transform[11-14] and the expansion of the plane wave factors in terms of SVWFs in isotropic medium[6], and the character of spherical Bessel functions[16,17], electromagnetic fields in homogenous gyrotropic spherical medium can be expressed as

$$\vec{E}=\sum_{l=1}^{2}\sum_{q=1}^{2}\sum_{mnn'}F_{mn'q}^{(l)}\int_0^{\pi}[A_{mnq}^{e}\vec{M}_{mn}^{(l)}(\vec{r},k_q)+B_{mnq}^{e}\vec{N}_{mn}^{(l)}(\vec{r},k_q)+C_{mnq}^{e}\vec{L}_{mn}^{(l)}(\vec{r},k_q)]\times P_{n'}^{m}(\cos\theta_k)k_q^2\sin\theta_k d\theta_k \qquad (3a)$$

$$\vec{H}=\sum_{l=1}^{2}\sum_{q=1}^{2}\sum_{mnn'}F_{mn'q}^{(l)}\int_0^{\pi}[A_{mnq}^{h}\vec{M}_{mn}^{(l)}(\vec{r},k_q)+B_{mnq}^{h}\vec{N}_{mn}^{(l)}(\vec{r},k_q)+C_{mnq}^{h}\vec{L}_{mn}^{(l)}(\vec{r},k_q)]\times P_{n'}^{m}(\cos\theta_k)k_q^2\sin\theta_k d\theta_k \qquad (3b)$$

in Eqs. (3), n' and n are summed up both from 0 to $+\infty$ while m is summed up from -n to n, and **r** is pointing in the (θ , Φ)-direction in the spherical coordinates. $A_{mnq}^{L}(\theta_k)$, $B_{mnq}^{L}(\theta_k)$ $C_{mnq}^{L}(\theta_k)$ (where L=e or h) and eigenvalues k_q (q=1,2) are defined in [6,9]. $F_{mnq}^{(l)}(l=1,2;\ q=1,2)$ are unknowns to be determined by the boundary conditions. $\vec{M}_{mn}^{(l)}$, $\vec{N}_{mn}^{(l)}$, and $\vec{L}_{mn}^{(l)}$ are SVWFs in isotropic media[6-9,10-12].

The incident plane waves ($\vec{E}^i,\vec{H}^i$) and scattering waves ($\vec{E}^s,\vec{H}^s$) in region 0 [6-15], electromagnetic fields($\vec{E}_2,\vec{H}_2$) in region 3 can be expressed in terms of SVWFs in isotropic medium(free space)[16].

The continue boundary conditions are in the interface of the gyrotropic anisotropic spherical shell can be given

$$\vec{E}\big|_t=\vec{E}^i\big|_t+\vec{E}^s\big|_t,\quad \vec{H}\big|_t=\vec{H}^i\big|_t+\vec{H}^s\big|_t,\quad r=a_1 \qquad (4a)$$

$$\vec{E}\big|_t=\vec{E}_2\big|_t,\qquad \vec{H}\big|_t=\vec{H}\big|_t\qquad r=a_2 \qquad (4b)$$

Submitting incident wave ($\vec{E}^i,\vec{H}^i$) and scattering wave ($\vec{E}^s,\vec{H}^s$) in region 0, electromagnetic fields in the gyrotropic anisotropic medium (region 1), region 2 ($\vec{E}_2,\vec{H}_2$) into boundary condition, the expansion coefficients in terms of SVWFS in gyrotropic medium can be obtained, and then the expansion coefficients of scattering filed in terms of SVWFs are derived, and in the later Radar cross sections(RCSs) of a plane wave from a gyrotropic anisotropic spherical shell can be given.

3. Numerical results and discussion

In the later section, some formula of a plane wave scattering by a gyrotropic anisotropic spherical shell has been derived, and the numerical results of a plane wave scattering by a gyrotropic anisotropic spherical shell is given in this section. The incident plane wave is assumed to have an electric-field amplitude equal to unity, to be polarized in parallel to +x, and to propagate in the +z-direction.

Because we didn't find some numerical results about the scattering by a gyrotropic shell in some reference, to demonstrate the accuracy of the solutions achievable by using the present method, we compare bistatic radar cross sections (RCSs) in E-plane (xoz-plane as shown in Fig. 1) and H-plane (yoz-plane as shown in Fig. 1) with the homogeneous gyrotropic anisotropic sphere [8], as shown in Fig. 2.

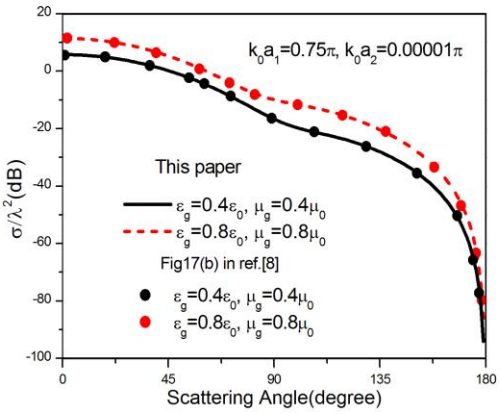

Fig.2 The RCSs between this paper with reference[8] where the inner radius approaches 0

Fig. 2 plots the radar cross sections (RCSs) versus the scattering angle for gyrotropic anisotropic spherical shell by comparison to the results from [8], in which the homogeneous gyrotropic anisotropic permittivity and permeability tensors are as follows: $\varepsilon_t=\varepsilon_0$, $\varepsilon_z=0.4\varepsilon_0$, $\mu_t=\mu_0$, $\mu_z=0.4\mu_0$, $\varepsilon_g=0.4\varepsilon_0$ and $\mu_g=0.4\mu_0$ or $\varepsilon_g=0.8\varepsilon_0$ and $\mu_g=0.8\mu_0$, the electric sizes are assumed to be $k_0a_1=0.75\pi$ and $k_0a_2=0.0004\pi$, and N is taken to be 6. From Fig. 2, it is shown that the results obtained by this proposed scheme agree very well with those from [8]. Note that the homogeneous gyrotropic sphere is a special case of the gyrotropic anisotropic shell.

Some other numerical results will be presented in the conference.

4. Conclusions

The SVWF expansion solution to the plane wave scattering by a gyrotropic anisotropic spherical shell is obtained analytically in this paper. The solution has only one-dimensional integral which can be calculated by Gauss integral[17] easily. Numerical results are obtained using the present method and compared with homogeneous gyrotropic sphere[8] and a fairly good agreement is observed. The present analysis is believed to be useful in antenna and satellite communication system designs.

Acknowledgements

This work is partially supported by the National Natural Science Foundation of China (NSFC), the No. is 60971047.

References

[1] H. F. Ma, J. F. Zhang, X. Chen, Q. Cheng, and T. J. Cui, "CG-FFT algorithm for three-dimensional inhomogeneous and biaxial metamaterials," *Waves in Random and Complex Media*, vol. 19, no. 1, pp. 49–64, 200

[2] X. Q. Sheng, and Z. Peng, "Analysis of scattering by large objects with off-diagobally annisotropic material using finite element-boundary integral-multilevel fast multipole algorithm," *IET Microw. Antennas Propag*., vol. 4, pp.492-500, 2010.

[3] L. Hu, L.-W. Li, and T.-S. Yeo, "Analysis of scattering by large inhomogeneous bi-anisotropic objects using AIM," *Progress In Electromagn. Res*., vol. 99, pp.21-36, 2009.

[4] C.-W. Qiu, L. W. Li, T. S. Yeo, and S. Zouhdi, "Scattering by and rotationally symmetric anisotropic spheres: Potential formulation parametric studies", *Physical Review E*, vol.75, 026609/1-8, 2007

[5] Papadakis S. N., N. K. Uzunoglu and C. N. Capsalis, Scatteing of a plane wave by a general anisotropic dielectric ellipsoid, *J. Opt. Soc. Am. A*, vol. 7, no. 6, pp.991-997, 1990

[6] Z. F. Lin and S. T. Chui, Electromagnetic scattering by optically anisotropic magnetic particle, *Physical Review E*, vol. 69, no. 5, p. 056614, 2004

[7] Le-Wei Li, Wee-Ling Ong. A new solution for charactering electromagnetic scattering by a gyroelectric sphere, *IEEE Trans. Antennas and Propagations*, vol. 59, No. 9, 2011.

[8] J. L.-W. Li, W.-L.Ong and K.H.-R. Zheng, Anisotropic scattering effects of a gyrotropic sphere characterized using the T-matrix method, *Physical Review E*, vol. 85, 2012.

[9] L. Cao, J. L. W. Li, J. Hu, A new T-matrix formulation for electromagnetic scattering by a radially multilayered gyroelectric sphere, *IEEE Trans. on Antennas and Propagation*, vol.61, no.2, pp.836-842, 2013

[10] D. Sarkar, and N. J. Halas, "General vector basis function of Maxwell's equations, " *Physical Review E*, vol.56, no.1, pp.1102-1112, 1997

[11] Y. L. Geng, X. B. Wu, L. W. Li, B. R. Guan, Mie scattering by a uniaxial anisotropic sphere, *Physical Review E*, vol. 70, pp. 056609/1-8, 2004

[12] Y. L. Geng, X. B. Wu, L. W. Li, Analysis of electromagnetic scattering by a plasma anisotropic sphere, *Radio Science*, vol.38, No.6, 1104/1-12, 2003

[13] Y. L. Geng, X. B. Wu, A plane electromagnetic wave scattering by a ferrite sphere, *Journal of Electromagnetic Waves and Applications*, vol.18, No.2, pp161-179, 2004

[14] Y. L. Geng, The analytical solution of electromagnetic scattering by a general gyrotropic sphere," *IET Microwaves, Antennas & Propagation*,vol.6, no.11, pp.1244-1250, 201

[15] Y. L. Geng, C. W. Qiu, Extended Mie theory for a gyrotropic-coated conducting sphere: an analytical approach," *IEEE Trans. Antennas and Propagation*, vol.59 No.11, pp.4364-4368, 2011

[16] W. C. Chew, *Waves and Fields in Inhomogeneous media*, Van Nostrand, New York, 1990

[17] M. Abramowitz, and I. A. Stegun, Handbook of Mathematical Functions with Formulas, Graphs, and Mathematical Tables, Dover Publications, Inc., New York, 1972.

An ultra-wideband monopole antenna achieved by using metamaterial cladding with an I-shaped structure array in S/C-band

Yan N. Jiang, Wen C. Zhang, Wei P. Cao, Jiao Wang*

Key Laboratory of Cognitive Radio and Information Processing (Guilin University of Electronic Technology), Ministry of Education, Guilin, China
*corresponding author, E-mail: wangjiao@guet.edu.cn

Abstract

We propose an ultra-wideband antenna comprising of a monopole antenna and a single-side I-shaped structure (ISS) metamaterial (MM) cladding. Presence of the ISS MM cladding improves significantly the performance of the antenna, i.e., the bandwidth of the UWB monopole antenna is broadened to 1.98–5.80 GHz (a part of the S/C-band) and the radiation patterns are also stable.

Index Terms: Monopole Antenna, Ultra-wideband (UWB), Metamaterial (MM) Clad, Bandwidth.

1. Introduction

Ultra-wideband (UWB) communication systems have become an increasing attractive wireless topic in both the academic and the industrial sectors as a result of commercial systems such as indoor and hand-held wireless communication [1]. Benefiting from UWB's wide frequency range, huge information capacity, and high data transmission capability, UWB antenna is widely investigated [2].

A quarter-wave monopole antenna has many applications because of their compact dimensions and potential usefulness for a wide variety of wireless application. However, it is well known a monopole antenna has limitations in bandwidth attributing to a large mismatch [3-4]. This is contradictory to many UWB applications. So, metamaterial (MM) techniques on bandwidth enhancement of the antennas have been proposed [5]. In this paper, we propose a single-side I-shaped structure (ISS) MM cladding which introduces a proper resonant frequency into a monopole to realize an UWB monopole antenna with stable radiation patterns in about 1.98–5.80 GHz (a part of the S/C-band).

2. ISS MM cladding characterization

The unit cell of the MM cladding is the ISS as shown in Fig. 1(a). The equivalent circuit can be seen in Fig. 1(b) [6]. As an inductive-capacitive resonator, the ISS has a strong electric response, that is, the central strip of the ISS provides an inductor and the small gap between the adjacent unit cells produces a capacitor. The thinner or longer the line, the higher ISS inductance; the smaller the gap, the larger ISS capacitance.

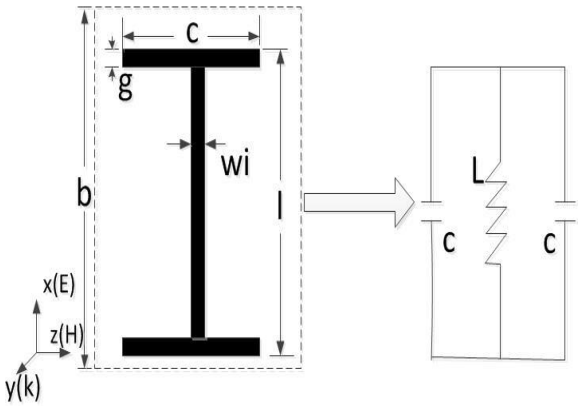

(a) (b)

Figure 1: Geometry (a) and equivalent circuit (b) of ISS unit cell. All dimensions being in millimeters: c=2, b=5, l=4.4, wi=0.6, g=0.2.

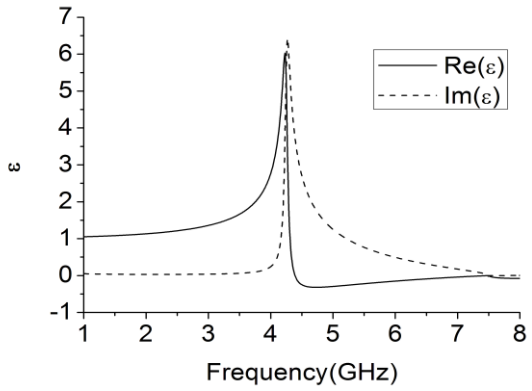

Figure 2: retrieved effective permittivity.

The periodic ISS array with capacitive loaded strips, namely, MM cladding is analyzed by effective permittivity (in order to extract the effective permittivity, S-parameters retrieval method is applied [7]). The retrieved effective permittivity, which is based on the single-side ISS only printed on one side of the FR-4 substrate, is shown in Fig. 2. It can be seen that the real part of the effective

permittivity is demonstrated to be negative in the band of about 4.4-6GHz.

3. Simulation and measurement

The proposed UWB monopole antenna system is shown in Fig. 3. The monopole is surrounded by a MM cladding. The MM cladding consists of 12×8 ISS copper unit cells printed on outer side of the FR-4 substrate with ε_r=4.9 and δ_{tan}=0.025. The thicknesses of the substrate and the copper are 0.150mm and 0.017mm respectively. The height of the monopole is 28mm, namely, theoretical resonant frequency is 2.5GHz.

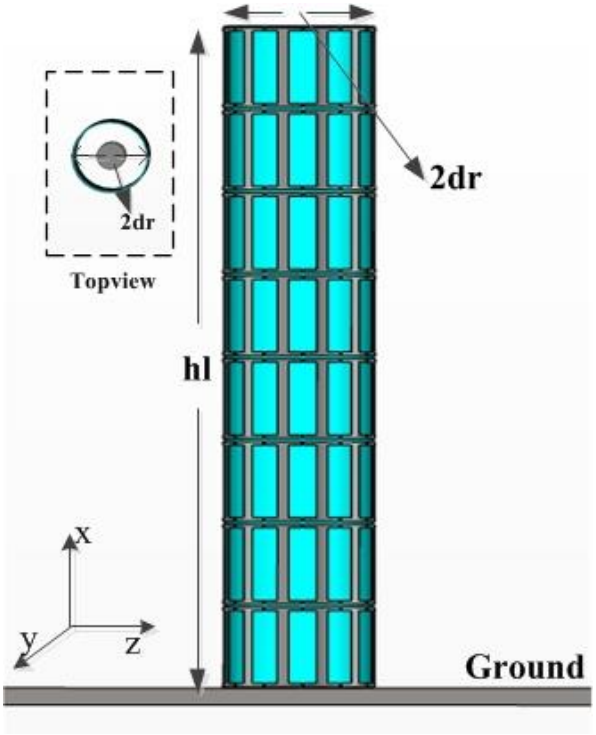

Figure 3: Configuration of the monopole antenna with the MM cladding. All dimensions are in mm: dr=5, hl=40.

3.1. Simulation

The antennas are simulated by using the CST Microwave Studio. The return losses of the monopole antenna with and without the MM cladding (i.e. the proposed UWB monopole antenna and the monopole antenna) are shown in Fig. 4. The monopole antenna yields a 2.2-2.87GHz bandwidth (i.e., the relative bandwidth is 26%) with a single resonance at 2.45GHz, whereas the bandwidth of proposed UWB monopole antenna is broadened to 1.98-5.80 GHz (the relative bandwidth is 100% increased by 74%) with two resonances. The first resonance is totally realized by the monopole structure and located at 2.31 GHz, which is a little lower than that of the monopole antenna; the new resonance appears at 4.8GHz, and the resonance range is about 4-6GHz, which is due to the negative effective permittivity of the MM cladding in the band of about 4.4-6GHz (as shown in Fig.2). Given all that, the MM cladding with an ISS array can realize UWB monopole antenna.

The simulated E-plane and H-plane radiation patterns of the proposed UWB monopole antenna are illustrated in Fig. 6 (the dash and solid lines denote the H-plane and E-plane radiation patterns respectively). It shows that the H-plane radiation patterns are omni-directional and the E-plane radiation patterns are stable in all cases.

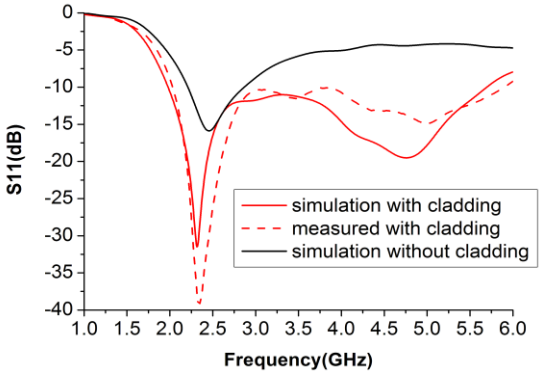

Figure 4: Simulation and measured return loss.

3.2. Measurement

Firstly, the MM cladding is realized by fabricating a planar MM sheet with the single-side ISS array, and then the sheet is curled into the desired cylindrical cladding as shown in Fig. 5. The MM-coated monopole situates on a square copper ground plane with the dimension of 32*32cm^2 and is excited via an SMA connector.

Then, a PNA-X Microwave Network Analyzer is used to measure the return loss versus frequency of the fabricated antenna. The measured S_{11} of the UWB antenna is shown in Fig. 4. It can be seen that the measured bandwidth is 3.85GHz (2.0-5.85GHz) and two obvious resonances approximate to these of simulation.

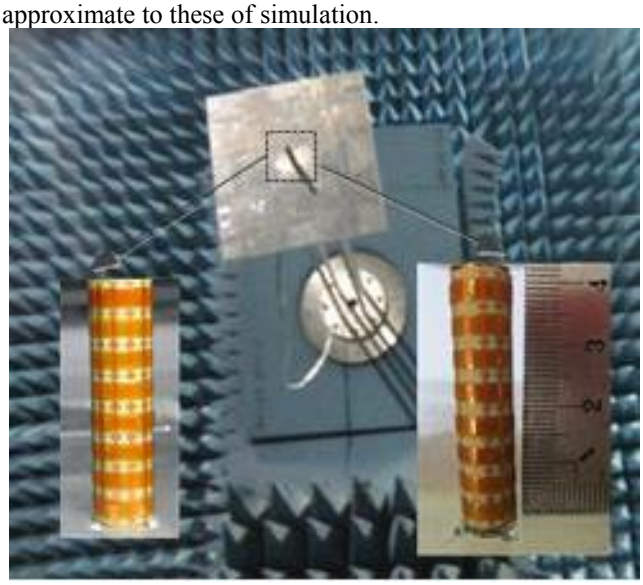

Figure 5: Measurement configuration in anechoic chamber.

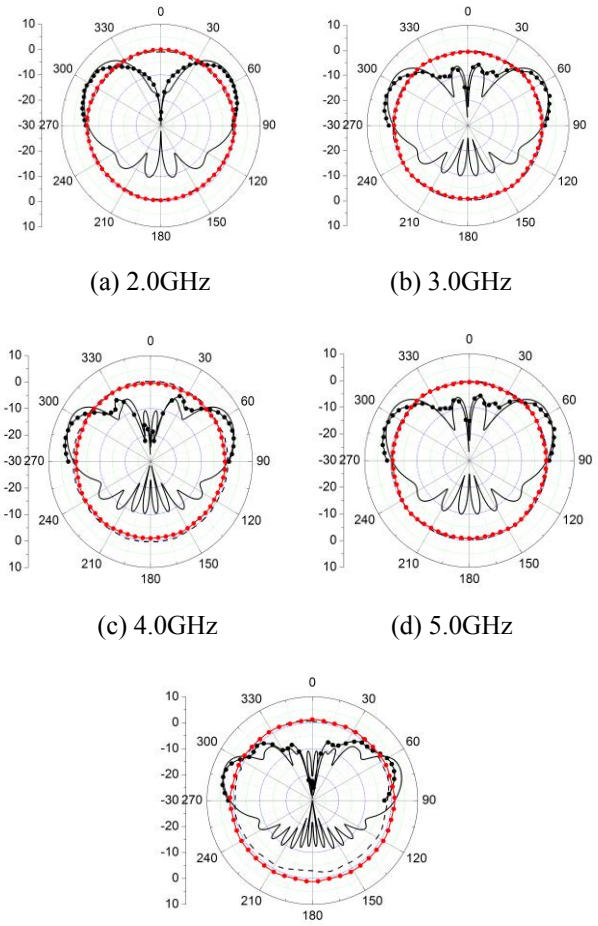

(a) 2.0GHz (b) 3.0GHz

(c) 4.0GHz (d) 5.0GHz

(e) 5.8GHz

Figure 6: Simulated and measured E-plane and H-plane patterns at five frequencies. (a) 2GHz, (b) 3GHz, (c) 4GHz,(d) 5GHz and (e) 5.8GHz.

Finally, as shown in Fig. 5, the radiation patterns of the antenna are also measured in the near field anechoic chamber. Due to the limitation of system, the E-plane patterns can only be measured from -90° to 90° in the *xsz*-plane. The measured E-plane and H-plane radiation patterns of the fabricated UWB monopole antenna are also illustrated in Fig. 6 (the solid and dash lines with dots show the measured E-plane and H-plan radiation patterns respectively).

It can be seen from Fig. 4 and Fig. 6 that the measured results of UWB antenna are in good agreement with the simulated result.

4. Conclusions

The proposed UWB antenna consists of a monopole antenna and single-side ISS MM cladding. Due to the single-side ISS MM cladding, the relative bandwidth of UWB antenna has increased by 74% and the radiation patterns retains stable in the 1.98-5.80GHz range. In addition, the simulations and measurements are in a good agreement. So, the UWB antenna can be widely used in the potable wireless device in S/C-band.

Acknowledgements

This work was supported by the Natural Science Foundation of China under Grant (61001020, 61361005, 61461016, 61161002), the Natural Science Foundation of Guangxi under Grant (2014GXNSFAA118283) and the Innovation Project of Guangxi Graduate Education under Grant (GDYCS201415).

References

[1] A. Foudazi, H.R. Hassani, S.M. Nezhad, A Small UWB planar monopole antenna with added GPS/GSM/WLAN bands, *Antennas and Propagation*, *IEEE Transactions on* 60(6): 2987-2992, 2012.

[2] S. Cimen, G. CAKIR, Planar Octagonal-Shaped UWB Antenna with Reduced Radar Cross Section, *Antennas and Propagation*, *IEEE Transactions on* 62(6): 2946-2953, 2014.

[3] B. D. Baal, A. Rohm, N.A. Mural, Small electrical metamaterial antenna based on coupled electric field resonator with enhanced bandwidth, *Electronics Letters*, 50(3): 138-139, 2014.

[4] A. Erentok, R.W. Ziolkowski, Metamaterial- inspired efficient electrically small antennas, *Antennas and Propagation*, *IEEE Transactions on* 56(3): 691-707, 2008.

[5] Z.-H. Jiang, M.D. Gregory, D.H. Werner, A broadband monopole antenna enabled by an ultrathin anisotropic metamaterial coating, *IEEE Antennas and Wireless Propagation Letters* 10: 1543-1546, 2011.

[6] R. W. Ziolkowski, Design, fabrication, and testing of double negative metamaterials, *IEEE Transactions on Antennas and Propagation* 51(7): 1516-1529, 2003.

[7] D.R. Smith, S. Schultz, P. Markoš, and C. M. Soukoulis, Determination of effective permittivity and permeability of metamaterials from reflection and transmission coefficient, *Phys. Rev. B*, (65): 195104, 2002.

Studying the CPML absorbing boundary condition in FDTD method modeling the TEM response

Yan N. Jiang, Wen Liu, Jiao Wang*

Key Laboratory of Cognitive Radio and Information Processing (Guilin University of Electronic Technology), Ministry of Education, Guilin, China
*corresponding author, E-mail: wangjiao@guet.edu.cn

Abstract

In FDTD modeling transient electromagnetic (TEM) response, Dirichlet boundary condition (DBC) is generally used. Hence, very large modeling region is required, and the computation amount increases rapidly. We propose the convolution perfectly matched layer (CPML) absorbing boundary condition (ABC) to overcome this problem. Considering the field approaching the dc limit at late times, magnetic field divergence equation should be incorporated explicitly, and then the proposed CPML ABC must be also suitable to deal with the divergence equation explicitly.

Index Terms: FDTD, transient electromagnetic, Dirichlet boundary condition, convolution perfectly matched layer.

1. Introduction

In the late time of transient electromagnetic (TEM) method, the displacement current can be neglected because of slow variation, and then the diffusion characteristic dominates the electromagnetic process under ground [1]. Two numerical methods are normally used to simulate the diffusion process, one is the DuFort-Frankel finite-difference method [2][4], the other is the explicit time-domain finite-difference (FDTD) method [5]-[7] involving the fictitious artificial displacement current. In the previous study of FDTD computing the TEM response [1]-[7] , there is normally an assumed condition, i.e., the subsurface boundaries are far enough away from the source and the abnormal body, and then the values at the boundary meet Dirichlet boundary condition (DBC). This assumption is consistent with the actual laws of physics and the DBC, moreover, is easy to be implemented. However, it could lead to the disadvantages that the enormous consumptions of computer memory and computing time.

In order to overcome the above disadvantages, we truncate the modeling region at the subsurface boundaries by using convolution perfectly matched layer (CPML) [8] absorbing boundary condition (ABC), which is also just applicable to the low frequencies response of TEM. Since the divergence equation of magnetic field must be incorporated explicitly in the iterative process and the magnetic induction component B_z is solved from the bottom boundary up to earth-air boundary, the proposed CPML ABC is also suitable to handle the explicit incorporation.

2. Formulation

Under the fictitious artificial displacement current being introduced into the diffusion equations to form explicit difference equations, the TEM fields in linear, isotropic, and source-free matched layer are described by Maxwell's equations in the frequency domain [9]:

$$\frac{1}{\mu_0}\nabla_s \times \boldsymbol{B} = \sigma \boldsymbol{E} + j\omega\gamma \boldsymbol{E}\ , \tag{1a}$$

$$\nabla_s \times \boldsymbol{E} = -j\omega \boldsymbol{B}\ , \tag{1b}$$

$$\nabla_s \cdot \boldsymbol{B} = 0\ , \tag{1c}$$

$$\nabla_s \cdot \boldsymbol{E} = 0\ , \tag{1d}$$

where $\boldsymbol{B}$ and $\boldsymbol{E}$ are the magnetic induction and electric field respectively, σ is the conductivity, μ_0 is the magnetic permeability of the free space, $\omega\gamma\boldsymbol{E}$ is the displacement current, and ∇_s is defined as [10]

$$\nabla_s = \hat{x}\frac{1}{s_x}\frac{\partial}{\partial x} + \hat{y}\frac{1}{s_y}\frac{\partial}{\partial y} + \hat{z}\frac{1}{s_z}\frac{\partial}{\partial z}\ , \tag{2}$$

in which s_x , s_y and s_z are the tensor coefficient in stretched coordinate, they are uniformly expressed as [10]

$$s_w = \kappa_w + \frac{\sigma_w}{\alpha_w + j\omega\varepsilon_0},\ \ (w = x, y, z)\ , \tag{3}$$

where ε_0 is the free-space permittivity, ω is the frequency, σ_w is the conductivity in the *w*-direction in matched layer, and $\sigma_w \geq 0$, $\kappa_w \geq 1$, $\alpha_w \geq 0$.

The study found that the low-frequency magnetic response can be erroneous if equation (1c) is ignored [5]. Therefore, we will discuss the incorporation of equation (1c) with equations (1a) and (1b). According to the basic theory of CPML, the discrete expressions of equation (1a) and (1b) are easy to be solved. In the following, we would focus on deriving the specific expression of equation (1c) in the CPML region.

Under the two-dimensional (2-D) TM_y mode and the expression (2) being directly inserted into the equation (1c), we can obtain

$$\frac{1}{s_z}\cdot\frac{\partial B_z}{\partial z} = -\frac{1}{s_x}\cdot\frac{\partial B_x}{\partial x}\ . \tag{4}$$

In addition, we can express the time-dependent expression as

$$\frac{1}{\kappa_z}\cdot\frac{\partial B_z}{\partial z}+\zeta_z(t)*\frac{\partial B_z}{\partial z}=-\left[\frac{1}{\kappa_x}\cdot\frac{\partial B_x}{\partial x}+\zeta_x(t)*\frac{\partial B_x}{\partial x}\right]. \quad (5)$$

It can be seen that equation (5) not only has the time-domain convolution items on both sides, but also the convolution form is $\zeta_w(t)*\partial B_w/\partial w$. However, the traditional CPML theory only has the convolution on one side and the form is $\zeta_v(t)*\partial B_w/\partial v$, namely, the traditional CPML process can't be directly implemented. In the following, we will conceive a method to calculate the time-domain convolution item of $\zeta_w(t)*\partial B_w/\partial w$ as

$$\psi_{Bw,w}\left(n+\frac{1}{2}\right)=\left[\zeta_w(t)*\frac{\partial B_w}{\partial w}\right]\Big|_{t=\left(n+\frac{1}{2}\right)\Delta t}$$
$$=b_w\cdot\psi_{Bw,w}\left(n-\frac{1}{2}\right)+c_w\cdot\frac{\partial B_w\left(n+\frac{1}{2}\right)}{\partial w} \quad (w=x,\ z) \quad (6)$$

where $b_w=\exp\left(-\left(\frac{\sigma_w}{\varepsilon_0\kappa_w}+\frac{\alpha_w}{\varepsilon_0}\right)\Delta t\right)$ and $c_w=\frac{\sigma_w}{\sigma_w\kappa_w+\kappa_w^2\alpha_w}\{b_w-1\}$.

Now, we can derive the recurrence formula of B_z.

3. Numerical examples

In order to verify the effectiveness of the proposed CPML ABC, the relative error of the TEM response relating to 2-D half-space model that the lower medium is homogeneous, lossy and non-magnetic media (as shown in figure 1) will be simulated. We define a rectangular coordinate system in Figure 1 with the origin of coordinate is on the earth-air interface, the *x*-axis parallel to the interface (positive to the right) and the *z*-axis perpendicular to the interface (positive down). The *x*-, *y*-, and *z*-axis complete a right-handed system. For TM_y problems, the electric vector will have only a *y* component.

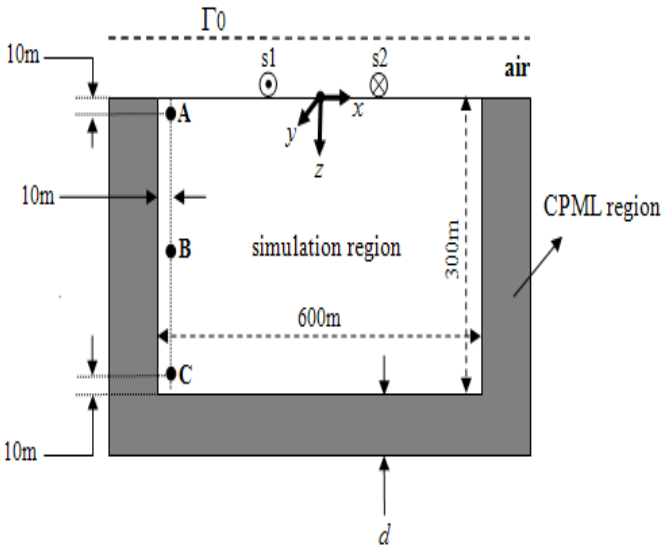

Figure 1: FDTD model truncated by CPML ABC. Points A, B and C are respectively placed at the grids of (-29,1), (-29,15) and (-29,29).

The grid spacing is $\delta=\Delta x=\Delta z=10m$ and the number of modeling grid is 60×30 cells. The conductivity of earth is $\sigma_g=1/300(s/m)$. Two infinite line sources s_1 and s_2 are placed respectively at $x=-100m$ and $x=100m$ along the *y* direction to make the 2-D loop that does not touch the ground and from which passes a positive and negative current. Let's assume that the current is shut-off at *t*=0, the initial time is $t_0=1.0472\mu s$, the time step is $\Delta t_n=a\sqrt{\mu_0\sigma_g t_n}\delta/D$ (where $a=0.2$, $D=2$ and $n=0,1,2\cdots$) and $\gamma=(\Delta t_n/\delta)^2 D/\mu_0$.

The excitation source is the same as Oristaglio's initial conditions [2]. The tangential magnetic induction B_x on the air boundary Γ_0 is computed by the upward continuation theory. The subsurface region is truncated by using CPML ABC with the thickness of *d*. The parameters of CPML are $\kappa_{\max}=6$, $\alpha_{\max}=0.05$, $\sigma_{factor}=300$, n=1, $m_a=1$, and *d* is 12 cells respectively.

3.1. Analyze the error of result

Figure 2 graphs the relative errors of the probed electronic field component E_y at points A, B and C over 1,000 time steps. It can be seen that the relative error is larger in the early time and the maximum value is -25 dB. However, the relative error become smaller and smaller as the time. Which indicates that the propose CPML ABC has the excellent absorbing properties.

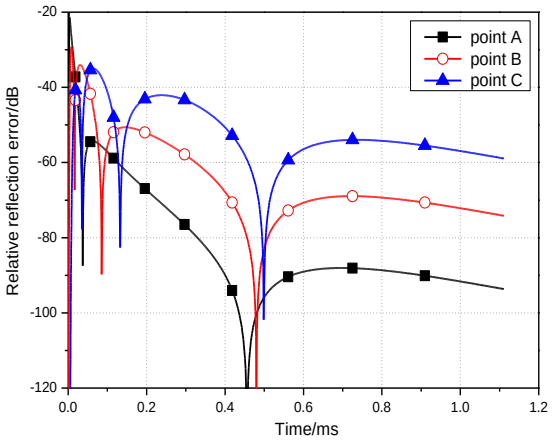

Figure 2: Relative reflection error at Points A, B and C.

3.2. The analysis of computing resource consumption

In 2-D FDTD, the formula of the memory consumption is[9]

$$M_{total}=N\times\left(3\frac{variable}{cell}\times 8\frac{Bytes}{variable}+1\frac{medium\ tag}{cell}\times 1\frac{Bytes}{medium\ tag}\right), \quad (7)$$

where *N* is the number of modeling grid. Each field components is stored by using a double precision variable and the medium is tagged by a single precision integer.

Under DBC, we suppose that the region is large enough and the number of grid is 800×400. By (7), 7.63MB memory is required for calculating three field components. In the computer simulation, 55.6s is consumed for running 1000 time steps. However, when the modeling region is reduced and truncated by CPML on the subsurface boundaries (the total grid number of FDTD and CPML region is 84×42, as shown in Figure 1), 0.12MB memory is required and 0.79s is consumed.

4. Conclusions

The proposed CMPL ABC is applicable to FDTD modeling TEM response. It can significantly reduce the modeling region and shorten the calculation time. The numerical results show that the relative error is less than -25dB and becomes smaller and smaller as the time, the consumption time, moreover, can be reduced by more than 90%.

Acknowledgements

This work was supported by the Natural Science Foundation of China under Grant (61001020, 61161002) and the Natural Science Foundation of Guangxi under Grant (2014GXNSFAA118283).

References

[1] Y.-B. Yan, D.-B. Ge, Analysis of Transient EM Scattering from Underground Targets with Pulse Excitations, *Acta Electronica Sinica*, 30(3): 325-327, 2002.

[2] M.L. Oristaglio, G.W. Hohmann, Diffusion of electromagnetic fields in two-dimensional earth: a finite difference approach, *Geophysics* 49 (7): 870-894, 1984.

[3] S. Yan, M.-S. Chen, J.-M. Fu, Direct time-domain numerical analysis of transient electromagnetic fields, *Chinese Journal of Geophysics* 45(2): 275-284, 2002.

[4] Y. Liu, X.-B. Wang, Y. Wang, Numerical modeling of the 2D time-domain transient electromagnetic secondary field of the line source of the current excitation, *Applied Geophysics* 10(2): 134-144, 2013.

[5] T. Wang, W.G. Hohmann, A finite-difference time-domain solution for three-dimensional electromagnetic modeling, *Geophysics* 58(6): 797-809, 1993.

[6] M. Commer, G. Newman, A parallel finite-difference approach for 3D transient electromagnetic modeling with galvanic sources, *Geophysics* 69(5): 1192-1202, 2004.

[7] H.-F. Sun, X. Li, S.-C. Li, et al, Three-dimensional FDTD modeling of TEM excited by a loop source considering ramp time, *Chinese Journal of Geophysics* 56 (3): 1049-1064, 2013.

[8] J.A. Roden, S.D. Gedney, Convolution PML (CPML): an efficient FDTD implementation of the CFS-PML for arbitrary media, *Microwave and Optical Technology Letters* 27(5): 334-339, 2000.

[9] D.-B. Ge, Y.-B. Yan, *Finite-Difference Time-Domain Method for Electromagnetic Waves* (in Chinese), Xidian University Press, Xi'an, 2005.

[10] A. Taflove, S.C. Hagness, *Computational Electrodynamics: The Finite-Difference Time-Domain Method*, Norwood, Artech House, 2005.

General Papers

Circuit emulator of meminductor based on memristor

Guohua Liu, Zhiqun Cheng, Tao Zhou, Huajie Ke and Zhihua Dong

School of Electronic and Information, Hangzhou Dianzi University, Hangzhou, China
*corresponding author, E-mail: ghliu@hdu.edu.cn

Abstract

A meminductor circuit emulator utilizing a flux-controlled tunneling memristor is proposed. It imitates the behavior of a current-controlled meminductor. The memristor used in the emulator is designed by normal electronic devices and is measured in laboratory. The emulator is built from off-the-shelf electronic components. The SPICE simulation outputs of the emulator are consistent with the numerical results. The meminductor emulator provides an alternative solution of meminductor model in real circuits.

High-Frequency Characterization of Through-Silicon Hole (TSH) Channel based on 3D Full-Wave Simulation

Jie Zheng, Wen-Sheng Zhao, and Gaofeng Wang*

Key Lab of RF Circuits and Systems of Ministry of Education, Microelectronics CAD Center,
Hangzhou Dianzi University, Hangzhou 310018, China
*corresponding author, E-mail: gaofeng@hdu.edu.cn

Abstract

In this paper, the electrical characteristics of through-silicon hole (TSH) structures are investigated. After validation with circuit model, the 3D full-wave simulations are employed to study the impacts of design parameters. The process variations including underfill and misalignment are also considered. Additionally, a single-end high-speed TSH channel is studied in the frequency-domain. The crack location is also presented by using *Z*-parameter variation.

1. Introduction

3-D integration with through-silicon via (TSV) has attracted a great deal of attention in the past several years [1]. It is believed that such technique is a potential solution for the realization of "more-Moore" and even "more-than-Moore" technologies. However, TSVs still have some critical issues need to be resolved, and alternative techniques are in development, such as coaxial and CNT-based TSVs [2, 3].

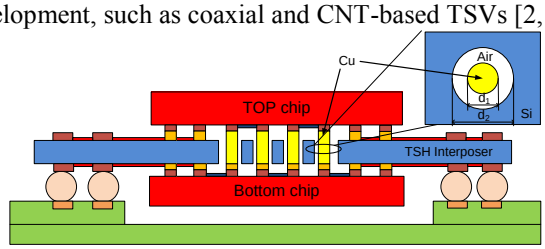

Figure 1: Schematic of TSH interposer.

Recently, Lau *et al.*, proposed a novel vertical interconnects named "through-silicon hole (TSH)", which are realized by inserting metal vias grown on the top chip into the interposer hole to connect the bumps on the bottom chip, as shown in Fig. 1 [4]. In this paper, the TSHs are investigated by using the 3D full-wave simulations.

2. Parametric Study

As shown in Fig. 2, the circuit model of TSH (TSV) pair is presented, and the expressions of these circuit elements can be referred in [5, 6]. Here, δ_{Si}=20 S/m, h=100 μm, d_1=15 μm, p =100 μm, and t_{diel}=7.5 μm for TSH and 0.5 μm for TSV. Evidently, the TSHs could provide superior performance over TSVs due to reduced substrate loss (see Figs. 2 and 3). In the following, the 3D full-wave simulations would be employed to study the impacts of design and process parameters (*e.g.*, silicon conductivity, underfill, and misalignment) on the electrical performance of TSHs.

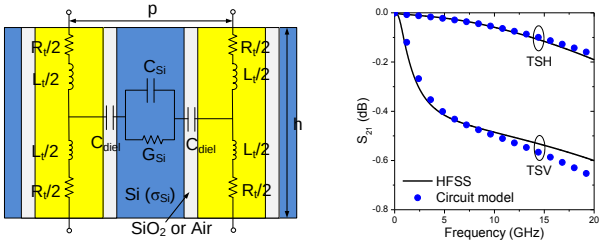

Figure 2: Circuit model and S_{21} of TSH (TSV) pair.

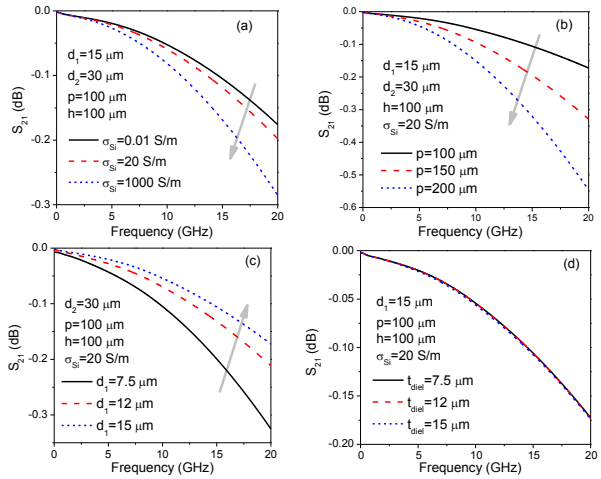

Figure 3: Impacts of design parameters on the S_{21} of TSH pair: (a) silicon conductivity; (b) pitch; (c) diameter; and (d) air thickness.

2.1. Design Parameters

The substrate loss is a key factor that determines the electrical performance of TSH pair. Therefore, with the increase of silicon conductivity σ_{Si}, the silicon conductance G_{Si} is increased, and thereby, the substrate loss becomes more significant. G_{Si}, as well as the silicon capacitance C_{Si}, is also affected by the pitch, which is the physical distance between the signal and ground vias. Therefore, the electrical performance of TSH pair is degraded by increasing the silicon conductivity and pitch (see Figs. 3(a) and (b)).

Keeping the other parameters unchanged, increasing the diameter would decrease both the resistance R_t and inductance L_t. It is shown in Fig. 3(c) that the electrical performance can be improved by increasing the diameter though C_{diel} is also increased, which means that the impacts of C_{diel} is negligible. The similar phenomenon can be observed in Fig. 3(d), which shows that the S_{21} is kept almost unchanged with the variation of air thickness.

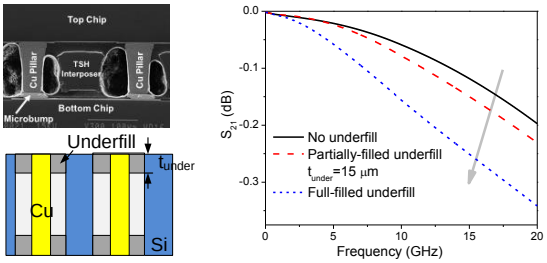

Figure 4: Impacts of underfill on the S_{21} of TSH pair.

2.2. Process Parameters

Here, we consider three kinds of process variations, *i.e.*, underfill, tapered via, and misalignment. As stated in [4], there are underfill filling the gap between the top/bottom chip and interposer. Inevitably, some underfill would flow through the holes. Therefore, it is necessary to study the impacts of partially- and full-filled underfill on the electrical performance of TSH pair in the frequency-domain. Here, the relative permittivity of underfill material is chosen as 7, and the thickness of top and bottom underfills are denoted by t_{under}. Obviously, as shown in Fig. 4, introducing the underfill increases the parasitic capacitance, thereby deteriorating the electrical performance of TSH pair. However, even the TSHs with full-filled underfill can still provide superior performance over TSVs (see Fig. 2).

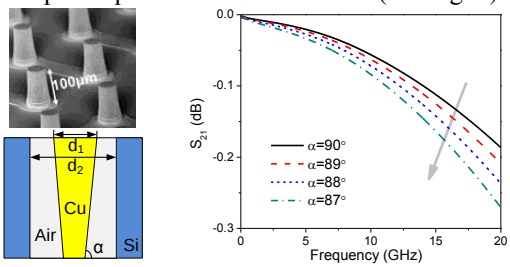

Figure 5: Impacts of slope angle on the S_{21} of TSH pair.

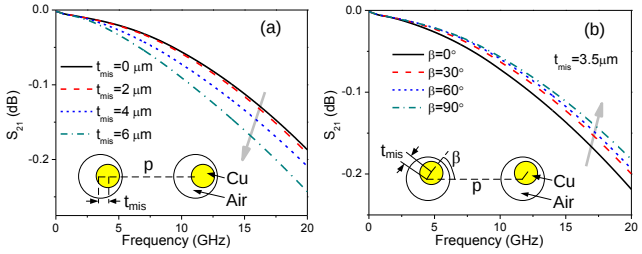

Figure 6: Impacts of misalignment on the S_{21} of TSH pair.

Fig. 5 shows the Cu pillars grown on the top chip. It is evident that the tapered vias would be formed and their impacts on the electrical performance should be investigated. Here, the slope angle α is defined as arctan($2h$/($d_2 - d_1$)). Assuming the diameter d_1 kept unchanged, it is found that the signal transmission can be improved by increasing α, which is due to the reduced R_t and L_t. Further, the impacts of misalignment on the electrical performance of TSH pair is evaluated in Figs. 6(a) and (b).

3. Structural Optimization

Here, we propose three structural optimization schemes in this paper. The first is to trench the substrate between the adjacent TSHs, as shown in Fig. 7(a). Such technique can be employed to improve the signal transmission or suppress the coupling noise. The second is to form coaxial TSH structure, which is shown in Fig. 7(b). As the integration technique given in [4] is to drill holes on interposer wafer, we can easily grow Cu layer around the hole (like annular TSVs) [7], and then insert the Cu pillars into the holes to form coaxial TSHs. Fig. 7(c) shows the unshielded symmetric TSH pair. It can also be formed as shield symmetric TSH pair, which can be utilized as differential interconnects. As shown in Fig. 7(d), the last one is to combine the multiinterconnected TSV with TSH to build a novel through-silicon vertical interconnect, which can provide the designers with more degree of freedom.

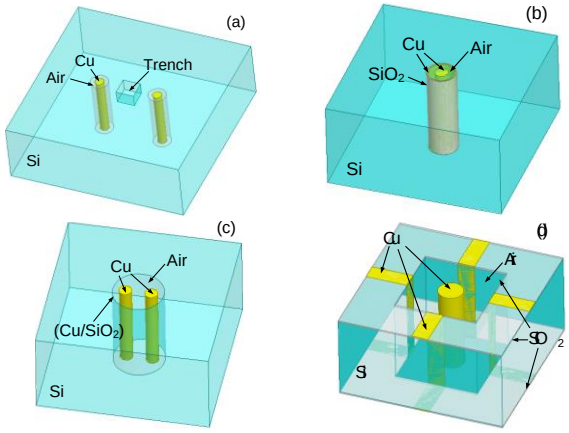

Figure 7: The proposed structural optimization schemes.

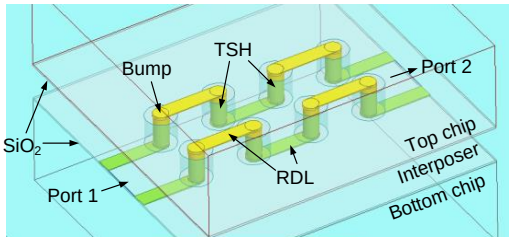

Figure 8: Schematic of a TSH channel.

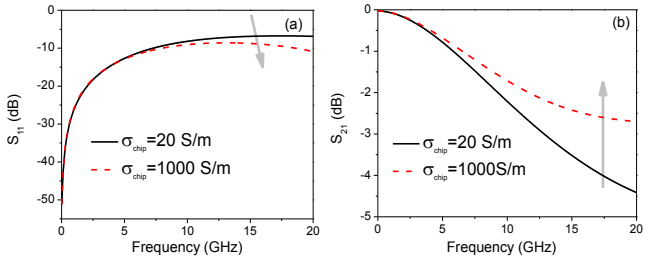

Figure 9: *S*-parameter of a TSH channel.

4. Characterization of a TSH Channel

4.1. Electrical Characterization

Finally, as shown in Fig. 8, a TSH channel, which is built with four signal and ground TSH pairs and redistribution-layer (RDL) lines, is studied in this section. The related geometrical and physical parameters are referred to [4], and the underfill is excluded in our simulation. The silicon conductivities of interposer, top and bottom chips are chosen to be 20 S/m.

As can be seen in Fig. 8, the electrical performances of top (bottom) RDL lines are demonstrated by the silicon conductivity of top (bottom) chip. In a heterogeneous integration, the top chip can be utilized for build RF front-end circuit, and therefore, the high-resistivity silicon (HRS) should be employed. Therefore, the impact of silicon conductivity of top chip on the total performance of TSH channel is evaluated. It is shown that with the increase of silicon conductivity of the top chip, the signal transmission performance can be improved significantly.

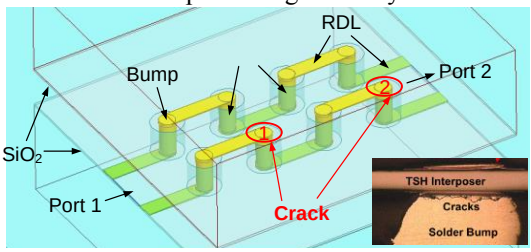

Figure 10: Schematic of crack failures in the TSH channel.

4.2. Crack Location

Inevitably, the crack failures occur during the fabrication and integration of TSV-based 3-D ICs. As shown in Fig. 10, similar phenomenon can be observed in the fabrication of TSH channels. In order to improve the yield, the cracks should be detected fast and accurately. To date, many techniques have been developed in this aspect, such as characterizing the signal degradation in TSVs. However, as TSVs have significant impacts on the mobility of the surrounding substrate, stable transistor performance cannot be guaranteed for crack detection in the time-domain. In this section, two kinds of crack detection are developed.

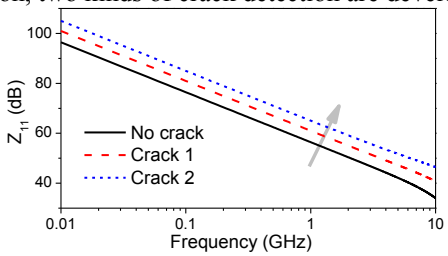

Figure 11: Z_{11}-parameter variation of the TSH channel.

The first is to capture the high-frequency Z_{11}-parameter variation. It is known that when there exist crack failures, a crack resistance and a crack capacitance would be introduced in the circuit model of TSH channel. Therefore, the Z_{11}-parameter will be increased due to the impacts of crack failures, and the crack location affects the magnitude of Z_{11}-parameter variation.

There is another approach to fast locate the crack failures in the TSH channel. As described in [8], a simple resistor chain can be established for crack location, which is shown in Fig. 12. When the resistor is much larger than the RDL and TSH resistances, the total resistance can be determined as R/N, where N denotes the number of resistors added. Evidently, where there is a crack failure, the total resistance will be increased, and it is given as R/n, where n denotes the location of crack failure.

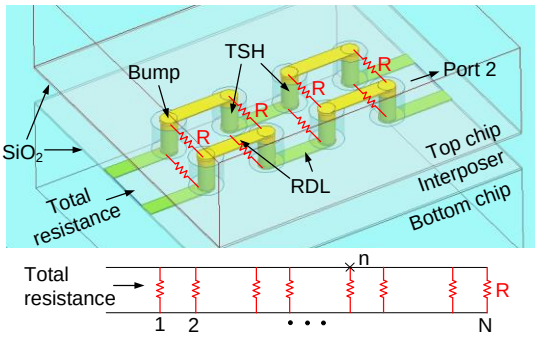

Figure 12: Simple resistor chain of the TSH channel.

5. Conclusions

In this paper, through-silicon holes (TSH) are investigated by using the 3D full-wave simulation. The impacts of design and process parameters on the signal transmission of TSH pair are studied. Several structural optimization schemes are proposed. Finally, the electrical performances of a TSH channel are characterized, with the crack location scheme presented.

Acknowledgements

This work was supported by Zhejiang Provincial NSFC under grants LZ14F010001 and LQ14F010010, and National NSFC under grant 61331007 and 61411136003.

References

[1] W.-S. Zhao *et al.*, "Electrothermal effects in high density through silicon via (TSV) arrays," *Prog. Electromagn. Res.*, 115: 226-242, 2011.

[2] F. Liang *et al.*, "Wideband impedance model for coaxial through-silicon vias in 3-D integration," *IEEE Trans. ED*, 60(8): 2498-2504, 2013.

[3] W.-S. Zhao *et al.*, "Electrothermal modelling and characterisation of submicron through-silicon carbon nanotube bundle vias for three-dimensional ICs," *Micro Nano Lett.*, 9(2): 123-126, 2014.

[4] J. H. Lau *et al.*, "Through-silicon hole interposers for 3-D IC integration," *IEEE Trans. CPMT*, 4(9): 1407-1419, 2014.

[5] J. Kim *et al.*, "High-frequency scalable electrical model and analysis of a through silicon via (TSV)," *IEEE Trans. CPMT*, 1(2): 181-195, 2011.

[6] W.-S. Zhao *et al.*, "Frequency- and temperature-dependent modeling of coaxial through-silicon vias for 3-D ICs," *IEEE Trans. ED*, 58(10): 3358-3368, 2011.

[7] J. Ye *et al.*, "Investigation of wet-etching- and multiinterconnected-based TSV and application in 3-D hetero-integration," *IEEE Trans. CPMT*, 4(10): 1567-1573, 2014.

[8] S. Hu *et al.*, "Fast location of opens in TSV-based 3-D chip using simpler resistor chain," *IEEE Trans. ED*, 61(7): 2584-2587, 2014.

The study on vibration and noise characteristics of small fan motors

Masaki Ogushi[1,2], Koki Shiohata[1], Takako Otsuka[2], Atsushi Taroda[2], Zhong Yan[2], Yoichi Kawai[3], and Miyuki Furuya[2]

[1] Graduate School of Science and Engineering, Ibaraki University, Ibaraki, Japan
[2]Minebea Co.,Ltd. Electric Device & Component Manufacturing HQ, Shizuoka, Japan
[3]Minebea Co.,Ltd. Electric Device & Component Manufacturing HQ, Nagano, Japan

*corresponding author, E-mail: mogushi@minebea.co.jp

Abstract

In this study, the vibration and the noise in the small fan motor caused by electromagnetic dynamics and fluid dynamics were analyzed. The noises in the fan motor caused by the blade-passing force and the electromagnetic force were prominent. Intense peaks were present at frequencies at which both the blade-passing force and the electromagnetic force had their harmonic components. In particular, noise became the maximum at a frequency where the harmonic frequency of the electromagnetic force matches the natural frequency in the fan motor in the axial direction.

1. Introduction

In current motor market, low noise and vibration is increasingly needed in addition to the higher power, and speed. A motor is requested to accomplish the low vibration and noise and high efficiency simultaneously. For the low vibration and noise of a motor, they have researched by both electromagnetic dynamics and structural dynamics [1] [2] [3] [4]. The fan motors consists of a motor and a fan for cooling of the equipments.

The fan motors are used in many equipments. Commonly the fan motors are required for high efficiency, high air capacity, and low vibration and noise. Recent changes in many people's lifestyles brought up reduction of vibration and noise of the fan motors as an important issue. In order to solve the issue, analyses on fluid dynamics, electromagnetic dynamics, and mechanical structural dynamics of the fan motors need to be performed not separately but simultaneously. This is because in a fan motor vibration and noise can be caused electromagnetically, mechanically, or fluid-dynamically at the operating speed. At present, few researches which are based on both electromagnetic dynamics and structural dynamics have been made on the vibration and noise in the fan motor. Especially, studies on the vibration in the axial direction cannot be found. This paper describes the mechanism that generates the vibration and noise in a small fan motor at its operation, and discusses the effects of harmonics components of electromagnetic dynamics and fluid dynamics, and vibration characteristics of the structure with a focus in the axial direction.

2. Measuring method

First, the vibration characteristics of a non-operating fan motor were obtained by hammer impact test, and experimental modal analysis was conducted. Next, vibration and noise characteristics of the operating fan motor were measured. Table 1 shows specifications of the fan motor model.

2.1. Vibration characteristics of the non-operating fan motor

Fig.1 shows the block diagram of measurement system. Solid lines indicate non operating conditions for modal analysis by hammer impact test, and dashed lines indicate operating conditions for frequency analysis of noise and vibration.

2.2. Vibration and noise characteristics of an operating fan motor

The noise and vibration were analyzed using measurement system shown with dashed line in Fig. 1 and the measurements of measuring three-dimensional accelerometer shown in Fig. 2.

Table 1: Specifications of the fan motor model

Size	□120 ㎜
Number of poles	4
Number of stator slots	4
Number of blades	9
Operating speed	2200 r/min

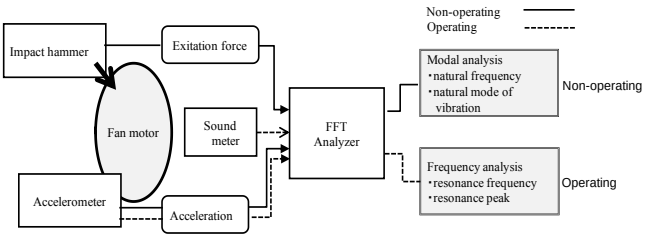

Figure 1: Block diagram of measurement system

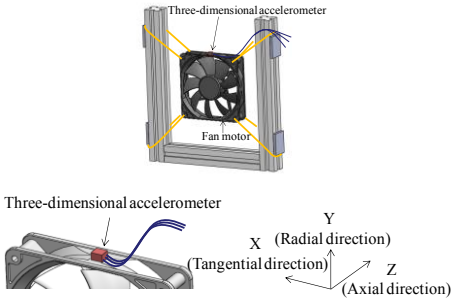

Figure 2 :Measurements of measuring three-dimensional acceleration

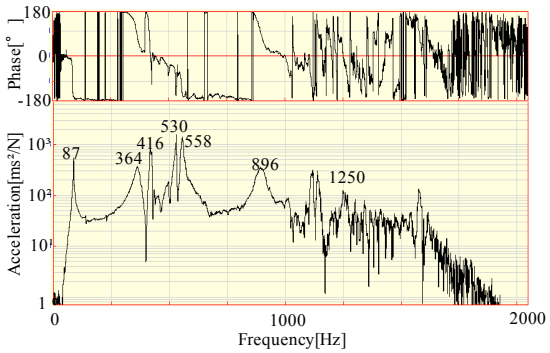

Figure 3: The Transfer functions in the axial direction

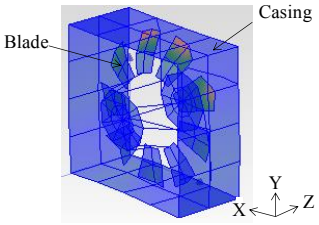

Figure 4: Natural vibration mode of the fan motor at 530Hz

3. Result of measurements

3.1. Vibration and noise characteristics of the non-operating fan motor

Fig. 3 shows transfer functions in the axial direction. The highest peak appeared at 530 Hz. Fig. 4 shows natural vibration mode of the fan motor at 530 Hz. The blades vibrate in the axial direction at 530 Hz.

3.2. Vibration characteristics of the non-operating fan motor

The rotational speed was continuously decreased from 2200 r/min to 1200 r/min while the measurements were taken. Fig. 5 shows the overall noise level. A significant noise peak was present at 1922 r/min. Fig. 6 shows noise level. Fluid noise which depends on the number of blades was present. And harmonic components on the noise caused by electromagnetic force were also confirmed.

The relationship between the harmonic components and frequency caused by blade-passing force and electromagnetic force is shown below.

The frequency f_z of the fluid noise caused by blade-passing force has the following relation.

$$f_z = mnz \quad (m=1,2,\cdots) \qquad (1)$$

Where, n is the rotational frequency and z is the number of blades. The frequency f_e of electromagnetic force has the following relation.

$$f_e = k \times (2n/p) \quad (k=1,2,\cdots) \qquad (2)$$

Where, k is the order of harmonic component, n is the rotational frequency and p is the number of poles. There is a relation of $f_e = f_z$ .Fig.7 shows frequency analysis results at 1922 r/min when the significant peak occurred. The squares indicate the points where the frequency the noise depending on the number of blades and the frequency of the noise caused by electromagnetic force are equal. Frequency of 512 Hz is the natural frequency of the structure that matches the 32nd component of electromagnetic force. Therefore, structural vibration and electromagnetic force were in a resonant condition and the significant peak was confirmed. Fig.8 shows noise level of the 32nd electromagnetic force versus rotational speed. The significant resonance occurred at 1922 r/min. Fig.9 shows vibration amplitude of the 32nd electromagnetic force in the axial direction versus rotational speed. The significant resonance occurred at 1922 r/min in the same manner as the noise (fig. 8).

As mentioned above, the significant vibration and noise occurred not by the fluid dynamics but by the electromagnetic dynamics, and moreover occurred in the axial direction.

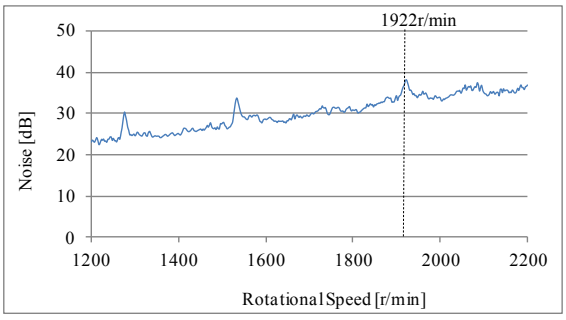

Figure 5: Overall noise level

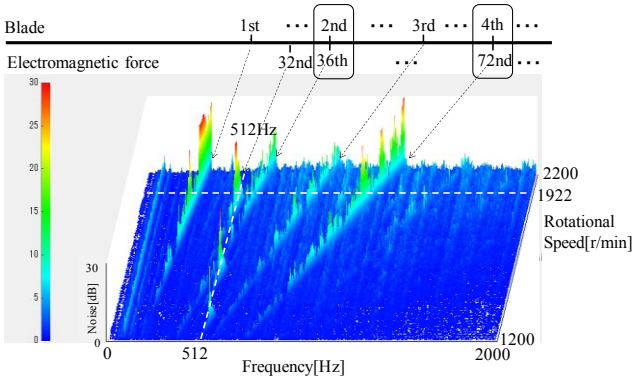

Figure 6: Noise level.

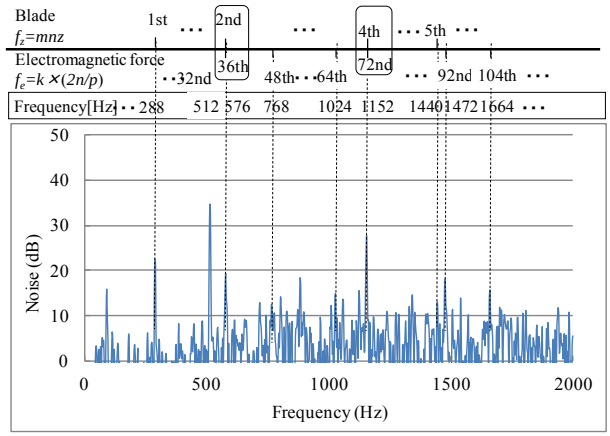

Figure 7: Noise level measured at 1922r/min

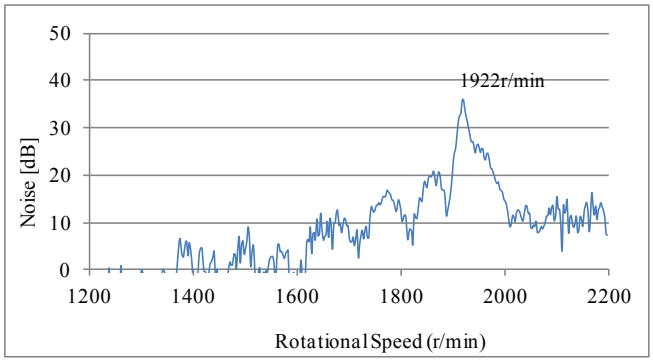

Figure 8: Noise level of the 32nd electromagnetic force

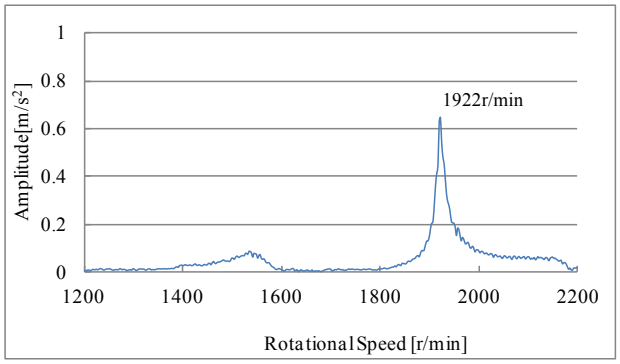

Figure 9: Vibration amplitude by the 32nd electromagnetic force

4. Calculation

Structural vibration analysis of the fan motor was carried out , and main vibration modes were investigated. Fig.10 shows the mode in which each blade vibrates in- phase in the axial

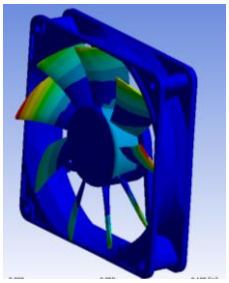

Figure 10: Natural frequency mode at 556Hz by simulation

direction. This vibration mode is equivalent to the experimentally observed mode at 530Hz (Fig. 4). The difference between the analytical results and experimental results of natural frequency were less than 5%, and were comparable each other.

5. Conclusion

The vibration and noise characteristic caused by the harmonic components of electromagnetic dynamics, fluid dynamics and structure's natural frequency were investigated for the phenomenon occurring small fan motor. From this study, following conclusions can be described:.

（1） The noises of the fan motor caused by the blade-passing force and the electromagnetic force were prominent. Intense peaks were present at frequencies at which both the blade-passing force and the electromagnetic force have their harmonic components.

(2) The significant vibration and noise was occurred not by the fluid dynamics but by the electromagnetic dynamics, and moreover occurred in the axial direction.

References

[1] K.Shiohata, Dong-Wei, Li, st al.:" Meted for Analyzing Electromagnetic-Force-Induced Noise From a Motor And Its Application", Proc. APVC Conf., Vol, Ⅱ,2001.

[2] T. Kobayashi, F.Tajima, F., M. Ito, S.Shibukawa, Effect of Slot Combination on Acoustic Noise from Induction Motors, IEEE TRANSACTION ON MAGNETICS, Vol.33. No.2, pp.2032-2035, 1993.

[3] D.Verdyck, R.Eimans, W.Geysen, An approach to Modeling of Magnetically an Excited Forces in Electrical Machines, IEEE TRANSACTION ON MAGNETICS, Vol.29. No.2, pp.2032-2035, 1993.

[4] D.verdyck,Ronnie J.M.Belmans:"An Acoustic Model for a Permanent Magnet Machine:Modal Shapes and Magnetic Force",IEEE TRANSACTION ON INDUSTRY APPLICATIONS, VOL.30,NO.6,1994

Tuning Optical Nonlinearity in Epoxy plates

Erik S. Lotfi[1,a], Kazem Jamshidi-Ghaleh[2,3,b] , and Hossein Masalehdan[2,4,5,c]

[1] College of Arts & Sciences, Department of Chemistry & Earth Sciences, Qatar University, Duha, Qatar 2713
[2] Department of Physics, Azarbaijan Shahid Madani University, Tabriz, Iran 51665-163
[3] Science and Research Group of Processing and Communication, Azarbaijan Shahid Madani University, Tabriz, Iran
[4] Optics & Laser Group, Department of Engineering Physics, Islamic Azad University, Bonab Branch, Iran 55518/134
[5] Young Research Club, Islamic Azad University, Bonab Branch, Iran 55518/134.
[a.] elotfi@qu.edu.qa
[b.] k-jamshidi@azaruniv.edu
[c.] masalehdan@azaruniv.edu

Abstract- In this paper we presented open and closed-aperture Z-Scan method investigating 1 and 2 mm thickness optical epoxy plate nonlinear optical responses. The samples heated up to 175 °C and the saturable absorption (SA) and two-photon absorption (TPA) processes reviewed. Since 2groups of the samples showed SA behavior for low intensity laser pulses then these plates promising candidate for saturable absorption devices. At the same excitation condition, the plates heated up to 90°C showed better SA response than the other samples.

Keywords: Optical Epoxy ; Saturable absorption ; Z-Scan method ; He:Ne laser

The Second-Harmonic Generation in a Dissipative and Dispersion Layered Structure

Erik S. Lotfi[1,a], Kazem Jamshidi-Ghaleh[2,4,b] , Afshin Arghand-Hesar[2], Jamshid Soltanmohammadi[3] and Hossein Masalehdan[2,3,5,c]

[1] College of Arts & Sciences, Department of Chemistry & Earth Sciences, Qatar University, Duha, Qatar 2713

[2] Department of Physics, Azarbaijan Shahid Madani University, Tabriz, Iran 51665-163

[3] Optics & Laser Group, Department of Engineering Physics, Islamic Azad University, Bonab Branch, Iran 55518/134

[4] Science and Research Group of Processing and Communication, Azarbaijan Shahid Madani University, Tabriz, Iran

[5] Young Research Club, Islamic Azad University, Bonab Branch, Iran 55518/134.

[a.] elotfi@qu.edu.qa

[b.] k-jamshidi@azaruniv.edu

[c.] masalehdan@azaruniv.edu

Abstract- The conversion efficiency of the fundamental radiation to the second harmonic wave is investigated under different linear absorptions of the interactive waves in a layered structure. We have considered that both the fundamental and the generated second harmonic waves are arbitrarily absorbed in each layer without any relation between them that has been considered on the previous studies. The layers of the structure are assumed to have different linear and nonlinear optical absorptions. The intensity-constant approximation on fundamental wave radiation is applied in the calculations. The behavior of the conversion efficiency after each layer, up to third layer, is graphically illustrated. Our results show that, as the linear losses increase, the conversion efficiency drops considerably.

Keywords*:* second harmonic generation, conversion efficiency, linear absorption, layered structure

1. Introduction

Frequency up-conversion processes have many applications in spectroscopy, optical communications, coherence measurements, etc. On the other hand, Periodic layered media such as one-dimensional multilayer photonic crystal structures are increasingly finding more applications in a wide range of telecommunications equipment due to their design flexibility [1-4]. In the nonlinear regime, periodic structures are also more engineering applications [5,6]. By adding an additional periodicity to a bulk crystal, it is possible to significantly alter its linear and nonlinear optical properties over a narrow wavelength range. In many different areas of nonlinear optics, ranging from second harmonic generation to supercontinuum generation [7], the main problem is the phase matching problem. On the harmonic conversion process in a bulk medium, under phase miss matching condition, because of the spatial biting between different frequencies, the complete conversion of the fundamental wave to the second harmonic is not possible. As the phase miss matching increases, the spatial

frequency increases and leads to a decrease on intensity of the generated second harmonic wave [8]. To overcome this problem, it is necessary to increase the length of the nonlinear medium. However, increasing of the medium length will be accompanied with occurrence of some phenomena such as inverse pumping from generated second harmonic wave to the fundamental radiation that decreases the conversion efficiency. In order to avoid this problem, instead of a homogenous nonlinear medium, a layered nonlinear medium with a suitable arrangement to compensating of the phase alteration is proposed [9,10]. This can be done with changing the sign of the phase miss matching of the interacting waves when passing from one layer to another one [11].

The process of second harmonic generation and other nonlinear phenomena are experimentally and theoretically investigated in the layered structures [12-16]. On the formulations, in some of those studies, the linear absorptions of fundamental radiation and second harmonic wave are also included. However, at the end when they are presenting their simulation results, the absorption coefficients are set to be zero. Meanwhile, the linearly decreasing of both, fundamental and generated harmonic waves can be an important parameter in practical results. On the previous studies [16], the linear absorption of the generated second harmonic wave have been considered twice that of the linear absorption of fundamental wave, i. e. ($\alpha_2(2\omega) = 2\alpha_1(\omega)$). This condition will be granted if the medium displays linear dispersion. But the material used to frequency conversion (nonlinear materials) has a more complicate dispersion relation, especially, near the resonance transition where maximum energy conversion occurs. In this work, we follow the formalisms that are presented by A.Z. Tagiov et al who clearly illustrated the effects of different linear absorptions on conversion efficiency layer to layer (i.e. after each layer). We have used the intensity constant approximation [15-17] in fundamental wave. In this approximation, the coherence length depends not only on the mismatch, but also on the so-called nonlinear length, i.e., on the nonlinearity parameters and the amplitude of the fundamental radiation [17]. The results are showing that the conversion efficiency can be significantly limited by the linear absorption at the fundamental radiation and the second harmonic wavelength.

2. Theoretical Model and Mathematical formulas

Here we consider the case where the periodic structure itself is inherently nonlinear. The medium that is considered to analyses the conversion efficiency of the fundamental harmonic to the SH is consisting of a structure with n layers, as depicted in Fig. 1. On each layer, deviation of the phases and linear absorptions of all interacting waves are considered. Different colors, in Fig. 1, indicate that for different layers the linear and nonlinear absorption coefficients and also other optical parameters can be different. The arrows show the fundamental and the generated second harmonic waves.

The subsequent layers consist from the nonlinear materials that can be had same or different linear and nonlinear optical materials. In order to analyses the phenomena, the reduced coupled equations, showing the second harmonic generation, should be independently considered in each layer. The boundary conditions for each layer

are based on the boundary conditions from the previous layer. In other words, the output waves from each layer determine the initial parameters for the next layer. The standard equations for the coupled complex amplitudes of the fundamental and generated second harmonic waves, inside the j[th] layer, in the approximation of slow varying amplitudes with considering of the losses are given by

$$\frac{dA_{1j}}{dz} + \alpha_{1j} A_{1j} = -i\gamma_{1j} A_{2j} A_{1j}^{*} \exp[-i\Delta_j z] \tag{1}$$

$$\frac{dA_{2j}}{dz} + \alpha_{2j} A_{2j} = -i\gamma_{2j} A_{1j}^{2} \exp[-i\Delta_j z], \tag{2}$$

where, A_{1j} and A_{2j} are complex amplitudes of the fundamental (pump) and second harmonic waves, α_{1j}, α_{2j}, γ_{1j}, γ_{2j} are the corresponding linear absorption coefficients and nonlinear coupling coefficients of interacting waves at the frequencies of $\omega_1 = \omega$ and $\omega_2 = 2\omega$, respectively, in j[th] layer. $\Delta_j = k_{2j} - 2k_{1j}$ is the phase mismatching between the interacting waves, k_{2j} and k_{1j} are modulus of the corresponding wave vectors. Differentiating of equation (2) with respect to z and then using of (1), the equation for A_{2j} can be rewritten as

$$\frac{d^2 A_{2j}}{dz^2} + (2\alpha_{1j} + \alpha_{2j} - i\Delta_j)\frac{dA_{2j}}{dz} A_{2j} + (2\alpha_{1j}\alpha_{2j} - i\Delta_j\alpha_{2j} + 2\gamma_{1j}\gamma_{2j} I_0) A_{2j} = 0 . \tag{3}$$

Assuming that in the iterance of the first layer ($z=0$) there is only the fundamental wave, that is; $A_{11}(z=0) = A_{10}\exp[i\varphi_{10}]$ and $A_{21}(0) = 0$, where φ_{10} is the initial phase of the fundamental wave at the input of the medium. Under those initial conditions and applying them to the equation (2), we obtain $dA_{21}/dz = -i\gamma_{21}A_{11}^2(0)$. By using of the initial values and constant intensity approximation for the fundamental radiation, i.e. $I_1(z) = I_1(0) = I_{10} = |A_0|^2 = I_0$, the solution of equation (3) at the outlet of first layer ($z = d_1$) with assumption that $\alpha_{21} = 2\alpha_{11}$ and it is given by

$$A_2(d_1) = -i\beta_{21}A_1^2(0)d_1 \sin c(\Omega_1 d_1)\exp[(2\varphi_{10} - \alpha_{21} + \frac{i\Delta_1}{2})d_1] . \tag{4}$$

The corresponding intensity would be as

$$I_2(d_1) = I_0^2 \gamma_{21}{}^2 d_1{}^2 \sin c^2(\Omega_1 d_1) \exp[-2\alpha_{21} d_1], \tag{5}$$

and conversion efficiency from the first layer is given by

$$\eta(d_1) = \frac{I_2(d_1)}{I_0^2} = \gamma_{21}{}^2 d_1{}^2 \sin c^2(\Omega_1 d_1) \exp[-2\alpha_{21} d_1] \tag{6}$$

here we have introduced $\Omega_1^2 = 2\Gamma_1^2 + \Delta_1^2/4$, $\Gamma_1^2 = \gamma_{11}\gamma_{21} I_0$ and $\sin cx = \sin x / x$.

With the same manner, the second harmonic wave generated from the second layer, by considering of the related optical parameters and again using of $\alpha_{22} = 2\alpha_{12}$ assumption (we remember that in general linear absorption coefficients can be different from corresponding parameters on the first layer), would be as follow;

$$A_{22}(d_2) = A_{21}(d_1) e^{[-\alpha_{22} d_2 + \frac{i\Delta_2 d_2}{2}]} [\cos(\Omega_2 d_2) - i(\frac{\gamma_{22} A_{11}^2(d_1) e^{[i(2\varphi_{11} - \varphi_{21})]}}{A_2 1(d_1)} + \frac{\Delta_2}{2})] \frac{\sin(\Omega_2 d_2)}{\Omega_2}] \tag{7}$$

here, $\Omega_2^2 = 2\Gamma_2^2 + \Delta^2/4$ and $\Gamma_2^2 = \gamma_{22}\gamma_{12} I_1(d_1)$, are the corresponding parameters of the second layer. The boundary conditions at the entrance to the second layer are used as; $A_{12}(z'=0) = A_{11}(d_1)\exp[i\varphi_{11}]$ and $A_{22}(z'=0) = A_{21}(d_1)\exp[i\varphi_{21}]$, where, φ_{11} and φ_{21} are the propagation phases at the entrance of the second layer at frequencies ω_1 and ω_2, respectively, and z' is equal to the first layer thickness plus additional free-space distance between first and second layer. From equation (6), the intensity of second harmonic wave at the end of second layer is given by:

$$I_2(d_2) = I_2(d_1) e^{-2\alpha_{22} d_2} [\cos^2(\Omega_2 d_2) + | \frac{\gamma_{22} A_{11}^2(d_1) e^{i(2\varphi_{11} - \varphi_{21})}}{A_{21}(d_1)} + \frac{\Delta_2}{2} |^2 \frac{\sin^2(\Omega_2 d_2)}{\Omega_2{}^2}]$$

Analogously, by the same procedure, the complex amplitude of second harmonic wave at the outlet of last layer (n^{th}) is obtained:

$$A_{2n}(d_n) = A_{2(n-1)}(d_{n-1})e^{[-\alpha_{2n}d_n + \frac{i\Delta_n d_n}{2}]}[\cos(\Omega_n d_n) - i(\frac{\gamma_{2n}A^2_{1(n-1)}(d_{n-1})e^{[i(2\varphi_{1(n-1)} - \varphi_{2(n-1)})]}}{A_{2(n-1)}(d_{n-1})} + \frac{\Delta_n}{2})\frac{\sin(\Omega_n d_n)}{\Omega_n}] \quad (8)$$

Here, again, it is assumed that $\alpha_{2n} = 2\alpha_{1n}$. Equation (8) will give the conversion efficiency of the fundamental wave to the second harmonic as the following;

$$\eta_2(d_n) = \eta_2(d_{n-1})[(\cos(\Omega_n d_n) + c_a\gamma_{2n}\frac{\sin(\Omega_n d_n)}{\Omega_n})^2 + (c_b\gamma_{2n}\frac{A_1^2(d_{n-1})}{A_2(d_{n-1})} + \frac{\Delta_n}{2})^2 \times \frac{\sin^2(\Omega_n d_n)}{\Omega_n{}^2}]\exp[-2\alpha_{2n}d_n] \quad (9)$$

In the last two equations (6) and (7), Γ_n and Ω_n are defined as: $\Gamma_n^2 = \gamma_{2n}\gamma_{1n}I_1(d_{n-1})$ and $\Omega_n^2 = 2\Gamma_n^2 + \Delta_n{}^2/4$, respectively, and c_a, c_b are constants that depend on the linear absorption coefficients α_{1n} and α_{2n}, nonlinear interaction parameters γ_{1n} and γ_{2n}, and the intensities of the interacting waves that their expressions are not shown owing to their bulkiness

3. Results and Conclusions

Figure 2, shows the conversion efficiency of the fundamental radiation to the second harmonic wave, after the first layer for two different length of d_1 =1cm (Fig. 2a) and d_1 = 5cm (Fig. 2b). On each figure, the curves 1-4 are plotted for various linear absorption coefficients of 0 cm^{-1} (curve 1), 0.01 cm^{-1}(curve 2), 0.05 cm^{-1} (curve 3) and 0.09 cm^{-1} (curve 4) respectively. It can be seen easily that in the absence of absorption (curves 1 in Fig. 2(a) and 2(b)) the conversion efficiency is same for both lengths of 1cm and 5cm. But considering of loss for the medium, at thicker sample, with increasing of the absorption coefficient, the conversion efficiency is decreased considerably (see curves 4). This result was predictable, because thicker sample absorbs more energy of the fundamental wave and the conversion efficiency will be decreased.

Now, we consider the conversion efficiency from two successive layers with thickness of d_1 and d_2. Figure 3(a)-3(d), shows the results for layer thickness of d_1=1cm, d_2=1cm (a), d_1=5cm, d_2=1cm (b), d_1=1cm, d_2=5cm (c) and d_1=5cm, d_2=5cm (d). On each figure, curves 1-3 are plotted for various linear absorption coefficients of

$\alpha_{21} = \alpha_{22} = 0\ cm^{-1}$(curve1), $\alpha_{21} = \alpha_{22} = 0.01 cm^{-1}$ (curve 2) and $\alpha_{21} = \alpha_{22} = 0.09 cm^{-1}$ (curve 3), respectively.

We have used the initial condition of $\alpha_{21} = 2\alpha_{11}$, $\alpha_{22} = 2\alpha_{12}$, $\gamma_{11} = \gamma_{21}$ and $\gamma_{12} = \gamma_{22}$. Other parameters are the same as the Fig. 2.

The same method can be extended to the n^{th} layer and the conversion efficiency can be obtained with respect to the various parameters of the layers. In order to extend our work, we have shown the results conversion efficiency up to third layer in figure 4.

4. Conclusion

The conversion efficiency of the fundamental radiation to the second harmonic wave in a layered structure was investigated under intensity constant approximation of the fundamental wave. The effect of arbitrary absorptions of the interacting waves on conversion efficiency was graphically illustrated, that is, it was assumed that both of the fundamental and generated second harmonic waves are linearly absorbed in each layer with different linear absorption coefficients. The behavior of the conversion efficiency after each layer, up to third layer, was graphically illustrated. The results were shown that, as the linear losses of the fundamental and second harmonic waves increase, the conversion efficiency drops considerably.

References

[1] B. Suthar, V. Kumar, Kh S. Singh, and A. Bhargava. "Tuning of photonic band gaps in one dimensional chalcogenide based photonic crystal." *Opt. Commun.* 285, 6, 1505-1509 (2012)

[2] J. D. Joannopoulos, S. G. Johnson, J. N. Winn, and R. D. Meade. *Photonic crystals: molding the flow of light*. Princeton university press (2011)

[3] E. Lotfi, K. Jamshidi-Ghaleh, F. Moslemi, and H. Masalehdan. "Optical multistability in 1D photonic crystals with nonlinear Thue–Morse structure."*Appl. Phys. A.* 103, 3, 669-672 (2011)

[4] Y. Ohtera, H. Ohkubo, K. Miura, T. Sato, T. Kawashima, and Sh. Kawakami. "Waveguide and guided-wave devices consisting of heterostructured photonic crystals." *Opt. eng.* 43, 5, 1022-1029 (2004)

[5] R. K. Narisetti, M. Ruzzene, and M. J. Leamy. "Study of wave propagation in strongly nonlinear periodic lattices using a harmonic balance approach." *Wave Motion* 49, 2, 394-410 (2012)

[6] M. Scalora, M. J. Bloemer, A. S. Manka, J. P. Dowling, C. M. Bowden, R. Viswanathan, and J. W. Haus. "Pulsed second-harmonic generation in nonlinear, one-dimensional, periodic structures." *Phys. Rev. A.* 56, 4, 3166 (1997)

[7] B. K. Canfield, H. Husu, J. Laukkanen, B. Bai, M. Kuittinen, J. Turunen, and M. Kauranen. "Local field asymmetry drives second-harmonic generation in noncentrosymmetric nanodimers." *Nano lett.*, 7, 5, 1251-1255 (2007)

[8] Z. H. Tagiev, and R. J. Kasumova. "Phase effects at second harmonic generation of powerful laser radiation in noncentrosymmetrical media." *Opt. commun.* 268, 2, 311-316 (2006)

[9] N. Blombergen, *Nonlinear Optics*, (W.A. Benjamin, 1955)

[10] V. D. Volosov and A. G. Kalintsev, “Degenerate parametric processes at three wave interactions in consecutively arranged crystals”, *Tech. Phys. Lett.* **2**, 85–90 (1976)

[11] A. S. Chirkin and D. B. Yusupov, “Quasi-synchrone parametric interactions of optical waves at equality of group velocities”, *Quantum Elektron.* (Moscow) **9**, 1625–1628 (1982)

[12] M. Scalora, M. J. Bloemer, A. S. Manka, J. P. Dowling, C. M. Bowden, R. Viswanathan, and J. W. Haus. "Pulsed second-harmonic generation in nonlinear, one-dimensional, periodic structures." *Phys. Rev. A.* 56, 4, 3166 (1997)

[13] N. S. Kazak, V. K. Pavlenko, and Yu. A. Sannikov, “Peculiarities SH generation in consecutively arranged crystals at strong energy exchange”, *J. Appl. Spectrosc.* **53**, 364–370 (1990)

[14] Z. H. Tagiev, “Theory of SH generation in consecutively arranged crystals”, *J. Appl. Spectrosc.* **53,** 136–139 (1990)

[15] Z. H. Tagiev, R. J. Kasumova, R. A. Salmanova, and N. V. Kerimova. "Constant-intensity approximation in a nonlinear wave theory." *J. Opt. B.*, 3, 3, 84. 4 (2001)

[16] Z.H. Tagiev, R.J. Kasumova, G.A. Safarova and A. Karimi, " Frequency conversion to the second harmonic in different layered nonlinear media", *Appl. Opt.*, **47,** 3681-3688 (2008)

[17] V.G. Dmitriev and L.V. Tarasov, *Prikladnaya nelineinaya optika* (Applied Nonlinear Optics) (Moscow; Radio I Svyaz, 1982)

Figures Caption

Fig. 1 Schematic of the periodic structure composed of various nonlinear layers to generate the SH wave. Different colors indicate that the layers can be having different optical parameters. The arrows show the fundamental and generated SH frequencies.

Fig.2 Conversion efficiency of the fundamental radiation to the second harmonic wave, from single layer for two different length of d_1 =1cm (a) and d_1 = 5cm (b). Curves, 1-4 are plotted for linear absorption coefficients of $\alpha_{11} = 0\ cm^{-1}$, 0.01 cm^{-1}, 0.05 cm^{-1} and 0.09 cm^{-1}, respectively. Other parameters are used as: $\varphi_{10} = 0$, $\alpha_{21} = 2\alpha_{11}$, $\gamma_{11} = \gamma_{21}$ and $\Delta_1 / 2\Gamma_1 = 3$.

Fig. 3 Conversion efficiency of the fundamental wave to the SH, after the 2^{end} layer at different lengths of a: $d_1 = d_2 = 1cm$, b: $d_1 = 1cm\ d_2 = 5cm$, c: $d_1 = 5cm\ d_2 = 1cm$ and d: $d_1 = d_2 = 5cm$. On each figure, curves 1-5 are plotted for various linear absorption coefficients of $\alpha_{21} = \alpha_{22} = 0\ cm^{-1}$(1), $\alpha_{21} = \alpha_{22} = 0.01cm^{-1}$ (2), $\alpha_{21} = 0.01\ \ \alpha_{22} = 0.09cm^{-1}$, $\alpha_{21} = 0.09\ \ \alpha_{22} = 0.01cm^{-1}$, $2\varphi_{11} - \varphi_{21} = 2\pi$ and $\alpha_{21} = \alpha_{22} = 0.09cm^{-1}$(5), respectively. The phase miss matching factors are $\Delta_1 / 2\Gamma_1 = -\Delta_2 / 2\Gamma_1 = 3$.

Fig. 4 Behaviour of the conversion efficiency, after 3rd layer at some selected layer thickness of (a): $d_1 = d_2 = 1cm$, (b): $d_1 = 1cm\ d_2 = 5cm$, (c): $d_1 = 5cm\ d_2 = 1cm$ and (d): $d_1 = d_2 = 5cm$. Same as the figure 3, here curves 1-5 are also plotted for different values of the linear absorption coefficients of $\alpha_{21} = \alpha_{22} = 0\ cm^{-1}$, $\alpha_{21} = \alpha_{22} = 0.01cm^{-1}$, $\alpha_{21} = 0.01\ \ \alpha_{22} = 0.09cm^{-1}$, $\alpha_{21} = 0.09\ \ \alpha_{22} = 0.01cm^{-1}$ and $\alpha_{21} = \alpha_{22} = 0.09cm^{-1}$, respectively. The relative phase miss match factors are set to be $\Delta_1 / 2\Gamma = -\Delta_2 / 2\Gamma = \Delta_3 / 2\Gamma_1 = 3$.

Figures

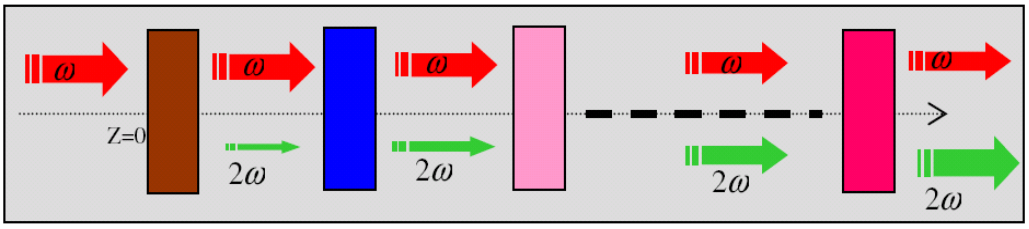

Fig. 1

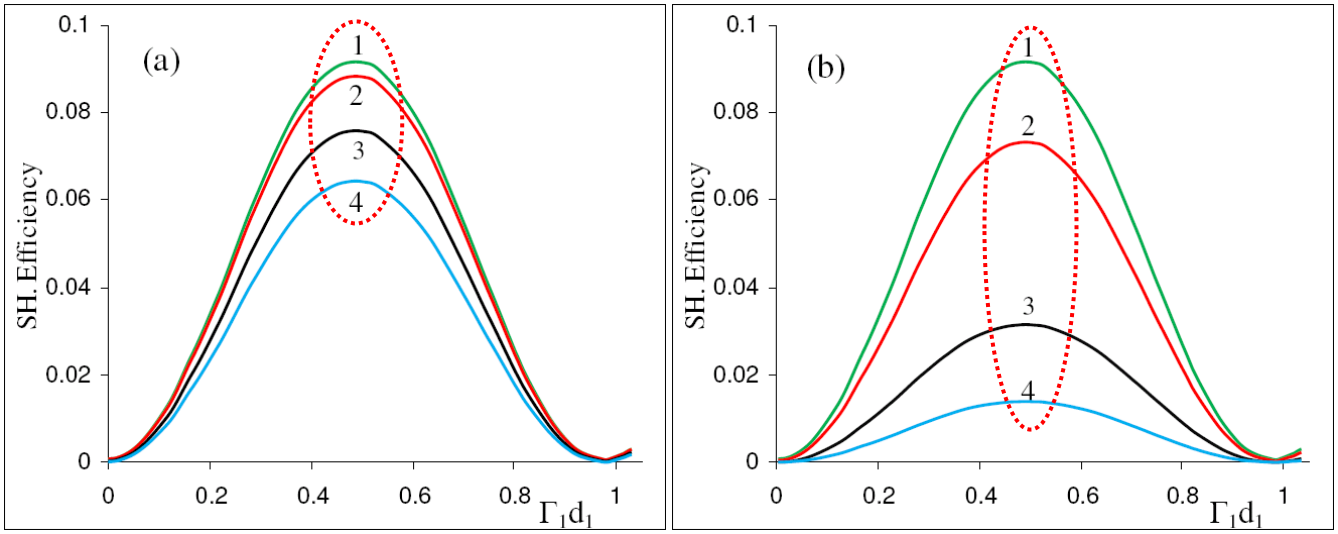

Fig. 2. a and b

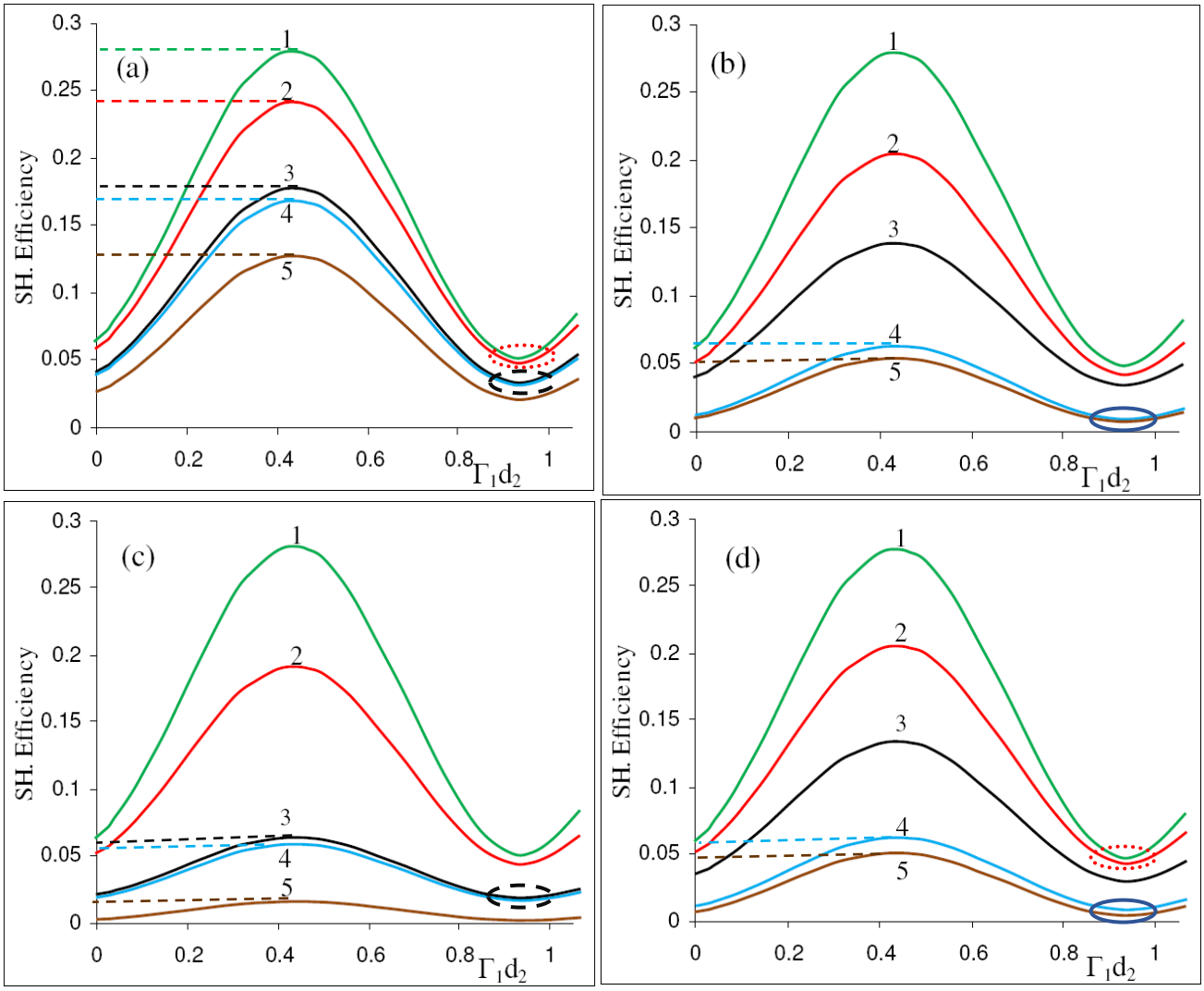

Fig. 3. a, b, c and d.

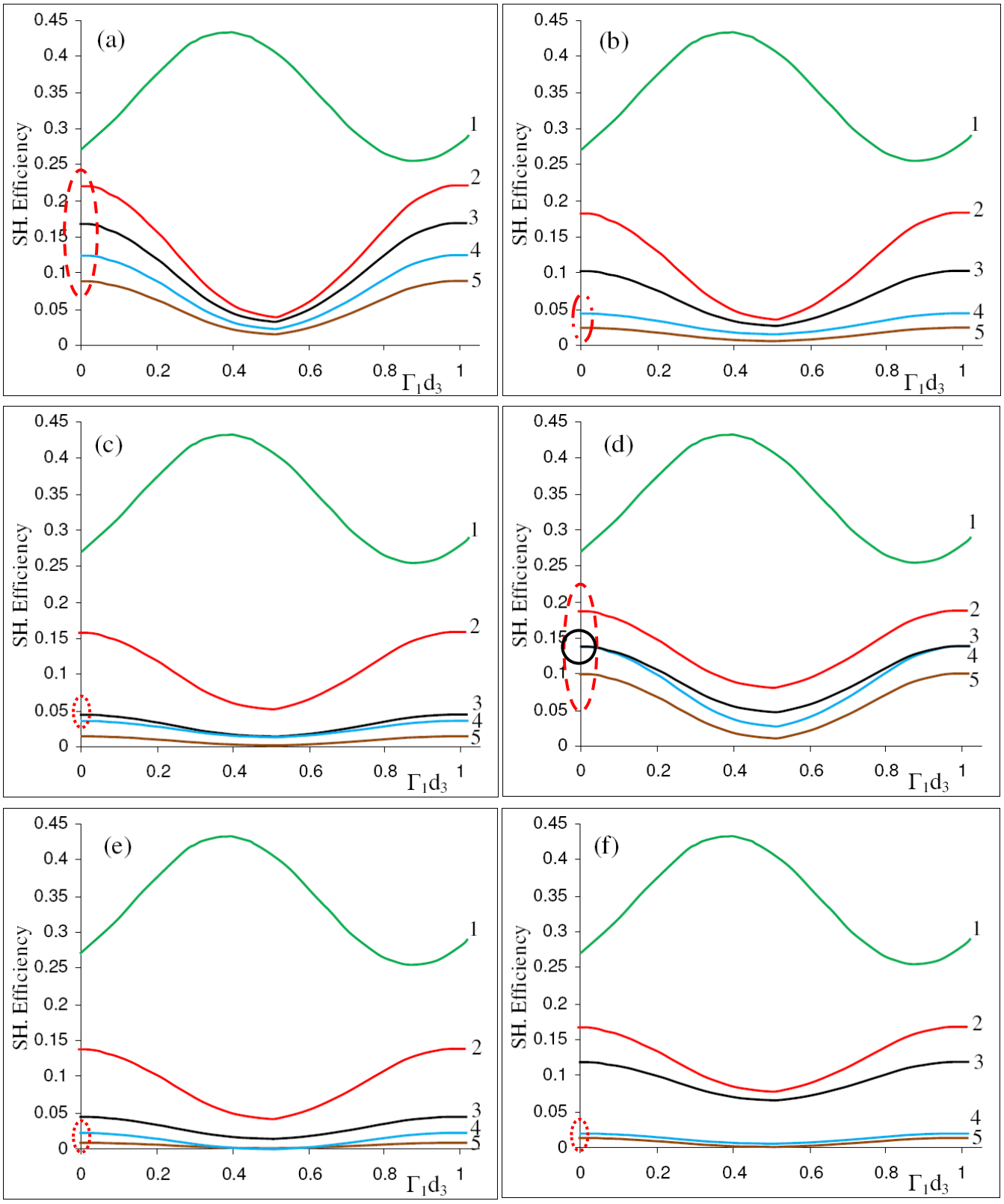
(a)
(b)
(c)
(d)
(e)
(f)
SH. Efficiency
$\Gamma_1 d_3$
0.45
0.4
0.35
0.3
0.25
0.2
0.15
0.1
0.05
0
0.2
0.4
0.6
0.8
1
1
2
3
4
5

Fig. 4. a, b, c, d, e and f.